

Selectivity in Catalysis

A C S S Y M P O S I U M S E R I E S **517**

Selectivity in Catalysis

Mark E. Davis, EDITOR
California Institute of Technology

Steven L. Suib, EDITOR
University of Connecticut

Developed from a symposium sponsored
by the Catalysis and Surface Science Secretariat
at the Fourth Chemical Congress of North America
(202nd National Meeting of the American Chemical Society),
New York, New York,
August 25–30, 1991



American Chemical Society, Washington, DC 1993



Library of Congress Cataloging-in-Publication Data

Selectivity in catalysis / Mark E. Davis, editor, Steven L. Suib, editor.

p. cm.—(ACS symposium series, ISSN 0097-6156; 517)

“Developed from a symposium sponsored by the Catalysis and Surface Science Secretariat at the Fourth Chemical Congress of North America (202nd National Meeting of the American Chemical Society), New York, New York, August 25–30, 1991.”

Includes bibliographical references and indexes.

ISBN 0-8412-2519-2

1. Catalysis—Congresses.

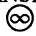
I. Davis, Mark E. II. Suib, Steven L., 1953- . III. American Chemical Society. Catalysis and Surface Science Secretariat. IV. Chemical Congress of North America (4th: 1991: New York, N.Y.). V. American Chemical Society. Meeting (202nd: 1991: New York, N.Y.). VI. Series.

QD505.S46 1993

541.3'.95—dc20

92-42872

CIP

The paper used in this publication meets the minimum requirements of American National Standard for Information Sciences—Permanence of Paper for Printed Library Materials, ANSI Z39.48-1984. 

Copyright © 1993

American Chemical Society

All Rights Reserved. The appearance of the code at the bottom of the first page of each chapter in this volume indicates the copyright owner's consent that reprographic copies of the chapter may be made for personal or internal use or for the personal or internal use of specific clients. This consent is given on the condition, however, that the copier pay the stated per-copy fee through the Copyright Clearance Center, Inc., 27 Congress Street, Salem, MA 01970, for copying beyond that permitted by Sections 107 or 108 of the U.S. Copyright Law. This consent does not extend to copying or transmission by any means—graphic or electronic—for any other purpose, such as for general distribution, for advertising or promotional purposes, for creating a new collective work, for resale, or for information storage and retrieval systems. The copying fee for each chapter is indicated in the code at the bottom of the first page of the chapter.

The citation of trade names and/or names of manufacturers in this publication is not to be construed as an endorsement or as approval by ACS of the commercial products or services referenced herein; nor should the mere reference herein to any drawing, specification, chemical process, or other data be regarded as a license or as a conveyance of any right or permission to the holder, reader, or any other person or corporation, to manufacture, reproduce, use, or sell any patented invention or copyrighted work that may in any way be related thereto. Registered names, trademarks, etc., used in this publication, even without specific indication thereof, are not to be considered unprotected by law.

PRINTED IN THE UNITED STATES OF AMERICA

**American Chemical
Society Library
1155 16th St. N. W.**

1993 Advisory Board

ACS Symposium Series

M. Joan Comstock, *Series Editor*

V. Dean Adams
Tennessee Technological
University

Robert J. Alaimo
Procter & Gamble
Pharmaceuticals, Inc.

Mark Arnold
University of Iowa

David Baker
University of Tennessee

Arindam Bose
Pfizer Central Research

Robert F. Brady, Jr.
Naval Research Laboratory

Margaret A. Cavanaugh
National Science Foundation

Dennis W. Hess
Lehigh University

Hiroshi Ito
IBM Almaden Research Center

Madeleine M. Joullie
University of Pennsylvania

Gretchen S. Kohl
Dow-Corning Corporation

Bonnie Lawlor
Institute for Scientific Information

Douglas R. Lloyd
The University of Texas at Austin

Robert McGorrin
Kraft General Foods

Julius J. Menn
Plant Sciences Institute,
U.S. Department of Agriculture

Vincent Pecoraro
University of Michigan

Marshall Phillips
Delmont Laboratories

George W. Roberts
North Carolina State University

A. Truman Schwartz
Macalaster College

John R. Shapley
University of Illinois
at Urbana-Champaign

L. Somasundaram
E. I. du Pont de Nemours and Company

Peter Willett
University of Sheffield (England)

Foreword

THE ACS SYMPOSIUM SERIES was first published in 1974 to provide a mechanism for publishing symposia quickly in book form. The purpose of this series is to publish comprehensive books developed from symposia, which are usually “snapshots in time” of the current research being done on a topic, plus some review material on the topic. For this reason, it is necessary that the papers be published as quickly as possible.

Before a symposium-based book is put under contract, the proposed table of contents is reviewed for appropriateness to the topic and for comprehensiveness of the collection. Some papers are excluded at this point, and others are added to round out the scope of the volume. In addition, a draft of each paper is peer-reviewed prior to final acceptance or rejection. This anonymous review process is supervised by the organizer(s) of the symposium, who become the editor(s) of the book. The authors then revise their papers according to the recommendations of both the reviewers and the editors, prepare camera-ready copy, and submit the final papers to the editors, who check that all necessary revisions have been made.

As a rule, only original research papers and original review papers are included in the volumes. Verbatim reproductions of previously published papers are not accepted.

M. Joan Comstock
Series Editor

Preface

AN EMPHASIS ON SELECTIVITY in this volume relates to increasing research in homogeneous catalysis and areas that bridge many fields of chemistry. The symposium on which this book is based is an outgrowth of the Catalysis and Surface Science Secretariat of the American Chemical Society and several divisions—the Divisions of Colloid and Surface Chemistry; Fuel Chemistry; Industrial and Engineering Chemistry, Inc.; Inorganic Chemistry, Inc.; Petroleum Chemistry, Inc.; and Physical Chemistry. A goal of the symposium was to assemble researchers from chemistry, chemical engineering, materials science, and related areas concerned with enhancement of selectivity in catalysis.

This book deals with four major areas of selectivity: stereoselectivity; clusters, alloys, and poisoning; shape selectivity; and reaction pathway control. An overview of the book and reviews of each of the four major areas are included as introductory chapters. Each review is followed by individual contributions by attendees of the symposium.

We thank Susan Lambert, secretary general of the Catalysis and Surface Science Secretariat, for her efforts in organizing sponsorship of this symposium. We also thank the attendees, the authors, and the American Chemical Society.

MARK E. DAVIS
California Institute of Technology
Pasadena, CA 91125

STEVEN L. SUIB
University of Connecticut
Storrs, CT 06269–3060

September 1, 1992

Chapter 1

Selectivity in Catalysis

An Overview

Steven L. Suib

Departments of Chemistry and Chemical Engineering Institute
of Materials Science, University of Connecticut,
Storrs, CT 06269-3060

This review encompasses the general area of selectivity in catalysis as well as the four major specific areas discussed in this book; Stereoselectivity; Clusters, Alloys and Poisoning; Shape Selectivity; and Reaction Pathway Control. Examples are taken from the literature for each of these four areas of recent articles that focus on selectivity in catalytic reactions. Specific reviews of the four areas listed above can be found in the overview chapters by D. Forster and coworkers, K. J. Klabunde, M. E. Davis and coworkers; and H. C. Foley and M. Klein.

I. INTRODUCTION

This review is an overview of recent literature research articles that deal with selectivity in catalysis. Four specific areas including stereoselectivity; clusters, alloys and poisoning; shape selectivity; and reaction pathway control will be discussed. This review is not meant to be a complete discussion of these areas. It represents a small fraction of the research presently underway and a very minor fraction of the available literature in this subject. The order of topics will follow the four major areas outlined above, however, there is no particular order for the articles discussed in each section.

Selectivity in catalysis is one of the most important factors to be controlled by researchers. Selectivity can be controlled in several ways such as by structural, chemical, electronic, compositional, kinetic and energy considerations. Certain factors may be more important in homogeneous catalytic reactions rather than heterogeneous reactions and vice versa. In most cases, however, little distinction will be made regarding the control of product selectivity for these two major types of catalysts.

Selectivity in catalysis might be controlled by preparation and use of new materials such as new zincosilicate molecular sieves such as VPI-7 having 3 membered rings,¹ gallophosphate molecular sieves with 20 atom ring pore openings having cloverleaf shaped windows,² 3 ring zeolitic ZSM-18 type materials,³ clays pillared with metal oxide clusters,⁴ and perhaps soccerball shaped C₆₀, C₇₀ buckyball cage structures.⁵

Besides new materials, it may be possible to modify surfaces of existing materials to provide sites to enhance selectivity. Considerable research has been

done in the area of molecular recognition at interfaces to control both chemical and physical properties of resultant materials. Such tailor-made surfaces can be used to control crystal nucleation, polymorphism, optical birefringence and nonlinear optical properties and the structure of materials.⁶

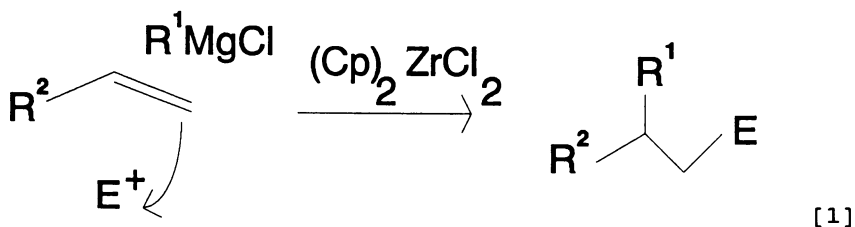
Control of pore sizes of known catalysts like zeolites has been known for some time although the use of chemical vapor deposition (CVD) of organosilanes to control pore sizes has been the focus of recent research.⁷ Other catalysts like silica have been treated with methods like CVD and sol-gel in order to deposit thin films. Monolayer coatings of titanium oxide prepared by sol-gel methods have been recently used to coat silica and such films are active in alcohol dehydrogenation reactions.⁸

Finally, new methods of analysis have recently been developed that may allow characterization of single atoms on surfaces such as atomic force microscopy.⁹ In certain cases, in situ experiments can be done such as the study of electrodes, enzymes, minerals and biomolecules. It has even been shown that one atom from a tip can be selectively placed on a desired surface.¹⁰ Such processes may one day be used to prepare catalysts that may enhance selectivity. Other methods that show promise as regards detection of surface catalytic intermediates are temperature programmed desorption techniques.¹¹ Selective poisoning of some surface intermediates with monitoring via temperature programming methods may also allow the preparation of more selective catalysts.

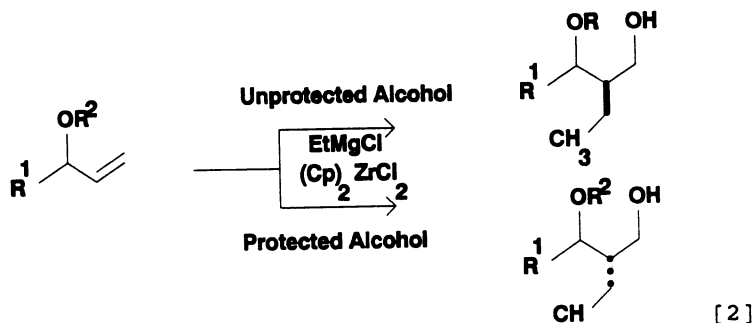
Such speculation suggests a tremendous potential for continued developments in the area of selectivity enhancement in catalysis. The remainder of this review focuses on current literature concerning selectivity in catalysis.

II. STEREOSELECTIVITY

Stereoselectivity in homogeneous catalytic reactions is well documented. Oftentimes mechanisms can be postulated regarding individual steps in contrast to heterogeneous systems. A recent detailed investigation of the stereoselective formation of C-C bonds catalyzed by $(C_5H_5)_2ZrCl_2$ has been reported by Hoveyda and Xu.¹² The initial step in these reactions is the addition of an alkyl Grignard reactant to an unactivated olefin followed by further bond formation as in Equation (Eq.) [1]:¹²



The above reactions are one pot syntheses, can be used for double alkylation or hydroxyalkylation of alkenes in good (55-65 %) yield, and with outstanding regiocontrol (> 99 %). Diastereochemical control in the formation of allylic alcohols and ethers has been shown to proceed with even better yields (up to 92 %) although the stereocontrol is somewhat decreased (95:5, highest; as low as 67:33) due to the use of THF as a solvent which can influence the stereochemistry. These studies are important since the different reaction pathways can lead to both protected and unprotected alcohols. Such pathways are shown in Eq. 2.¹²

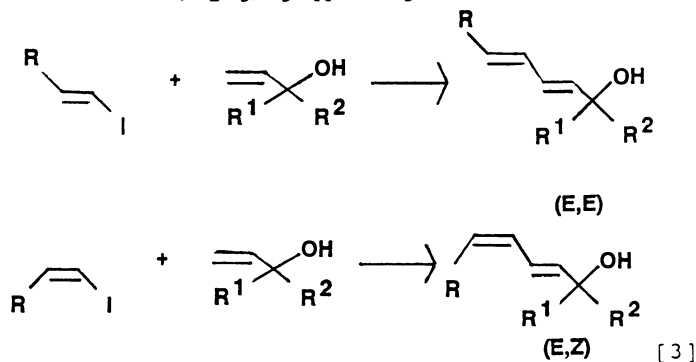


Both syn and anti carbometalation products were prepared with excellent stereochemistry in the above reactions. The role of solvent was not well studied, however, it is clear that stereocontrol is influenced in these systems by the nature of the solvent. It was suggested that a 16 electron intermediate zirconocene [(Cp)₂Zr] species is the active catalyst in such systems.

Giles and coworkers have recently reported the use of TiCl₄ in CH₂Cl₂ at -78°C for the stereoselective isomerization of naphthyl- and phenyl-dioxolanes to yield pyrans that are important in aphid pigments.¹³ Other Lewis acids besides TiCl₄ such as BF₃, SnCl₄, Ti(IsoPr)₂Cl₂ and Ti(IsoPr)₃Cl are not effective in such reactions. ¹H NMR and nuclear Overhauser effect spectroscopies were used to establish stereochemistry. Some diol side product (13 %) was also formed. The major effort in this research was to clearly identify products of the isomerization.

The preparation of highly chemo-, regio- and stereo-selective (E,E) and (E,Z) conjugated dienols important in several biological systems such as leucomycins and oxazolomycins has been reported by Jeffery.¹⁴ These homogeneous reactions were done in the presence of different silver salts and palladium acetate catalysts. These reactions were highly dependent on the nature of the solvent but also dependent on the nature of the silver salt. Silver carbonates, nitrates and acetate salts gave conjugated diols with yields from 60 to 82 % with either (E,E) or (E,Z) type double bonds. The role of the anion of the silver salt was not studied in any great detail. The process was reported to be generally useful for primary, secondary and tertiary allylic alcohols.

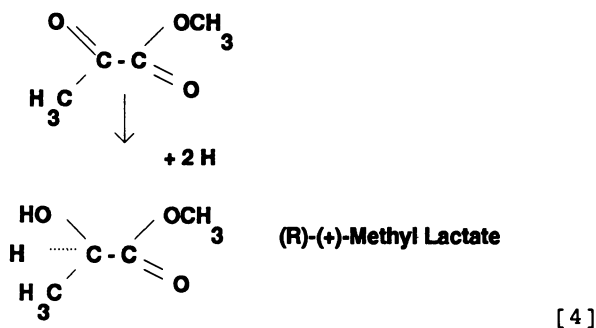
A general scheme for the formation of (E,E) and (E,Z) conjugated diols is given in Eq. 3.¹⁴ In the following scheme (Eq. 3) R = C₆H₁₃, R¹ is either H or CH₃, and R² can be H, C₂H₅, C₅H₁₁ or CH₃.



Biocatalysts such as *Candida cylindracea* lipase enzymes have recently been used in enantioselective hydrolyses of racemic esters by Fowler, Macfarlane and Roberts.¹⁵ The (R,R) diastereoisomer was the main product (91 +/- 0.5 %) as determined by NMR spectroscopic analysis of the products. These authors point out the difficulty of measuring such diastereoisomer ratios by using NMR methods, however, their results show a clear selectivity towards the (R,R) diastereoisomer.

Sutherland, Ibbotson, Moyes and Wells have published a detailed account of the heterogeneous enantioselective hydrogenation of methyl pyruvate ($\text{CH}_3\text{COCOOCH}_3$) to R-(+)-methyl lactate over Pt/silica surfaces modified by sorbed cinchona alkaloids.¹⁶ Kinetic, isotherm and molecular modeling calculations were used to develop an idea of the role of the cinchonidine modifier. This system is quite unusual; high enantioselectivity is achieved only with Pt, only in the presence of cinchonidine modifiers and only for the hydrogenation of α -ketoesters.

The order of reaction for methyl pyruvate was zero and for hydrogen was unity indicating that the ketoester is strongly adsorbed and the hydrogen is weakly adsorbed. By assuming that hydrogenation occurs via addition of two H atoms from below the plane of the adsorbed methyl pyruvate, the configuration outlined in Eq. 4¹⁶ (which generates the major product (R)-(+)-Methyl Lactate) is necessary since its mirror image leads to the formation of (S)-(-)-Methyl Lactate.



Molecular modeling studies suggested that the lowest energy configuration of sorbed cinchonidine was a structure where the two aromatic rings were parallel to the Pt surface in a close-packed array. The quinuclidine groups of cinchonidine lie above the Pt thereby leaving access for sorption of methyl pyruvate in a unique surface orientation. The authors stress the importance of using a well known catalyst/support system and have carried out several other experiments to suggest that the high enantioselectivity is limited to date to the above system.

A final example of a stereoselective heterogeneous catalytic system is the work of Laycock, Collacott, Skelton and Tchir.¹⁷ Layered double hydroxide (LDH) synthetic hydrotalcite materials were used to stereospecifically polymerize propylene oxide [PO] to crystalline isotactic and liquid atactic poly(propyleneoxide) [PPO]. These authors suggest that the LDH surface acts as other inorganic or organometallic coordination initiators or catalysts by providing specific surface orientations for propylene oxide monomer. X-ray powder diffraction showed some loss of crystallinity after calcination and X-ray photoelectron spectroscopy showed an enhancement of Mg/Al content due to restructuring of the Mg and Al surface atoms. The surface was also rich in Cl^-

(anion precursor) as well as carbonate ions which have been shown to incorporate into LDH materials during synthesis.

No characterization of the catalysts after reaction was reported. Detailed ^{13}C NMR analyses were used to identify structures in the PPO products. A mechanism involving ring opening of PO after coordination of a PO monomer to the surface of the LDH leading to discrete sterically hindered catalytic sites was invoked to explain the high stereodirecting influence of the mixed oxide catalyst.

There are clearly some interesting observations reported in the above papers¹²⁻¹⁷ that seem to pervade stereoselective reactions. First of all, the nature of the solvent in homogeneous stereoselective reactions is critical. Secondly, unique steric requirements for reactants on solid surfaces appear to lead to enhanced stereoselectivity. Thirdly, modifiers and promoters in both solution phase and solid phase catalysis appear to have marked effects on product selectivity.

III. CLUSTERS, ALLOYS AND POISONING.

Clusters and alloys are molecular species that may show different catalytic activity, selectivity and stability than bulk metals and alloys. Small metal clusters and alloy clusters have been studied recently for potential use as catalysts, ceramic precursors, and as thin films. Several fundamental questions regarding such clusters are apparent. How many atoms are needed before metallic properties are observed? How are steric and electronic properties related to the number, type and structure of such clusters? Do mixed metal clusters behave like bulk alloy phases?

A major focus of our research program has been the preparation of small ($< 5 \text{ \AA}$) Co, Fe and Fe/Co alloy clusters in zeolites.¹⁸ Catalytic reactions of cyclopropane and hydrogen over such clusters have shown that turnover frequencies are 3 orders of magnitude lower for the isomerization of cyclopropane to propylene than for bulk ($>20 \text{ \AA}$) Co particles supported on Al_2O_3 . Such clusters are selective towards propylene at temperatures of 120°C and towards propane via hydrogenation at 160°C as the cluster size grows to 10 \AA size particles. Further sintering at 180°C leads to 15 \AA particles on the surface of the zeolite as well as a shift in products to methane and ethane. Such structure sensitive reactions with rates measured as a function of particle size clearly show that Co clusters have different structural, catalytic and physical properties than bulk Co metal or large Co particles on various supports.

Another focus of this section involves the role of poisons in catalysis. In general, poisons are impurity species that decrease the selectivity towards a desired product. In the area of fluid cracking catalysis, metal poisons or contaminants in the feed deposit on the zeolite/matrix fluid cracking catalysts (FCC) and can cause severe changes in activity and selectivity. For example, we have shown that vanadium poisons decrease the activity of FCC materials almost immediately by destroying the structure of the Y zeolite portion of the FCC even at 1 ppm levels of vanadium.¹⁹ Nickel poisons on the other hand, lead to overcracking of gasoline to light gases. Several methods have been used to prevent such poisoning such as demetallization and addition of passivating agents to the catalyst.

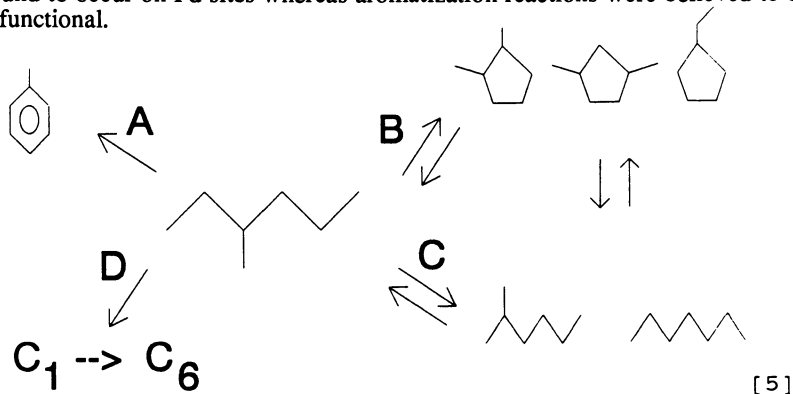
Pine has recently focused on the role of vanadium in the destruction of USY zeolite.²⁰ Kinetic studies of the reaction of vanadium and steam (used in catalyst regeneration) have been carried out for vanadium levels of 0-4000 ppm and at temperatures of 740 to 800°C . Kinetic data suggest that vanadium acts as a catalyst for the breakdown of the zeolite lattice via a solid state mechanism.

Further studies showed that vanadium also attacks silicalite implying that framework decomposition occurs via Si-O bond breakage. The rate limiting step of the destructive role of vanadium was proposed to be the attack of vanadium on surface hydroxyl groups.

Espeel, Tielens and Jacobs have recently shown that metal clusters in zeolites can be used in electron transport chain conversions of ethylene to acetaldehyde in an analogous fashion to that of homogeneous Wacker catalysts.²¹ The electron transport chain involves transfer of electrons from ethylene to the metal clusters to oxygen. Infrared, kinetic and isotope labeling studies were done that suggested an electron transfer mechanism first involving coordination of ethylene to Pd²⁺ followed by an intramolecular hydrogen transfer leading to the production of acetaldehyde. The combination of Cu²⁺ and Pd²⁺ leads to a synergistic effect with overall activity increased by a factor of 5. Advantages of such a system are the avoidance of high chloride concentrations as in homogeneous solution which leads to incorporation of Cl⁻ in products and use of solid acids rather than highly acidic solutions.

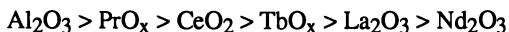
The role of iron clusters in Fischer-Tropsch catalysis has been the focus of considerable studies. Cagnoli et al. have recently studied the role of Fe clusters on silica and alumina supports for methanation.²² Chemisorption, catalysis and Mössbauer spectroscopy experiments were used to study the effect of dispersion and the role of various supports. Although several oxidation states of iron were observed, the focus of this research was on Fe clusters which were found to be on the order of 12 Å crystal size. The authors proposed that metal support interactions were greater for silica than alumina supports and that selectivity differences between these catalysts were due to differences in surface properties of silica vs. alumina. Differences in selectivity for Fe/SiO₂ catalysts at different H₂/CO ratios were attributed to differences in coadsorption of H₂ and CO. Selectivity differences are difficult to explain in such systems even when only one metal is present.

Normand et al. have studied Pd deposited on several metal oxide supports in reactions of methylcyclopropane hydrogenolysis, 3-methylhexane aromatization, and in Fischer-Tropsch catalysis.²³ Three classes of oxides were studied, those that were not reducible such as Re₂O₃, those with anion vacancies produced during reduction like CeO₂, and those with intrinsic anion vacancies such as nonstoichiometric Pr₆O₁₁ and Tb₄O₇. Hydrogenolysis reactions were found to occur on Pd sites whereas aromatization reactions were believed to be bifunctional.



Reactions of 3-methylhexane were found to occur on the support alone which complicated the above studies. Besides aromatization to toluene (A), isomerization to cyclopentane derivatives (B), isomerization to heptane and other branched hexanes (C) and cracking to C₁ to C₆ hydrocarbons (D) were all observed as depicted in Eq. 5.²³

For aromatization, the following order of decreasing activity in aromatization was observed for the supports themselves:



The Pd/Al₂O₃ system and Pd/PrO_x systems were studied in more detail than the others and kinetic and thermodynamic results suggest that the Pd/PrO_x catalysts have a much higher density of specific sites (about 1.6 times) for aromatization than on the alumina support.

Effects of additives are often difficult to unravel, perhaps because they serve more than one role in catalytic reactions. Nitta, Hiramatsu and Imanaka have suggested recently that Cl⁻ additives in the hydrogenation of cinnamaldehyde and crotonaldehyde over supported Co catalysts serve to enhance selectivity by influencing both the hydrogen reduction and hydrogenation steps in these reactions.²⁴ Crystallite sizes of cobalt are markedly influenced by the nature of the cobalt anion precursor ranging from < 40 Å for acetate precursors to 180 Å for chloride precursors as determined by X-ray line broadening experiments. The other role of Cl⁻ anions is to decrease the hydrogenation of C=C double bonds during hydrogenation of cinnamaldehyde and crotonaldehyde. Anions, mean crystallite sizes, initial selectivities and selectivities at 50 % conversion are summarized in Table I.²⁴

The above studies show that Cl⁻ anions may play several roles in enhancing the selectivity in such reactions. A maximum in both selectivity and activity was found when the Cl/Co ratio was 0.2. Studies with various supports suggested that metal support interactions were also important.

A final example of the role of additives is that of Larkins and Nordin.²⁵ Li₂CO₃ when added to MgO catalysts increases the selectivity to C₂ hydrocarbons in oxidative coupling reactions of methane as has been found by others. Catalytic, scanning electron microscopy, X-ray powder diffraction, temperature programmed reactions and electron microprobe studies have been used to show that additives of both Zn and Mn can enhance selectivity to C₂ hydrocarbons in these systems.

If Mn additives are added at too high a loading (8%) then selectivity to C₂ hydrocarbons is lowered and total oxidation prevails. Catalytic data are summarized in Table II²⁵ for such systems.

These data show that small amounts of Mn (0.1 mol %) incorporated into Li/MgO considerably enhance the selectivity to C₂ hydrocarbons. Additives of Zn also enhance the C₂ selectivity, however, not as significantly as Mn dopants.

In the absence of Li, the Mn doped materials produce a significant amount of CO and CO₂. In the absence of Li, the Zn doped materials primarily yield CO₂. As temperature is lowered from 805°C to 710°C the overall conversion is decreased as expected and it may be difficult to make valid comparisons for catalysts having significantly different conversions. Nevertheless, these data suggest that the role of additives can markedly influence selectivity as was observed in other systems noted above. The exact role of Li, Mn and Zn in these systems is not well known.

There are several features of the different systems described above for the cluster, alloy and poisoning section that are common. First of all, the structural

Table I. Effect of Anion for Hydrogenation of Cinnamaldehyde *

Anion	D _C	S _O	S ₅₀
Chloride	180	94	93
Nitrate	70	81	77
Acetate	<40	76	68
Sulfate	a	70	a

* - 0.2 M Cinnamaldehyde in C₂H₅OH, 30°C, 1 MPa H₂,
Co supported on SiO₂. a - not measured.
D_C - mean crystallite size from X-ray diffraction.
S_O - Initial selectivity to cinnamyl alcohol.
S₅₀ - Selectivity to cinnamyl alcohol at 50 % conversion.

SOURCE: Data are taken from reference 24.

Table II. Conversion and Selectivity Data for Doped Li/MgO Catalysts

Dopant (%)	p O ₂	p CH ₄	Conversion		Carbon Selectivity			
			C ₁	O ₂	C ₂	C ₂ ⁼	CO	CO ₂
Zn(0), [800]	117	219	27	49	30.3	33.8	0	35.9
Zn(2.6), [805]	107	214	22	42	32.5	33.4	0	34.1
Zn(2.6), [760]	107	214	12	18	51.1	22.7	0	26.2
Zn*(2.4), [805]	105	207	28	100	9.3	0	0	90.7
Mn(0.1), [805]	112	233	36	84	23.6	31.4	0	45.1
Mn(0.1), [760]	112	233	24	49	35.0	25.9	0	39.1
Mn(0.3), [710]	109	228	10	18	48.9	16.6	0	34.5
Mn(8.8), [805]	108	227	31	100	16.5	10.4	0	73.1
Mn*(0.1), [805]	114	218	28	100	4.6	0	14.3	81.1

Mn() - mol % metal; [] - temperature, °C; * - no Li.
p in torr, Conversion in %, Selectivity in %.
Total flow rate 25 mL/min.

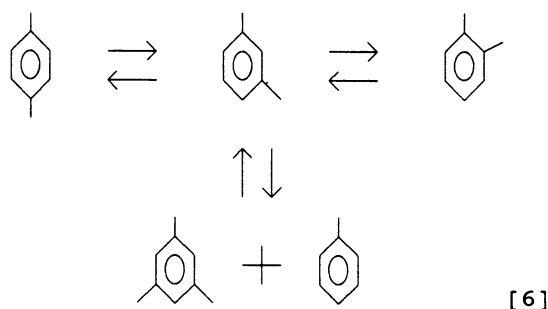
SOURCE: Data are taken from reference 25.

and electronic properties of clusters markedly influence selectivity of a variety of reactions. Secondly, the role of the support is critical; metal support interactions were invoked in practically all of these studies to explain differences in selectivity and activity. Thirdly, the role of additives and poisons provides several mechanisms for enhancing selectivity in catalytic reactions including the control of metal particle size, the control of reaction pathways, control of local electronic properties and other factors.

IV. SHAPE SELECTIVITY

Shape selective reactions are typically carried out over zeolites, molecular sieves and other porous materials. There are three major classifications of shape selectivity including (1) reactant shape selectivity where reactants of sizes less than the pore size of the support are allowed to enter the pores to react over active sites, (2) product shape selectivity where products of sizes smaller than the pore dimensions can leave the catalyst and (3) transition state shape selectivity where sizes of pores can influence the types of transition states that may form. Other materials like porphyrins, vesicles, micelles, cryptands and cage complexes have been shown to control product selectivities by shape selective processes.

Catalytic isomerizations of ethylbenzenes and xylenes over zeolites are commercial processes and have been used as test reactions of acid catalysts. Corma and Sastre²⁶ have recently suggested that xylenes can form via transalkylation of trimethylbenzene which is believed to be an intermediate in the isomerization of p-xylene. A general scheme as that shown in Eq. 6²⁶ was proposed on the basis of kinetic and mass spectrometric data. The reactant p-xylene was believed to produce m-xylene as a primary product but also rearranges in the pores of ultrastable faujasite zeolites to form o-xylene which appears as a primary product. In addition, trimethylbenzenes were formed along with toluene.



Further isomerization of m-xylene as well as transalkylation of trimethylbenzene and toluene to form m-xylene can occur. Evidence for the bimolecular transalkylation mechanism was provided by observation of a peak at m/e 109 in the mass spectra for CD_3 substitution of toluene. These data rule out unimolecular 1,2-methyl shifts as the sole means of formation of xylenes. The higher the Al content of the ultrastable faujasite the greater the extent of bimolecular transalkylation. These observations have significant implications for unimolecular kinetic models that have been proposed as well as reported activation energies and turnover frequencies.

Disproportionation of 2-methylnaphthalene over ZSM-5 zeolite to dimethylnaphthalenes (DMN) has recently been reported to be shape selective by

Matsuda, Yogo, Mogi and Kikuchi.²⁷ ZSM-5 and ZSM-5 dealuminated with $(\text{NH}_4)_2\text{SiF}_6$ were used as catalysts in these reactions. ZSM-5 gave rise to several DMN isomers in contrast to selective formation of the 2,6 and 2,7 DMN isomers over dealuminated ZSM-5 as shown in Figure 1 (After 27).²⁷

The authors suggest that isomerization reactions occur predominantly on external surface sites of ZSM-5 and by using dealumination procedures that such sites are rendered inactive. Selectivities of 2,6-DMN and 2,7-DMN increased from 23.4 and 24.9 % before dealumination to 39.9 and 60 % after dealumination, respectively. The disproportionation reaction was proposed to occur in the pores of the zeolite.

Lafyatis and Foley have developed molecular models for studying shape selectivity in Fischer-Tropsch reactions using a trifunctional catalyst system.²⁸ A classical Fischer Tropsch catalyst for converting CO and H₂ to water and CH₂ was combined with a hydrogenolysis catalyst to promote cracking and with a carbon molecular sieve to impart shape selectivity. A structure of such trifunctional catalysts is given in Figure 2 (After 28).²⁸ Analyses of catalytic data led to the conclusion that a non-Schulz-Flory distribution of hydrocarbons was observed with high selectivity to light hydrocarbons. A diffusional model was proposed for these systems that helped explain the shape selectivity of these systems.

A final example of shape selective catalysis is the selective hydrogenation of alkynes, alkenes and other hydrocarbons over Pd complexes anchored to montmorillonite clay supports.²⁹ In these studies, phosphines and amine ligands were first reacted with montmorillonite and then reacted with palladium (II) salts to form anchored Pd(II) complexes in the interlamellar spacings of the montmorillonite clay.

Styrene and 1-hexene have been selectively hydrogenated as well as substituted acetylenes, alkyne diols, stilbene and other unsaturated hydrocarbons with these palladium montmorillonites. A size selectivity was invoked to explain the enhanced hydrogenation activity of certain clay catalysts presumably due to the differences in interlamellar spacings of the clay which will depend on degree of hydration, concentration of Pd(II) complex, dielectric constant of the solvent used to disperse the reactants and other factors.

The catalysts were characterized with infrared, X-ray photoelectron spectroscopy, NMR, and X-ray powder diffraction to determine the Pd content, nature of coordinated and uncoordinated ligands, oxidation states (both Pd²⁺ and Pd³⁺ were observed) of Pd complexes and the symmetry of Pd complexes. Metal leaching was prevented by using an excess of phosphine ligand. A preferential hydrogenation of alkynes was noted, especially for complexes with smaller (14.2 Å) interlamellar spacings vs. 18.3 Å for the larger spacings.

The above examples of shape selective reactions show the complexity of such systems and that several factors need to be considered before shape selective control can be realized. The use of other porous supports besides zeolites such as carbon molecular sieves, clays, pillared clays and related materials to catalyze shape selective reactions appears to be growing. Molecular modeling of the spatial constraints of various pores is also an area of increased research effort.

V. REACTION PATHWAY CONTROL

Reaction pathway control is a general term implying that reactions can occur by more than one path. Use of specific paths might be governed by a variety of phenomena which may be different for each different reaction. For example, thermal reactions may have entirely different pathways than photochemical, electrochemical, sonochemical and other systems. Electron

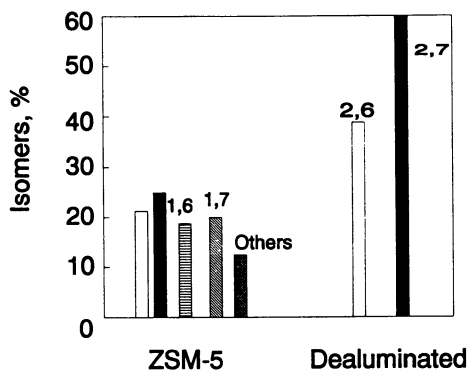


Figure 1. Dimethylnaphthylene Isomers Produced over ZSM-5 and Dealuminated ZSM-5.

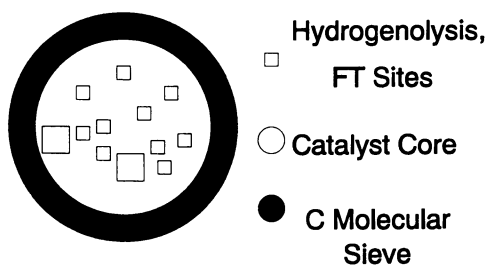


Figure 2 Model of Trifunctional Catalyst System.

transfer rates may control a pathway. A variety of structures and sites may be available that can be selectively populated in order to control selectivity. Finally, specific types of materials like membranes, films, wires and meshes may afford pathways not accessible with more typical supported metal or solid acid catalysts.

Homogeneous reactions such as the isomerization of triphenylformazanes and olefin hydrogenation by Rh(I) complexes have also been described with this compensation effect model where the solvent cage molecules around the homogeneous catalyst act like the support and surroundings of a heterogeneous catalyst.

Oxidation reactions have been the focus of several researchers in recent years. Several pathways are available for the activation of methane with two predominant ones being partial oxidation via oxidative coupling and the other being formation of oxygenates. Sojka, Herman and Klier have recently reported that formaldehyde selectivity can be enhanced by using a doubly promoted (Cu-Fe) doped ZnO with yields of 76 g HCHO (kg cat.)⁻¹h⁻¹.³¹ These reactions were carried out at 750°C at 2.5% conversion. Singly doped Cu-ZnO catalysts yielded CO₂ and H₂O via deep oxidation whereas singly doped Fe-ZnO primarily yielded HCHO. Doubly doped Cu-Fe-ZnO minimized the formation of C₂ products and therefore, the Cu-Fe-ZnO catalyst decreased C₂ products and enhanced HCHO formation.

The above system is believed to show enhanced selectivity towards oxygenates due to the variable redox (Cu^{2+/1+}; Fe^{3+/2+}) and Lewis acid (Fe³⁺) functionalities of these catalysts. It is interesting that copper and iron when doped at equimolar levels give the best selectivity towards oxygenates.

Smits, Seshan and Ross have studied the selective oxidative dehydrogenation of propane to propylene over Nb₂O₅ and Nb₂O₅ supported on alumina.³² Vanadia supported on MgO has typically been used in these reactions, although reduced surface vanadyl ions can give rise to decreasing selectivity to propylene. Niobia on the other hand, is much more difficult to reduce than vanadyl but there have been few studies with this oxide in such reactions.

When unsupported niobia is calcined above 500°C, selectivities to propylene as high as 85 % were observed albeit at conversions less than 2 mol % propane. Supported niobia on alumina gave selectivities as high as 62 % to propylene with conversion of about 1 mol % propane. The good selectivity of niobia in these systems may be related to the inertness of niobia with respect to vanadia and perhaps due to specific Nb-O interactions in the unsupported oxide catalyst.

Oyama and Somorjai have studied the oxidation of ethanol and ethane over vanadia supported on silica.³³ Ethane oxidation yielded ethylene and acetylene with considerable CO₂ for highly dispersed catalysts. Ethanol oxidation to acetaldehyde, on the other hand was shown to be structure insensitive. Conversions and selectivities for reaction of ethanol are shown in Table III.³³

Selectivities and conversions for ethane conversion are summarized in Table IV³³ for comparison.

Oxygen chemisorption methods were used to titrate surface vanadium sites in these studies. Raman, X-ray diffraction and isotopic labeling were done to support the dispersion results from chemisorption. A further conclusion was that as the % V increased for ethane oxidation reactions that the catalytic activity and selectivity was similar to that of unsupported vanadia.

Methane can also be selectively oxidized using photochemical methods over MoO₃/ZnO at 500-550 K as shown by Wada and coworkers.³⁴ These observations are somewhat surprising since photooxidation of methane over supported semiconductors often leads to deep oxidation. For a 5 wt. % MoO₃ on ZnO catalyst, 4.0 μ mol HCHO/hr and 0.1 μ mol CH₃OH/hr were produced (no

Table III. Conversion and Selectivities for Ethanol Oxidation Over V_2O_5/SiO_2

% V	Conv.	S, CH_3CHO	S, CH_2CH_2	S, CH_3COOH	S, CO_2
0	0.4	100			
1.4	2	84	4	6	6
3.5	3.5	77	2	11	10
5.6	5.5	77	1	11	11
7.7	3.9	65	1	17	17
9.8	3.8	74	1	14	11

S in %, T = 490 K, Conv. in %.

SOURCE: Data are taken from reference 33.

Table IV. Conversions and Selectivities for Ethane Oxidation Over V_2O_5/SiO_2

% V	Conv.	S, CH_3CHO	S, CH_2CH_2	S, CO	S, CO_2
0	0				
0.3	1	7	30	0	63
1.4	1.5	3	19	5	73
3.5	0.6	12	63	10	15
5.6	0.5	7	73	9	11
7.7	0.8	9	65	7	19
9.8	0.5	8	59	5	28

S in %, Conv. in %, T = 800 K.

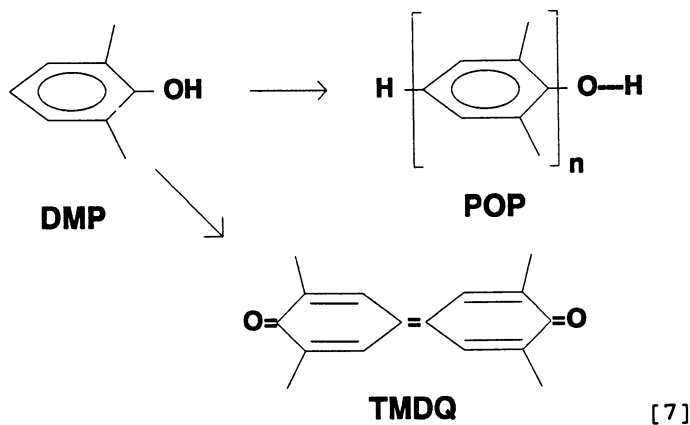
SOURCE: Data are taken from reference 33.

CO or CO₂) at 493 K after 5 h with photolysis while unirradiated catalysts gave no products.

Similar studies³⁴ with ethane as a feed led to yields of CH₃CHO of 11 μ mol/hr, 3 μ mol/hr HCHO, and 5 μ mol/hr CO₂ on irradiation and no products again without irradiation. Data for ZnO itself showed higher selectivities to CH₃CHO for unirradiated catalysts than for irradiated catalysts. Photochemical and thermal pathways are clearly different for these materials. A 200 W Hg arc lamp with broad band ultraviolet wavelengths was used for excitation.

Talsi et al. have shown that certain Cu²⁺ complexes can efficiently catalyze the selective oxidation of 2,6-dimethylphenol [DMP] to polyoxophenylene polymers on the basis of detailed electron paramagnetic resonance and NMR spectroscopy.³⁵ Six different copper(II) complexes were observed with mixed Cu²⁺ complexes of either monomeric or oligomeric phenolate, and acetate, amine or formate ions. Highest selectivities are achieved when monomeric phenoxy radicals react with coordinated phenolate ligands to yield the final desired product, pol[oxy-2,6-dimethyl-1,4-phenylene], [POP]. A quinone byproduct, 3,3',5,5'-tetramethyldiphenoquinone [TMDQ] is the major side product of these reactions. A reaction scheme showing the different products is given in Eq. 7.³⁵

The driving force for these reactions is believed to be the electron transfer from monomeric or oligomeric phenolate ions to Cu²⁺ ions in these transition metal catalysts. Some structures of the proposed active catalysts are shown in Fig. 3 (After 35).



A reaction mechanism for the above reactions was proposed which consists of initial formation of the copper precursor complexes of Fig. 3 (without coordinated phenolate), coordination of phenolate, electron transfer from phenolate to Cu²⁺ and subsequent reduction to Cu¹⁺ with formation of a phenoxy radical, and reoxidation of Cu¹⁺ to Cu²⁺ with oxygen. Various copper(II) catalysts having different stereochemistries (octahedral or tetrahedral coordination) due to coordination of amines like pyridine (Py) or acetate (OAc) groups in different ligand sites were observed by NMR and electron paramagnetic resonance techniques.

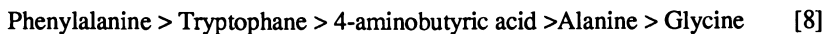
Alternative pathways for reactions such as decomposition of acetaldehyde and ethanol over single crystal surfaces such as shown in the work of Houtman

and Barteau on Rh(111) crystal faces often can be used as model systems to help interpret catalytic data for supported metal catalysts.³⁶ Decarbonylation of acetaldehyde was found to be dependent on the initial coverage of acetaldehyde with saturated monolayer coverage giving rise to selectivity to methane of 50 %. On the other hand, for acetaldehyde coverage of 0.05, no methane was observed. Deuterium labeling studies suggest that the ability of these catalysts to hydrogenate sorbed acetaldehyde surface species critically depends on surface hydrogen atoms. Since the primary product observed by temperature program methods was monodeuterated methane, it was suggested that a methyl migration mechanism was responsible for decarbonylation of acetaldehyde.

In contrast to the acetaldehyde decarbonylation, reactions with ethanol over Rh (111) did not lead to formation of methane but rather to an oxametallocycle via methyl hydrogen abstraction. These data suggest that ethanol formed over supported rhodium catalysts may not be due to hydrogenation of acetaldehyde. This study shows how surface science studies of model catalysts and surfaces can be used to extract information about reaction mechanisms since the nature of surface intermediates can often be identified by methods such as temperature programmed desorption and high resolution electron energy loss spectroscopy.

Chang et al. have recently used calixarene liquid membranes to enhance the selective transport of amino acid esters of phenylalanine and tryptophane over glycine, alanine and 4-aminobutyric acid.³⁷ While these are not catalytic reactions and the membrane is only being used for separation purposes, it appears that use of such membranes in catalytic reactions is attractive. Transport rates of the phenyl alanine ethyl ester were about two orders of magnitude greater than corresponding glycine derivatives. Binding of ester complexes in the calixarene and crown ether cavities are shown in Fig. 4 After 37) for comparison.³⁷

Ultraviolet and infrared spectroscopies were used to verify the symmetry of the ester complexes of Fig. 4. The transport efficiency was related to the relative degree of hydrophobicity of the amino acids with an ordering as shown in Eq. 8.³⁷



Statistical methods can often be used to understand what variables are important for the preparation of catalysts, for the optimization of selectivity and conversion and other phenomena. Screening and experimental design methods have been used by Ebert et al. to optimize the selectivity of isomerization of 1,5-cyclooctadiene to 1,4-cyclooctadiene.³⁸ Silica supported Ir₄(CO)₁₂ was used as a catalyst and experimental data from the experimental design were used to optimize the yield of 1,4-cyclooctadiene with selectivity of 50 %.

The most important parameter for the optimization of this isomerization is reaction temperature. Better yields of 1,4 cyclooctadiene are obtained at higher temperatures, however selectivity to 1,3 cyclooctadiene is also enhanced. The metal loading and flow rate are also important parameters with low metal loading and high flow rate being optimal. The partial pressure of reactant 1,5 cyclooctadiene does not appear to be important. Time of reaction was found to be somewhat important because some catalyst deactivation occurs.

Wu, Yuan and Xu have studied nonuniform pellets in the hydrogenation of CO over Ni on alumina supports.³⁹ Selectivity is directly related to the CO/H₂ ratio inside the pellets. The active Ni particles were deposited as a narrow band in order to approximate a Dirac delta distribution. Experimental data followed theoretical predictions of the researchers regarding enhanced selectivity to

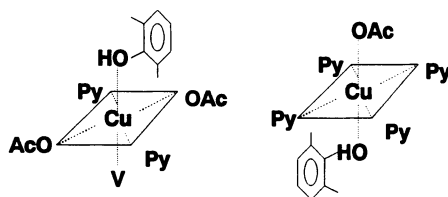


Figure 3. Structures of Oxidation Catalysts

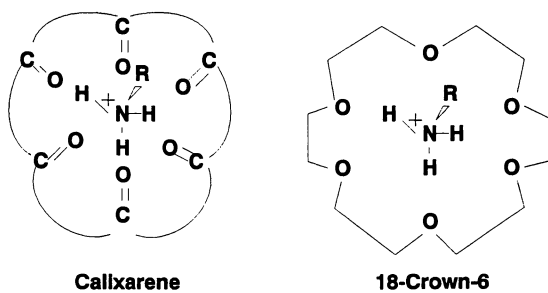


Figure 4. Structure of Calixarene and 18-Crown-6

methane. A Langmuir-Hinshelwood mechanism was assumed and coke deposition was minimized.

A final example of reaction pathway control is the selective hydrogenation of CO to C₁ to C₁₂ hydrocarbons and oxygenates with Co/Ni alloys on various supports. Electron donating metal oxide supports such as MgO, PbO, and ZnO decrease the overall activity of Co/Ni alloys. Supports like TiO₂ and MnO₂ lead to enhanced conversion and selectivity to higher hydrocarbons. Metal support interactions were proposed to be important in the control of activity and selectivity as were the electronegativities of the supports. Highly electron accepting metal oxides like TiO₂ and SiO₂ were proposed to weaken the adsorption of CO whereas hydrogen coverage was strong leading to enhanced rates of CO hydrogenation.

As in the other 3 sections, catalytic processes controlled by specific reaction pathways have several similar requirements. In many of the above systems the degree of electron transfer between the metal and support was proposed to be important. Various surface structures were also believed to play an important role in enhancement of selectivity. In this particular section it is clear that the type of input energy such as photochemical, thermal or other energy forms may markedly influence product distributions of catalytic reactions.

VI. CONCLUSIONS.

The above literature review gives a comparison of different ways to control selectivity for both homogeneous and heterogeneous catalytic reactions. There are several common features for the four areas of stereoselectivity: metal clusters, alloys and poisoning; shape selectivity; and reaction pathway control. In fact, many times more than one of these areas may be involved in a catalytic system. Some common features for all of these areas include precise control of the structural and compositional properties of the catalysts. This paper serves as an overview for the other manuscripts in this book. Specific review chapters on each of the four areas can be found in reviews that follow by D. Forster et al., K. J. Klabunde et al., M. E. Davis et al., and H. C. Foley and M. Klein et al.

VII. ACKNOWLEDGMENTS.

The author acknowledges the support of the National Science Foundation under grant CBT 8814974 and the Department of Energy, Office of Basic Energy Sciences, Division of Chemical Sciences for research in the area of selectivity in catalysis.

VIII. REFERENCES.

1. Annen, M. J.; Davis, M. E.; Higgins, J. B.; Schlenker, J. L. *J. Chem. Soc. Chem. Comm.*, 1991, 1175-1176.
2. Estermann, M.; McCusker, L. B.; Baerlocher, C.; Merrouche, A.; Kessler, H. *Nature*, 1991, **352**, 320-323.
3. Lawton, S. L.; Rohrbaugh, W. J. *Science*, 1990, **247**, 1319-1322.
4. Amato, I. *Science*, 1991, **253**, 1212-1213.
5. Amato, I. *Science*, 1991, **254**, 30-31.
6. Weissbuch, I.; Addadi, L.; Lahav, M.; Leiserowitz, L. *Science*, 1991, **253**, 637-645.
7. Niwa, M.; Murakami, Y. *J. Phys. Chem. Solids*, 1989, **50**, 487-496.
8. Srinivasan, S.; Datsy, A. K.; Hampden-Smith, M.; Wachs, I. E.; Deo, G.; Jehng, J. M.; Turek, A. M.; Peden, C. H. F. *J. Catal.*, 1991, **131**, 260-275.

9. Friedbacher, G.; Hansma, P. K.; Ramli, E.; Stucky, G. D. Science, 1991, **253**, 1261-1263.
10. Bard, A. J.; Fan, F. F.; Pierce, D. T.; Unwin, P R.; ipf, D. O.; Zhou, F. Science, 1991, **254**, 8-74.
11. a) Gorte, R. J. J. Catal., 1982, **75**, 164-174.
b) Biaglow, A. I.; Adamo, A. T.; Kokotailo, G. T; Gorte, R. J. J. Catal., 1991, **131**, 252-259.
12. Hoveyda, A. H.; Zhongmin, X. J. Am. Chem. Soc., 1991, **113**, 5079-5080.
13. Giles, R. G. F.; Green, I. R.; Knight, L. S.; Son, V. R. L.; Rickards, R. W.; Senanayake, B. S. J. Chem. Soc. Chem. Comm., 1991, 287-288.
14. Jeffery, T. J. Chem. Soc. Chem. Comm., 1991, 324-325.
15. Fowler, P. W.; Macfarlane, E. L. A.; Roberts, S. M. J. Chem. Soc. Chem. Comm., 1991, 453-454.
16. Sutherland, I. M.; Ibbotson, A.; Moyes, R. B.; Wells, P. B. J. Catal., 1990, **125**, 77-88.
17. Laycock, D. E.; Collacott, R. J.; Skelton, D. A.; Tchir, M. F. J. Catal., 1991, **130**, 354-358.
18. (a) Efstathiou, A.; Suib, S. L.; Bennett, C. O. J. Catal., 1991, **131**, 94-103.
(b) Nam, S. S.; Iton, L. E.; Suib, S. L.; Zhang, Z. Chem. Mater., 1989, **1**, 529-534.
19. (a) Kurihara, L. K.; Occelli, M. L.; Suib, S. L. ACS Symposium Series **452**, 1991, 224-241.
(b) Anderson, M. W.; Occelli, M. L.; Suib, S. L. J. Catal., 1990, **122**, 374-383.
20. Pine, L. A. J. Catal., 1990, **125**, 514-524.
21. Espeel, P. H.; Tielen, M. C.; Jacobs, P. A. J. Chem Soc. Chem. Comm., 1991, 669-671.
22. Cagnoli, M. V.; Marchetti, S. G.; Gallegos, N. G.; Alvarez, A. M.; Mercader, R. C.; Yeramian, A. A. J. Catal., 1990, **123**, 21-30.
23. Le Normand, F.; Barrault, J.; Breault, R.; Hilaire, L.; Kiennemann J. Phys. Chem., 1991, **95**, 257-269.
24. Nitta, Y.; Hiramatsu, Y.; Imanaka, T. J. Catal., 1990, **126**, 235-245.
25. Larkins, F. P.; Nordin, M. R. J. Catal., 1991, **130**, 147-160.
26. Corma, A.; Sastre J. Chem. Soc. Chem. Comm., 1991, 594-596.
27. Matsuda, T. Yogo, K.; Mogi, Y.; Kikuchi, E. Chem. Lett., 1990, 1085-1088.
28. Lafyatis, D. S.; Foley, H. C. Chem. Eng. Sci., 1990, **45**, 2567-2574.
29. Choudhary, B. M.; Kumar, K. R.; Kantam, M. L. J. Catal., 1991, **130**, 41-51.
30. Larsson, R. J. Mol. Catal., 1989, **55**, 70-83.
31. Sojka, Z.; Herman, R. G.; Klier, K. J. Chem. Soc. Chem. Comm., 1991, 185-186.
32. Smits, R. H. H.; Seshan, K.; Ross, J. R. H. J. Chem. Soc. Chem. Comm., 1991, 558-559.
33. Oyama, S. T.; Somorjai, G. A. J. Phys. Chem., 1990, **94**, 5022-5028.
34. Wada, K.; Yoshida, K.; Watanabe, Y.; Suzuki, T. J. Chem. Soc. Chem. Comm., 1991, 726-727.
35. Talsi, E. P.; Shaikhtudinova, N. I.; Shubin, A. A.; Chinakov, V. D.; Khlebnikov, B. M.; Yudkin, B. I.; Nekipelov, V. M.; Zamaraev, K. I. J. Mol. Catal., 1990, **57**, 325-351.

36. Houtman, C. J.; Barteau, M. A. *J. Catal.*, 1991, 130, 528-546.
37. Chang, S. K.; Hwang, H. S.; Son, H.; Youk, J.; Kang, Y. S. *J. Chem. Soc. Chem. Comm.*, 1991, 217-218.
38. Ebert, C.; Gianferrara, T.; Graziani, M.; Kaspar, J.; Linda, P.; Trovarelli, A. *J. Catal.*, 1990, 124, 433-440.
39. Wu, H.; Yuan, Q.; Zhu, B. *Ind. Eng. Chem. Res.*, 1990, 29, 1771-1776.
40. Ishihara, T.; Horiuchi, N.; Eguchi, K.; Arai, H. *J. Catal.*, 1991, 130, 202-211.

RECEIVED September 15, 1992

Chapter 2

Stereoselectivity

The Ultimate Challenge in Catalysis

D. Forster

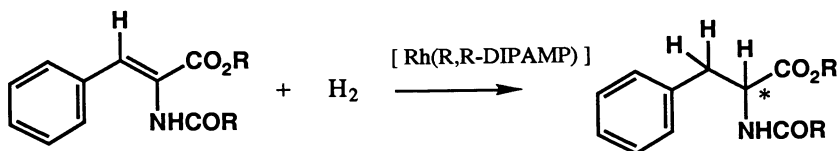
Department of Chemical Sciences, Monsanto Corporate Research,
Monsanto Company, 800 North Lindbergh Boulevard, St. Louis, MO 63167

The need for stereoselective synthesis of organic molecules has been growing rapidly over the past fifteen years. There has been a heightened awareness of the differentiation of biological effects by enantiomer. This is a logical result of the exposure of pharmaceutical and pesticidal agents into the biological milieu in which they have to extend their mode of action. The biological environment is chiral and therefore clear distinctions are frequently encountered between stereoisomers. This issue has been receiving increasing scrutiny by regulatory agencies and we appear to be evolving to a situation where single optical isomer drugs will become the norm unless the financial burden on the consumer to produce such a material is excessive (in the absence of strong bio-effect). Clearly the traditional resolution approach to making single optical isomer materials can only be more expensive than the racemic mixture. Additional impetus for asymmetric synthesis of bio-active molecules is coming from the rapidly expanding knowledge base in structural biology. Thus, as the biological targets for human health and agricultural pesticides become better characterized at the molecular level by X-ray and NMR techniques, the starting point for a synthetic program has stereochemical information as a key component.

While there are now many ways to pursue asymmetric synthesis, certainly for commercial production, direct catalytic synthesis of the desired enantiomer is intrinsically the most attractive. However, the attainment of high selectivity in an asymmetric catalytic reaction is a major challenge. Thus, in most forms of catalysis, one is usually attempting to achieve differentiation in selectivity among potential products with different thermodynamic energy levels. Asymmetric catalysis poses an additional challenge insofar as enantiomers are energetically equivalent in an achiral environment. Therefore, the subtle energetic differences allowing catalytic selectivity must be achieved by utilizing chiral transition states in the catalytic cycle.

While there were attempts to produce heterogeneous asymmetric catalysts over 30 years ago, such systems gave such minor enhancement of stereoselectivity that they were never considered practical. The modern age of asymmetric catalysis began with the work of W. S. Knowles *et al.* (1), (2), who showed that by combining a soluble metal species (rhodium) with a chiral ligand effective asymmetric catalysts for hydrogenation of olefins could be formed. The initial catalyst systems had serious limitations with respect to the olefin substrates capable of giving high stereoselectivity (typically measured by enantiomeric excess or % e.e.). Neverthe-

less, the early systems were highly effective with (2)- α -acetamidocinnamic acids which were precursors to amino acids and the new catalyst concept was introduced into a commercial facility for L-Dopa production in 1972. The initial commercial production was accomplished with a catalyst system based on a monodentate chiral



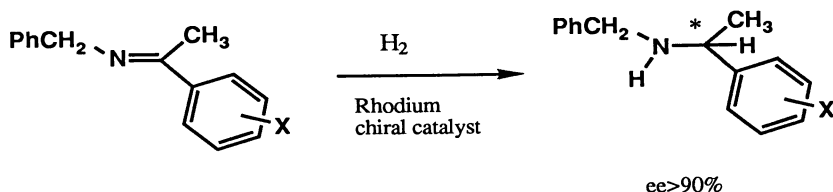
phosphine-cyclohexylisyl methylphosphine (CAMP), but the catalyst was changed over to a chelating chiral phosphine (DIPAMP) as it became established that chelating phosphines generally bestowed higher stereoselectivity on the reaction.

The mechanism of asymmetric catalytic reactions is clearly of fundamental importance and has been intensively investigated in the case of asymmetric hydrogenation. The mechanistic studies of Halpern *et al.* (3) (4) and the structural studies of Knowles *et al.* (5) of asymmetric hydrogenation of α -acylamino-acrylic and -cinnamic acid derivatives with cationic rhodium complexes containing chiral phosphine ligands have uncovered several important facets of these highly effective catalysts: (a) The substrate initially binds in a relatively rigid "chelating" mode to the metal (in the case of the unsaturated acid derivatives, the binding is provided both by the olefin bond and the carbonyl oxygen) and the chiral metal complex forms diastereomers with the olefinic substrate; (b) The predominant diastereomeric metal species observed under reaction conditions was on the pathway to the minor stereo-isomeric product. In other words the greater thermo-dynamic stability of the pre-dominant isomer reduces its reactivity with respect to the subsequent steps necessary for productive catalysis. This interpretation is clearly at odds with the familiar "lock and key" interpretation of enzymic catalysis.

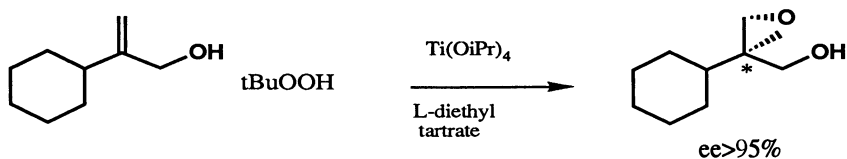
Another facet of these asymmetric hydrogenations, which has been quantified by the detailed studies referred to above, are the extraordinary rates of reaction. Thus the turnover rates of several of these systems approach or exceed 10^2 sec^{-1} and therefore are comparable to many classes of enzymic catalysis. This high reactivity was important for the utilization of such catalysts for commercial operation. It should be appreciated that use of the expensive rhodium together with a very expensive ligand system presents a potential bar to commercial utility. However, the extremely high turnover rates that can be realized with these systems at low temperatures allows their use in such minute amounts that intact recycle is not required and they are merely recovered for their precious metal content.

Over the past fifteen years there has been a rapid expansion of the field of asymmetric catalysis with approximately twenty classes of reactions now having been achieved with high (> 70% e.e.) optical purity. Some representative examples follow.

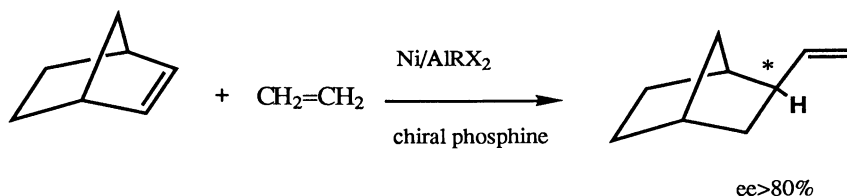
Hydrogenation of Imines (6)



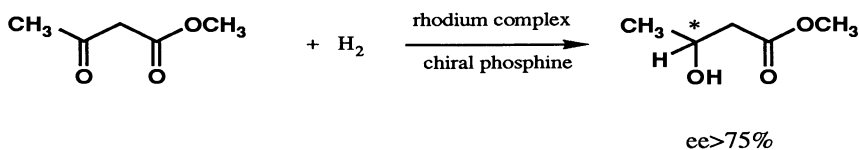
Oxidation of Allylic Alcohols (7)



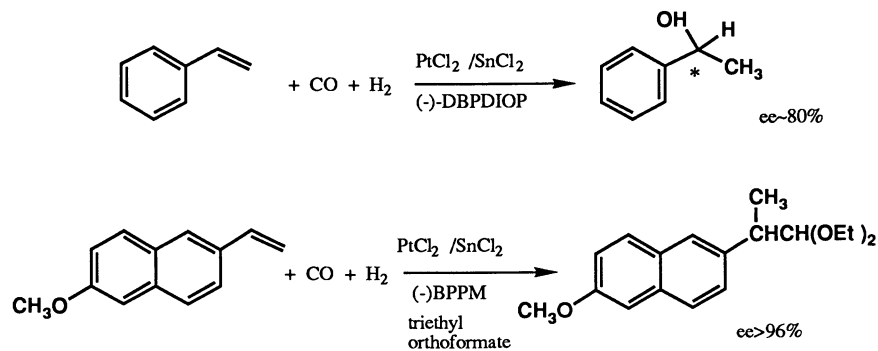
Codimerization of Olefins (8)



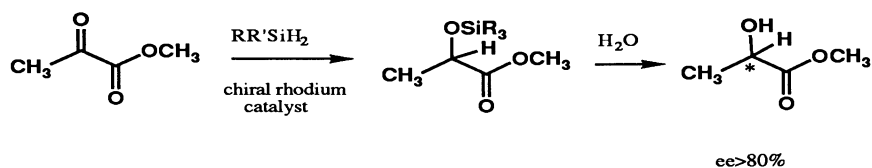
Hydrogenation of Ketones (9)



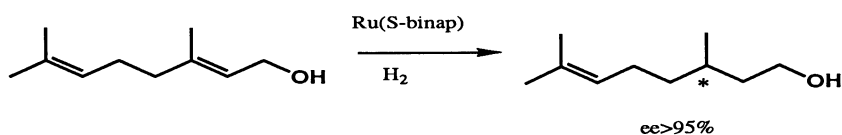
Hydroformylation of Alkenes (10) (11)



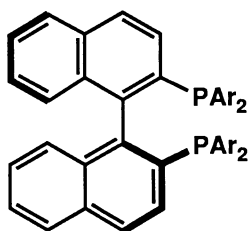
Hydrosilylation of Ketones (12)



Hydrogenation of Allylic Alcohols (13)

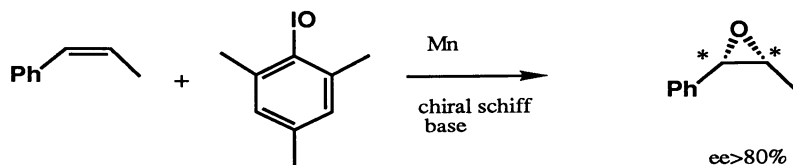


This is but one example of the many new reactions which have become practical as a result of the discovery and exploitation of the BINAP ligand by Noyori *et al.* (14).

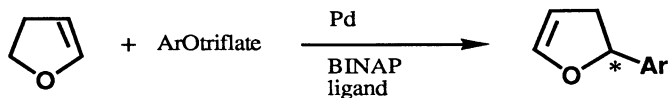


(S)-BINAP

Epoxidation of Olefins (15)



Asymmetric Heck Reactions (16)



This field continues to advance at a rapid rate and it is reasonable to expect asymmetric catalytic synthesis to become more and more commonplace in the armormentarium of the synthetic organic chemist.

Literature Cited

1. Knowles, W. S., and Sabacky, M. J. *J. Chem. Soc., Chem. Commun.*, **1968**, p. 1445.
2. Knowles, W. S., Sabacky, M. J., and Vineyard, B. D. *J. Chem. Soc., Chem. Commun.*, **1972**, p. 10.
3. Landis, C. R., and Halpern, J. *J. Organomet. Chem.*, **1983**, *250*, 485.
4. Halpern, J. In *Asymmetric Synthesis*; Editor, J. D. Morrison; Academic Press, **1985**, Vol. 5; p. 41.
5. Koenig, K. E., Sabacky, M. J., Bachman, G. L., Christopfel, W. C., Barnstoff, H. D., Friedman, R. B., Knowles, W. S., Stults, B. R., Vineyard, B. D., and Weinkauff, D. *J. Ann. N.Y. Acad. Sci.*, **1980**, *333*, 16.
6. Bakos, J., Orosz, A., Heil, B., Laghmari, M. Lhoste, P., and Sinou, D. *J. Chem. Soc., Chem. Commun.*, **1991**, p. 1684.
7. Katsuki, T., and Sharples, K. B. *J. Am. Chem. Soc.*, **1980**, *102*, 5974.
8. Bogdanovic, B., Henc, B., Meister, B., Pauling, H., and Wilke, G. *Angew. Chem., Int. Ed. Engl.*, **1972**, *11*, 1023.
9. Toros, S., Heil, B., Kollar, L., and Marko, C. *J. Organomet. Chem.*, **1980**, *197*, 85.
10. Consiglio, G., Pino, P., Flowers, L. I., and Pittman, C. V. *J. Chem. Soc., Chem. Commun.*, **1983**, p. 612.
11. Parrinello, G., and Stille, J. K. *J. Am. Chem. Soc.*, **1987**, *109*, 7122.
12. Ojima, I., and Kogure, T. *Organometallics*, **1982**, *1*, 1390.
13. Takaya, H., Ohta, T., Sayo, N., Kumobayashi, H., Akutagawa, S., Inone, S., Kasahara, I., and Noyori, R. *J. Am. Chem. Soc.*, **1987**, *109*, 1596.
14. Noyori, R. *Science*, **1990**, *248*, 1194.
15. Zhang, W., Loebach, J. L., Wilson, S. R., and Jacobsen, E. N. *J. Am. Chem. Soc.*, **1990**, *112*, 2801.
16. Ozawa, F., Kubo, A., and Hayashi, T., this volume.

RECEIVED July 15, 1992

Chapter 3

Asymmetric Catalytic Hydrogenation of 2-Arylacrylic Acids as a Low-Cost Route to Pharmaceutical Products

A. S. C. Chan, S. A. Laneman, and R. E. Miller

Monsanto Corporate Research, Monsanto Company, 800 North Lindbergh Boulevard, St. Louis, MO 63167

The homogeneous catalytic asymmetric hydrogenations of 2-arylacrylic acids have been studied. Both rhodium and ruthenium catalysts have been examined. The reaction temperatures and hydrogen pressures have profound effects on the optical yields of the products. The presence of a tertiary amine such as triethylamine also significantly increases the product enantiomer excess. Commercially feasible processes for the production of naproxen and S-ibuprofen have been developed based on these reactions.

Chiral compounds are important for the food, pharmaceutical, and agrochemical industries. Although the optical isomers of each specific compound possess many similar physical properties such as melting and boiling points, solubilities in common solvents, etc., they often show distinctly different physiological properties when applied to biological systems. This difference is due to the different interactions of the optical isomers with the host receptors which are also optically active.

Traditionally, most optically pure compounds are produced via one or more of the following methods:

(1) Preferential crystallization. Preferential crystallization is one of the oldest methods for the resolution of racemates. It involves seeding of the racemate solution with pure crystals of the desired enantiomer which induce the preferential crystallization of that isomer from the solution. The technology is used in the commercial production of α -methyl-L-dopa (1).

(2) Diastereomeric crystallization. In this approach an optically pure auxiliary compound is added to the mixed optical isomers of the product to form the corresponding diastereomers which are then separated via crystallization. For example, S-naproxen is produced by reacting a chiral amine with the racemic mixture of 2-(6'-methoxy-2'-naphthyl)propionic acid to form the corresponding organoammonium salts of the S- and R- isomers followed by crystallization and re-acidification (2).

(3) **Kinetic resolution.** Kinetic resolution is a separation process based on the different rates of the transformation of the enantiomers into certain products under the influence of chiral reagents or catalysts. In recent years the use of enzyme-catalyzed enantioselective hydrolysis of chiral esters has attracted much attention (3). A large rate difference in the transformation of the starting enantiomers is an important criteria for this technology to be of practical use.

(4) Use of existing chiral compounds as starting materials or templates in a stoichiometric fashion. The use of existing chiral compounds as a source of chiral center is popular among organic chemists. Natural amino acids have been extensively used for this purpose (4). While this method is most convenient, it is limited by the availability and the cost of the existing chiral pool.

(5) **Catalytic asymmetric synthesis.** This technology probably has the best economic potential because large quantities of optically pure compounds can be made in high yields with only small amounts of chiral catalysts. Mother nature has been producing a large variety of chiral materials via enzyme-catalyzed reactions for millenniums. More recently, the use of chiral transition metal catalysts have attracted much attention (5). The advantage of studying the homogeneous asymmetric catalysts is that one can characterize the catalytic species with modern instrumentation and significantly improve the efficacy of the catalyst systems via appropriate modifications.

In the late sixties, several research groups in the U.S. (6), Europe (7), and Japan (8) initiated studies of homogeneous catalytic asymmetric syntheses. Of these efforts, the catalytic asymmetric hydrogenation of prochiral olefins reported by Knowles, *et al.* (6,9) attracted most attention. The importance of this technology was shown by its application in the Monsanto L-DOPA process which had since become an industrial flagship in catalytic asymmetric syntheses (Figure 1).

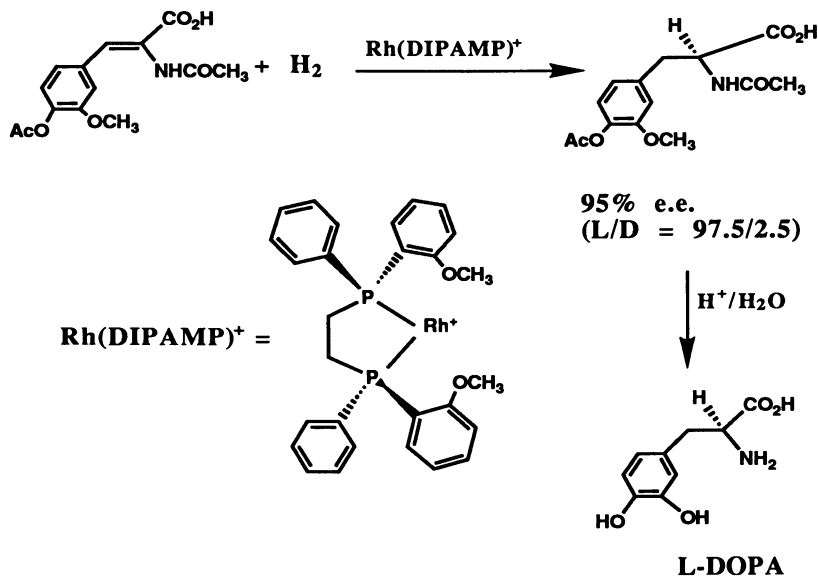
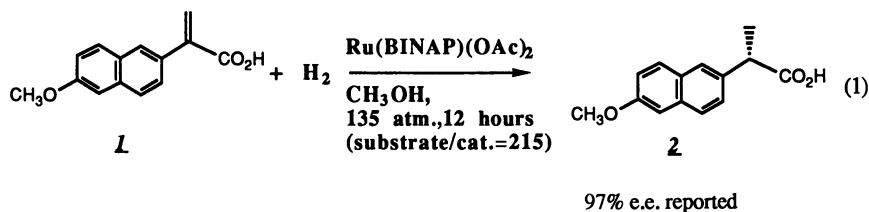


Figure 1. Monsanto L-DOPA Process

The scientific interest in the L-DOPA process was further enhanced by the clear, detailed elucidation of the mechanism of the catalytic reaction (10). To this date, thousands of papers and patents have been published on the subject of catalytic asymmetric hydrogenation.

Although the Rh-catalyzed asymmetric hydrogenations of prochiral enamides have been extensively studied and excellent results have been frequently achieved, the catalytic asymmetric hydrogenations of 2-arylacrylic acids have been less successful. Until recently most catalyst systems gave only moderate optical yields for the 2-arylpropionic acid products (11). An important breakthrough in the study of these reactions was reported by Noyori *et al.* By using Ru(BINAP)(OAc)₂ as a catalyst precursor, these researchers obtained excellent optical yields in the asymmetric hydrogenation of 2-(6'-methoxy-2'-naphthyl)acrylic acid (12).



The optical yields in this reaction are very sensitive to the hydrogen pressure. For example, under moderate pressure (<100 psig), the enantiomeric excess (e.e.) has been found to be below 75%. Since naproxen and many other chiral 2-arylpropionic acids are high-valued pharmaceutical products, there is great economic potential for the development of a practical process based on the efficient asymmetric hydrogenation of 2-arylacrylic acids. A practical process should have high turnover rates and high optical yields under moderate operating pressures.

In this paper we present a study of the catalytic asymmetric hydrogenation which leads to commercially feasible processes for the production of (S)-2-(6'-methoxy-2'-naphthyl)propionic acid (naproxen) and (S)-2-(*p*-isobutylphenyl)propionic acid (S-ibuprofen).

Results and Discussions

Improved Conditions for the Asymmetric Hydrogenation of 2-Arylacrylic Acids.

In our initial study of the Rh-catalyzed asymmetric hydrogenation of 2-(6'-methoxy-2'-naphthyl)acrylic acid, we observed that the relationship between the optical yields and the reaction conditions was substantially different from that observed in the enamide hydrogenation. While high H₂ pressure and low reaction temperature lowered the optical yields in the asymmetric hydrogenation of enamides, just the opposite was observed in the hydrogenation of 2-arylacrylic acids. In addition, we also observed that the presence of a tertiary amine such as triethylamine in the reaction system improved the optical yields of the product. Some examples illustrating these effects are shown in Table 1. The best optical yield obtained from the Rh catalyst system was about 85% when Rh(DIOP)⁺ was used as a catalyst. Although that was a significant improvement over the previous Rh catalyst systems, the optical yields were still not high enough for the technology to be commercially feasible. (For the technology to be commercially attractive, optical yields higher than 95% are needed.)

TABLE 1. [Rh(DIOP)]⁺-Catalyzed Asymmetric Hydrogenation of 2-(6'-methoxy-2'-naphthyl)acrylic Acid^{a,b}

Base ^c /Substrate (M/M)	H ₂ pressure (psig)	Temp. (°C)	e.e (%)
1.0	1000	-5	85.2
1.0	45	23	65.4
0.1	1000	-5	86
0.1	1000	23	70
-	1000	-5	45.4
-	1000	23	39
-	45	23	33

a) catalyst precursor = [Rh(COD)((-)-DIOP)]ClO₄.

b) substrate/catalyst (M/M) = 29-100.

c) base = NEt₃.

When we applied the improved reaction conditions to the Ru(BINAP) type catalyst, we found that a variety of Ru(BINAP) catalysts could be used to effect the asymmetric hydrogenation under relatively mild conditions. Table 2 summarizes the results of the use of typical Ru(BINAP) catalysts in the production of naxopen.

Table 2. Asymmetric Hydrogenation of 2-(6'-methoxy-2'-naphthyl)acrylic Acid Catalyzed by Ru(BINAP) Catalysts^a

Catalyst	Pressure (psig)	Temp. (°C)	%ee
[RuCl ₂ (S-BINAP)] ₂ ·NEt ₃	2000	-7	98.5
Mixed [RuCl ₂ (S-BINAP)] _n ^b	1000	-5	97
[Ru(S-BINAP)](BF ₄) ₂ (from 1/2[RuCl ₂ (S-BINAP)] ₂ +2Ag BF ₄)	1000	-6	97
RuCl ₂ (DMSO) ₄ +S-BINAP ^c	1000	-4	97
1/2[Ru(Benzene)Cl ₂] ₂ +S-BINAP ^c	500	-7	97
RuHCl(BINAP) ₂	500	-6	97.7

a) NEt₃/substrate = 1.0 (M/M); substrate/catalyst = 500-3000;
solvent = CH₃OH.

b) Mixed [RuCl₂(S-BINAP)] complexes were prepared by heating S-BINAP with [Ru(COD)Cl₂]_n and NEt₃ in toluene. ³¹P NMR showed at least 5 species having NMR patterns similar to that of [RuCl₂(S-BINAP)]₂·NEt₃.

c) Refluxed in toluene for 16-20 hours and utilized *in situ*.

The effects of pressure, temperature, and tertiary amine in the Ru system are similar to those observed in the Rh catalyst systems. These effects are illustrated in tables 3 and 4.

Table 3. The Temperature and Pressure Effects of the Asymmetric Hydrogenation of **1^{a,b}**

H ₂ Pressure (psig)	Temperature (°C)	%e.e.
100	25	70.6
100	11	85
100	-7	95.3
200	25	82.6
200	11	89.8
200	-7	96.7
500	25	93.3
500	11	95.2
500	-7	98.1

a) Catalyst = [Ru(S-BINAP)Cl₂]_n (n=1 to 3).

b) Solvent = methanol; NEt₃/substrate (M/M) = 1.

Table 4. The Effect of Base Promoter in the Asymmetric Hydrogenation of **1^{a,b}**

Catalyst	T (°C)	NEt ₃ /substrate (M/M)	% e.e.
[Ru(S-BINAP)Cl ₂] ₂ (NEt ₃)	-5	0	92
[Ru(S-BINAP)Cl ₂] ₂ (NEt ₃)	-5	1	97
[Ru(S-BINAP)(η ⁶ -C ₆ H ₆)Cl]Cl	0	0	86
[Ru(S-BINAP)(η ⁶ -C ₆ H ₆)Cl]Cl	0	1	96
[Ru(S-BINAP)][BF ₄] ₂	-3	0	87
[Ru(S-BINAP)][BF ₄] ₂	-3	1	95

a) Solvent = methanol.

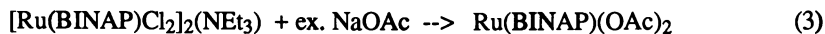
b) Pressure of H₂ = 500 psig.

It is quite clear from these data that by employing a tertiary amine in the Ru(BINAP) catalyst system and by modifying the reaction conditions in the production of naproxen, one can achieve excellent e.e.'s even under moderate H₂ pressure.

Improvements in Catalyst Preparation.

The widely studied Ru(BINAP)(OAc)₂ catalyst is derived from [Ru(BINAP)Cl₂]₂(NEt₃) which is in turn obtained from reacting [Ru(COD)Cl₂]_n with BINAP ligand in the presence of excess triethylamine (12,13).





(The isolated yield of $\text{Ru}(\text{BINAP})(\text{OAc})_2$ in the two step reaction was about 65-70% (12).)

From a practical standpoint, it is of interest to devise a one-step synthesis of the catalyst. Since both reactions 2 and 3 are ligand substitution reactions, it is quite conceivable that both steps can be carried out at the same time. When we reacted $[\text{Ru}(\text{COD})\text{Cl}_2]_n$ with BINAP and sodium acetate in acetic acid, we indeed obtained $\text{Ru}(\text{BINAP})(\text{OAc})_2$ in good yields (70-80%). Interestingly, when the reaction was carried out in the absence of sodium acetate, no $\text{Ru}(\text{BINAP})(\text{OAc})_2$ was obtained. The product was a mixture of chloro-ruthenium-BINAP complexes. A ^{31}P NMR study revealed that the mixture contained a major species (3) (^{31}P [^1H] (CDCl_3): $P_1=70.9$ ppm; $P_2=58.3$ ppm; $J = 52.5$ Hz) which accounted for more than 50% of the ruthenium-phosphine complexes (Figure 2). These complexes appeared to be different from previously characterized and published $\text{Ru}(\text{BINAP})$ species (12,13). More interestingly, these mixed complexes were found to catalyze the asymmetric hydrogenation of 2-(6'-methoxy-2'-naphthyl)acrylic acid with excellent rates and enantioselectivities.

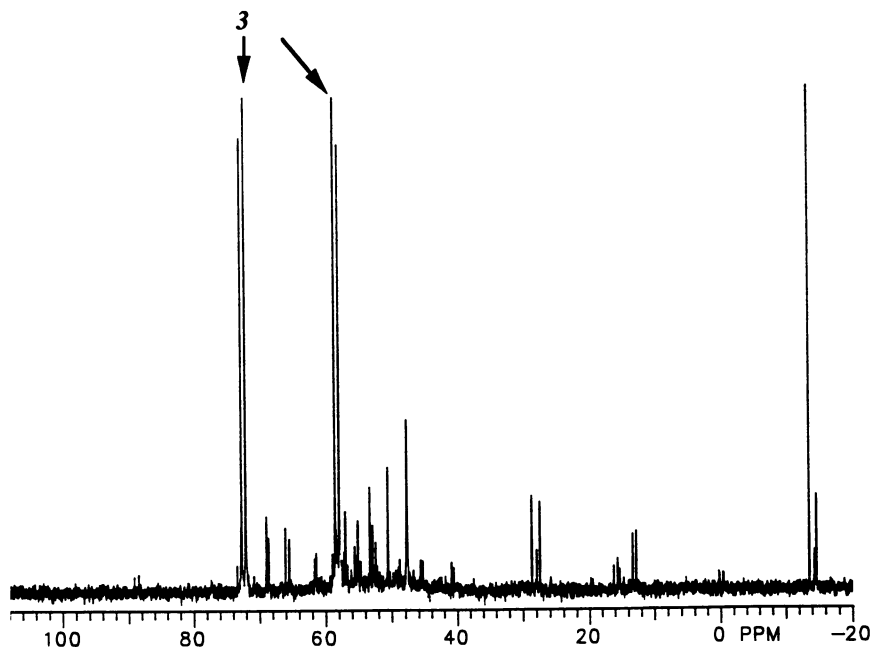
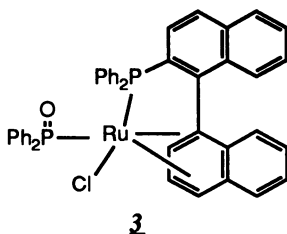


Figure 2. ^{31}P NMR of the crude mixed catalysts.

By carefully crystallizing these complexes in acetone, we were able to isolate complex **3** in the form of single crystals. An X-ray diffraction study revealed the structure of this complex as shown below.



An unusual feature of this complex was that one of the phosphorus-naphthyl bonds in the BINAP ligand was ruptured. Based on the mechanisms elucidated for the P-C bond cleavage on Rh-phosphine complexes (14), we speculated a possible path for the formation of **3** via oxidative addition of the phosphorus-naphthyl bond to the Ru center (Figure 3).

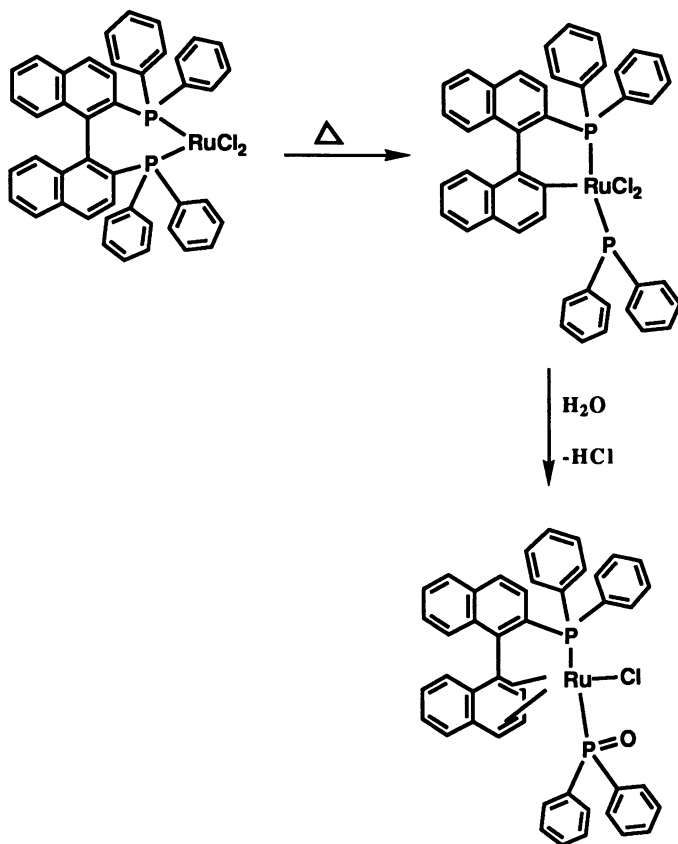


Figure 3 . A Speculated Mechanism for the Formation of **3**.

Complex **3** was found to be inactive in the catalytic asymmetric hydrogenation of 2-(6'-methoxy-2'-naphthyl)acrylic acid. Since **3** accounted for a large portion of the mixed complexes, it was quite clear that the catalytic activity of the mixed species would be substantially increased if the formation of **3** could be avoided. It appeared that preventing the rupture of the phosphorus-naphthyl bond was most critical in an improved synthesis of the mixed Ru-BINAP-chloride catalysts.

Since the oxidative addition of a P-C bond from an organic phosphine to a transition metal center is most facile when the transition metal complex is coordinatively unsaturated, in our attempt to prevent the formation of **3** in the synthesis of the mixed catalysts, we chose to use an aromatic co-solvent as a weakly coordinating agent to suppress the formation of the speculated, "unsaturated species" which was thought to be the culprit for the formation of **3**. When a mixture of toluene and acetic acid was used as solvent in the reaction of $[\text{Ru}(\text{COD})\text{Cl}_2]_n$ with BINAP ligand, complex **3** was not found in the final mixed catalyst product. This new catalyst mixture was indeed found to be two to three-fold more active than the catalyst mixture which contained **3** as a major species. In fact, in the asymmetric hydrogenation of 2-(6'-methoxy-2'-naphthyl)acrylic acid, this catalyst mixture was among the most active when compared with all previously established Ru(BINAP) catalysts. In a typical hydrogenation experiment that was carried out at ambient temperature under 1000 psig H_2 with a substrate-to-catalyst ratio of 10,000, 100% conversion of 2-(6'-methoxy-2'-naphthyl)acrylic acid to naproxen can be achieved in less than one hour. The exact structures of the species in the mixture have not been characterized yet. A mass spectrometric study revealed a general formula of $[\text{Ru}(\text{BINAP})\text{Cl}_2]_n$ ($n=1-3$). (It is possible that higher oligomers of Ru(BINAP) species existed but were not detected because their molecular weights exceeded the limitation of our instrument.)

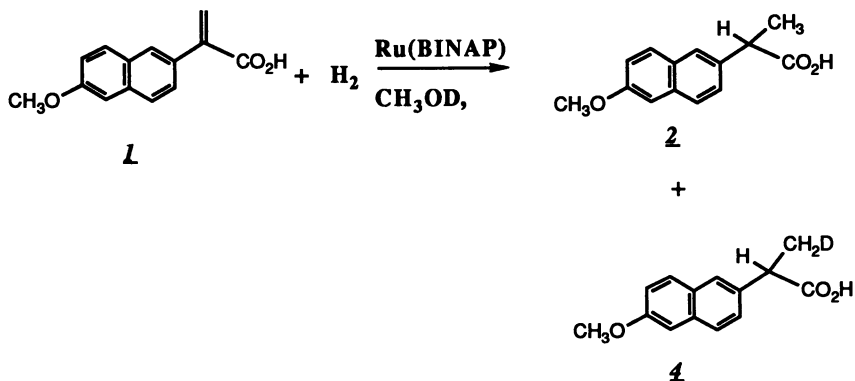
It must be emphasized that this study of the Ru(BINAP) catalysts is still at a preliminary stage. Much has to be done to characterize the active catalysts and elucidate their roles in the asymmetric hydrogenation. However, even at this early stage, it is reasonable to suggest that there is great potential for the development of even more active Ru(BINAP) type catalysts. This direction is currently being aggressively pursued in our laboratory and some promising results have been obtained (15). These results will be published later when more complete data are obtained.

Probing the Reaction Mechanism via a Deuterium Labelling Study.

Recently, Halpern *et al.* (16) and Noyori *et al.* (17) independently reported the deuterium labelling effect on the Ru(BINAP)(OAc)₂-catalyzed hydrogenation of tiglic acid. Two important conclusions were drawn regarding the mechanism of the reaction:

- (1) the activation of hydrogen was via heterolytic splitting of H_2 by the Ru(II) complex;
- (2) the solvolysis of a Ru-alkyl bond was important in the product formation.

Noyori also observed that under high pressure of H_2 , the solvolysis of the ruthenium-alkyl species was less important for the product formation. In our study of the Ru(II)-catalyzed hydrogenation of 2-(6'-methoxy-2'-naphthyl)acrylic acid in CH_3OD , we found the deuterium labelling in the naproxen product to be similar to those reported on the hydrogenation of tiglic acid:



The deuterium label was found to be exclusively on the β -carbon; no deuterium was found in the α -position of the propionic acid moiety. The degree of deuterium incorporation varied widely, depending on the reaction conditions.

Several observations on the factors which affect the degree of deuterium incorporation are summarized as follows:

- (1) β -deuterated naxopren (4) was the dominant species (>60%) when the hydrogenation of concentrated **1** (>5%) in CH_3OD was carried out under low H_2 pressure (<10 psig) and in the absence of a base (such as triethylamine).
- (2) Non-deuterated naxopren (2) was the dominant species (>60%) when the hydrogenation of dilute **1** (<0.5%) in CH_3OD was carried out even under low H_2 pressure and in the absence of a base.
- (3) Under high H_2 (>1000 psig) pressure, non-deuterated naxopren **2** was the dominant product (>80%) even when higher concentration of **1** was used in the absence of a base.
- (4) In the presence of triethylamine (1:1 molar ratio with **1**), non-deuterated naxopren was the dominant species (>90%) even when the reaction was carried out under low H_2 pressure.

These results can be explained by a mechanism proposed in Figure 4. Under low H_2 pressure, the reaction of the ruthenium alkyl species with H_2 was slow. The rate of solvolysis of the ruthenium alkyl species depended on the acidity of solution. Higher acidity of the solution (e.g. higher concentration of **1** in the absence of triethylamine) increased the rate of solvolysis. The presence of triethylamine essentially shut off this route by quenching the acid and lowering the availability of free D^+ which was needed for the solvolysis. High pressure of hydrogen gas increased the rate of the reaction of ruthenium alkyl with H_2 and consequently increased the ratio of **2** to **4**. It should be noted that no deuterium incorporation was observed when rhodium chiral phosphine species were used as catalysts for this reaction. These results were consistent with a different mechanism of H_2 activation by $\text{Rh}(\text{I})$ and $\text{Ru}(\text{II})$ complexes. The mechanism of the rhodium-catalyzed hydrogenation involved mainly the oxidative addition of H_2 to Rh , hydride migration to the coordinated olefin and then reductive elimination of the product from the alkyl hydridorhodium species.

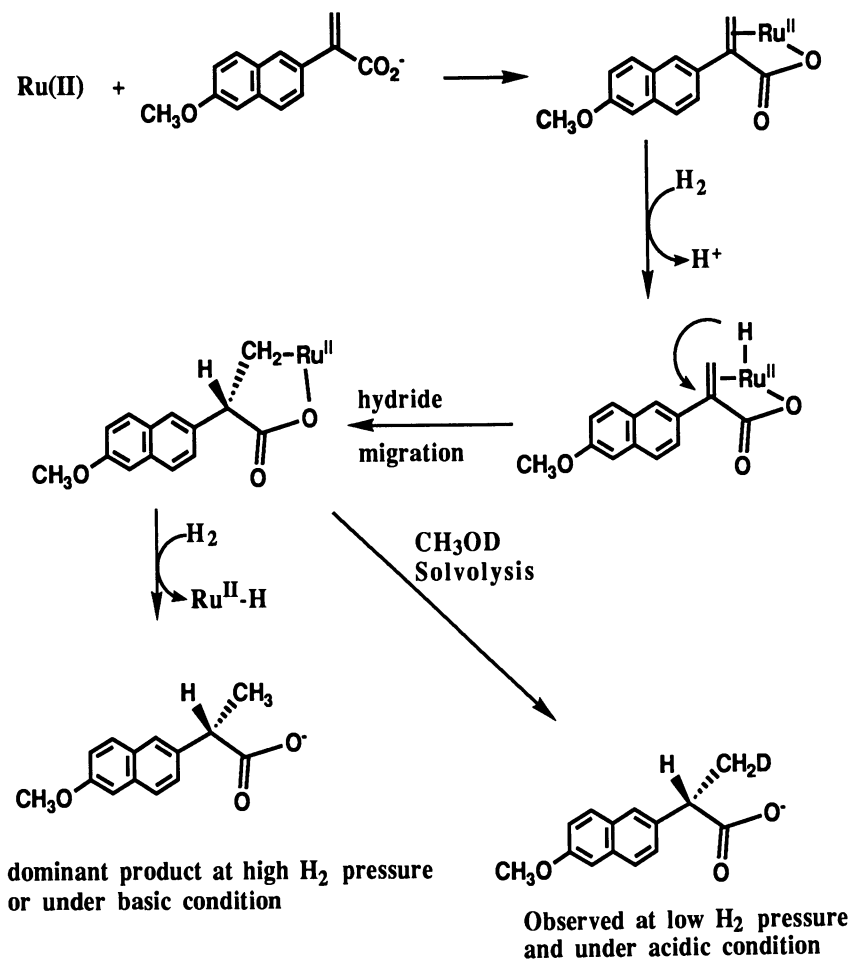


Figure 4. A Possible Mechanism of Ru(II)-catalyzed Hydrogenation of **L**.

Commercially Feasible Processes Based on the Asymmetric Hydrogenation of 2-Arylacrylic Acids.

The ultimate goal in most industrial research is to develop economically attractive processes or products. The technology of asymmetric hydrogenation of 2-arylacrylic acids is probably most useful for the production of naproxen and S-ibuprofen. Naproxen is currently one of the top ten prescription drugs in the world; S-ibuprofen is the active isomer in the popular anti-inflammatory drug ibuprofen. Figures 5 and 6 summarize two commercially feasible processes for the manufacturing of these products.

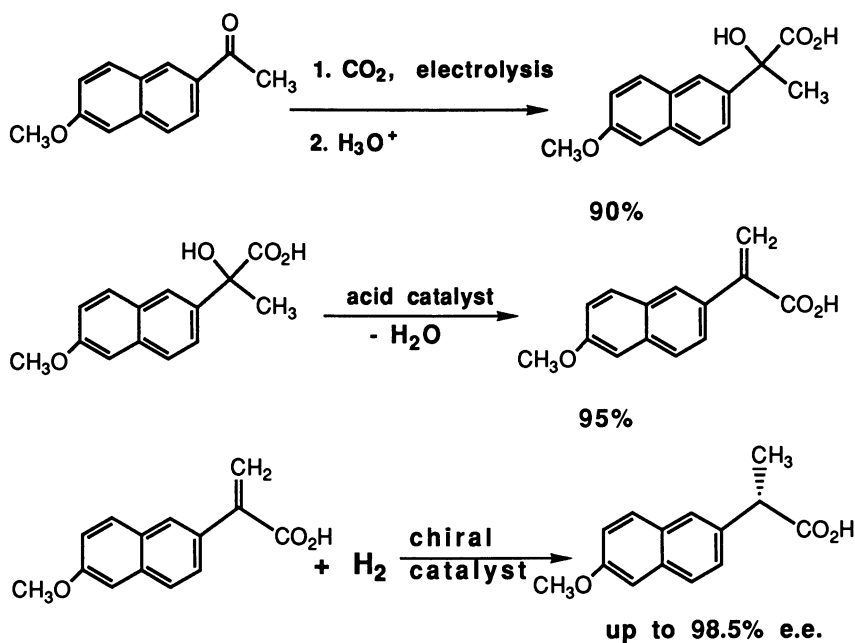


Figure 5. Monsanto Naproxen Process.

There is no doubt that catalytic asymmetric synthesis has a significant advantage over the traditional diastereomeric resolution technology. However, it is important to note that for the asymmetric hydrogenation technology to be commercially useful, a low-cost route to the precursor olefins is just as crucial. The electrocarboxylation of methyl aryl ketone and the dehydration of the substituted lactic acids in Figures 5 and 6 are highly efficient. Excellent yields of the desired products can be achieved in each reaction. These processes are currently under active development. However, since the subjects of electrochemistry and catalytic dehydration are beyond the scope of this article, these reactions will be published later in a separate paper.

Experimental Section

1) Hydrogenation of 2-(6'-methoxy-2'-naphthyl)acrylic Acid.

A typical screening experiment is carried out as follows: In an inert atmosphere glove-box a 25 mL autoclave with a glass liner and a magnetic stirring bar is charged with 20 mg 2-(6'-methoxy-2'-naphthyl)acrylic acid, 9 mg triethylamine, 2 mL methanol (solvent), and 0.1 g of catalyst solution (prepared by dissolving 3 mg of the catalyst in 30 g methylene chloride, methanol, or tetrahydrofuran). The autoclave is then closed and placed in a constant temperature bath on a magnetic stirrer. The reaction was carried out by magnetically stirring the solution at a set bath temperature under constant H_2 pressure. After the reaction is terminated in

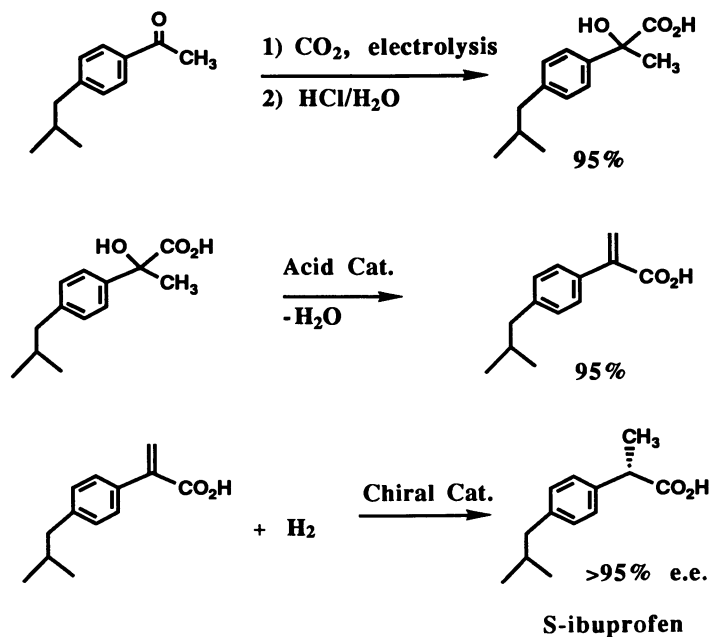


Figure 6. Monsanto S-ibuprofen Process.

each experiment, the solution is taken out of the reactor. The solvent is evaporated and the residue is analyzed by ^1H NMR (for conversion level) and by chiral GLC (for optical yield).

2) Analysis of Naproxen Products with Chiral GLC.

To analyze the optical purity of a naproxen product, the material is first converted to a (+)-menthyl ester by reacting it with excess of (+)-menthol in the presence of dicyclohexylcarbodiimide and an amine catalyst. The resulting material is analyzed on a Varian 370 GC with a 25-meter Chrompack Chirasil-L-Val column.

A typical procedure is as follows: An esterification solution was prepared by dissolving 3.5 g (+)-menthol, 0.12 g DCC, 3 mg 4-dimethylaminopyridine (4-DMAP), and 3 mg 4-DMAP-HCl in one mL dry CH_2Cl_2 . For the analysis of a product sample, about 0.05 mg of the compound in about 10 microliter dichloromethane is mixed well with 10 μl esterification solution at ambient temperature for 30 minutes. The final solution was analyzed on a Varian 370 GC with a 25-meter Chirasil-L-Val column at 195°C isothermally. Excellent baseline separations of the diastereomers are usually obtained. A calibration with naproxen of known optical purity is carried out before using this method for analysis.

Acknowledgment

We thank D. Forster, D. P. Riley and J. Allman for helpful discussions and thank F. Fronczek of Louisiana State University for performing the x-ray diffraction study.

Literature Cited

1. Reinhold, D. F.; Firestone, R. A.; Gaines, W. A.; Chmerda, J. M.; Sletzing, M.: J. Org. Chem., 1968, 33, 1209.
2. Harrison, I. T.: J. Med. Chem. 1970, 13, 203.
3. Kagan, H.: Top Stereochem., 1988, 18, p.249.
4. Coppola, G. M.; Schuster, H. F.: "Asymmetric Synthesis", John Wiley & Sons, New York, New York, 1987.
5. Morrison, J. D.; Ed: "Asymmetric Synthesis", Vol. 5, Academic Press, New York, New York, 1985.
6. Knowles, W. S.; Sabacky, M. J.: J. Chem. Soc. Chem. Commun. 1968, 1445.
7. Horner, L.; Siegel, H.; Buthe, H.: Angew Chem., 80, 1968, 1034.
8. Nozaki, H.; Moriuti, S.; Takaya, H.; Noyori, R.; Tet. Lett., 1966, 5329.
9. Vineyard, B. D.; Knowles, W. S.; Sabacky, M. J.; Bachman, G. L.; Weinkauff, D. J.: J. Amer. Chem. Soc., 1977, 99, 5946.
10. Halpern, J.: "Asymmetric Synthesis", Vol. 5, Morrison, J. D. Ed., pp.41-69, Academic Press: New York, New York, 1985.
11. Campolmi, S.; Felicioli, M. G.; Carkettum V.; Santi, R.: U.S. Pat. 4239914 (Dec. 16, 1980).
12. Noyori, R.; Takaya, H.: J. Org. Chem., 52, 1987, 3176.
13. Ikariya, T.: J. Chem. Soc. Chem. Commun., 1985, 922.
14. Abatjoglou, A. G.; billig, E.; Brian, D. R.: Organometallics, 1984, 3, 923.
15. Chan, A. S. C.; Laneman, S. A.: U.S. Pat. Appl., 1991.
16. Ashby, M. T.; Halpern, J.: J. Amer. Chem. Soc., 1991, 113, 589.
17. Ohta, T.; Takaya, H.; Noyori, R.: Tet. Lett., 1990, 7189.

RECEIVED July 15, 1992

Chapter 4

Chiral Rhodium(II) Carboxamides

Remarkably Effective Catalysts for Enantioselective Metal Carbene Transformations

Michael P. Doyle

Department of Chemistry, Trinity University, San Antonio, TX 78212

Dirhodium(II) tetrakis(carboxamides), constructed with chiral 2-pyrrolidone-5-carboxylate esters so that the two nitrogen donor atoms on each rhodium are in a *cis* arrangement, represent a new class of chiral catalysts with broad applicability to enantioselective metal carbene transformations. Enantiomeric excesses greater than 90% have been achieved in intramolecular cyclopropanation reactions of allyl diazoacetates. In intermolecular cyclopropanation reactions with monosubstituted olefins, the *cis*-disubstituted cyclopropane is formed with a higher enantiomeric excess than the *trans* isomer, and for cyclopropanation of 1-alkynes extraordinary selectivity has been achieved. Carbon-hydrogen insertion reactions of diazoacetate esters that result in substituted γ -butyrolactones occur in high yield and with enantiomeric excess as high as 90% with the use of these catalysts. Their design affords stabilization of the intermediate metal carbene and orientation of the carbene substituents for selectivity enhancement.

A select number of transition metal compounds are effective as catalysts for carbenoid reactions of diazo compounds (*I-3*). Their catalytic activity depends on coordination unsaturation at their metal center which allows them to react as electrophiles with diazo compounds. Electrophilic addition to diazo compounds, which is the rate limiting step, causes the loss of dinitrogen and production of a metal stabilized carbene. Transfer of the electrophilic carbene to an electron rich substrate (S:) in a subsequent fast step completes the catalytic cycle (Scheme I). Lewis bases (B:) such as nitriles compete with the diazo compound for the coordinatively unsaturated metal center and are effective inhibitors of catalytic activity. Although carbene complexes with catalytically active transition metal compounds have not been observed as yet, sufficient indirect evidence from reactivity and selectivity correlations with stable metal carbenes (*4, 5*) exist to justify their involvement in catalytic transformations.

Transition metal catalysts that are effective for carbenoid transformations include those of copper(I), palladium(II) or platinum(II), cobalt(II), and rhodium(II) (*I-3, 6-8*), but only copper and rhodium catalysts have been routinely employed.

Copper catalysts have historically been the most widely used, but many of their applications are limited by competing reactions (1). With rhodium catalysts, specifically dirhodium(II) tetrakis(carboxylates), carbenoid transformations have undergone a renaissance in synthetic applications because of the high yields and selectivities that characterize their uses. Rhodium(II) carboxylates (1) are structurally well defined, having D_{2h} symmetry (9-11), with axial coordination sites at which metal carbene formation occurs in reactions with diazo compounds (1). Two limiting structures portray the primary functional characteristics of these dirhodium(II) carbenes (Scheme II): metal carbene 3 and the metal-stabilized carbocation 2, whose inherent stability arises from electron donation through the dirhodium(II) framework (1, 2). In fact, the metal-stabilized carbocation concept for these carbenes explains a broad selection of observations concerning their highly electrophilic character.

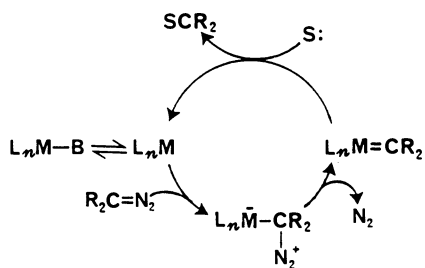
A major advantage of dirhodium(II) catalysts for use in carbenoid reactions results from the electronic influences of their bridging ligands on reactivity and selectivity. In the series, $Rh_2(pfb)_4$ (pfb = perfluorobutyrate), $Rh_2(OAc)_4$ (OAc = acetate), and $Rh_2(acam)_4$ (acam = acetamide), where electron withdrawal by the ligand increases from $Rh_2(acam)_4$ to $Rh_2(pfb)_4$, $Rh_2(pfb)_4$ exhibits the highest reactivity for both metal carbene formation from diazo compounds and metal carbene reactions, and $Rh_2(acam)_4$ has the highest selectivity (12,13). These electronic influences, which are consistent with the description of dirhodium(II) carbene complexes as metal stabilized carbocations, expand the utility of dirhodium(II) catalysts beyond that possible with other transition metal catalysts. Their applications for carbenoid reactions are too numerous to list exhaustively, but several general processes are described in Figure 1. This chapter will focus on the development of chiral dirhodium(II) catalysts that are effective for three of the four transformations.

Chiral Catalysts

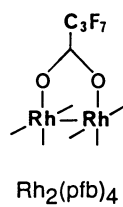
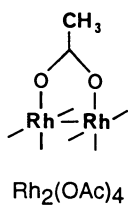
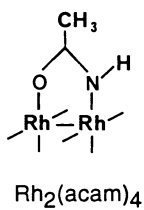
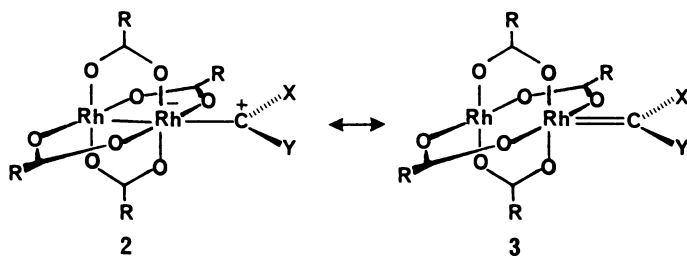
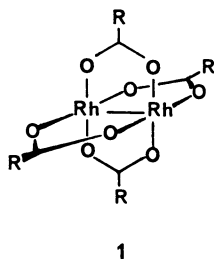
The design and development of chiral catalysts for asymmetric carbenoid transformations have been actively pursued since the first reports by Nozaki of enantioselective cyclopropanation reactions with a copper(II) chelate complex possessing a chiral salicylaldehyde ligand (14,15). Although optical yields of cyclopropane products using the Nozaki catalyst were low (6% ee in reactions of ethyl diazoacetate with styrene), elaboration of the design for this catalytic system by Aratini and coworkers (16-19) provided a copper(II) complex (A-Cu) with which enantioselectivities exceeding 90% ee could be achieved (Figure 2) in selected cases (syntheses of permethrin, cilastatin, and *trans*-chrysanthemic acid) (19-22).

More recently, Pfaltz has reported high enantioselectivities for the cyclopropanation of monosubstituted alkenes and dienes with diazo carbonyl compounds using chiral (semicorrinato)copper complexes (P-Cu) (23-25), and Evans, Masamune, and Pfaltz subsequently discovered exceptional enantioselectivities in intermolecular cyclopropanation reactions with the analogous bis-oxazoline copper complexes (26-28). With the exception of the chiral (camphorquinone dioximato)cobalt(II) catalysts (N-Co) reported by Nakamura and coworkers (29, 30), whose reactivities and selectivities differ considerably from copper catalysts, chiral complexes of metals other than copper have not exhibited similar promise for high optical yields in cyclopropanation reactions (31).

The approach that we have taken for the design of chiral rhodium(II) catalysts is based on the selectivity obtained in the preparation of geometric isomers with a limited number of rhodium(II) carboxamides. Although four different orientations of amide



Scheme I: Catalytic Cycle for Metal Carbene Transformations



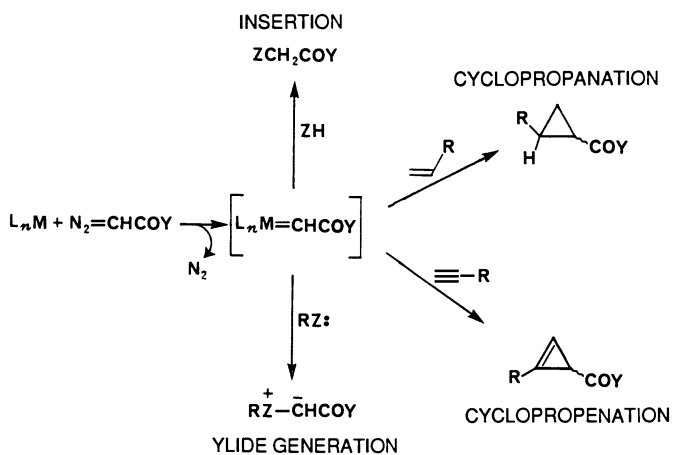
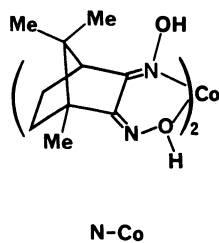
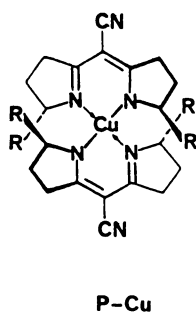
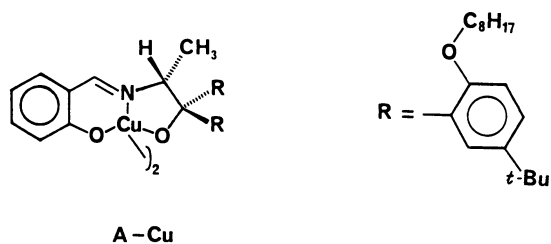


Figure 1. Catalytic Metal Carbene Transformations



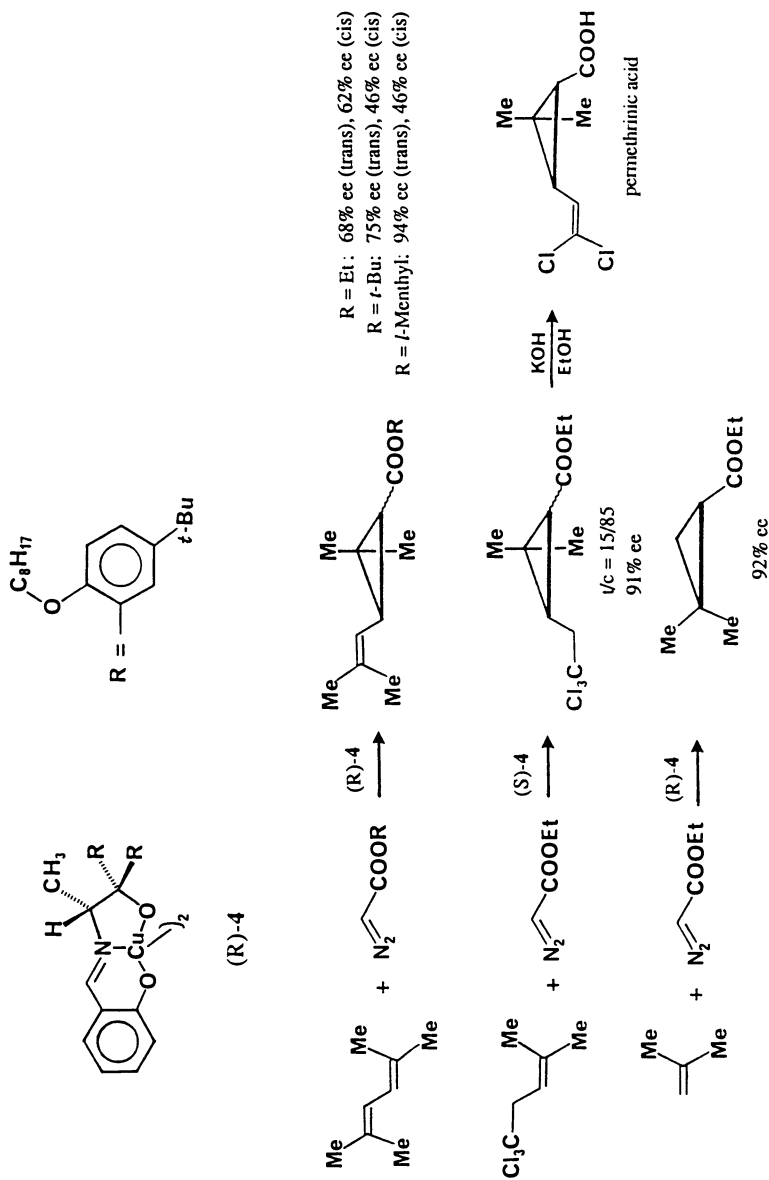


Figure 2. Representative Applications of the Aratani Catalysts for Intermolecular Cyclopropanation

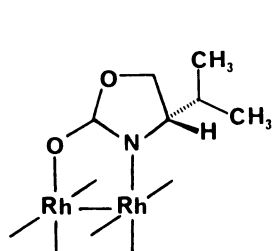
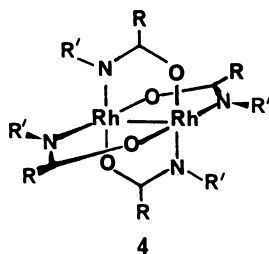
ligands on one face of the dirhodium tetrakis(carboxamide) are conceptually possible, only one (**4**) has been isolated with acetamide or trifluoroacetamide as the bridging ligand (32,33). With chiral amides whose asymmetric center is adjacent to nitrogen, the construction of rhodium(II) carboxamides allows placement of a chiral attachment at nitrogen close to the reactive carbene center. When the bridging amide ligands are positioned such that each rhodium has a pair of nitrogen donor atoms in a *cis* arrangement, the resulting rhodium(II) carboxamide presents an asymmetric environment for the metal stabilized carbene that can be expected to provide substantial facial selectivity in carbenoid transformations.

Chiral catalysts of copper and cobalt have been constructed to effect enantiocontrol in cyclopropanation reactions by limiting access to the carbenoid carbon through steric interactions enforced by substituents of the chiral ligand in close proximity to the reacting carbene-alkene (19, 25, 30). Based on this rationale we prepared a series of chiral dirhodium(II) 4-alkyloxazolidinones, **5-8** (IPOX = isopropylloxazolidinone, BNOX = benzyloxazolidinone [**6** = 4S and **7** = 4R], MPOX = methyl-5-phenyloxazolidinone) in which the chiral center is adjacent to the rhodium-bound nitrogen, and with which only steric interactions emanating from the protruding alkyl substituent should control enantioselectivity.

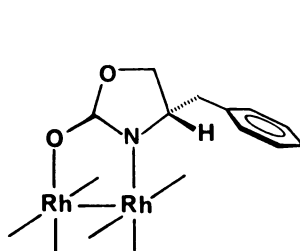
The capabilities of **5-8** for enantioselective cyclopropanation were determined (34) from reactions at room temperature of *d*- and/or *l*-menthyl diazoacetate (MDA) with styrene (Table 1), which allows direct comparison with results from both the Aratani (A-Cu) and Pfaltz (P-Cu) catalysts (19, 24). Cyclopropane product yields ranged from 50 to 75%, which were comparable to those obtained with chiral copper catalysts, but enantiomeric excesses were considerably less than those reported from use of either P-Cu or A-Cu. Furthermore, these reactions were subject to exceptional double diastereoselectivity not previously seen to the same degree with the chiral copper catalysts. Although chiral oxazolidinone ligands proved to be promising, the data in Table 1 suggested that steric interactions alone would not sufficiently enhance enantioselectivities to advance Rh_2L_4^* as an alternative to A-Cu or P-Cu.

An alternative approach to the design of Rh_2L_4^* presented itself in the form of readily accessible chiral 2-pyrrolidone-5-carboxylate ligands (**9**) in which the carboxylate carbonyl group can be viewed to reside above or perpendicular to the "empty" p orbital of the electrophilic carbene. Electronic interaction of the ligand's carboxylate carbonyl group with the carbene's p orbital could be expected to stabilize the bound carbene, orient the carbene substituents into two limiting configurations (10a and 10b), of which one (10a) is more stable, and direct incoming nucleophiles such as alkenes to backside attack on the side of the carbene opposite to the stabilizing carbonyl. An indication of the success of this approach to the design of Rh_2L_4^* can be seen from the enantioselectivities achieved with the use of $\text{Rh}_2(\text{5S-MEPY})_4$ at 1.0 mol % in refluxing CH_2Cl_2 (Table 2). Product yields were similar to those with the chiral dirhodium(II) oxazolidinones, and optical purities similar to those of the Aratani catalysts were obtained (34). The enantiomeric $\text{Rh}_2(\text{5R-MEPY})_4$, which is also readily accessible, gave identical % ee's but opposite chirality in cyclopropanation reactions, and reversed diastereomeric preferences were obtained from reactions with MDA. Since the *trans* isomer has C_2 symmetry, the geometry of the $\text{Rh}_2(\text{MEPY})_4$ catalysts could be established by NMR spectroscopy to be that of the *cis*-isomer **9**.

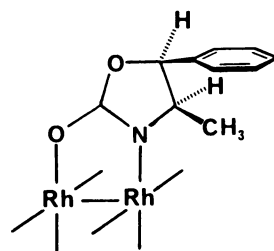
Intramolecular Cyclopropanation with Chiral Rhodium(II) 2-Pyrrolidone-5-carboxylates. Applications of chiral copper and cobalt catalysts, including

 $\text{Rh}_2(4\text{S-IPOX})_4$

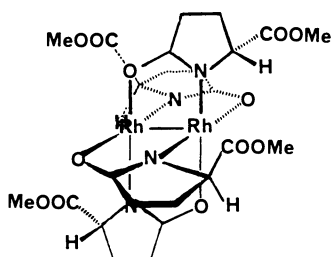
5

 $\text{Rh}_2(4\text{S-BNOX})_4$

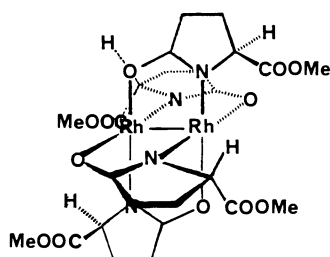
6

 $\text{Rh}_2(4\text{R-MPOX})_4$

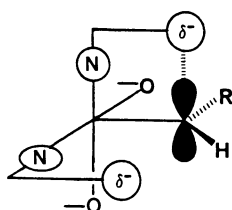
8



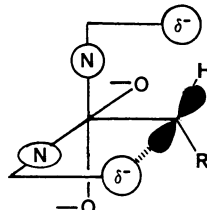
R-9



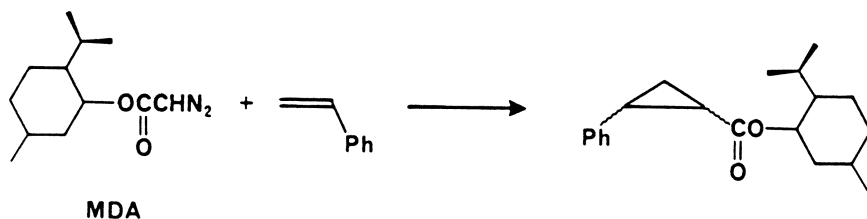
S-9



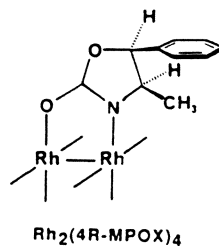
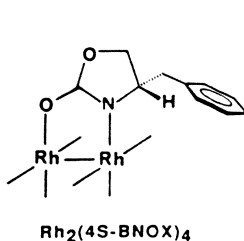
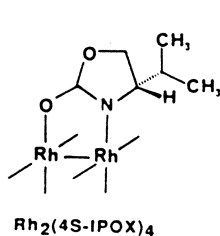
10a



10b

Table 1. Diastereoselectivities for the Cyclopropanation of Styrene by Menthyl Diazoacetate with Chiral Rhodium(II) Oxazolidinone Catalysts

catalyst	MDA	trans:cis	% de trans	% de cis
P-Cu	<i>l</i>	85:15	91 (1 <i>S</i> ,2 <i>S</i>)	90 (1 <i>S</i> ,2 <i>R</i>)
P-Cu	<i>d</i>	82:18	97 (1 <i>S</i> ,2 <i>S</i>)	95 (1 <i>S</i> ,2 <i>R</i>)
Rh ₂ (OAc) ₄	<i>l</i>	68:32	5 (1 <i>R</i> ,2 <i>R</i>)	13 (1 <i>R</i> ,2 <i>S</i>)
Rh ₂ (OAc) ₄	<i>d</i>	55:45	9 (1 <i>S</i> ,2 <i>S</i>)	13 (1 <i>S</i> ,2 <i>R</i>)
Rh ₂ (4 <i>S</i> -IPOX) ₄	<i>l</i>	70:30	34 (1 <i>R</i> ,2 <i>R</i>)	56 (1 <i>R</i> ,2 <i>S</i>)
Rh ₂ (4 <i>S</i> -IPOX) ₄	<i>d</i>	75:25	2 (1 <i>R</i> ,2 <i>R</i>)	4 (1 <i>R</i> ,2 <i>S</i>)
Rh ₂ (4 <i>S</i> -BNOX) ₄	<i>l</i>	61:39	34 (1 <i>R</i> ,2 <i>R</i>)	63 (1 <i>R</i> ,2 <i>S</i>)
Rh ₂ (4 <i>S</i> -BNOX) ₄	<i>d</i>	63:37	4 (1 <i>R</i> ,2 <i>R</i>)	24 (1 <i>R</i> ,2 <i>S</i>)
Rh ₂ (4 <i>R</i> -BNOX) ₄	<i>l</i>	62:38	4 (1 <i>S</i> ,2 <i>S</i>)	25 (1 <i>S</i> ,2 <i>R</i>)
Rh ₂ (4 <i>R</i> -BNOX) ₄	<i>d</i>	67:33	30 (1 <i>S</i> ,2 <i>S</i>)	60 (1 <i>S</i> ,2 <i>R</i>)
Rh ₂ (4 <i>R</i> -MPOX) ₄	<i>l</i>	71:29	4 (1 <i>R</i> ,2 <i>R</i>)	4 (1 <i>R</i> ,2 <i>S</i>)
Rh ₂ (4 <i>R</i> -MPOX) ₄	<i>d</i>	77:23	23 (1 <i>R</i> ,2 <i>R</i>)	20 (1 <i>S</i> ,2 <i>R</i>)



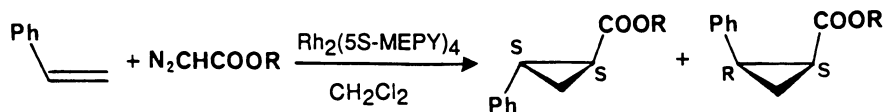
A-Cu, **N-Co**, and **P-Cu** to carbenoid transformations have been limited to intermolecular reactions, for which they remain superior to chiral dirhodium(II) catalysts for intermolecular cyclopropanation reactions. Few examples other than those recently reported by Dauben and coworkers (eq 1) (35) portray the effectiveness of these chiral catalysts for enantioselective intramolecular cyclopropanation reactions, and these examples demonstrate their limitations. However, with $\text{Rh}_2(5\text{S-MEPY})_4$ intramolecular cyclopropanation of 3-methyl-2-buten-1-yl diazoacetate (eq 2) occurs in high yield and with 92% enantiomeric excess (36).

Chiral rhodium(II) oxazolidinones **5-7** were not as effective as $\text{Rh}_2(\text{MEPY})_4$ for enantioselective intramolecular cyclopropanation, even though the steric bulk of their chiral ligand attachments (COOMe versus *i*-Pr or CH_2Ph) are similar. Significantly lower yields and lower enantiomeric excesses resulted from the decomposition of **11** catalyzed by either $\text{Rh}_2(4\text{S-IPOX})_4$, $\text{Rh}_2(4\text{S-BNOX})_4$, or $\text{Rh}_2(4\text{R-BNOX})_4$ (Table 3). In addition, butenolide **12**, the product from carbenium ion addition of the rhodium-stabilized carbenoid to the double bond followed by 1,2-hydrogen migration and dissociation of Rh_2L_4^* (Scheme II), was of considerable importance in reactions performed with **5-7** but was only a minor constituent ($\leq 1\%$) from reactions catalyzed by $\text{Rh}_2(5\text{S-MEPY})_4$. This difference can be attributed to the ability of the carboxylate substituents to stabilize the carbocation form of the intermediate metal carbene.

The directional orientation of chiral ligand substituents on $\text{Rh}_2(5\text{S-MEPY})_4$ establishes relatively unimpeded pathways for intramolecular cyclization whose preferred route is determined from the relative stability of two limiting configurations (**13a** and **13b**). According to this model *Z*-olefins should afford higher enantioselectivities than do *E*-olefins. The exceptional capabilities of $\text{Rh}_2(5\text{S-MEPY})_4$ and $\text{Rh}_2(5\text{R-MEPY})_4$ for asymmetric induction in intramolecular cyclopropanation reactions are evident in the results obtained with a series of allyl diazoacetates (eq 3). The % ee's determined for **14b-e** by the use of chiral NMR shift reagent showed none of the corresponding enantiomers; since the limit of detection by this method is generally considered to be 97:3, the % ee's are denoted as ≥ 94 even though only one enantiomer was detected. Identical yields and % ee's of these products were obtained using $\text{Rh}_2(5\text{R-MEPY})_4$ but, of course, having opposite product chirality.

Intermolecular Cyclopropanation of Alkynes. Functionalized cyclopropenes are viable synthetic intermediates whose applications (37, 38), which extend to a wide variety of carbocyclic and heterocyclic systems, have been largely ignored because of the relative inaccessibility of these strained compounds. However, recent advances in the synthesis of cyclopropenes, particularly from rhodium(II) carboxylate catalyzed decomposition of diazo esters in the presence of alkynes (39-42), has made available an array of stable 3-cyclopropenecarboxylate esters. Previously, copper catalysts provided low to moderate yields of cyclopropenes in reactions of diazo esters with disubstituted acetylenes (43, 44), but the higher temperatures required for these carbenoid reactions often led to thermal or catalytic ring opening and products derived from vinylcarbene intermediates (45-48). Potential uses of the cyclopropene ring as a template in enantiocontrolled synthesis have been recognized, but until now synthetic chiral cyclopropene derivatives have been accessible only through resolution (49).

Chiral rhodium(II) carboxamides are exceptional catalysts for highly enantioselective intermolecular cyclopropanation reactions (50). With ethyl diazoacetate and a series of alkynes, use of dirhodium(II) tetrakis[methyl 2-pyrrolidone-5-(*R*)-carboxylate], $\text{Rh}_2(5\text{R-MEPY})_4$, in catalytic amounts (≤ 1.0 mol %) results in the formation of ethyl cyclopropene-3-carboxylates (eq 4) with enantiomeric excesses

Table 2. Diastereoselectivities for the Cyclopropanation of Styrene by Representative Diazo Esters with $\text{Rh}_2(5\text{S-MEPY})_4$ Catalyst

Diazo Compound	trans:cis	% de trans	% de cis
ODA	73:27	67	83
<i>t</i> -MDA	67:33	56	79
<i>d</i> -MDA	67:33	48	86
<i>t</i> -BDA	66:34	52	66
EDA	54:46	58	33

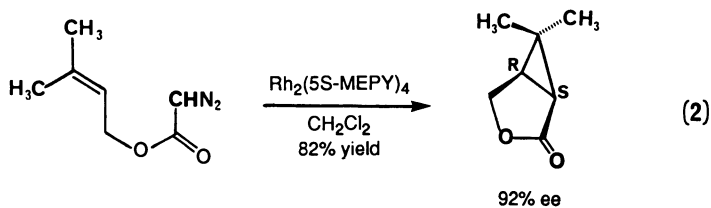
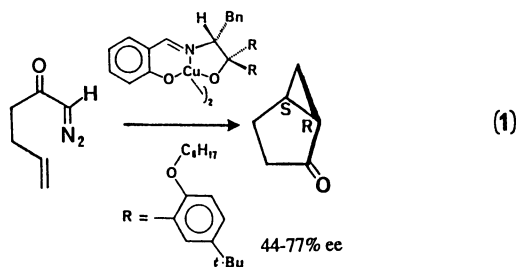
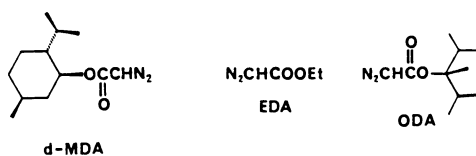
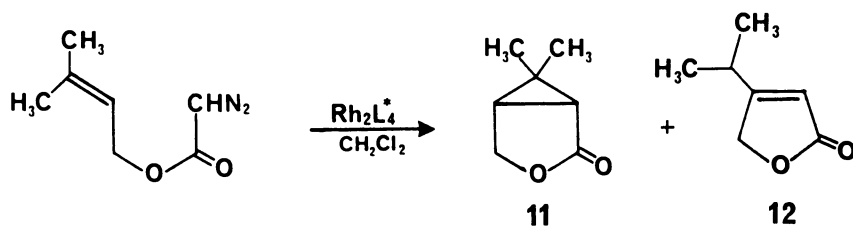
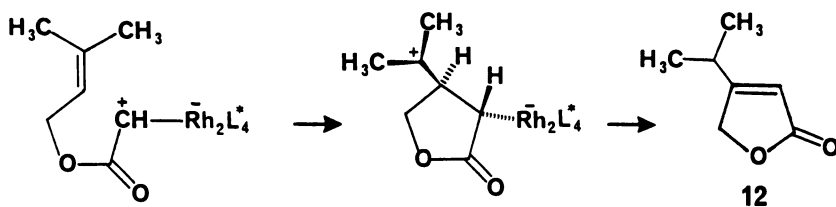
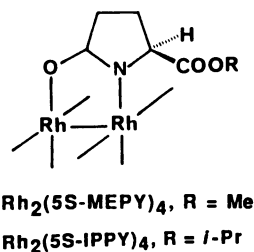
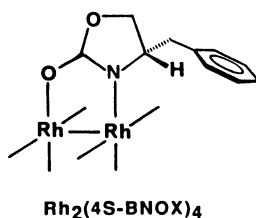
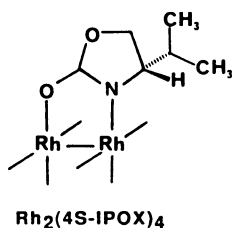


Table 3. Intramolecular Reactions of 3-Methyl-2-buten-1-yl Diazoacetate Catalyzed by Chiral Dirhodium(II) Carboxamide Catalysts

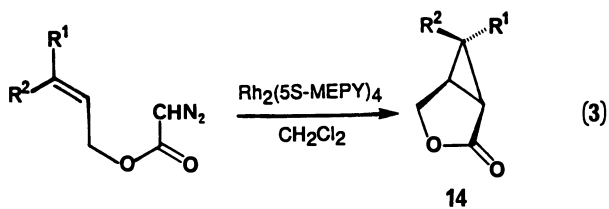
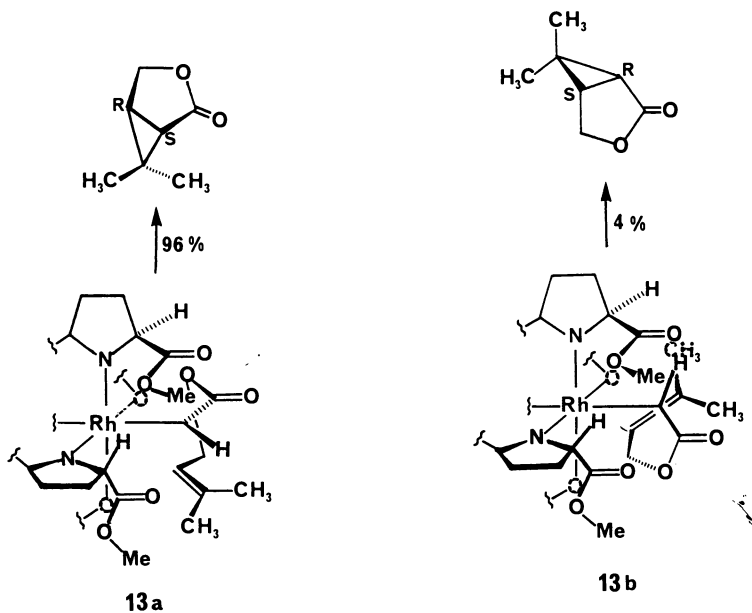


catalyst	yield, %		% ee 11
	11	12	
$\text{Rh}_2(4\text{S-IPOX})_4$	44	5	44 (1R,5S)
$\text{Rh}_2(4\text{S-BNOX})_4$	52	11	54 (1R,5S)
$\text{Rh}_2(4\text{R-BNOX})_4$	50	12	56 (1S,5R)
$\text{Rh}_2(5\text{S-MEPY})_4$	82	<1	92 (1S,5R)
$\text{Rh}_2(5\text{S-IPPY})_4$	83	<1	89 (1S,5R)



$\text{Rh}_2(4\text{S-BNOX})_4$	12%
$\text{Rh}_2(4\text{R-BNOX})_4$	11%
$\text{Rh}_2(4\text{S-IPOX})_4$	5%
$\text{Rh}_2(5\text{S-MEPY})_4$	< 1%

Scheme II: Butenolide Formation in Catalytic Intramolecular Cyclopropanation



	R ¹	R ²	% yield	% ee		R ¹	R ²	% yield	% ee
(a)	H	H	74	88	(f)	CH ₃	CH ₃	82	92
(b)	H	Ph	45	≥ 94	(g)	Ph	H	59	65
(c)	H	CH ₂ CH ₃	88	≥ 94	(h)	CH ₂ CH ₂ CH ₃	H	74	75
(d)	H	CH ₂ Ph	80	≥ 94	(i)	H	C ₆ H ₁₁ CH ₂	45	68
(e)	H	Sn(<i>n</i> -Bu) ₃	78	≥ 94	(j)	H	(CH ₃) ₂ CHCH ₂	29	72

ranging from 54 to 69% in good yields (70-85%). Virtually identical results, except in the opposite stereocontrol sense, are obtained with the use of $\text{Rh}_2(5S\text{-MEPY})_4$. With *d*-menthyl diazoacetate and the same series of alkynes, selectivities as high as 98% de have been achieved (eq 5). Enantioselectivities increase with the steric size of the diazo ester, and the polarity of the alkyne substituent also appears to influence enantiocontrol. That % ee's of cyclopropenes from reactions with propargyl methyl ether are higher than those from reactions with 1-hexyne and 3,3-dimethyl-1-butyne suggest that polar interactions of the alkyne with ligands of the catalyst may be operative. Carbene dimers and azine are the principal competing reactions, but dimer formation can be minimized by using higher alkene:diazo ester ratios and by decreasing the rate of addition.

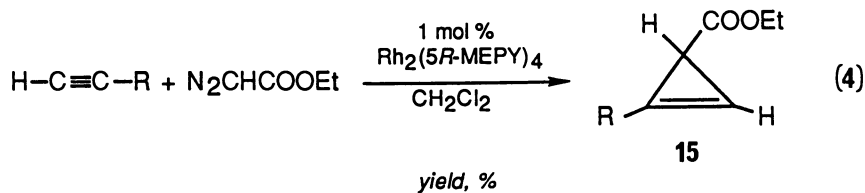
The use of $\text{Rh}_2(5R\text{-MEPY})_4$ and $\text{Rh}_2(5S\text{-MEPY})_4$ for reactions with menthyl diazoacetates (MDA) also produces an enormous double diastereoselection not previously observed to the same degree in cyclopropanation reactions. With methyl propargyl ether, for example, $\text{Rh}_2(5R\text{-MEPY})_4$ catalyzed reactions of *d*-MDA yield **16** ($\text{R} = \text{CH}_3\text{OCH}_2$) in 98% diastereomeric excess (de), but *l*-MDA produces its diastereoisomer in only 40% de; with $\text{Rh}_2(5S\text{-MEPY})_4$, *l*-MDA gives the higher de (98%) and *d*-MDA gives the lower de (43%). Similar results are obtained from reactions of MDA with 1-hexyne and 3,3-dimethyl-1-propyne. The diazocarboxylate substituent obviously plays a critical role in establishing the more effective carbene orientation for addition to the alkyne.

Alternative rhodium(II) carboxamide catalysts derived from 4-(*R*)-benzyloxazolidinone (4*R*-BNOXH) and 4-(*S*)-isopropylloxazolidinone (4*S*-IPOXH) provided only a fraction of the enantioselection obtained with $\text{Rh}_2(\text{MEPY})_4$ catalysts. Whereas cyclopropanation of 1-hexyne with ethyl diazoacetate in the presence of $\text{Rh}_2(5R\text{-MEPY})_4$ resulted in **15** (eq 4, $\text{R} = n\text{-Bu}$) with 54% ee, $\text{Rh}_2(4R\text{-BNOX})_4$ gave the same compound in 5% ee, and $\text{Rh}_2(4S\text{-IPOX})_4$ provided only 6% ee.

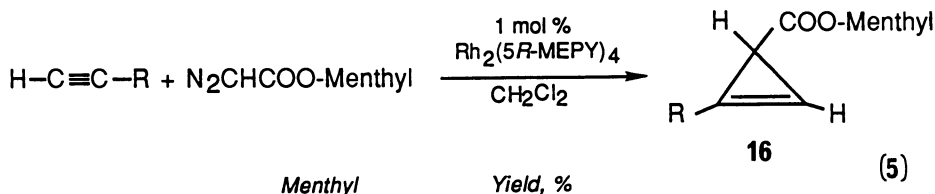
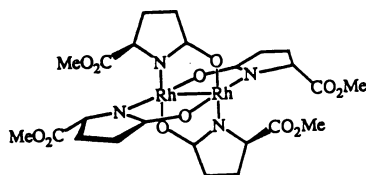
Enantiocontrol in cyclopropanation reactions is obviously highly dependent on the carboxylate substituent of the dirhodium(II) carboxamide ligand and on the carboxylate substituent of the intermediate carbene. High enantioselectivity is achieved with the use of $\text{Rh}_2(\text{MEPY})_4$ catalysts and menthyl diazoacetates in reactions with 1-alkynes, and further enhancement in % ee can be anticipated.

Intramolecular Carbon-Hydrogen Insertion. The advantages of rhodium(II) catalysts for carbenoid transformations are nowhere more evident than with carbon-hydrogen insertion reactions. Exceptional regio- and diastereocontrol has been observed for $\text{Rh}_2(\text{OAc})_4$ catalyzed transformations of a broad selection of diazo-ketones, α -diazo- β -ketoesters, α -diazo- β -keto-sulfones and -phosphonates which yield cyclopentanone derivatives in moderate to good yields (51-54). In contrast, poor yields and low regioselectivities characterize the corresponding copper catalyzed reactions. Applications of dirhodium(II) catalysts for C-H insertion reactions have even been extended to the synthesis of γ -lactones (55), 3(2*H*)-furanones (56,57), β -lactones (58), and β -lactams (59,60).

The suitability of $\text{Rh}_2(5S\text{-MEPY})_4$ and $\text{Rh}_2(5R\text{-MEPY})_4$ for enantioselective intramolecular C-H insertions is exemplified in the results from preliminary experiments with a series of 2-alkoxyethyl diazoacetates and 2-phenethyl diazoacetate (61). Addition of diazo ester **17** to a solution of the chiral $\text{Rh}_2(\text{MEPY})_4$ catalyst (0.5-1.0 mol %) in refluxing anhydrous CH_2Cl_2 provided the corresponding 3-substituted γ -butyrolactones **18** (eq 6) in moderate to high yields and with consistently high enantioselectivities. The exceptional correspondence in enantioselection between



R = CH ₃ OCH ₂	73	69% ee
CH ₃ (CH ₂) ₃	70	54% ee
(CH ₃) ₃ C	85	57% ee

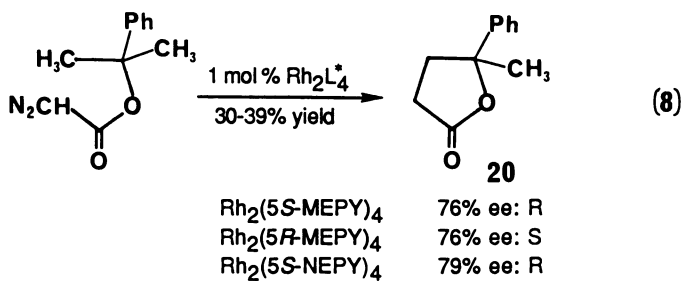
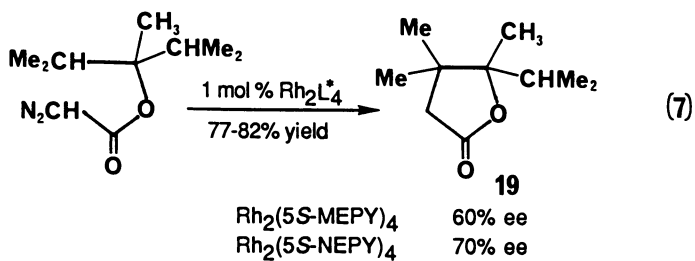
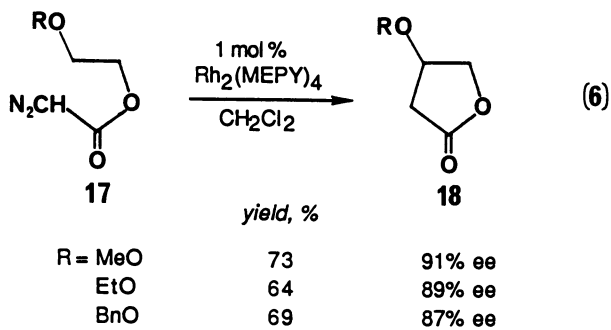


R = CH ₃ OCH ₂	<i>d</i>	43	98% ee
	<i>l</i>	45	43% ee
CH ₃ (CH ₂) ₄	<i>d</i>	46	82% ee
	<i>l</i>	46	20% ee
(CH ₃) ₃ C	<i>d</i>	51	77% ee
	<i>l</i>	50	56% ee

d-Menthyl = (+)-(1*S*,2*R*,5*S*)-2-isopropyl-5-methyl-1-cyclohexyl

enantiomeric dirhodium(II) catalysts defines their versatility. For comparison, chiral dirhodium(II) carboxylates, whose architecture places the chiral center perpendicular to the rhodium-carbene bond axis, have recently been reported to catalyze intramolecular C-H insertion reactions of α -diazo- β -keto esters (62) and a α -diazo- β -keto sulfone (63) to form 3-substituted cyclopentanone derivatives with enantiomeric excesses ranging from 10 to 46%.

Applications with diazo esters that undergo insertion into a C-H bond vicinal to the incipient chiral center demonstrated further advantages of this catalytic methodology for asymmetric synthesis. 2,3,4-Trimethyl-2-pentyl diazoacetate formed lactone **19** exclusively (eq 7) in 60% ee (77% isolated yield) with Rh₂(5*S*-MEPY)₄ and Rh₂(5*R*-MEPY)₄ and in 70% ee with the neopentyl ester analog, Rh₂(5*S*-NEPY)₄ (82% isolated yield). Cumyl diazoacetate underwent insertion into the normally disfavored 1° C-H bond (eq 8) to yield lactone **20** in 76% ee (30% isolated yield) with



$\text{Rh}_2(5S\text{-MEPY})_4$ (predominantly (*R*)-**20**) and $\text{Rh}_2(5R\text{-MEPY})_4$ (predominantly (*S*)-**20**) and in 79% ee (39% isolated yield) with $\text{Rh}_2(5S\text{-NEPY})_4$ (predominantly (*R*)-**20**).

The high degree of enantiocontrol in C-H insertion reactions with such a diversity of diazoacetates suggests unique advantages for chiral dirhodium(II) catalysts derived from pyrrolidone-5-carboxylates. Both lactone enantiomers are accessible from a single diazo ester, and the absence of by-products of similar composition allows convenient product isolation.

Acknowledgments. The financial support to conduct research on chiral dirhodium(II) carboxamides from the National Science Foundation and National Institutes of Health is gratefully acknowledged.

Literature Cited

- (1) Doyle, M. P. *Chem. Rev.* **1986**, *86*, 919.
- (2) Doyle, M. P. *Acc. Chem. Res.* **1986**, *19*, 348.
- (3) Maas, G. *Topics in Current Chem.* **1987**, *137*, 75.
- (4) Doyle, M. P.; Griffin, J. H.; Bagheri, V.; Dorow, R. L. *Organometal.* **1984**, *3*, 53.
- (5) Doyle, M. P.; Griffin, J. H.; Conceição, J. *J. Chem. Soc., Chem. Commun.* **1985**, 328.
- (6) Tomilov, Y. V.; Kostitsyn, A. B.; Shulishov, E. V.; Nefedov, O. M. *Synthesis* **1990**, 246.
- (7) Tamblyn, W. H.; Hoffmann, S. R.; Doyle, M. P. *J. Organometal. Chem.* **1981**, *216*, C64.
- (8) Hanks, T. W.; Jennings, P. W. *J. Am. Chem. Soc.* **1987**, *109*, 5023.
- (9) Cotton, F. A.; Walton, R. A. *Multiple Bonds Between Metal Atoms*; Wiley: New York, NY, 1982; Chapter 7.
- (10) Felthouse, T. R. *Prog. Inorg. Chem.* **1982**, *29*, 73.
- (11) Boyar, E. B.; Robinson, S. D. *Coord. Chem. Rev.* **1983**, *50*, 109.
- (12) Doyle, M. P.; Bagheri, V.; Wandless, T. J.; Harn, N. K.; Brinker, D. A.; Eagle, C. T.; Loh, K.-L. *J. Am. Chem. Soc.* **1990**, *112*, 1906.
- (13) Doyle, M. P.; Bagheri, V.; Pearson, M. M.; Edwards, J. D. *Tetrahedron Lett.* **1989**, *30*, 7001.
- (14) Nozaki, H.; Monuti, S.; Takaya, H.; Noyori, R. *Tetrahedron Lett.* **1966**, 5239.
- (15) Nozaki, H.; Takaya, H.; Moriuti, S.; Noyori, R. *Tetrahedron* **1968**, *24*, 3655.
- (16) Aratani, T.; Yoneyoshi, Y.; Nagase, T. *Tetrahedron Lett.* **1975**, 1707.
- (17) Aratani, T.; Yoneyoshi, Y.; Nagase, T. *Ibid.* **1977**, 2599.
- (18) Aratani, T.; Yoneyoshi, Y.; Nagase, T. *Ibid.* **1982**, *23*, 685.
- (19) Aratani, T. *Pure Appl. Chem.* **1985**, *57*, 1839.
- (20) Baldwin, J. E.; Carter, C. G. *J. Am. Chem.* **1982**, *104*, 1363.
- (21) Kunz, T.; Reissig, H.-U. *Tetrahedron Lett.* **1989**, *30*, 2079.
- (22) Becalski, A.; Cullen, W. R.; Fryzuk, M. D.; Herb, G.; James, B. R. Kutney, J. P.; Piotrowska, K.; Tapiolas, D. *Can. J. Chem.* **1988**, *66*, 3108.
- (23) Fritschi, H.; Leutenegger, U.; Siegmann, K.; Pfaltz, A.; Keller, W.; Kratky, Ch. *Helv. Chim. Acta* **1988**, *71*, 1541.
- (24) Fritschi, H.; Leutenegger, U.; Pfaltz, A. *Ibid.* **1988**, *71*, 1553.

- (25) Pfaltz, A. *Modern Synthetic Methods* **1989**, 5, 199.
- (26) Evans, D. A.; Woerpel, K. A.; Hinman, M. M. *J. Am. Chem. Soc.* **1991**, 113, 726.
- (27) Lowenthal, R. E.; Abiko, A.; Masamune, S. *Tetrahedron Lett.* **1990**, 31, 6005.
- (28) Müller, D.; Umbricht, G.; Weber, B.; Pfaltz, A. *Helv. Chim. Acta* **1991**, 74, 232.
- (29) Nakamura, A.; Konishi, A.; Tsujitani, R.; Kudo, M.; Otsuka, S. *J. Am. Chem. Soc.* **1978**, 100, 3449.
- (30) Nakamura, A.; Konishi, A.; Tatsuno, Y.; Otsuko, S. *J. Am. Chem. Soc.* **1978**, 100, 3443, 6544.
- (31) Salaün, J. *Chem. Rev.* **1989**, 89, 1247.
- (32) Ahsan, M. Q.; Bernal, I.; Bear, J. L. *Inorg. Chem.* **1986**, 25, 260.
- (33) Dennis, A. M.; Korp, J. D.; Bernal, I.; Howard, R. A.; Bear, J. L. *Inorg. Chem.* **1983**, 22, 1522.
- (34) Doyle, M. P.; Brandes, B. D.; Kazala, A. P.; Pieters, R. J.; Jarstfer, M. B.; Watkins, L. M.; Eagle, C. T. *Tetrahedron Lett.* **1990**, 31, 6613.
- (35) Dauben, W. G.; Hendricks, R. T.; Luzzio, M. J.; Ng, H. P. *Tetrahedron Lett.* **1990**, 31, 6969.
- (36) Doyle, M. P.; Pieters, R. J.; Martin, S. F.; Austin, R. E.; Oalman, C. J.; Müller, P. *J. Am. Chem. Soc.* **1991**, 113, 1423.
- (37) Baird, M. S. *Top. Curr. Chem.* **1988**, 144, 137.
- (38) Binger, P.; Buch, H. M. *Top. Curr. Chem.* **1986**, 135, 77.
- (39) Protopopova, M. N.; Shapiro, E. A. *Russ. Chem. Rev.* **1989**, 58, 667.
- (40) Petiniot, N.; Anciaux, A. J.; Noels, A. F.; Hubert, A. J.; Teyssie, P. *Tetrahedron Lett.* **1978**, 1239.
- (41) Dowd, P.; Schappert, R.; Garnver, P.; Go, C. L. *J. Org. Chem.* **1985**, 50, 44.
- (42) Shapiro, E. A.; Romanova, T. N.; Dolgii, I. E.; Nefedov, O. M. *Izv. Akad. Nauk SSSR, Ser. Khim.* **1984**, 2535.
- (43) Shapiro, E. A.; Lun'kova, G. V.; Nefedov, A. O.; Dolgiii, I. E.; Nefedov, O. M. *Izv. Akad. Nauk SSR, Ser. Khim.* **1981**, 2535.
- (44) Maier, G.; Hoppe, M.; Reisenauer, H. P.; Kruger, C. *Angew. Chem. Int. Ed. Engl.* **1982**, 21, 437.
- (45) Wenkert, E.; Alonso, M. E.; Buckwalter, B. L.; Sanchez, E. L. *J. Am. Chem. Soc.* **1983**, 105, 2021.
- (46) Müller, P.; Pautex, N.; Doyle, M. P.; Bagheri, V. *Helv. Chim. Acta* **1990**, 73, 1233.
- (47) Padwa, A.; Chiacchio, U.; Garreau, Y.; Kassir, J. M.; Krumpe, K. E.; Schoffstall, A. M. *J. Org. Chem.* **1990**, 55, 414.
- (48) Hoye, T. R.; Dinsmore, C. J.; Johnson, D. S.; Korkowski, P. F.; *J. Org. Chem.* **1990**, 55, 4519.
- (49) Pincock, J. A.; Moutsokapas, A. A. *Can. J. Chem.* **1977**, 55, 979.
- (50) Protopopova, M. N.; Doyle, M. P.; Müller, P.; Ene, D., *J. Am. Chem. Soc.* **1992**, 114, 2755.
- (51) Taber, D. F.; Ruckle Jr., R. E. *J. Am. Chem. Soc.* **1986**, 108, 7686.
- (52) Wenkert, E.; Davis, L. L.; Mylari, B. L.; Solomon, M. F.; da Silva, R. R.; Shulman, S.; Warnet, R. J.; Ceccherelli, P.; Curini, M.; Pellicciari, R. *J. Org. Chem.* **1982**, 47, 3242.

- (53) Monteiro, H. J. *Tetrahedron Lett.* **1987**, *28*, 3459.
- (54) Corbel, B.; Hernot, D.; Haelters, J.-P.; Sturtz, G. *Tetrahedron Lett.* **1987**, *28*, 6605.
- (55) Doyle, M. P.; Bagheri, V.; Pearson, M. M.; Edwards, J. D. *Tetrahedron Lett.*, **1989**, *30*, 7001.
- (56) Adams, J.; Poupart, M.-A.; Grenier, L. *Tetrahedron Lett.* **1989**, *30*, 1753.
- (57) Adams, J.; Poupart, M.-A.; Grenier, L.; Schaller, C.; Quimet, N.; Frenette, R. *Tetrahedron Lett.* **1989**, *30*, 1749.
- (58) Lee, E.; Jung, K. W.; Kim, Y. S. *Tetrahedron Lett.* **1990**, *31*, 1023.
- (59) Doyle, M. P.; Taunton, J.; Pho, H. Q. *Tetrahedron Lett.* **1989**, *30*, 5397.
- (60) Doyle, M. P.; Shanklin, M. S.; Oon, S.-M.; Pho, H. Q.; Veal, W. R. *J. Org. Chem.* **1988**, *53*, 3384.
- (61) Doyle, M. P.; van Oeveren, A.; Westrum, L. J.; Protopopova, M. N.; Clayton Jr., T. W. *J. Am. Chem. Soc.* **1991**, *113*, 8982.
- (62) Hashimoto, S.; Watanabe, N.; Ikegami, S. *Tetrahedron Lett.* **1990**, *31*, 5173.
- (63) Kennedy, M.; McKervey, M. A.; Maguire, A. R.; Roos, G. H. P. *J. Chem. Soc., Chem. Commun.* **1990**, 361.

RECEIVED September 1, 1992

Chapter 5

Discrete Chiral Rhodium Phosphine Complexes as Catalysts for Asymmetric Hydrosilation of Ketones

T. E. Waldman, G. Schaefer, and D. P. Riley

Monsanto Corporate Research, Monsanto Company, 800 North Lindbergh Boulevard, St. Louis, MO 63167

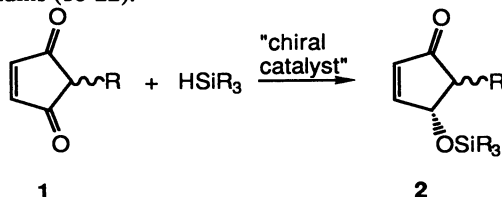
The synthesis of discrete, well-characterized rhodium(I) complexes containing chiral phosphine ligands and their utility as asymmetric hydrosilation catalysts for ketones is described. Electron and ligand deficient cationic Rh(I) complexes of the type, $[\text{Rh}_2(\text{di-phosphine})_2]^{2+}$ are excellent catalysts for the asymmetric hydrosilation of non-enolizable ketones using trisubstituted silanes. Such cationic Rh(I) complexes are particularly useful for the 1,2-monohydrosilation of cyclopentene-1,4-dione (CPDK) generating chiral siloxycyclopentenone derivatives with optical yields approaching 70% under optimal conditions. With enolizable ketones these Lewis acidic, ligand deficient catalysts do not function as catalysts, but promote the enolization of the ketone and deactivate via trimerization to form cationic complexes of the type $[\text{Rh}_3(\text{diphosphine})_3(\mu_3\text{-O-enolate})_2]^+$.

Extremely high activity catalysts for the selective generic ketone 1,2-hydrosilation using diarylsilanes were developed by moderating the Lewis acidity of the $[\text{Rh}_2(\text{diphosphine})_2]^{2+}$ ligand deficient catalysts with the addition of monodentate phosphines to form air-stable $[\text{Rh}(\text{diphosphine})(\text{monophosphine})_2]^+$ complexes. When the monophosphine is sterically demanding the fastest rates are achieved; e.g., with menthyl-diphenylphosphine (MDP) or neomenthyl-diphenylphosphine (NMDP) the turnover numbers based on initial rates exceed $10^5/\text{hr}$. The complex with (*S,S*)-Binap and either MDP or NMDP also afford the highest optical yields for the hydrosilation of simple model ketones with optical yields exceeding 70% under unoptimized conditions. The utility of these two new classes of well-defined rhodium complexes is demonstrated here and the probable mechanism of these catalysts are discussed.

The catalytic asymmetric hydrosilation of a prochiral ketone to the corresponding chiral silyl ether followed by a mild hydrolysis is in principle an attractive route for the preparation of chiral alcohols that has the advantage that it would not require high hydrogen pressure to effect the reduction (1-6). Despite the synthetic potential only limited application of this technique to the synthesis of complex organic molecules has been made (7-9). This is in part due to the relatively low optical

yields that have been generally obtained (10-15). Another major factor that limits the commercial attractiveness of such technology is that virtually all the catalyst systems reported to date have relied upon generating the active catalyst species in solution using a convenient source of active catalytic metal (most generally $\{\text{Rh}(\text{diolen})\text{Cl}\}_2$) and a large excess of a chiral chelating ligand. Such systems are invariably of low catalytic activity due to the large excess of excellent chelating ligand and they present a very unsatisfactory situation with regard to catalyst recycle and the separation of catalyst and excess expensive ligand from the product. For these reasons we have developed catalyst systems that are based on well-defined and characterized rhodium/ phosphine complexes which contain no excess phosphine ligand. These complexes are of two types: a) so-called "ligand deficient" rhodium complexes where the P:Rh ratio is 2 and the complexes are dimeric in non-coordinating solvents, $\{\text{Rh}(\text{P}_2)\}_2^{2+}$ (16, 17); and b) and tetraphosphine $[\text{Rh}(\text{P}_2)(\text{P})_2]^+$ complexes.

An important potential target of asymmetric hydrosilation catalysis is to the reduction of the cyclopenten-1,4-diones, **1**, producing the 4-silyloxycyclopentenones, **2**, which are key intermediates in the synthesis of single-isomer prostaglandins (18-22).



The diketones, **1**, represent an unusual class of ketone substrates in that they will not enolize. For example, **1** ($\text{R}=\text{H}$), has been studied by DePuy, et. al. and is very acidic, $\text{pH}_a \sim 6$, but the anion is localized on the carbon (23,24). Molecules such as **1** are in fact unstable to base undergoing an anionic polymerization. When rhodium (phosphine) catalysts prepared according to literature methods (25-31) were employed using excess chiral ligand and H_2SiPh_2 , only 1,4-addition to **1** ($\text{R}=\text{H}$) was observed and when trisubstituted silanes were employed no reactions occur even at 60°C after several days. The failure of the trisubstituted silanes to react even at elevated temperature was ascribed to the presence of an excess of chelating phosphine ligand which effectively blocks the available coordination sites on Rh effectively "poisoning" the catalyst. To circumvent this we developed the "ligand deficient" catalysts of type a) described above in which the rhodium has only two bound phosphine atoms (from the chelating phosphine). These complexes have been characterized previously and are dimeric in the absence of any additional ligands, with the phenyl rings of one phosphine bridging to the adjacent Rh center and π -binding in an η_6 -mode (16,17). These complexes in non-coordinating solvents serve as very efficient catalysts for the hydrosilation of the diketone substrates of structure **1** with the highest activities ever achieved for the asymmetric hydrosilation of ketones using trisubstituted silanes. The reactivity of these catalysts with a variety of silanes and phosphine-rhodium combinations are reported here and preliminary mechanistic studies are described. In addition, we have discovered that these very Lewis acidic Rh complexes will not hydrosilate enolizable ketones due to the formation of stable Rh(I)enolate trimers. This chemistry is also described in detail. (See Figure 1.)

To generate active, well-defined Rh catalysts for the generic hydrosilation of ketones we have synthesized a new class of Rh(I) complexes (type (b) above) which are synthesized by addition of two additional moles of Phosphine/Rh to the

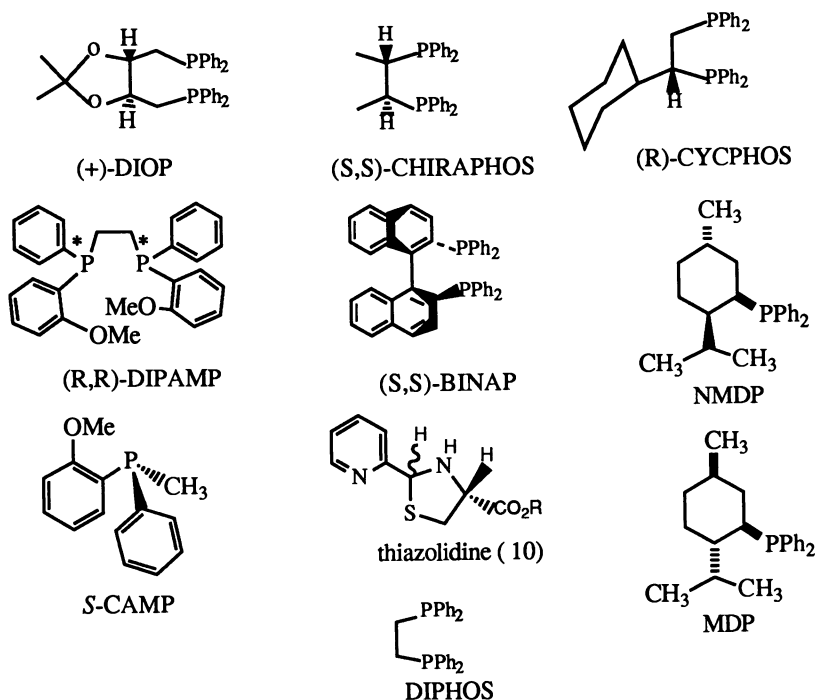


Figure 1. List of ligands used in this work.

{Rh(P₂)}₂²⁺ dimers. The new [Rh(P₂)(P)₂]⁺ complexes can be isolated as their PF₆⁻ complexes. These Rh(I) complexes are air-stable in the solid state and serve as extremely active and selective (1,2- vs. 1,4-hydrosilation) asymmetric hydrosilation catalysts for the reduction of ketones with disubstituted silanes.

Experimental

Materials. (Bicyclo[2.2.1]hepta-2,5-diene) rhodium(I) chloride dimer and silver hexafluorophosphate were purchased from Strem Chemical; the rhodium complex was recrystallized from acetone prior to use. All silanes (Aldrich) were distilled under a nitrogen atmosphere, freeze-thaw degassed and stored under a nitrogen atmosphere. 4-cyclopentene-1,3-dione (CPDK) from Aldrich was recrystallized from diethyl ether and stored in the dark under a nitrogen atmosphere at -40°C. All solvents were distilled under nitrogen from appropriate drying agents immediately prior to use.

Catalyst Preparation. The "ligand deficient" rhodium(I) dimer dications (e.g. [(DIPHOS)₂Rh₂](PF₆)₂), were prepared according to a slight modification of the literature procedure (16,17). Yields of greater than 85% were obtained in all cases. The cationic rhodium(I) tetra(phosphine) complexes were prepared by adding stoichiometric amounts of the desired monophosphine to a methanolic solution of the "ligand deficient" dimer. Removal of the solvent *in vacuo*, followed by recrystallization of the resulting solids from CH₂Cl₂/Et₂O gave the air-stable rhodium(I) tetra(phosphine) complexes in nearly quantitative yields. Representative

analytical data for $[\text{Rh}(\text{S,S-Chiraphos})(\text{PEt}_3)_2](\text{PF}_6)$, **5**: ^1H NMR (CD_2Cl_2) δ 8.15 (broad m, 4H, Ph); 7.83 (broad m, 8H, ph); 7.51 (broad m, 8H, Ph); 1.73 (broad s, 2H); 1.44 (broad q, 12H, $J_{\text{C-H}} = 11$ Hz, PCH_2CH_3); 0.82 (m, 24H, PCH_2CH_3 and CH_3 -chiraphos). ^{31}P NMR (CD_2Cl_2) δ 60.01 (d of d, 2P, $J_{\text{Rh-P}} = 197$ Hz, $J_{\text{P-P}} = 52$ Hz, chiraphos); 9.07 (d of d, 2P, $J_{\text{Rh-P}} = 195$ Hz, $J_{\text{P-P}} = 59$ Hz, PEt_3) Note: Numerous hyperfine couplings are present in the ^{31}P spectrum. Elemental Analysis calculated for $\text{C}_{40}\text{H}_{58}\text{F}_6\text{P}_3\text{Rh}$, calculated(found): C, 52.76(52.54); H, 6.42(6.00); P, 17.01(17.24).

Hydrosilylation of CPDK. Hydrosilylation reactions involving CPDK were carried out under an inert atmosphere as follows: CPDK (0.25 g, 2.6 mmol) and the desired rhodium(I) catalyst (100:1 mol ratio CPDK:Rh) were dissolved in five mL of CH_2Cl_2 and rapid stirring was initiated. Dropwise addition of the silane (1:1 mol ratio CPDK:silane) caused an immediate color change from orange-red to pale yellow and, in the case of disubstituted silanes an exothermic reaction occurs causing the solvent to boil vigorously if the addition is not slow and the solution cooled. Reactions with disubstituted silanes were complete within minutes whereas reactions involving trisubstituted silanes required up to 15 hr for completion. Removal of the solvent *in vacuo* followed by flash column chromatography on neutral alumina afforded the products as pale yellow liquids which were characterized according to standard procedures (elemental analysis or high resolution mass spectrometry and ^1H and ^{13}C NMR).

Hydrosilylation of Generic Ketones. All other hydrosilylation reactions were performed in a similar fashion to that stated previously. Thus, the desired ketone and catalyst (5000:1 mol ratio ketone:catalyst) were dissolved in CH_2Cl_2 and a stoichiometric amount of the appropriate disubstituted silane was added to the rapidly stirred solution. After addition of the silane, stirring was continued for two hours at room temperature. Evaporation of the solvent and hydrolysis of the resulting silyl ether in 10% HCl (2 hr room temperature) followed by addition of a saturated Na_2CO_3 solution and extraction with diethyl ether gave the expected chiral alcohol. Isolated yields are reported for the alcohols following purification by distillation or column chromatography.

Kinetic Studies. Reaction rates were determined by integration of selected ^1H NMR resonances and are reported as turn-over numbers ($k_{\text{obs}}/\text{mol catalyst}$). All reactions were performed in 5 mm NMR tubes at 25°C with one mL CD_2Cl_2 solvent and were monitored until complete. Pseudo-first order conditions were employed throughout these studies with a minimum [substrate] / [catalyst] ratio of 100 and the order of the reactants and catalysts were determined by the method of initial rates.

Preparation and Isolation of Rhodium μ_3 -Fluoro Trimers. The addition of triethylsilane, (0.16 mL, 1 mmol) to a rapidly stirred solution of $[(\text{Diphos})_2\text{Rh}_2](\text{PF}_6)$ (0.13 g, 0.1 mmol) in acetone caused a slow (2 days) color change from orange to deep red. Removal of the solvent *in vacuo* and crystallization of the resulting red solids from $\text{CH}_2\text{Cl}_2/\text{Et}_2\text{O}$ gave 48 mg (28% isolated yield) of the μ -fluoro trimer, $[(\text{Diphos})_3\text{Rh}_3(\mu_3\text{-F})_2](\text{PF}_6)$, **6**. Alternatively, **6** was prepared by the addition of an excess of KF to a methanolic solution of $[(\text{Diphos})_2\text{Rh}_2](\text{PF}_6)$ and following removal of the solvent and crystallization from $\text{CH}_2\text{Cl}_2/\text{Et}_2\text{O}$, **6** was isolated in 68% yield. The related Dipamp substituted trimer, $[(\text{Dipamp})_3\text{Rh}_3(\mu\text{-F})_2](\text{BF}_4)(\text{CH}_2\text{Cl}_2)$ **7**, was prepared in an exactly analogous manner as above by the addition of excess KF to the "ligand deficient" dimer $[(\text{Dipamp})_2\text{Rh}_2](\text{BF}_4)_2$ in

methanol. Single crystals of sufficient quality for an X-ray diffraction study were obtained by slow vapor diffusion of diethyl ether into a concentrated dichloroethane solution of the rhodium trimer. Analytical Data for [(Diphos)₃Rh₃(μ-F)₂](PF₆), **6**: ¹H NMR (CD₂Cl₂) δ 7.93 (br, 24 H, Ph); 7.87 (m, 12 H, Ph); 6.85-7.68 (m, 24 H, Ph); 2.15 (d of d, 12 H, PCH₂CH₂P) ³¹P NMR (CD₂Cl₂) δ 74.6 (d of d, 6 P, J_{P-F} = 50 Hz, J_{Rh-P} = 201 Hz); m. p. = 232 - 234°C (decomp.); Elemental Analysis: calculated (found): C, 55.54 (55.44); H, 4.3 (4.60); P, 12.85 (12.35).

Structural Determination of [Rh₃(Dipamp)₃(μ₃-F)₂](BF₄)-(CH₂Cl₂)₂, **7**. Single crystals of **7** were obtained by slow vapor diffusion of diethyl ether into a saturated CH₂Cl₂ solution of **7** at room temperature. Selected crystals were transferred to glass X-ray capillaries that had been filled with the mother liquor from which the crystals were grown and the capillaries were sealed. Crystallographic studies were performed by Crystallitics Company and revealed a triclinic unit cell, space group P₁-C₁ (No. 1) with a = 13.137(3) Å, b = 13.366(3) Å, c = 15.828(4) Å, α = 76.62(2)°, β = 60.98(2)°, γ = 68.05(2)°, v = 225(1) Å³, and Z = 1 (d_{calcd.} = 1.460 g, cm⁻³). A total of 10711 independent reflections having 2θ(MoKα < 55°) were obtained using full (1.00° wide) ω scans and graphite-monochromated MoKα radiation. Out of the total number of reflections obtained, 7575 had intensities judged to be above background (I > 3σ(I)) and were utilized in subsequent calculations. The structure was solved using "Direct Methods" techniques using Siemens SHELXTL-PLUS software as modified by Crystallitics Company. The resulting structural parameters were refined to convergence {R₁ (unweighted, based on F) = 0.040} using counter-weighted full-matrix least-squares techniques. All nonhydrogen atoms (except B₁) were refined anisotropically whereas isotropic thermal parameters were used for all hydrogen atoms. The methyl hydrogens were included as rigid rotors with sp³-hybridized carbon atoms and a C-H bond length of 0.96 Å. The remaining hydrogen atoms were placed at idealized positions, assuming sp²- or sp³-hybridization of the carbon atoms and a C-H bond length of 0.96 Å, on their respective carbon atoms.

Preparation and Isolation of Rhodium μ₃-Enolate Trimers. Triethylsilane, (0.16 mL, 1.0 mmol), was added via syringe to an acetone solution of [(Diphos)₂Rh₂](ClO₄)₂ (120 mg, 0.1 mmol) and the resulting orange-red colored solution was stirred for 36 hr at room temperature during which time the color became blood red. The solvent was removed *in vacuo* and the black-red solids were dissolved in a minimum amount of hot acetone/CH₂Cl₂. Upon cooling the solution to room temperature, dark red microcrystals precipitated that were isolated by filtration and dried under vacuum to give pure [(Diphos)₃Rh₃(μ-OC(CH₂)CH₃)₂](ClO₄)-(CH₂Cl₂), **8**. Further cooling of the supernatant at -40°C overnight gave additional product for an overall yield of 86% (154 mg). Compound **8** was prepared independently by the addition of excess diisopropyl(ethyl)amine to a concentrated solution of the (Diphos)rhodium(I) dimer, [(Diphos)₂Rh₂](PF₆)₂ in acetone. The reaction mixture was stirred for 10 minutes and then allowed to stand overnight at room temperature during which time the desired product precipitated as a bright red powder. The powder was isolated by filtration and then dissolved in minimum amount of CH₂Cl₂ from which dark red microcrystals of the product were isolated following slow evaporation (3-4 days) of the CH₂Cl₂. Analytical Data for [(Diphos)₃Rh₃(μ₃-OC(CH₂)CH₃)₂](ClO₄)(CH₂Cl₂), **8**: ¹H NMR (acetone-d₆): δ 7.85-6.91 (m, 60 H, Ph); 5.29 (br, 2 H, CH₂Cl₂); 2.15 (broad s, 3 H, CH₃C(O))

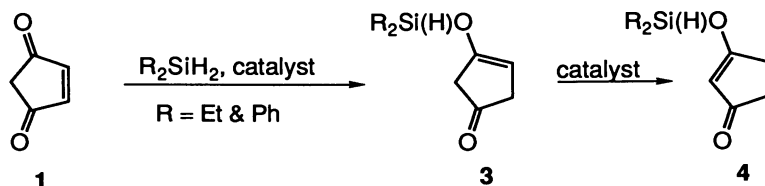
2.05 (broad m, 12 H, PCH_2); 1.5 (broad m, 2 H, C(O)CH_2). ^{31}P NMR (CD_2Cl_2): δ 74.9 (d, 6P, $J_{\text{Rh-P}} = 198.5$ Hz). Elemental Analysis calculated for $\text{C}_{85}\text{H}_{84}\text{Cl}_3\text{O}_5\text{P}_6\text{Rh}_3$: calculated(found) C, 57.10 (57.22); H, 4.74 (4.60); P, 10.40 (11.39).

Determination of Optical Yields. Optical yields of the siloxycyclopentenones derived from CPDK were determined by chiral HPLC (Chiracel OC column (J. T. Baker)) with the exception of the triphenylsilane derivative which was determined by optical rotation. 2-Butanol was derivatized to the corresponding diastereomeric urethanes with *R*-methylbenzylisocyanate according to literature procedures (32); the optical yield was then determined by G.C analysis using a Chirasil-*L*-Val column (Chrompack). The optical purity of the remaining alcohols (with the exception of α -tetralol; optical rotation) was determined by chiral G.C. analysis of the underivatized alcohol using a CP-Cyclodextrin-B-2,3,6-M-19 column (Chrompack). Baseline resolution of the enantiomeric alcohols was achieved in all cases and it was observed that the *R*-isomer was eluted first without exception (confirmed by both optical rotation and G.C. analysis of independently prepared optically pure samples).

Results

Hydrosilation of CPDK. Rhodium phosphine catalysts prepared according to literature methods (25-31) using excess chiral ligand (Diop, Dipamp, 2-(2-pyridyl)-4-carboethoxy-1,3-thiazolidine, etc.-see Figure 1) gave only 1,4-addition of disubstituted silanes to **1**; whereas, no reaction was observed with trialkylsilanes. Upon standing in the presence of the catalyst, the 1,4-addition product 3-siloxy-3-cyclopentenone, **3**, undergoes a rearrangement to the conjugated enone 3-siloxy-2-cyclopentenone, **4**. Notably, no 1,2-hydrosilation or bis(hydrosilation) products were observed using these rhodium(I) phosphine catalysts generated *in situ*, and no reaction was observed between CPDK and trisubstituted silanes (e.g. triethylsilane) in the presence of these catalyst systems even at elevated temperatures ($\sim 60^\circ\text{C}$).

The "ligand deficient" rhodium dimers were found to be highly active catalysts for the addition of both di- and trisubstituted silanes to CPDK. Turnover numbers ($k_{\text{obs}}/\text{mol catalyst}$) for the addition of trisubstituted silanes ranged from $34.8 \text{ M}^{-1} \text{ sec}^{-1}$ to $9.32 \times 10^2 \text{ M}^{-1} \text{ sec}^{-1}$ depending upon the catalyst and silane combination (Table I). The addition of disubstituted silanes to CPDK gave exclusively **4** following rearrangement of **3**. However, the addition of trisubstituted silanes afforded the desired 1,2-monohydrosilation product **2** in high yield (>90% isolated) with only trace amounts of **4** (<5%). (Table II) No bis(hydrosilation) products were observed even in the presence of excess silane.



catalyst = $[\text{Rh}(\text{NBD})\text{Cl}]_2 + 5\text{-}6 \text{ eqv. of DIOP or Thiazolidine (10)}$

The reaction temperature was found to have a marked effect on the regioselectivity of silane addition, namely 1,2-addition of trisubstituted silanes is

Table I. Rates of Addition of Trisubstituted Silanes to **1**

Catalyst	Silane	Rate (M ⁻¹ , sec. ⁻¹) ^a
[[<i>(S,S)</i> -(-)-Chiraphos]Rh] ₂ [PF ₆] ₂	Et ₃ SiH	90.1
[[<i>(S,S)</i> -(-)-Chiraphos]Rh] ₂ [PF ₆] ₂	(Ph) ₂ MeSiH	69.4
[[<i>(R)</i> -Dipamp]Rh] ₂ [PF ₆] ₂	Et ₃ SiH	7.29 x 10 ²
[[<i>(R)</i> -Cycphos]Rh] ₂ [PF ₆] ₂	Et ₃ SiH	34.8
[[<i>(+)</i> -Diop]Rh] ₂ [PF ₆] ₂	Et ₃ SiH	9.32 x 10 ²
[(Diphos)Rh] ₂ [PF ₆] ₂	Et ₃ SiH	54.2

^aDetermined by ¹H NMR of **1** (s, 2H, 7.22 d), reported as turn-over numbers (k_{obs}/mol catalyst).

avored at lower temperatures. For example, the *S,S*-Chiraphos rhodium(I) catalyzed addition of diphenylmethylsilane to **1** at 0°C catalyzed by the "ligand deficient" rhodium(I) dimers again gave **1** in 98% yield as compared to a 1:1 mixture of **2** and **4** obtained at 40°C. The reaction temperature also directly effected the enantioselectivity of the addition with higher temperatures resulting in higher optical yields. The *S,S*-Chiraphos rhodium(I) catalyzed addition of diphenylmethylsilane to **1** gave 54% e.e. at 45°C, 46% at 25°C, and 12% e.e. at 0°C. Further, the e.e. is also dependent upon the nature of the silane; namely, increasing the steric bulk of the silane leads to higher e.e.'s (Table II). Without exception the addition of trialkylsilanes also gives rise to products having the same stereochemistry as that of the bis(phosphine) ligand. Notably, substitution of a single alkyl group by an aryl moiety on the silane results in inversion of the asymmetric induction for all catalyst systems.

Attempts to use the "ligand deficient" rhodium(I) dimers as catalysts for the addition of trisubstituted silanes to enolizable ketones led to catalyst deactivation via formation of either the di-μ₃-fluoro rhodium(I) trimer, [(Diphos)₃Rh₃(μ₃-F)₂](PF₆), **6**, with the PF₆ or BF₄ salts or to the μ₃-enolate trimer, [(Diphos)₃Rh₃(μ₃-O-enolate)₂](ClO₄), **8**, when non-hydrolyzable counterions were employed. When more reactive disubstituted silanes (e.g. diphenylsilane), were used in conjunction with the ligand deficient catalysts, silyl enol ethers resulting from dehydrogenative silylation were the major products (>80%). An X-ray diffraction study performed on single crystals of the related Dipamp rhodium μ-fluoro trimer, [Rh₃(Dipamp)₃(μ₃-F)₂](BF₄)·(CH₂Cl₂)₂, **7**, confirmed the trimeric arrangement of the rhodium atoms capped by triply bridging fluorine atoms. A perspective view and numbering scheme for **7** is shown in Figure 2.

Development of Tetraphosphine Rh(I) catalysts. The tetra(phosphine) rhodium(I) cations, prepared by adding stoichiometric amounts of a monophosphine to the ligand deficient dimers, were subsequently found to be very active hydrosilylation catalysts. Although the addition of trisubstituted silanes was slow (1-2 days) and required elevated temperatures (~55°C), high regioselectivity to the 1,2-hydrosilylation products was obtained. Importantly, no products arising from catalyst deactivation in the form of trimeric rhodium(I) complexes were observed. More interestingly, these tetraphosphine rhodium complexes are extremely efficient catalysts for the 1,2-addition of *disubstituted* silanes to enolizable ketones. Turn-over numbers up to 10⁵/hr at room temperature have been observed for a number of catalyst and ketone/silane combinations.

The nature of the monophosphine has a dramatic effect on the catalyst

Table II. Enantioselectivity of Silane Addition to **1**^a

Catalyst ^b	Silane	% 2 vs 4	% e.e. (config.) ^c
<i>S,S</i> -Chiraphos	Et(Me) ₂ SiH	97:3	19(S)
"	(Et) ₂ MeSiH	96:4	24(S)
"	Et ₃ SiH	95:5	30(S)
"	Ph(CH ₃) ₂ SiH	83:17	38(R)
"	Ph ₂ (Me)SiH	95:5	46(R)
"	Ph ₃ SiH	71:29	46(R)
(+)-DIOP	(Et) ₂ MeSiH	92:8	<1(R)
"	Et ₃ SiH	53:45	2(R)
"	Ph(Me) ₂ SiH	80:20	8(S)
"	Ph ₂ (Me)SiH	75:25	12(S)
"	Ph ₃ SiH	61:38	12(S)
<i>R,R</i> -Dipamp	Et(Me) ₂ SiH	57:40	7(R)
"	(Et) ₂ MeSiH	80:20	6(R)
"	Et ₃ SiH	95:5	14(R)
"	Ph(CH ₃) ₂ SiH	82:17	25(S)
"	Ph ₂ (Me)SiH	87:10	43(S)
"	Ph ₃ SiH	75:25	34(S)
<i>S</i> -(-)-Binap	Et ₃ SiH	59:41	54(S)
"	Ph ₃ SiH	95:5	26(R)
"	<i>t</i> -Bu(Me) ₂ SiH ^d	87:12	52(S)
<i>R</i> -Cycphos	Et ₃ SiH	95:5	30(R)

^aReaction conditions: **1** (50 mg, 0.5 mmol), silane (0.5 mmol), catalyst (5 X 10⁻³ mmol) except *S*-Binap catalyst (5 X 10⁻⁴ mmol). All reactions were run at 25°C and were monitored by ¹H NMR until all of **2** was converted to either **1** or **4**. ^bLigand deficient dimer based on the bidentate bis(phosphine) listed. ^cSee Experimental ^dLess than 20% conversion after 24 hrs at room temperature.

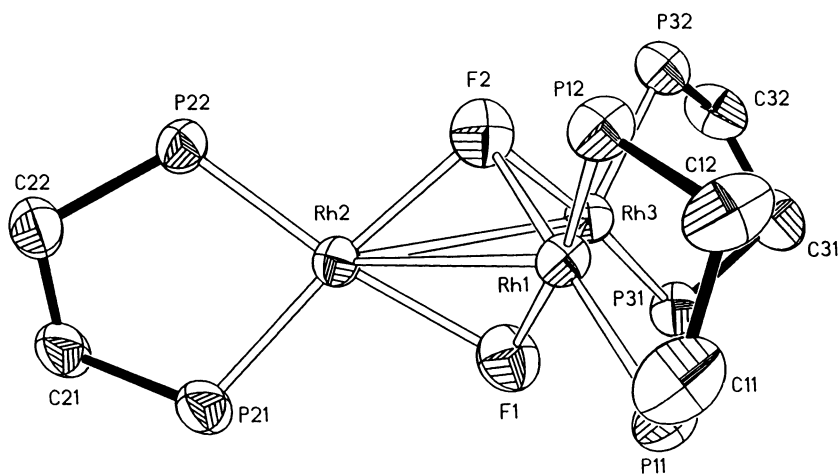


Figure 2. The solid state structure of $[\text{Rh}_3(\text{Dipamp})_3(\text{F})_2](\text{BF}_4) \cdot 2\text{CH}_2\text{Cl}_2$, **7**; the phenyl rings have been omitted for clarity.

activity. Under identical conditions ($[\text{H}_2\text{SiPh}_2] = [\text{sub}]$, and $[\text{sub}]/[\text{cat}] = 5000$, CH_2Cl_2 , 21°C .) the reduction of acetophenone with diphenylsilane catalyzed by $[\text{Rh}(\text{Diphos})(\text{PPh}_3)_2](\text{PF}_6)$ was complete in less than 10 minutes as compared to 20% conversion after 48 hours and no reaction at all for the triethylphosphine and trimethylphosphite substituted analogues, respectively.

The reduction of α,β -unsaturated ketones is equally fast and remarkably selective for 1,2-addition of the silane. A variety of both cyclic and acyclic α,β -unsaturated ketones were reduced with diphenylsilane under the standard conditions with yields ranging from 66-99% for 1,2-addition. Cyclic enones were reduced with a higher degree of regioselectivity than the acyclic enone, mesityl oxide. (Table III)

In all cases, the absolute configuration of the secondary alcohol isolated was identical to that of the bis(phosphine) ligand attached to the rhodium. Additionally, the nature of the bis(phosphine) ligand itself was found to have a significant impact on the degree of enantioselectivity. Thus, rhodium catalysts derived from Binap gave consistently higher e.e.'s for all substrates as compared to the analogous catalyst systems using other chiral bis(phosphine) ligands. Tetraphosphine rhodium(I) complexes prepared using chiral monophosphines such as menthylidiphenylphosphine or Camp gave generally higher e.e.'s as compared to their triphenylphosphine analogues although no direct additivity of the chiral centers was observed. In particular, the reduction of acetophenone catalyzed by triphenylphosphine, *S*-Camp menthylidiphenylphosphine, and neomenthylidiphenylphosphine derivatives of (*S*-Binap)Rh(PR₃)₂ gave 26%, 54%, 53%, and 51% e.e., respectively, of the expected *S*-sec alcohol. Further, the analogous combinations (triphenylphosphine, menthylidiphenylphosphine, neomenthylidiphenylphosphine and *S*-Camp) with the *R*-Binap substituted rhodium complex gave nearly identical e.e.'s (27%, 53%, 52%, and 49% , respectively) of the *R*-sec-phenylethanol. Although no additivity of the two chiral ligands was observed, the $[(\text{Diphos})\text{Rh}(\text{S-Camp})_2](\text{PF}_6)$ catalyst, in which *S*-Camp is the only source of chirality, gave *S*-sec-phenylethanol in 19% e.e.

Interestingly, the enantioselectivity for the hydrosilation of acetophenone was found to be independent of the amount of chiral ligand present in the reaction mixture, although the reactions slow down as excess ligand is added. Thus, catalyst solutions prepared by adding from 1-10 equivalents of MDPP per rhodium to the (*S*-Binap)Rh dimer all gave ca. 55% e.e. of the expected *S*-sec alcohol. The addition of excess achiral phosphines such as triphenylphosphine or tricyclohexylphosphine did not effect the optical yield of the alcohol as compared to reactions involving stoichiometric amounts of the monophosphine.

Concentration of the reagents, solvent, and rate of addition of the silane have no significant effect on the optical yield for the reduction of acetophenone or 2,2-dimethylcyclopentanone. Reductions performed in neat ketone gave the identical e.e. as those run in CH_2Cl_2 , THF or $\text{ClCH}_2\text{CH}_2\text{Cl}$ with concentrations of the ketone ranging from .01 M to 5 M. A significant decrease in the rate of the reduction was noted when THF or neat ketone (both of which are strongly coordinating) were used as the solvent. Similarly, dropwise addition of a dilute CH_2Cl_2 solution of diphenylsilane (10 mmol, 5 mL CH_2Cl_2) to the ketone/catalyst solution (10 mmol $\text{PhC}(\text{O})\text{CH}_3$ 5 mL CH_2Cl_2) over 45 minutes gave the same e.e. as the analogous reaction to which the silane had been added rapidly via syringe. The addition of a large excess (10-20 fold) of diphenylsilane to the reaction solutions cause no change in either the optical or chemical yield of the chiral alcohol.

The order of addition of reagents was critical to the success of the hydrosilation reaction for all ketone and catalyst systems. When the silane was added to the ketone and catalyst solution or the catalyst was added to a mixture of the

Table III. Regioselectivity of Addition to α,β -Unsaturated Ketones

Ketone	catalyst	1,2-/1,4-addition ¹	e.e.
2-cyclohexenone	[(<i>S</i> -Binap)Rh(MDPP) ₂] ⁺	88 : 12	7(<i>S</i>)
"	[(<i>R</i> -Dipamp)Rh(MDPP) ₂] ⁺	99 : 1	4 (<i>R</i>)
mesityl oxide	[(<i>S</i> -Binap)Rh(MDPP) ₂] ⁺	80 : 20	8 (<i>S</i>)
"	[(<i>R</i> -Dipamp)Rh(MDPP) ₂] ⁺	90 : 10	3 (<i>R</i>)
2-methyl-2-cyclopentenone	[(<i>S</i> -Binap)Rh(MDPP) ₂] ⁺	98 : 2	13 (<i>S</i>)
"	[(<i>R</i> -Dipamp)Rh(MDPP) ₂] ⁺	92 : 8	7 (<i>R</i>)
2-cyclopentenone	[(<i>S</i> -Binap)Rh(MDPP) ₂] ⁺	94 : 6	12(<i>S</i>)
"	[(<i>R</i> -Dipamp)Rh(MDPP) ₂] ⁺	95 : 5	2 (<i>R</i>)
<i>R</i> -carvone	[(<i>R</i> -Dipamp)Rh(MDPP) ₂] ⁺	99 : 1	32(<i>R</i>)

¹ Product ratios determined by ¹H NMR.

silane and ketone, the reduction proceeded smoothly to give the silyl ether in high yield. If, however, the silane was added to a CH₂Cl₂ or THF solution of the catalyst followed by addition of the ketone, a mixture of dehydrogenative silylation and hydrosilylation products were obtained. Interestingly, the order of addition did not alter the enantioselectivity of the hydrosilylation reaction.

The reaction temperature had a dramatic impact on the enantioselectivity of the silane addition. Using acetophenone, diphenylsilane and the (*S*-Binap)Rh(PPh₃)₂ catalyst as a model system, the initial reaction temperature was varied from -40°C to 55°C. When carried out under the standard conditions (*vide supra*), the reduction gave an optical yield of 26% (*S*-isomer). Lowering the initial temperature to 0°C caused a decrease in the e.e. to 12% and decreasing the temperature further still to -40°C resulted in an optical yield of only 7%. Increasing the initial temperature, on the other hand, to 55°C (1,2-dichloroethane solvent) raised the optical yield to 55%.

The integrity of the rhodium catalyst over the course of the reaction was confirmed by the observation that the optical yield was not a function of the percent conversion. Hydrolysis and chiral G.C. analysis of one mL aliquots taken at one minute intervals from a CH₂Cl₂ solution of 2,2-dimethylcyclopentanone, diphenylsilane and the [(*S*-Binap)Rh(MDPP)₂]⁺ catalyst revealed that the e.e. is invariant over the course of the reaction. Thus, at 26% conversion the optical yield was 69% e.e., the same as that obtained at 68% conversion, 100% conversion (30 minutes) and after stirring overnight. Further studies involved the addition of a second ketone and stoichiometric silane to the precatalyst to generate an active catalyst species followed by addition of the ketone of interest. Under the standard conditions (*vide supra*), acetophenone (1.0 mmol) was added to the catalyst followed by 1.0 mmol of diphenylsilane. The reaction mixture was stirred for 10 minutes after which time 2,2-dimethylcyclopentanone (100 mmol) and diphenylsilane (100 mmol) were added to the solution in that order. Reduction of the cyclopentanone proceeded smoothly at room temperature to give 98% product yield and 71% e.e. Vice versa, with use of 2,2-dimethyl-cyclopentanone (1 mmol) as a secondary ketone, the reduction of acetophenone gave 92% isolated yield and 27% e.e., nearly identical to the straightforward reduction for each ketone.

Substituents on the silane (e.g. phenyl, methyl etc.) do effect the enantioselectivity of the reductions; however, the nature of the effect (enhancement or reduction of the e.e.) appears to depend upon the particular catalyst, ketone and silane combination employed. An example being the reduction of acetophenone with diphenyl or phenylmethylsilane catalyzed by either [(*S*-Binap)Rh(PPh₃)₂]⁺ or [(*S,S*-Chiraphos)Rh(PPh₃)₂]⁺. The optical yield for the [(*S*-Binap)Rh(PPh₃)₂]⁺ catalyzed reduction increases from 22% to 35% e.e when phenylmethylsilane is used in place of diphenylsilane; whereas, no change in the optical yield was observed for the analogous reductions using the [(*S,S*-Chiraphos)Rh(PPh₃)₂]⁺ catalyst (29% e.e. in both cases). When diethylsilane was employed in the reductions, the e.e.'s were generally lower. The substituents adjacent to the ketone greatly effected the enantiofacial selectivity of the reduction. An overview of the results obtained using the [(*S*-Binap)Rh(MDP)₂]⁺ catalyst and diphenylsilane to reduce a wide variety of ketones under the standard conditions are presented in Table IV.

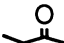
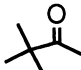
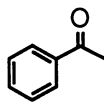
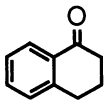
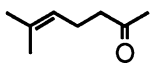
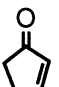
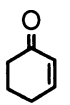
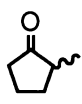
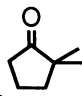
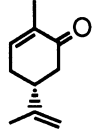
A preliminary mechanistic investigation of the tetraphosphine rhodium(I) catalyzed hydrosilation reaction has revealed that the reaction is zero-order in ketone at [ketone] > 0.5M and first-order in both diphenylsilane and catalyst. Under pseudo-first order conditions ([ketone] ≥ 10 x [silane] = 5000 x [catalyst]), the initial rate of addition of diphenylsilane to 2,2-dimethyl-cyclopentanone in the presence of [Rh(Diphos)(PPh₃)₂]⁺ was invariant over a 10 fold concentration range of the ketone ($k_{obs.} = 2.39 \times 10^{-3} \text{ sec.}^{-1}$). Using identical conditions as above, the catalyst concentration was varied over a 10 fold range ($1.43 \times 10^{-4} \text{ M}$ to $1.43 \times 10^{-3} \text{ M}$) and a subsequent plot of the initial rate vs. [catalyst] gave a line of slope = 1. Initial studies varying the concentration of the silane suggests a first-order dependence of the rate on the concentration of silane. The rate of reaction was inversely dependent upon the concentration of added phosphine. Using ³¹P NMR to monitor the concentration of free PPh₃, an equilibrium constant of 2.6×10^{-5} was determined for the dissociation of PPh₃ from [Rh(Diphos)(PPh₃)₂]⁺ in the presence of excess ketone.

Discussion

Enantiomerically enriched 4-siloxycyclopentenones, precursors to a wide variety of prostaglandin derivatives, are easily prepared in high isolated yield via rhodium(I) catalyzed addition of trisubstituted silanes to 2-cyclopentene-1,4-dione. The reactions proceed rapidly under very mild conditions in noncoordinating solvents such as CH₂Cl₂ to give exclusively the monohydrosilated products with a high degree (>95%) of regioselectivity for 1,2-addition. Disubstituted silanes were shown to undergo 1,4-addition to the enone moiety of CPDK in all cases.

The characteristics of the asymmetric hydrosilation of CPDK using the "ligand deficient" rhodium(I) dimers are as follows: 1) "ligand deficient" dimers are cleaved in the presence of CPDK to give symmetric CPDK adducts as characterized by ³¹P and ¹H NMR spectroscopy 2) no reaction occurs between silanes and the catalyst in the absence of CPDK, and 3) no interconversion of the 1,2- and 1,4-addition products was observed under the reaction conditions. With this in mind a possible reaction mechanism for the addition of silanes to CPDK catalyzed by "ligand deficient" rhodium(I) complexes is presented in Figure 3. The salient features of the proposed mechanism are the equilibrium formation of a CPDK adduct of the catalyst followed by oxidative addition of the silane to yield a rhodium(III) silyl hydride species. Insertion of the ketone into the rhodium silicon bond would give the alkyl

Table IV. Enantioselectivity of Diphenylsilane Addition
Catalyzed by [(*S*-Binap)Rh(MDP)₂](PF₆)¹

Ketone	% Yield	e.e. (config.)
	98	26 (<i>S</i>)
	97	63 (<i>S</i>)
	94	52 (<i>S</i>)
	99	33 (<i>S</i>)
	20	19 (<i>S</i>)
	92	12 (<i>S</i>)
	96	6.6 (<i>S</i>)
	98	22 (<i>S</i>) ²
	99	71 (<i>S</i>)
	93	32 (<i>S</i>)

¹ See Experimental Section. ² 70% cis addition

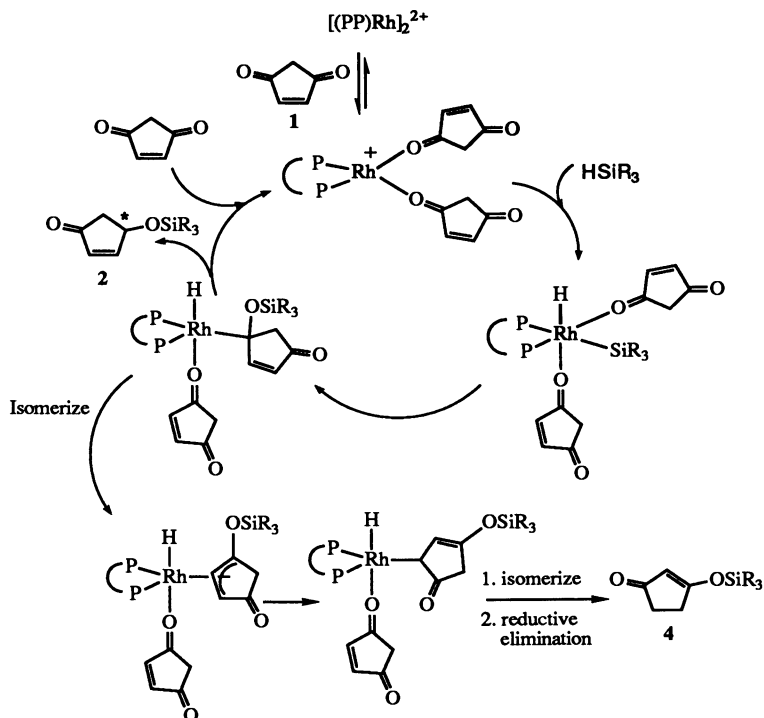


Figure 3. Proposed mechanism for the hydrosilation of CPDK.

rhodium hydride species at which point the reaction may follow one of two proposed pathways.⁽³³⁾ Reductive elimination from the α -siloxy alkyl species gives the desired 4-siloxy-2-cyclopentenone or alternatively, isomerization via a rhodium(III) allyl species followed by reductive elimination would yield the corresponding 1,4-addition by-product.⁽³⁴⁾

The success of the "ligand deficient" catalysts for the hydrosilation of CPDK is most likely due to the inability of CPDK to form a stable enol tautomer and subsequently trap the catalyst. In the case of enolizable ketones, the electron and "ligand deficient" rhodium(I) metal center may act as a Lewis acid promoting the enolization of coordinated ketones. With trisubstituted silanes and enolizable ketones, the catalyst is trapped by the enol or by fluoride generated from the degradation of the PF_6^- or BF_4^- counterions. The more reactive disubstituted silanes, on the other hand, yield silyl enol ethers corresponding to dehydrogenative silylation of the ketone.

In order to moderate the Lewis acidity of the rhodium(I) catalysts as well as inhibit catalyst deactivation via trimerization, the new class of rhodium(I)(tetraphosphine) hydrosilation catalysts was developed. The reactivity of these rhodium(I) catalyst species is directly related to the steric properties of the monodentate phosphine, namely the larger the monophosphine the more active the catalyst. A possible explanation for this trend lies in the following observation. Basic trialkylphosphines having relatively small cone angles (e.g. trimethyl or triethylphosphine) readily form stable tetraphosphine species; whereas, larger phosphines containing aryl substituents or highly bulky alkyl groups such as menthylidiphenylphosphine or tricyclohexylphosphine yield tris(phosphine) adducts

such as (*S*-Binap)Rh(MDP)⁺ in solution. Assuming that dissociation of a monophosphine from the tetraphosphine Rh(I) center is required for further reaction, catalyst systems containing bulky monophosphines should exhibit a higher degree of reactivity than those which form stable 18 electron tetraphosphine complexes.

The effect of chiral monodentate phosphines on the enantioselectivity of the hydrosilation reaction is less clear. The lack of additivity between the chiral centers of bis(phosphines) and chiral monodentate phosphines such as menthyl or neomenthylidiphenylphosphine might be attributed to the fact that the chiral center (the menthyl substituent) is not proximal to the metal center. Thus, any enhancement of the enantioselectivity resulting from the use of these ligands might be due to a simple steric effect as opposed to a direct chiral interaction with the substrate. Chiral at phosphorous ligands such as *S*-Camp, in which the chiral center is directly attached to the metal, might be expected to have a more direct impact on the enantiofacial selectivity of the reduction. The observation that [(Rh(Diphos)(*S*-Camp)₂](PF₆) afforded an optical yield of 19% (*S*-isomer) for the addition of diphenylsilane to acetophenone confirms that "chiral at phosphorus" ligands can impart stereoselectivity to the metal catalysts. Unfortunately, no additive (or deleterious) effect on the optical yield was observed between chiral bis(phosphine) ligands and *S*-Camp regardless of the chirality of the bis(phosphine) ligand employed.

Characteristics of the asymmetric hydrosilation reaction involving tetraphosphine rhodium(I) catalysts are as follows: 1) the order of addition (ketone first) is critical suggesting the formation of a rhodium(I) ketone adduct prior to oxidative addition of silane and, 2) little if any catalytic activity was seen for rhodium(I) catalysts containing small, highly basic monophosphines implying that phosphine dissociation is essential for hydrosilation to occur. These observations, combined with the preliminary kinetic data acquired using the achiral [Rh(Diphos)(PPh₃)₂](PF₆) catalyst (*vide supra*), support the proposed mechanism outlined in Figure 4. Key features of the proposed mechanism are the initial loss of a monophosphine to form an L₃Rh(ketone)_n complex that undergoes oxidative addition of the silane Si-H bond. Insertion of the ketone into the rhodium-silyl bond gives the α-siloxy Rh(III) intermediate that upon reductive elimination yields the product silyl ether and regenerates the active catalyst species. The formation of the α-siloxy intermediate is supported by the fact that 2-methylcyclopentanone is selectively reduced to the *cis*-2-methylcyclopentanol (ca. 4:1 ratio *cis:trans*) using the rhodium catalysts and diphenylsilane. The *cis* arrangement is preferred due to steric interactions between the α-methyl substituent and the phenyl rings attached to the bis(phosphine) ligand. Such steric interactions are greatly reduced in the alternative rhodium(III) alkoxide type intermediate (resulting from hydride transfer to the carbonyl carbon) and little if any *cis/trans* selectivity would be expected.

Conclusions

A series of new asymmetric hydrosilation catalysts based on previously reported "ligand deficient" rhodium(I) complexes has been developed. These "ligand deficient" rhodium complexes were found to be the most active rhodium based catalysts known for the addition of trisubstituted silanes to ketones. Importantly, the preparation of enantiomerically enriched 4-siloxy-2-cyclopentenones under mild conditions (CH₂Cl₂, 21°C, < 15 hr) from readily available CPDK utilizing these catalysts has been demonstrated. These chiral siloxycyclopentenones are versatile intermediates in the synthesis of a number of prostaglandin derivatives including both PGD and PGE type prostaglandins. In order to avoid catalyst deactivation or undesired dehydrogenative silation by-products observed with enolizable ketones, a new class of hydrosilation catalyst, namely tetraphosphine rhodium(I) complexes

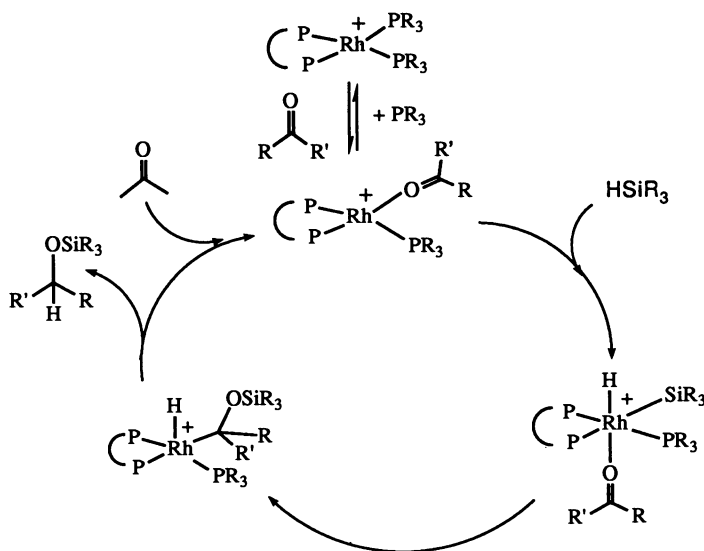


Figure 4. Proposed mechanism for asymmetric hydrosilation using tetraphosphine Rh(I) catalysts.

containing one bidentate and two monodentate phosphines, was developed. These tetraphosphine rhodium catalysts are extremely efficient catalysts for the addition of disubstituted silanes to a variety of ketone substrates with turn-over numbers as high as $10^5/\text{hr}$ observed at 21°C in noncoordinating solvents such as CH_2Cl_2 . Addition of diphenylsilane to α,β -unsaturated ketones proceeds with a high degree of regioselectivity (typically greater than 95% 1,2-addition) and optical yields as high as 75% have been obtained using these catalysts.

Literature Cited

- Ojima, I. in *The Chemistry of Organic Silicon Compounds*; Patai, S.; Rappoport, Z., Eds.; John Wiley and Sons Ltd., 1989 Chap. 25.
- Ojima, I.; Hirai, K. in *Asymmetric Synthesis* Vol. 5; Morrison, J. O., Ed.; Academic Press, New York; 1985 pp 104-125.
- Nishiyama, H.; Kondo, M.; Nakamura, T.; Itoh, K. *Organometallics*, **1991**, *10*, 500-508.
- Brunner, H.; Obermann, U. *Chem. Ber.* **1989**, *122*, 499.
- Brunner, H.; Kurzinger, A. *J. Organomet. Chem.*, **1988**, *346*, 413.
- Brunner, H.; *J. Organomet. Chem.* **1984**, *3*, 1354.
- Yoshii, E.; Koizumi, T.; Ikeshima, H.; Ozaki, K.; Hayashi, I. *Chem. Pharm. Bull.*, **1975**, *23*, 2496.
- Yoshii, E.; Ikeshima, H.; Ozaki, K. *Ibid.* **1972**, *20*, 1827.
- Kobayashi, M.; Koyama, T.; Ogura, K.; Seto, S.; Ritter, F. F.; Bruggeman-Rotagne, I. E. M. *J. Am. Chem. Soc.*, **1980**, *102*, 6602.
- Brunner, H.; Fisch, H. *J. Organomet. Chem.* **1987**, *335*, 1.
- Brunner, H.; Fisch, H. *J. Organomet. Chem.* **1988**, *346*, 413.
- Kogure, T.; Ojima, I. *J. Organomet. Chem.* **1982**, *234*, 249.
- Kogure, T.; Ojima, I. *J. Organomet. Chem.* **1976**, *122*, 83.

14. Brunner, H.; Brandl, P. *J. Organomet. Chem.* **1990**, *390*, C90.
15. Balvoine, G.; Clinet, J. C.; Lellouche, I. *Tet. Lett.* **1989**, *30(38)*, 5141.
16. Halpern, J.; Riley, D. P.; Chan, A. S. C.; Pluth, J. *J. Am. Chem. Soc.* **1977**, *99*, 8055.
17. Riley, D. P. *J. Organomet. Chem.* **1982**, *234*, 85.
18. Morita, Y.; Suzuki, M.; Koyano, H.; Noyori, R. *Tetrahedron* **1990**, *46*, 4809.
19. Morita, Y.; Suzuki, M.; Noyori, R. *J. Org. Chem.* **1989**, *54*, 1785.
20. Suzuki, M.; Yanagisawa, A.; Noyori, R. *J. Am. Chem. Soc.* **1988**, *110(14)*, 4718.
21. Noyori, R.; Suzuki, M. *Chemtracts* **1990**, *3*, 173.
22. Crabbe, P. In *Prostaglandin Research*, Blomquist, T.; Wasserman, H. H. Eds.; Organic Chemistry, A Series of Monographs; Academic Press: New York, 1977, Vol. 36.
23. DePuy, C. H.; Zaweski, E. F. *J. Am. Chem. Soc.*, **1959**, *81*, 4920.
24. DePuy, C. H.; Wells, P. R. *J. Am. Chem. Soc.*, **1960**, *82*, 2909.
25. Wright, M. E.; Svejda, S. A.; Jin, M. J.; Peterson, M. A. *Organometallics* **1990**, *9(1)*, 136.
26. Abicht, H. P.; Kreuzfeld, H. J.; Kinting, A. *J. Organomet. Chem.* **1989**, *370*, 343.
27. Dobler, C.; Kinting, A. *J. Organomet. Chem.* **1989**, *370*, 351.
28. Ojima, I.; Hirai, K. *Asymmetric Synth.* **1985**, *3*, 103.
29. Ojima, I.; Clos, N.; Bastos, C. *Tetrahedron* **1989**, *45(22)*, 690.
30. Kokel, N.; Mortreux, A.; Petit, F. *J. Mol. Cat.* **1989**, *57*, L5-L7.
31. Yamamoto, K.; Hayashi, T.; Kazuyuki, K.; Omizu, H.; Kumada, M. *J. Organomet. Chem.* **1976**, *113*, 127-137.
32. Brunner, H.; Reiter, B.; Riepl, G. *Chem. Ber.* **1984**, *117*, 1330.
33. The formation of an α -siloxy Rh(III) intermediate resulting from initial transfer of the silyl moiety to the ketone oxygen (as opposed to a Rh(III) alkoxide) has been postulated based on spin-trapping experiments and EPR studies. Ojima, I.; Kogure, T. *Organometallics* **1982**, *1(10)*, 1390 and references therein.
34. An alternative mechanism for the formation of the 1,4-addition product could involve olefin coordination to the rhodium metal center followed by hydride transfer and reductive elimination of the silyl enol ether as suggested by a reviewer.

RECEIVED June 22, 1992

Chapter 6

Catalytic Asymmetric Heck Reaction

Fumiyuki Ozawa, Akihiko Kubo, and Tamio Hayashi

Catalysis Research Center and Graduate School of Pharmaceutical Science, Hokkaido University, Sapporo 060, Japan

Catalytic asymmetric arylation of 2,3-dihydrofuran with phenyl triflate in benzene in the presence of 1,8-bis(dimethylamino)naphthalene (proton sponge) and a chiral palladium catalyst, generated in situ from Pd(OAc)₂ and 2 equiv/Pd of (*R*)-BINAP, at 40 °C gave optically active (*R*)-2-phenyl-2,3-dihydrofuran in extremely high enantioselectivity (>96% ee), together with a small amount of the regioisomer (*S*)-2-phenyl-2,5-dihydrofuran. Under similar conditions, various aryl triflates (ArOTf; Ar = *p*-ClC₆H₄, *m*-ClC₆H₄, *o*-ClC₆H₄, *p*-AcC₆H₄, *p*-NCC₆H₄, *p*-FC₆H₄, *p*-MeOC₆H₄, *p*-MeC₆H₄, and 2-naphthyl) reacted with 2,3-dihydrofuran to yield the corresponding (*R*)-2-aryl-2,3-dihydrofurans of >96–87% ee. The mechanism and factors governing this novel catalytic asymmetric reaction are discussed in detail.

The palladium-catalyzed arylation and alkenylation of olefins, which were first discovered in the 1970's by Heck (1, 2) and Mizoroki (3) and have been often called the "Heck reaction", are versatile synthetic means for making a carbon-carbon bond. These reactions have been extensively used for organic synthesis during the past two decades (4–7). However, no reports on the "asymmetric Heck reaction" have been appeared until very recently. Shibasaki reported an asymmetric intramolecular cyclization of alkenyl iodides to give *cis*-decalin derivatives of 80–91% ee (8–10). Overman reported an intramolecular cyclization of alkenyl triflate, giving a chiral quaternary carbon center of 45% ee (11). We report herein the first example of intermolecular asymmetric Heck-type arylation of cyclic olefins catalyzed by (*R*)-BINAP-coordinated palladium complexes (Scheme 1) (12,13).

Catalytic Asymmetric Arylation of Olefins

Scheme 2 shows the mechanism generally accepted for the catalytic arylation of olefins with aryl iodides in the presence of a tertiary phosphine-coordinated palladium catalyst and a base (4). Oxidative addition of aryl iodide (ArI) to a Pd(0) species (A), which is most commonly generated from palladium diacetate and a tertiary phosphine ligand, forms an arylpalladium iodide complex (B). Coordination of olefin on B followed by insertion of the coordinated olefin into the Pd-Ar bond forms a σ -alkylpalladium species (C), which undergoes β -hydrogen elimination reaction to give the arylation

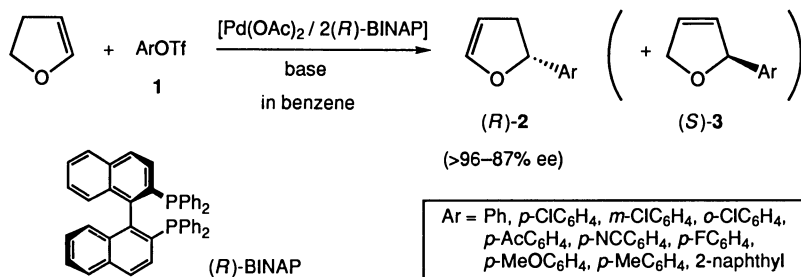
product and a hydridopalladium complex (D). Complex D thus formed further interacts with a base to regenerate the Pd(0) species (A) which further carries the catalytic cycle.

The main reason why the Heck reaction has not been applied to asymmetric synthesis until very recently is that the Heck reaction generally does not create new chiral carbon centers in the products. The chiral carbon center formed by the olefin-insertion is lost at the subsequent β -hydrogen elimination step. An exception to this was found in the reaction of a cyclic olefin such as 2,3-dihydrofuran where the chiral carbon center remains in the arylation product (Scheme 3). The reaction of 2,3-dihydrofuran with an arylpalladium species via the common cis insertion process forms alkylpalladium intermediate E. In this intermediate, the hydrogen bound to the arylated carbon, that is trans to the palladium, can not participate in the β -hydrogen elimination. Alternatively, the cis β -hydrogen at another β -carbon may be abstracted by palladium. Dissociation of the coordinated olefin from the resulting hydrido-olefin complex F gives 2-aryl-2,5-dihydrofuran (3), whereas insertion of the olefin into the Pd-H bond in F followed by β -hydrogen elimination forms the thermodynamically more stable 2-aryl-2,3-dihydrofuran (2), in which the arylated carbon center remains chiral.

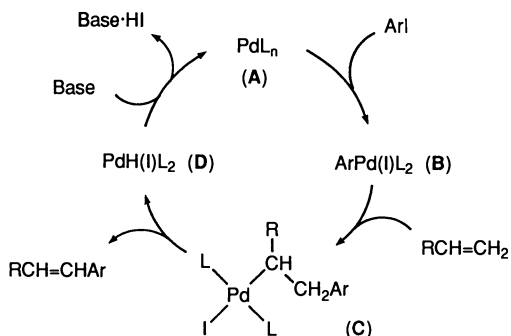
We therefore studied asymmetric arylation of 2,3-dihydrofuran. In our initial attempts, we applied chiral diphosphine ligands to a common arylation system using phenyl iodide as the arylating reagent, but no or little asymmetric induction has been observed. For example, the reaction of 2,3-dihydrofuran with phenyl iodide in THF in the presence of triethylamine and 3 mol% of a palladium catalyst, prepared in situ from Pd(OAc)₂ and (*R*)-BINAP, at 40 °C for 44 h gave racemic 2-phenyl-2,3-dihydrofuran (2a) and 2-phenyl-2,5-dihydrofuran (3a) in 23% and 2% yields, respectively. This reaction must involve a [PdPh(I)(BINAP)] intermediate formed by oxidative addition of phenyl iodide to a [Pd(0)(BINAP)] species generated in the system. Recent mechanistic studies on olefin-insertion into the related acylpalladium halide complexes [Pd(COR)(X)L₂] having two tertiary phosphine ligands (L) revealed that the insertion process involves displacement of one of the phosphine ligands with olefin to give a [Pd(COR)(olefin)X(L)] type intermediate (14,15). Therefore, we reasoned that the absence of asymmetric induction in the arylation system with phenyl iodide is attributable to partial dissociation of BINAP ligand during the olefin-insertion process.

On the other hand, we recently found that a cationic acetyl-palladium complex bearing 1,2-bis(diphenylphosphino)ethane (dppe) as a potent bidentate ligand [Pd(COMe)(NCMe)(dppe)]⁺BF₄⁻ (4) possesses extremely high reactivity toward olefin-insertion (Scheme 4) (16). Complex 4 reacted with cyclic olefins, including cyclopentene and cycloheptene, under very mild conditions (-40 °C) to give the olefin-inserted complexes. Cationic complex 4 has a coordination site that is weakly coordinated with acetonitrile and easily accessible for coordination of olefins. The presence of bidentate ligand allows the acetyl group and the coordinated olefin to come to the adjacent sites (cis) required for the subsequent olefin-insertion. The overall situation results in facile olefin-insertion without involving the partial dissociation of phosphine ligand.

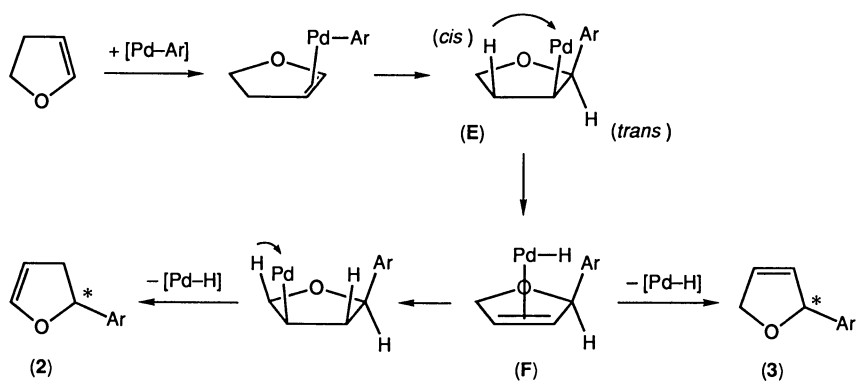
Taking the above mechanistic information into account, we next sought the catalytic asymmetric arylation system that involves a cationic arylpalladium intermediate. First, we examined the reaction of 2,3-dihydrofuran with phenyl iodide and Et₃N in the presence of AgClO₄ and a palladium catalyst coordinated with (*R*)-BINAP ligand. The silver salt employed may react with the [PdPh(I)(BINAP)] intermediate to generate a desirable cationic phenylpalladium species. The reaction carried out in THF at 40 °C for 44 h actually gave optically active (*R*)-2-phenyl-2,3-dihydrofuran (2a) of 65% ee (25% yield) together with a small amount of its regioisomer (3a) (1% yield). Secondly, we tried to employ arylpalladium triflate intermediate [Pd(Ar)(OTf)(BINAP)] (5) which may be generated in the catalytic system by oxidative addition of aryl triflate to a Pd(0) species (12). Complex 5 having the triflate ligand as a good leaving group was expected to form a cationic olefin-



Scheme 1.



Scheme 2.



Scheme 3.

coordinated species $[\text{Pd}(\text{Ar})(\text{olefin})(\text{BINAP})]^+\text{OTf}^-$ (**6**) with retention of the chelate coordination of the BINAP ligand, leading to the highly enantioselective Heck reaction.

Reaction of 2,3-dihydrofuran with aryl triflate in benzene in the presence of a base and a palladium catalyst, prepared in situ from $\text{Pd}(\text{OAc})_2$ and 2 equivalents of (*R*)-BINAP, gave (*R*)-2-aryl-2,3-dihydrofuran (**2**) and a small amount of the regioisomer (*S*)-2-aryl-2,3-dihydrofuran (**3**) (Scheme 1). Table I demonstrates that the arylation reaction proceeds in extremely high enantioselectivity with a variety of aryl triflates. Particularly, almost enantiomerically pure (*R*)-**2** was obtained with 2-naphthyl triflate and phenyl triflates bearing an electron-withdrawing substituent at the para or meta position.

The regioselectivity and the enantiomeric purities of the arylation products are strongly affected by the base employed (Ozawa, F.; Kubo, A.; Hayashi, T., *Tetrahedron Lett.*, in press). Table II lists the results of catalytic reactions of 2,3-dihydrofuran with phenyl triflate in the presence of a variety of bases. Extremely high enantioselectivity for (*R*)-**2a** (>96% ee) was obtained with highly basic and sterically demanding 1,8-bis(dimethylamino)naphthalene (proton sponge) (run 1). On the other hand, the enantiomeric purity of (*R*)-**2a** was lower in the reactions using more compact aliphatic amines and less basic amines including pyridine derivatives (runs 2–6). Inorganic bases such as sodium acetate and sodium carbonate also gave lower enantioselectivities (runs 7 and 8). It is interesting to note that increasing product ratio of the minor product (*S*)-**3a** tends to increase the enantiomeric purity of major product (*R*)-**2a**.

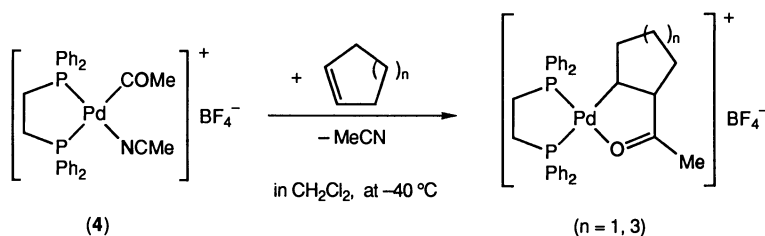
Under similar reaction conditions, *N*-substituted pyrrolines were arylated in 68–83% ee (Scheme 5) (Ozawa, F.; Hayashi, T., *J. Organomet. Chem.*, in press).

Reaction Mechanism

Figure 1 depicts a molecular view of $[\text{PdPh}\{(R)\text{-BINAP}\}]^+$ species which was drawn with the *Chem 3D* computer program using the partial X-ray structure of $[\text{PdCl}_2\{(R)\text{-BINAP}\}]$. It is seen that the lower part of the empty coordination site widely opens whereas the upper part is blocked by one of the phenyl groups of the BINAP ligand.

Scheme 6 shows the two possible modes for coordination of 2,3-dihydrofuran to the $[\text{PdPh}\{(R)\text{-BINAP}\}]^+$ species. As suggested from the molecular model in Figure 1, dihydrofuran may coordinate to the palladium center more easily in mode (a) than (b). The olefin-coordination in mode (a) followed by olefin-insertion and β -hydrogen elimination reactions forms the phenylation product having (*R*)-configuration, that is the observed configuration in major regioisomer **2** in the actual catalytic reactions.

An interesting feature of this asymmetric reaction is that the arylation products **2** and **3** have the opposite configurations to each other, indicating that a kinetic resolution process enhances the enantiomeric purity of major product (*R*)-**2** by selective elimination of (*S*)-isomer as minor product **3** from the catalytic cycle (Scheme 7). Coordination of dihydrofuran on arylpalladium intermediate **5** forms two types of olefin-coordinated complexes **6_R** and **6_S**, depending on the selection of enantiofaces of olefin. Complexes **6_R** and **6_S** thus formed undergo the subsequent olefin-insertion and β -hydrogen elimination reactions to give a pair of diastereomers of hydrido-olefin complexes having (*R*)-2-aryl-2,5-dihydrofuran and (*S*)-2-aryl-2,5-dihydrofuran ligands, **8_R** and **8_S**, respectively. Molecular inspection using CPK models has suggested that **8_R** has a preferable structure for further olefin-insertion and β -hydrogen elimination reactions to give major product (*R*)-**2** (see Scheme 3). On the other hand, the diastereomer **8_S** suffers considerable steric repulsion between the coordinated olefin



Scheme 4.

Table I. Catalytic Asymmetric Arylation of 2,3-Dihydrofuran with Aryl Triflates^a

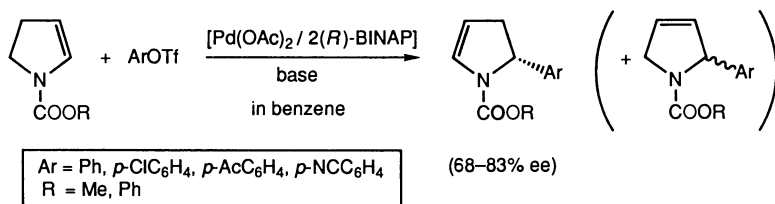
run	ArOTf (Ar)	% ee ^b			yield (%) ^c	
		(R)-2	(S)-3	2/3 ^d	(R)-2	(S)-3
1	Ph (1a)	>96	17	71/29	46	24
2	<i>p</i> -ClC ₆ H ₄ (1b)	>96	6	70/30	54	21
3	<i>m</i> -ClC ₆ H ₄ (1c)	>96	39	72/28	66	22
4	<i>o</i> -ClC ₆ H ₄ (1d)	92	53	73/27	53	21
5	<i>p</i> -AcC ₆ H ₄ (1e)	>96	7	e	50	24
6	<i>p</i> -NCC ₆ H ₄ (1f)	>96	4 (R)	66/34	52	26
7 ^f	<i>p</i> -FC ₆ H ₄ (1g)	>96	24	71/29	46	19
8 ^g	<i>p</i> -MeOC ₆ H ₄ (1h)	87	11 (R)	63/37	42	25
9 ^f	<i>p</i> -MeC ₆ H ₄ (1i)	88	42	77/23	52	15
10	2-naphthyl (1j)	>96	10	69/31	52	26

^a The reaction was carried out in benzene at 40 °C under a nitrogen atmosphere in the presence of 1,8-bis(dimethylamino)naphthalene (proton sponge) as the base for 2–9 days unless otherwise noted. Initial conditions: ArOTf/2,3-dihydrofuran/base/Pd(OAc)₂/(R)-BINAP = 1/5/3/0.03/0.06. ^b Determined by ¹H NMR analysis using an optically active shift reagent Eu(hfc)₃. ^c Isolated yield by silica gel column chromatography at 100% conversion of aryl triflate. ^d Product ratio in the catalytic solution as determined by GLC. ^e Not measured. ^f The reaction was carried out at 60 °C. ^g The reaction was carried out at 50 °C.

Table II. Effect of Base on the Catalytic Asymmetric Arylation of 2,3-Dihydrofuran with Phenyl Triflate (1a)^a

run	base ^b	reaction time	conversion ^c of 1a (%)	2a/3a ^c	% ee ^d	
					(<i>R</i>)-2a	(<i>S</i>)-3a
1		9 d	100	71/29	>96	17
2	Cy ₂ NH	17 h	100	86/14	82	43
3	<i>i</i> -Pr ₂ NEt	24 h	100	92/8	82	60
4	Et ₃ N	26 h	100	98/2	75	9
5		5 d	88	100/0	77	—
6		9 d	38	100/0	69	—
7 ^e	MeCOONa	2 d	82	96/4	71	3 (<i>R</i>)
8 ^e	Na ₂ CO ₃	1 d	100	97/3	75	93 (<i>R</i>)

^a The reaction was carried out in benzene under a nitrogen atmosphere at 40 °C unless otherwise noted. Initial conditions: 1a/2,3-dihydrofuran/base/Pd(OAc)₂/*R*-BINAP = 1/5/3/0.03/0.06. ^b Cy₂NH = dicyclohexylamine. ^c Determined by GLC. ^d Determined by ¹H NMR analysis using an optically active shift reagent Eu(hfc)₃. ^e The reaction was carried out at 60 °C.



Scheme 5.

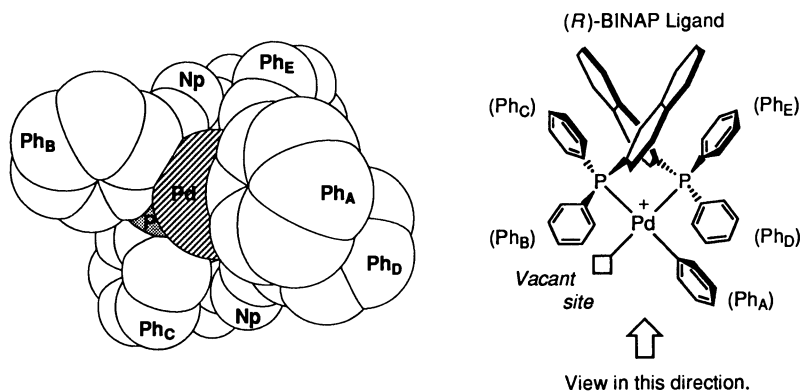
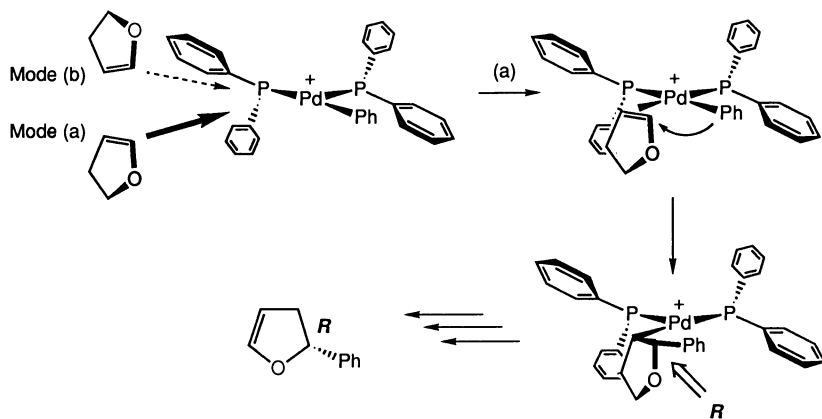
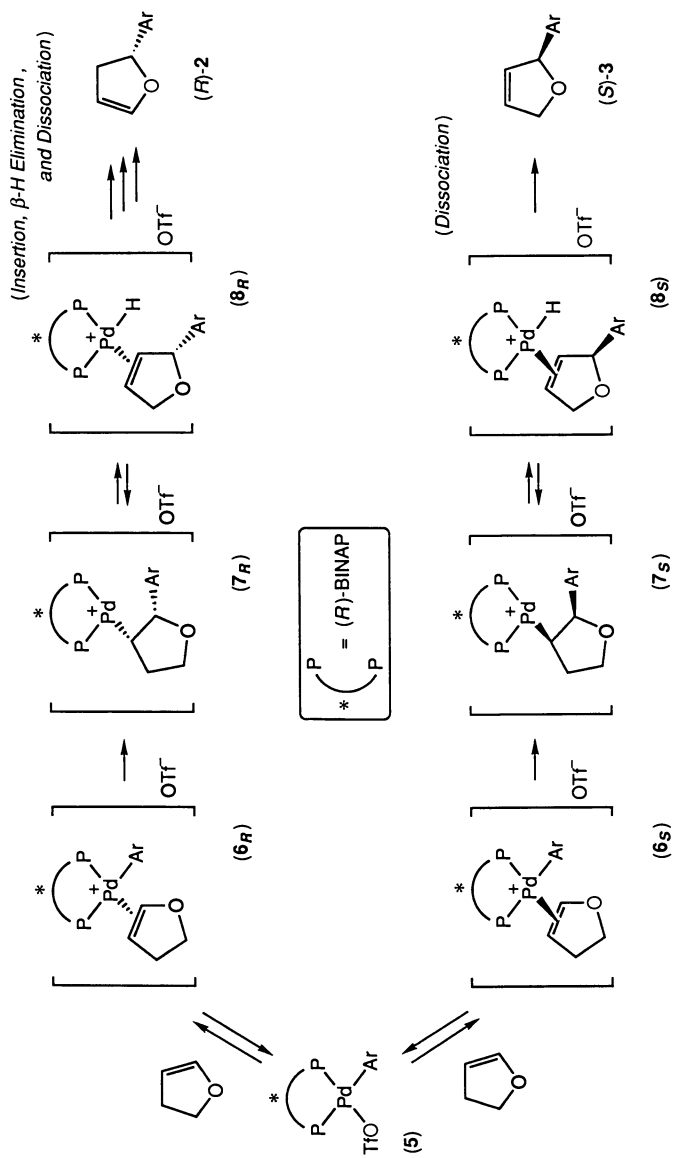


Figure 1. Molecular model of $[\text{PdPh}\{(R)\text{-BINAP}\}]^+$ species.



Scheme 6. A schematic process for the enantioselective insertion of 2,3-dihydrofuran into the Pd-Ph bond in $[\text{PdPh}\{(R)\text{-BINAP}\}]^+$ species, showing the two possible modes (a) and (b) for olefin-coordination. The binaphthyl group in (R)-BINAP ligand is omitted for clarity.



Scheme 7. Proposed mechanism for the kinetic resolution process.

and one of the phenyl groups in the BINAP ligand. Consequently, **8_S** is prone to release the coordinated olefin (*S*)-**3**. The overall process gives rise to the enhancement in the enantiomeric purity of major product (*R*)-**2**.

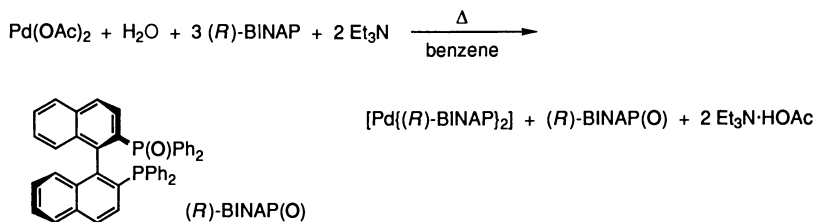
For example, based on the product ratio of (*R*)-**2a** to (*S*)-**3a** and the enantiomeric purities of both compounds, the relative ratio of **8_R** to **8_S** in run 1 in Table I may be calculated as 83 : 17. Therefore, if both diastereomers gave the same regioisomer **2a**, the catalytic reaction should give (*R*)-**2a** of 66% ee; the value being much lower than that observed in the actual catalytic system (>96% ee).

The initial step of the catalytic cycle is oxidative addition of aryl triflate to a BINAP-coordinated Pd(0) species. Since, in the actual catalytic system, Pd(OAc)₂ and (*R*)-BINAP are used as the precursors of the Pd(0) species, reduction of Pd(OAc)₂ into the BINAP-coordinated Pd(0) species should be operative prior to the catalytic reaction. Although Pd(OAc)₂ is the most commonly used precursor of a Pd(0) species in many palladium-catalyzed organic reactions, no direct information has been reported so far on its reduction process. In this study, we confirmed for the first time that the reduction proceeds according to the process involving a combination of tertiary phosphine (BINAP) and water as the reducing reagent (Scheme 8) (Ozawa, F.; Kubo, A.; Hayashi, T., submitted for publication).

Treatment of a benzene solution of Pd(OAc)₂ and 3 equivalents of (*R*)-BINAP with an excess amount of Et₃N resulted in change in the color of the solution from yellow to red. ³¹P{¹H} NMR study of the resulting solution revealed the formation of [Pd{(R)-BINAP}₂] and (*R*)-BINAP monoxide ((*R*)-BINAP(O)) in a 1 : 1 ratio. Labeling experiments showed the participation of 1 equivalent of residual water in the reduction system. Thus, the reaction carried out in solution saturated with ¹⁸OH₂ gave ¹⁸O-labeled (*R*)-BINAP(¹⁸O).

On the basis of the well-defined information on the catalytic system, our attention was directed toward further details of the kinetic resolution process. Thus, the catalytic reaction was examined with isolated [Pd{(R)-BINAP}]₂ catalyst and *i*-Pr₂NEt as the base (Table III). Surprisingly, **2a** was exclusively formed in the catalytic reaction using the [Pd{(R)-BINAP}]₂ catalyst (run 1), indicating that no kinetic resolution takes place. Addition of BINAP(O) did not cause the kinetic resolution (run 2). In contrast, the kinetic resolution occurred in the presence of added acetic acid (runs 3 and 4). The larger amount of acetic acid gave rise to the higher ratio of **3a** and the higher enantiomeric purity of (*R*)-**2a**. In the presence of 5 equiv/Pd of acetic acid, almost enantiomerically pure (*R*)-**2a** was obtained.

Since the catalytic system contains an excess amount of amine, acetic acid added to the system forms the ammonium acetate salt, which is also formed in the catalytic system starting with Pd(OAc)₂ as the catalyst precursor during the conversion of Pd(OAc)₂ into a Pd(0) species (Scheme 8). The results described above demonstrate that the acetate anion thus formed serves as the promoter of the kinetic resolution process. Since the hydrido-olefin complex **8_S** in Scheme 8 has a 16e square planar structure, dissociation of the coordinated olefin should proceed via an associative mechanism involving an 18e transition state formed by nucleophilic attack of an incoming ligand to the palladium center. The acetate anion may possess the high nucleophilicity toward the cationic palladium center in **8_S** to cause the dissociation of the olefin. The nucleophilicity of acetate anion should be defined by the counter cation particularly in nonpolar media such as benzene. The marked difference in effect of bases in the kinetic resolution process is attributable to the difference in the nucleophilicity of acetate anion that is controlled by the ammonium cation. Proton sponge as one of the most strong bases for trapping proton in organic solvents may generate the highly reactive acetate anion that promotes the efficient kinetic resolution giving (*R*)-**2** of extremely high enantiomeric purity.



Scheme 8.

Table III. Catalytic Asymmetric Arylation of 2,3-Dihydrofuran with Phenyl Triflate (1a) Promoted by [Pd{(R)-BINAP}₂] Catalyst^a

run	additive (equiv./Pd)	2a/3a ^c	% ee ^b	
			(R)-2a	(S)-3a
1	—	100/0	77	—
2	BINAP(O) (1)	100/0	76	—
3	AcOH (2)	89/11	83	64
4	AcOH (5)	84/16	>96	60

^a The reaction was carried out in benzene at 40 °C under a nitrogen atmosphere in the presence of *i*-Pr₂NEt as the base for 1–2 days. Initial conditions: 1a/2,3-dihydrofuran/*i*-Pr₂NEt/catalyst = 1/5/3/0.03. ^b Determined by ¹H NMR analysis using an optically active shift reagent Eu(hfc)₃. ^c Product ratio in the catalytic solution as determined by GLC.

Literature Cited

1. Heck, R. F.; Nolley, Jr., J. P. *J. Org. Chem.* **1972**, *37*, 2320.
2. Dieck, H. A.; Heck, R. F. *J. Am. Chem. Soc.* **1974**, *96*, 1133.
3. Mori, K.; Mizoroki, T.; Ozaki, A. *Bull. Chem. Soc. Jpn.* **1973**, *46*, 1505.
4. Heck, R. F. *Org. React.* **1982**, *27*, 345.
5. Heck, R. F. *Acc. Chem. Res.* **1979**, *12*, 146.
6. Heck, R. F. In *Palladium Reagents in Organic Synthesis*; Academic Press: New York, 1985.
7. Daves, Jr., G. D.; Hallberg, A. *Chem. Rev.* **1989**, *89*, 1433.
8. Sato, Y.; Sodeoka M.; Shibasaki, M. *J. Org. Chem.* **1989**, *54*, 4738.
9. Sato, Y.; Sodeoka M.; Shibasaki, M. *Chem. Lett.* **1990**, 1953.
10. Kagechika, K.; Shibasaki, M. *J. Org. Chem.* **1991**, *56*, 4093.
11. Carpenter, N. E.; Kucera, D. J.; Overman, L. E. *J. Org. Chem.* **1989**, *54*, 5846.
12. Ozawa, F.; Kubo, A.; Hayashi, T. *J. Am. Chem. Soc.* **1991**, *113*, 1417.
13. (R)-BINAP: (R)-2,2'-bis(diphenylphosphino)-1,1'-binaphthyl. Takaya, T.; Mashima, K.; Koyano, K.; Yagi, M.; Kumobayashi, H.; Taketomi, T.; Akutagawa, S.; Noyori, R. *J. Org. Chem.* **1986**, *51*, 629, and references cited therein.
14. Brumbaugh, J. S.; Whittle, R. R.; Parvez, M.; Sen, A. *Organometallics* **1990**, *9*, 1735.
15. Samsel, E. G.; Norton, J. R. *J. Am. Chem. Soc.* **1984**, *106*, 5505.
16. Ozawa, F.; Hayashi, T.; Koide, H.; Yamamoto, A. *J. Chem. Soc., Chem. Commun.* **1991**, 1469.

RECEIVED July 9, 1992

Chapter 7

Clusters, Alloys, and Poisoning

An Overview

Kenneth J. Klabunde and Yong-Xi Li

Department of Chemistry, Kansas State University, Manhattan, KS 66506

A brief overview of bimetallic catalysts is presented. Electronic *vs.* ensemble effects are discussed, and literature is reviewed on single crystal bimetallics, and supported bimetallic clusters. Bimetallic cluster compounds are considered as models. Structural considerations, effects of potential poisons, particles from bimetallic cluster compounds, and catalytic activity/selectivity studies are briefly reviewed and discussed.

Bimetallic particles are playing a key role both in industrial catalysis and in aiding our understanding of fundamental gas-solid reaction mechanisms and dynamics. The study of bimetallic clusters/particles takes on new dimensions as scientists are better able to control their synthesis and unravel their complex structures.

A fundamental question that has driven this substantial effort in such materials is "are catalytic reactions governed by geometrical effects on the metal surface, or are subtle electronic effects more important?" Practical aspects have also given an important impetus to the work since unexplained and sometimes remarkable new properties are imported to a metallic catalyst by the addition of a second metal.

The topics of great current interest in this field range from the most basic studies of molecular cluster compounds to the more applied aspects of catalyst testing. A brief overview of certain aspects will now be presented, which is not intended to be exhaustive.

Molecular Bimetallic Cluster Compounds

A few illustrative examples dealing with bimetallic cluster compounds will now be presented. For example, mixed cluster compounds $[M_2Ru_4(\mu-CO)_3(CO)_{10}(PPh_3)_2]$ where $M = Cu, Ag,$ and Au have been prepared and structurally characterized.⁽¹⁾ Metal core structures consist of a Ru_4 tetrahedron with $M-PPh_3$ groups capping two

Ru₃ faces. Such structures are significantly different from similar hydrido-clusters. Cluster compounds of Re-Pt such as Cp(CO)(NO)Re₂(PR₃)PtH(PPh₃)₂⁺ have also been of interest, and have provided evidence of a secondary reaction pathway for Pt assisted CO substitution.(2)

Indeed there are numerous bimetallic clusters now prepared and characterized and the recent book by Mingos and Whales summarizes the field very well.(3)

Bimetallic Crystal Surfaces

Somorjai and coworkers(4) have codeposited Rh vapor on the (111) face of platinum, and Pt vapor on the (0001) face of rhenium under ultrahigh vacuum. Then a high pressure microreactor was employed for the study of ethane hydrogenolysis. The reaction was shown to be structure sensitive. It was also shown that a bimetallic surface of the stoichiometry Re₂Pt was found to be the most active (about ten fold more active than the Re(0001) surface). Their results suggested that an electronic interaction exists between platinum and rhenium metals which strongly influenced the catalytic hydrogenolysis of ethane. Furthermore, carbonaceous deposits adhered the least tenaciously to Pt-Re bimetallic surfaces. Additional studies by Godbey(5) supported this electronic effect according to XPS, because the 4f7/2 peaks shifted to higher binding energies for both metals when Re was deposited on Pt. Further studies by Godbey and Somorjai(6) showed that the growth mode of Pt on Re(0001) was layer by layer. On the other hand, Re evaporated onto Pt(111) grows with a hcp (hexagonal close packed) structure exposing the (0001) face, while on Pt(100) it grows with a fcc (face centered cubic) structure exposing the (100) face. The presence of platinum on a partially oxidized Re(0001) surface was found to catalyze the decomposition of rhenium oxides as low as 400°C.

Additional strong evidence for electronic effects in bimetallic systems comes from the recent work of Goodman and coworkers.(7) Employing temperature programmed desorption (TPD) and XPS, it was shown that CO adsorption to thin layers of Pd on Ta or W crystals was significantly altered by the Ta or W crystalline substrate. It was found that XPS (Pd(3d 5/2)) core level shifts correlated with the changes in CO adsorption strength. Similar results have been observed with Cu on Rh crystals.

These and other recent results demonstrate that bimetallic systems can be catalytically interesting because of both geometrical and electronic effects. This is certainly encouraging for further research --- a very rich field of investigation still awaits elucidation by chemists, physicists, and engineers.

Heterogeneous Catalysts Derived from Bimetallic Cluster Compounds

Driven by the desire to prepare well characterized bimetallic clusters on catalyst supports, a great deal of work has been carried out where cluster compounds have been deposited on catalyst supports in the hope of preparing "well defined" catalytic particles. For example H₂FeOs₃(CO)₁₃, H₂FeRu₃(CO)₁₃, and H₂FeCo₃(CO)₁₂ have been supported on partially dehydroxylated MgO.(8) After H₂ treatment at 400°C, very small bimetallic particles were produced having the same bulk composition as that of the starting cluster compound (based on high spacial resolution analytical

microscopy). Adsorption (from CH_2Cl_2 solution) of separate clusters $\text{Fe}_3(\text{CO})_2 + \text{M}_3(\text{CO})_{12}$ did not yield bimetallic clusters.

Shapley and coworkers(9) have reported analogous findings with $\text{CpMoIr}_3(\text{CO})_{11}$, and $\text{Cp}_2\text{Mo}_2\text{Ir}_2(\text{CO})_{10}$. After H_2 treatment at 500°C Ir containing materials $[\text{Mo}_2\text{Ir}_2]$, $[\text{MoIr}_3]$, $[\text{Ir}_4]$ and $[\text{Ir}_4 + 2 \text{Mo}_2]$ were active catalysts for hydrogenolysis of n-butane, but the $[\text{MoIr}_3]$ system was most active. Overall, the data supported the concept of a unique bimetallic effect in catalysis.

Ichikawa and coworkers have also reported promising results.(10) Carbonyl clusters as precursors were deposited on SiO_2 . Thus, $[\text{FeRh}_4]$ and $[\text{Fe}_2\text{Rh}_4]$ cluster derived catalysts showed high selectivity for formation of ethanol and methanol in CO hydrogenation. Analogously, $[\text{Fe}_3\text{Pt}_3]$, $[\text{Fe}_6\text{Pt}_6]$ and $[\text{FeIr}_4]$ cluster derived catalysts yielded methanol in high selectivity while $[\text{Fe}_4\text{Pt}]$ and $[\text{Fe}_4\text{Pd}]$ were not selective. Mössbauer and EXAFS indicated, surprisingly, that the iron existed on the SiO_2 surface as primarily Fe^{3+} even after H_2 reduction. This suggested that Fe reacted with surface $[\text{SiO}_2]\text{-OH}$ groups so that iron was oxidized and this anchored the cluster to the surface. Additional work utilizing $\text{Rh}_6\text{-xIr}_x(\text{CO})_{16}$ clusters was carried out in order to synthesize RhIr clusters inside cages of NaY zeolite.(11) EXAFS, FTIR and ^{129}Xe NMR studies demonstrated that the bimetallic particles were very small, less than 10\AA , with homogeneous metal compositions. Butane hydrogenolysis activities were suppressed greatly by small increases in Ir content.

In a similar approach Gates and coworkers(12) prepared $\text{H}_2\text{RuOs}_3(\text{CO})_{13}$, $\text{H}_4\text{RuOs}_3(\text{CO})_{12}$, $\text{Et}_4\text{N}[\text{HRuOs}_3(\text{CO})_{13}]$, and $\text{Et}_4\text{N}[\text{H}_3\text{RuOs}_3(\text{CO})_{12}]$, and these were allowed to react with basic -OH groups on Al_2O_3 . Surface bound anions were formed. Upon mild heating additional reactions were observed. For example $[\text{H}_3\text{RuOs}_3(\text{CO})_{12}]\text{-(Al)}$ was formed, and served as a precursor of a catalyst active for the isomerization of 1-butene to 2-butenes. Interestingly, this $[\text{H}_3\text{RuOs}_3(\text{CO})_{12}]\text{-(Al)}$ species was, according to spectroscopic analyses, the principle surface moiety on the working catalyst. It was also found that when C_2H_4 hydrogenation was attempted, the clusters were degraded and metal particles were formed. In this case, the particles or perhaps even mononuclear metal complexes served as the catalytic species. Bimetallic Re-Os and Re-Pt cluster compounds were also supported on Al_2O_3 .(13) Characterization by XPS and EXAFS after hydrogen reduction showed that Re valence states were variable depending on the metal partner. These results were interpreted in terms of multifunctional catalysis, rather than alloy participation.

The cluster compounds $(\text{RCN})_2\text{M}_2\text{Ru}_6\text{C}(\text{CO})_{16}$ where $\text{R}=\text{C}_1\text{-C}_6$ alkyl, Ph; or $\text{C}_6\text{-C}_{10}$ aralkyl, and $\text{M} = \text{Cu}, \text{Ag}, \text{or Au}$, are useful bimetallic systems for converting $\text{CO} + \text{H}_2$ to CH_3OH .(14) No catalyst support was employed, and a static reactor operating at 275°C at moderate pressures was effective (no hydrocarbons were produced).

Polymer supported anionic clusters of $\text{Ru}_{3,4}$ and $\text{Os}_{3,4}$ as well as RuOs_3 have been studied as hydroformylation catalysts.(15) The supported clusters were more active than solution analogs, and the mixed metal clusters were the most active.

A somewhat different approach has been employed by Sachtler and coworkers.(16) Conventionally prepared Pt/NaY (platinum particles on NaY zeolite) was treated with the $\text{Re}_2(\text{CO})_{10}$ vapor. After deposition, heating in a

reducing atmosphere caused CO removal, and the formation of PtRe bimetallic particles.

Solvated Metal Atom Dispersed (SMAD) Bimetallic Catalysts

Another non-conventional preparative route to bimetallic catalysts has been developed where metal atoms (vapors) have been trapped at low temperature in solvating media. (A review has recently appeared).(17) By solvating two metals at the same time (eg. Co in toluene and Mn in toluene), followed by warming, bimetallic clusters/particles form. In the presence of a catalyst support, surface -OH groups can have a dramatic effect on the structure of the small bimetallic cluster produced. For example, with Co and Mn, a layered structure of MnO_x covered by Co^* in a particle of about 25 Å was formed.(18) With Fe and Co combinations, a layer of FeO_x followed by Fe^*Co^* alloy and a surface rich in Co^* was formed.(19)

When less oxophilic metals were employed, such as Pt-Sn and Au-Sn combinations, more "alloy-like" particles were formed.(20) However, when SiO_2 or Al_2O_3 were present, some surface richness in Pt on the bimetallic particle was suggested by catalysis and spectroscopic studies. Finally, in the case of Au-Sn, under the conditions of slow growth of bimetallic particles, a tendency toward formation of stable intermetallic small particles was noted.(21)

All of the bimetallic SMAD catalysts have shown unusual catalytic properties. Several laboratories are now reporting similar findings.(22,23) Both geometric/ensemble effects and electronic effects have been considered in trying to explain these unusual properties.

Bimetallic Catalysts - Structural Considerations

Although typical catalyst preparation procedures vary slightly from one laboratory to another, the "conventional approach" is to deposit a metal salt on a support, convert this salt to the oxide, and then reduce to the metallic state. When two metals are simultaneously so treated and reduced, bimetallic clusters may form. However, it cannot be assumed that bimetallic clusters are produced since monometallic separate particles may predominate. In fact, it is perhaps the unusual case where bimetallics do form since there are many possible paths, both thermodynamic and kinetic, that can lead to (1) separate monometallics, (2) one metal not reduced, (3) thermal segregation of bimetallic precursor particle, and/or (4) volatilization or migration of one metal.

Since there are many problems with regards to establishing cluster/particle structure, studies reported often only deal with catalyst activity/selectivity experiments. A summary of recent work along this line will be given later. At this time, structural aspects of bimetallic particles will be summarized. By far the most widely used techniques for deducing cluster/particle structure are EXAFS and

Mössbauer (and Mössbauer is only applicable for Fe, Ir, Eu, Au and Sn). Powder X-Ray diffraction and chemisorption studies are not as useful for characterizing such bimetallic particles due to their small size and poorly understood synergistic chemisorption properties.

Sinfelt and coworkers have been true pioneers in this area of structural elucidation and EXAFS has been a valuable tool. Since so many studies have been reported, we will attempt to summarize by use of Table I. The bimetallic particles formed, conditions treated, techniques employed, comments and literature references are given. Reports dealing primarily with structures of the particles are included. Actually, only gross structural features can usually be ascertained. The reader should note the date of the reports. Since 1980 the data has steadily improved allowing better and better structural elucidation.

Catalysts --- Poisoning and General Reactivity Studies

Frequently, studies of bimetallic catalysts are carried out primarily with an eye toward effects of poisoning and catalysts lifetime. Afterall, these are the most important parameters that are the most sensitive and important from an industrial viewpoint.

Table II summarizes some pertinent information. It is useful to point out some particular features of all these data. First of all, the predominance of work on Pt-Re, Pt-Ir, and Pt-Sn is due to the industrial importance of these commercial catalysts. In recent years, the member of combinations has grown, and this will certainly continue.

Some unusual preparative procedures should also be noted, such as photoimpregnation,(31,32) Pt-Sn complexes in acetone,(37) vapor deposition of Sn and Pt,(43) surface reactions of tin alkyls with Pt particles,(45) and ion exchange in zeolites.(53) However, no matter what the preparative method, the data clearly indicate that enhancement in catalytic activities/selectivities/lifetimes depend on a variety of factors; no single parameter, such as alloy formation, can satisfactorily explain the results. Thus, alloy or bimetallic cluster formation definitely can occur depending on the metals in question and treatment conditions. However, metal ions (metal oxides) also can be important, especially with regard to anchoring of metallic particles to the support. It becomes increasingly evident that multiple effects can be important and each bimetallic catalysts can have its own unique electronic/geometric/anchoring behavior.

On the other hand, a few generalities can be gleaned from these data. First of all, "alloy like" or bimetallic particles will likely form if the two metals have similar and favorable tendencies toward forming the metallic state; i.e. Pt, Ir, Cu, Ag, Au, etc. However, oxophilic metals such as Mn, Fe, Ru, Re, Os, etc. have a strong tendency toward forming/retaining the form of surface oxides, and the presence of surface -OH groups on the catalyst support can serve as oxidizing agents (if needed) and can govern this behavior.

Bimetallic catalysts will continue to entice the curiosity of chemists for a long time to come. And then, what about multimetallics?

Table I. A Brief Summary of Literature Relating Generally to Structural Elucidations of Bimetallic Catalysts

Bimetallic Combination	Method or Prep./Particle Size (Å)/ Treatment Cond.	Techniques Employed
Pt-Ir	Cl salts on SiO ₂ reduced 200-300 °C / ~ 10 / 200-300 °C	¹⁹³ Ir Mossbauer
	Strong segregation tendencies. ²⁴	
Re-Cu Ir-Cu Pt-Cu	coimpregnation of salts on SiO ₂ , reduced at 500 °C / ~ 17 / 400-450 °C	EXAFS EXAFS EXAFS
	Bulk miscibility is less of a governing factor in the smallest particles. M-M' bonding is prevalent. ²⁵	
Ag-Cu Au-Cu	coimpregnation of salts on SiO ₂ , reduced at 500 °C / < 100, ~ 65 / 400-450 °C	EXAFS
	Extensive segregation. Cu in center with Ag on surface. Au in interior, Cu on exterior. ²⁶	
Pt-Cu	coimpregnation on NaY zeolite, 500 °C / 10-20 / 500 °C outgassing	EXAFS
	Cu atoms leached from surface leaving more Pt on surface. Pt rich in center before outgassing. ²⁷	
Pt-Re	coimpregnation on SiO ₂ , 500 °C reduction / > 100 / 500 °C reduction, then cool H ₂ .	Synchrotron anomalous X-ray diffraction
	hcp and fcc Re; strong Pt-Re interaction. ²⁸	
Pt-Re Pd-Re	coimpregnation on Al ₂ O ₃ , reduced at 500 °C / - / -	EXAFS
	Pd-Re less mixed than Pt-Re. ²⁹	
Pt-Ir	Ionic, bimetallic mixed complexes impregnated on Al ₂ O ₃ / - / -	EXAFS
	Ir(IV) present. ³⁰	
Pt-Rh	salts photo-impregnated on TiO ₂ / 10-30 / photolysis at room temp.	TEM STEM-EDX
	Bimetallic particle formation dependent on reduction rates. ^{31,32}	

Continued on next page

Table I. A Brief Summary of Literature Relating Generally to Structural Elucidations of Bimetallic Catalysts (Continued)

Bimetallic Combination	Method or Pre./Particle Size (Å)/ Treatment Cond.	Techniques Employed
Pt-Re Pt-Rh	coimpregnation on Al ₂ O ₃ / - / Not reduced. A study of drying and calcination steps.	EXAFS
	Upon drying oxygen substitutes chlorine around Pt ^{x+} . Anchoring sites on Al ₂ O ₃ vary in strength. ^{33,34}	
Pt-Rh Pt-Re	coimpregnation on Al ₂ O ₃ . Calcined at 530°C. / - / successive H ₂ reduction temperatures.	EXAFS
	First moments of formation of bimetallic cluster monitored. Controlled by Al ₂ O ₃ network initially. Metal segregation occurs later after particle growth. ³⁵	
Pt-Sn	Coimpregnation on Al ₂ O ₃ or SiO ₂ . Calcined at 500°C. / - / Reduced at 400°C.	Chemisorption methods, XPS
	Sn(II) and Sn(IV) present on Al ₂ O ₃ after reduction step. However, Sn ⁰ present on SiO ₂ . Sn ⁰ may be present to alter catalyst selectivity/activity. ³⁶	
Pt-Sn	Pt-Sn complex in acetone impregnated on Al ₂ O ₃ / - / Reduced in situ at 375°C at elevated H ₂ pressure.	XPS
	Sn ⁰ probably alloyed with Pt ⁰ . ³⁷	
Pt-Re Pt-Ir	Coimpregnation on SiO ₂ / - / -	Acetylene hydrogenation activity/selectivity
	Addition of Re or Ir to Pt resulted in decreased activity and increased selectivity. ³⁸	
Cu-Ir Au-Ir	Coimpregnation / - / -	Hexane/H ₂ activity/select. Acetylene/H ₂ activity/select.
	Mixed Ir/Cu ensembles are important. Dissociative adsorption suppressed by alloying. ³⁹	

Table I. Continued

Bimetallic Conditions	Method or Prep./Particle Size (Å)/ Treatment Cond.	Techniques Employed
Fe-Ru, Fe-Rh Fe-Pd, Fe-Ir Fe-Pt, Co-Ir Co-Pt, Ni-Ir Ni-Pt	Coimpregnation on SiO ₂ / - / -	Co hydrogenation to CH ₄ and methanol.
	Active sites for the Fe-Ir/SiO ₂ system contain Ir ⁺ and Fe ^{2+/3+} . ⁴⁰	
Pt-Re	Coimpregnation on Al ₂ O ₃ , SiO ₂ , or Y-zeolite, reduced in H ₂ / - / -	Hydrocarbon hydrogenolysis
	Mixed clusters much more active. Formation of bimetallic clusters depends on surface migration of Re oxide to hydrogen covered Pt particle; and coalescence of migrating metal particles (especially on zeolites). ⁴¹	
Pt-Sn	Coimpregnation on Al ₂ O ₃ . Reduced in H ₂ / - / -	Temperature programmed reduction and desorption.
	Average oxidation state of tin was Sn ²⁺ . Small amounts of Sn ⁺ and/or Pt-Sn alloys are possible. Beneficial affect of tin can be attributed to enhanced hydrogen mobility from Sn sites to Pt sites. ⁴²	
Pt-Sn	Vapor deposition of Sn and Pt. / - / -	TEM, X-Ray diffraction
	SnO is formed, but H ₂ reduction causes SnO to disappear, and PtSn alloy remains. Electronic interaction and support modifications are functions of tin. ⁴³	
Pt-Ir	Coimpregnation on SiO ₂ . Reduced in H ₂ / - / -	¹⁹³ Ir Mossbauer
	Strong tendencies toward segregation. ⁴⁴	
Pt-Sn	Surface reactions of SnR ₄ with Pt/Al ₂ O ₃ , and by Sn halide reduction by Li/H ₂ on Al ₂ O ₃ / - / -	Hexane dehydrocyclization
	New preparative methods yielded Pt-Sn particles. ⁴⁵	

Continued on next page

Table I. A Brief Summary of Literature Relating Generally to Structural Elucidations of Bimetallic Catalysts (Continued)

Bimetallic Combination	Method or Prep./Particle Size (Å) Treatment Cond.	Techniques Employed
Pt-Re Pd-Re	Coimpregnation of Al ₂ O ₃ / - / -	EXAFS
	Pt-Re and Pd-Re clusters are present, but they have regions rich in one metal (partial segregation). Sulfur treatment has little effect on these structures. ⁴⁶	
Pt-Sn Pt-In	Coimpregnation on Al ₂ O ₃ / - / -	Photoelectron spectra
	Pt exists in an electron deficient state, and this deficiency increases with addition of Sn or In. ⁴⁷	
Pt-Ir	Coimpregnation on Al ₂ O ₃ / - / -	Deuterium exchange reactions and hydrogenolysis of alkanes.
	Ir ensembles of 3 atoms possibly required. Depth of hydrogenolysis increases with Ir content, probably due to increased strength of adsorption. ^{48,49}	
Pt-Sn	Impregnation / - / -	High resolution electron microscopy
	Industrial Pt-Sn catalyst studied. Sn is dissolved in Pt forming a solid solution at low Sn concentrations. Sn crystallinities observed at higher concentrations. ⁵⁰	
Pt-Re	Coimpregnation / - / -	XPS
	Pt is metallic, but most of the Re is in oxidized state. ⁵¹	
Pt-Ir	Coimpregnation on Al ₂ O ₃ / - / Reduced in H ₂ .	Temperature Programmed Reduction.
	Pt mobilization prior to interaction with anchored Ir phase. ⁵²	

Table I. Continued

Bimetallic Combination	Method or Prep./Particle Size (Å)/ Treatment Cond.	Techniques Employed
Cu-Pt, Cu-Ir Cu-Rh, Cu-Ru	Ion exchange on zeolites, H ₂ reduction at 500°C. / - / -	XPS, TEM, H ₂ chemisorption, IR of adsorbed CO.
	Bimetallic clusters are homogeneously dispersed with constant size over a range of compositions. Cu addition decreased activities. ⁵³	
Pt-Ir	Coimpregnation on Al ₂ O ₃ / - / Calcined at various temperatures. Then H ₂ reduction.	Chemisorption of H ₂ and CO
	By choice of calcining temperature, and then reduction, segregation into Pt rich and Ir rich clusters could be accomplished. Catalyst activity degraded with increased segregation of Pt and Ir. ⁵⁴	
Pt-Sn Pt-Re	Coimpregnation on Al ₂ O ₃ . Promoted with K / - / Reduced in H ₂ .	XPS
	Aluminate of K or Sn had metallic Re on its surface. ⁵⁵	
Pt-Sn	Coimpregnation on Al ₂ O ₃ . / - / Reduced in H ₂ .	Hydrogenation, hydrogenolysis, aromatization of hydrocarbons.
	Sn ⁰ dilutes Pt surface. Aromatization goes through a maximum as a function of Sn content. Sn also has an electronic effect on the Pt. ⁵⁶	
Pt-Re	Coimpregnation on Al ₂ O ₃ . / - / -	EXAFS
	Role of Re is to fix the Pt on the support (during the drying/calcination of the catalyst). ⁵⁷	
Cu-Os Pt-Ir Cu-Ru	Coimpregnated on Al ₂ O ₃ or SiO ₂ . / - / Reduced in H ₂	EXAFS
	For Pt-Ir both metals interact strongly with the support and the Pt-Ir clusters exist as rafts, with Ir at the core. For Cu-Os, Os occupies the core of the particle. ^{58,59}	

Continued on next page

Table I. A Brief Summary of Literature Relating Generally to Structural Elucidations of Bimetallic Catalysts (Continued)

Bimetallic Combination	Method or Prep./Particle Size (Å) Treatment Cond.	Techniques Employed
Pt-Ir	Coimpregnated on Al ₂ O ₃ or SiO ₂ / 25-50 / Reduced in H ₂	EXAFS
	One of the earliest EXAFS studies of highly dispersed Pt-Ir Systems. ⁶⁰	
Pt-Sn	Coimpregnating on Al ₂ O ₃ in acetone. / - / Reduced in H ₂	Temperature Program reduction
	Pt catalyzes the reduction of Sn(IV) to Sn(II). Presence of Sn increases dispersion of Pt. No Pt-Sn alloys form. ⁶¹	
Pt-Ir	Coimpregnating on Al ₂ O ₃ . / - / -	High resolution weak beam images.
	Alloys are not formed. ⁶²	
Pt-Re	Coimpregnated on Al ₂ O ₃ . / - / sulfided	Proton induced X-ray emission, Rutherford backscattering, electron microscopy.
	Sulfur is bound to Pt. ⁶³	
Pt-Sn Pt-Zn	Alloys supported on ZnAl ₂ O ₄ spinel. / - / -	Hydrocarbon reforming
	Alloys of fcc structure increase catalyst activity/selectivity. Too much Sn or Zn deactivated catalyst, and form alloy of structure different from that of Pt. ⁶⁴	

Table II. A Brief Summary of Literature Relating Generally to Reactivity–Selectivity–Poisoning Studies of Bimetallic Catalysts

Bimetal. Catal.	Conditions	Catal. Processes Studied (Cond.)
Pt-Zn/Al ₂ O ₃ Pt-Ga	Al ₂ O ₃ and HZSM-5 supports	Dodecane and Isobutane dehydrog. 480°, 0.1 MPa, H ₂ /RH = 8/1) Aromatization of C ₃ /C ₄ hydrocarbons.
	Zn addition promotes C ₃ H ₈ formation and restricts its reactivity; Ga promotes alkene aromatization. ⁶⁵	
Pt-Re Pt-Ir	Al ₂ O ₃ support	Hydrog. of C ₆ H ₆ in presence of thiophene and coke.
	Hydrogenolysis of adsorbed thiophene (poison) is the rate determining step. Sulfur resistance was Pt > Pt-Ir > Pt-Re. ^{65,66}	
Pt-Ir	Calcining at various temps.	Studies of H ₂ O vapor effects on Cl content and IrO ₂ particle size after calcination.
	Cl level and calcination temperature often control Ir agglomeration in Pt-Ir catalysts. H ₂ O vapor also promotes IrO ₂ agglomeration. Actually, H ₂ O vapor removes Cl from surface, leading to more IrO ₂ agglomeration. ⁶⁷	
Pt-Sn	Coking allowed, then regeneration cycles carried out	n-Butane dehydrogenation, TEM, Mossbauer, H ₂ chemisorption.
	Coking - regeneration cycle was examined. Surface area diminished while Pt-Sn alloy increased. Sn ²⁺ and Al ₂ O ₃ interaction important in catalyst stability. CeO ₂ addition enhanced stability. ⁶⁸	
Pt-Re Pt-Sn	none	Kinetics of coking during hydrocarbon reforming.
	Coke formation is inverse first order in H ₂ , 0.75 order in feedstock pressure, and inverse first order in coke already present; E _a = 37 kcal/mole. Coking is more pronounced with heavier feedstocks, especially polycyclic hydrocarbons. ⁶⁹	

Continued on next page

Table II. A Brief Summary of Literature Relating Generally to Reactivity–Selectivity–Poisoning Studies of Bimetallic Catalysts (continued)

Bimetal. Catal.	Conditions	Catal. Processes Studied (Cond.)
Pt-Re	Al ₂ O ₃ support	Hydrocarbon reforming
	Coke deposition begins on metal site and then continues on acidic catalysts sites. When combustion of coke is carried out in order to regenerate the catalyst, it is removed from the metal sites first. ⁷⁰	
Pt-Ir, Pt-Re Pt-Sn, Pt-Ge	Al ₂ O ₃ support	Reforming of n-heptane
	Coke deposition less extensive on bimetallics. Coke on Pt-Ir richer in hydrogen and more reactive. ⁷¹	
Pt-Re	Al ₂ O ₃ support	Partial coke burning. C ₆ H ₆ hydrogenation and n-pentane isomerization.
	Coke burning recovers metal sites first. Coke on support can later migrate to metal sites. ⁷²	
Pt-Re	Sulfided and chlorided, Al ₂ O ₃ support	Coking allowed, and coke characterized by temp-programmed oxidation. Also catalyst testing.
	Smaller coke deposition on sulfided and chlorided catalysts. ⁷³	
Pt-Ir	Sulfided, Al ₂ O ₃ and SiO ₂ supports	n-Hexane hydrogenolysis/reforming. Temp. programmed reduction and X-ray diffraction.
	Alloy formation in Pt-Ir/SiO ₂ catalyst. After sulfiding all catalysts showed a "Pt-like" behavior with respect to selectivity. High dehydrogenating activity of Re probable. ⁷⁴	
Pt-Sn Pt-Re	Nitrogenated, sulfided, Al ₂ O ₃ support	Reforming of C ₇ hydrocarbons.
	Nitrogenating promoted dealkylation. Sulfiding lowered aromatics yield, but prolonged catalyst life. ⁷⁵	
Pt-Re	sulfided, Al ₂ O ₃ support	Hydrogenolysis and reforming of n-hexane and methylcyclopentane. Coke deposition measured.
	Introduction of Re and S increased selectivity more effectively than coke formation. Coke deposited on metal sites first. Presulfiding deactivates metal sites toward coke formation. Metal sites control overall deactivation. ⁷⁶	

Table II. Continued

Bimetal. Catal.	Conditions	Catal. Processes Studied (Cond.)
Pt-Cu, Pt-Zn Pt-Cd, Pt-In Pt-Ge, Pt-Tl Pt-Sn, Pt-Pb Pt-Se	Al ₂ O ₃	Dehydrogenation of n-dodecane
	Bimetallic systems showed more stable performance, even in the presence of intense coke formation. Bimetallic systems showed a high tolerance to coke formation. ⁷⁷	
Pt-Re Pt-Ge	Pt-Re sulfided, Al ₂ O ₃ support	Hydrocarbon reforming
	Activity trend Pt/Al ₂ O ₃ > Pt-Re-S/Al ₂ O ₃ > Pt-Ge/Al ₂ O ₃ ; Pt best for hydrocracking, Pt-Re-S best for aromatization, Pt-Ge for isomerization. Complex phenomenon and dangerous to extrapolate results to different experimental conditions. ⁷⁸	
Pt-Cu, Pt-Zn Pt-Ga, Pt-Ge Pt-As, Pt-Re Pt-S	none	Paraffin dehydrogenation and hydrogenolysis
	Bimetallics prevent coke deposition and decrease unsaturated products adsorption. Re suppresses coke formation and cause coke redistribution on catalyst components. ⁷⁹	
Pt-Sn	none	Dehydrocyclization of n-octane at 1 atm and 2.7 MPa.
	Sn promotion effects independent of H ₂ and hydrocarbon pressure. Sn decreases isomerization activity, but increases dehydrocyclization activity. ⁸⁰	
Pt-Re	sulfided, Al ₂ O ₃ support	Hydrocarbon reforming
	Stability of catalysts not affected by drying temperatures, but is affected by sulfiding. Sulfided catalyst fouled by different mechanism. ⁸¹	
Pt-Ir Pt-Re	Coke formation, Al ₂ O ₃ support	Cyclopentane reforming
	Coke deposition is lowered by presence of Ir on Re. Amount of coke oxidizable at low temperatures decreases in the order Pt-Re > Re > Pt > Pt-Ir > Pt. Poisoning by coke lowest on Pt-Re and highest on Pt-Ir. ⁸²	

Continued on next page

Table II. A Brief Summary of Literature Relating Generally to Reactivity–Selectivity–Poisoning Studies of Bimetallic Catalysts (continued)

Bimetal. Catal.	Conditions	Catal. Processes Studied (Cond.)
Pt-Sn Pt-Pb	Initial catalyst lifetime, Al ₂ O ₃ support	Hexane reforming.
	Pt-Sn and Pt-Pb produce large amounts of hexadienes that are intermediates in aromatization. Their desorption is facilitated by Sn and Pb; cracking is decreased and isomerization is increased. ⁸³	
Pt-Sn Pt-Re Pt-Pb	Initial catalyst lifetime, Al ₂ O ₃ support	Hexane and heptane reforming. Radiotracer studies.
	Cracking suppressed by carbonaceous deposits and aromatics became predominant. This trend was enhanced by Sn and Pb. Small amounts of C ₁ species can act as inert additives like Sn, but at higher concentrations can form coke. ⁸⁴	
Pt-Re	chlorided with CCl ₄ , Al ₂ O ₃ support	Hydrocarbon hydrogenolysis
	Chloriding has less effect on Pt-Re vs. Pt. Alloy formation suggested. However, Pt and Re segregation can occur depending on conditions. ⁸⁵	
Pt-Sn Pt-Pb Pt-Sb	Alloy formation, Al ₂ O ₃ support	Hydrocarbon reforming.
	Hydrogenolysis strongly suppressed by alloy formation. With Pt-Sn, 20% alloying of Sn occurs. ⁸⁶	
Pt-Re	Surface carbonaceous material determined and its reactivity studied.	n-Hexane reforming.
	Presence of Re allows an increase in amount of reactive hydrogen available, and so lowers formation of carbonaceous material. ⁸⁷	

Table II. Continued

Bimetal. Catal.	Conditions	Catal. Processes Studied (Cond.)
Pt-Sn Ni-Mo	none	Hexane reforming.
	Formation of a solid solution of Ni and Mo resulted in drastic reduction in activity and changes in selectivity. For Pt-Sn, Sn is mainly Sn ²⁺ after reduction, and its presence improves catalyst stability. ⁸⁸	
Pt-Ir	Industrial catalyst regeneration, Al ₂ O ₃ support	Hydrocarbon reforming (industrial)
	Temperature, gas flow rate, oxychlorination studied. Careful control necessary. Sintered catalysts could be redispersed somewhat by oxychlorination, especially with higher Cl levels. ^{89,90}	
Pt-M	Industrial catalysts	Hydrocarbon reforming (industrial)
	A review of bimetallic industrial catalysts used for gasoline production. ⁹¹	
Pt-Sn Pt-Re	Activities and selectives, Al ₂ O ₃ support	n-Hexane reforming, cyclopentadiene reactions.
	One role of Re and of Sn may be to selectively hydrogenate dienes to alkenes. ⁹²	
Pt-Re Pt-Ir	sulfided with H ₂ S, Al ₂ O ₃ support	Hydrocarbon reforming.
	With same sulfur coverage, Pt-Re catalysts are more deactivated than Pt or Pt-Ir. However, Ir presence increases sulfur poisoning resistance. ⁹³	
Pt-Ir	Catalytic gasification of graphite.	Electron microscopy. Channel propagation.
	Channeling has different stages, apparently due to Pt-Ir alloy formation. In oxygen atmosphere alloy contains excess Ir, but in hydrogen atmosphere the alloy particles are surface enriched in Pt. ⁹⁴	

Continued on next page

Table II. A Brief Summary of Literature Relating Generally to Reactivity–Selectivity–Poisoning Studies of Bimetallic Catalysts (continued)

Bimetal. Catal.	Conditions	Catal. Processes Studied (Cond.)
Pt-Re Pt-Ir	Al ₂ O ₃ support	Chemisorption of H ₂ and CO. Reforming of heptane, methylcyclopentane, and naptha.
	The Pt-Re and Pt-Ir catalysts can be combined to take advantage of the properties of both. ⁹⁵	
Pt-Ir	Dispersion of metals. Thermal treatments in oxygen (300-600%) and hydrogen (500-800°C), Al ₂ O ₃ support	Chemisorption
	Segregation of Pt and Ir occurred during oxygen treatment. Pt and Pt-Ir catalysts sintered in similar ways upon hydrogen treatment. ⁹⁶	
Pt-Sn Pt-Pb	Al ₂ O ₃ support	Dehydrogenation of cyclohexane, dehydrocyclization of n-heptane, chemisorption of H ₂ .
	Sn and Pb have similar effects. Reaction conditions determine effectiveness of Sn or Pb additions; reactions inhibited under mild conditions while aromatization increased and hydrogenolysis decreased under more severe conditions. ⁹⁷	

Acknowledgements

The support of the National Science Foundation is acknowledged with gratitude.

Literature Cited

1. Brown, S.S.D.; Salter, I.D.; *J. Organomet. Chem.*, **1987**, *332*, C6-C10
2. Powell, J.; Sawyer, J.F.; Stainer, M.V.R. *Inorg. Chem.*, **1989**, *28*, 4461-70.
3. Mingos, M.D.; Wales, D.J.; "Introduction to Cluster Chemistry", Prentice Hall, Englewood Cliffs, New Jersey, **1990**.
4. Godbey, D.J.; Garin, F.; Somorjai, G.A. *J. of Catal.*, **1989**, *117*, 144-154.
5. Godbey, D.J.; Energy Res. Abstr. 1988, 13(8), Abstr. No. 18773, **1987**, 245.
6. Godbey, D.J.; Somorjai, G.A. *Surface Science*, **1988**, *202*, 204-226.
7. a. Rodrigues, J.A.; Campbell, R.A.; Goodman, D.W.; *J. Phys. Chem.*, **1991**, *95*, 2477.
b. Radriguez, J.A.; Goodman, D.W.; *J. Phys. Chem.*, **1991**, *95* 4196.
c. He, J.W.; Kuhn, W.K.; Goodman, D.W.; *J. Phys. Chem.*, **1991**, *95*, 5220.
d. Private communications with D.W. Goodman.
8. Choplin, A.; Huang, L.; Theolier, A.; Gallezot, P.; Basset, J.M.; Siriwardane U.; Shore, S.G.; Mathieu, R., *J. Am. Chem. Soc.*, **1986**, *108*, 4224-4225.
9. Shapley, J.R.; Uchiyama, W.S.; Scott, R.A.; *J. Phys. Chem.*, **1990**, *94*, 1190-1196.
10. Fukuoka, A.; Kimura, T.; Kosugi, N.; Kuroda, H.; Minai, Y.; Sakai, Y.; Tominaga, T.; Ichikawa, M. *J. Catal.*, **1990**, *126*, 434-450.
11. Ichikawa, M.; Rao, L-F; Kimura, T.; Fukuoka, A. *J. of Molec. Catal.*, **1990**, *62*, 15-35
12. Scott, J.P.; Budge, J.R.; Rheingold, A.L.; Gates, B.C. *J. Am. Chem. Soc.* **1987**, *109*, 7736-44.
13. Kelley, M.J.; Fung, A.S.; McDevitt, M.R.; Tooley, P.A.; Gates, B.C. *Mater. Res. Soc. Symp. Proc.*, **1988**, *111*, 23-33.
14. Pruet, R.L.; Bradley, J.S. U.S. 4, 301,086 **1984**, cont. in part.
15. Marrakchi, H.; Haimour, M.; Escalant, P.; Lieto, J.; Aune, J.P. *Nouv. J. Chim.*, **1986**, *10*, 159-63.
16. Tsang, C.M.; Augustine, S.M.; Butt, J.B.; Sachtler, W.M.H. *Appl. Catal.*, **1989**, *46*, 45-46.
17. Klabunde, K.J.; Li, Y.X.; Tan, B.J.; *Chem. Materials*, **1991**, *3*, 30.
18. Tan, B.J.; Klabunde, K.J.; Sherwood, P.M.A.; *J. Am. Chem. Soc.*, **1991**, *113*, 855.
19. Tan, B.J.; Klabunde, K.J.; Sherwood, P.M.A., *Chem. Materials*, **1990**, *2*, 186.
20. a. Li, Y.X.; Klabunde, K.J.; *J. Catal*, **1990**, *126*, 123.
b. Li, Y.X.; Klabunde, K.J.; *Langmuir*, **1987**, *3*, 558.
c. Li, Y.X.; Zhang, Y.F.; Klabunde, K.J.; *Langmuir*, **1988**, *4*, 385.

21. Wang, Yi, Li, Y.X.; Klabunde, K.J.; this volume.
22. Wang, Z.; Wu, S.; *J. Catal*, **1992**, in press.
23. Akhmedov, V.M.; *Metalloorg. Khim.* (Russian), **1989**, 2, 198.
24. Wagner, F.E.; Sawicki, J.A.; Rolston, J.H. *Hyperfine Interactions*, **1988**, 41, 733-736.
25. Meitzner, G.; Via, G.H.; Lytle, F.W.; Sinfelt, J.H. *J. Chem. Phys.*, **1985**, 83, 353-360.
26. Meitzner, G.; Via, G.H.; Lytle, F.W.; Sinfelt, J.H. *J. Chem. Phys.*, **1985**, 83, 4793-4799.
27. Tzou, M-S; Kusunoki, M.; Asakura, K.; Kuroda, H.; Moretti, G.; Sachtler, W.M.H. *J. Phys. Chem.*, **1991**, 95, 5210-5215.
28. Liang, K.S.; Hughes, G.J.; Sinfelt, J.H. *Physica B*, **1989**, 158, 135-137.
29. Meitzner, G.; Via, G.H.; Lytle, F.W.; Sinfelt, J.H. *Physica B*, **1989**, 158, 138-141.
30. Elbiyyadh, A.; Guerin, M.; Kappenstein, C.; Bazin, D.; Dexpert, H. *Physica B*, **1989**, 158, 170-171.
31. Herrmann, J-M; Disdier, J.; Pichat, P.; Fernandez, A.; Gonzalez-Elipse, A.; Munuera, G.; Leclercq, C. *J. Catal.*, **1991**, 132, 490-497.
32. Fernandez, A.; Munuera, G.; Gonzalez-Elipse, A.R.; Espinos, J.P.; Herrmann, J.M.; Pichat, P.; Leclercq, C. *Appl. Catal.*, **1990**, 57, 191-202.
33. Bazin, D.; Dexpert, H.; Lagarde, P.; Bournonville, J.P. *J. Catal.*, **1988**, 110, 209-215.
34. Bazin, D.; Dexpert, H.; Bournonville, J.P.; Lynch, J. *J. Catal.*, **1990**, 123, 86-97.
35. Bazin, D.; Dexpert, H.; Lagarde, P.; Bournonville, J.P.; *J. Phys.*, **1986**, 47, 293.
36. Balakrishnan, K.; Schwank, J. *J. of Catal.*, **1991**, 127, 287-306.
37. Stencel, J.M.; Goodman, J.; Davis, B.H.; "Proc. 9th Int. Cong. Catal. Calgary," Phillips, M.J.; Ternan, M.; editors, Vol. 3, p. 1291, The Chemical Inst. Canada, **1988**.
38. Pestman, R.; Den Hartog, A.J.; Adrianus, J.; Ponec, V. *Catal. Lett.*, **1990**, 4, 287-97.
39. Den Hartog, A.J.; Adrianus, J.; Holderbusch, M.; Rappel, E.; Ponec, V. *Int. Congr. Catal.*, **1988**, 3, 1174-881.
40. Niemantsverdriet, J.W.; Louwers, Stefan, P.A.; Van Grondelle, J.; Van der Kraan, A.M.; Kampers, F.W.H.; Koningsberger, D.C. *Int. Congr. Catal.*, **1988**, 2, 674-81.
41. Augustine, S.M.; Nacheff, M.S.; Tsang, C.M.; Butt, J.B.; Sachtler, W.M.H. *Int. Congr. Catal.*, **1988**, 3, 1190-7.
42. Sachdev, A.; Schwank, J. *Int. Congr. Catal.*, **1988**, 3, 1275-82.
43. Kumar, J.; Ghosh, M. *NATO ASI Serv., Ser. B*, **1987**, 158, 819-24.
44. Wagner, F.E.; Sawicki, J.A.; Rolston, J.H. *Hyperfine Interact.*, **1988**, 41, 733-6.
45. Margitfalvi, J.; Talas, E.; Hegedus, M.; Gobolos, S. *Heterog. Catal.*, **1987**, 2, 345-50.
46. Meitzner, G.; Via, G.H.; Lytle, F.W.; Sinfelt, J.H. *J. Chem. Phys.* **1987**, 87, 6354-63.

47. Podkletnova, N.M.; Shpiro, E.S.; Kogan, S.B.; Minachev, Kh. M.; Bursian, N.R. *Kinet. Katal.*, **1987**, *28*, 712-16.
48. Garden, D.; Kemball, C.; Whan, D.A.; *J. Chem. Soc.*, Faraday Trans. 1, **1986**, *82*, 3113-23.
49. Faro Jr., A.C.; Kemball, C. *J. Chem. Soc.*, Faraday Trans. 1, **1986**, *82*, 3125-39.
50. Qiao, G.W.; Zhou, J.; Kuo, K.H. *Int. Congr. Catal.* **1985**, *3*, 93-111.
51. Adkins, S.R.; Davis, B.H. *ACS Symp. Ser.*, **1985**, *288*, 57-66.
52. Wang, X.K.; Schwarz, J.A. *Appl. Catal.* **1985**, *18*, 147-55.
53. Tebassi, L.; Sayari, A.; Ghorbel, A.; Dufaux, M.; Ben Taarit, Y.; Naccache, C. *Proc. Int. Zeolite Conf.*, **1984**, *6th*, 368-76.
54. McVicker, G.B.; Ziemiak, J.J. *Appl. Catal.*, **1985**, *14*, 229-43.
55. Adkins, S.R.; Davis, B.H. *Preprint. Am. Chem. Soc., Petro. Div.*, **1984**, *29*, 708-13.
56. Coq, B.; Figueras, F. *J. Mol. Catal.* **1984**, *25*, 87-98.
57. Dexpert, H.; Lagarde, P.; Bournonville, J.P. *J. Mol. Catal.* **1984**, *25*, 347-55.
58. Via, G.H.; Sinfelt, J.H.; Lytle, F.W.; Greegor, R.B., *Preprint. Am. Chem. Soc., Petro. Div.*, **1983**, *28*, 460-3.
59. Lytle, F.W.; Greegor, R.B.; Via, G.H.; Sinfelt, J.H. *Preprint. Am. Chem. Soc., Petro. Div.*, **1981**, *26*, 400-6.
60. Sinfelt, J.H.; Via, G.H.; Lytle, F.W. *J. Chem. Phys.*, **1982**, *76*, 2779-89.
61. Burch, R. *J. Catal.*, **1981**, *71*, 348-59.
62. Yacaman, M.J.; Zenith, J.; Contreras, J.L. *Appl. Surf. Sci.* **1980**, *6*, 71-5.
63. Srivastava, R.D.; Prasad, N.S.; Pal, A.K., *Chem. Eng. Sci.*, **1986**, *41*, 719-24.
64. Pakhomov, N.A.; Buyanov, R.A. *Adv. Catal.*, **1985**, *7*, 305-13.
65. Apesteguía, C.R.; Garetto, T.F.; Borgna, A.; *Stud. Surf. Sci. Catal.*, **1991**, *68*, 399-406.
66. Gregori, L.; Desmay, A.; Agorreta, E.; Menendez, M.; Monzon, A. *Stud. Surf. Sci. Catal.*, **1991**, *68*, 581-4.
67. Huang, Y.J.; Fung, S.C. *J. Catal.*, **1991**, *131*, 378-84.
68. Fan, Y.; Xu, Z.; Zang, J. Liwu, L. **1991**, *Stud. Surf. Sci. Catal.*, **1991**, *68*, 683-90.
69. Mieville, R.L. *Stud. Surf. Sci. Catal.*, **1991**, *68*, 151-9.
70. Parera, J.M. *Stud. Surf. Sci. Catal.* **1991**, *68*, 103-10.
71. Beltramini, J.N.; Datta, R. *React. Kinet. Catal. Lett.* **1991**, *44*, 353-9.
72. Pieck, C.L.; Jablonski, E.L.; Parera, J.M. *Appl. Catal.*, **1991**, *70*, 19-28.
73. Grau, J.M.; Parera, J.M. *Appl. Catal.*, **1991**, *70*, 9-18.
74. Dees, M.J.; Ponec, V. *J. Catal.*, **1989**, *115*, 347-55.
75. Das, S.; Srivastava, R.D.; Saraf, D.N. *J. Chem. Technol. Biotechnol.*, **1988**, *43*, 95-105.
76. Parera, J.M.; Beltramini, J.N. *J. Catal.*, **1988**, *112*, 357-65.
77. Podkletnova, N.M.; Kogan, S.B.; Bursian, N.R. *Zh. Prikl. Khim. (Leningrad)* **1987**, *60*, 2028-31.

78. Parera, J.M.; Querini, C.A.; Beltramini, J.N.; Figoli, N.S. *Appl. Catal.*, **1987**, *32*, 117-32.
79. Bursian, N.R.; Aharkov, B.B.; Kogan, S.B.; Lastovkin, G.A.; Podkletnova, N.M.; *Int. Cong. Catal.*, **1985**, *2*, 11481-11490.
80. Davis, B.H.; *Int. Congr. Catal.*, **1985**, *2*, 469-480.
81. Pachecho, M.A.; Petersen, E.E. *J. Catal.*, **1985**, *96*, 499-506.
82. Barbier, J.; Corro, G.; Zhang, Y.; Bournville, J.P.; Franck, J.P. *Appl. Catal.*, **1985**, *16*, 169-77.
83. Paal, Z.; Dobrovolszky, M.; Voelter, J.; Lietz, G. *Appl. Catal.*, **1985**, *14*, 33-46.
84. Lietz, G.; Voelter, J.; Dobrovolszky, M.; Paal, Z. *Appl. Catal.* **1984**, *13*, 77-87.
85. Menon, P.G.; Froment, G.F. *J. Mol. Catal.*, **1984**, *25*, 59-66.
86. Voelter, J.; Hoang, D.L.; Ho Si Thoang; Lieske, H.; Kuerschner, U.; Lietz, G. *Geterog. Katal.* **1983**, *1*, 303-8.
87. Margitfalvi, J.; Gobolos, S.; Kwaysser, E.; Hegedus, M.; Nagy, F.; Koltai, L. *React. Kinet. Catal. Lett.*, **1984**, *24*, 315-21.
88. Burch, R.; Garla, L.C.; Hennessy, J.S. *Preprint. Am. Chem. Soc., Petro. Div.*, **1983**, *28*, 451-9.
89. Bishara, A.; Murad, K.M.; Stanislaus, A.; Ismail, M.; Hussain, S.S. *Appl. Catal.*, **1983**, *7*, 351-9.
90. Bishara, A.; Murad, K.M.; Stanislaus, A.; Ismail, M.; Hussain, S.S. *Appl. Catal.* **1983**, *7*, 337-49.
91. Hughes, T.R. *Chem. Ind. Eng. Soc. China Am. Inst. Chem. Eng.*, **1982**, *2*, 672-87.
92. Burch, R.; Mitchell, A.J. *Appl. Catal.* **1983**, *6*, 121-8.
93. Apesteguia, C.R.; Barbier, J. *J. Catal.* **1982**, *78*, 352-9.
94. Baker, R.T.K.; Sherwood, R.D.; Dumesic, J.A. *Electron Microsc. Soc. Am., 40th Annual Meeting*, **1982**, 644-7.
95. Carter, J.L.; McVicker, G.B.; Weissman, W.; Kmak, W.S.; Sinfelt, J.H. *Appl. Catal.*, **1982**, *3*, 327-46.
96. Graham, A.G.; Wanke, S.E.; Sieghard, E. *J. Catal.*, **1981**, *68*, 1-8.
97. Voelter, J.; Lietz, G.; Uhlemann, M.; Hermann, M. *J. Catal.* **1981**, *68*, 42-50.

RECEIVED July 6, 1992

Chapter 8

Platinum–Tin–Alumina Catalysts

Comparison of Alkane Dehydrocyclization Activity and Characterization Data

Burtron H. Davis

Center for Applied Energy Research, University of Kentucky, 3572 Iron Works Pike, Lexington, KY 40511

Surface and bulk characterization results for Pt-Sn-alumina catalysts are reviewed. For co-impregnated Pt and Sn catalysts, XPS, Mössbauer, and XRD data are consistent with the formation of an alloy of PtSn, and the fraction of Pt that is present as an alloy increases with increasing Sn/Pt ratio. XRD and electron microdiffraction data indicate that the alloy has a Pt:Sn = 1:1 composition over the Sn/Pt range investigated (1:1 to 1:12). For a catalyst where the support was prepared by coprecipitating tin and aluminum oxide followed by impregnation with chloroplatinic acid, the data indicated that little or no Pt was present as an alloy. XANES and EXAFS data indicated that tin increased Pt dispersion, but the data did not permit a definitive conclusion about alloy formation. The data clearly show that the addition of Pt and Sn by co-impregnation leads to alloy formation but this is not the case for Pt on a coprecipitated tin and alumina oxide. For the co-impregnated catalyst on a non-acidic alumina support, tin acts as a promoter. However, on an acidic support, where dehydrocyclization occurs predominantly by a bifunctional pathway, tin may act as a catalyst poison.

The introduction of the bifunctional platinum-alumina catalyst for naphtha reforming shortly following the end of WWII led to a revolution in petroleum processing (1). On the commercial side, the reforming process provided a means to meet the dramatic increase in octane rating for gasoline, to provide an abundant source of aromatics for the rapidly developing petrochemicals industry, and to provide surplus hydrogen to permit the development of other processes such as hydrotreating and hydrocracking. On the scientific side, the studies needed to define the mechanisms underlying the effectiveness of this

bifunctional catalyst led to significant advances in the understanding of catalysis as well as the reforming process.

While the Pt-alumina catalysts were an outstanding success, they had to be regenerated at rather frequent intervals, every three months or so. Thus, the introduction in the late 1960s of a platinum-rhenium bimetallic catalyst that could remain on-stream for a period of a year or even longer led to a second revolution in naphtha reforming (2). The Pt-Re-alumina catalyst had to be activated and brought on stream using a rather lengthy procedure that usually involved poisoning the catalyst with sulfur during a break-in period. Today, with the potential for a naphtha reforming process utilizing continuous catalyst regeneration other bimetallic catalysts which do not require complex activation procedures must be utilized; Pt-Sn-alumina appears to be an attractive catalyst for this process.

The reasons for the superior catalytic properties of these bimetallic catalysts are not adequately understood even after 30 years of active research in this area. Many of the explanations for the superior properties of the bimetallic catalysts are based on a structural point of view. Many argue that the bimetallic components form an alloy which has better catalytic properties than Pt alone. For example, alloy formation could influence the d-band electron concentration, thereby controlling selectivity and activity (3). On the other hand, the superior activity and selectivity may be the result of high dispersion of the active Pt component, and the stabilization of the dispersed phase by the second component (4). Thus, much effort has been expended to define the extent to which metallic alloys are formed (*for example*, 5-18). These studies have utilized a variety of experimental techniques.

Platinum and tin present a complex situation since a number of alloy compositions are possible, depending upon the Sn/Pt ratio. The phase diagram in Figure 1 shows that as the Sn/Pt ratio increases it should be possible to form a series of alloys with increasing Sn fractions (19,20).

In the following, we summarize some data from methods that make a more direct measure of the chemical or physical state of the Pt and/or Sn present in Pt-Sn-alumina catalysts.

Catalyst Characterization

Temperature Programmed Reduction. Temperature-programmed reduction (TPR), one of the indirect analysis methods, yielded data that suggested that Sn was not reduced to zero-valent state (10,16). Burch (15) has reviewed early work on the characterization of this type of catalyst. Lieske and Volter (21) reported, based on the results obtained from TPR studies, that a minor part of the tin is reduced to the metal, and this Sn(O) combined with Pt to form "alloy clusters" but the major portion of the tin is reduced to only the

Sn(II) state. They also reported that the amount of alloyed tin increases with increasing tin content.

X-Ray Photoelectron Spectroscopy. X-ray photoelectron spectroscopy (XPS) studies permit one to determine the chemical state of an element but the data does not permit one to define whether Sn(0), if present, is in the form of a Pt-Sn alloy. Furthermore, the major Pt XPS peak coincides with a large peak from the alumina support. Thus, XPS can only provide data to indicate whether an alloy is possible; it cannot be used to prove the presence of a Pt-Sn alloy.

The early XPS studies, including those from our laboratory, revealed that the tin is present only in an oxidized state (10,16). These results were consistent with those for the Pt-Re bimetallic catalysts where only oxidized Re was observed (9,22). Li et al. (23,24) reported that a portion of the tin in Pt-Sn-alumina catalysts was present in the zero valence state; furthermore, it appears that the composition of the Pt-Sn alloy, based upon the amount of Pt in the catalyst and the Sn(0) detected by XPS, increases with increasing ratios of Sn/Pt.

Stencel et al. (25) utilized XPS together with scanning electron microscopy (SEM) to follow the interaction and migration of Cl in Pt, Rh and Pt-Sn-containing catalysts. In-situ reduction with hydrogen decreased the surface concentration of chloride while increasing the chloride concentration interior to particles and extrudates. Subsequent oxygen treatment of these reduced catalysts caused the surface concentration of chloride to increase. In the case of Rh/alumina, the characteristics of the Al 2p peak after hydrogen reduction suggest the formation of AlCl₃-type species.

Tin Mössbauer. ¹¹⁹Sn Mössbauer data also provide a bulk diagnostic and this method has been utilized in a number of studies (for example, 7,26-39). Direct evidence for PtSn alloy formation was obtained from Mössbauer studies (for example, 7,34,35,38,39); however, many of these studies were at high metal loadings and even then a complex spectrum was obtained so that there was some uncertainty in assigning Sn(0) to the exclusion of tin oxide phases.

Li et al. (40) utilized the same series of catalysts that had been utilized earlier in their XPS studies (23); each sample in the three series contained 1 wt.% Pt and a varying amount of Sn. Tin was observed in forms whose isomer shifts were similar or the same as SnO₂, SnO, SnCl₄, SnCl₂, Sn(0) and PtSn alloy when alumina was the support. If it is assumed that the Pt/Sn alloy corresponds only to PtSn alloy as was found to be the case in X-ray diffraction (XRD) data to be described below, one obtains the results shown in Figure 2. For lower Sn:Pt ratios (5 or less) little difference is observed in the extent of alloy formation and the distribution of the oxidized species for a low and high surface area alumina support. In this respect, there is general agreement

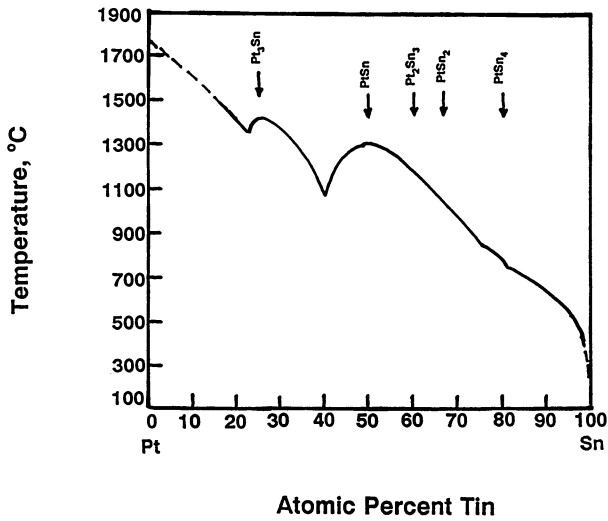


Figure 1. Phase diagram of platinum-tin (reference 19).

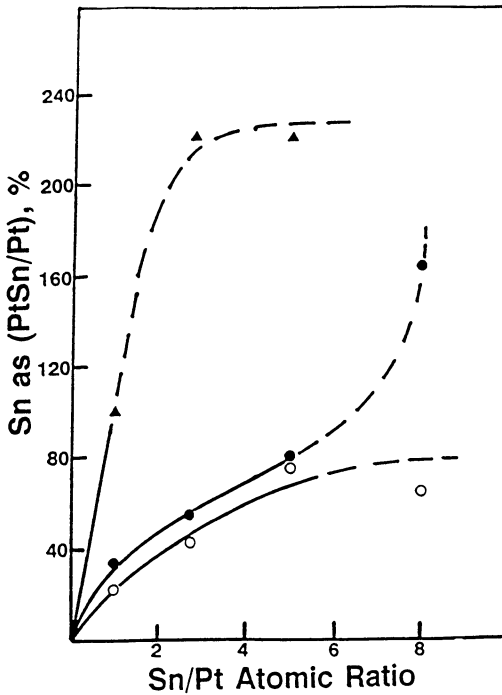


Figure 2. Amount of tin calculated to be present as PtSn alloy versus tin:Pt ratio: ▲, silica support ●, low surface area alumina support; ○, high surface area alumina support.

with data observed in some of the earlier Mössbauer studies. The Mössbauer data in Figure 2 show a similar trend in the extent of alloy formation for the alumina supported materials; the fraction of Pt present in an alloy phase increases with increasing tin concentration and only approaches complete alloy formation at Sn:Pt \geq ca. 5.

For Pt supported on a co-precipitated tin oxide-alumina catalyst, alloy formation occurs to a much smaller extent than it does on a material prepared by impregnation with the chloride complex of the two metals (40,41). Since most commercial catalyst formulations are based on tin-alumina co-precipitated support materials, it appears that the studies using Pt and Sn co-impregnation techniques, while interesting, are not directly applicable to the commercial catalysts.

X-Ray Diffraction. A catalyst was prepared by impregnating a Degussa Aluminum Oxide C (a nonporous alumina with a surface area of 110 m²/g) with an acetone solution of Pt₃(SnCl₃)₂₀²⁻ (42). A sample of a catalyst containing 5 wt.% Pt was reduced in situ in the chamber of an XRD instrument; thus the material was not exposed to the atmosphere prior to recording the X-ray diffraction pattern (43). The X-ray diffraction patterns match very well, both in position and intensity, the pattern reported for PtSn alloy. With the 5 wt.% Pt catalyst, a small fraction of the Pt is present as crystalline Pt but crystalline Pt was not observed for the 0.6 wt.% Pt catalyst. It is noted that similar results for the PtSn alloy are obtained for a catalyst that contains only 0.6 wt.% Pt, and with the same Sn/Pt ratio as the 5% Pt catalyst. These in situ XRD studies therefore support alloy formation with a stoichiometry of Pt:Sn = 1:1. The Sn in excess of that needed to form this alloy is present in an X-ray "amorphous" form, and is postulated to be present in a shell layer with a structure similar to tin aluminate. A series of catalysts were prepared to contain 1 wt.% Pt and Sn:Pt ratios ranging from ca. 1 to 8 using a low (110 m²/g) and high (300 m²/g) surface area alumina (44). XRD studies indicated that, irrespective of the Sn/Pt ratio, the only crystalline phase detected by XRD was PtSn (1:1). The XRD intensity of lines for the SnPt alloy phase increase with increasing Sn:Pt ratios, indicating the presence of unalloyed Pt in the samples containing low tin loadings.

X-Ray Absorption Fine Structure. X-ray absorption near edge structure (XANES) and extended X-ray absorption fine structure spectra (EXAFS) were obtained for a series of Sn/Pt on alumina or silica samples (45,46). The data suggest the possibility of Pt/Sn alloy formation, but do not provide conclusive proof for this.

Transmission Electron Microscopy. An electron microdiffraction technique was employed to identify crystal structures developed in two Pt-Sn-alumina catalysts (47). One catalyst was prepared by co-precipitating Sn and Al oxides and then impregnating the calcined material with chloroplatinic acid to give

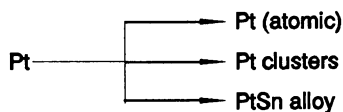
a Pt:Sn = 1:3 atomic ratio. The second catalyst was prepared by co-impregnating Degussa alumina with an acetone solution of chloroplatinic acid and stannic chloride to provide a Pt:Sn = 1:3. Pt-Sn alloy was not detected by X-ray diffraction for the co-precipitated catalyst although evidence for PtSn alloy was found for the co-impregnated catalyst.

EDX data was obtained for a number of the metal particles present in the two catalysts. Both Pt and Sn were observed in the impregnated catalyst. The relative amounts of Pt and Sn present in an individual metal particle indicates that the dominant alloy is Pt:Sn = 1:1 (Figure 3). The EDX data for the co-precipitated Sn- and Al-oxide give contrasting results to the impregnated catalyst. Only rarely is it possible to find a metal particle that contains both Pt and Sn. It is therefore concluded that the majority of Pt is present as metallic Pt, and not in an alloy form. The tin is also viewed to be incorporated in the bulk of the sample as well as on the surface.

Pt-Sn-Alumina Structure. No single model will adequately describe the above catalyst characterization data and the published data that has not been included because of space limitations. The relative distribution of both the Pt and Sn species depend upon a number of factors such as surface area of the support, calcination and/or reduction temperature, Sn/Pt ratio, etc. Furthermore, it appears that the "co-impregnated" and "co-precipitated" catalysts are so different that their structure should be considered separately.

For a "co-impregnated" catalyst all, or the dominant fraction of, both Pt and Sn are located on the surface alumina support. For the following discussion we consider the role of only the support surface area, the metal concentration and the Sn/Pt ratio. First consider the case of a series of catalysts with a constant Pt loading but with variable Sn/Pt ratios.

Our view of the catalyst surface is schematically depicted in Figure 4. The indirect and direct characterization data for Pt indicates that it is present in a zero valence state. The Pt will therefore be distributed among Pt atoms, Pt clusters that are larger than one atom and Pt present as a Pt/Sn alloy. Thus, a description of the state of Pt in the Pt-Sn-alumina catalyst involves determining the fraction present in each of the three states. Furthermore, both of the direct methods for determining the Pt/Sn alloy composition, XRD and TEM, indicates that only the PtSn = 1:1 alloy is formed. Thus,



These three Pt states are represented schematically in Figure 4.

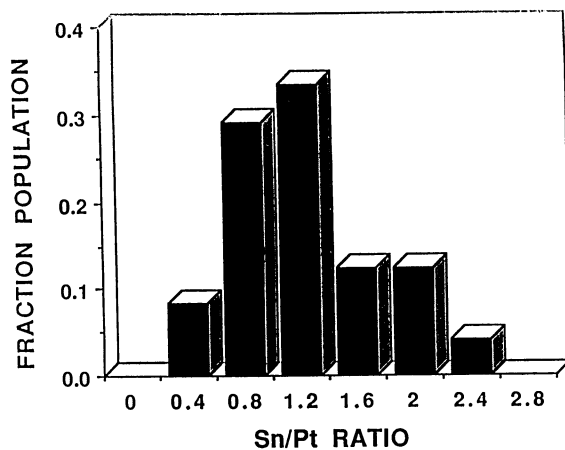


Figure 3. Frequency distribution of EDX intensity of Sn/Pt ratios for increasing Sn/Pt concentration.

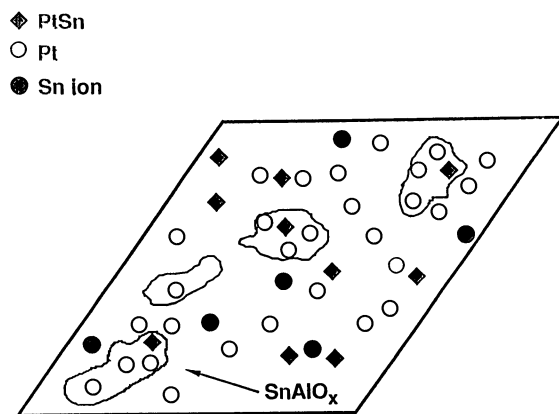
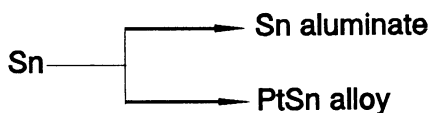


Figure 4. Schematic of proposed surface structure of a low (1:1) Pt/Sn-alumina catalyst.

The possible states of the tin are more numerous than for Pt. Many investigators believe they have presented strong evidence for the three stable valence states - Sn^{4+} , Sn^{2+} and Sn^0 - as well as for a host of compounds ranging from SnO_2 to metallic tin. It appears certain that the ratio of the oxidized to Sn^0 will vary with support surface area and Sn/Pt ratio. For a number of reasons we favor a "surface layer" of a tin compound that resembles tin aluminate, whether the oxidized tin is present as Sn^{2+} or Sn^{4+} . Even at 10 wt.% Sn on alumina, XRD does not detect any three dimensional tin compounds, including SnO_2 . Furthermore, for most of the techniques utilized to determine the chemical compounds containing tin would not be able to distinguish between the tin oxide and a corresponding tin aluminate.

Even if the tin does not actually form a species corresponding to a surface tin aluminate compound, the oxidized tin is widely dispersed, the anion associated with it must be an oxide anion, or possibly a chloride ion if the catalyst still contains this element, and the oxidized tin interacts strongly with the alumina support. Thus, even if the tin is not present in a specific tin aluminate compound containing either Sn^{2+} or Sn^{4+} , the actual structure will resemble a tin aluminate widely dispersed over the surface. Thus, we only consider two states for tin: a surface species for the oxidized tin that is or resembles a tin aluminate and Sn^0 that is essentially all present as $\text{PtSn} = 1:1$ alloy. Thus,



For the impregnated catalysts, the fraction of Pt present as PtSn alloy increases with increasing Sn/Pt until, for a given Pt loading, further increases in Sn/Pt does not produce additional PtSn. The Sn/Pt ratio where the limiting amount of PtSn alloy occurs depends upon both Pt loading and surface area of the support. The lower the surface area, the smaller the Sn/Pt ratio that is needed to produce the limiting value. As the Pt loading is increased on a given support, the lower the Sn/Pt ratio needed to attain the limiting value.

The situation appears to be very different for the catalyst where the support was prepared by coprecipitation of a mixed tin and aluminum hydroxide. In this case it appears that a high fraction of the tin is present in the interior of the solid, with the fraction located on the surface being small. Thus, when Pt is added to the surface by impregnation, even when the bulk Sn/Pt ratio is on the order of 1 to 4, the actual surface ratio of Sn/Pt will be very much smaller.

It is therefore believed that the limited published data for the coprecipitated catalyst is consistent with Pt interacting with tin only through isolated tin aluminate clusters containing only one, or at most, a few tin ions.

Alkane Dehydrocyclization with Pt-Sn-Alumina

As noted in the Introduction, the Pt-Sn system has been studied extensively, both from the standpoint of the structure of the catalyst as well as the reason for the superior catalytic properties. Davis utilized Pt-Sn complexes, including $\text{Pt}_3\text{Sn}_8\text{Cl}_2^{2-}$, in an organic solvent to prepare supported catalysts (42). It was proposed that the reason for the superior activity of catalysts prepared in this manner was the formation of a PtSn alloy (48,49).

Burch and coworkers (50-53) have reported on the use of Pt-Sn catalysts for hydrocarbon conversions. It was concluded that no proper alloys of Pt and Sn were formed so that this could not account for the changes in the catalytic properties imparted by the presence of Sn (50). Burch and Garla concluded for their catalysts that: (i) *n*-hexane is isomerized by a bifunctional mechanism, (ii) benzene and methylcyclopentane are formed directly from *n*-hexane at metal sites, and (iii) the conversion of methylcyclopentane requires acidic sites (51). It was also concluded that the Sn (II) ions modified the Pt electronically with the result that self-poisoning by hydrocarbon residues is reduced. However, these later observations were based upon conversions at one bar.

Völter and coworkers (54-61) have also reported extensively on the PtSn catalyst system for a number of years. In an early study, the tin was found to decrease both hydrogen adsorption and the rate of cyclohexane dehydrogenation but to increase the activity for *n*-heptane dehydrocyclization (54,55). It was also reported that bimetallic catalysts can have both a positive and negative shift of activity and selectivity. The negative effect is connected with mild reaction conditions, and the positive effect with the severe deactivation reaction of aromatization. For dehydrocyclization the role of Sn is to decrease poisoning by carbonaceous residues. Lank *et al.* (57) obtained similar results for *n*-hexane conversion using an alumina supported and an unsupported Pt-Sn catalyst; thus, they attributed the impact of tin to a direct interaction with Pt, and not to an interaction of Sn with alumina. Völter and Kürschner (58) found that the addition of tin caused an increased production of benzene from methylcyclopentane, and at the same time a decrease in hydrogenolysis and deactivation even though coke formation was not diminished from that of the Pt-alumina catalyst. Völter and Kürschner attributed the effect to PtSn alloy formation. Paál *et al.* (60) reported evidence for hexatrienes during *n*-hexane conversion, and that their amount was markedly higher over the bimetallic PtSn or PtPb catalyst. Lieske *et al.* (61) reported that added tin increased the extent of coking by hexene but at the same time a larger part of the Pt remains free of carbon. They explained this by a "drain-off" effect of the

alloying tin: on Pt-Sn/Al₂O₃ the coke precursors are more easily transferred to the alumina support. The hydrocarbon conversion studies by Völter and coworkers were at normal pressure.

Figueras and coworkers (62-64) have also investigated the catalytic activity of PtSn catalysts for hydrocarbon conversions. For the conversion of *n*-heptane with Pt-Sn supported on a nonporous Degussa alumina, the authors concluded that tin poisons the strong acid sites of the support and part of the platinum; these authors expressed surprise that Pt-Sn based catalysts found commercial applications (62). For methylcyclopentane conversion, Coq and Figueras (63,64) found that tin provides a stabilizing effect on Pt and imparts a decrease in the extent of hydrogenolysis. An enhancement in the aromatization of methylcyclopentane was observed as the tin loading was increased; the aromatization passed through a maximum and then decreased with further increase in the Sn/Pt ratio. The dehydrogenation of methylcyclopentane to methylcyclopentene remained unchanged as the Sn/Pt ratio was increased. These authors also conducted their studies at normal pressures.

Dautzenberg *et al.* (65) tested a number of unsupported PtSn alloys as well as a number of alumina supported PtSn catalysts. *n*-Hexane conversion was effected at atmospheric pressure for the unsupported alloy catalysts and for some supported catalysts; other supported catalyst studies were at 3 bar. These authors reported that the addition of tin decreased the amount of methylcyclopentane and that coke was dramatically reduced during the conversion of *n*-hexane.

Sexton *et al.* (66) also examined the activity for the dehydrogenation of cyclohexane and conversion of methylcyclopentane of a series of PtSn alumina catalysts where the Sn/Pt ratio was varied. They found that the activity decreased as the Sn/Pt ratio increased. Selectivity for benzene formation from methylcyclopentane increased to a maximum at *ca.* 1.5 to 2.5 wt.% Sn (Sn/Pt = 4.9 to 8.2) and then declined. These conversions were conducted at normal pressures.

Beltramini and Trimm (67) utilized Pt-, Sn- and Pt-Sn- supported on γ -alumina for the conversion of *n*-heptane at 500°C and 5 bar. They observed that during six hours less coke per mole of heptane converted was deposited on the Pt-Sn-alumina catalyst than on Pt-alumina; however, the total amount of coke formed during six hours was much greater on Pt-Sn-alumina than on Pt-alumina. The addition of tin increased the selectivity of dehydrocyclization. Since hydrocracking and isomerization activity of a Sn-alumina catalyst remained high in spite of coke formation, the authors concluded that there was little support for the suggestion that tin poisons most of the acid sites on the catalyst. These authors (68) also measured activity, selectivity and coking over a number of alumina supported catalysts: Pt, Pt-Re, Pt-Ir, Pt-Sn and Pt-

Ge. Coke formation was significantly reduced on bimetallic catalysts compared to Pt-alumina; the results show that it is not only the amount but the location of coke that is important in determining catalyst performance. The greater efficiency of the bimetallics was due to both the amount of coke formed and its location.

Karpiński and Clarke (69) compared the results of the conversion of *n*-pentane and *n*-hexane on Pt-Sn and Pt-Rh alloy films in the temperature range 320-400°C (~ 10 torr pressure with H₂/hydrocarbon = 10/1). They found the ratio of 1,5 and 1,6 ring closure, S₅/S₆, is less than unity for pure Pt, goes through a maximum and then decreases as the amount of alloy increases. The authors conclude that surface carbiding (70) controls S₅/S₆ for Pt; as the carbide forms there is a shift from 1,5 to 1,6 ring closure. The addition of Sn decreases carbide formation; thus at low Sn/Pt ratios S₅/S₆ increases. The 1,5 cyclization selectivity patterns were interpreted in terms of the change in active site number, with possible modification by carbiding. Tin addition markedly decreased hydrogenolysis. Clarke *et al.* (71) also presented preliminary data obtained in a pulse reactor for silica Pt-Sn catalysts.

Li and Klabunde (72) utilized a pulse reactor (normal pressure) to carry out *n*-heptane conversions. Pt and Sn were evaporated into a solvent at low temperature; following evaporation the solvent was allowed to warm to room temperature where agglomeration of atoms took place to produce a dispersion of colloidal particles that were then added to an alumina support. These catalysts were compared to conventional Pt-Sn-alumina catalysts for *n*-heptane conversion. The authors proposed that the presence of small amounts of Sn⁰ on the surface of Pt can cause both an increase in catalytic activity and a decrease in hydrogenolysis.

Margitfalvi and coworkers (*e.g.* 73-76) have utilized as a means of catalyst preparation a controlled surface reaction in which a volatile Sn (or Pt) compound is allowed to react with Pt (or Sn) already present on a support. They employed conventional and transient kinetic approaches to study the mechanism of hydrocarbon reactions on these catalysts; conversions were effected at atmospheric or lower pressures. These authors found a perplexing variety of activity patterns, depending upon the manner and sequence in which Pt and Sn was added. Depending upon preparation conditions, the added tin may either enhance or decrease Pt activity and increase or decrease the selectivity for hydrogenolysis (73).

Lin *et al.* (77) reported that there are two types of sites on Pt-Sn-alumina catalysts: M₁ sites adsorb hydrogen that can react with ethene while hydrogen adsorbed on M₂ sites does not react with ethene. Aromatization and hydrogenolysis activity increased rapidly with an increase of M₁ sites while isomerization activity increased sharply with an increase in M₂ sites. Zhang

et al. (78) argue that the addition of Sn reduces the carbon deposited on metal surfaces.

Gault et al. (79) converted ^{13}C labeled hydrocarbons over catalysts containing 10% Pt and varying amounts of tin (0.2 to 5 wt.%) on alumina catalysts at low (5.5 torr) or atmospheric pressure. The support was an inert alumina and, even though the catalysts contained 1 to 1.2% Cl, the authors did not consider the catalyst to have acidic character. They reported that the 10% Pt loaded catalyst, when loaded with small amounts of Sn, has the same catalytic properties as very highly dispersed Pt-alumina catalysts.

Sárkány et al. (80) considered the formation of carbon deposition from hydrocarbons using normal pressure. They conclude that carbon deposition is decreased by the addition of tin but the rate of formation of carbon deposits through a "polyene" route is increased with the addition of tin. Wilde et al. (81), also using normal pressure conditions, also emphasize the high activity and selectivity for dehydrogenation and dehydrocyclization by 1,6 ring closure due to lower carbon deposition.

For the most part, the data for alkane and cycloalkane conversion with Pt-Sn catalysts have been at atmospheric pressure. For commercial reforming operations, a much higher pressure is utilized.

Davis (82) compared the conversion of *n*-octane at 1 atmosphere and 200 psig and found that the metal catalyzed dehydrocyclization selectivity, based upon the distribution of C_8 -aromatic isomers, was the same at both pressures. Thus, for the Pt or Pt-Sn catalyst the dominant metal catalyzed cyclization pathway to produce aromatics was a 1,6-ring closure provided the support did not have acidity to effect isomerizations.

Davis (83) later proposed that both 1,5- and 1,6-cyclization pathways occurred with these catalysts; however, at atmospheric pressure the 1,5-cyclization pathway led to coking whereas at higher pressures the 1,5-cyclization pathway led to the production of C_8 isoalkanes through hydrogenolysis of the cyclopentanes that were formed through 1,5-cyclization.

Aromatics may be formed by a bifunctional pathway when an acidic alumina support is used. Furthermore, it has been reported that the bifunctional pathway leads to aromatics at least 20 times faster than the metal only pathway (84). In addition, the bifunctional pathway is more selective for aromatics formation than the metal cyclization pathway (84).

A series of catalysts, each with 1 wt.% Pt but containing 1 to 8 atomic ratio of Sn/Pt on an acidic support, were utilized for the conversion of *n*-octane at 100 psig. As the data in Figure 5 clearly show, the addition of tin caused a

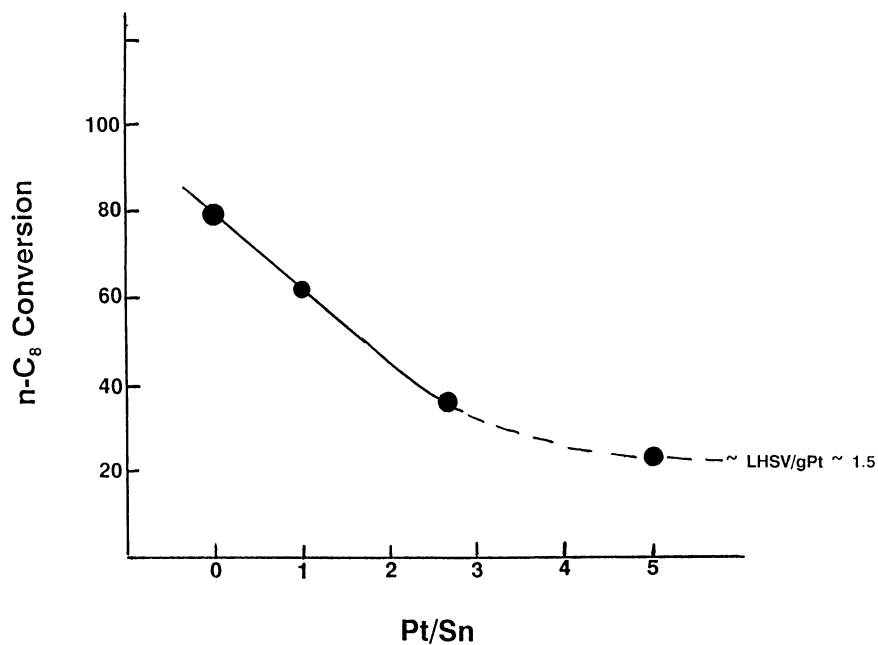


Figure 5. Total n-octane conversion for catalysts with constant Pt (1 wt.%) and increasing Sn/Pt at 482°C and 100 psig.

decrease in the conversion of *n*-octane. There was likewise a decrease in aromatics production that paralleled the decrease in total conversion.

Summary - Dehydrocyclization

The alkane conversion data, like the catalyst characterization, should not be considered to fit only one model. In the discussion that follows we consider first a catalyst with a nonacidic support and then consider the case where the support is acidic. An interpretation of the conversion data for atmospheric or lower pressure conversions are complicated by rapid catalyst aging. Thus, we will rely on data generated at greater than one atmosphere (i.e., 100 to 400 psig) in the following discussion.

For PtSn supported on a nonacidic alumina the addition of Sn causes an increase in activity up to Sn/Pt = ~ 4 , and then a decline in activity for low pressure operation (42). The increase in activity is much less at 400 psig operation than the two-fold increase observed at atmospheric pressure. However, there is a change in the selectivity of aromatic isomers produced from *n*-octane at both 15 and 400 psig as Sn is incorporated into the catalyst. Thus, both Pt and Pt/Sn catalysts produce only (> 90-95%) ethylbenzene and *o*-xylene as the dehydrocyclization products from *n*-octane. However, Pt produces ethylbenzene:*o*-xylene = 1:1 whereas a catalyst with Sn/Pt = 4 produces ethylbenzene:*o*-xylene = 1:2. This change in aromatic isomerization leads to two postulates:

- (1) for Sn to be able to alter the ethylbenzene:*o*-xylene ratio requires that there be intimate contact between Pt and Sn, or they be at least close enough to each other to permit electronic interactions, and
- (2) the increase in *o*-xylene relative to ethylbenzene follows from breaking two weaker secondary C-H bonds to produce *o*-xylene in contrast to breaking one secondary and one primary C-H bond to form ethylbenzene. It is believed that the change to break weaker bonds is due to the Pt being altered by donation of electrons from Sn to Pt.

The situation is much different when an acidic support is used. First, the C₈ aromatic products have a distribution that approaches an equilibrium composition. The Pt catalyst on an acidic support is both more active and produces aromatics more selectively than Pt on a nonacidic support (84). It is concluded that the bifunctional mechanism involving cyclization by the acid site followed by a bifunctional ring expansion/dehydrogenation reactions is much more rapid than the monofunctional metal catalyzed dehydrocyclization reaction. For the catalyst based on an acidic support, the tin added initially acts as a catalyst poison (Figure 5), at least during the initial 1-2 weeks of usage.

The activity data indicate that the state of Pt desired in the most active alkane dehydrocyclization is not the form that is easily detected by most characterization techniques. Thus, the catalysts where crystalline Pt is easily detected, either as the metal or the alloy, are usually not the optimum catalysts from the point of view of activity. It appears that for a catalyst utilizing an acidic alumina support, alloy formation is not desirable. Likewise, a surface tin concentration that decreases acidity to a significant extent is not desirable.

LITERATURE CITED

1. V. Haensel in "Chemistry of Petroleum Hydrocarbons", (B. T. Brooks, C. E. Boord, S. S. Kurtz, Jr., and L. Schmerling, Eds.) Vol. 2, p 189. Reinhold, New York, 1955.
2. R. L. Jacobson, H. E. Kluksdahl, C. S. McCoy and R. W. Davis, *Proc. Amer. Pet. Inst., Div. Ref.*, 49, 504 (1969).
3. O. Beeck, *Discuss. Faraday Soc.*, 8, 118 (1950).
4. G. B. McVicker, R. L. Garten, and R. T. K. Baker, *J. Catal.*, 54, 129, (1978).
5. B. D. McNicol, *J. Catal.*, 46, 438, (1977).
6. V. I. Kuznetsov, E. N. Yurchenka, A. S. Belyi, E. V. Zatolokina, M. A. Smolnikov, and V. K. Duplakin, *React. Kinet. Catal. Lett.*, 21, 419, (1982).
7. R. Bacaud, P. Bussiere and F. Figueras, *J. Catal.*, 69, 399, (1981).
8. R. Burch, *J. Catal.*, 71, 348, (1981).
9. D. R. Short, S. M. Dhalid, J. R. Katzer and M. J. Kelley, *J. Catal.*, 72, 288, (1981).
10. S. R. Adkins and B. H. Davis, *J. Catal.*, 89, 371, (1984).
11. B. H. Davis, *J. Catal.*, 46, 348, (1977).
12. J. H. Sinfelt, "Bimetallic Catalysis: Discoveries, Concepts, and Applications." Wiley, New York, 1983.
13. G. Bolivar, M. Charcosset, R. Ferty, M. Primet and L. Tournayan, *J. Catal.*, 37, 424, (1975).
14. N. Wagstaff and R. Prins, *J. Catal.*, 59, 434, (1979).
15. R. Burch, *Platinum Metals Rev.*, 22, 57, (1978).
16. B. A. Sexton, A. E. Hughes and K. Folger, *J. Catal.*, 88, 466, (1984).
17. V. I. Kuznetsov, A. S. Belyi, E. N. Yurchenko, M. D. Smolnikov, M. T. Protasova, E. V. Zatolokina and V. K. Duplyakin, *J. Catal.*, 99, 159, (1986).
18. A. C. Müller, P. A. Engelhard and J. E. Weisang, *J. Catal.*, 56, 65, (1979).
19. M. Hansen, "Constitution of Binary Alloys", McGraw-Hill, New York, 1958, pg 1142.
20. F. Doerinckel, *Z. Anorg.*, 54, 349 (1907).
21. H. Lieske and J. Volter, *J. Catal.*, 90, 46, (1984).
22. S. R. Adkins and B. H. Davis in "Catalyst Characterization Science" (M. L. Deviney and J. L. Gland, Eds.) ACS Symp. Series, 22, 57, (1985).

23. Y.-X. Li, J. M. Stencel and B. H. Davis, *Reaction Kin. Catal. Lett.*, **37**, 273 (1988).
24. Y.-X. Li, J. M. Stencel and B. H. Davis, *Appl. Catal.*, **64**, 71, (1990).
25. J. M. Stencel, J. Goodman and B. H. Davis, *Proc. 9th Int. Congr Catal.*, **3**, 1291, (1988).
26. V. H. Berndt, H. Mehner, J. Völter and W. Meise., *Z. Anorg. Allg. Chem.*, **429**, 47 (1977).
27. R. Bacaud, P. Bussiere, F. Figueras and J. P. Mathieu, *C.R. Acad. Sci. Paris Ser. C.*, **281**, 159, (1975).
28. R. Bacaud, P. Bussiere and F. Figueras, *J. Phys. Colloq.*, **40**, C2-94 (1979).
29. J. S. Charlton, M. Cordey-Hayes and I. R. Harris, *J. Less-Common Met.*, **20**, 105, (1970).
30. Y.-X. Li, Y.-F.- Zhang and K. J. Klabunde, *Langmuir*, **4**, 385, (1988).
31. K. J. Klabunde, Y.-X. Li and K. F. Purcell, *Hyperfine Interact.*, **41**, 649, (1988).
32. L. Lin, R. Wu, J. Zang and B. Jiang, *Acta Petrol Sci. (China)*, **1**, 73 (1980).
33. N. A. Pakhomov, R. A. Buyanov, E. N. Yurchenko, A. P. Cherynshev, G. R. Kotel'nikov, E. M. Moroz, N. A. Zaitseva and V. A. Patanov, *Kinet. Katal.*, **22**, 488, (1981).
34. V. I. Kuznetsov, A. S. Belyi, E. N. Yurchenko, M. D. Smolikov, M. T. Protasova, E. V. Zatolokina and V. K. Duplyakin, *J. Catal.*, **99**, 159, (1986).
35. P. R. Gray and F. E. Farha in "Mössbauer Effect Methodology" (I. J. Grunerman and Seidel, Eds.), Vol. 10, p. 47, Plenum, New York, 1976.
36. E. N. Yurchenko, V. I. Kuznetsov, V. P. Melnikova and A. N. Startsev, *React. Kinet. Catal. Lett.*, **23**, 137, (1983).
37. P. Zhang, H. Shao, X. Yang and L. Pang, *Cuihua Xuebao*, **5**, 101, (1984).
38. Y.-X. Li, Y.-F. Zhang and Y.-F. Shia, *Cuihua Xuebao*, **5**, 311, (1985).
39. S. Zhang, B. Xie, P. Wang and J. Zhang, *Cuihua Xuebao*, **1**, 311, (1980).
40. Y.-X. Li, K. J. Klabunde and B. H. Davis, *J. Catal.*, **128**, 1, (1991).
41. G. Meitzner, G. H. Via, F. W. Lytle, S. C. Fung, and J. H. Sinfelt, *J. Phys. Chem.*, **92**, 2925, (1988).
42. B. H. Davis, "Bimetallic Catalyst Preparation", U.S. Patent 3,840,475, October 8, 1974.
43. R. Srinivasan, R. J. De Angelis and B. H. Davis, *J. Catal.*, **106**, 449, (1987).
44. R. Srinivasan, R. J. De Angelis and B. H. Davis, *Catal. Lett.*, **4**, 303 (1990).
45. Y.-X. Li, N.-S. Chiu, W.-H. Lee, S. H. Bauer and B. H. Davis, "Characterization and Catalyst Development. An Interactive Approach.", ACS Symp. Series, 411, 328, (1989).

46. N.-S. Chiu, W.-H. Lee, Y.-X. Li, S. H. Bauer and B. H. Davis, "Advances in Hydrotreating Catalysts," (M. L. Occelli and R. G. Anthony, Eds.), Elsevier Sci. Pub., Amsterdam, **1989**, pp. 147-163.
47. R. Srinivasan, L. A. Rice and B. H. Davis, *J. Catal.*, **129**, 257 (1991).
48. B. H. Davis, G. A. Westfall, J. Watkins and J. O. Pezzanite, *J. Catal.*, **42**, 247 (1976).
49. B. H. Davis, *J. Catal.*, **46**, 348 (1977).
50. R. Burch, *J. Catal.*, **71**, 348 (1981).
51. R. Burch and L. C. Garla, *J. Catal.*, **71**, 360 (1981).
52. R. Burch and A. J. Mitchell, *Appl. Catal.*, **6**, 121 (1983).
53. R. Burch, L. C. Garla and J. S. Hennessy, *Prepr. Am. Chem. Soc., Div. Pet. Chem.*, **28** (2), 451 (1983).
54. H. Berndt, H. Mehner, J. Völter and W. Meisel, *Z. anorg. allg. Chem.*, **429**, 47 (1977).
55. J. Völter, H. Lieske and G. Lietz, *React. Kinet. Catal. Lett.*, **16**, 87 (1981).
56. J. Völter, G. Lietz, M. Uhlmann and M. Hermann, *J. Catal.*, **68**, 42 (1981).
57. H. D. Lanh, G. Lietz, H. S. Thoang and J. Völter, *React. Kinet. Catal. Lett.*, **21**, 429 (1982).
58. J. Völter and U. Kürschner, *Appl. Catal.*, **8**, 167 (1983).
59. A. Palazov, Ch. Bonev, D. Shopov, G. Lietz, A. Sarkany and J. Völter, *J. Catal.*, **103**, 249 (1987).
60. Z. Paál, M. Dobrovolszky, J. Völter and G. Lietz, *Appl. Catal.*, **14**, 33 (1985).
61. H. Lieske, A. Sarkany and J. Völter, *Appl. Catal.*, **30**, 69 (1987).
62. R. Bacaud, P. Bussiere, F. Figueras and J. P. Mathieu, "Preparation of Catalysts" (B. Delmon, P. A. Jacobs and G. Poncelet, eds.) Elsevier Sci. Pub. Co., Amsterdam, **1976**, pp 509-523.
63. B. Coq and F. Figueras, *J. Mol. Catal.*, **25**, 87 (1984).
64. B. Coq and F. Figueras, *J. Catal.*, **85**, 197 (1984).
65. F. M. Dautzenberg, J. N. Helle, P. Biloen and W. M. H. Sachtler, *J. Catal.*, **63**, 119 (1980).
66. B. A. Sexton, A. E. Hughes and K. Forger, *J. Catal.*, **88**, 466 (1984).
67. J. Beltramini and D. L. Trimm, *Appl. Catal.*, **31**, 113 (1987).
68. J. Beltramini and D. L. Trimm, *Appl. Catal.*, **32**, 71 (1987).
69. Z. Karpinski and Clarke, *J. Chem. Soc., Trans. Faraday Soc., II*, **71**, 893 (1975).
70. J. K. A. Clarke and J. J. Rooney, *Adv. Catal.*, **25**, 125 (1975).
71. J. K. A. Clarke, I. Manninger and T. Baird, *J. Catal.*, **54**, 230 (1978).
72. Y.-X. Li and K. J. Klabunde, *J. Catal.*, **126**, 173 (1990).
73. J. Margitfalvi, M. Hegedüs, S. Göbölös, E. Kern-Tálas, P. Szedlaczek, S. Szabó and F. Nagy, *Proc. 8th Int. Congr. Catal., Vol. II*, pp 903-914 (1984).
74. J. L. Margitfalvi, P. Szedlaczek, M. Hegedüs, E. Tálas and F. Nagy, *Proc. 9th Int. Congr. Catal.*, pp 1283-1290 (1988).

75. J. L. Margitfalvi, M. Hegedüs and E. Tálas, *J. Mol. Catal.*, **51**, 279 (1989).
76. E. Kern-Tálas, M. Hegedüs, S. Göbölös, P. Szedlacsek and J. Margitfalvi in "Preparation of Catalysts. IV", (B. Delmon, P. Grange, P. A. Jacobs and P. Poncelet, eds.) Elsevier, Amsterdam, **1986**, pp 689-700.
77. L. Lin, J. Zang, R. Wu, C. Wang and H. Du, Proc. 8th Int. Congr. Catal., Vol. IV, pp 565-576 (1984).
78. T. Zhang, J. Zang and L. Lin, "Catalyst Deactivation 1991" (C. H. Bartholomew and J. B. Butt, eds.) Elsevier, Amsterdam, **1991**, pp 143-150.
79. F. G. Gault, O. Zahraa, J. M. Dartigues, G. Maire, M. Peyrot, E. Weisang and P. A. Engelhardt, *Proc. 7th Int. Congr. Catal.*, (T. Seiyama and K. Tanabe, eds.) Elsevier, Amsterdam, **1981**, pp 199-210.
80. A. Sárkány, H. Lieske, T. Szilágyi and L. Toth, *Proc. 8th Int. Congr. Catal., Vol. II*, **1984**, pp 613-621.
81. M. Wilde, R. Feldhaus, K. Anders and H.-D. Neubauer, *Z. Phys. Chemie, Leipzig*, **271**, 919 (1990).
82. B. H. Davis, *J. Catal.*, **42**, 376 (1976).
83. B. H. Davis, *Preprint, Am. Chem. Soc., Div. Pet. Chem.*, **28**, 420 (1983).
84. D. E. Sparks, R. Srinivasan and B. H. Davis, *J. Catal.*, submitted.

RECEIVED July 6, 1992

Chapter 9

Alkyne Coordination, Dimerization, and Scission on a Tungsten–Triiridium Cluster Core

Reaction Modeling Studies Related to Cluster-Derived Butane Hydrogenolysis Catalysts

John R. Shapley, Mark G. Humphrey, and Colin H. McAteer

School of Chemical Sciences and Materials Research Laboratory,
University of Illinois, Urbana, IL 61801

From the reaction of $\text{CpWIr}_3(\text{CO})_{11}$ with excess diphenylacetylene in refluxing toluene, two products have been isolated as crystalline solids: brown $\text{CpWIr}_3(\text{CO})_7(\mu_3, \eta^2\text{-C}_2\text{Ph}_2)_2$ (**1a**) and red $\text{CpWIr}_3(\text{CO})_5(\mu\text{-CPh})(\mu_3\text{-CPh})\{\mu, \eta^4\text{-C}(\text{Ph})\text{C}(\text{Ph})\text{C}(\text{Ph})\text{C}(\text{Ph})\}$ (**1b**) in 40% and 37% yields, respectively. Analytical and spectroscopic data in support of these formulations as well as the results of single-crystal X-ray diffraction studies of both compounds are reported. Compound **1a** has two distinct alkyne units bonded to separate faces of the closed (tetrahedral) WIr_3 cluster core. In contrast compound **1b** has an open (butterfly) core with the tungsten atom at a 'hinge' position, and the alkyne ligands have undergone either $\text{C}\equiv\text{C}$ scission to give μ_2 - and μ_3 -coordinated alkylidyne moieties or dimerization via C-C coupling to give an iridacyclopentadienyl system. The possible relationship of these transformations to the pathways involved in catalytic butane hydrogenolysis over Ir/W(Mo) cluster-derived catalysts are discussed.

The mixed-metal cluster compounds $\text{CpM}_2\text{Ir}_3(\text{CO})_{11}$ and $\text{Cp}_2\text{M}_2\text{Ir}_2(\text{CO})_{10}$ ($\text{Cp}=\eta^5\text{-C}_5\text{H}_5$, $\text{M}=\text{Mo}$, W) adsorbed onto alumina are precursors to heterogeneous catalysts that are active for alkane hydrogenolysis (1,2). For both $\text{M}=\text{Mo}$ and $\text{M}=\text{W}$ the selectivity patterns of the derived catalysts (and for $\text{M}=\text{Mo}$ EXAFS data) provide evidence for bimetallic interactions at the catalytic sites. Since experimental studies of ethane hydrogenolysis suggest that C-C cleavage occurs in an adsorbed, dehydrogenated C_2H_{6-x} , $x=2-4$, intermediate, (3,4) reaction modeling studies can focus on direct access to an analogous dehydrogenated species by the use of alkenes or alkynes as reactants (5). As an aid in understanding the origins of the selectivity differences displayed by the cluster-derived catalysts, we have examined the reactivity of the molecular precursors $\text{CpWIr}_3(\text{CO})_{11}$ and $\text{Cp}_2\text{W}_2\text{Ir}_2(\text{CO})_{10}$ toward an alkyne, specifically, diphenylacetylene. We have previously reported (6) that the reaction of $\text{Cp}_2\text{W}_2\text{Ir}_2(\text{CO})_{10}$ with diphenylacetylene afforded both a complex of the intact alkyne, $\text{Cp}_2\text{W}_2\text{Ir}_2(\text{CO})_8(\text{C}_2\text{Ph}_2)$, and a complex exhibiting the effects of $\text{C}\equiv\text{C}$ bond scission and C-C bond formation, $\text{Cp}_2\text{W}_2\text{Ir}_2(\text{CO})_6(\mu_3\text{-CPh})(\mu_3\text{-}\eta^3\text{-C}_3\text{Ph}_3)$. We report herein the results of treating $\text{CpWIr}_3(\text{CO})_{11}$ with diphenylacetylene and show that the products derive from a combination of alkyne coordination, alkyne dimerization (to give an iridacyclopentadienyl system), and alkyne ligand scission (to give μ_2 - and μ_3 -

coordinated alkylidyne moieties). The connection between metal framework structure and the associated hydrocarbon moieties may have a significant relationship to the selectivity differences displayed by the catalysts derived from the parent cluster compounds.

Experimental Section

CpWIr₃(CO)₁₁ was prepared as previously described (2). Diphenylacetylene (Aldrich) was used as received. Preparative thin-layer chromatography was carried out on (20 x 20 cm) silica gel Si250F plates (J.T. Baker). Infrared spectra were recorded on a Perkin-Elmer 1750 FT-IR spectrophotometer. ¹H NMR (360 MHz) spectra were obtained on a Nicolet NT-360 spectrometer. Fast atom bombardment (FAB) mass spectra were obtained by the staff of the Mass Spectrometry Laboratory of the School of Chemical Sciences on a VG ZAB-SE mass spectrometer, using a matrix of dithioerythritol/dithiothreitol; calculated masses are referenced to ¹⁸⁴W and ¹⁹³Ir. Elemental analyses were performed by the School Microanalytical Laboratory.

Reaction of CpWIr₃(CO)₁₁ with diphenylacetylene. Under a nitrogen atmosphere a dry toluene solution (25 mL) of CpWIr₃(CO)₁₁ (26.3 mg, 23.2 μmol) and diphenylacetylene (21.3 mg, 119.5 μmol) was quickly brought to reflux. The solution color changed from orange to black over 15 min, after which time the reaction was allowed to cool to room temperature. The solvent was removed *in vacuo*, and preparative TLC (1:4 dichloromethane/hexane eluant) of a dichloromethane extract of the residue afforded two major bands. Crystallization from dichloromethane/methanol at -10 °C afforded CpWIr₃(CO)₇(μ₃,η²-C₂Ph₂)₂ (12.9 mg, 40%) (**1a**) and CpWIr₃(CO)₅(μ-CPh)(μ₃-CPh){μ,η⁴-C(Ph)C(Ph)C(Ph)C(Ph)} (12.8 mg, 37%) (**1b**) as brown and red crystals, respectively.

Characterization of 1a. Anal. Calcd for C₄₀H₂₅Ir₃O₇W: C, 34.86; H, 1.83. Found: C, 34.72; H, 1.90. Mass spectrum: *m/z* 1380 (M⁺), 1380 - 28x, x = 1-7 (M⁺ - xCO). IR (C₆H₁₂): ν(CO), 2055 (m), 2030 (s), 2020 (s), 1986 (s), 1963 (m), 1949 (w) cm⁻¹. ¹H NMR (CDCl₃): δ 6.90 (20H, br, Ph), 5.27 (5H, s, Cp).

Characterization of 1b. Anal. Calcd for C₅₂H₃₅Ir₃O₅W: C, 41.63; H, 2.35. Found: C, 41.23; H, 2.46. Mass spectrum: *m/z* 1502 (M⁺), 1502 - 28x, x = 1-5 (M⁺ - xCO). IR (C₆H₁₂): ν(CO), 2045 (m), 2035 (s), 1998 (s), 1981 (m), 1975 (w) cm⁻¹. ¹H NMR (CDCl₃): δ 7.10 (30H, br, Ph), 4.94 (5H, s, Cp).

Results

The reaction of CpWIr₃(CO)₁₁ with diphenylacetylene in refluxing toluene for 15 minutes afforded two major products, **1a** (40%) and **1b** (37%), after chromatographic separation. Compound **1a** has six IR bands in the CO stretching region, whereas compound **1b** has five IR bands in this region. The mass spectrum of **1a** was consistent with the molecular ion being CpWIr₃(CO)₇(C₂Ph₂)₂, whereas that for **1b** suggested that the molecular ion was CpWIr₃(CO)₅(C₂Ph₂)₃. The molecular structures of the products have been determined by single crystal X-ray diffraction analyses. Details of this study will be presented elsewhere (Humphrey, M. G.; McAteer, C. H.; Wilson, S. R.; Shapley, J. R. Manuscript in preparation), but salient features of the structures will be discussed, and a summary of important bond distances is given in Table I.

Table I. Important Bond Distances (Å) in Compounds **1a** and **1b**

Cmpd	M-M distances	M-C distances	C-C distances
1a	W-Ir(1) = 2.700(1)	W-C(70) = 2.18(1)	C(50)-C(60) = 1.40(2)
	W-Ir(2) = 2.755(1)	W-C(80) = 2.20(1)	C(70)-C(80) = 1.44(2)
	W-Ir(3) = 2.798(1)	Ir(2)-C(70) = 2.21(1)	
	Ir(1)-Ir(2) = 2.682(1)	Ir(3)-C(80) = 2.12(1)	
	Ir(1)-Ir(3) = 2.672(1)	Ir(1)-C(50) = 2.25(1)	
	Ir(2)-Ir(3) = 2.598(1)	Ir(1)-C(60) = 2.17(1)	
		Ir(2)-C(50) = 2.12(1)	
	Ir(3)-C(60) = 2.15(1)		
1b	W-Ir(1) = 2.698(3)	W-C(40) = 2.07(5)	C(60)-C(70) = 1.44(6)
	W-Ir(2) = 2.711(3)	Ir(1)-C(40) = 2.19(5)	C(70)-C(80) = 1.47(6)
	W-Ir(3) = 2.896(3)	Ir(2)-C(40) = 2.08(4)	C(80)-C(90) = 1.40(6)
	Ir(1)-Ir(2) = 2.814(3)	W-C(50) = 1.90(5)	
	Ir(2)-Ir(3) = 2.644(3)	Ir(1)-C(50) = 2.11(5)	
		Ir(2)-C(60) = 2.14(5)	
		Ir(2)-C(90) = 2.05(4)	
		Ir(3)-C(60) = 2.33(5)	
		Ir(3)-C(70) = 2.31(4)	
		Ir(3)-C(80) = 2.35(4)	
		Ir(3)-C(90) = 2.19(4)	

The molecular structure of compound **1a** is depicted in Figure 1. The molecule has a WIr_3 tetrahedral framework with two ($2\sigma + \pi$)-bound acetylene ligands, an η^5 -coordinated cyclopentadienyl group and seven terminal CO ligands. The WIr_3 core distances ($W-Ir_{av}$ 2.75(5) Å, $Ir-Ir_{av}$ 2.65(5) Å) are shorter than the comparable distances for the precursor cluster $CpWIr_3(CO)_{11}$ ($W-Ir_{av}$ = 2.82(4) Å, $Ir-Ir_{av}$ = 2.699(2) Å) (2,7). Both alkyne ligands are bonded with their C-C vectors parallel to a metal-metal vector, the most common bonding mode of alkynes in clusters (8,9), with $C\equiv C$ alkyne distances within the usual range of values for this bonding type (1.33 - 1.47 Å) (8). The tungsten-alkyne carbon distances are symmetrical (2.19(1) Å), whereas the corresponding distances involving the iridium atoms show a considerable range (2.12(1) - 2.25(1) Å).

Compound **1b**, as shown in Figure 2, has a WIr_3 "butterfly" framework (10), with the lone tungsten atom occupying one of the "hinge" positions; a cyclopentadienyl ligand is η^5 -bound to the tungsten atom and five terminal CO ligands are distributed among the iridium atoms. The η^5 -iridacyclopentadienyl system defined by Ir(2), C(60), C(70), C(80), and C(90) is planar and coordinates Ir(3). The W-Ir(3) and Ir(1)-Ir(2) bonds are considerably elongated relative to the W-Ir and Ir-Ir distances in the precursor complex $CpWIr_3(CO)_{11}$ (*vide supra*). The dihedral angle between the W-Ir(1)-Ir(2) and W-Ir(2)-Ir(3) planes is 115.8°. The μ_3 -phenylmethylidyne ligand capping the W-Ir(1)-Ir(2) face is displaced markedly toward the W-Ir(2) vector. The μ_2 -phenylmethylidyne group spanning the W-Ir(1) edge is also asymmetric; the W-C(50) distance of 1.90(5) Å is significantly shorter than any other W-C distance in either **1a** or **1b** and may be considered formally as a W=C bond.

Treatment of **1a** with excess diphenylacetylene failed to afford **1b** (toluene, 110°C, 1 hr). Also, we were not able to effect the reverse reaction (**1b** → **1a**) by carbonylation (2.5 atm CO, dichloromethane, 70°C, 3 hr).

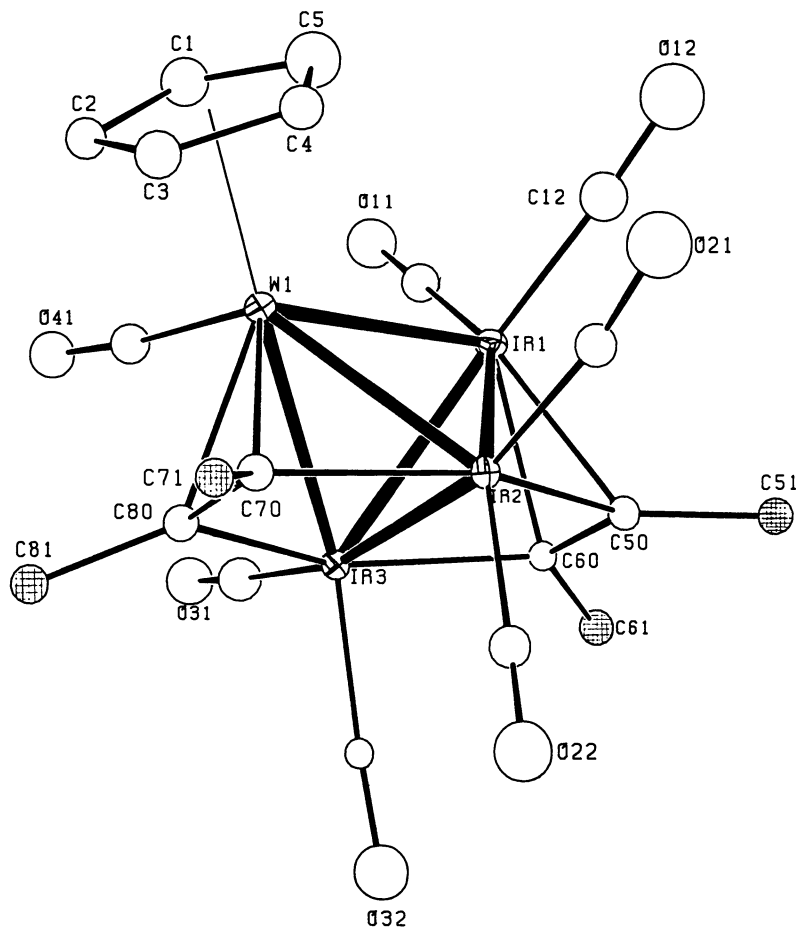


Figure 1. Diagram showing the core structure of compound 1a, $\text{CpWIr}_3(\text{CO})_7(\mu_3, \eta^2\text{-C}_2\text{Ph}_2)_2$. The cross-hatched circles indicate the ipso carbons of the substituent phenyl groups.

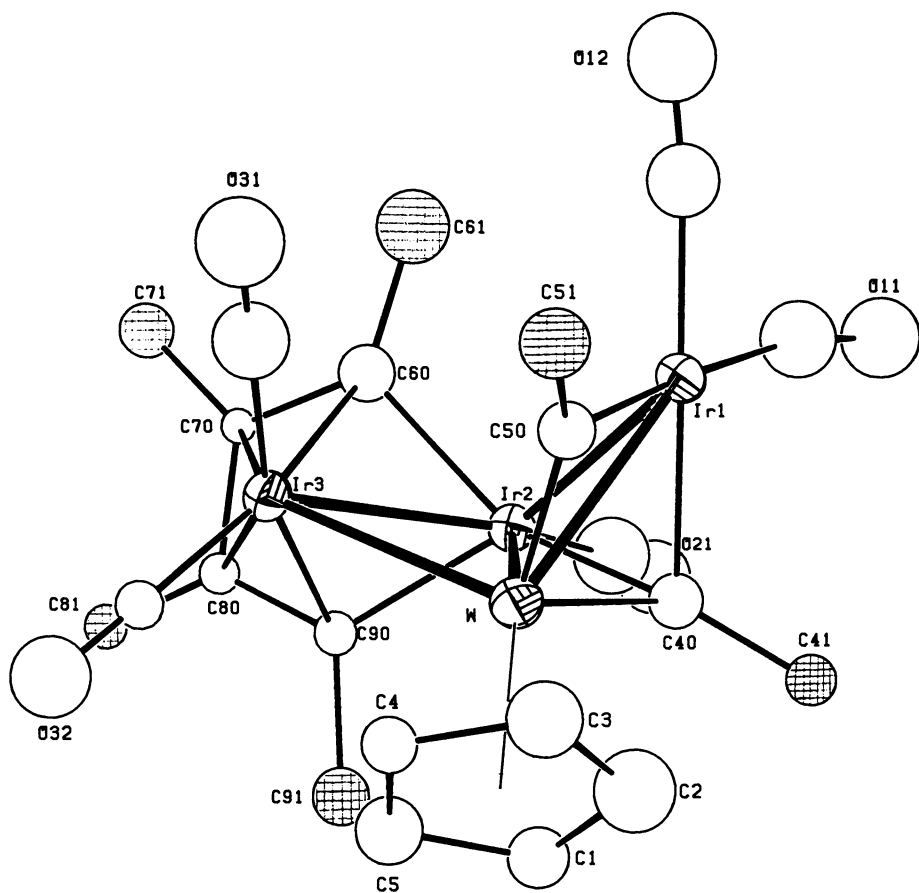


Figure 2. Diagram showing the core structure of compound **1b**, $\text{CpWIr}_3(\text{CO})_5(\mu_2\text{-CPh})(\mu_3\text{-CPh})(\mu, \eta^4\text{-C}_4\text{Ph}_4)$. The cross-hatched circles indicate the ipso carbons of the substituent phenyl groups.

Discussion

Reaction Patterns of Molecular W/Ir Clusters with Alkynes. The reaction between an alkyne and either $\text{Cp}_2\text{W}_2\text{Ir}_2(\text{CO})_{10}$ or $\text{CpWIr}_3(\text{CO})_{11}$ appears to proceed in each case by two independent pathways that are signaled by differences in the morphology of the products' metallic frameworks. As depicted in Figure 3, the reaction of $\text{Cp}_2\text{W}_2\text{Ir}_2(\text{CO})_{10}$ with diphenylacetylene has been shown (6) to afford both a complex of the intact alkyne, $\text{Cp}_2\text{W}_2\text{Ir}_2(\text{CO})_8(\mu_4, \eta^2\text{-C}_2\text{Ph}_2)$, resulting from insertion into a W-W bond, and a complex resulting from a combination of C-C scission and C-C coupling, $\text{Cp}_2\text{W}_2\text{Ir}_2(\text{CO})_6(\mu_3\text{-CPh})(\mu_3, \eta^3\text{-C}_3\text{Ph}_3)$, with cleavage of a W-Ir bond. The corresponding results reported in this paper are shown in Figure 4. The reaction of $\text{CpWIr}_3(\text{CO})_{11}$ with diphenylacetylene affords one product that involves only coordination of the intact alkyne ligand (1a), whereas the other product (1b) shows evidence for both $\text{C}\equiv\text{C}$ scission (to give μ_2 - and μ_3 -coordinated alkyldiylne moieties) and C-C coupling (alkyne dimerization to give an iridacyclopentadienyl system). For neither cluster system can the two types of products be interconverted.

The alkyne ligand transformations suggested by the product structures shown in Figures 3 and 4 have individual precedents in previous work with trinuclear clusters but have received relatively little previous attention for tetranuclear systems. Thus, the coupling of alkyldiylne moieties with alkyne ligands to give the face-bridging dimetallaallyl ligand ($\mu_3, \eta^3\text{-CRCRCR}$) has been observed in several instances with trinuclear frameworks (11) but not previously with tetranuclear ones. Furthermore, there are many examples of metallacyclopentadienyl ligands for trinuclear clusters, but they are almost unknown for tetranuclear clusters (12). Finally, alkyne ligand $\text{C}\equiv\text{C}$ cleavage has been studied for a number of trinuclear compounds, but it has been observed previously for tetranuclear compounds only with two mixed-metal clusters: $\text{CpWOs}_3(\text{CO})_9(\mu_3\text{-CTol})_2\text{H}$ (13) and $\text{Cp}_2\text{Fe}_2\text{Co}_2(\text{CO})_5(\mu_3\text{-CCF}_3)_2$ (14).

The products of the reaction schemes shown in Figures 3 and 4 have some important common features. In the two cases where the alkyne is coordinated intact, tungsten atoms are sited at the less highly coordinated "wingtip" positions. Compound 1a is probably formed via an intermediate with a butterfly structure that loses carbon monoxide and closes to the observed structure (Humphrey, M. G.; Shapley, J. R. Unpublished results). In both cases where scission of the alkyne ligand occurs, the resulting phenylmethylidyne moieties are bonded to a tungsten atom at the "hinge" position by relatively short tungsten-carbon bonds. The opportunity to form strong $\text{W}=\text{C}$ bonds at a relatively oxidized tungsten center has previously been deemed significant for alkyne scission in both a tetranuclear (W_4Os_3) (13) and a trinuclear (W_2Os) (15) cluster system. Furthermore, the wingtip iridium atoms are π -bonded to a chain of three or four carbon atoms in this configuration. Thus, the picture that emerges from these reaction studies is that W atoms at hinge positions promote C-C scission and Ir atoms at tip positions support chains of unsaturated carbon atoms.

Behavior of W/Ir and Mo/Ir Cluster-Derived Catalysts. In our catalysis studies (1,2) the clusters $\text{CpM}_2\text{Ir}_3(\text{CO})_{11}$ and $\text{Cp}_2\text{M}_2\text{Ir}_2(\text{CO})_{10}$ (M=Mo, W) were deposited onto alumina as catalyst precursors. Comparable materials were prepared from $\text{Ir}_4(\text{CO})_{12}$ and $\text{Cp}_2\text{M}_2(\text{CO})_6$ as well as from a stoichiometric mixture (Ir:M=1:1) of these compounds. The supported compounds were activated by heating to 500 °C in flowing H_2 , and the resulting materials, designated as $[\text{M}_x\text{Ir}_y]$ to indicate the precursor, were examined as catalysts for the hydrogenolysis of n-butane at 215 °C. The iridium-containing materials $[\text{Ir}_4]$, $[\text{M}_2\text{Ir}_3]$, $[\text{M}_2\text{Ir}_2]$, and $[\text{M}_2\text{Ir}_4]$ were all comparably active catalysts, but $[\text{M}_2]$ was inactive. The selectivity for ethane

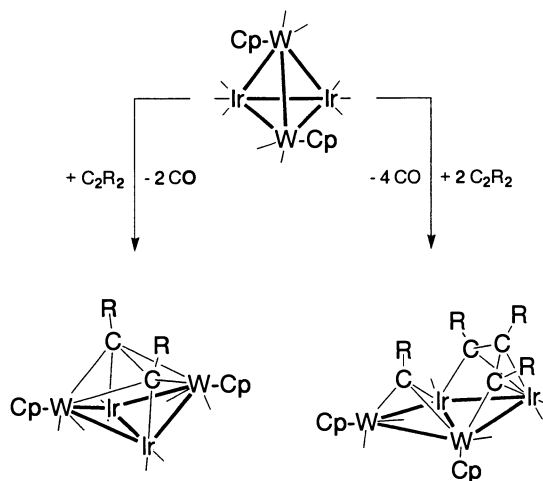


Figure 3. Reaction scheme showing the products derived from the reaction of $\text{Cp}_2\text{W}_2\text{Ir}_2(\text{CO})_{10}$ with diphenylacetylene (6).

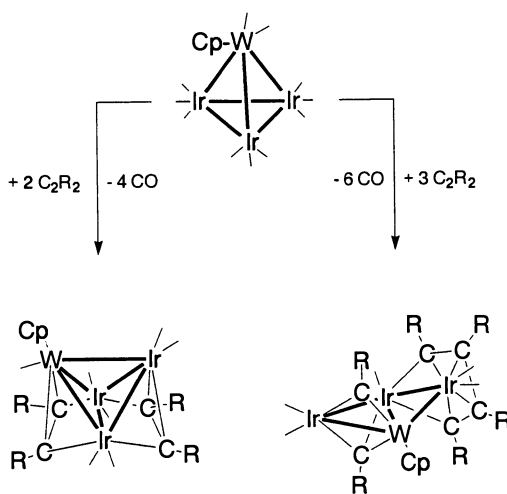


Figure 4. Reaction scheme showing the products derived from the reaction of $\text{CpWIr}_3(\text{CO})_{11}$ with diphenylacetylene.

production (the balance being methane and propane) was 70-75% for the $[\text{Ir}_4]$, $[\text{M}\text{Ir}_3]$, and $[\text{2M}_2+\text{Ir}_4]$ catalysts, but the $[\text{M}_2\text{Ir}_2]$ catalysts showed ethane selectivity of ca. 50%. Thus, the $[\text{M}\text{Ir}_3]$ catalysts showed preferential cleavage of a terminal methyl group from the butane substrate, whereas the $[\text{M}_2\text{Ir}_2]$ catalysts demonstrated a significantly greater degree of cleavage at the interior carbon-carbon bond. These different selectivity patterns were attributed to the presence of differing bimetallic interactions in the activated $[\text{M}\text{Ir}_3]$ and $[\text{M}_2\text{Ir}_2]$ materials. This idea was further supported by EXAFS data in the case of the molybdenum-containing catalysts (1).

Foger and Anderson's (16) studies of supported iridium catalysts showed that the selectivity pattern for butane hydrogenolysis is highly correlated with particle size in that the selectivity for ethane production increased dramatically as the catalyst dispersion increased (decreasing particle size). Engstrom, et al. (4) provided closely related information from their study of butane hydrogenolysis over two different single crystal iridium surfaces: first, the smooth (111) plane, akin to the surface of large particles; and second, the more open (110)-(1x2) plane, with lower coordination number iridium sites more similar to those on the surfaces of small particles. In the former case there was a preference for terminal cleavage, producing methane, whereas in the latter situation there was much more internal cleavage, leading to ethane. These workers suggested that the different cleavage patterns result from different structures for the partially dehydrogenated C_4 surface intermediates on the two surfaces due to different degrees of steric congestion, viz., the (111) plane favors a 1, 2-coordinated species but the (110) plane allows a 1, 4-coordinated metallocyclic intermediate that preferentially forms two C_2 units.

The specific structures of our alumina-supported cluster-derived catalysts are not known, but both indirect (chemisorption) and direct (EXAFS) measurements provide evidence that the catalytic particles formed by cluster decomposition are well-dispersed (i.e., small) and at least in part retain some close metal-metal interactions. It is expected that the more electropositive metal will interact strongly with the alumina support upon ligand loss, whereas the iridium centers may not bond strongly. A highly simplified model is shown in Figure 5, wherein one M is 'inactive' by being incorporated into the surface through strong bonding, but the remaining three metal centers are 'active', that is, exposed to and able to interact with the reactant stream. On the basis of this model the $[\text{M}_2\text{Ir}_2]$ catalysts will have one active M center in addition to the two iridium centers, whereas the $[\text{M}\text{Ir}_3]$ catalysts will have only active iridium centers and an inactive M center.

The model in Figure 5 is consistent overall with the observation that the $[\text{M}\text{Ir}_3]$ catalysts display the same selectivity pattern as the iridium-only $[\text{Ir}_4]$ catalyst. The iridium centers in these catalysts will have relatively low coordination, leading to the

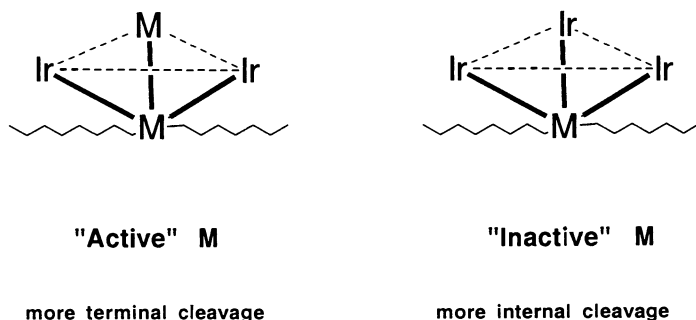


Figure 5. Model for the alumina-supported, $\text{Cp}_2\text{M}_2\text{Ir}_2(\text{CO})_{10}$ and $\text{CpM}\text{Ir}_3(\text{CO})_{11}$ cluster-derived catalysts.

possibility of extensive dehydrogenation and internal cleavage, as observed. The metallacyclic structure observed for compound **1b** may represent a model for an intermediate along this pathway. On the other hand the reaction modeling studies suggest that the presence of a reactive tungsten or molybdenum center is important for the stabilization of C₁ moieties through strong multiple bonding. Thus, an active M center in the [M₂Ir₂] catalysts would be expected to lead to more terminal cleavage, which is consistent with the observed selectivity pattern.

Acknowledgments

This work was supported by National Science Foundation grant DMR 89-20538 and its predecessors to the Materials Research Laboratory of the University of Illinois. We acknowledge Dr. Scott R. Wilson of the School of Chemical Sciences X-ray Crystallographic Service for providing the results of the structure determinations of compounds **1a** and **1b**.

Literature Cited

- (1) Shapley, J. R.; Uchiyama, W. S.; Scott, R. A. *J. Phys. Chem.* **1990**, *94*, 1190.
- (2) Shapley, J.R.; Hardwick, S.J.; Foose, D.S.; Stucky, G.D.; Churchill, M.R.; Bueno, C.; Hutchinson, J.P. *J. Am. Chem. Soc.* **1981**, *103*, 7383.
- (3) Sinfelt, J. H. *J. Catal.* **1972**, *27*, 468.
- (4) Engstrom, J. R.; Goodman, D. W.; Weinberg, W. H. *J. Am. Chem. Soc.* **1988**, *110*, 8305.
- (5) Wang, P.-K.; Slichter, C. P.; Sinfelt, J. H. *J. Phys. Chem.* **1990**, *94*, 1154.
- (6) Shapley, J.R.; McAteer, C.H.; Churchill, M.R.; Biondi, L.V. *Organometallics* **1984**, *3*, 1595.
- (7) Churchill, M.R.; Hutchinson, J.P. *Inorg. Chem.* **1981**, *20*, 4112.
- (8) Sappa, E.; Tiripicchio, A.; Braunstein, P. *Chem. Rev.* **1983**, *83*, 203.
- (9) Raithby, P.R.; Rosales, M.J. *Adv. Inorg. Chem. Radiochem.* **1985**, *29*, 169.
- (10) Sappa, E.; Tiripicchio, A.; Carty, A.J.; Toogood, G.E. *Prog. Inorg. Chem.* **1987**, *35*, 437.
- (11) Adams, R.D.; Belinski, J.A. *Organometallics* **1991**, *10*, 2114, and references therein.
- (12) Riaz, U.; Curtis, M.D.; Rheingold, A.; Haggerty, B.S. *Organometallics* **1990**, *9*, 2647.
- (13) Park, J.T.; Shapley, J.R.; Bueno, C.; Ziller, J.W.; Churchill, M.R. *Organometallics* **1988**, *7*, 2307.
- (14) Rumin, R.; Robin, F.; Petillon, F.; Muir, K.W.; Stevenson, I. *Organometallics* **1991**, *10*, 2274.
- (15) Chi, Y.; Shapley, J.R. *Organometallics* **1985**, *4*, 1900.
- (16) Fogar, K.; Anderson, J.R. *J. Catal.* **1979**, *59*, 325.

RECEIVED June 22, 1992

Chapter 10

Platinum–Tin and Gold–Tin Bimetallic Particles Prepared from Solvated Metal Atoms

Structure and Catalysis

Yi Wang, Yong-Xi Li, and Kenneth J. Klabunde¹

Department of Chemistry, Kansas State University, Manhattan, KS 66506

Deposition of metal atoms into cold frozen solvents followed by warming leads to cluster formation through solvated metal atom intermediates. The use of two metals, such as Pt and Sn, leads to ultra-fine particles of PtSn that can be trapped on Al₂O₃. In this way PtSn/Al₂O₃ catalysts were prepared that showed very good properties for n-heptane reforming to benzene/toluene, especially better selectivity compared with conventional catalysts. These results also strongly suggest that metallic tin is important in this class of reforming catalysts. Further studies employing Au and Sn bimetallic particle formation were carried out. Attempts to control the solvated metal atom clustering step were made by varying solvent polarity, viscosity, functional group, and by solvent warming procedure. It was determined that slow warming of the cold solvent led to the smallest crystallites (about 12 nm) of AuSn (as well as smaller amounts of Au₅Sn and Sn). Viscosity only was a factor in select cases. These results were rationalized by considering the competitive rates of atom growth to clusters *vs.* cluster reaction with the host solvent (which ligand stabilizes the cluster and stops growth). One important finding was that some selective growth to AuSn and Au₅Sn was possible by temperature control of the solvated metal atom media.

Although nano-scale metal particles have been of leading importance in heterogeneous catalysis for decades, these particles have generally been prepared by high temperatures reduction methods.^(1,2,3) Under such conditions approach to the most thermodynamically stable state has often moved further than desirable. That is, metastable mono-metallic phases cannot be prepared because they convert to the most stable crystalline phase, and metastable bimetallic particles would phase separate according to thermodynamic tendencies.

¹Corresponding author

In order to prepare metastable states or possibly new phases of nano-scale metal particles, low temperature, kinetic growth methods should be used.(4) And atoms should be used, rather than salts or oxides since in the former case the high temperature reduction step can be avoided. In actuality, in recent years we have witnessed the development of several methods for the low temperature kinetically controlled growth of clusters from free atoms. Perhaps the most dramatic development has been the "cluster beam" approach where evaporated metal atoms are allowed to cluster in low temperature gaseous helium or argon streams.(5-20) Unusual cluster structures and reactivities have been realized.

Clustering of metal atoms in frozen or liquid rare gases has also attracted attention, and both annealing and photo induced clustering have been reported.(21-24)

A similar method is to allow metal atoms to cluster in cold organic solvents. This method can be practiced on large scale with relatively low expense, and so has been widely practiced for almost 20 years, serving as a forerunner of all of those clustering methods.(25-30) Kinetic control of cluster growth may be realized, and unique structure/reactivity of such materials has been demonstrated many times.(4) Magnetic and electrical properties of such clusters are often unusual as well.(29,31)

Metal clusters formed in this way are always contaminated by adsorbed host solvent and fragments of this solvent.(29) In one way this is an advantage since this adsorption tends to "ligand stabilize" the cluster and stop further growth --- thus nano-scale particles are isolable. However, the complex nature of these fragments do complicate study of these particles. Another frequent problem is that growth is less controllable than desirable.

What is usually observed when metal atoms are codeposited with excess organic solvents at -196°C is the formation of a frozen matrix where the atoms are isolated and weakly solvated. Upon warming atoms begin to migrate in the cold liquid phase, and thousands of atoms cluster into particles of 4-9 nm. Continued warming and/or solvent evaporation leads to flocculation (without amalgamation) of these "monomer" clusters into super clusters or chains, and eventually yielding powders(29) or films(32-34).

In this report we wish to consider the initial clustering process in some detail. Are there experimental procedures which will allow more control of this growth to monomer clusters? Can new metastable phases be formed and detected? And do bimetallic particles formed in this way possess any unique catalytic properties?

The Pt-Sn System

The commercial importance of the Pt-Sn/ Al_2O_3 catalyst system (35-39) as well as the poor understanding of the role of tin led us to investigate this bimetallic combination in some detail.(40-42) These solvated metal atom dispersed (SMAD) catalysts have been prepared in two general ways: the "half-SMAD" process refers to treating preformed, conventional Pt/ Al_2O_3 catalysts with solvated Sn atoms, thereby ensuring the deposition of metallic tin on the Pt clusters.(41-42) The "full-SMAD" process refers to the simultaneous evaporation/trapping/solvation of Pt and

Sn atoms simultaneously followed by warming, bimetallic cluster formation and trapping on high surface area Al_2O_3 .(40)

Two conventional procedures for Pt-Sn/ Al_2O_3 catalyst preparations were carried out for comparisons. The first one involved the co-impregnation of Al_2O_3 with aqueous Pt^{2+} and Sn^{4+} chloride salts. The second involved the co-precipitation of $\text{Al}(\text{OH})_3$ with Pt^{2+} and Sn^{4+} salts.

Figure 1 illustrates these four catalyst preparation methods and the anticipated Pt-Sn cluster structures. Note that the conventional preparation methods are expected to yield Pt° and $\text{Sn}^{4+}/\text{Sn}^{2+}$ oxides on Al_2O_3 , while the SMAD methods are expected to yield Pt° and Sn° combinations of differing morphologies.

There is still debate as to whether any Sn° is formed when conventional catalysts go through the reduction step. Usually Sn° is not detected spectroscopically.(43,44) However, recent work from Davis' laboratory demonstrates that at least a small amount of Sn° can be formed and this may be significant in affecting catalyst performance.(45,46)

Through the combined use of catalytic probe reactions, Mössbauer, EXAFS, XPS, XRD, it has been demonstrated that the anticipated particle structures for the half-SMAD and full SMAD procedures are close to reality.(40-42) Thus, ^{119}Sn Mossbauer, a bulk solid analysis technique, revealed the relative amounts of Sn, Pt-Sn alloy, SnO , and SnO_2 present in the catalysts. It was possible to differentiate Sn° from Pt-Sn alloy through supporting evidence of XPS and selective oxidation, since it was found that ultra-fine Sn° particles were much more susceptible to oxidation than Pt-Sn alloy particles. Also, since the full SMAD $\text{Pt}^\circ\text{-Sn}^\circ/\text{Al}_2\text{O}_3$ catalysts behaved much differently than $\text{Pt}^\circ/\text{Al}_2\text{O}_3$, it is clear that the SMAD catalysts are not made up of separate Pt° and Sn° particles.

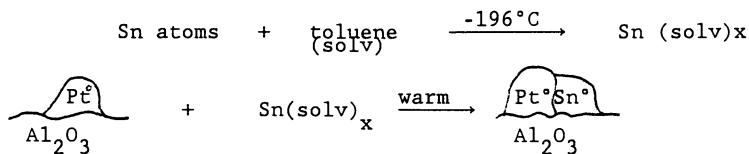
All of this information combined to suggest the most likely morphology of the full SMAD $\text{Pt}^\circ\text{-Sn}^\circ$ particles, and this is shown in Figure 2.

Catalytic reactions over these four types of Pt-Sn/ Al_2O_3 catalysts were studied using n-heptane reforming as a model. In particular the production of benzene and toluene (desirable products) was compared with production of undesirable hydrogenolysis products, methane and ethane. Hydrogenolysis was significantly depressed on the full SMAD catalysts. Figure 2 illustrates a particle where Pt ensembles would be decreased in surface population. Accordingly, it seems likely that hydrogenolysis decrease is a result of this lack of necessary ensembles to carry out this structure sensitive reaction.(40)

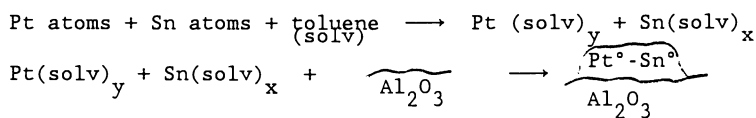
These results also demonstrate that zero-valent tin does affect catalytic performance in beneficial ways. So, although zero-valent tin is rarely detected in conventional Pt-Sn/ Al_2O_3 catalysts, small amounts possibly formed on the Pt particles (by H_2 reduction of Sn^{2+}) may be at least partially responsible for beneficial changes in this important class of bimetallic catalysts.(44)

A comparison of catalytic properties for all four catalyst systems suggested some generalizations: (1) the presence of SnO_2 and SnO in the conventional catalysts may play a role in improving lifetime/stability by blocking Pt particle sintering; (2) the presence of Sn° in combination with Pt° can affect catalytic activity and selectivity; (3) the presence of $\text{Pt}^\circ\text{-Sn}^\circ$ alloy (rich in Sn°) can depress unwanted hydrogenolysis while activity for the desired dehydrocyclization is only lowered slightly.(40,47)

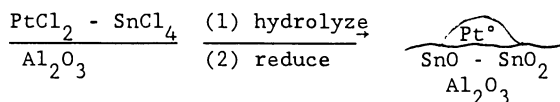
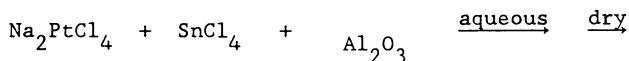
Half SMAD



Full SMAD



Co-Impregnation (conventional)



Co-Precipitation

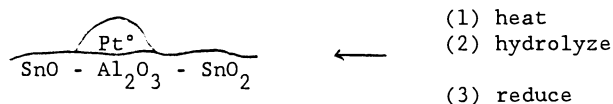
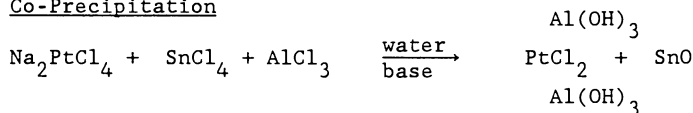


Figure 1. Pt-Sn/Al₂O₃ Catalyst Preparation Schemes

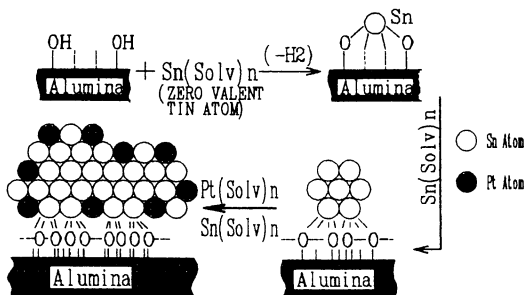


Figure 2. Proposed sequence for formation of a full SMAD Pt-Sn Bimetallic Particle on Al₂O₃ (Sn/Pt atomic ratio of 2.5 is illustrated). Reproduced with permission of Ref. 40. Copyright 1990 Academic Press.

The Au-Sn System

The rationale for study of this bimetallic system is based on the goal of learning if cluster growth could be controlled more precisely. The choice of Au/Sn was based on several things: (1) similarity with the Pt-Sn system; (2) relatively low reactivity of Au and Sn atoms; (3) ease of evaporation of gold and tin and similarity in vapor pressures (in contrast to Pt vs. Sn); (4) the fact that gold and tin form several well characterized intermetallic compounds through the entire composition range of the two substituents, and (5) the ability to study both gold and tin by Mössbauer techniques (although this proved less useful than anticipated).

Experimental parameters such as evaporation method, solvent polarity and viscosity, and warming rate during cluster formation were varied. Cluster/crystallite size and particle surface area were monitored. Additional information was gleaned from Mössbauer, Differential Scanning Calorimetry (DSC), and X-Ray Photoelectron Spectroscopy (XPS).

Background. An introduction to the Au-Sn alloy system is appropriate before our experimental results are summarized. The AuSn alloy (1:1 atomic ratio) has been of interest as an optical recording material.(48) Considerable work on the interdiffusion of thin layers of gold on tin has been carried out --- rapid diffusion occurs even at room temperature. Thus, the formation of AuSn is a very favorable process,(49,50) and the properties of this material have interested physicists for some time.(51-55) By this diffusion process, grain sizes of 20-60 nm for the AuSn have been observed.(56) Other stoichiometries have been observed if excess Au or Sn was present, although formation of such species as Au₅Sn, AuSn₂, and AuSn₄ is usually slower than formation of AuSn.(57)

In fact, many Au-Sn stoichiometric ratios are possible, as illustrated by the phase diagram of this system, Figure 3. However, the favored species, according to film diffusion studies, appear to be AuSn, AuSn₂, AuSn₄ and Au₅Sn. Mossbauer of ¹¹⁹Sn in these phases are summarized in Table I.(58) These results were explained in terms of the number of Au nearest neighbors for the Sn atoms and the specific volume of Sn atoms.

Electronic behavior of Au-Sn alloys has been studied by XPS.(54,55) Positive shifts in core level binding energies for both Au 4f_{7/2} and Sn 3d_{5/2} were observed for Au_{0.96}Sn_{0.04}, AuSn, and AuSn₄. The average shifts for AuSn were 0.9 eV for Au and 0.3 eV for Sn. Similarly, the valence band of this alloy was narrowed and shifted to higher binding energy.

These intermetallic species in molecular form have been examined by Knudson Cell-Mass Spectroscopy techniques. The dissociation energy D₀^o of AuSn(g) was reported as 252.6 ± 7.2 kJ/mol and its heat of formation as 414.6 ± 7.2 kJ/mol, a rather substantial value.(59) Other molecular species AuSn₂, Au₂Sn, Au₂Sn₂, and AuSn₃ were also evaluated. These results further point out that the formation of these intermetallics is energetically quite favorable.

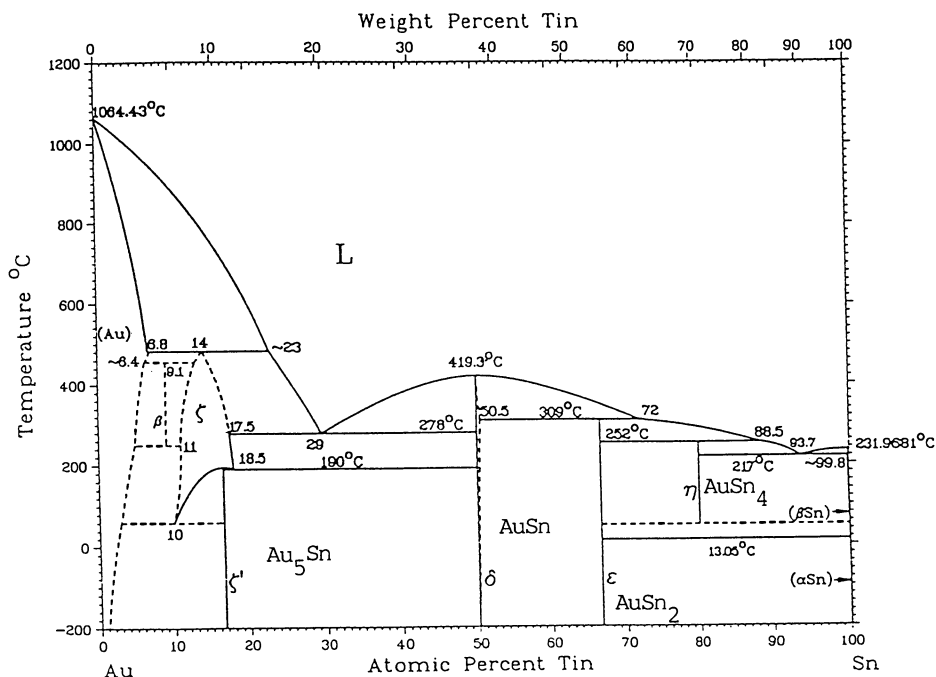


Figure 3. Au-Sn Alloy Phase Diagram. Okamoto, H.; Massalski, T.B.; *Bull Alloy Phase Diagrams*, 1984, 5(5), October. Reproduced with permission. Copyright 1984.

Table I. ^{119}Sn Isomer Shifts (ΔS^I) and Quadrupole Splitting (ΔE_Q) for Some Au-Sn Binary Alloys

Sample	ΔS^I (mm/sec)	ΔE_Q (mm/sec)
ξ^*	2.02(3)	0.25(2)
$AuSn$	2.28(2)	0.25(2)
$AuSn_2$	2.35(2)	0.71(2)
$AuSn_4$	2.73(6)	0.17(3)

(a) ξ represents the cph ξ phase solid solution with homogeneity ranging between about 10 and 18.5 atomic % Sn.

Experimental Results on Au Atom - Sn Atom Clusters in Cold Solvents.

Cluster Growth. Would solvated atoms, allowed to slowly warm and nucleate to Au-Sn intermetallic alloy particles, show any selectivity toward growth of particular Au_xSn_y species? What properties of the solvent or other experimental parameters affect this selectivity? These are the questions we attempted to answer with the following experiments.

Indeed, with mono-metallic studies, we have found that solvent polarity and warm-up procedure can drastically affect resultant crystallite sizes,(29) magnetic properties,(29,31) and ability to form stable colloidal solutions.(32,34) However, a bimetallic such as Au-Sn has not been examined in this way before (although other bimetallics have yielded interesting SMAD catalysts).(40,60,61,62,63)

In the present study, gold and tin were usually evaporated simultaneously from two separate crucibles, and the atoms cocondensed simultaneously with a high excess of the vapor of the solvent of choice. This resulted in the almost complete matrix isolation of the atoms at -196°C (the ratio of Au:Sn could be determined by weighing the used crucibles later). Upon warming the atom clustering took place, mainly in the cold liquid solvent as it melted.

Figure 4 exhibits a typical x-ray powder diffraction (XRD) pattern for the isolated, dry Au-Sn powder from an experiment where the Au:Sn ratio was 1.3:1. The spectrum is compared with known diffraction patterns of Sn, AuSn, and Au_5Sn and it can be seen that AuSn is the major component with the remaining smaller peaks assignable to Sn and Au_5Sn . So some selectivity is exhibited, considering all of the possibilities for other compositions, and statistical/random clustering does not appear to dominate.

Other experiments bear on this point more strongly. Layering experiments, where gold and tin were evaporated at different times, were carried out. In this way a layer of frozen Sn atoms/acetone was covered by a layer of frozen Au/acetone with about the same molar ratio of Au:Sn overall. Upon warming and clustering, the same product distribution was obtained (Figure 5). These results show that the clustering process takes place mostly after solvent liquification and mixing of solvated atom solutions. If this were not true, large amounts of Sn and Au particles should have been formed due to the proximity of these species with each other. In addition, such results prove that the clustering process does not take place in the gas phase prior to codeposition and that pyrolysis of trace of amounts of solvent on the hot crucibles does not affect the clustering process.

The results of the layering experiments allowed our experimental design to be much simplified, if we so desired.(64) That is, we placed gold and tin metals in the same crucible and simply evaporated all the metal. Tin evaporates at a lower temperature and so this is really another type of layering experiment. Again, the same products were obtained, further supporting that cluster formation of the intermetallic compounds occurs in the matrix during and after solvent liquification and complete mixing.

The next series of experiments dealt with solvent variation. Table II summarizes solvent properties, matrix warm-up procedure, and properties of the resultant ultra-fine powder of AuSn obtained. (In these studies gold and tin were

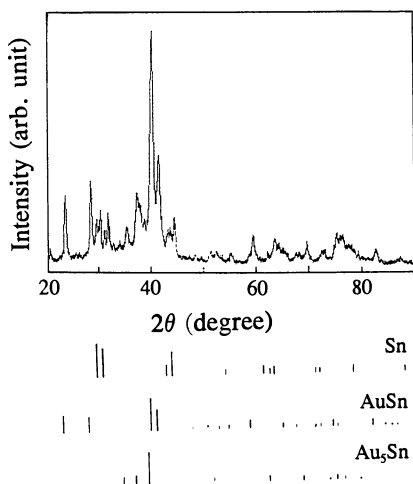


Figure 4. XRD Pattern of Au-Sn Powder Prepared in Acetone. The Molar Ratio of Au:Sn Evaporated is 1.3:1.

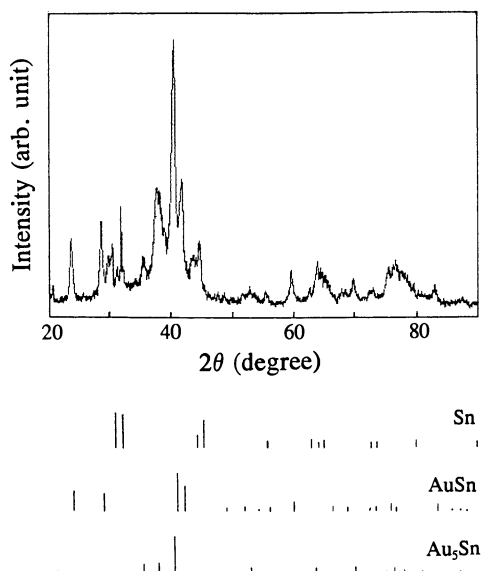


Figure 5. XRD Pattern of Au-Sn of Powder Prepared in Acetone by evaporating Each Metal Successively (layering experiment).

Table II. Solvent Properties Compared with Surface Areas and Crystallite Sizes of Resultant AuSn Powders

Solvent	m.p. C°	Dielectric Constant E°	viscosity ^a	warm- up ^b	SA (m ² /g) ^c	Cryst Size (nm) ^d
				fast	16.5	16.3
Pentane	-130	1.8	0.289	slow	23.8	10.2
				fast	14.9	17.8
Acetone	-95	20.7	0.399	slow	18.3	11.2
				fast	17.6	17.6
Toluene	-95	2.4	0.772	slow	43.7	17.1
				fast	11.6	26.9
Ethanol	-117	24.3	1.733	slow	16.5	23.6
				fast	19.4	13.1
Cyclo- hexane	6.5	2.0	1.02(20)	slow	28.0	12.7
				fast	16.6	17.8
Ether	-116	4.3 (20)	0.284	slow	-----	9.3
				fast	23.4	13.1
Hexane	-95	1.9 (20)	0.401	slow	19.8	12.5

(a) Viscosities are at 0°C unless indicated otherwise in parentheses.

(b) Fast warm-up: -196°C to 25°C in ~0.5 hrs.

Slow warm-up: -196°C to 25°C in 3~4 hrs.

(c) BET method using nitrogen adsorption.

(d) From XRD data using Scherrer equation.

(e) Dielectric constants are at 25°C unless indicated otherwise in parentheses.

evaporated from the same crucible). It soon became apparent that the product mix of AuSn, Sn, and Au₅Sn did not change significantly with variation in solvent, if warm-up procedures were kept constant. Thus, selectivity was not changing, according to XRD. However, product morphology did change. For example, with ethanol the largest crystallite size and lowest surface area was encountered. However, warm-up procedure had the most striking effect --- note that in every case a slow warm-up yielded smaller average AuSn crystallite sizes and larger surface areas. Moreover, this effect was minimized for solvents of higher viscosity, but was marked for solvents of lowest viscosity.

These results tell us that the cluster growth process in this case does exhibit same selectivity toward the formation of the more stable phases. Also, for similar functional groups in the solvents, viscosity has a limited effect on the crystallinity on particle size. And although the warm-up rate had the most striking effect, note that for the lowest viscosity solvents the largest changes were caused by warm-up variation. These points suggest that the growth process occurs within a rather narrow temperature and viscosity range.

As an illustration one could imagine a competition between processes: solvated atoms nucleate and begin to grow vs. the reaction of the growing particles with the solvent and surface ligation occurs and particle growth is slowed or stopped. With earlier work on Ni-pentane nucleation and growth, we expressed this as a competition between particle growth and reaction with the pentane host.(29,65) With bimetallic systems it is more complex, and we express these concepts as shown in Figure 6. It is likely that reactions 1-3 are quite rapid when the solvent just liquifies, but these rates can be affected by large viscosity changes as would be encountered when a solvent melts to a very non-viscous liquid over a small temperature range. As the particle grows, and mobility decreases, (with simultaneous increase in temperature), reaction 3 would become slower. However, the rate of reaction 4 would increase rapidly once the minimum temperature for reaction with the solvent is reached. In other words, reactions 1, 2, and 3 occur below the temperature where reaction 4 becomes competitive.

The slower warming rate and minimization of large viscosity gradients tend to allow reaction 4 to compete better with reaction 3. Thus, solvent fragmentation/ligation (reaction 4) competes better over the slow warm-up period.

One additional interesting point is that the most polar solvents allow the growth of the largest crystallites. This, again, can be explained by the logical assumption that reaction 1, 2, and 3 become slower and more selective since displacement of more strongly ligating solvent ligands (due to higher polarity) would be more difficult. Thus, these growth steps become more selective and crystal growth more favorable. In other words, fewer nucleation sites would be formed, and larger crystallites would grow.

These findings might be summed up by saying that slow warm-up causes a "milder" clustering process to occur, while fast warm-up causes a "wilder" process to occur.

Heat Treatment of AuSn Particles. Differential Scanning Calorimetry. Heat treatment of these ultra-fine particles caused the expected increase in crystallite

sizes. Also, the formation of small amounts of SnO_2 , presumably from reaction with adsorbed acetone fragments and/or adventitious oxygen was apparent (Figure 7 and 8).

Differential scanning calorimetry (DSC) studies were particularly interesting for these samples. DSC provides information about exothermic and endothermic reactions and phase changes upon controlled heating, and can be quite useful when dealing with intermetallic compounds. Figure 9 illustrates spectra for AuSn particles prepared in acetone by fast and slow warm-up procedures. Endothermic processes show upward peaks while exothermic are downward. The sharp endothermic peaks represent phase changes in the small particles, and correspond to melting points of the various compositions:

<u>Temperature(°C)</u>	<u>Alloy</u>
219	Sn
275	eutectic mix of Au_5Sn and AuSn
419	AuSn

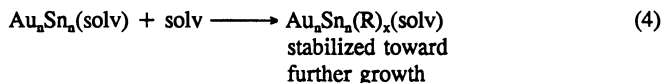
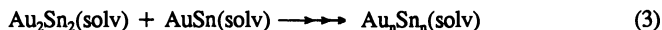
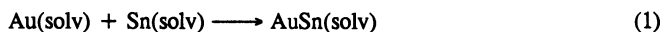
The most interesting features are the sharpness of the melting, and the fact that the sample from slow warming exhibits a less complex mixture. This clearly shows more selectivity in product formation, and is perhaps the most promising result demonstrating the potential for control of cluster growth for atom clustering in cold solvents.

Further Spectroscopic Characterization. Mössbauer (^{119}Sn) proved to be of limited value due to overlap of spectral lines for Sn^0 and $\text{Au}^0\text{-Sn}^0$ alloys. Figure 10 shows a bulk AuSn alloy that we prepared by melt-annealing; $\text{IS}=2.31$ mm/sec and $\Delta E_Q = 0.22$ which agree with literature discussed earlier (Table I). The Sn and AuSn samples prepared in acetone show the presence of a small amount of tin oxide demonstrated by the broad peak at $\text{IS} = 0$, and this absorption increased with length of spectral collection time suggesting that the Sn particles were slowly being oxidized by adventitious oxygen rather than by adsorbed solvent fragments (acetone).

X-ray photoelectron (XPS) studies of the core and valence electrons were also carried out (see Tables III -Table V and Figures 11 and 12). The Sn core level peaks were shifted to higher energies; 1.2 eV shift for Sn 3p and 0.4 eV for Sn 3d. These results could be explained by considering that there is considerable charge delocalization toward Au in these small particles, which is consistent with electronegativity



considerations. It might be expected that the Au core level binding energies would then be shifted to lower energies, and our data supports this, although the changes are very small.



- Mobility decreases with size. Therefore k_3 decreases.
- Mobility is low at high viscosities. Therefore, k_4 competes with k_3 more effectively.
- Interdiffusion of Au and Sn does not occur from particle to particle, because each particle is a separate entity due to the solvation shell.

Figure 6. A Generalization of Rate Processes for cluster growth and cluster reactions with host solvent. solv = solvent molecule, R = fragment of solvent that serves as a ligand.

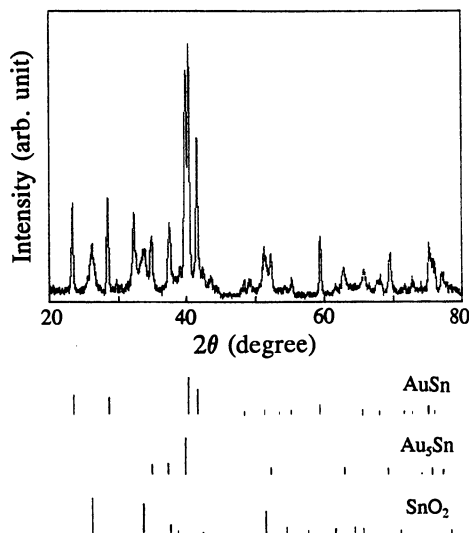


Figure 7. X-Ray Diffraction Pattern of a AuSn Sample (prepared in acetone) Heated to 275°C Under Argon.

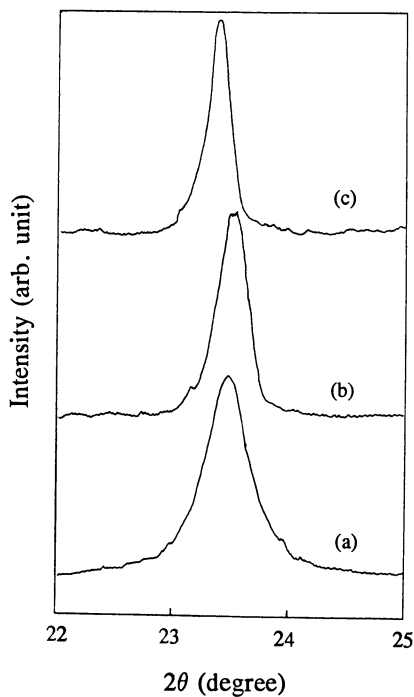


Figure 8. A comparison of X-ray diffraction lines for AuSn particles upon heating to 275 °C and 450 °C. (a) as received, 18 nm average crystallite size; (b) 275 °C, 25 nm; (c) 450 °C, 36 nm (according to Scherrer Treatment of crystallite sizes).

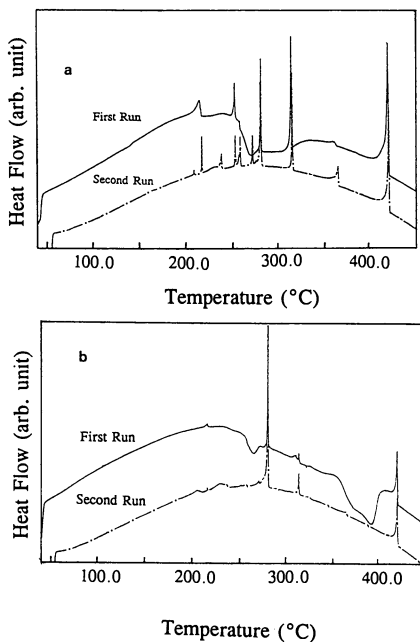


Figure 9. DSC spectra of AuSn particles prepared in acetone by (a) fast warm-up (b) slow warm-up

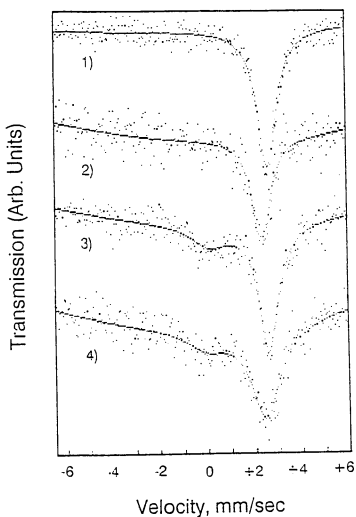


Figure 10. ^{119}Sn Mossbauer Spectra for (1) β -Sn foil; (2) bulk AuSn alloy (3) Sn particles prepared in acetone (4) AuSn particles prepared in acetone

Table III. XPS of AuSn Particles Prepared in Acetone; Binding Energies in eV

	Sample 1 ^a	Sample 1 (etched)	Sample 2 ^b	Sample 2 (etched)	Au foil	Sn foil
Au 4f	88.00	87.70	88.05	87.90	88.25	-
	84.30	84.00	84.25	84.00	84.35	-
Au 4d	353.45	353.30	353.45	353.30	353.55	-
	335.50	335.30	335.55	335.60	335.40	-
Sn 3p	715.50	715.10	715.45	715.10	-	714.10
	757.40	756.90	757.25	757.00	-	756.00
Sn ⁿ⁺	494.65	494.60	494.45	494.50	-	-
	486.20	486.10	486.05	486.10	-	-
Tab. III con't	493.40	493.10	493.20	493.25	-	492.85
	484.90	484.65	484.90	484.85	-	484.45

(a) Au-Sn/acetone, vaporized from separate crucibles.

(b) Au-Sn/acetone, vaporized from the same crucible.

Table IV. XPS of AuSn Particles Prepared in Acetone;
Spin Orbit Splittings

	$\Delta\text{Sn } 3p$	$\Delta\text{Sn } 3d$		$\Delta\text{Au } 4f$	$\Delta\text{Au } 4d$	ΔVB
		Sn^{n+}	Sn^0			
Sample 1	41.90	8.45	8.50	3.70	17.95	1.45
Sample 1 (etched)	41.80	8.50	8.45	3.70	18.00	2.00
Sample 2	41.80	8.40	8.40	3.80	17.90	1.15
Sample 2 (etched)	41.90	8.40	8.40	3.90	17.90	1.45
Au foil	-	-	-	3.90	18.15	2.60
Sn foil	41.90	-	8.40	-	-	-

Table V. XPS of AuSn Particles Prepared in Acetone;
Peak Area Ratios

	$\text{Sn}3d/$	$\text{Sn}3d/$	$\text{Au}4f/$	$\text{Au}4d/$	$\text{Au}4d/$	$\text{Au}4f/$
	Ols	Cls	Sn3d	Sn3d	Sn3p	Sn3p
Sample 1	0.87	0.90	0.24	0.22	0.024	0.03
Sample 1 (etched)	1.52	1.23	0.63	0.47	0.078	0.11
Sample 2	1.26	2.12	0.19	0.15	0.022	0.03
Sample 2 (etched)	2.39	4.05	0.25	0.21	0.038	0.05

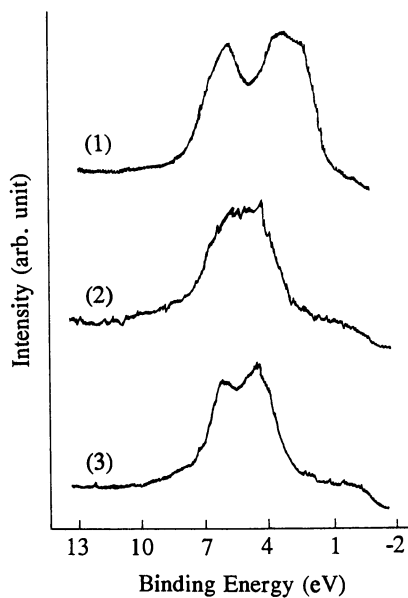


Figure 11. Gold XPS Valence Band Spectra of (1) Bulk gold; (2) AuSn particles prepared in acetone; (3) after Ar ion etching.

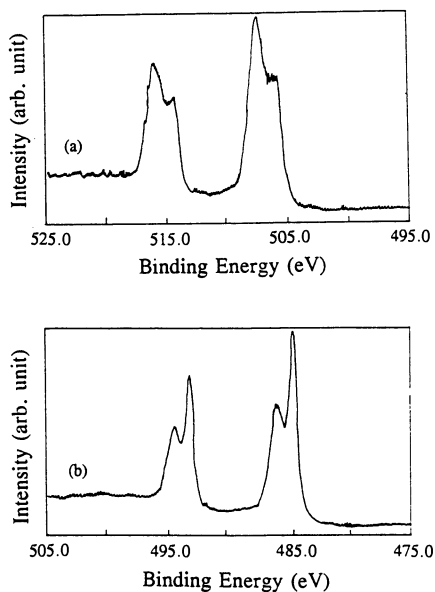


Figure 12. Tin XPS (3d) Spectra of (a) AuSn particles prepared in acetone; (b) after Ar ion sputtering.

Valence band spectra for Au 5d (Figure 11) show a slight shift to higher energy compared with bulk gold, and decrease in spin-orbit splitting. These features are characteristic of crystalline AuSn alloys.

Interestingly, XPS results for these ultra-fine particles are somewhat different from bulk samples. As discussed earlier, for bulk AuSn *vs.* Sn⁰ core electron shifts for Sn 3d were smaller than we found for these fine particles of AuSn. However, it is perhaps not appropriate to speculate about these differences without further, more careful studies.

Acknowledgments

The support of the National Science Foundation is acknowledged with gratitude. We thank Dr. B.J. Tan and Dr. Steve Suib for obtaining XPS data.

Literature Cited

1. Haensel, V.; Burwell, R.; *Sci. Am.*, **1971**, *225*, 46.
2. Anderson, J. R. "*Structure of Metallic Catalysts*", Academic Press, New York, 1975.
3. Srivastava, R. D. "*Heterogeneous Catalytic Science*", CRC Press, Boca Raton, Florida, 1988.
4. Klabunde, K. J.; Jeong, G. H.; Olsen, A. W. In *Molecular Structures and Energetics: Selective Hydrocarbon Activation*; Davies, J. A.; Watson, P. L.; Liebman, J. F.; Greenberg, A., Eds.; VCH: New York, 1990, pp. 433-463.
5. Geusic, M. E.; Morse, M. D.; O'Brien, S. C.; Smalley, R. E. *Rev. Sci. Inst.* **1985**, *56*, 2123.
6. Cox, D. M.; Trevor, D. J.; Whetten, R. L.; Kaldor, A. J. *J. Phys. Chem.* **1988**, *92*, 421. Ruatta, S. A.; Anderson, S. L. *J. Chem. Phys.* **1988**, *89*, 273.
7. Richtsmeier, S. C.; Parks, E. K.; Lin, K.; Pobo, L. G.; Riley, S. J. *J. Chem. Phys.* **1985**, *82*, 3659.
8. Parks, E. K.; Nieman, G. C.; Pobo, L. G.; Riley, S. J. *J. Chem. Phys.* **1988**, *88*, 6260.
9. Parks, E. K.; Weiller, B. H.; Bechthold, P. S.; Hoffman, W. F.; Nieman, G. C.; Pobo, L. G.; Riley, S. J. *J. Chem. Phys.* **1988**, *88*, 1622.
10. Morse, M. D.; Geusic, M. E.; Heath, J. R.; Smalley, R. E. *J. Chem. Phys.* **1985**, *83*, 2293.
11. Whetten, R. L.; Cox, D. M.; Trevor, D. J.; Kaldor, A. J. *J. Phys. Chem.* **1985**, *89*, 566.
12. Trevor, D. J.; Whetten, R. L.; Cox, D. M.; Kaldor, A. J. *Am. Chem. Soc.* **1985**, *107*, 518.
13. Christmann, K.; Ertl, G.; Pignet, T. *Surf. Sci.* **1976**, *54*, 365. Also see Anderson, A. B.; Maloney, J. J. *J. Phys. Chem.* **1988**, *92*, 809.
14. St. Pierre, R. J.; El-Sayed, M. A. *J. Phys. Chem.* **1987**, *91*, 763.
15. St. Pierre, R. J.; Chronister, E. L.; El-Sayed, M. A. *J. Phys. Chem.* **1987**, *91*, 5228.

16. St. Pierre, R. J.; Chronister, E. L.; Li, S.; El-Sayed, M. A. *J. Phys. Chem.* **1987**, *91*, 4648.
17. Geusic, M. E.; Morse, M. D.; Smalley, R. E. *J. Chem. Phys.* **1985**, *82*, 590.
18. Alford, J. M.; Weiss, F. D.; Laaksonen, R. T.; Smalley, R. E. *J. Phys. Chem.* **1986**, *90*, 4480.
19. Brucat, P.J.; Piettiette, C.L.; Yang, S.; Zheng, L.S.; Craycraft, M.J. Smalley, R. E. *J. Chem. Phys.* **1986**, *85*, 4747.
20. Morse, M. D. *Chem. Rev.* **1986**, *86*, 1049.
21. Bier, K. D.; Haslett, T. L.; Kirkwood, A. D.; Moskovits, M. *J. Chem. Phys.* **1988**, *89*, 6.
22. Moskovits, M.; Ozin, G. A.; Eds. "*Cryochemistry*". Wiley Interscience, New York, 1976.
23. Moskovits, M.; Ed, "*Metal Clusters*", Wiley: New York, 1986.
24. Klotzbucher, W. E.; Ozin, G. A. *Inorg. Chem.* **1980**, *19*, 3767.
25. Klabunde, K. J.; Efner, H. F.; Satek, L.; Donley, W. J. *Organomet. Chem.* **1974**, *71*, 309.
26. Murdock, T. O.; Klabunde, K. J. *J. Org. Chem.* **1976**, *41*, 1076. Murdock, T.O.; Klabunde, K. J.; *Inorg. Syn.* **1979**, *19*, 70. Klabunde, K. J.; Murdock, T. O.; *J. Org. Chem.* **1979**, *44*, 3901.
27. Klabunde, K. J.; *Accts. Chem. Res.* **1975**, *8*, 393.
28. Klabunde, K. J.; Efner, H. F.; Murdock, T.; Roppel, R. *J. Am. Chem. Soc.* **1976**, *98*, 1021.
29. Davis, S. C.; Severson, S.; Klabunde, K. J. *J. Am. Chem. Soc.* **1981**, *103*, 3024.
30. Imamura, H.; Nobunaga, T.; Kawahigashi, M.; Tsuchiya, S. *Inorg. Chem.* **1984**, *23*, 2509.
31. Kernizan, C. F.; Klabunde, K. J.; Sorensen, C. M.; Hadjapanayis, G. C. *Chem. Materials*, **1990**, *2*, 70.
32. Lin, S. J.; Franklin, M. J.; Klabunde, K. J.; *Langmuir*, **1986**, *2*, 259.
33. Cardenas-Trivino, G.; Klabunde, K. J.; Dale, B.; *Langmuir*, **1987**, *3*, 986.
34. Franklin, M. T.; Klabunde, K. J.; "*High Energy Processes in Organometallic Chemistry*," *ACS Sym. Series 333*, Suslick, K. S., editor; **1986**, pg. 246.
35. Sinfelt, J. H. U.S. Patent 3,953,368. 1976.
36. Davis, B. H. *J. Catal.* **1976**, *42*, 376.
37. Roberti, A.; Ponec, V.; Sachtler, W. M. H. *J. Catal.* **1973**, *28*, 381.
38. Bacaud, R.; Bussiere, R.; Figueras, F. *J. Catal.* **1981**, *69*, 399.
39. Sinfelt, J. A. *AICHE J.* **1973**, *19*, 678.
40. Li, Y.X.; Klabunde, K.J.; *J. Catal.* **1990**, *126*, 173.
41. Li, Y. X.; Klabunde, K. J.; *Langmuir*, **1987**, *3*, 558.
42. Li, Y. X.; Zhang, Y. F.; Klabunde, K. J.; *Langmuir*, **1988**, *4*, 385.
43. Li, Y. X.; Chiu, N. S.; Lee, W. H.; Bauer, S. H.; Davis, B. H. *ACS Symp. Ser.* **1989**, *411*, 328.
44. The concept that Pt-Sn alloy particles are important in determining activity

- and selectivity of supported Pt-Sn catalysts has been presented by earlier workers: (a) Biloen, P.; Helle, J. N.; Verbeek, H.; Dautzenberg, F. M.; Sachtler, W. M. H. *J. Catal.* **1980**, *63*, 63. (b) Verbeek, H.; Sachtler, W. M. H. *J. Catal.* **1976**, *42*, 257. (c) Dautzenberg, F. M.; Helle, J. N.; Biloen, P.; Sachtler, W. M. H.; *J. Catal.* **1980**, *63*, 119.
45. Li, Y. X.; Klabunde, K. J.; Davis, B. H.; *J. Catal.*, **1991**, *128*, 1.
 46. Davis, B. H.; see accompanying paper in this volume.
 47. Klabunde, K. J.; Li, Y. X.; Tan, B. J. *Chem. Materials*, **1991**, *3*, 30.
 48. Nakamura, N.; Suzuki, K.; Kobayashi, T. *Jpn. Kokai Tokyo Koho*, JP62,275,337,[87,275,337](C1, G11B7/24)
 49. Chang, C.; Callcott, T. A.; Arkawa, E. T. *J. Appl. Phys.* **1982**, *53*, 7362.
 50. Neel, S. Arkawa, E. T., Inagaki, T. *J. Appl. Phys.* **1984**, *55*, 4132.
 51. Chekin, V. V. *Soviet Physics Jet P*, **1968**, *27*, 983.
 52. Chou, T. S.; Perlman, M. L.; Watson, R. E. *Phys. Rev. B*, **1976**, *14*, 3248.
 53. Castelijns, J. H. P.; de Vroomen, A. R. *Solid State Comm.* **1978**, *25*, 461.
 54. Friedman, R. M.; Hudis, J.; Perlman, M. L.; Watson, R. E. *Phys. Rev. B*, **1973**, *8*, 2433.
 55. Th M van Atteknm, P. M.; Trooster, J. M. *J. Phys. F.* **1979**, *9*, 2287.
 56. Buene, L.; Falkenberg-Arell, H. and Tafto, J. *Thin Solid Films* **1980**, *67*, 95.
 57. Simic, V.; Marinkovic, Z. *J. Less Common Metals*, **1983**, *95*, 259.
 58. Tanaka, I.; Nasu, S.; Fujita, F.E. *Nippon Kinzoku Gakkaishi*, **1986**, *50*, 523.
 59. Kingcade, Jr., J. E.; Gingerich, K. A. *J. Chem. Phys.* **1986**, *84*, 3432.
 60. a. Klabunde, K. J.; Tanaka, Y. *J. Mol. Catal.* **1983**, *21*, 57.
b. Klabunde, K. J.; Imizu, Y. *J. Am. Chem. Soc.* **1984**, *106*, 2721.
c. Tan, B. J.; Klabunde, K. J.; Tanaka, T.; Kanai, H.; Yoshida, S. *J. Am. Chem. Soc.* **1988**, *110*, 5951.
 61. Tan, B. J.; Klabunde, K. J.; Sherwood, P. M. A. *Chem. Mater.*, **1990**, *2*, 186.
 62. Li, Y.; Chiu, N. S.; Lee, W. H.; Bauer, S. H.; Davis, B. H.; *ACS Symp. Ser.* **1988**, *411*, 328.
 63. Glavee, G. N.; Klabunde, K. J.; Sorensen, C. M.; Hadjapanayis, G. C.; *Chem. Materials*, in press.
 64. It is experimentally difficult to heat two metal evaporation sources (crucibles) simultaneously so that both metals evaporate at the desired rate. It is much easier to load both metals into one crucible and just evaporate all the metal.
 65. Davis, S. C.; Klabunde, K. J. *J. Am. Chem. Soc.* **1978**, *100*, 5973.

RECEIVED July 16, 1992

Chapter 11

Mechanism and Selectivity in Catalytic Olefin Polymerization

A. R. Siedle, W. M. Lamanna, J. M. Olofson, B. A. Nerad, and
R. A. Newmark

3M Corporate Research Laboratories, 201-2E-02 3M Center,
St. Paul, MN 55144

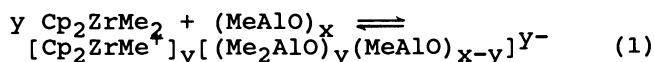
We describe a mechanistic and kinetic study of polymerization of ethylene and 1-hexene by the homogeneous catalyst $\text{Cp}_2\text{ZrCl}_2-(\text{MeAlO})_x$ -toluene.

Introduction Homogeneous catalysis of olefin polymerization is a research area having very significant technological potential. Achieving a fundamental understanding of this science necessitates addressing issues that lie at the very core of organometallic and physical chemistry. In this contribution, we describe the results of a mechanistic study of an exemplary catalyst system. It will be seen that there exist multiple, competing reaction pathways. The outcome of this competition translates into selectivity and it is reflected in the structure and physical properties of the product polymers.

The Catalyst System Eleven years ago, Kaminsky invented a novel olefin polymerization catalyst derived from Cp_2ZrCl_2 ($\text{Cp} \equiv \eta^5\text{-C}_5\text{H}_5$) and methylaluminumoxane (1), a result that has stimulated intense interest in synthesis and reactions of metallocenium ions. Important questions still remain, however, regarding the nature of the Kaminsky catalyst. These include (1) what is methylaluminumoxane and how does it interact with Cp_2ZrMe_2 to initiate polymerization; and (2) what are the mechanisms of chain initiation, propagation, transfer and termination? A collateral question is how these steps may be controlled.

Methylaluminumoxane is produced by the controlled hydrolysis of trimethylaluminum. GPC data

indicate that it is a mixture of oligomers. (2) The ^{27}Al NMR spectrum of $(\text{MeAlO})_x$ in toluene at 25°C comprises a broad resonance centered at 154 ppm (relative to external $\text{Al}(\text{H}_2\text{O})_6^{3+}$). This is assigned to four-coordinate Al arising from Al-O-Al or Al-CH₃-Al bridge bonding. At 90°C , an additional, broad resonance at 100 ppm appears reversibly. We attribute this to three-coordinate Al. Although aluminum with lower coordination number would be expected to resonate at lower field, the chemical shift matches that of the model compound $\text{MeAl}(2,6\text{-di-}t\text{-butyl-4-methylphenoxy})_2$ in which aluminum is constrained to be three-coordinate by the bulky aryloxy ligands. (3) ^{27}Al has $I = 5/2$ and so the spin lattice relaxation time varies inversely with temperature. Only at elevated temperature is this resonance distinguishable from the base line. The presence of three-coordinate Al in $(\text{MeAlO})_x$ is to be expected for two reasons. First, there seems to be no logical way to arrange that all aluminum atoms be coordinatively saturated in an oligomer in which $x > 4$. Second, $(\text{MeAlO})_x$ rapidly exchanges methyl groups with $\text{Cp}_2\text{Zr}(\text{}^{13}\text{CH}_3)_2$, a reaction which appears to require aluminum having $\text{CN} < 4$. (4) This exchange reaction, which will be seen to represent an important chain transfer process, is believed to occur via an ionic mechanism, Eq 1.



Precedent for intermediacy of an ionic species comes from the seminal work of Marks who observed Zr- $\underline{\text{C}}\text{H}_3$ - B- $\underline{\text{C}}\text{H}_3$ exchange in $[\text{Cp}_2\text{ZrMe}][\text{MeB}(\text{C}_6\text{F}_5)_3]$. (5)

When Cp_2ZrMe_2 was combined with ≤ 10 equivalents of $(\text{MeAlO})_x$ in toluene, an orange oil separated that contained all the Zr in the system and that was capable of catalyzing ethylene polymerization. The ^{91}Zr NMR spectrum of this material in dichloromethane exhibited two resonances at +100 and -100 ppm relative to external Cp_2ZrBr_2 in THF. The former is attributed to Cp_2ZrMe^+ and the chemical shift agrees well with 115 ppm for $[\text{Cp}_2\text{Zr}(\text{Me})\text{THF}][\text{BPh}_4]$. (6) The ^{13}C NMR spectrum shows a CH_3 resonance at 39.3 ppm which is close to the 40.9 ppm observed in $[\text{Cp}_2\text{ZrMe}][\text{MeB}(\text{C}_6\text{F}_5)_3]$. (5) Taken together, ^{13}C and ^{91}Zr NMR provide strong evidence for the presence of Cp_2ZrMe^+ in the Kaminsky catalyst system. We believe that this metallocenium ion is solvated, possibly by coordination to the weakly basic oxygen atoms in $(\text{MeAlO})_x$ or by Zr-CH₃-Al interactions

which can be classical or agostic. The higher field ^{91}Zr resonance occurs in a region characteristic of $\text{Cp}_2\text{ZrMe}(\text{OR})$ compounds. We suggest that it arises from a $\text{Cp}_2\text{Zr}(\text{Me})(\text{OAl}=\text{O})$ species derived by cleavage of Al-O bonds in methylaluminoxane.

Ethylene Polymerization Many important clues to the mechanism of ethylene polymerization can be obtained from analysis of the organic products. In a typical experiment, ethylene at an initial pressure of 250 mm was polymerized in a closed reactor so that the amount of monomer was limited. The catalyst was prepared from Cp_2ZrCl_2 and a commercial (Ethyl Corp.) toluene solution 0.9M each in both Me_3Al and $(\text{MeAlO})_x$ so that $[\text{Zr}] = 0.04\text{M}$, $[\text{Al}] = 0.72$, $[\text{Al}]/[\text{Zr}] = 18$ and $[\text{Me-Al}]/[\text{Zr}] = 36$. By restricting the amount of monomer used, ethylene oligomers rather than high polymers were obtained so that, following quenching with methanol, the products could be analyzed by GC/MS. Such analysis reveals several significant facts about the organic products:

(1) Odd-numbered hydrocarbons predominate with $C_{\text{odd}}/C_{\text{even}} = 2.6$.

(2) The C_{odd} hydrocarbons are predominantly linear alkanes.

(3) The C_{even} hydrocarbons are predominantly mono-unsaturated alkenes.

(4) When the reaction was quenched with CH_3OD , about 60% of both C_{odd} and C_{even} hydrocarbons were monodeuterated, the remainders being non-deuterated.

Structurally, the alkenes formed are quite varied. $^{13}\text{C}_2\text{H}_4$ at 100 mm pressure was similarly polymerized. Analysis of the products by 1- and 2-D ^{13}C NMR spectroscopy indicated that hydrocarbons of the types $\text{CH}_2=\text{CH}-\text{R}^1$, $\text{CH}_2=\text{C}(^{12}\text{CH}_3)\text{R}^2$ and $\text{CH}_2=\text{CR}^3\text{R}^4$ were present. R^{1-4} are alkyl groups indistinguishable, and undefined in length, by NMR. The unlabeled $^{12}\text{CH}_3$ group arises from the metallocenium initiator (vide infra).

We account for these observations by the reaction scheme shown in Figure 1. In it, polymerization begins by coordination of ethylene to (putatively solvated) Cp_2ZrMe^+ ; the number of ethylene molecules that bind is not established. Sequential coordination then insertion of ethylene into the Zr- CH_3 metal-carbon sigma bond leads to a growing alkyl chain on zirconium. These groups undergo rapid chain transfer to aluminum in an alkyl-methyl exchange process 4 that is favored

because of the high $[\text{Me-Al}]/[\text{Zr}]$ ratio; Cp_2ZrMe^+ is concomitantly regenerated. Quenching with CH_3OD generates the observed monodeuterated C_{odd} alkanes. Alternatively, the Zr-oligomer bond can be cleaved by ethylene in a sigma bond metathesis reaction thus generating the observed non-deuterated C_{odd} alkanes along with a new vinyl metallocenium initiator, $\text{Cp}_2\text{ZrCH}=\text{CH}_2^+$. This species too can coordinate and insert ethylene to give a growing alkenyl chain. Transfer of this chain to aluminum by transalkylation followed by quenching with CH_3OD gives the observed C_{even} monodeuterated alkenes. Alternatively, its cleavage by sigma bond metathesis leads to non-deuterated C_{even} alkenes. According to Figure 1, alkanes derived from ethylene originate from $\text{Cp}_2\text{ZrCH}_3^+$ and thus must have an odd number of carbon atoms. Alkenes derived from ethylene originate with $\text{Cp}_2\text{ZrCH}=\text{CH}_2^+$ and have an even number of carbon atoms. Unless the ethylene concentration drops to such a low value that the substituted alpha-olefin products compete with ethylene, beta hydrogen elimination from Cp_2ZrR^+ (where R here is an unbranched alkyl chain) is not an important pathway to oligomers and polymers.

The structural types of alkenes that are observed are explicable in terms of Figure 1 if it is recalled that, because the initial amount of ethylene in the test system is fixed, the concentration of product olefins rises as that of ethylene falls. A point is reached where product olefins compete with ethylene in insertion reactions. These product olefins bear alkyl substituents which tend to favor beta hydrogen elimination. (7) Thus, the $\text{CH}_2=\text{C}(\text{CH}_3)\text{R}^2$ compounds can arise from addition of $\text{Cp}_2\text{ZrCH}_3^+$ or Cp_2ZrR^+ to such olefins followed by beta hydrogen elimination. The internal olefins, $\text{CH}_3-\text{CH}=\text{CH}-\text{R}^1$ cannot be accommodated by the scheme of Figure 1. We adopt the proposal by Turner and Hlatky (8) that they arise from ethylene insertion into $\text{Cp}_2\text{ZrCH}=\text{CH}_2^+$ to give $\text{Cp}_2\text{ZrCH}_2\text{CH}_2\text{CH}=\text{CH}_2^+$ which rapidly rearranges to $\text{Cp}_2\text{ZrCH}_2\text{CH}=\text{CHCH}_3^+$. Subsequent ethylene insertion into this 2-butenylmetallocene would then produce 2-olefins by the chemistry in Figure 1.

Hexene Polymerization Polymerization of 1-hexene (and also propylene) by the Kaminsky catalyst $[(\text{Cp}_2\text{ZrCl}_2/(\text{MeAlO})_x/\text{toluene})_x]$ differs fundamentally from that of ethylene in that beta hydrogen elimination is the only detectable chain transfer mechanism. Insertion of 1-hexene into the Zr-C bond in $\text{Cp}_2\text{ZrCH}_3^+$ produces $\text{Cp}_2\text{ZrCH}_2\text{CH}(\text{CH}_3)\text{C}_4\text{H}_9^+$. The electron donating

alkyl group promotes beta hydrogen elimination and this leads to 2-methyl-1-hexene (observed) and the metallocenium hydride Cp_2ZrH^+ . This hydride species can coordinate and insert olefin into the Zr-H bond. Repetition of this process followed by beta hydrogen elimination yields 2-butyl-1-octene as the hexene dimer along with higher, vinylidene-terminated oligomers.

We find that sigma bond metathesis is not an important chain transfer process in the polymerization of hexene by the Kaminsky catalyst. Were it to occur, $\text{Cp}_2\text{ZrCH}_2\text{CH}(\text{R})\text{CH}_2\text{CH}_2\text{R}$ ($\text{R} = n\text{-C}_4\text{H}_9$) would be converted to $\text{Cp}_2\text{ZrCH}=\text{CHR}^+$ and $\text{CH}_3\text{-CH}(\text{R})\text{CH}_2\text{CH}_2\text{R}$. The latter compounds contain branch methyl groups. Careful examination of the 19-20 ppm region of the high gain ^{13}C NMR spectrum of the organic products fails to disclose a signal due to such methyl groups; this also indicates that alkyl ligand exchange is likewise not an important chain transfer process.

The ^1H NMR spectrum of polyhexene of M_w 20,000 that was prepared using $[(\text{Me}_3\text{SiCp})_2\text{ZrMe}][\text{MeB}(\text{C}_6\text{F}_5)_3]$ as the catalyst shows a resonance at 4.7 ppm due to vinylidene $=\text{CH}_2$ end groups. However, another peak at 5.36 ppm is also present and it is assigned to a different type of unsaturated end group, a 1,2-disubstituted olefin. The origin of these two end group types is shown in Figure 2. The 1,1-disubstituted olefin groups arise from sequential [1,2] insertion of hexene with beta hydrogen elimination as the chain transfer step. Chains with internal unsaturation are thought to arise from occasional [2,1] insertion or "mis-insertion". Steric crowding results from mis-insertion because a bulky butyl group is on the alpha carbon next to zirconium. We suggest that this crowding disfavors continued chain propagation and instead favors chain transfer via beta hydrogen elimination that leads to the observed internal olefinic end groups. In high molecular weight polyhexene prepared with metallocenium catalysts, this process accounts for up to half of the chain ends. In the Kaminsky catalyst system, we find that the relative number of end groups derived from [2,1] insertion increases with increasing initial concentration of hexene. $\text{CHR}=\text{CHR}$ groups account for 3, 17 and 18% of the total end groups at $[\text{hexene}]_{\text{initial}}$ 1.6, 3.2 and 7.9M respectively.

Kinetics of Hexene Polymerization We have measured the kinetics of 1-hexene polymerization by the Kaminsky catalyst by following monomer consumption with time.

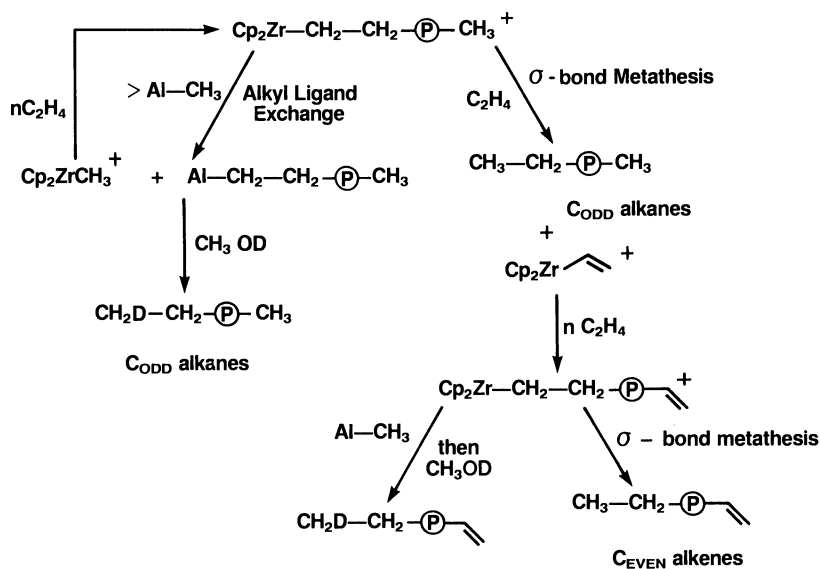
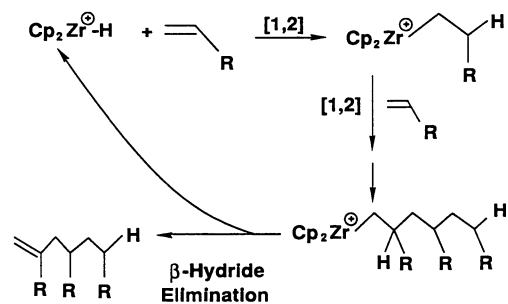


Figure 1. Scheme showing steps in ethylene polymerization by Kaminsky catalyst

$\text{Cp}_2\text{ZrCl}_2/\text{MAO}$ Catalyzed 1-Hexene Polymerization

Mechanism:



Formation of Internal double bonds:

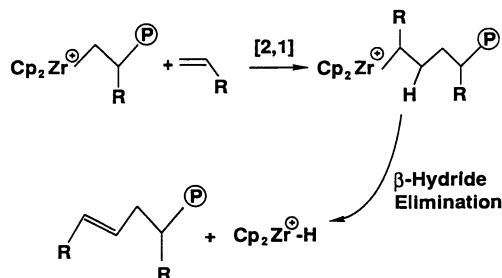


Figure 2. Origin of two types of unsaturated end groups in polyhexene

Hexene is well suited to such a study because it is a liquid at room temperature and can be readily quantitated without use of complex gas handling equipment. Further, propagation is sufficiently slow that rates can be measured in real time and the temperature rise due to exothermic polymerization reaction is easily controlled. Finally, the oligomer and polymer products remain soluble in the homogeneous reaction medium. Initial experiments at high (3.6M) hexene concentrations appeared, deceptively, to indicate simple second order (in monomer) kinetics. Significant deviations from a second order rate law became manifest at [hexene] <1.2M yet the order in [hexene] never reached 1.0. This is in contradiction to the commonly held belief that propagation proceeds through a 14 electron Zr-alkyl cation by equilibrium complexation of one molecule of monomer followed by intramolecular insertion into the Zr-alkyl bond, according to which, one predicts a reaction order in monomer no greater than one.

By following the initial rate of hexene consumption as a function of initial hexene concentration, we have sought to develop a mechanistic understanding of the propagation steps in hexene polymerization. The reaction mechanism most consistent with the initial rate data contains six elementary steps as shown in Figure 3. Zr refers to Cp_2Zr^+ ; R' is hexyl and R is an alkyl group derived from higher hexene oligomers corresponding to a degree of oligomerization >2. O denotes olefin (i.e 1-hexene) and P polymer.

Significant features of this mechanistic model are:

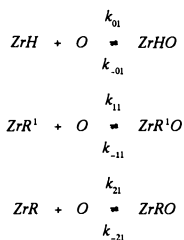
(1) Three distinct propagating species, each having different equilibrium olefin binding constants and insertion rate constants, are present. They are $\text{Cp}_2\text{ZrH(olefin)}^+$, $\text{Cp}_2\text{ZrR'(olefin)}^+$ and $\text{Cp}_2\text{ZrR(olefin)}^+$.

(2) Beta hydrogen elimination is the sole chain transfer pathway and the source of the propagating species Cp_2ZrH^+ .

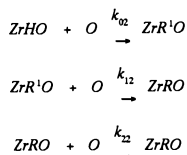
(3) All beta hydrogen elimination occurs from the 14-electron species Cp_2ZrR^+ where, by definition, R is branched. In contrast, beta hydrogen elimination from $\text{Cp}_2\text{ZrR}'^+$ is slow (because the alkyl group, n-hexyl, is linear) and the rate of this reaction is taken to be zero.

(4) In order to fit the data, it is not necessary to assume that beta hydrogen elimination from the monolefin complexes $\text{Cp}_2\text{ZrR'O}^+$ or Cp_2ZrRO^+ occurs. The model therefore ignores these reactions.

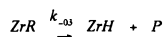
Equilibrium Complexation:



Insertion:



Elimination:



Rate Law:

$$-\frac{d[\text{O}]}{dt} = \frac{2[\text{O}]^2 + A[\text{O}]^3 + B[\text{O}]^4}{C + D[\text{O}] + E[\text{O}]^2 + F[\text{O}]^3}$$

Reaction Conditions:

Temperature = 0°C

[Zr] = 1.64 · 10⁻⁴ M

Me₃Al / MAO = 1.0 (supplied by Ethyl Corp.)

[Al] = 1.64 · 10⁻¹ M

Parameter	Expression
A (1/M)	$\frac{k_{22}}{k_{-21}}$
B (1/M ²)	$\frac{k_{-21} k_{22}}{k_{-03} k_{-21}}$
C (M min)	$\frac{k_{-01}}{k_{01} k_{02} [\text{Zr}]} + \frac{k_{-11}}{k_{11} k_{12} [\text{Zr}]}$
D (min)	$\frac{1}{k_{01} [\text{ZrR}]} + \frac{1}{k_{02} [\text{Zr}]} + \frac{1}{k_{12} [\text{Zr}]}$
E (min/M)	$\frac{1}{k_{-03} [\text{Zr}]} + \frac{1}{k_{-21} [\text{Zr}]}$
F (min/M ²)	$\frac{k_{21}}{k_{-03} k_{-21} [\text{Zr}]}$

Figure 3. Elementary steps in polyhexene polymerization with rate constant expressions

(5) Insertion of olefin proceeds in a concerted, bimolecular reaction between a second molecule of olefin and any of the monoolefin species Cp_2ZrHO^+ , $\text{Cp}_2\text{ZrR}'\text{O}^+$ and Cp_2ZrRO^+ . This provides a second order component to the propagation kinetics and, at the same time, accommodates possible agostic interactions between Zr and an alpha C-H group in the growing alkyl chains. (9,10) An alternative model involving intramolecular insertion in a bis(olefin) complex cannot be rigorously distinguished. It is disfavored on the ground that complexation of a second molecule of olefin should produce a much higher energy structure because of repulsive steric interactions.

(6) In order to fit the initial rate data, it is not required that the bound olefin in Cp_2ZrHO^+ , $\text{Cp}_2\text{R}'\text{O}^+$ or Cp_2RO^+ also inserts directly, in an intramolecular fashion. A reaction mechanism based solely on intramolecular insertion of this bound olefin, without assuming the existence of either a bis(olefin) intermediate or the concerted, bimolecular insertion reaction of a monoolefin species with a second equivalent of monomer does not fit the data.

The rate law derived from this model is

$$-d[\text{O}]/dt = \frac{2[\text{O}]^2 + A[\text{O}]^3 + B[\text{O}]^4/C + D[\text{O}] + E[\text{O}]^2}{+ F[\text{O}]^3}$$

The parameters A-F, which each contain several rate constants, are defined in Figure 3. Figure 4 shows a graphical fit of the data to a plot of the experimental normalized rates [i.e. initial rate/initial hexene concentration] versus initial 1-hexene concentration. The agreement is gratifyingly good for so complex a chemical system and this lends credence to our model.

Substituent Effects So reactive are the coordinatively unsaturated metallocenium cations that one would expect that introduction of substituents into the cyclopentadienyl rings would modulate catalytic activity. (11) If substituent effects could be understood, it should be possible to modify the catalyst system to produce polymers having predetermined properties. We suspect that the needed detailed understanding will be hard to achieve for two reasons. First, the polymerization involves a multi-step mechanism and substituents may affect different steps differently. Second, steric and electronic effects of substituents may act in concert or in opposition and they must therefore be disentangled. Table 1 shows the effect of structural changes

in the zirconocene dichloride component of the Kaminsky catalyst on relative rates of reaction (measured, relative to Cp_2ZrCl_2 , during the early stages of the reaction), on the relative molecular weight of the final polymer; and on the prevalence of "mis-insertion" of monomer (i.e. [2,1] rather than [1,2] insertion). Introduction of one or two bulky trimethylsilyl groups accelerates the polymerization and leads to a modest increase in molecular weight; four Me_3Si groups lead to deceleration. The 1,2-bis(indenyl)ethylene ligand (12) appears to increase reaction rate, molecular weight and tendency for monomer [2,1] insertion.

In an effort to obtain more quantitative data, we have examined the variable temperature ^1H and ^{13}C NMR spectra of metallocenium salts of the type $[(\text{RCp})_2\text{ZrMe}][\text{MeB}(\text{C}_6\text{F}_5)_3]$ in toluene. Two processes are observed. The first, occurring at lower temperature, leads to exchange of diastereotopic CH units in the cyclopentadienyl rings. We suggest that this results from cleavage of the weakest bond in the system, the agostic $\text{Zr}\dots\text{H}-\text{CH}_2$ bond linking the $(\text{RCp})_2\text{ZrMe}^+$ cation with the $\text{MeB}(\text{C}_6\text{F}_5)_3^-$ anion, that is, the components of the ion pair move further apart. In this more separated ion pair, rapid intramolecular migration of the $\text{Zr}-\text{CH}_3$ group can lead to a shift from one lateral position on Zr to the other, thereby adding a mirror plane of symmetry to the cation. This fluxional process in $(\text{RCp})_2\text{ZrMe}^+$ leaves the relative positions (and line-widths) of the $\text{Zr}-\text{CH}_3$ and $\text{B}-\text{CH}_3$ groups unaffected. The second process, which has a slightly higher activation energy, is associated with interconversion of these two types of methyl groups and concomitant exchange broadening. We surmise that this process involves cleavage of the next weakest bond, that between Me and $\text{B}(\text{C}_6\text{F}_5)_3$ in $\text{MeB}(\text{C}_6\text{F}_5)_3^-$; and equilibrium transfer of CH_3^- from the anion to the cation to form $(\text{RCp})_2\text{ZrMe}_2$ and $\text{B}(\text{C}_6\text{F}_5)_3$, the neutral precursors of $[(\text{RCp})_2\text{ZrMe}][\text{MeB}(\text{C}_6\text{F}_5)_3]$. In the reverse reaction, either of two equivalent methyl groups may be abstracted by $(\text{C}_6\text{F}_5)_3\text{B}$. Some free energies of activation for the lower energy process are given in Table 2; entropies of activation are experimentally negligible. Onset of the higher energy, dissociative process occurs at temperatures near those at which the compounds begin to decompose and so, in two cases, only lower limits are given. Interestingly, ΔG^\ddagger for the methyl shift process in $(\text{RCp})_2\text{ZrMe}^+$ scales approximately with the steric bulk of the substituent R, increasing in the order $\text{R} = \text{Me}_3\text{SiCH}_2 > \text{Me}_3\text{Ge} > \text{Me}_3\text{Si} > \text{t-Bu}$, a trend

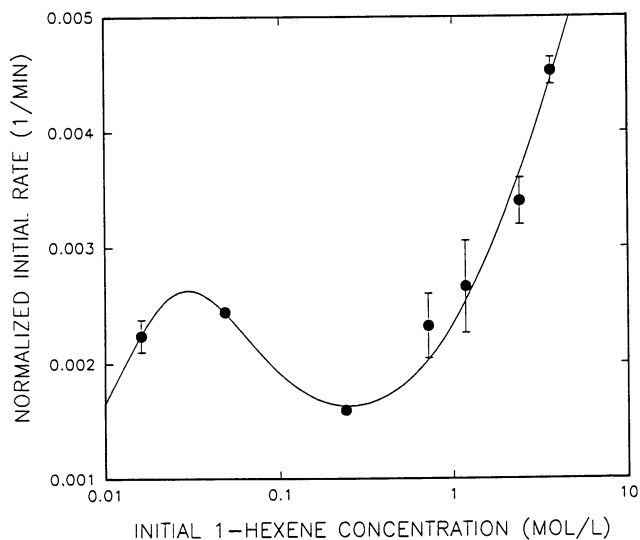


Figure 4. Plot of normalized initial rate of hexene polymerization versus initial hexene concentration.

Table 1. Effect of Variation in Organometallic Component of Kaminsky Catalyst on Relative Rate of Polymerization, Molecular Weight and Ratio of [1,2] to [2,1] Insertion

Organometallic	Rel. Rate	Rel. M.W.	[1,2]/[2,1] Insertion
$(C_5H_5)_2ZrCl_2$	1.0	1.0	1.0
$(C_9H_7)_2ZrCl_2$	0.9	6.2	4.0
$[1,2-(C_9H_6)_2C_2H_4]ZrCl_2$	7.1	9.5	7.7
$(Me_3SiC_5H_4)_2ZrCl_2$	3.2	1.8	1.5
$[1,3-(Me_3Si)_2C_5H_3]_2ZrCl_2$	0.3	1.5	14.5
$(C_5H_5)(Me_3SiC_5H_4)ZrCl_2$	3.2	1.2	0.9

Table 2. Free Energies of Activation in kcal mole⁻¹ for Methyl Shift (Lower Temperature Process) and Methyl Transfer (Higher Temperature Process) in Some Metallo-cenium Ions

Cation ^a	ΔG^\ddagger , Me Shift	ΔG^\ddagger , Me Transfer (°C)
$(Me_3SiC_5H_4)_2ZrMe^+$	15.1±0.1	>18.5 (63)
$(Me_3SiC_5H_4)_2HfMe^+$	15.4	16.4±0.1 (53)
$(t-C_4H_9C_5H_4)_2ZrMe^+$	12.3	>17.5 (23)
$(Me_3GeC_5H_4)_2ZrMe^+$	15.7	18.6±0.2 (73)
$(Me_3SiCH_2C_5H_4)_2ZrMe^+$	16.6	17.7±0.2 (63)
$(C_9H_7)_2HfMe^+$	15.4	16.2±0.1 (53)

(a) $MeB(C_6F_5)_3^-$ salts in toluene-d₈

presaged by the work of Marks et al. (5). ΔG^\ddagger for the CH_3 transfer reaction in $(\text{Me}_3\text{SiCp})_2\text{MMe}^+$ ($\text{M} = \text{Zr}, \text{Hf}$) is larger for Zr than Hf, consistent, given Hammond's postulate, with a larger bond disruption enthalpy for $\text{Hf}-\text{CH}_3$ than for $\text{Zr}-\text{CH}_3$. (13) These reactions are conceptually quite simple and their further study may shed more light on the polymerization chemistry that transpires on metallocenium ions.

REFERENCES

- (1) (a) Sinn, H.; Kaminsky, W.; Vollmer, H. J.; Woldt, R. Angew. Chem. Int. Ed. **1980**, 19, 390. (b) Transition Metals and Organometallics as Catalysts for Olefin Polymerization, Kaminsky, W.; Sinn, H. eds. Springer Verlag, New York, N.Y. (1988).
- (2) Cam, D.; Albizzati, E.; Cinquina, P. Makromol. Chem. **1990**, 191, 1641.
- (3) Healey, M. D.; Wierda, D. A.; Barron, A. R. Organometallics **1988**, 7, 2543.
- (4) Siedle, A. R.; Newmark, R. A.; Lamanna, W. M.; Schroepfer, J. N. Polyhedron **1990**, 9, 301. (b) Siedle, A. R.; Newmark, R. A.; Gleason, W. B.; Lamanna, W. M. Organometallics **1990**, 9, 1290.
- (5) Yang, X.; Stern, C. L.; Marks, T. J. J. Am. Chem. Soc. **1991**, 113, 3263.
- (6) (a) Jordan, R. F.; Bajgur, C. S.; Willett, R.; Scott, B. J. Am. Chem. Soc. **1985**, 105, 7410. (b) Jordan, R. F. Adv. Orgmet.Chem. **1991**, 32, 325.
- (7) Burger, B. J.; Thompson, M. E.; Cotter, W. D.; Bercaw, J. D. J. Am. Chem. Soc. **1990**, 112, 1566.
- (8) Private communication from G. Hlatky and H. W. Turner.
- (9) Krauledat, H.; Brintzinger, H. H. Angew. Chem. Int. Ed. **1990**, 29, 1412.
- (10) Piers, W. E.; Bercaw, J. E. J. Am. Chem. Soc. **1990**, 112, 9406.
- (11) (a) Gassman, P. G.; Winter, C. H. J. Am. Chem. Soc. **1988**, 110 6130. (b) Gassman, P. G.; Macomber, D. W.; Hershberger, J. W. Organometallics, **1983**, 2, 1470. (c) Gassman, P. G.; Campbell, W. H.; Macomber, D. W. Organometallics **1984**, 3, 385. (e) Erker, G.; Nolte, R.; Aul, R.; Wilker, S.; Kruger, C.; Noe, R. J. Am. Chem. Soc. **1991**, 113, 7594.
- (12) Kaminsky, W.; Kulper, K.; Brintzinger, H. H.; Wild, F. R. W. P. Angew. Chem. Int. Ed. **1985**, 24, 507.
- (13) Schock, L. E.; Marks, T. J. J. Am. Chem. Soc. **1988**, 110, 7701.

RECEIVED June 22, 1992

Chapter 12

Effect of a Model Hydrogenation on a Catalytic Palladium Membrane

Henry C. Foley¹, A. W. Wang^{1,2}, B. Johnson¹, and J. N. Armor²

¹Center for Catalytic Science and Technology, Department of Chemical Engineering, University of Delaware, Newark, DE 19716

²Corporate Science and Technology Center, Air Products and Chemicals, Inc., Allentown, PA 18195

The hydrogenation of ethylene with a hydrogen permselective palladium membrane catalyst was examined to evaluate the changes in the structure and performance with extended time on stream. Changes in both catalyst activity and morphology were highly dependent on the reaction temperature. At 150 and 200°C, considerable increases in catalyst activity and extensive cracking and pitting of the catalyst surface were observed during the course of a 40 h experiment. However, the permeability of the membrane to hydrogen remained nearly constant. At higher temperatures, both the catalytic activity and morphological changes were suppressed. The drop in catalyst activity in going from 200 to 300°C was shown to be reversible, indicating that the low activity at high temperatures does not result from irreversible catalyst poisoning. These data are consistent with mechanisms for surface rearrangement involving participation of carbon atoms or adsorbed hydrocarbons in the formation of mobile palladium-containing species.

The use of an inorganic oxide “guard” phase has been investigated as a method to preserve the palladium surface. A layer of titania has been synthesized over the palladium foil using the sol-gel method. The layer is between 0.1 and 0.5 μ thick. Hydrogen permeation rates have been measured over a range of temperatures with this hybrid membrane structure (TiO_x -Pd) and they are as high or higher than those for palladium alone. Ethylene hydrogenation is nearly as efficient over Pt/ TiO_x -Pd as it is over pure Pd and does not display the matched transient in activity with time on stream. Interestingly, ethylene conversion over TiO_x -Pd is lower than that over pure Pd but it also shows much more stable conversion behavior than the latter. These results point to increased stability of the “guarded” palladium membrane, suggesting that hydrocarbon reactant does not reach the surface in sufficient quantities to drive the restructuring processes that underlie the transient behavior displayed in the catalytic reactivity.

Membrane transport and catalysis used in concert offer new opportunities for chemical process technology. Membrane transport is quite a familiar unit operation. More specifically, the use of metal membranes for hydrogen purification brings to mind palladium or palladium alloy "diffusers." The diffuser takes advantage of the permselectivity of palladium for hydrogen transport. When a matrix of gases including hydrogen is imposed on one surface of the diffuser hydrogen is transported to the other side where its concentration can approach a mole fraction of one. The other gases in the original matrix are rejected by the metal.

The opportunity lies in combining membrane separation with catalytic reaction. In principle, a reaction like a dehydrogenation of a hydrocarbon can be carried out on one side of the membrane to generate the dehydro-product and dihydrogen. The dihydrogen is transported through the membrane continuously, thereby driving the reaction closer to completion than would be predicted on the basis of the thermodynamics for a closed system. Run in the opposite direction, hydrogen can be permeated through palladium in order to drive hydrogenation reactions on the opposite side of the membrane.

The potential in this approach is two-fold. In combination, two normally separate unit operations are integrated into one. Although this may not be of general advantage, since in most cases one would want to design and optimize, reactor and separation units independently, it may prove quite advantageous for certain types of reaction. This leads to the second potential advantage of the integrated approach. If a dehydrogenation reaction is equilibrium limited, then by opening the system selectively to hydrogen, equilibrium is shifted in favor of products and higher conversions. It is because of these properties and potential features that palladium and palladium alloys are of considerable interest as catalysts and catalytic reactors.

Background

In dehydrogenation reactions, the continuous and selective removal of hydrogen from the reaction zone via transport through the membrane permits one to shift the reaction equilibrium towards the product (1-5), in accordance with LeChatelier's principle. In hydrogenation and hydrogenolysis reactions, the hydrogen is typically fed to one side of the membrane, where it undergoes dissociation and then diffuses through to the other side as active hydrogen atoms. Markedly higher rates are often claimed as compared with those obtained when conventional supported palladium catalysts are used under the same partial pressure of hydrogen (5-10). It has also been demonstrated that a dehydrogenation can be conducted on the side of the membrane with hydrogen transported to the other side where a hydrogenation reaction can be driven. In turn the heat generated by the exothermic hydrogenation reaction is conducted by the metal membrane back to the endothermic dehydrogenation reaction. This provides a coupling of the two reactions by both mass and heat transport through the metal. Alloys of palladium with ruthenium, nickel, or a variety of other metals have been evaluated as membrane catalysts and in many cases it has been found that they provide enhanced permeability or activity without sacrificing the permselectivity of the membrane (5,6,11-13).

Although considerable attention has been given to discovering applications for palladium membrane technology; less work has gone into understanding the changes in the nature of these materials during use, and how these changes affect their behavior. It has been known for some time that exposing palladium to heating and cooling cycles in hydrogen leads to the formation of cracks along the grain boundaries of the metal (13,14). These result from internal stresses due to volume changes which accompany phase transformations between α - and β -palladium hydride. Palladium alloys are attractive in part because they exhibit superior durability during extended use (15). Gryaznov and co-workers have reported

numerous instances in which surfaces of palladium alloy membranes were altered under the influence of chemical reactions and regeneration by heating in air followed by flowing hydrogen (11,16-18). In most cases they observed increases in catalytic activity as a function of the number of experiment/regeneration cycles to which a membrane was subjected. Skakunova, Gryaznov and co-workers found that a 6% ruthenium in palladium alloy membrane displayed no activity for the hydrogenolysis of propane prior to alternating reaction-regeneration treatment, and that stable activity was not observed until after thirteen cycles. Electron microscopy revealed that the surface of the membrane had undergone considerable restructuring; the authors refer to "disintegration," which suggests both increased surface area and erosion. Significantly, cyclic oxidation-reduction of the membrane was not effective in activating the catalyst. Interestingly, the authors concluded that the presence of carbon is necessary to facilitate the migration of surface metal atoms (17).

Gryaznov et. al. observed a "loosening" of the surface structure in a large number of palladium alloy membrane catalyzed reaction-regeneration processes, including the dehydrogenation of cyclohexane over 5% ruthenium alloy (12), the dehydrogenation of isoamylene on 5.5% nickel alloy (18), and the hydrogenation of cyclooctadiene or cyclopentadiene using a 10% ruthenium membrane (16). In the latter study, the authors observed that the extent of surface restructuring was greater and the regeneration time shorter with cyclooctadiene than with cyclopentadiene. They attributed this to the stronger adsorption of cyclooctadiene on palladium. Furthermore, while the enhanced surface area led to an increase in catalytic activity, little or no increase in membrane permeability to hydrogen was measured. It was the authors' hypothesis that potential increases in permeability due to the increased surface area for recombination and desorption of hydrogen atoms were suppressed by the presence of carbonaceous deposits on the surface. This supposition is consistent with the work of Roshan, Gryaznov and co-workers (18), who experimented with palladium-ruthenium alloy tubular membranes which had been pretreated with boiling CCl_4 and rinsed in HCl to increase the area of the membrane surface by selective removal of ruthenium. These materials exhibited enhanced catalytic activity and hydrogen permeabilities up to two orders of magnitude greater than untreated tubes in spite of the fact that the inherent diffusivity of hydrogen in the palladium was presumably unchanged.

Changes in the composition of the membrane surface have also been observed. Carbon deposition has been reported in many studies. Ziemecki and Jones have shown by x-ray diffraction and neutron scattering that carbon atoms readily occupy the octahedral holes in the face-centered cubic palladium lattice forming a new structure with formula $\text{PdC}_{0.15}$ (19,20). It is likely that the promoter effect of carbon towards palladium alloy surface restructuring is largely due to this propensity for carbon incorporation into the palladium structure. However, different alloy membranes can exhibit either enhancement or depletion of the alloying element at the surface as a result of reaction-regeneration cycling. These effects could also explain changes in catalytic activity. In one case Gryaznov and co-workers reported surface enrichment of rhodium when cyclohexane dehydrogenation was carried out over 10% rhodium alloy foil catalyst, and demonstrated a correlation between the surface concentration of rhodium and the extent of cyclohexane dehydrogenation (12).

In spite of the advances made by these researchers, it remains unclear how membrane surfaces undergo restructuring and how these changes influence the catalytic and transport properties of the material. Furthermore, there is a need to link surface structure and composition with long-term performance of palladium membranes under continuous reaction conditions. One

objective of this work was to gain insight into these issues by examining a simple model reaction: the hydrogenation of ethylene over a pure palladium membrane catalyst.

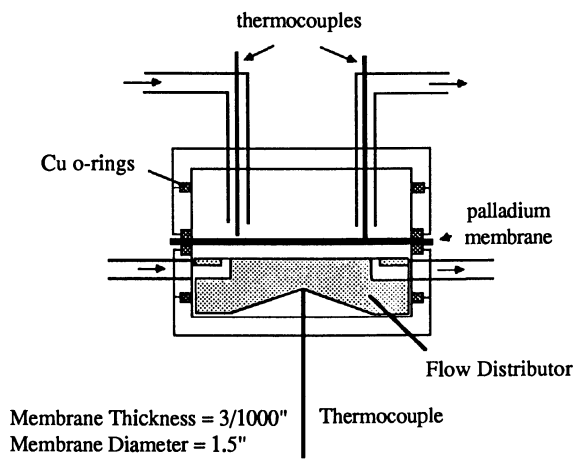
A logical extension of this work was to prepare multifunctional or hybrid membranes in which a palladium foil is modified by the addition of a porous ceramic coating. Such a coating could serve to stabilize the membrane's catalytic activity by protecting the palladium surface from attack by adsorbed hydrocarbons. For example in an alkene hydrogenation reaction, hydrogen atoms would be expected to diffuse out of the membrane, spillover to the inorganic oxide and consume reactant molecules that are diffusing toward the palladium surface. When operated under proper conditions the concentration of active organic species reaching the palladium surface would be diminished, ideally, to zero. In practice this might be expected to result in much less poisoning and surface restructuring of the palladium membrane since these processes are most likely driven by carbon incorporation. Recently, it has been shown that a layer of transition metal on palladium, especially titanium, can produce a marked diminution in the rate of surface poisoning (21). Although a metal and not a metal oxide was used, the concept is similar. Also, such a coating could serve as a catalyst itself or as a support phase for a catalytic metal such as platinum. Intimate contact between the ceramic and the palladium could modify or even enhance hydrogen transport through the membrane by providing a route for spillover of atomic hydrogen away from the palladium surface.

Ceramic and semiconductor thin films have been prepared by a number of methods including chemical vapor deposition (CVD), spray-coating, and sol-gel techniques. In the present work, the sol-gel method was chosen to prepare uniform, thin films of titanium oxides on palladium. Titanium oxide was chosen because of its versatility as a support material and also because the sol-gel synthesis of titania films has been clearly described by Takahashi and co-workers (22). The procedure utilized herein follows the work of Takahashi, but is modified to take advantage of the hydrogen permeability of the palladium substrate. Our objective was to develop a reliable procedure for the fabrication of thin titania films on palladium, and then to evaluate the performance of the resulting metalloceramic membranes for hydrogen transport and ethylene hydrogenation for comparison to the pure palladium membrane results.

Experimental Methods

Membranes and Reactor Studies. The 4.0 cm diameter circular membranes used in this study were cut from .003 inch (7.62×10^{-3} cm) palladium foil (Johnson-Matthey, Ltd.). The reactor consisted of a set of four Conflat flanges (Kurt J. Lesker, Co.) and the membrane was pressed between two of the flanges using annealed copper o-rings to provide the seal (see Figure 1.) A flow distributor was used to provide more uniform delivery of the gases on the reaction (bottom) side of the reactor. Thermocouples in contact with the membrane surface were used to monitor the temperature on either side of the membrane and to provide feedback control to the heating tape which surrounds the reactor.

Analysis of the reactant and product streams was accomplished using two gas chromatographic systems: an 8'x1/8" Hayesep Q 80/100 column equipped with a Gow-Mac 40-250 thermal conductivity detector, and a 12'x1/8" Hayesep Q 80/100 column installed in a Gow-Mac 69-750P Gas Chromatograph with a flame ionization detector. Two selection valves permitted analysis of all four reactor flows with either column. The eight-foot column was used for hydrogen analysis and utilized argon as the carrier gas and a sample size of 500 μL . The twelve-foot column was used in the analysis of ethane and ethylene, at a sample size of 2 mL. Data from this column was tabulated and recorded using a Spectra-Physics SP4270 Integrator.



Flow Distributor --

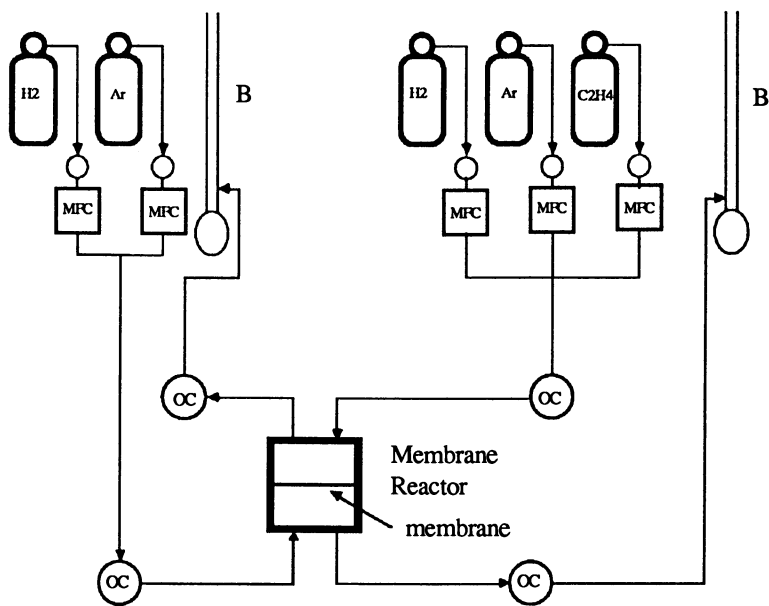
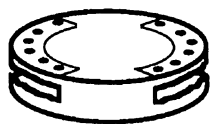


Figure 1. Schematic of membrane reactor.

X-Ray Photoelectron Spectroscopy was performed using a Perkin-Elmer ESCALAB Model 551 spectrometer. Scanning Electron Micrographs were obtained on a Philips 501 Scanning Electron Microscope equipped with an EDX detector.

Membranes were washed with acetone prior to installation in the reactor and pretreated for one hour at reaction temperature with a 50% hydrogen/argon feed (24 sccm) admitted to the top of the membrane (hereafter referred to as the feed side) and a pure argon flow (12 sccm) on the reaction side. Measurements of the initial permeability of the membrane were taken at this time by measuring the hydrogen flux through the foil at these standard conditions.

Argon (Ultra High Purity, 99.999%), hydrogen (Research Purity, 99.9995%) and ethylene (Research Purity, 99.99%) were purchased from Matheson. The argon was further purified using a Matheson Gas Purifier Model 6406 in conjunction with an Alltech indicating oxy-trap.

Preparation of Thin Films of TiO_2 on Palladium Foils. Following the procedure reported by Takahashi, an isopropanol based sol of titanium tetra-isopropoxide (TTIP) was prepared (10 mL of TTIP in 48.4 mL of 2-propanol), to which 6.7 mL of diethanolamine was added to inhibit the formation of oxides. This mixture was stirred for two hours, at which time gel formation was initiated by the addition of 28.1 mL of a dilute water solution (1.42 mL water in 30 mL of 2-propanol). The resulting molar ratio of water to TTIP was 2:1, as was recommended by Takahashi and co-workers (22). The palladium substrates were dipped vertically into this solution and then clamped on edge while draining to allow the excess to drip off and to prepare as even a coating as possible. The membranes were then air-dried in a vertical position at 100°C for one hour, followed by a post-treatment with hydrogen (see Figure 2).

A variety of post-drying heat treatments were investigated. Calcination at 330°C in air for three hours resulted in coatings which were rough, poorly adhered and black in color, suggesting the presence of considerable carbon within the titania film. More gradual temperature ramping led to some improvement in both the morphology and the adhesion of the coating, however the grayish-brown color of the product indicated that carbon was still being retained within the film. Further treatment of one such membrane with hydrogen permeation at 330°C produced a gold-brown film with modest adhesion, suggesting that some of the carbon had been removed.

It appears that carbon formation results from the inability of isopropoxide, 2-propanol and diethanolamine to escape from the coating during drying and calcination. The permeability of the composite membrane (palladium and coating) to hydrogen permits the use of hydrogen atoms to remove carbon from the coating via reaction. Since this method showed some promise when applied as a post-calcination step, the procedure was modified to include hydrogen permeation during the calcination process.

Palladium substrates were dipped and dried according to the standard procedure outlined above. The dried membranes were then sealed between two copper o-rings into the reactor shown in Figure 1. Hydrogen and argon were fed to opposite sides of the membrane at 330°C for three hours. The resulting films had a bright gold color and very smooth morphology, but suffered from poor adhesion, particularly on the surface exposed to the hydrogen feed. Reducing the flux of hydrogen through the use of a 70% feed of hydrogen (in argon) on one side and a 30% feed of hydrogen on the permeate side resulted in better apparent adhesion on both sides without visibly sacrificing the quality of the film. Extending the drying time beyond one hour had no apparent effect on the product. The extensive cracking of the

coating under pure hydrogen is probably a result of the differences in the coefficients of thermal expansion between the coating and the substrate. This appears to be unavoidable.

The reducing environment present during the heat-treatment process makes it likely that the final film is of composition TiO_x ($1 < x < 2$). Depth-profiling studies with XPS indicate that the films are at least 1640\AA thick; scanning electron microscopy suggests that the film thickness is less than 5000\AA . Thus, it seems reasonable to assume a film thickness on the order of several thousand angstroms.

Preparation of Pt-TiO₂/Pd membranes. It was also desirable to prepare metal/ceramic membranes in which the catalytic activity of the ceramic phase was enhanced through the addition of a noble metal. The very low surface area of the titania films prepared as described above made them difficult to impregnate with adequate dispersion by traditional incipient wetness techniques. Instead, finely ground titania (>200 mesh) was impregnated with platinum via the incipient wetness method with a chloroplatinic acid solution. This powder was then sprinkled onto the surface of a freshly dipped membrane, which was dried and heat treated as described. These materials were activated before use at 350°C in hydrogen for three hours.

Results

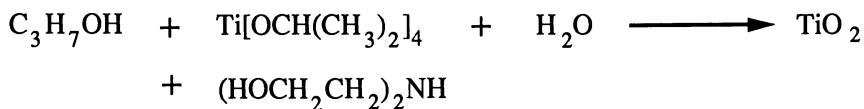
Pure Palladium Membranes.

Time and Temperature Dependence of Ethylene Hydrogenation. Changes in the steady-state activity of the palladium membranes as catalysts for ethylene hydrogenation were examined in a series of experiments at various temperatures in which continuous feeds (45 mol% ethylene in argon to the reaction side of the membrane and 50 mol% hydrogen in argon to the opposite side) were maintained for forty hours. The reactor performance was monitored periodically by gas chromatographic analysis of the product streams. At the end of each run, the reactor was cooled in flowing argon and the membrane was reexamined with electron microscopy and EDX.

The dependence of ethylene conversion with time on stream is shown in Figure 3. The corresponding SEM micrographs of the reaction side of the membranes are given in Figure 4 (a-d), along with a micrograph of a membrane surface prior to reaction. The micrographs of the reacted foils reveal varying extents of cracking and pitting of the membrane surface as compared with the unreacted sample. The conversion profiles exhibit a marked dependence on temperature; conversions ranging from 3% to 75% were observed over a temperature range of 150°C . Hydrogenation activity decreased with temperature above 200°C . With the exception of the 300°C run, the observed ethylene conversion initially increased with time. This increase was most gradual at 150°C , where the conversion increased steadily by approximately 7% per 1000 minutes. The most rapid and short-lived activation was observed in the 250°C reaction, in which the conversion increased from 32% to 37% in the first 30 minutes of reaction and thereafter underwent gradual deactivation. The increase in conversion over a given run correlates qualitatively with the extent of surface texturing. The 200, 250 and 300°C experiments all eventually achieved a state of gradual deactivation, but at 150°C the membrane displayed monotonically increasing activity even after 3000 minutes on stream.

Hydrogen Permeability. The permeation rates of hydrogen through the membrane at various points in each run are tabulated in Table 1. As noted elsewhere in the literature, the apparent permeation rate of hydrogen during reaction is considerably higher than that

Sol Gel Synthesis:



Removal of Carbon Remaining after Calcination and Drying

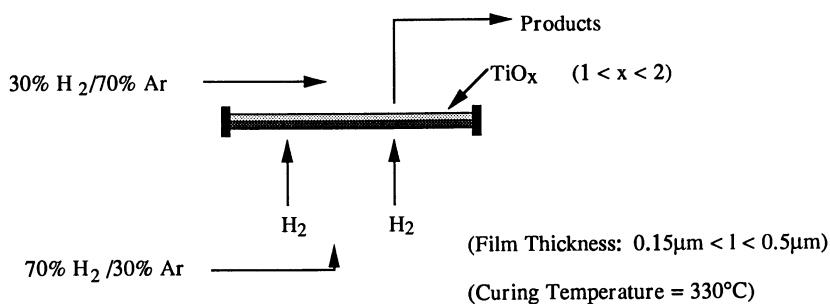


Figure 2. Preparation of titania films on palladium by sol-gel synthesis and thermal treatment.

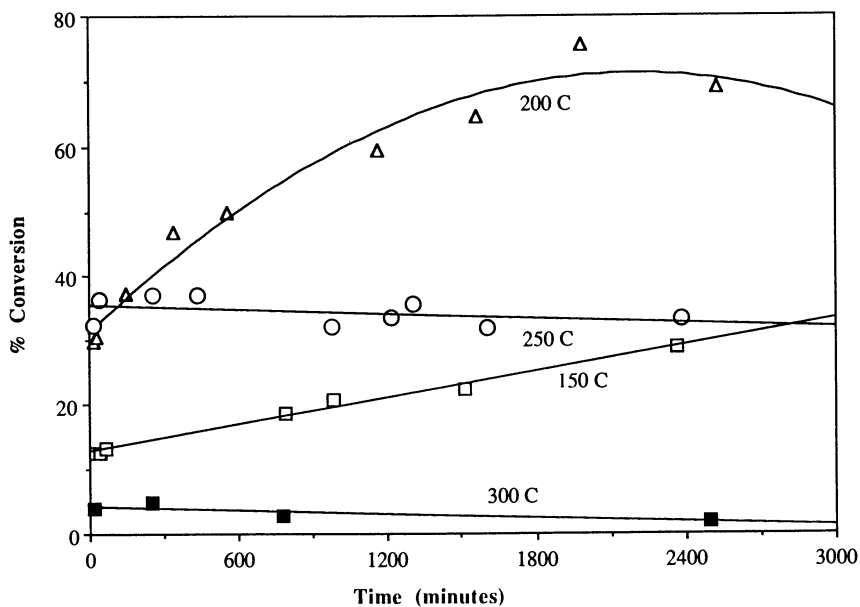


Figure 3. Ethylene hydrogenation conversion as a function of time on stream.

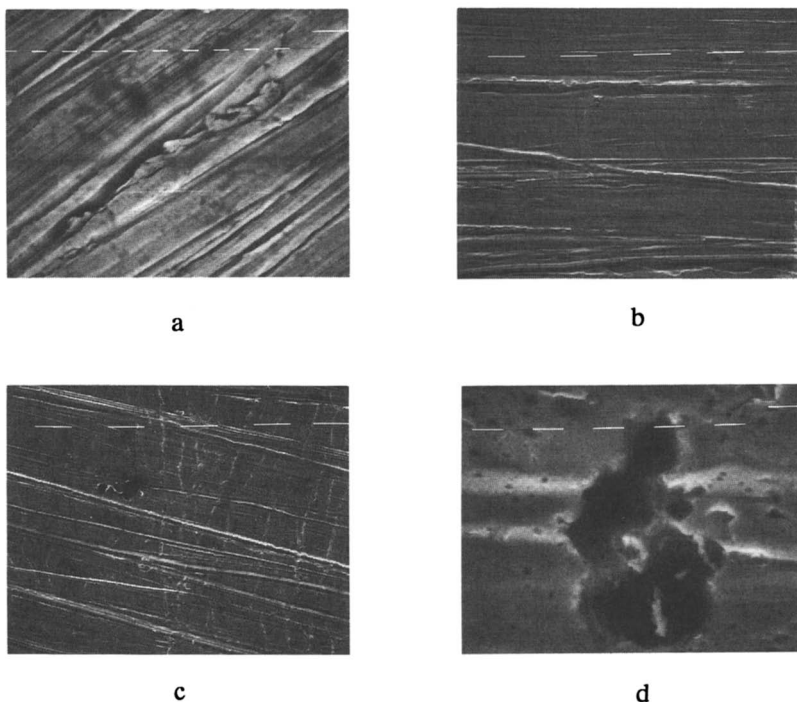


Figure 4 Scanning electron micrographs of a) virgin palladium foil (2000x), b) after 40 hr of ethylene hydrogenation at 150 °C (500x), c) after 40 hr of ethylene hydrogenation at 200 °C (400x), d) close of etch-pit on 200 °C sample (4000x).

Table 1
Permeation Rates of Hydrogen ($\mu\text{mol}/\text{cm}^2/\text{min}$)*

Condition	Temperature (°C)				
	150°C	200°C	250°C	300°C	200°C**
Prior to C ₂ H ₄ Addition	7.6	10.9	12.2	12.8	11.4
Immediately after C ₂ H ₄ Addition	11.5	20.1	23.6	17.2	
After 30 hours on Stream	15.2	30.6	24.4	18.5	31.7
After reaction Without C ₂ H ₄					10.9

* Through 0.003 in palladium foil, the hydrogen permeation rate was taken as the sum of hydrogen and ethane in the product stream.

** The 200°C run with just hydrogen was conducted to obtain post reaction permeation rates.

observed in the absence of ethylene. This indicates that the surface reaction assists the permeation of hydrogen through the membrane by removing hydrogen atoms from the surface or near-surface layers. The duplicate experiment at 200°C is especially revealing, in that the rate of hydrogen diffusion in the absence of ethylene was measured again at the end of the experiment, and found to be approximately equal to the initial value. It is apparent that the increase in hydrogen flux during the reaction at 200°C is a reflection of the increased activity of the catalyst surface and is not due to an increase in the overall permeability of the membrane itself.

The XPS/Auger spectrum of a membrane prior to reaction revealed the presence of sulfur uniformly distributed throughout the palladium as an impurity (see Figure 5a). Spectra of the membrane after reaction at 200°C for forty hours indicated that both surfaces of the membrane had been preferentially enriched with traces of sulfur (see Figure 5b). Depth-profiling experiments revealed the formation of a trace sulfur surface layer which is approximately 20 Å thick. Spectra of both the raw and used foils showed carbon on the surface, however the concentration was too low to differentiate from possible sample contamination.

Suppression of Activity at High Temperatures. One notable aspect of the temperature dependence experiments was the low activity demonstrated by the catalyst above 200°C. It was of interest to determine whether this results from an irreversible form of catalyst poisoning or is a consequence of the equilibrium temperature dependence of the adsorption of ethylene. To investigate this point, an experiment was performed in which the hydrogenation of ethylene was carried out at several temperatures, increasing from 100°C to 300°C and then cooling back to 100°C. At each temperature, the reactor was allowed to come to steady state for one hour before the product streams were analyzed. To minimize the effect of changes in the membrane morphology, a membrane which had been previously used in a 200°C reaction was utilized.

The results of the experiment are shown in Figure 6. It is evident that the loss of activity in going from 200 to 300°C is largely reversible. This supports the hypothesis that the lower activity of the palladium membrane at higher temperatures is due more to the suppression of ethylene adsorption than it is to irreversible poisoning at these temperatures. It is also worth noting that similar temperature dependencies have been noted for the permeation of hydrogen through palladium (23). A coupling of this phenomenon with that of the ethylene adsorption thermodynamics may be involved. The hysteresis in this data reflects the aforementioned deactivation process which, although slow, is clearly observed at 250 and 300°C.

Titania-Palladium Hybrid Membranes.

Hydrogen Permeability. The ability of the metalloceramic membranes to transport hydrogen was evaluated by measuring the flux of hydrogen through them at various temperatures at a standard feed of 50% hydrogen in argon (25 sccm) and a purge of 100% argon (25 sccm). The Pt-TiO₂/Pd membranes were tested for permeability in both directions; within experimental error, no difference in hydrogen transport was observed when the feed was switched from the non-impregnated side to the platinum doped side at any of the temperatures examined. Since one would expect that the presence of platinum would affect the ability of the membrane surface to perform surface-sensitive processes such as recombination of hydrogen atoms or adsorption/desorption of hydrogen molecules, this suggests that such processes are not the rate-determining step in hydrogen permeation over the temperature range of the study.

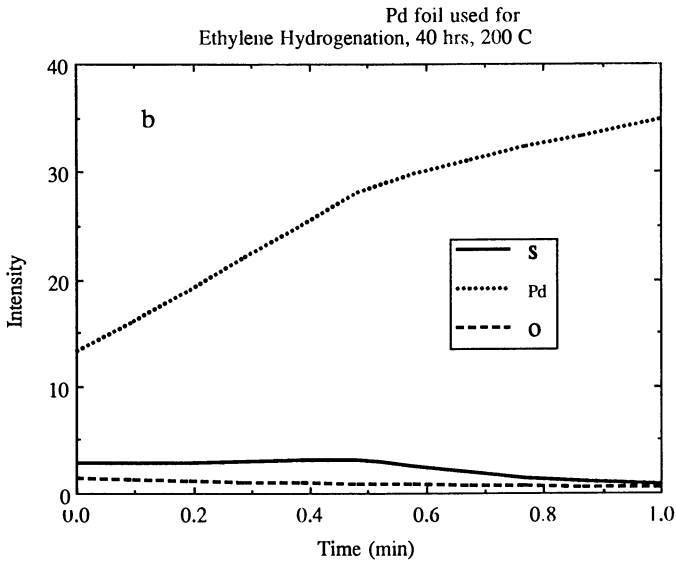
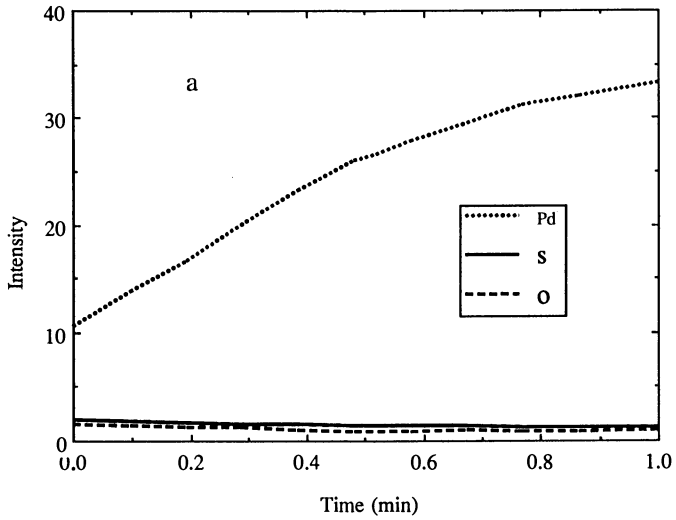


Figure 5 Auger electron spectroscopy depth profiles of a) unused and b) used palladium membranes.

The permeability parameter used in this study, Π , is the ratio of the observed flux to a concentration driving force defined as the difference in bulk gas-phase concentration on the two sides of the membrane divided by the thickness of the membrane. Thus, Π has dimensions of $(\text{length})^2/\text{time}$. This definition was chosen for its simplicity as a basis of comparison between membranes and does not take into account the relationship between gas-phase concentration and surface metal concentration, or the possibility of bulk gas-phase hydrogen transfer limitations. Figure 7 shows the temperature dependence of Π for pure palladium foil, TiO_x/Pd and $\text{Pt-TiO}_x/\text{Pd}$. It is interesting to note that the presence of the titania overlayer does not significantly undermine the ability of the membrane to transport hydrogen; in fact, at temperatures below 150°C and above 300°C the metalloceramic membranes appear to outperform the unmodified foil. One possible explanation for this is that the ceramic phase assists the removal of hydrogen from the permeate surface by providing a surface for hydrogen spillover. If this is the case, then it is quite possible that at temperatures greater than 300°C, surface recombination or desorption of hydrogen is the rate-limiting step in the absence of a ceramic overlayer, and that the addition of the ceramic phase allows the rate of hydrogen transport through the bulk palladium to continue to dominate.

Stability of TiO_x/Pd membranes as catalysts for ethylene hydrogenation. We have previously observed that unmodified palladium foils underwent impressive changes in activity when utilized as membrane catalysts for ethylene hydrogenation. This behavior generally consisted of two steps: a period of increasing activity followed by a period of gradually decreasing activity. Two features of this phenomenon were particularly noteworthy: (1) the extent and duration of the increase in activity was a function of temperature, and (2) increases in activity were accompanied by the formation of cracks and pits in the palladium surface. Our conclusion was that surface reconstruction was the result of strongly adsorbed hydrocarbons forming organopalladium moieties which could be removed by a coupling of surface and gas phase processes. Therefore, a ceramic coating might produce a more stable membrane catalyst by preventing the adsorption of hydrocarbons directly on the palladium surface. In the case of a TiO_x/Pd membrane, it was envisioned that the ethylene could adsorb onto the titania where it would react with hydrogen spilled over from the palladium. Further modification of these materials through the addition of platinum to the ceramic phase would provide a more effective site for the adsorption and activation of ethylene.

This hypothesis was examined by carrying out forty-hour ethylene hydrogenation reactions on both a TiO_x/Pd and a $\text{Pt-TiO}_x/\text{Pd}$ membrane and comparing the changes of conversion over time with those observed on pure palladium foil. These experiments were performed at 200°C because this temperature produced the most dramatic increase in activity when unmodified palladium was used. The feeds to the reactor consisted of 25 mL/min flows of 50% hydrogen in argon and 50% ethylene in argon to the feed and reaction surfaces respectively. The results of these experiments are shown in Figure 8. It is evident that the addition of the titania coating prevents the activation process from occurring; only the gradual deactivation is observed. These data also demonstrate that although modification of the palladium surface with titania leads to a reduction in the catalytic activity of the membrane, the activity can be restored through the addition of platinum to the ceramic phase. In this composite membrane, the palladium foil is envisioned as a source of hydrogen atoms which are spilled over onto the ceramic coating and subsequently react with ethylene chemisorbed on the platinum.

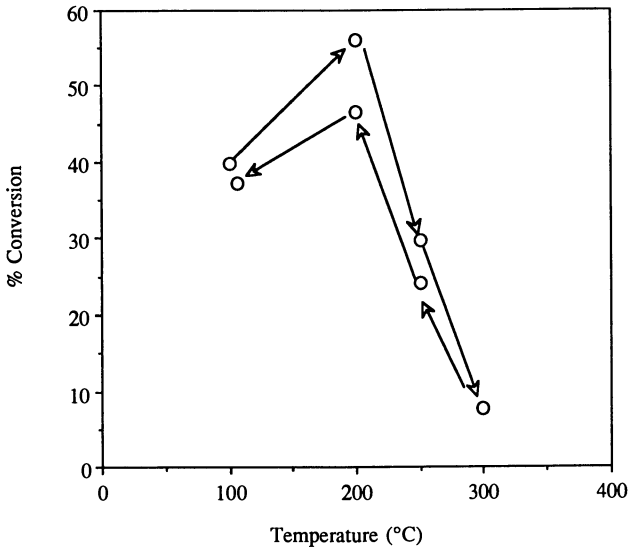


Figure 6. Temperature dependence of ethylene conversion to ethane over a palladium membrane.

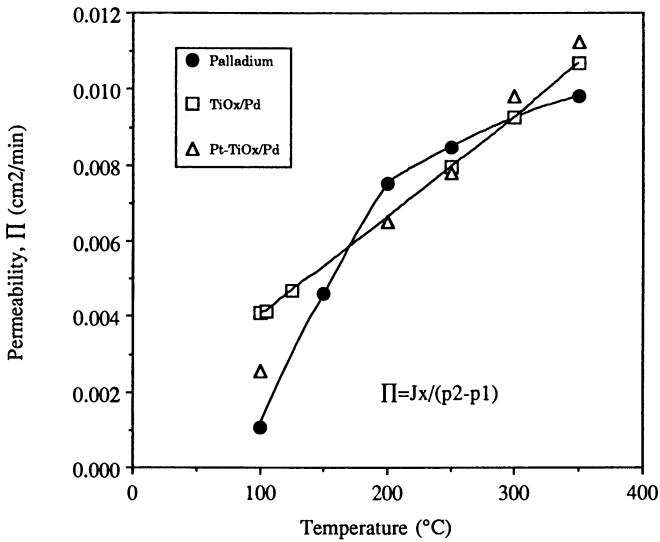


Figure 7. Temperature dependence of hydrogen permeabilities in Pd, TiO_x-Pd and Pt/TiO_x-Pd membranes.

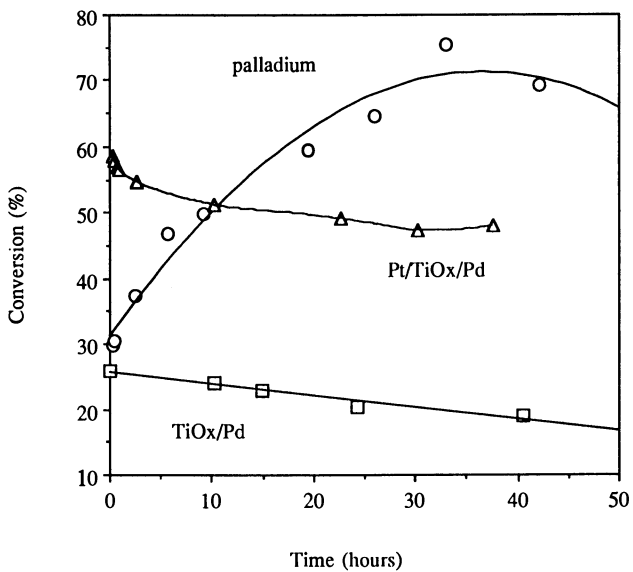


Figure 8. Time dependence of ethylene conversions to ethane over Pd, TiO_x-Pd, and Pt/TiO_x-Pd membranes.

Discussion

Figures 3 and 6 demonstrate that the activity of palladium foils as membrane catalysts for hydrogenation reactions is a strong function not only of temperature but also of time on stream. This transient nature of the catalyst behavior underscores the difficulty of reporting "steady-state" reactivity data for these materials, particularly over timescales of twelve hours or less. The correlation between the increase in activity of a catalyst at a given temperature, and the amount of surface restructuring observed by SEM, supports the hypothesis that the enhancement of catalytic activity, observed most clearly at 150 and 200°C, results from changes in the nature of the surface. The absence of an alloying metal further simplifies this picture by eliminating the possibility that changes in the surface metal composition are involved. Furthermore, consistent with Gryaznov's results (16,18), it appears that the roughening of the reaction surface through etching and cracking does not have a significant effect on the capability of the membrane to transport hydrogen. Therefore, our results indicate that the increased flux of hydrogen through the membrane is a result, not a cause, of the greater reaction rate at the surface. However, this conclusion is inconsistent with the acid etch experiment of Roshan and co-workers (18), and also with the theory that the rate-limiting process in hydrogen diffusion through palladium is the recombination and/or desorption of hydrogen molecules from the surface into the permeate stream.

It is reasonable to assume that the same process of catalyst activation via surface restructuring is active at all of the temperatures studied, but proceeds more rapidly at higher temperatures. Two reasonable sources of the effect of surface restructuring on catalyst activity are the resulting increase in surface area available for reaction, and the removal of an inactive surface layer or contaminant. Upon completion of this restructuring process, the slower deactivation process becomes evident in the three higher temperature experiments. Presumably the 150°C reaction would likewise enter a period of gradual deactivation once the benefits of surface restructuring were fully realized. The migration of traces of sulfur to the surface during reaction, demonstrated by the XPS/Auger data, may provide one possible explanation for this deactivation.

A significant issue is how the surface is restructured and why much more extensive restructuring is seen at 150 and 200°C. Ermilova and co-workers have suggested that surface restructuring is related to the strength of the adsorption of the hydrocarbon (16). This hypothesis is consistent with this work in that at higher temperatures the equilibrium adsorption constant for ethylene is lower and surface restructuring is suppressed. Skakunova and co-workers' hypothesis that carbon atoms are necessary to facilitate surface migration of metal atoms (18) could also help explain our data; higher temperatures result in higher rates of hydrogen permeation which should reduce surface concentrations of carbon and retard surface restructuring. However, neither one of these theories provides a completely satisfactory explanation for the fact that faster rates of catalyst activation were observed at 200°C than at 150°C. One possible explanation is that at temperatures as low as 150°C the advantage offered by increased concentrations of ethylene or carbon is outweighed by reduced mobility of the moiety they form on the surface which is responsible for the restructuring. A second possibility is that intrinsic carbon deposition rates are lower, so that even in the presence of a decreased hydrogen flux surface carbon concentrations are comparatively low.

The pitting of the membrane surface is interesting since the micrographs shown in Figure 4 provide evidence for removal of metal, but no indications of its accumulation or redistribution on the surface. Thus, it is conceivable that the surface "restructuring" observed

in this system is actually an etching process, involving removal of surface atoms via gas phase transport, as opposed to a purely surface transport mechanism as has been proposed by Ermilova and co-workers (16). The high concentration of hydrogen and hydrocarbon radicals on the surface could provide the driving force for the mechanism of surface pitting through radical etching. A possible pathway for etching of the palladium surface may involve formation of a volatile ethyl or ethyl-hydride palladium species.

This hypothesis provides a more satisfactory explanation of the comparatively rough surface morphology associated with restructuring, since intuition suggests that increased surface mobility ought to yield a smoother surface rather than a rougher one. The unevenness of the etching process might result from either nucleation of pits at surface impurities or preferential etching along grain boundaries or machining defects.

Conclusion

The ethylene hydrogenation data provide strong evidence to support the hypothesis that pitting and cracking of palladium membrane catalysts result from the interaction of hydrocarbons with the palladium surface, and not merely from the diffusion of hydrogen through the bulk metal. The addition of a ceramic overlayer to a palladium foil effectively separates the palladium from the reacting molecules, protecting the metal from attack and stabilizing the catalytic activity of the membrane. It has been demonstrated that the extent of palladium surface reconstruction during ethylene hydrogenation is dramatically reduced by the ceramic coating. The presence of this overlayer does not significantly impede the transport of hydrogen through the membrane and, at sufficiently high or low temperatures, may actually facilitate it. This behavior may be due to the capability of the ceramic phase to induce hydrogen spillover from the pool of permeate hydrogen on the surface of the palladium, which suggests interesting possibilities for performing chemistry involving hydrogen transport at comparatively low temperatures. The ceramic phase could serve both as a material on which to anchor organometallic catalysts, as well as a conduit for hydrogen atoms to drive reactions at low temperatures, especially at temperatures below the decomposition temperature of the organometallics.

Acknowledgment

The authors are grateful to Air Products and Chemicals, Inc., the State of Delaware Research Partnership, and the National Science Foundation PYI Award to HCF for providing funding for this project. We would also like to acknowledge Dr. Nikos Maris, who designed and constructed much of the equipment used in this research, and Dr. Alejandro Cabrera, who obtained and interpreted the XPS/Auger spectra.

Literature Cited

1. Itoh, N.; *AIChE Journal*, **33**, 1576 (1987).
2. Itoh, N.; Govind, R.; *AIChE Symp. Ser. No. 268*, **85**, 10 (1988).
3. Itoh, N.; Govind, R.; *AIChE Journal*, **34**, 1493 (1988).
4. Sun, Y.; Khang, S.; *Ind. Eng. Chem. Res.*, **27**, 1136 (1988).
5. Armor, J.N.; *Appl. Catal.*, **49**, 1 (1989).
6. Gryaznov, V.M.; Ermilova, M.M.; Morozova, L.S.; Orekhova, N.V.; Polyakova, V.P.; Roshan, N.R.; Savitsky, E.M.; Parfenova, N.I.; *J. Less Common Metals*, **89**, 529 (1983).
7. Kokes, R.J.; Rennard, R.J.; *J. Phys. Chem.*, **70**, 2543 (1966).

8. Nagamoto, H.; Inoue, H.; *Chem. Eng. Commun.*, **34**, 315 (1985).
9. Nagamoto, H.; Inoue, H.; *Bull. Chem. Soc. Jap.*, **59**, 3935 (1986).
10. Gryaznov, V.M.; Smimov, V.S.; Slinko, M.G.; *Proc. Seventh. Int. Congr. Catal.*, Vol. 1 (Elsevier Scientific Publishing Co., Amsterdam-Oxford-New York), 224 (1980).
11. Gryaznov, V.M.; Smimov, V.S.; Slinko, M.G.; *Proc. Fifth. Int. Congr. Catal.*, Vol. 2 (North-Holland Publishing Co., Amsterdam-London), 1139 (1973).
12. Gryaznov, V.M.; Smimov, V.S.; Slinko, M.G.; *Proc. Sixth. Int. Congr. Catal.*, Vol. 2 (The Chemical Society, Burlington House, London), 894 (1977).
13. Hsieh, H.P.; *AIChE Symp. Ser.*, No. 268, 85, 53 (1989).
14. Darling, A.S.; *Plat. Met. Rev.*, **2**, 16 (1958).
15. Hsieh, H.P.; *AIChE Symp. Ser.*, No. 261, 84, 1 (1988).
16. Ermilova, M.M.; Orekhova, N.V.; Skakunova, E.V.; Gryaznov, V.M.; *Izvestiya Akademii Nauk SSR, Seriya Khimicheskaya*, No. 4, 750, (1988).
17. Skakunova, E.V.; Ermilova, M.M.; Gryaznov, V.M.; *Izvestiya Akademii Nauk SSR, Seriya Khimicheskaya*, No. 5, 986 (1988).
18. Roshan, N.R.; Mishchenko, A.P.; Polyakova, V.P.; Parfenova, N.I.; Savitsky, E.M.; Voitekhova, E.A.; Gryaznov, V.M.; Sarylova, M.E.; *J. Less Common Metals*, **89**, 423 (1983).
19. Ziemecki, S.B.; Jones, G.A.; *J. Catal.*, **95**, 621 (1985).
20. Ziemecki, S.B.; *Catalysis 1987*, Elsevier Scientific Publishing Co. (J.W. Ward, ed.), 625 (1988).
21. Harris, J. R.; U. S. Pat. No. 4,536,196 (1985).
22. Takahashi, Y.; Matsuoka, Y.; *J. Mat. Sci.* **23**, 2266 (1988).
23. Maganyuk, A.P.; Naumov, V.A.; in *Metals and Alloys as Membrane Catalysts*, ed.: V. M. Gryaynov, E.D. Klabrunovsky; Nauka Publishers, Moscow, 1981, pp. 45-55.

RECEIVED July 9, 1992

Chapter 13

Vanadium Migration between Model Components of Fluid Cracking Catalysts

SEM-EDX Studies

Yan-Fei Shen¹, Steven L. Suib^{1,2}, and Mario L. Occelli³

¹Department of Chemistry, University of Connecticut,
Storrs, CT 06269-3060

²Department of Chemical Engineering, University of Connecticut,
Storrs, CT 06269-0139

³Zeolites and Pillared Clays Program, Georgia Technical Research
Institute, Atlanta, GA 30332

Scanning electron microscopy/energy dispersive X-ray (SEM/EDX) analyses have been used to probe the migration of vanadium in model fluid cracking catalysts (FCC). At the experimental conditions used, vanadium can migrate either from a Eu³⁺-exchanged Y (EuY) zeolite to an AAA-alumina gel or vice versa, depending on the type of vanadium precursor used.

If vanadyl naphthenate is used, minimal migration from the matrix to the zeolite and little or no V-migration from the zeolite to the matrix occur during calcination. Steaming induces some V-migration from the matrix to the zeolite but does not enhance V-migration from the zeolite to the matrix suggesting that vanadium is preferentially associated with the zeolite.

In contrast, if vanadium porphyrin is used, calcination causes about 80% of the vanadium initially deposited onto the zeolite to move to the matrix. There is much less metal migration of the porphyrin complex from the matrix to the zeolite, indicating that vanadium prefers to remain in the matrix after calcination. During steaming, additional V-migration occurs and V-losses attributed to the formation of volatile V-compounds are observed.

Metal contaminants when deposited onto fluid cracking catalysis (FCC) have a serious detrimental effect on the catalysts' physicochemical properties (1-21). Vanadium (at levels < 2,000 ppm) generally yield less hydrogen and coke than nickel contaminants in FCC's and its deleterious effects depend on its concentration and

location in the catalyst particle (microsphere). Larger amounts of hydrogen and coke are observed in vanadium loaded non-zeolitic material than in zeolite particles (3,22). At higher (>2,000 ppm) loading, the irreversible destruction of the zeolite structure together with loss of surface area, acid sites and catalytic activity occur in the FCC (2,15,16).

Vanadium is much more mobile than nickel and its mobility is controlled by the nature of the matrix or passivating agent present in the FCC. Sepiolite, attapulgite, MgO and Al₂O₃ appear to be more active for trapping vanadium than other matrices such as metakaolin and AAA-alumina (1,5,10,23,24,25), because of the ability that these supports have to form heat stable V-compounds (5,23).

In addition to interparticle migration (23), intraparticle transport has also been reported (1,5,21). Vanadium has been observed to migrate preferentially from the interior to the exterior of a sepiolite particle during high temperature calcination (1,5). Steaming causes vanadium, initially evenly distributed throughout the catalyst particle, to migrate to the FCC cracking component (the zeolite) (18,21,25-27).

At microactivity test conditions (MAT), the mechanism of vanadium migration has been found to be a gas-phase transport phenomena (20,23). However, a particle contact interaction mechanism has also been suggested (21). Formation of surface compounds, such as heat stable vanadates (5), may help explain V migration and V induced FCC deactivation. Few experimental investigations of metal migration between the various FCC components have been reported.

The present study attempts to elucidate mechanisms for vanadium migration between a Eu³⁺-exchanged zeolite Y and an AAA-alumina matrix. Eu³⁺ was used since it can readily be tracked with various spectroscopies. Moreover, effects of different vanadium precursors on migration will be a major focus of the paper because the nature of such precursors has been reported to control zeolite-vanadium interactions (28). SEM/EDX analyses are useful tools for tracking metal migration. Spot analyses on either Y zeolite or matrix particles will be reported since these FCC components show quite different morphologies.

EXPERIMENTAL

Sample Preparation. A sample of NH₄Y zeolite, supplied by Alfa Ventron, was exchanged with Eu³⁺ cations by stirring 10 g of the zeolite in 1000 mL of a 0.025 M EuCl₃·6H₂O solution at room temperature for 48 hours. The product was then washed sparingly with distilled deionized water until no Cl⁻ anions could be detected in the filtrate via reaction with a solution of 0.10 N AgNO₃. Finally, the zeolite was dried at 110°C overnight in an oven.

AAA-alumina (75% SiO₂/25% Al₂O₃ aluminosilicate gel provided by Davison) was used without further pretreatment. Benzene solutions of either vanadyl porphyrin (5, 10, 15, 20-tetraphenyl-21H, 23H-porphine vanadium oxide) or vanadyl naphthenate were impregnated by incipient wetness onto the EuY or the gel to generate a loading of 1.0 wt % vanadium. Vanadyl naphthenate has been widely utilized as a model V-contaminant and metalloporphyrins have been identified as metallic species in crude oil (29-30). The solvent was removed under

reduced pressure. The metal loaded material (such as EuYV or AAV) was then mixed mechanically with a V-free component (AAA or EuY) at a 1:1 weight ratio. In some cases, metal-doped components were calcined, before mixing with the V-free zeolite or gel.

Calcination of the mixtures was performed in a quartz reactor of diameter of about 2" and length of 1 foot with flowing air at 540°C for 10 hours to decompose the organic ligands. About 1 g catalyst was used for these studies. Steam aging was conducted at 740°C for 10 hours in a flowing 95% H₂O/5% N₂ mixture with a water flow rate of 4 mL/hr.

Nomenclature of Samples. The nomenclature used to describe various samples and treatments has been outlined in detail elsewhere (8). In this study, EuYV(p)AAACS means that EuY has been loaded with 1.0 wt % vanadium porphyrin (p), then mixed with the AAA-alumina (AAA), calcined (C) and subsequently steamed (S). Naphthenate precursor will be labeled n.

SEM/EDX Measurements. Sample powder was sprayed onto a carbon coated aluminum sample holder. After drying at room temperature, the sample holder was put into the analysis chamber of an AMRAY 1810D scanning electron microscope and evacuated.

SEM/EDX analyses were done with a Philips PV9800 EDX spectrometer. An acceleration potential of 25 or 30 kV was used for the EDX measurement (2 micron depth analysis). Care was taken to find both pure matrix and pure zeolite spots. Multi-spot analyses were performed on different particles of a sample in order to obtain more accurate information. Quantitative calculations were done with the Super Quant program with a ZAF correction to obtain relative concentrations.

RESULTS AND DISCUSSION

Energy dispersive X-ray (EDX) analyses (data in Tables I-III) represent semiquantitative analyses of elemental distributions of vanadium, europium and elements of the zeolite and gel structure. EDX data arise from about 2 mm area and, therefore, are more indicative of bulk analyses than surface analyses such as the data obtained by X-ray photoelectron spectroscopy.

A. Porphyrin Precursors

Vanadium Porphyrin on EuY. SEM-EDX spectra of EuYV(p)AAAC are shown in Fig. 1. A sharp V K α peak can be detected in the matrix (Fig. 1b) and only a small V K α peak is observed in the zeolite (Fig.1a), indicating movement of vanadium from the zeolite to the gel after calcination. The large (8.45) V% reported in Table I may be due to V₂O₅ crystallites at the surface produced during calcination. Formation of vanadium is consistent with luminescence results obtained with these materials (10).

Table I. Effects of pretreatments on vanadium migration between the zeolite and the AAA-alumina

Sample	elemental concentrations(wt %)									
	EuY					AAA-alumina				
	Al	Si	V	Eu	V/Eu	Al	Si	V	Eu	V/Eu
AAAV(p)EuY	15.54	66.51	0	17.96	0	18.07	79.43	1.87	0.54	3.44
AAAV(p)EuYC	17.07	70.29	0.43	12.20	.035	18.73	77.39	1.75	0.91	1.92
AAAV(p)EuYCS	17.15	65.36	0.78	16.52	.047	23.37	72.42	1.82	1.26	1.29
EuYV(p)AAA	18.95	61.13	2.45	11.47	0.21	23.54	73.21	0.44	2.81	0.16
EuYV(p)AAAC	19.14	63.84	0.51	16.51	.031	21.16	69.73	8.45	0.67	12.61
EuYV(p)AAACS	17.37	70.63	0.62	11.32	.055	18.71	78.19	1.83	0.79	2.44
EuYV(p)CAAAS	20.67	68.96	0.58	9.79	.059	20.83	74.19	2.42	2.56	0.95
AAAV(p)CEuYS	23.45	65.46	0.52	10.57	.049	23.04	73.54	1.26	2.16	0.57

Table II. Elemental concentrations of calcined and uncalcined EuYV(p) samples

Sample	Elemental concentrations (wt%)				
	Al	Si	V	Eu	V/Eu
EuYV(p)C(...AAA)S	20.23	68.49	0.82	10.46	.079
EuYV(p)(...AAA)C	16.17	63.74	1.61	18.49	.088
EuYV(p)	17.01	64.86	1.32	16.81	.089

Table III. Elemental concentrations on different zeolite particles

Sample	Spot analysis No.	Elemental concentration(wt %)				
		Al	Si	V	Eu	V/Eu
EuYV(p)	1	17.81	59.62	1.05	21.52	0.049
	2	17.75	65.74	1.55	14.96	0.10
	3	17.40	61.47	1.50	19.63	0.076
	4	17.71	65.27	1.32	15.70	0.084
	5	15.66	65.71	0.22	18.41	0.012
	6	15.74	71.32	2.28	10.66	0.214
EuYV(p)(...AAA)C	1	16.71	62.71	1.55	19.03	0.082
	2	16.37	69.69	1.15	12.79	0.090
	3	15.60	58.98	1.99	23.43	0.085
	4	15.99	63.57	1.75	18.69	0.094
EuYV(p)C(...AAA)S	1	19.79	69.69	0.79	9.74	0.081
	2	20.53	67.97	0.82	10.69	0.077
	3	20.38	67.81	0.86	10.96	0.079

In order to quantitatively estimate the degree of vanadium migration, EDX data were used to calculate surface composition; results are presented in Table 1. As in the case for Ni (31), the relative V concentrations or the V-to-Eu ratios are used to quantify V migration, since Eu^{3+} cations are evenly distributed and do not move to the matrix during calcination or steaming. Observation of small amounts of Eu on the gel are due to adhesion of some zeolite crystals to the gel during mixing. The quantitative data in Table 1 show that about 80% of the vanadium initially deposited on the zeolite moves to the matrix after decomposition, indicating that after calcination of the porphyrin complex, vanadium preferentially moves to the matrix.

A trace of vanadium is detected on the matrix component of EuYV(p)AAA (Table 1). The similarity of the V/Eu ratio for the zeolite ((0.21) vs. the matrix (0.16)) for EuYV(p)AAA suggests that there are zeolite particles on the matrix.

After steaming EuYV(p)AAAC , the V $K\alpha$ peak and V/Eu ratio are smaller in the matrix (Fig 2b, Table 1) and a little larger in the zeolite (Fig. 2a, Table 1) than corresponding peaks in the calcined sample (Fig. 1, Table 1). Therefore, some of the vanadium that migrated to the matrix or was present on the surface as V_2O_5 during calcination moves back to the zeolite during steaming. Formation of volatile V-compounds is believed to be the main reason for the decreased peak intensity observed in Figure 2b.

In order to clarify the role of steaming on vanadium migration, the EuY component doped with V (EuYV) was calcined, prior to being mixed with the gel. The SEM-EDX spectra of the steamed sample, (EuYV(p)CAAAS), are illustrated in Fig. 3. Corresponding analytical data are given in Table 1.

As observed in EuYV(p)AAAC , a strong V $K\alpha$ peak is seen in the gel of the EuYV(p)CAAAS mixture (Fig. 3b); however some of the vanadium is still retained in the zeolite (Fig. 3a). Data in Table 1 show that the vanadium concentration is much smaller in the matrix component of this sample than in EuYV(p)AAAC . Thus, it appears that, after steaming a mixture containing calcined EuYV and fresh AAA-alumina, V-transport to the gel still occurs (as observed in EuYV(p)AAAC). However, greater vanadium levels are retained by the gel, Figure 3b, indicating a decreased tendency of the vanadium compounds present to form volatile species.

Vanadium Porphyrin on AAA-alumina. SEM-EDX spectra of AAAV(p)EuYC are presented in Fig. 4. A small vanadium $K\alpha$ peak at 4.96 kV can be observed for the zeolite particles (Fig. 4a) indicating that only small amounts of vanadium initially deposited on the matrix move to the zeolite during calcination, Fig. 4b. Eu K peaks seen for the gel are attributed to the presence of small EuY crystals embedded into the gel macroporous structure, Figure 4b.

When the calcined sample is subsequently steamed, Figure 5 reveals a small increase of the V $K\alpha$ peak in the zeolite component (Fig. 5a) and a decrease of the V peak in the matrix (Fig. 5b) attributed

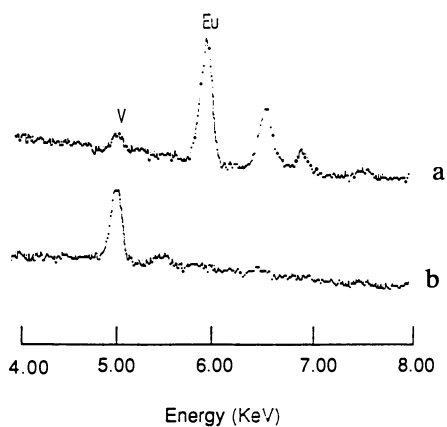


Figure 1. SEM/EDX spectra of EuYV(p)AAAC: (a) zeolite (b) matrix

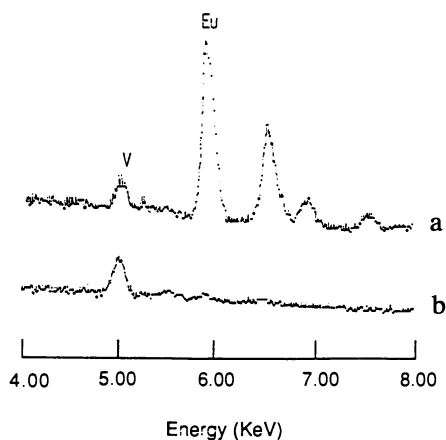


Figure 2. SEM/EDX spectra of EuYV(p)AAACs: (a) zeolite (b) matrix

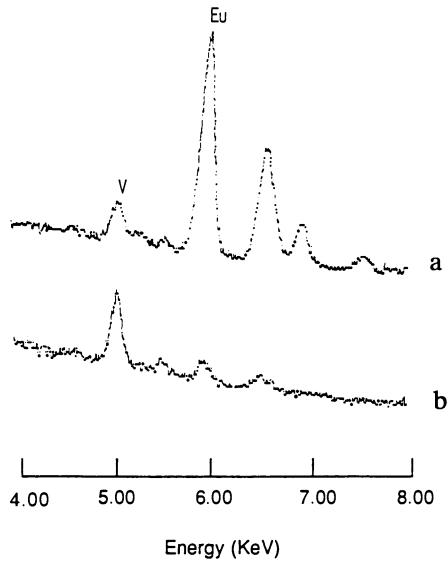


Figure 3. SEM/EDX spectra of EuYV(p)CAAAS: (a) zeolite
(b) matrix

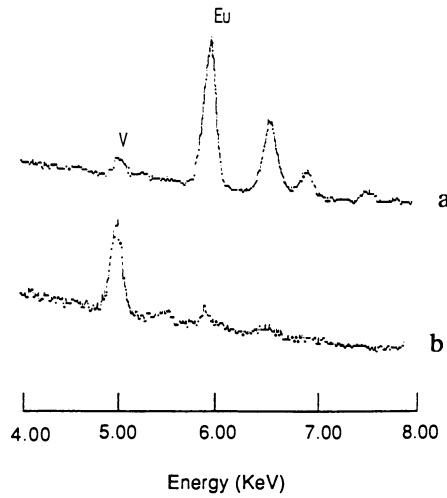


Figure 4. SEM/EDX spectra of AAVV(p)EuYC: (a) zeolite
(b) matrix

mainly to V-losses resulting from the formation of volatile V-compounds. Changes in the V K α peaks shown in Figures 4-5 are in qualitative agreement with changes in V concentrations given in Table I. The similarity between Figures 4 and 6 suggest that after calcination V-loaded gels minimize the formation of volatile V-compounds during steaming. Surface migration of vanadium during calcination has been reported by Jaeras and co-workers (16). Vanadium mobility on solid surfaces has also been observed by luminescence (10) and EPR methods (12).

In the case of AAV(p)CEuYS, a large V K α peak is detected on the zeolite particles (Fig. 6a) and a large peak is observed for the matrix (Fig. 6b), indicating that a small amount of vanadium moves to the zeolite on steaming.

Data of Table I show that the V/Eu ratios in the EuY component of EuYV(p)AAACS and EuYV(p)CAAAS are almost the same, as are the ratios for AAV(p)EuYCS and AAV(p)CEuYS mixtures. Moreover, these V/Eu ratios are larger than those of the other samples. These results suggest that an equilibrium may exist for vanadium migration between the two components during steaming. The larger V/Eu ratio may be due to the interaction of vanadium and europium in the lattice (5, 12).

In summary, the results of Figs. 1-6 reveal that calcination of the porphyrin complex induce vanadium migration and that V mobility is minimized when V is initially placed on the gel. Calcination of V-loaded supports prior to mixture formation minimizes V-losses during steaming.

B. Naphthenate Precursors

To understand the effects of the different ligands on V-migration during thermal treatments, vanadyl naphthenate precursor has also been used as dopants. The results for two calcined samples (EuYV(n)AAAC and AAV(n)EuYC), are presented in Figs. 7 and 8, respectively. In contrast to the results shown in Fig. 1-6, no measurable V migration occurs from the zeolite to the matrix (Fig. 7) and only a trace of V moves from matrix to the zeolite (Fig. 8). Thus vanadium precursors can alter V mobility during calcination

Figures 9 and 10 show that during steaming only a trace of vanadium can move from the zeolite (in EuYV(n)AAACS mixtures) to the matrix (Fig. 9), while considerable V migration from the matrix of AAV(n)EuYCS to the zeolite occurs (Fig. 10) after steaming. As before, the decrease in V K peak intensity in Figure 10b is attributed (in part) to V losses due to the formation of volatile V-compounds.

By comparing these results to those obtained using the vanadium porphyrin precursor, it can be concluded that vanadium from the porphyrin tends to stay on the matrix after thermal pretreatments (see Fig. 4), whereas vanadium from the naphthenate is preferentially associated with the zeolite after steaming, Fig. 9. These observations are in agreement with the report (1) that vanadium impregnated from vanadyl naphthenate migrated to the zeolite from the matrix surface during steam treatment. This different behavior of the two precursors

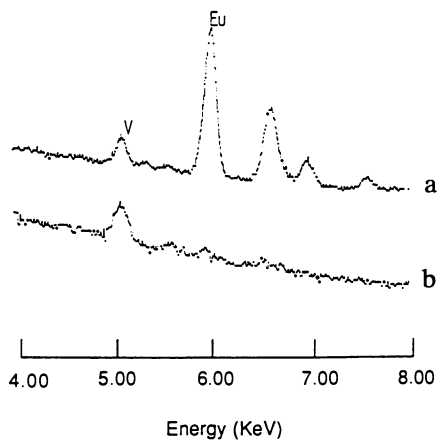


Figure 5. SEM/EDX spectra of AAV(p)EuYCS: (a) zeolite (b) matrix

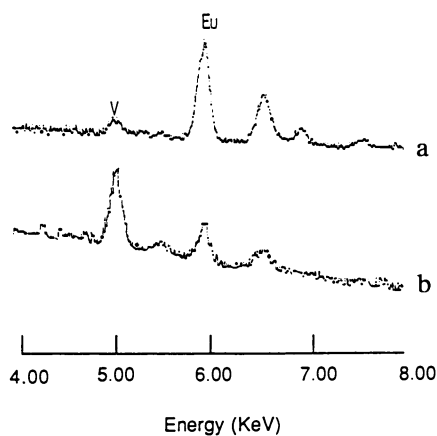


Figure 6. SEM/EDX spectra of AAV(p)CEuYS: (a) zeolite (b) matrix

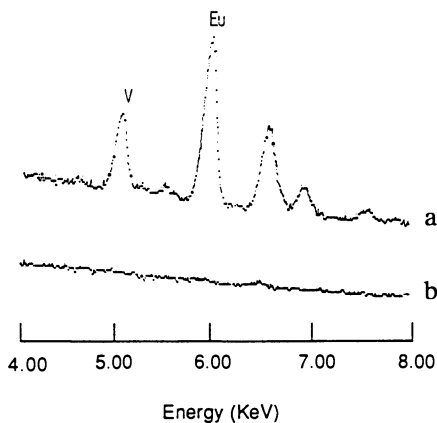


Figure 7. SEM/EDX spectra of EuYV(n)AAAC: (a) zeolite (b) matrix

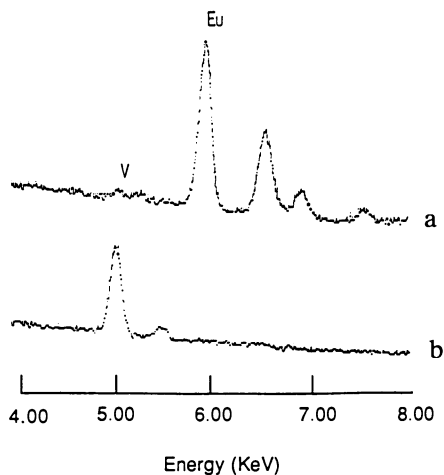


Figure 8. SEM/EDX spectra of AAAV(n)EuYC: (a) zeolite (b) matrix

may be due to different vanadium surface species in the matrix and in the zeolite produced during steam aging, as well as to different migration mechanisms.

C. Migration Mechanisms

Calcination. Based on the above data and other reports concerning surface vanadium species (12), migration mechanisms may be different for catalysts loaded with metals containing porphyrin or naphthenate ligands.

During calcination, vanadium precursors are initially oxidized to some intermediates. Such intermediates may be produced at the interface of the zeolite and the matrix. Moreover, they are probably different for the two precursors and act as active gettering species for vanadium migration. In the case of vanadyl porphyrin, it is found that if calcination of EuYV(p)AAA is conducted at 200°C, the sample keeps its initial brown color and no migration to the gel occurs (Fig. 11a). This is in agreement with a report (6) that after calcination below 200°C, vanadyl porphyrin was intact, indicating that molecularly-adsorbed vanadyl porphyrin does not migrate. Calcination at 390°C, induces the sample to be lighter in color, indicating a transformation of the porphyrin into some intermediates, and vanadium migration to the gel takes place (Fig. 11b). This result is also in accord with reports (1, 32) that calcination or heating in N₂ at 300°C resulted in loss of the conjugated ring structure of the porphyrin and formation of an intermediate. Such intermediates may be responsible for migration during calcination.

When calcination was performed at 470°C, the sample turns light yellow, indicating the conversion of intermediates probably into oxides and other species, accompanied by further V migration to the gel (Fig. 11c). Luminescence measurements from our laboratory (33) have shown that calcination at 470°C results in complete disappearance of vanadyl porphyrin peaks and appearance of some new excitation peaks which can not be observed in the corresponding excitation spectrum of the EuYV(p)AAAC sample. These data suggest that intermediates exist after calcination and that these species may play a critical role during V migration.

Furthermore, it has been reported (1) that porphyrin deposited on a Nd-Y zeolite completely decomposes at about 420°C, but deposition on an amorphous silica-alumina begins to decompose at ca. 400°C and extends over at least a 150°C temperature range, indicating that the thermal stability of the porphyrin is higher on the silica-alumina gel than on the zeolite. The light yellow color of the EuYV(p)AAA sample calcined at 470°C (and corresponding luminescence results (33) suggests that surface intermediates are also present on the matrix surface. It is believed that intermediates act as active species for migration between the two FCC components. In addition, the formation of such intermediates may enhance V dispersion on the zeolite particles (Table III).

In order to see whether intermediate species are associated with aluminum or silicon (or both) in the matrix, EuYV(p) was mixed with

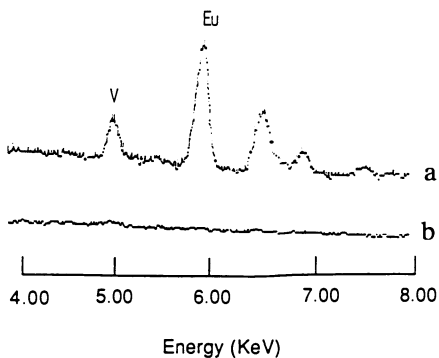


Figure 9. SEM/EDX spectra of EuYV(n)AAACS: (a) zeolite (b) matrix

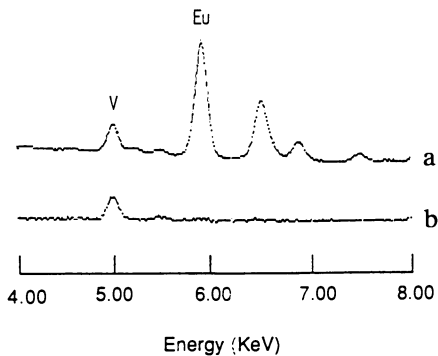


Figure 10. SEM/EDX spectra of AAV(n)EuYCS: (a) zeolite (b) matrix

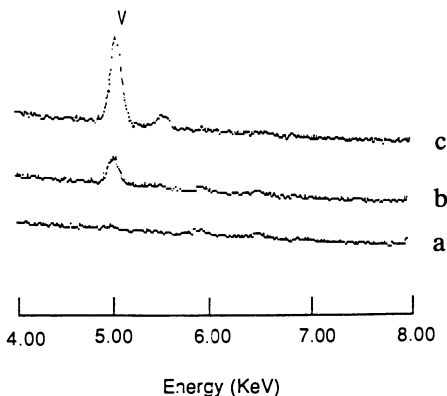


Figure 11. SEM/EDX spectra of the gel for a EuYV(p)AAA mixture calcined at: (a) 200°C; (b) 390°C and (c) 470°C.

either a SiO₂ gel (from Cabot Corporation) or γ -Al₂O₃ from (Engelhard Corporation) and then the mixture was calcined as above. The results are presented in Fig. 12. No V K α peak can be detected in the SiO₂ matrix (Fig. 12a), indicating that migrating V was not retained by the silica surface or that little migration from the zeolite during calcination has occurred. However, vanadium can move from the zeolite to γ -Al₂O₃ (Fig. 12b) as it does with the AAA-alumina matrix (Fig. 1b). Therefore, these results indicate that stable surface intermediates after migration are associated with aluminum in the matrix rather than silicon, probably due to the formation of V⁺⁵-O-Al linkages (34-37).

As for vanadyl naphthenate, intermediates formed on calcination may be different than in the porphyrin system, since little migration can be found in the EuYV(n)-AAA or in the EuYV(n)- γ -Al₂O₃ systems mentioned above (Fig 12b). Moreover, such intermediates are probably more stable on the zeolite than on the matrix, since migration from the AAA-alumina matrix to the zeolite occurs, but not vice versa, Figs. 9-10.

Calcination products of the two vanadium precursors are different. Calcination of the deposited vanadyl naphthenate gives rise mainly to VO²⁺ in the zeolite and V₂O₅ in the matrix (12, 28). However, luminescence measurements (33) of EuYV(p)AAAC and AAAP(p)C do not show the formation of V₂O₅, as reported elsewhere for vanadyl porphyrin (28). Instead, a small amount of EuVO₄ can be observed in EuYV(p)AAAC and EuYV(p)C, indicating the formation of EuVO₄ in the zeolite after calcination. In the matrix, V⁺⁵-O-Al species may be present.

A reviewer has suggested that V(n) and V(p) decomposition may be different during calcination. For V(n), decomposition may involve intermediates of V that migrate to sodalite cages or hexagonal prisms. On the other hand, V species from V(p) may result in decomposition products either in supercages or on external surfaces of the zeolite.

Steaming. Migrating V species generated by the two precursors during steaming should also differ. In fact, little migration from the zeolite to the matrix occurs for EuYV(n)AAACS (Fig. 9), while significant transport can be observed for EuYV(p)CAAAS (Table I). Moreover, different vanadium species, due to different precursors, have been implicated elsewhere (37). In the case of vanadyl naphthenate, the existence of bulk V₂O₅ species on the AAA-alumina should (at least in part) be responsible for vanadium migration from the matrix to the zeolite, as is the case for vanadium on kaolin (5) and other supports (1). Although, after steaming, V₂O₅ was still found to be the main species present in the matrix (12, 28) at hydrothermal conditions, vanadates, such as EuVO₄, can form in the zeolite (5, 12).

The irreversible formation of EuVO₄ may favor the migration of vanadium to the zeolite and eventually causes the collapse of the zeolite structure. As for the porphyrin system, luminescence studies (33) have shown the formation of more EuVO₄ in EuYV(p)CAAAS than in EuYV(p)AAAC, indicating the importance of water vapor in the

formation of EuVO_4 thus lending support to mechanism of EuVO_4 formation (5, 12). In the matrix, luminescence results (33) suggest the absence of V_2O_5 at these V-loadings, but HO-V-O-Al species have been proposed (34).

As for calcination, intermediates formed during steaming appear to play a role in vanadium migration. This is supported by a comparison of Fig. 7 with Fig. 13, which shows that V migrates from the zeolite to $\gamma\text{-Al}_2\text{O}_3$ during steaming. There is no migration in the $\text{EuYV}(n)\text{AAACS}$ system (Fig. 7), whereas substantial migration is observed from the zeolite to $\gamma\text{-Al}_2\text{O}_3$ in $\text{EuYV}(n)\text{-}\gamma\text{-Al}_2\text{O}_3\text{CS}$ (Fig.13). Since little migration occurs in either of the two systems during calcination, starting species for V migration may be the same. Thus, the nature of intermediates and/or products formed in the matrix during steaming might be responsible for vanadium migration. Further experiments need to be undertaken to understand the nature of these intermediates.

Data for calcined and dried $\text{EuYV}(p)$ samples of Table II show similar Si/Al and V/Eu ratios before and after calcination. Elemental concentration data for different zeolite particles of Table III show that the reproducibility of these experiments is quite good and that the samples are laterally uniform. One noted exception is point 6 of sample $\text{EuYV}(p)$ with respect to the other 5 points.

CONCLUSIONS

The presence or absence and mechanism of vanadium migration are found to depend largely on the vanadium precursors used to contaminate the solid surface. If vanadium naphthenate is used, no migration occurs from the zeolite to the matrix during calcination and a little vanadium migrates to the zeolite from the matrix. Steaming induces trace amounts of vanadium on the $\text{EuYV}(n)\text{AAAC}$ sample to move to the matrix, in contrast to the considerable migration observed from the matrix to the zeolite for $\text{AAAV}(n)\text{EuYC}$. These observations indicate that vanadium prefers to remain on the zeolite probably in the form of VO^{2+} ions after calcination and in the form of EuVO_4 after steaming. However, if vanadium porphyrin is used, about 80 % of the vanadium initially impregnated onto the zeolite can move to the matrix during calcination. For vanadium initially deposited on the matrix, only a trace of vanadium migrates to the zeolite during calcination. These data demonstrate that vanadium prefers to remain on the matrix after calcination of the porphyrin loaded system. Steaming causes some of the vanadium that migrated to the matrix during calcination to move back to the zeolite and also results in further transport of vanadium initially deposited on the matrix to the zeolite. Therefore vanadium migration during calcination and steaming in vanadium migration appears to be different, probably due to different vanadium intermediates produced by the two thermal treatments.

The nature of the matrix is found to significantly influence migration. During calcination, $\text{V}(p)$ initially deposited on the zeolite can move to $\gamma\text{-Al}_2\text{O}_3$ as significantly as it does with AAA-alumina, but it is not retained

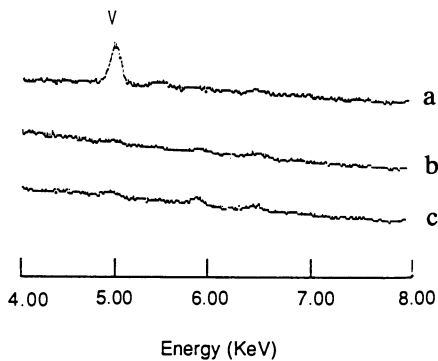


Figure 12. SEM/EDX spectra of (a) SiO_2 in $\text{EuYV(p)SiO}_2\text{C}$ mixture; (b) $\gamma\text{-Al}_2\text{O}_3$ in $\text{EuYV(n)-}\gamma\text{-Al}_2\text{O}_3\text{C}$ mixture. and (c) $\gamma\text{-Al}_2\text{O}_3$ in EuYV(p)-mixture

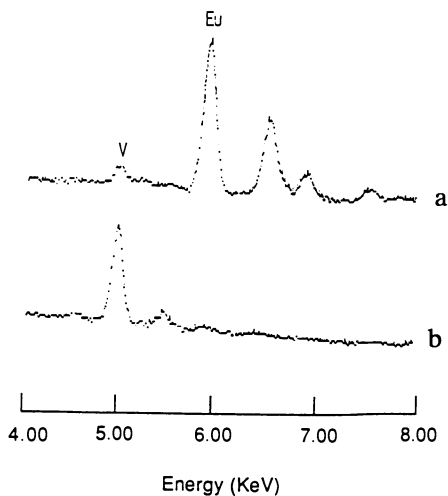


Figure 13. SEM/EDX spectra of $\text{EuYV(p)-}\gamma\text{-Al}_2\text{O}_3\text{CS}$ mixture: (a) zeolite (b) matrix.

on SiO₂ gel. Therefore, migration of vanadium in EuYV(p)AAAC is associated with the aluminum in the AAA-alumina probably by V-O-Al linkages. No migration to γ -Al₂O₃ is observed during calcination if the naphthenate is used, but steaming does induce significant migration of vanadium from the zeolite to the alumina. Therefore, the ability of matrices to trap vanadium decreases in the order: γ -Al₂O₃ > AAA-alumina > SiO₂. In addition to migrate between the two components, vanadium can move between zeolite particles during calcination and in particular during steaming.

Intermediates may be different for the two vanadium precursors. For the porphyrin, calcination intermediates are found to be associated with aluminum in the matrix. No such relation has been found for the naphthenate. Pretreatment products are also different for the two precursors. Some amounts of EuVO₄ are formed in the zeolite and no V₂O₅ is present in the matrix (at the V-loaded area) after calcination of the porphyrin-doped sample. The naphthenate-doped samples after calcination contain VO²⁺ in the zeolite and V₂O₅ in the matrix (12). Steaming induces the formation of EuVO₄ in the zeolite for samples prepared from either precursor. V₂O₅ is the main surface species generated by naphthenates (12), but it is not observed on samples loaded with V-porphyrin precursor.

ACKNOWLEDGEMENTS

Support for this research from the National Science Foundation under the Kinetics and Catalysis Program through grant CBT-08814974 is gratefully acknowledged.

REFERENCES

1. Andersson, S.L.T., Lundin, S.T., Jaeras, S. and Otterstedt, J.E. *Applied Catal.*, **9** (1984) 317.
2. Beyerlein, R.A., Tamborski, G.A., Marshall, C.L., Meyers, B.L., Hall, J.B. and Huggins, B.J. *Prepr. Div. Pet. Chem. Amer. Chem. Soc.*, **35** (1990) 694.
3. Schubert, P.F. *Prepr. Div. Pet. Chem. Amer. Chem. Soc.*, **32** (1987) 673.
4. Chester, A.W. *Ind. Eng. Chem. Res.*, **26** (1987) 863.
5. Occelli, M.L. and Stencel, J.M. in " Fluid Catalytic Cracking: Its Role in Modern Refining ", ACS Book Series No.375, M. L. Occelli, Ed., p.195 (1988).
6. Roth, S.A., Iton, L.E., Fleisch, T.H., Meyers, B.L., Marshall, C.L. and Delgass, W.N. *J. Catal.*, **108** (1987) 214.
7. Otterstedt, J.E., Gevert, S.B., Jaeras, S. and Menon, P.G. *Applied Catal.*, **22** (1986) 159.
8. Occelli, M.L., Psaras, D. and Suib, S.L. *J. Catal.*, **96** (1985) 363.
9. Occelli, M.L., Psaras, D. and Suib, S.L. *Acta Chim. Phys.*, (1985) 423.

10. Anderson, M.W., Suib, S.L. and Occelli, M.L. *J. Catal.*, **118** (1989) 31.
11. Anderson, M.W., Suib, S.L. and Occelli, M.L. *J. Mol. Catal.*, **61** (1990) 295.
12. Anderson, M.W., Suib, S.L. and Occelli, M.L. *J. Catal.*, **122** (1990). 374.
13. Suib, S.L., Anderson, M.W. and Occelli, M.L. in "Characterization and Catalyst Development", S.A. Bradley, M.J. Gatusso, R.J. Bertolacini, Eds., ACS Symposium Series, 411, Washington, DC, Chapter 5, 40-45, **1989**.
14. Altomare, C.A., Koermer, G.S., Schubert, P.F., Suib, S.L. and Willis, W.S. *Chem. of Mater.*, **1** (1989) 459.
15. Ritter, R.E., Rheahme, L., Welsh, W.A. and Magee, J.S. *Oil and Gas J.*, **79** (1981) 103.
16. Jaeras, S. *Applied Catal.*, **2** (1982) 207.
17. Mitchell, B.R., *I. E. D. Prod. Res. Dev.*, **19** (1980) 209.
18. Pompe, R., Jaeras, S., Vannerberg, N.-G. *Applied Catal.*, **13** (1984) 171.
19. Masuda, T., Ogata, M., Yoshida, S. and Nishimura, Y. *Int. Chem. Eng.*, **25** (1985) 340.
20. Wormsbecher, R.F., Peters, A.W. and Maselli, J.M. *J. Catal.*, **100** (1986) 130.
21. Kugler, E.L. and Leta, D.P. *J. Catal.*, **109** (1988) 387.
22. Schubert, P.F., Altomare, C.A. in "Fluid Catalytic Cracking", ACS, Washington, DC, p.182 (1989).
23. Occelli, M.L. in "Fluid Catalytic Cracking: Its Role in Modern Refining", ACS Book Series No. 375, M. L. Occelli, Ed., p.162 (1988).
24. Woolery, G.L., Chin, A.A., Kirker, G.W. and Huss, A. Jr., *Physica B*, **158** (1989) 213; in "Fluid Catalytic Cracking: Its Role in Modern Refining", ACS Book Series No. 375, M. L. Occelli, Ed., p.215 (1988)
25. Maselli, J.A. and Peters, A.W. *Catal. Rev. Sci. Eng.*, **26** (1984) 525.
26. Masuda, T., Ogata, M., Ida, T., Takaura, K. and Nishimura, Y. *J. Japan. Pet. Inst.*, **26** (1983) 344.
27. Nishimura, Y., Masuda, T., Sato, G. and Egashira, S. *Prepr. Div. Pet. Chem. Amer. Chem. Soc.*, **28** (1983) 707.
28. Kurihara, L., Occelli, M.L. and Suib, S.L. in "Fluid Catalytic Cracking II: Concepts in Catalyst Design", ACS Symposium Series 452, M.L. Occelli, p.224 (1990).
29. Marriott, P.J., Gill, J.P., Evershed, P.R, Hill, C.S. and Eglinton, G. *J. Chromatogr.* **301** (1984) 107.
30. Wolff, G.A., Chicarelli, M.I., Shaw, G.J., Evershed, R.P., Quirke, J.M.E. and Maxwell, J.R. *Tetrahedron*, **40** (1984) 3786.
31. Shen, Y.-F., Suib, S.L. and Occelli, M.L. "SEM-EDX Study of Nickel Migration in Model FCC Catalysts", in preparation.
32. Streusand, B.J. and Schrader, G.L. *Appl. Spectrosc.*, **38** (1984) 433.
33. Shen, Y.-F., Suib, S.L. and Occelli, M.L. in preparation.

34. Ocelli, M.L. and Stencel, J.M. in "Fluid Catalytic Cracking II: Concepts in Catalyst Design", ACS Symposium Series 452, M.L. Ocelli, p.252 (1990).
35. Anpo, M., Sunamoto, M., Che, M. *J. Phys. Chem.*, 93 (1989) 1187.
36. Anpo, M., Suzuki, T., Yamada, Y., and Che, M. Proc. 9th Int. Congr. Catal., 1513 (1988).
37. Iyer, P.S., Eckert, H., Ocelli, M.L. and Stencel, J.M. *Prepr. Div. Pet. Chem. Amer. Chem. Soc.*, 35 (1990) 770.

RECEIVED July 10, 1992

Chapter 14

Shape-Selective Catalysis with Zeolites and Molecular Sieves

Charles B. Khouw and Mark E. Davis

Department of Chemical Engineering, California Institute of Technology,
Pasadena, CA 91125

The types of shape selective catalysis that occur in zeolites and molecular sieves are reviewed. Specifically, primary and secondary acid catalyzed shape selectivity and encapsulated metal ion and zero valent metal particle catalyzed shape selectivity are discussed. Future trends in shape selective catalysis, such as the use of large pore zeolites and electro- and photo-chemically driven reactions, are outlined. Finally, the possibility of using zeolites as chiral shape selective catalysts is discussed.

Zeolites are crystalline aluminosilicates that are constructed from TO_4 tetrahedra (T = tetrahedral atom, e.g., Si, Al); each apical oxygen atom is shared with an adjacent tetrahedron. Thus, the ratio of O/T is always equal to 2. A SiO_4 unit in a framework (structure) is neutral since an oxygen atom bridges two T atoms and shares electron density with each (Figure 1). However, since Al is +3, for every aluminum containing tetrahedron there is a net -1 charge which must be balanced by a cation. The tetrahedra are coordinated such that the zeolites have open framework structures with high surface areas. Access to the cavities is possible through voids of various sizes which are of the size of small molecules. Because of these unique properties, zeolites are able to be shape and size selective in catalytic molecular rearrangements.

Approximately 70 distinct structures of zeolites and molecular sieves are known (2). There are natural zeolites, synthetic analogues of natural zeolites, and synthetic zeolites with no natural counterparts. Their pore sizes range from 4 Å to 13 Å as illustrated in Figure 2. Zeolites with pores that are comprised of eight T-atoms (and eight oxygen atoms) are considered small pore zeolites. They have free diameters of 3.0-4.5 Å, e.g., zeolite A. Medium pore zeolites have pores formed by ten T-atom rings with 4.5-6.0 Å free diameter, e.g., ZSM-5. Zeolites with twelve or more T-atoms in rings that make-up the pores are considered large pore zeolites. They have free diameters of 8.0 Å or more, e.g., zeolite X and Y (3). To date, no zeolite (aluminosilicate) exists with pores larger than ~ 8 Å. In addition to zeolites, there are now many non-aluminosilicate molecular sieves. Referring to Figure 1, if tetrahedra containing aluminum and phosphorous are connected in a strict Al/P = 1, a neutral framework is obtained. The aluminophosphate or AlPO_4 is the "3-5" analogue of the "4-4" pure SiO_2 . Also, other elements can be incorporated into the AlPO_4 framework

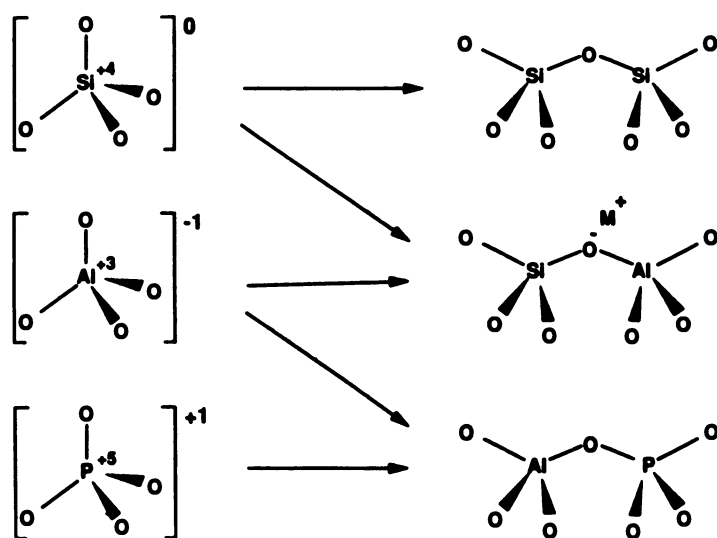


Figure 1. Basic building blocks of zeolites—molecular sieves. (Reproduced from reference 1. Copyright 1991 American Chemical Society.)

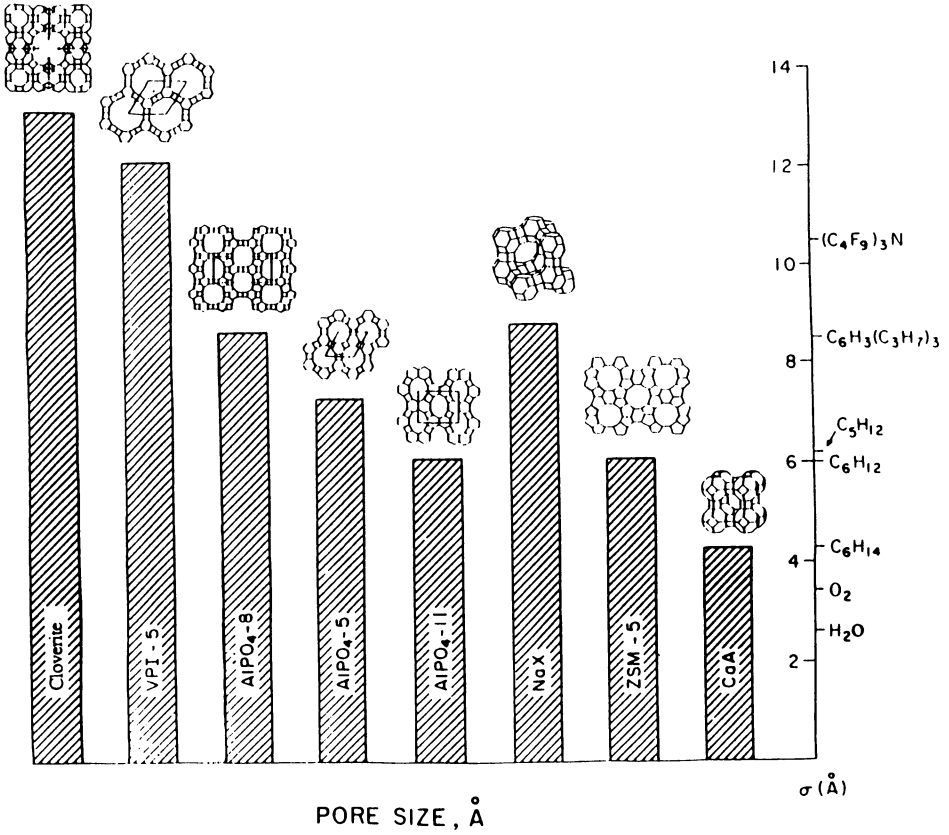


Figure 2. Typical zeolite pore sizes compared to the diameter of various molecules. (Adapted from ref. 1.)

to make them charged, e.g., silicoaluminophosphates or SAPO's. Of particular importance to this review is the fact that phosphate-based molecular sieves have extended the pore size range from 8 Å to 13 Å. Figure 2 shows some typical framework projections containing various rings (pores) of different sizes. However, it should be noted that the data shown for cloverite and $\text{AlPO}_4\text{-8}$ are the maximum dimension as determined from the crystal structure. For $\text{AlPO}_4\text{-8}$, the structure is faulted and the adsorption behavior that would be expected from the crystal structure can not be obtained (4). Also, adsorption data revealing the pore size of cloverite is not yet reported.

In this paper, we review primary and secondary shape selective acid catalysis with zeolites. Next, we discuss shape selectivity with metal containing zeolites. We conclude with a section that deals with future trends in shape selective catalysis.

Acid Catalyzed Shape Selectivity in Zeolites

Primary Shape Selectivity. There are several types of shape and size selectivity in zeolites. First, the reactant molecules may be too large to enter the cavities. A particularly good illustration of this behavior is given by Weisz and co-workers (5). Zeolites A and X were ion exchanged with calcium salts to create acid sites within the zeolite. These acid sites are formed as the water of hydration around the calcium ions hydrolyzes. When these zeolites are contacted with primary and secondary alcohols in the vapor phase, both alcohols dehydrate on CaX but only the primary one reacts on CaA. Since the secondary alcohol is too large to diffuse through the pores of CaA, it can not reach the active sites within the CaA crystals. This kind of selectivity is called reactant shape selectivity and is illustrated in Figure 3.

Product shape selectivity occurs when reaction products of different sizes are formed within the interior of the zeolite crystals and some of the products formed are too bulky to diffuse out (6). The products which cannot escape from the cavities may undergo secondary reactions to smaller molecules or may deactivate the catalyst by blocking the pores. A classic example of this type of selectivity is the monomolecular isomerization reactions of alkylaromatics as depicted in Figure 3. The diffusion coefficient for para-xylene in ZSM-5 is approximately a thousand times that of either ortho or meta-xylene. Hence, essentially pure para-xylene is observed leaving the zeolite. Direct evidence for this type of shape selectivity has been reported by Anderson and Klinowski (7) for the catalytic conversion of methanol to hydrocarbons in ZSM-5. During the reaction, methanol is dehydrated to dimethyl ether (DME). The equilibrium mixture between methanol and DME reacts to form olefins, aliphatics and aromatics. By using *in situ* magic angle spinning NMR, 29 different organic species were identified in the adsorbed phase; however not all of these were observed with gas chromatography. For example, the tetramethylbenzenes that are formed in the pores of ZSM-5 do not diffuse out from the zeolites to be observed with gas chromatography.

Another type of shape selectivity is transition-state shape selectivity. For this type of selectivity, certain types of transition-state intermediates are too large to be accommodated within the pores/cavities of the zeolites. However, neither the reactants or the products are restricted from diffusing through the pores of the zeolites. A good example of this type of selectivity is the transalkylation of dialkylbenzenes. In this reaction, an alkyl group is transferred from one molecule to another through a diphenylmethane transition state. For meta-xylene, this reaction will produce 1,3,5- as well as 1,2,4-trialkylbenzene. However, the transition state for the reaction that yields 1,3,5-trialkylbenzene is too large to be accommodated within the pores of mordenite. Consequently, only 1,2,4-trialkylbenzene is selectively formed inside the zeolite as illustrated in Figure 3.

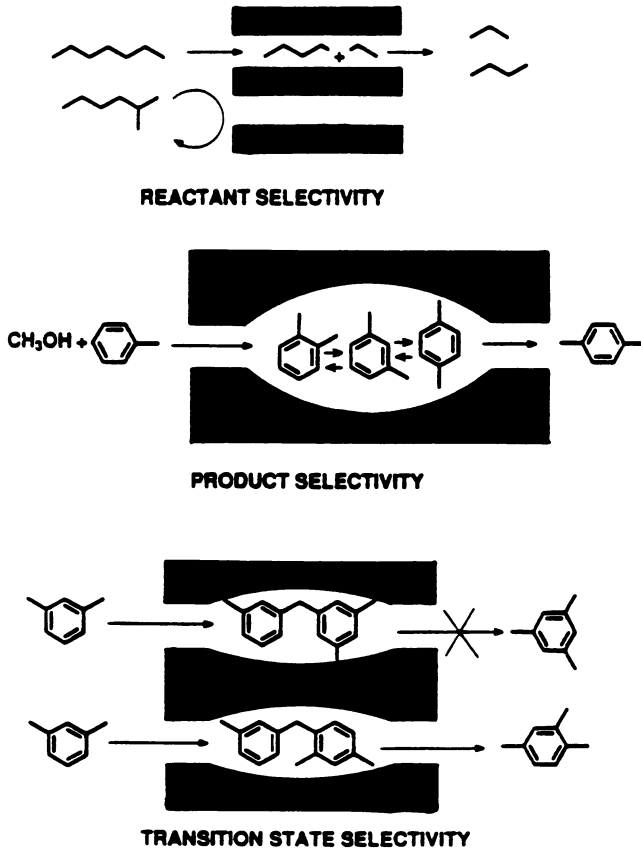


Figure 3. Schematic representation of the types of shape selectivity exhibited by zeolites. (Reproduced from reference 1. Copyright 1991 American Chemical Society.)

Transition-state selectivity is sometimes difficult to distinguish from product shape selectivity. A recent study by Kim et al. (8) shows that the high para-selectivity for the alkylation of ethylbenzene with ethanol in metallosilicates (MeZSM-5) is not due to product selectivity alone. They conclude that the primary product of the alkylation on ZSM-5 type metallosilicates is p-diethylbenzene which isomerizes further inside the cavity of ZSM-5 to other isomers. As the acid sites of zeolites becomes weaker (achieved by substituting different metals into the framework of the zeolite), the isomerization of the primarily produced p-isomer is suppressed. Although Kim et al. attribute this suppression of the isomerization activity to restricted transition-state selectivity, it is more likely that this suppression is due to the decrease in acid strength.

Direct observation of transition-state selectivity has been observed from the low-temperature cyclization of dienes inside H-mordenite and H-ZSM-5 (9). By using electron spin resonance (ESR) spectroscopy, it has been possible to explore radical formation upon the sorption of dienes on H-mordenite and H-ZSM-5. From the analysis obtained, it was found that the dienes are not very reactive for oligomerization inside H-mordenite channels. Heating H-mordenite with presorbed 1,4-pentadiene or 1,5-hexadiene yields selective cyclization of molecules via cycloalkenic radicals inside the H-mordenite channel. However, in the smaller pores of H-ZSM-5 (although the nature of both acid and redox sites in both zeolites are the same) no cyclo-olefinic radicals are formed as shown by the ESR spectrum. These experiments illustrate the reality of transition-state selectivity inside the pores of zeolites.

Secondary Shape Selectivity. The shape selectivity behavior of zeolites can be altered when other molecules are present in addition to the reactant molecules. (This phenomenon does not happen in unrestricted environments.) This type of selectivity is called "secondary shape selectivity" (10) or "coreactant-induced modification" (11). Santili et al. (10) showed that over SSZ-16 n-hexane inhibits the cracking of n-hexadecane under hydrocracking conditions, and that the cracking of n-hexane is only slightly affected by the presence of n-hexadecane. This inhibition is attributed to a steric effect in which n-hexane and the SSZ-16 pores keep the n-hexadecane from reacting. Although the specific interaction between the reactants and the zeolite pores has not been elucidated, it is likely that n-hexane causes the n-hexadecane concentration in the zeolite pores to decrease when these two molecules are present together in the feed. Namba et al. (12) showed that 2,2-dimethylbutane retards the cracking of n-octane in ZSM-5. They believe that this inhibition is due to the very hindered diffusion of 2,2-dimethylbutane in the pores of ZSM-5. As a result, the diffusion of the sterically smaller n-octane is severely restricted by the larger molecule, 2,2-dimethylbutane. Since the behavior illustrated by these two examples does not occur in an unrestricted environment, these systems can be classified as "secondary shape selectivity." Nevertheless, there is a difference between these two experiments. In the first case, a smaller molecule inhibits the cracking of a larger molecule while the latter shows that the cracking of a smaller molecule is inhibited by a larger molecule.

Another example of secondary shape selectivity is shown by John and co-workers (11,13). They found that the hydroisomerization/hydrocracking of n-hexane over Pt/H-mordenite is significantly inhibited by the presence of benzene. They also found a correlation between the aromatic size relative to zeolite pore size on the inhibition of the hexane reaction and the changes in isomer selectivities. Figure 4 illustrates the relation between the various aromatics co-fed and the n-hexane isomerization rates on H-mordenite. From Figure 4, it is shown that as the kinetic diameter of the aromatics is increased, the isomer formation rate appears to pass through a minimum. This result can be explained by considering the size of the zeolite pore and the kinetic

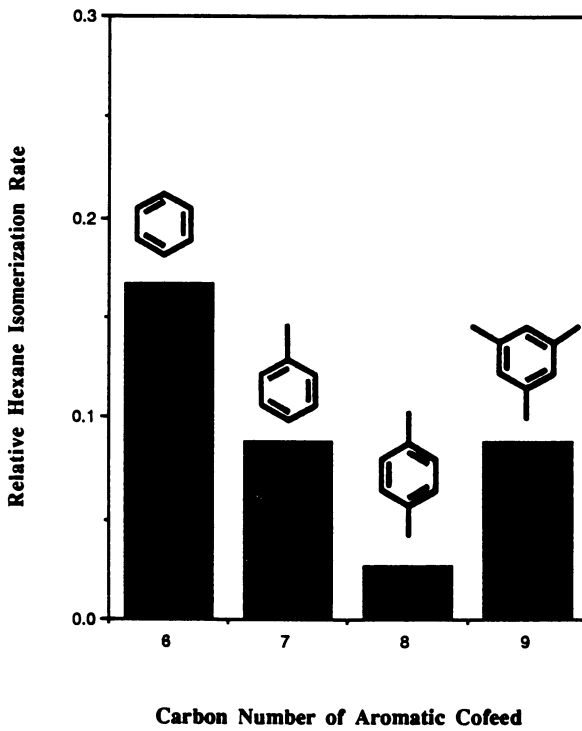


Figure 4. Correlation between relative n-hexane reaction rate and various aromatic co-fed (1.0 refers to pure n-hexane feed).

diameters of the aromatics. Benzene, toluene and p-xylene have kinetic diameters of 6.75 Å each while mesitylene has an effective size of 8.4 Å (14). H-mordenite has a reported effective size of 6-7 Å (15). Since benzene, toluene and p-xylene can diffuse easily into the pores of H-mordenite, the paraffin reaction is more inhibited as the molecule size increases. For mesitylene, competition by the aromatic for access to the interior sites is reduced which allows the paraffin reaction to proceed unperturbed. Both inhibition and modification of the isomer selectivity of the paraffin reaction by aromatic co-feeds are attributed to a site suppression mechanism in which the effective number of the catalytic sites available for the paraffin reaction is reduced and to a pore blockage mechanism which creates diffusional barriers for both the reactants and products.

Metal Catalyzed Shape Selectivity in Zeolites

In addition to performing acid/base catalysis, zeolite structures can serve as hosts for small metal particles. Transition metal ions, e.g., platinum, rhodium, can be ion exchanged into zeolites and then reduced to their zero valent state to yield zeolite encapsulated metal particles. Inside the zeolite structure, these particles can perform shape selective catalysis. Joh et al. (16) reported the shape selective hydrogenation of olefins by rhodium encapsulated in zeolite Y (specifically, cyclohexene and cyclododecene). Although both molecules can be hydrogenated by rhodium supported on nonmicroporous carbon, only cyclohexene can be hydrogenated by rhodium encapsulated in zeolite Y since cyclododecene is too large to adsorb into the pores of zeolite Y.

When metal centers act in conjunction with acid sites on the zeolite, bifunctional catalysis can occur (e.g., Pd/HY). This type of catalysis is used mainly for the hydrocracking and isomerization of long-chain n-alkanes. For example, the rates of formation of 2- and 5-methylnonane isomers obtained from n-decane isomerization over bifunctional zeolite catalysts depend on the size and structure of the zeolites used. This reaction has been developed as a test reaction to characterize zeolite structures (17-19).

The ability of zeolites to be ion-exchanged with metal ions broadens their uses as supports for active components such as Pd, Cu, V, Fe by performing shape selective redox reactions. The oxidative acetoxylation of propene to give allyl acetate has been shown to be selectively catalyzed by ion-exchange zeolites: Pd/Cu-erionite, Pd/Cu-mordenite and Pd/Cu-faujasite give 90%, 70% and 40% selectivity, respectively. However, the alkali metal ions present in the zeolite before replacement by Pd and Cu may also affect the activity and selectivity of this reaction (20). The direct catalytic oxidation of ethylene with dioxygen to give acetaldehyde with Pd^{II} and Cu^{II} in concentrated chloride solution is known as the homogeneous Wacker process. Recently Espeel et al. (21) demonstrated the use of a zeolite as a "solid solvent". They showed that faujasite-type zeolites with specific Si/Al ratios exchanged with Pd(NH₃)₄²⁺ and Cu²⁺ catalyzed the oxidation of ethylene to acetaldehyde in a manner similar to the homogeneous Wacker system. The active center was assumed to be the partially ammoniated Pd²⁺ ion; the chloride ion in the homogeneous phase is replaced by the anionic zeolite framework.

The unique structure and the ability of zeolites to be ion exchanged with metal ions show promise for the development of inorganic mimics of various enzymes. Herron (22) prepared a mimic of Cytochrome P-450 by exchanging Pd^{II} and Fe^{II} ions into different zeolite structures. The Pd^{II} was then reduced to Pd⁰ by reduction in hydrogen. Pd⁰ has been found to convert hydrogen and oxygen into hydrogen peroxide which is used by the Fe^{II} ions to hydroxylate the organic substrates. The partial oxidation of n-octane on Pd⁰/Fe^{II}-ZSM-5 shows that this catalyst has a

remarkable regioselectivity. Since it is believed that the oxidation actually proceeds via a direct combination of hydrogen and oxygen over the Pd⁰ catalyst producing hydrogen peroxide, a direct feed of hydrogen peroxide into iron zeolites should yield the same net oxidation effect. Table I depicts some of the results from the n-octane/cyclohexane reactions over Fe^{II}/zeolites with hydrogen peroxide.

Table I. Selectivity in oxidations using Fe^{II}/zeolites and hydrogen peroxide (22)

Catalyst	Substrate Selectivity n-octane: cyclohexane	Regio Selectivity n-octane			
		1	2	3	4
Carbon position		1	2	3	4
Fe on amorphous silica-alumina	1 : 1	4	35	32	27
Fe on zeolite A	205 : 1	35	27	22	16
Fe on ZSM-5	5 : 1	45	23	19	13

It is interesting that selectivity for oxidation toward the end of the octane chain is increased when using the zeolite catalysts, especially at the terminal methyl group (unusual for alkane oxidation). It has been postulated that the conformation of the reactant approaching the active sites inside the zeolite framework dictates the selectivity. In zeolite A, only the extended linear conformation of n-octane is capable of moving through the pores from cage to cage (15) where the Fe active sites are located so that the terminus of the molecule is preferentially presented to the active sites.

The substitution of other ions for Al³⁺ and Si⁴⁺ in the zeolite frameworks may change the zeolite properties (although they still have the same topology and channel system). These materials are no longer called zeolites (they are normally called metallosilicates if the Al³⁺ is replaced). Several metals have been claimed to be incorporated into zeolite frameworks, e.g., iron, boron, chromium, beryllium, gallium, germanium, cobalt, vanadium and titanium (23). The discovery of titanium substituted ZSM-5 (TS-1) has led to remarkable progress in new technology for the production of chemicals which are obtained through selective oxidation reactions; especially with aqueous hydrogen peroxide as the oxidant. Aromatic hydrocarbons are hydroxylated to phenol or substituted phenols; phenol is hydroxylated to catechol and hydroquinone, olefins are oxidized to the corresponding epoxides, and primary and secondary alcohols are converted to aldehydes and to ketones, respectively. The interesting feature of these oxidations is that all of the reactions use aqueous solutions of hydrogen peroxide (40% aqueous H₂O₂ or less) as oxidant with no loss in selectivity (in almost all cases is higher than 80% to the desired product). TS-1 is now operating in a commercial facility in Italy for the production of catechol and hydroquinone from phenol (24). Recently, it has been shown that TS-1 can oxidize alkanes at relatively low temperatures. Huybrechts et al. (25) and Tatsumi et al. (26) showed that n-alkanes can be oxidized to alcohols and ketones at 100° C over TS-1 with aqueous H₂O₂ as the oxidant. For the oxidation of linear alkanes, no activation of primary C-H bonds was observed. Oxidation at the secondary carbon atom occurred statistically. However, this catalyst can differentiate linear from branched and cyclic alkanes. The selectivity arises from the transport restrictions which inhibit branched/cyclic molecules from passing through the pores. Although no extensive

mechanistic study has been performed with the alkane oxidation on TS-1, it has been postulated that the oxidation proceeds through a homolytic mechanism that gives rise to radical intermediates (26).

Finally, Rossin et al. (27) showed that Co^{2+} can be incorporated into tetrahedral atom positions in the framework of ZSM-5. Recently, the framework $\text{Co}^{2+} \leftrightarrow \text{Co}^{3+}$ redox reaction has been demonstrated for cobalt-containing molecular sieves (28-30). These results illustrate the possibility of using framework atoms as isolated redox centers within microporous environments.

Trends in Shape Selectivity of Zeolites

Molecular sieve science is growing rapidly. The uses of molecular sieves as shape selective catalysts for various chemical reactions continue to increase. Below, we illustrate several new trends in the use of zeolites and other molecular sieves as shape selective catalysts.

Most zeolites that have proven utility for shape selective reactions contain pores of ten member rings, e.g., ZSM-5. However, little is known about the use of larger pore zeolites. Recently, Lee et al. (31) utilized a novel dealuminated H-mordenite catalyst (DHM) for the liquid phase alkylation of biphenyl with propene to produce 4,4'-diisopropylbiphenyl (DIPBP) in high yields. This reaction illustrates the potential of zeolites to perform alkylation of polynuclear aromatics with olefins to produce para-para dialkylates of polynuclear aromatic hydrocarbons (important intermediates in the preparation of monomers for thermotropic liquid crystal polymers). The yield of DIPBP increases with increasing $\text{SiO}_2/\text{Al}_2\text{O}_3$ ratio, due to the improved diffusion via the creation of additional mesopores and also to a lower deactivation rate in the DHM. Dealumination not only reduces the number of acid sites but also modifies the pore distribution of the catalysts such that there is an increase in the total pore volume, especially the mesopore volume. In addition, it reduces the partial polymerization of the propene in a side reaction and the tendency for nonpore reactions such as isomerization of para-para to para-meta isomers. The authors suggest that the shape selectivity of the catalyst is due to the spatial constraints imposed on the biphenyl and alkylated biphenyl molecules within the 12-member ring channels of mordenite. The propene diffuses primarily through the smaller eight-member ring channels, thereby illustrating a kind of "molecular traffic control". However, it is also probable that there is some propene diffusion in the larger ring channels.

Similar work by Katayama et al. (32) illustrates the use of H-mordenite as a shape selective catalyst for the liquid phase alkylation of naphthalene with propene or propan-2-ol to produce 2,6-dialkyl-naphthalene (2,6-DIPN). As in the previous example, 2,6-DIPN is a useful monomeric starting material for the preparation of polymers. It is difficult to obtain 2,6-DIPN under the conventional alkylation conditions since naphthalene has eight hydrogen atoms that are easily replaced by alkyl groups. Also, various reactions such as isomerization and transalkylation may occur at the same time under the conventional alkylation conditions. The activities and selectivities for this alkylation of various zeolites were tested. Katayama et al. found that the activities of the zeolites decrease in the order $\text{HY} > \text{HL} > \text{H-mordenite} > \text{H-ZSM-5}$. From the reactions using HY and HL as catalysts, they suggested that the isopropylation occurs initially at the α -positions of naphthalenes, which are more active and thermodynamically less stable. Then, the isopropyl substituents rearrange to the thermodynamically more stable β -positions. The channels of HY and HL are large enough for the rearrangement of the isopropyl groups to occur. Although H-ZSM-5 should have adequate acidity for isopropylation (as it does with HY and HL), it shows little activity and that can be attributed to the fact that the pores of H-ZSM5 are too small to allow the isopropylation of naphthalene to occur. The reaction using H-mordenite as catalyst yields a completely different product distribution from those

obtained using other zeolites. The selectivities for the formation of the β,β' -isomers (2,6-, 2,7-) are much higher than those for the α,α' -isomers (1,4- and 1,5-) or the α,β -isomers (1,3-, 1,6- and 1,7-) and do not change with time. Generally the β,β' -isomers of dialkylnaphthalene are smaller in molecular size than the α,α' - or the α,β -isomers. From the above result, it is concluded that the pores in H-mordenite are sufficiently small so that propene or propan-2-ol cannot directly attack at the α -positions of the naphthalene. It is also suggested that the activated complex which promotes the production of the 2,6-isomer is formed more easily than that of the 2,7-isomer with naphthalene, propene and the wall of H-mordenite channels. Molecular models show that the 2,6-isomer is more linear than the 2,7-isomer. As a result, the structure of the 2,6-isomer is more suited to move in the tight one-dimensional channels of H-mordenite than the 2,7-isomer. This argument explains why the formation of the 2,6-isomer is more favorable than that of the 2,7-isomer despite a similar molecular size.

Another example of using a 12-membered ring zeolite as a shape selective catalyst is given by Keating (33). He reported data for the disproportionation of cumene to diisopropylbenzene (DIPB) and benzene over ZSM-12. In addition to disproportionation, cumene is alkylated with propene to give DIPB. A large amount of para-DIPB is formed over ZSM-12 indicating a shape selective effect inside the channel. As in the production of para-xylene over ZSM-5, the para-isomer of DIPB has the smallest minimum dimension and can diffuse out of the pores much faster than the larger ortho- and meta- isomers. However, with long contact times, isomerization reactions occur and the mixture of isomers more nearly approaches the thermodynamic equilibrium favoring meta. This example suggests that the large pore openings of ZSM-12 are ideal for the alkylation of benzene analogues with propene to produce the corresponding isopropyl derivatives. It also indicates a high potential for the commercial production of meta- and para- diisopropylbenzene, which are useful chemical intermediates.

The discovery of zeolite-like phosphate-based molecular sieves now extends the possibilities for shape selective catalysts toward larger molecules (34). The extra-large pore aluminophosphate VPI-5 (35) (one-dimensional 18-ring channels), $\text{AlPO}_4\text{-8}$ (36) (one-dimensional 14-ring channels) and the very new gallophosphate cloverite (37, 38) (supercage of 30 Å diameter and three-dimensional 20-ring channels) are well-known examples of extra-large pore phosphate-containing molecular sieves. These extra-large pore molecular sieves will allow for the adsorption and reaction of larger molecules than is possible with zeolites.

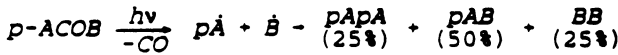
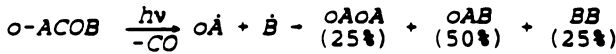
Our work on the alkylation of meta-diisopropylbenzene with propene over the acid form of various 12-member ring zeolites and molecular sieves shows that these catalysts can reveal shape selective behavior (39). As the effective size of the voids increases, the ratio of the formed 1,3,5- to 1,2,4-triisopropylbenzene increases; e.g., mordenite and zeolite Y give 1.1 and 2.5, respectively. Additionally, an amorphous $\text{SiO}_2/\text{Al}_2\text{O}_3$ catalyst yields a ratio of 3.5. Thus, the "smaller" 12-ring materials show shape selective behavior. Based on these results, extra-large pore materials such as VPI-5 may show some shape selectivity for this reaction, if acid sites can be incorporated into the material.

Photochemical and Electrochemical Reactions.

The effect of zeolites on the photochemical reaction pathway of organic molecules has been studied recently. Turro et al. (40, 41) have shown that the photochemistry of methyl benzyl ketones (ACOB) in the presence of pentasil zeolites follows a different pathway depending on the location of adsorbed ketones. Figure 5 illustrates the photochemical reaction pathways in the gas phase and on ZSM-5. Para-ACOB is readily adsorbed by the pentasil framework, so that the radicals formed upon



GAS PHASE



ZEOLITE

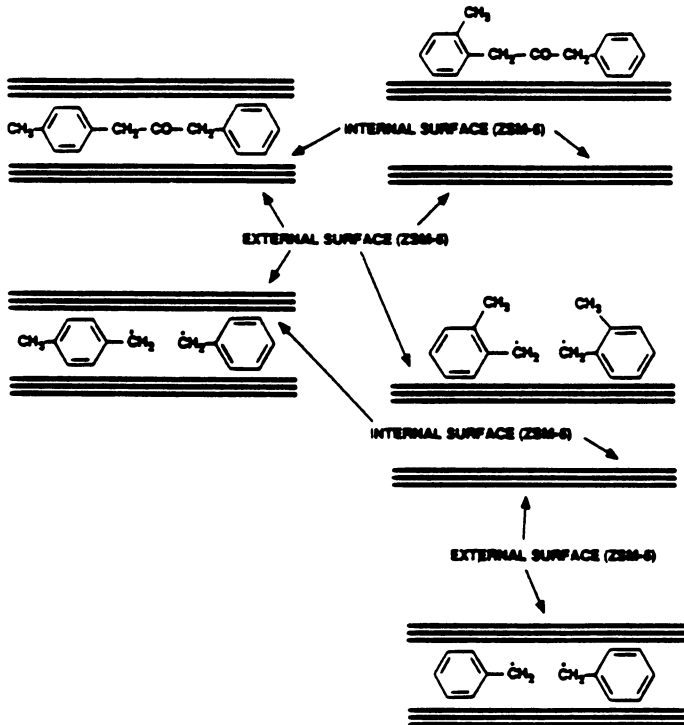
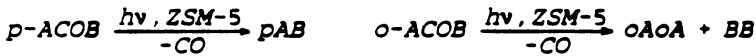


Figure 5. Photochemical reaction pathways in the gas phase and on ZSM-5. (Reproduced from reference 1. Copyright 1991 American Chemical Society.)

photolysis occur inside the zeolite framework ($p\dot{A}$ and \dot{B}). The steric hindrance imposed by the framework induces these radical pairs to combine producing p -AB as the primary product. However, photolysis of o -ACOB yields different product distributions depending upon the extent of the adsorption into the framework. Ortho-ACOB is too large to fit inside the zeolite framework. Upon photolysis, the radicals ($o\dot{A}$ and \dot{B}) are formed at the external surface of zeolites. Although $o\dot{A}$ radical cannot go inside the framework, \dot{B} radical is small enough to diffuse into the internal framework of zeolites and it diffuses faster than it can react to form o -AB. Consequently, $o\dot{A}$ radical combines with itself to form oA_oA at the external surface of zeolites and \dot{B} radical combines with itself inside the zeolite framework to form BB. Hence, the major products from the photolysis of o -ACOB are oA_oA and BB. In addition, the photolysis product distributions can be systematically varied depending upon the aluminum content of the framework. Non-reactive material, such as water may also change the product distribution of both p - and o -ACOB. The water molecules will displace the p -isomer from the framework, and in the case of o -ACOB, it will block the access of \dot{B} radical formed to the internal surface.

Zeolites have been used as modifiers for electrode surfaces. A recent review by Rolison (42) outlines the advantages and applications of these materials. Most of the zeolite-modified electrodes are prepared as composites which form a durable coating on or as part of an electrode surface. An interesting example of using a zeolite-modified electrode for shape selective photochemical reactions was demonstrated by Krueger et al. (43) in the study of artificial photosynthesis in zeolites. Electrodes were prepared with a coating that contained zeolite L in an inert polystyrene binder. Then they were ion-exchanged with a small electroactive cation (benzylviologen) which can diffuse into the zeolite channel and with a large cation ($Ru(bpy)_3^{2+}$ -diquat $^{2+}$ cation) which cannot diffuse into the zeolite channel. The kinetics of the light-induced electron transfer in this system were studied using flash photolysis/transient diffuse reflectance techniques. Figure 6 summarizes the electron transfer in this system. The ruthenium complex is too large to fit into the channel of zeolite L, however the smaller diquat moiety can be accommodated into the pore openings so that the two ends of the ruthenium containing molecule are kept apart. This argument is postulated as the cause for the relatively long lifetime of the charge-separated state of $Ru(bpy)_3^{3+}$ -diquat $^{+}$ cation. The electron is transferred to the zeolite-encapsulated benzylviologen (BV^{2+}) forming a Ru^{3+} -benzylviologen $^{+}$ state which has a lifetime of 35 μs . This long lifetime is attributed to the physical separation of the two molecules imposed by the zeolite. The long-lived charge-separated state is similar to what happens in natural photosynthesis. In both cases, the forward electron transfer step is faster than the reverse step and the ultimate electron acceptor is well separated from the electron donor.

Chiral Catalysis

Quartz can be chiral. A study by Bernal et al. (44) showed that quartz may have played a role as an adsorptive substrate which served as a template in the abiotic evolution of biopolymers. Additionally, it has been reported that the stereospecific adsorption of various organic molecules such as vitamin B $_{12}$ and d,l camphor can occur on quartz. Moreover, it is also possible to separate the two enantiomers by adsorption onto powdered d or l quartz (45).

Schwab et al. (46, 47) showed that nickel, copper and platinum supported on optically-active quartz behave as enantioselective catalysts for the dehydrogenation and oxidation of racemic *sec*-butyl alcohol. At low conversion, a measurable optical rotation of the reaction solution is observed, showing that one enantiomer has reacted

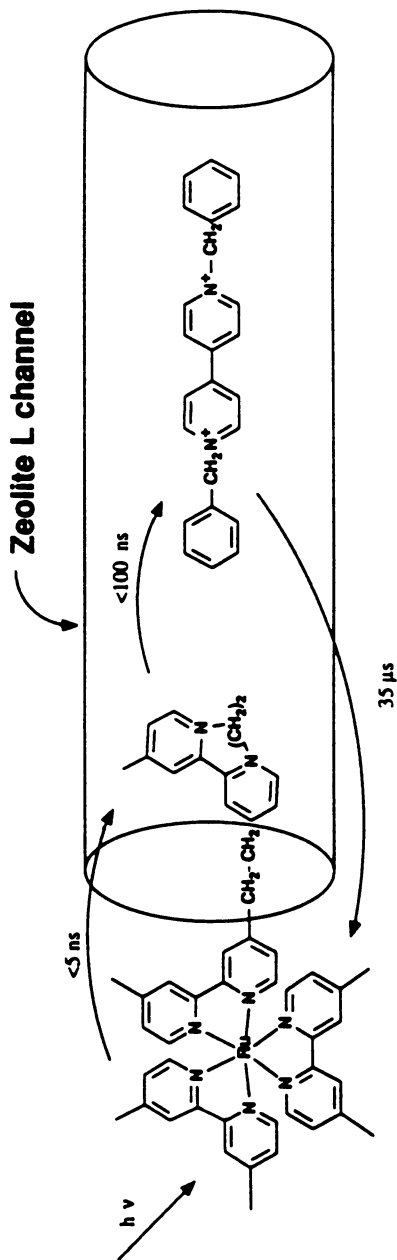


Figure 6. Schematic representation of an artificial photosynthesis system. (Reproduced from reference 1. Copyright 1991 American Chemical Society.)

preferentially. It is thought that the chiral arrangement of the crystal is the cause for this resolution. The asymmetric conversion depends on the kind and the amount of metal loaded onto the quartz. Optimum enantioselectivity was achieved at metal loading which was roughly a monolayer.

To date, no chiral zeolite or molecular sieve has been obtained. However, Newsam et al. (48) have shown that zeolite beta is an intergrowth of two distinct structures: polymorph A and B. Polymorph A forms an enantiomeric pair. Thus, synthesis of one of the enantiomorphs of polymorph A would yield the first chiral zeolite and initiate the possibility of performing intrazeolitic asymmetric catalysis. Shape selective asymmetric catalysis would be the ultimate achievement in shape selective catalysis, and would certainly be a step closer toward truly mimicking enzyme catalysis.

Literature Cited

1. Davis, M. E. *Ind. Eng. Chem. Res.* 1991, 30, 1675-1683.
2. Meier, W. M.; Olson, D. H. *Atlas of Zeolite Structure Types*; Butterworths: Boston, 1987.
3. Moscou, L. *Stud. Sur. Sci. Catal.* 1991, 58, 559-568.
4. Vinje, K.; Ulan, J.; Szostak, R.; Gronsky, R. *Appl. Catal.* 1991, 72, 361-372.
5. Weisz, P. B.; Frilette, V. J.; Maatman, R. W.; Mower, E. B. *J. Catal.* 1962, 1, 307-312.
6. Csicsery, S. M. *Zeolites* 1984, 4, 202-213.
7. Anderson, M. W.; Klinowski, J. *Nature* 1989, 339, 200-203.
8. Kim, J. H.; Namba, S.; Yashima, T. *Zeolites* 1991, 11, 59-63.
9. Kucherov, A. V.; Slinkin, A. A.; Gitis, K. M.; Isagulants, G. V. *Catal. Lett.* 1988, 1, 311-316.
10. Santilli, D. S.; Zones, S. I. *Catal. Lett.* 1990, 7, 383-388.
11. John, V. J.; Martin, M., A.; Chen, J., K.; Dadyburjor, D., B. *Ind. Eng. Chem. Res.* 1989, 28, 1613-1618.
12. Namba, S.; Sato, K.; Fujita, J. H.; Kim, J. H., and Yashima, T. H. *Stud. Sur. Sci. Catal.* 1986, 28, 661-668.
13. John, V. J.; Martin, M. A.; Chen, J. K. *J. Catal.* 1988, 111, 425-428.
14. Moore, R. M.; Katzer, J. R. *AIChE J.* 1972, 18, 816-824.
15. Breck, D. W. *Zeolites Molecular Sieves*; Krieger: Malabar, FL, 1984.
16. Joh, T.; Harada, A.; Takahashi, S. *Mem. Inst. Sci. In. Res., Osaka Univ.* 1989, 46, 37-50.
17. Martens, J. A.; Tielen, M.; Jacobs, P. A.; Weitkamp, J. *Zeolites* 1984, 4, 98-107.
18. Martens, J. A.; Jacobs, P. A. *Zeolites* 1986, 6, 334-348.
19. Jacobs, P. A.; Martens, J. A. *Stud. Sur. Sci. Catal.* 1986, 28, 23-32.
20. Minachev, Kh. M.; Nefedov, O. M.; Kharlamov, V. V.; Panov, S. Y.; Politanskii, S. F. *Izv. Akad. Nauk SSSR Ser. Khim.* 1981, 1490-1495.
21. Espeel, P. H.; Tielen, M. C.; Jacobs, P. A. *J. C. S., Chem. Commun.* 1991, 669-671.
22. Herron, N. *New J. Chem.* 1989, 13, 761-766.
23. Szostak, R. *Molecular Sieves: Principle of Synthesis and Identification*; Van Nostrand Reinhold: New York, 1989.
24. Notari, B. *Stud. Sur. Sci. Catal.* 1988, 37, 413-425.
25. Huybrechts, D. R. C.; De Bruyker, L.; Jacobs, P. A. *Nature* 1990, 345, 240-242.
26. Tatsumi, T.; Nakamura, M.; Negishi, S.; Tominaga, H. *J. C. S., Chem. Commun.* 1990, 476-477.
27. Rossin, J. A.; Saldarriaga, C.; Davis, M. E. *Zeolites* 1987, 7, 295-300.

28. Schoonheydt, R. A.; de Vos, R.; Pelgrims, J.; Leeman, H. *Stud. Sur. Sci. Catal.* 1989, *49A*, 559-568.
29. Iton, L. E.; Choi, I.; Desjardins, J. A.; Maroni, V. A. *Zeolites* 1989, *9*, 535-538.
30. Montes, C.; Davis, M. E.; Murray, B.; Narayana, M. *J. Phys. Chem.* 1990, *94*, 6425-6430.
31. Lee, G. S.; Maj, J. J.; Rocke, S. C.; Garces, J. M. *Catal. Lett.* 1989, *2*, 243-248.
32. Katayama, A.; Toba, M.; Takeuchi, G.; Mizukami, F.; Niwa, S.; Mitamura, S. *J. C. S., Chem. Commun.* 1991, 39-40.
33. Keading, W. W. *J. Catal.* 1989, *120*, 409-412.
34. Flanigen, E. M.; Lok, B. M.; Patton, P. L.; Wilson, S. T. *Stud. Sur. Sci. Catal.* 1986, *28*, 103-112.
35. Davis, M. E.; Saldarriaga, C.; Montes, C.; Garces, J.; Crowder, C. *Nature* 1988, *331*, 698-699.
36. Dessau, R. M.; Schlenker, J. L.; Higgins, J. B. *Zeolites* 1990, *10*, 522-524.
37. Estermann, M.; McCusker, L. B.; Baerlocher, C.; Merrouche, A.; Kessler, H. *Nature* 1991, *352*, 320-323.
38. Davis, M. E. *Nature* 1991, *352*, 281-282.
39. Kim, M. H.; Chen, C. Y.; Davis, M. E., in this volume.
40. Turro, N. J.; Chen, C. C.; Abrams, L.; David, R. C. *J. Am. Chem. Soc.* 1987, *109*, 2449-2456.
41. Turro, N. J. *Pure Appl. Chem.* 1986, *58*, 1219-1228.
42. Rolison, D. R. *Chem. Rev.* 1990, *90*, 867-878.
43. Krueger, J. S.; Lai, C.; Li, Z.; Mayer, J. E.; Mallouk, T. E. *Proc. 5th Int. Symp. on Inclusion Phenom. Mol. Recogn.*, Orange Beach, AL, 1988.
44. Bernal, J. D. *The Physical Basis of Life*; Routledge and Kegan Paul: London, 1951.
45. Kavasmaneck, P. R.; Bonner, W. A. *J. Am. Chem. Soc.* 1977, *99*, 44-50.
46. Schwab, G. M.; Rudolph, L. *Naturwiss.* 1932, *20*, 363-364.
47. Schwab, G. M.; Rost, F.; Rudolph, L. *Kolloid-Zeitschrift* 1934, *68*, 157-165.
48. Newsam, J. M.; Tracy, M. M. J.; Koetsier, W. J.; de Gruyter, C. B. *Proc. R. Soc. London, A* 1988, *420*, 375-405.

RECEIVED September 9, 1992

Chapter 15

Reactions of *meta*-Diisopropylbenzene on Acid Molecular Sieves

Man-Hoe Kim¹, Cong-Yan Chen¹, and Mark E. Davis¹

Department of Chemical Engineering, Virginia Polytechnic Institute and State University, Blacksburg, VA 24061

Meta-diisopropylbenzene is reacted with propylene over the acid form of the molecular sieves SAPO-5, mordenite, offretite, beta, hexagonal and cubic faujasite (EMT and FAU), L, SAPO-37, and an amorphous silica-alumina at temperatures around 463 K in a flow-type fixed-bed reactor. A small amount of cracking is observed. However, the main reactions of meta-diisopropylbenzene are isomerization and alkylation. It is proposed that this alkylation can be used as a new test reaction to characterize the effective size of the voids in larger pore (12 T-atom rings or above) molecular sieves by measuring the weight ratio of 1,3,5- to 1,2,4-triisopropylbenzene formed. In most cases, this ratio increases with the increasing effective void size of the molecular sieves in the order: SAPO-5 < mordenite < offretite < beta < EMT \approx FAU < L < SAPO-37 < amorphous silica-alumina.

Zeolites have been widely used as shape selective catalysts for a great variety of processes in the refining and petroleum industry (1). The discovery of the zeolite-like phosphate-based molecular sieves now extends the possibilities for shape selective catalysts (2). Notable phosphate-containing molecular sieves are the extra-large pore aluminophosphates VPI-5 (3) (one-dimensional 18-ring channels) and AlPO₄-8 (4) (one-dimensional 14-ring channels) and the very new gallophosphate cloverite (5,6) (superpore of 30 Å diameter and three-dimensional 20-ring pore openings).

Recent efforts in the synthesis of new molecular sieves and their modification have resulted in a very large number of molecular sieve materials with vastly different pore sizes and void structures. For example, in Figure 1 the structures of the molecular sieves SAPO-5, offretite, mordenite, L, beta, cubic and hexagonal faujasite, and SAPO-37 are schematically illustrated. It is apparent that the tetrahedral units of SiO_{4/2}, AlO_{4/2} and PO_{4/2} connect in different ways to form crystalline structures with cavities and/or channels of different size and shape. Although techniques such as HREM (High Resolution Electron Microscopy) (7), MAS-NMR (Magic Angle Spinning NMR) (8), Neutron Diffraction (9), etc. can be used to gain insight into the void structure of the

¹Current address: Chemical Engineering, California Institute of Technology, Pasadena, CA 91125

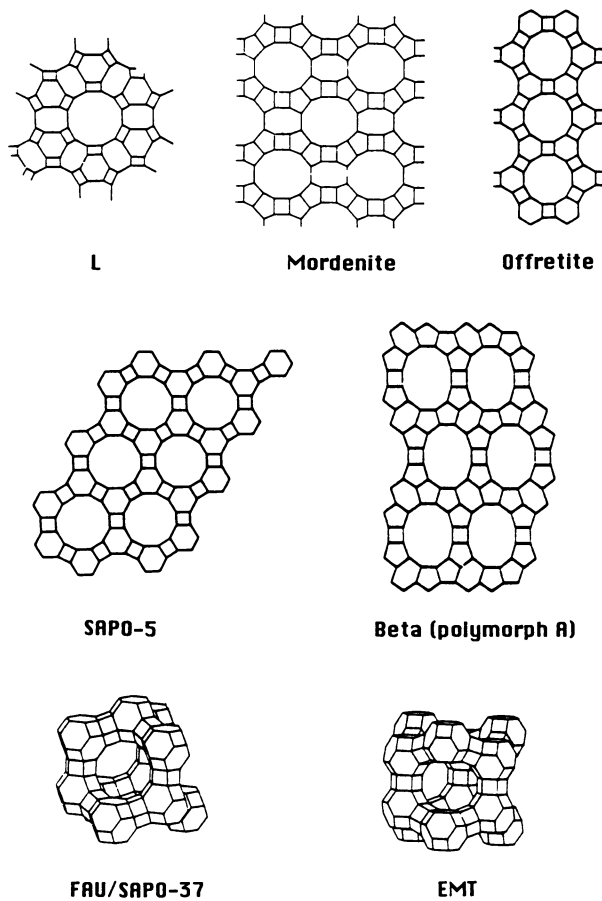


Figure 1. Schematic structures of molecular sieves.

molecular sieve materials, they can rarely be applied at conditions suitable for catalytic reactions to occur. The sorption of molecules with systematically increasing diameters can also be used to characterize the pore structure of molecular sieve materials (10). However, this technique is subject to temperature regions where catalysis is not occurring and can only provide information on total pore volume and effective pore size. (Variation in effective pore size with changing temperatures has been clearly established.)

The use of a catalytic test reaction is another method to determine the effective pore and/or void space sizes of molecular sieve materials (11). A new test reaction must first be tested using known molecular sieve materials with different pore structures to establish a correlation between the shape selectivities and the effective pore/void sizes. Subsequently, the reaction can be applied to molecular sieve materials with unknown crystal structures in order to formulate an estimate of their effective pore structures on the basis of shape selectivities. For the characterization of acid zeolites, workers at Mobil Research Laboratories have suggested the determination of the Constraint Index CI (12). This index involves the relative cracking rate of n-hexane and 3-methylpentane and is used for probing the effective pore size of 10-membered ring zeolites. Other acid-catalyzed test reactions are the conversion of alkylaromatics, e.g., meta-xylene (13,14), ethylbenzene (15), methylethylbenzene (16). In addition to acid-catalyzed reactions, bifunctional molecular sieves (metal particles in addition to acid sites) have been tested. The Refined Constraint Index CI* (17,18) and the Spaciousness Index SI (19,20) have found success in characterizing the effective pore size of 10- and 12-membered ring molecular sieves, respectively. The Refined Constraint Index CI* is based on the bifunctional hydrocracking and isomerization of n-decane and the Spaciousness Index SI is based on the bifunctional hydrocracking of C₁₀-naphthenes.

In this paper, a new test reaction is suggested for characterizing the effective pore size of larger pore (12-membered rings or above) molecular sieve materials. Meta-diisopropylbenzene is alkylated with propylene and the weight ratio of 1,3,5- to 1,2,4-triisopropylbenzene formed is calculated. This ratio is used to characterize the effective void space size of molecular sieves.

Experimental

Catalyst Preparation. The molecular sieves used in this study were either purchased from commercial suppliers (Union Carbide: zeolites mordenite and L) or obtained by hydrothermal synthesis according to the information published in the literature (offretite, beta, cubic and hexagonal faujasite, SAPO-5, and SAPO-37). The hexagonal polytype of faujasite (21,22) is designated EMT as assigned by the IZA structure commission. The as-made samples were washed with deionized water, recovered by filtration, dried at 383 K and subsequently calcined in air at 873 K for 6 hours (except SAPO-37) to remove the organic species occluded in the pore systems. The resulting materials were then transformed into their NH₄⁺-forms by an ion-exchange with a 1 M aqueous solution of NH₄Cl. The H⁺-forms of the catalysts (except SAPO-37) were obtained by activating their NH₄⁺-forms *in-situ* in the reactor with a helium flow of 5 L/h at 623 K. The as-made SAPO-37 which does not contain any alkali-cations was calcined *in-situ* in the reactor in an oxygen flow of 6 L/h at 793 K for 10 hours in order to obtain its H⁺-form without any observable losses in structural integrity. The amorphous silica-alumina (87 wt.-% silica and 13 wt.-% alumina) was purchased from Strem. To obtain the H⁺-form of the silica-alumina, it was pretreated in the same way as the molecular sieve catalysts studied here (except SAPO-37).

Adsorption Measurement. The capacities of the molecular sieves to adsorb vapor phase 1,3,5-triisopropylbenzene (97 %, Aldrich) and 1,2,4-triisopropylbenzene (99%, Carnegie-Mellon University) were measured at 373 K using a McBain-Bakr balance. The adsorption temperature was chosen such that no chemical reactions of the adsorbates were observed. Prior to the adsorption experiment, the NH_4^+ -forms of the solids (except SAPO-37) were dehydrated at 573 K under a vacuum of 10^{-2} Torr. The as-made SAPO-37 was calcined at 793 K in an oxygen flow of 6 L/h *in-situ* in the adsorption system for removal of organic species and dehydration. The vapor pressure at 296 K of 1,3,5- and 1,2,4-triisopropylbenzene is approximately 0.45 Torr. The adsorption experiments were conducted at this pressure.

Ammonia TPD Measurement. The acidic properties of the catalysts were characterized using temperature programmed desorption (TPD) of ammonia. The experiments were carried out on a flow-type apparatus equipped with a fixed-bed and a thermal conductivity detector. The samples were activated in a helium flow of 5 L/h at 773 K for 1 hour. 300 mg of the H^+ -form of each dehydrated sample were used to perform the ammonia TPD. Pure ammonia, with a flow rate of 3 L/h, was then passed through the sample at 423 K for 30 min. The sample was subsequently purged with helium at the same temperature for 1.5 hours in order to remove the physisorbed ammonia. The TPD was performed under a helium flow of 6 L/h from 423 K to 873 K with a heating rate of 10 K/min and subsequently at the final temperature for 30 min.

Catalytic Experiment. The alkylation of meta-diisopropylbenzene with propylene was performed at 463 K in a flow-type fixed-bed reactor. The carrier gas nitrogen was first saturated with the vapor of meta-diisopropylbenzene (97 %, Aldrich) and then admixed with propylene (99 %, Matheson). The partial pressure of propylene and meta-diisopropylbenzene was 42.6 and 6.0 Torr, respectively. (The molar ratio of propylene and meta-diisopropylbenzene at the reactor inlet was 7.1 : 1). The modified residence time of propylene and meta-diisopropylbenzene $W/F_{\text{propylene}}$ and $W/F_{\text{m-DIPB}}$ ranged from 4 to 20 and from 25 to 150 gh/mol, respectively, where W indicates the weight of dehydrated catalyst at 623 K and F_i indicates the molar flow rate of reactant i at the reactor inlet. The reaction conditions, viz. the reaction temperature, amount of catalyst, partial pressure and modified residence time of reactants, were chosen in order to obtain conversions of meta-diisopropylbenzene around 25 %.

The products were analyzed with an on-line gas chromatograph using a 1.8 m packed column that contained 5 % SP-1200 and 75 % Bentone 34 as the stationary phase. The saturator and reactor system have been described in greater details elsewhere (23).

Results and Discussion

Adsorption Capacities. The adsorption capacities of the various molecular sieves and the amorphous silica-alumina for 1,3,5- and 1,2,4-triisopropylbenzene are listed in Table I. 1,3,5-Triisopropylbenzene does not adsorb into the channels of the acid form of SAPO-5, mordenite and offretite at an adsorption temperature of 373 K. The small adsorption capacity of around 0.005 g/g most likely is indicative of some surface and/or intercrystalline adsorption of 1,3,5-triisopropylbenzene in these three samples. On the other hand, all the other samples studied in this work possess cavities and/or channels large enough to accommodate 1,3,5-triisopropylbenzene. In addition, all the sieves used here are capable of adsorbing 1,2,4-triisopropylbenzene.

It is obvious that the samples exhibit observable differences in adsorption capacity as a consequence of their different pore structures. These effects can be nicely

Table I. Adsorption data for 1,2,4- and 1,3,5-triisopropylbenzene at 373 K*

Sample	<i>g/g solid</i>		$W_{1,3,5-TIPB}$
	<i>1,2,4-TIPB</i>	<i>1,3,5-TIPB</i>	$W_{1,2,4-TIPB}$
SAPO-5	0.045	0.006	0.13
Mordenite	0.039	0.005	0.13
Offretite	0.039	0.007	0.18
Beta	0.129	0.052	0.40
EMT	0.179	0.115	0.64
FAU	0.141	0.143	1.01
L	0.032	0.027	0.84
SAPO-37	0.243	0.200	0.82
SiO ₂ -Al ₂ O ₃	0.028	0.026	0.93

*Pressure of adsorbate is the vapor pressure at room temperature

illustrated by calculating the adsorption capacity ratio $W_{1,3,5-TIPB}/W_{1,2,4-TIPB}$ as shown in Table I. Interestingly, this ratio ranges between 0.64 and 1.01 for the molecular sieves L, EMT, FAU, SAPO-37 and the amorphous silica-alumina, i.e., those solids that can adsorb both triisopropylbenzene isomers. The ratio of 0.40 for zeolite beta and 0.64 for EMT is unexpected and may upon further study reveal interesting features attributable to their unique structures.

TPD Results. Figure 2 shows the results of ammonia TPD from the H⁺-form of the molecular sieves SAPO-37, L, FAU, EMT, mordenite, beta, SAPO-5 and the amorphous silica-alumina. Two different types of acid sites are distinguished which are related to the maximum ammonia desorption rates in the temperature region of 540 - 610 K and at ca. 770 K, respectively. The total amount of acid sites correlates to the area integrated below the ammonia TPD curve. The ammonia TPD curves of H-FAU and H-EMT illustrate that these two samples possess very similar acidity, which is in good agreement with the fact that they have the same Si/Al ratio of 3.4. The tailings of their TPD curves after the peak maxima are indicative of the presence of some strong acid sites the peaks of which are not resolved in these experiments. For SAPO-37, the narrow TPD profile reveals that this sample has slightly stronger acid sites than the majority of those in H-FAU and H-EMT. On the other hand, according to their TPD peak areas these three samples have very similar total amount of acid sites. For H-L, H-beta and H-mordenite, there is some NH₃ desorption near 770 K that indicates the presence of strong acid sites. However, in contrast to H-L and H-beta, H-mordenite has a greater number density of strong acid sites than weak ones. Finally, for H-SAPO-5 and H-SiO₂/Al₂O₃, only weak acid sites of small amount are observed.

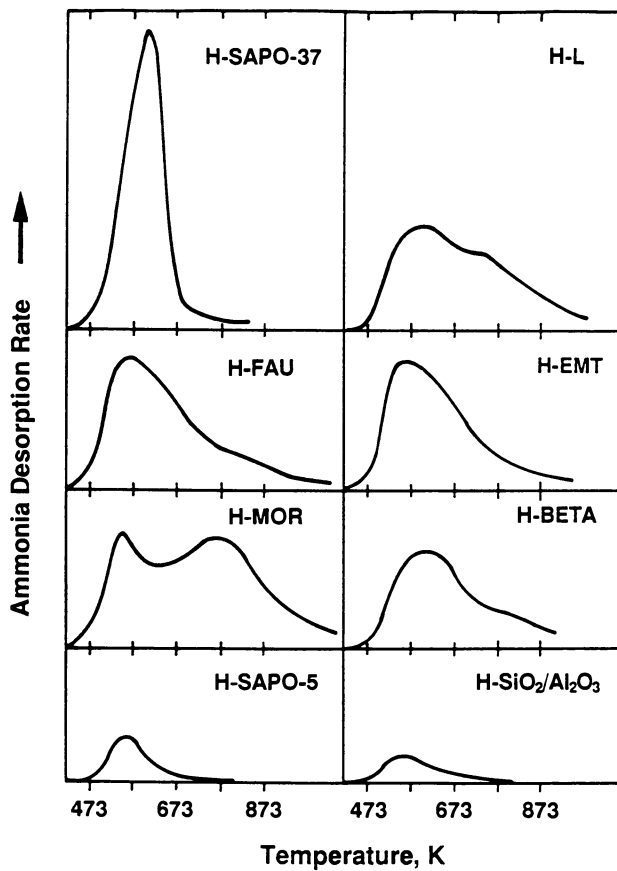


Figure 2. Ammonia TPD curves of molecular sieves and amorphous silica-alumina.

Reactions of meta-diisopropylbenzene. The adsorption data given above clearly reveal that within the series of 12-ring molecular sieves studied here, 1,2,4-triisopropylbenzene can be distinguished from 1,3,5-triisopropylbenzene. Also, it is known that at room temperature, VPI-5 adsorbs 1,3,5-triisopropylbenzene while NaY does not (equilibrium reached in several days) (24). Thus, it is speculated that the alkylation of meta-diisopropylbenzene with propylene to form triisopropylbenzenes may be useful for characterizing the size of the void spaces in molecular sieves with 12-ring pores or larger (ZSM-5 does not sorb and react meta-diisopropylbenzene at the conditions employed here). The premise is that as the void space increases in size the catalyst will produce a greater amount of 1,3,5-triisopropylbenzene since it is the thermodynamically preferred product. Also, it is important to point out that the reactions of diisopropylbenzene are very facile in that they do not require strong acid sites. This may be helpful when attempting to characterize phosphate-based molecular sieves (in general they have weaker acid sites than zeolites). Also, differences in acid site strength may not affect the selectivity results and thus allow direct comparison of a large number of materials with varying acid strength distributions.

A problem with monofunctional reactions, e.g., cracking, alkylation, etc. is that they have a tendency to quickly deactivate because of coke deposition. This problem is usually not of concern with bifunctional reactions, e.g., those that employ a metal function in addition to the acid sites. However, we avoided the use of metal function because of the possible unknown modifications that could be introduced to a given sample by the metal deposition procedure. This is especially important when dealing with samples like VPI-5. Thus, to minimize the rate of deactivation, the alkylation experiments were conducted at 463 K. This low temperature introduces another problem, namely, the adsorption of reactants and products. At the experimental conditions employed here, the catalyst bed becomes saturated at time of 10 minutes or less (depending on sample). From this point onward, deactivation is clearly observable via the decrease in conversion with time. The data reported here were obtained at 11-13 minutes on-line. Since meta-diisopropylbenzene proceeds through several reaction pathways that lead to a number of products, it is most appropriate to compare the catalytic data at the constant level of conversion. Here we report selectivities at approximately 25 % conversion. For each catalyst, the results near 25 % conversion were repeated three times to ensure reproducibility.

Table II shows the results obtained from contacting meta-diisopropylbenzene and propylene with the various catalysts at 463 K. For all the catalysts except SAPO-5, the amount of cracked products is low (included in column labelled others). In addition, no ortho-diisopropylbenzene and trace 1,2,3-triisopropylbenzene were observed. Two trends are illustrated by the data in Table II. First, the ratio A/I of alkylated products (1,3,5- and 1,2,4-TIPB) to that formed by isomerization (p-DIPB) increases roughly as the size of the pore/void spaces increase. The exception is EMT. For EMT a very high isomerization rate is observed. However, it is interesting to note that EMT has a lower than expected $W_{1,3,5-TIPB}/W_{1,2,4-TIPB}$ adsorption capacity ratio which may be correlated to the catalytic results. Second, the ratio of 1,3,5- to 1,2,4-triisopropylbenzene (1,3,5/1,2,4-TIPB) follows the trends in A/I with increasing void space size. Clearly these ratios (especially 1,3,5/1,2,4-TIPB) are an outcome of the catalyst structure.

When isomerization competes with alkylation, then there is the possibility that some of the isomerized diisopropylbenzene (para) is alkylated as well. In order to test for this possibility, two other experiments were performed. At higher conversion, a greater amount of products formed by secondary reactions should be observable. Additionally, reactions with para-diisopropylbenzene will reveal the presence of secondary reaction if 1,3,5-triisopropylbenzene is formed (assuming that at lower conversion the small amount of 1,2,4-triisopropylbenzene will not produce a significant amount of 1,3,5-triisopropylbenzene by isomerization). Table III gives the

Table II. Comparison between the pore size of catalysts and the product distributions of meta-diisopropylbenzene alkylation with propylene at 463 K

Catalyst	Conv. mol-%	Yield, mol-%				<i>1,3,5-TIPB</i>		A/I*
		<i>p-DIPB</i>	<i>1,3,5-TIPB</i>	<i>1,2,4-TIPB</i>	Others	<i>1,2,4-TIPB</i>		
SAPO-5	24.3	74.9	2.0	8.9	14.2	0.2	0.15	
Mordenite	25.6	62.3	17.8	15.6	4.3	1.1	0.83	
Offretite	25.1	53.2	26.4	17.6	2.8	1.5	0.54	
Beta	24.2	55.4	25.1	14.3	5.2	1.8	0.71	
EMT	25.3	42.0	35.0	15.4	7.6	2.3	1.20	
FAU	27.4	21.0	54.0	21.5	3.5	2.5	3.60	
L	25.5	23.8	53.4	18.5	4.3	2.9	3.02	
SAPO-37	26.2	21.9	55.5	18.3	4.3	3.0	3.37	
SiO ₂ -Al ₂ O ₃	24.2	17.9	62.1	17.9	2.1	3.5	4.47	

*A/I: total alkylated products/total isomerized products

results of these experiments performed on SAPO-5 and zeolite L. Notice that 1,3,5-triisopropylbenzene is formed from a para-diisopropylbenzene feed in both cases. Thus, the secondary reactions of isomerized diisopropylbenzenes do contribute to the formation of triisopropylbenzenes. These results clearly demonstrate that the isomerization and alkylation processes (both primary and secondary) must be considered when attempting to rationalize the product distributions.

Table III. Reaction of diisopropylbenzenes over SAPO-5 and zeolite L

Catalyst	Reactant	T, K	Conv. mol-%	Yield, mol-%			<i>1,3,5-TIPB</i>	
				<i>DIPB</i>	<i>1,3,5-TIPB</i>	<i>1,2,4-TIPB</i>	<i>1,2,4-TIPB</i>	
SAPO-5	m-DIPB	463	24.3	74.9(p)*	2.0	8.9	0.2	
SAPO-5	m-DIPB	473	46.0	64.0(p)	5.0	15.0	0.3	
SAPO-5	p-DIPB	473	32.0	47.0(m)	6.0	28.0	0.2	
L	m-DIPB	463	25.5	23.8(p)	53.4	18.5	2.9	
L	m-DIPB	473	51.0	35.0(p)	46.0	14.0	3.3	
L	p-DIPB	473	19.0	32.0(m)	45.0	20.0	2.3	

*p: para; m: meta

It is interesting to note that EMT and FAU give different results. Since the only difference between these two samples is the structure, clearly in this case we are observing the difference in structure-property relationships. Because the amount of the isomerized product is so high for EMT, one must be careful not to overinterpret these differences. Further syntheses and reaction experiments with FAU and EMT will be performed in order to verify these results. Also, one might expect similar data from FAU and SAPO-37. Since SAPO-37 contains no alkali, the supercage will be slightly larger in SAPO-37 than in FAU. This may be the cause of the differences in the 1,3,5/1,2,4-TIPB ratios.

Table IV shows a comparison of indexes derived from various test reactions. It is clear that CI and CI* can not discriminate well between 12-membered ring molecular sieves while SI can. It is not clear at this time whether the SI will continue to increase in magnitude with larger pore materials. Also, as previously mentioned, the use of a bifunctional reaction may prove difficult for testing materials with low stability. This point may not be as important as we initially believed since we recently have shown that platinum can be impregnated into VPI-5 and n-hexane reacted at temperature as high as 800 K. The ratio 1,3,5/1,2,4-TIPB does increase with increasing pore/void size and does reveal a difference between 10-13 Å sized microporous materials and the mesoporous SiO₂-Al₂O₃. Thus, with further refinements this ratio may prove useful for characterizing larger pore molecular sieves.

Table IV. Comparison of Indexes

<i>Catalyst</i>	<i>CI</i>	<i>CI*</i>	<i>SI</i>	$\frac{1,3,5\text{-TIPB}}{1,2,4\text{-TIPB}}$	<i>A/I</i>
SAPO-5	-	1.5	4.0	0.2	0.15
Offretite	3.7	1.8	5.0	1.1	0.83
Mordenite	0.4	1.8	7.8	1.5	0.54
Beta	0.6	1.4	18.9	1.8	0.71
EMT	-	-	-	2.3	1.20
FAU	0.3	1.2	20.8	2.5	3.60
L	-	1.0	17.2	2.9	3.02
SAPO-37	-	1.3	-	3.0	3.37
SiO ₂ -Al ₂ O ₃	-	-	-	3.5	4.47

Conclusions

The alkylation of meta-diisopropylbenzene with propylene over the acid form of molecular sieves is suggested as a new test reaction to characterize the effective pore size of larger (12 T-atom rings or above) molecular sieves. The ratio of 1,3,5- and 1,2,4-triisopropylbenzene formed at conversions near 25 % shows a strong correlation with the size of the pore/void space, i.e., the ratio increases with increasing size.

Acknowledgement

We thank the Akzo America, Inc. for the financial support of this work.

Literature Cited

1. Chen, N.Y.; Garwood, W.E.; Dwyer, F.G. *Shape Selective Catalysis in Industrial Applications*; Marcel Dekker, Inc.: New York, Basel, 1989; pp 67–250.
2. Flanigen, E.M.; Lok, B.M.; Patton, P.L.; Wilson, S.T. in *New Developments in Zeolite Science and Technology*; Murakami, Y.; Iijima, A.; Ward, J.W., Ed.; Studies in Surface Science and Catalysis 28; Kodansha: Tokyo and Elsevier: Amsterdam, Oxford, New York, Tokyo, 1986; pp 103–112.
3. Davis, M.E.; Saldarriaga, C.; Montes, C.; Garces, J.; Crowder, C. *Nature* 1988, 331, pp 698–699.
4. Dessau, R.M.; Schlenker, J.L.; Higgins, J.B. *Zeolites* 1990, 10, pp 522–524.
5. Estermann, M.; McCusker, L.B.; Baerlocher, C.; Merrouche, A.; Kessler, H. *Nature* 1991, 352, pp 320–323.
6. Davis, M.E. *Nature* 1991, 352, pp 281–282.
7. Treacy, M.M.J.; Newsam, J.M. *Nature* 1988, 332, pp 249–251.
8. Fyfe, C.A.; Gies, H.; Kokotailo, G.T.; Feng, Y.; Strobl, H.; Marler, B.; Cox, D.E. in *Zeolites: Facts, Figures, Future*; Jacobs, P.A.; Van Santen, R.A., Ed.; Studies in Surface Science and Catalysis 49; Elsevier: Amsterdam, Oxford, New York, Tokyo, 1989; pp 545–557.
9. Briscoe, N.A.; Johnson, D.W.; Shannon, M.D.; Kokotailo, G.T.; McCusker, L.B. *Zeolites* 1988, 8, pp 74–76.
10. Wu, E.L.; Landolt, G.R.; Chester, A.W. in *New Developments in Zeolite Science and Technology*; Murakami, Y.; Iijima, A.; Ward, J.W., Ed.; Studies in Surface Science and Catalysis 28; Kodansha: Tokyo and Elsevier: Amsterdam, Oxford, New York, Tokyo, 1986; pp 547–554.
11. Jacobs, P.A.; Martens, J.A. in *New Developments in Zeolite Science and Technology*; Murakami, Y.; Iijima, A.; Ward, J.W., Ed.; Studies in Surface Science and Catalysis 28; Kodansha: Tokyo and Elsevier: Amsterdam, Oxford, New York, Tokyo, 1986; pp 23–32.
12. Frilette, V.J.; Haag, W.O.; Lago, R.M. *J. Catal.* 1981, 67, pp 218–222.
13. Dewing, J. *J. Mol. Catal.* 1984, 27, pp 25–33.
14. Joensen, F.; Blom, N.; Tapp, N.J.; Derouane, E.G.; Fernandez, C. in *Zeolites: Facts, Figures, Future*; Jacobs, P.A.; Van Santen, R.A., Ed.; Studies in Surface Science and Catalysis 49; Elsevier: Amsterdam, Oxford, New York, Tokyo, 1989; pp 1131–1140.
15. Weitkamp, J.; Ernst, S.; Jacobs, P.A.; Karge, H.G. *Erdöl, Kohle-Erdgas-Petrochem.* 1986, 39, pp 13–18.
16. Csicsery, S.M. *J. Catal.* 1987, 108, pp 433–443.
17. Martens, J.A.; Tielen, M.; Jacobs, P.A.; Weitkamp, J. *Zeolites* 1984, 4, pp 98–107.
18. Martens, J.A.; Jacobs, P.A. *Zeolites* 1986, 6, pp 334–348.

19. Weitkamp, J.; Ernst, S.; Kumar, R. *Appl. Catal.* 1986, *27*, pp 207–210.
20. Weitkamp, J.; Ernst, S.; Chen, C.Y. in *Zeolites: Facts, Figures, Futures*; Jacobs, P.A.; Van Santen, R.A., Ed.; Studies in Surface Science and Catalysis 49; Elsevier: Amsterdam, Oxford, New York, Tokyo, 1989; pp 1115–1129.
21. Delprato, F.; Delmotte, L.; Guth, J.L.; Huve, L. *Zeolites* 1990, *10*, pp 546–552.
22. Annen, M.J.; Young, D.; Arhancet, J.P.; Davis, M.E.; Schramm, S. *Zeolites* 1991, *11*, pp 98–102.
23. Weitkamp, J. in *Innovation in Zeolite Materials Science*; Grobet, P.J.; Mortier, W.J.; Vansant, E. F.; Schulz-Ekloff, G., Ed.; Studies in Surface Science and Catalysis 37; Elsevier: Amsterdam, Oxford, New York, Tokyo, 1988; pp 515–534.
24. Davis, M. E.; Saldarriaga, C.; Montes, C.; Garces, J.; Crowder, C. *Zeolites* 1988, *8*, pp 362–366.

RECEIVED September 9, 1992

Chapter 16

Methyl *tert*-Butyl Ether and Ethyl *tert*-Butyl Ether

Synthesis over Triflic Acid Modified Y-Zeolite

R. Le Vanmao, H. Ahlafi, and T. S. Le

Department of Chemistry and Biochemistry, Catalysis Research Laboratory, and Laboratories for Inorganic Materials, Concordia University, 1455 De Maisonneuve West, Montreal, Quebec H3G 1M8, Canada

The apparent activation energy for the synthesis reaction of methyl *tert*-butyl ether or MTBE, was found to be 64 KJ/mole. The best activity and selectivity for MTBE were observed at temperatures of 85 - 90 °C, and contact times of circa 2.5 h when the methanol / isobutene molar ratio was kept within the 1.2 - 1.5 range. There was a fierce competition between the ethyl *tert*-butyl ether formation and that of diethylether at reaction temperatures higher than 85 °C.

As lead antiknock additives in gasoline will be banned in most industrialized countries by the end of this decade, octane boosters for fuels such as light alcohols, methyl-*tert*-butyl ether (MTBE) have been increasingly used in gasoline blend. When compared to aromatic hydrocarbons which can be used to upgrade gasoline, MTBE evolves no toxic products from the incomplete combustion in engines. Furthermore, MTBE does not provoke demixing when blended with gasoline, which is not the case with methanol, for instance. MTBE, which is characterized with specifications close to those of gasoline, does not require dramatic modifications in engine technology. MTBE being an oxygenate and having a fairly high octane number, accordingly favors the "clean" combustion of gasolines and other fuels.

MTBE is currently synthesized industrially from methanol and isobutene over an acidic ion-exchange resin, mostly Amberlyst 15 which is in fact a macroreticular cation-exchange resin [1,2]. ETBE which is obtained by reaction of isobutene with ethanol, is also an attractive octane enhancer for gasoline [3]. Although the commercial catalyst is very efficient, it suffers from several drawbacks such as thermal instability, acid leaching from the resin

surface and high methanol/isobutene ratio requirement. ZSM-5 zeolite was thus proposed as a remedy to such inconveniences [4]. However, the activity of the ZSM-5 zeolite catalyst is relatively low if compared to the Amberlyst 15 resin [3]. Increasing the surface acidity of the ZSM-5 zeolite by coating with triflic acid, a well-known organic superacid, results in a catalytic system which is strongly limited by diffusion phenomena due to pore narrowing [5]. However, with the larger pore sized Y-type zeolite, coating with triflic acid has provided an acid catalyst which shows catalytic activity and product selectivities comparable to those of the Amberlyst 15 in the synthesis of MTBE [5]. One of the advantages in the use of zeolite based catalysts is the significantly reduced production of (undesired) diisobutene and other oligomers of isobutene. This is due to the shape selectivity of the zeolite pore system.

In this work, the triflic acid modified Y-zeolite catalyst has been investigated for the atmospheric synthesis of MTBE and ETBE. In particular, the apparent activation energy for MTBE was determined, and this value is compared with those reported in the literature [1,6]. In addition, for both syntheses, the product selectivities are reported as functions of the contact time at the temperature where the catalyst activity is the highest. The catalyst stability for the MTBE synthesis was also examined.

EXPERIMENTAL

CATALYST PREPARATION

The acid form of the Y zeolite was obtained by activating the LZY-82 sample (Y-type zeolite, ammonium-form, powder, supplied by Linde) in air at 550 °C for 10 h. The triflic acid loading (3 wt %) was done according to the following procedure. Triflic acid (0.75 g; trifluoromethane-sulfonic acid, $\text{CF}_3\text{SO}_3\text{H}$, 8 % from Fluka Chemie AG, hereafter called TFA) was dissolved in 40 ml of pure acetone. This solution was added to 25 g of zeolite (powder, acid form) contained in a small beaker. The resulting suspension was allowed to settle in the beaker, which was covered with a glass watch, and dried overnight at room temperature. The solid obtained was heated at 120 °C in air for 12 h.

The final catalyst extrudates were prepared according to the procedure described elsewhere [5]. This catalyst is hereafter referred to as H-Y/TFA.

CATALYST CHARACTERIZATION

The catalyst powder was characterized by atomic absorption (chemical composition), X-ray powder diffraction (structure identification and degree of crystallinity) and nitrogen adsorption/desorption. For the latter method, an automatic Micromeritics ASAP 2000 apparatus was used, which also allowed the determination of the pore size distribution in the mesopore and macropore region (2 nm to 300 nm).

CATALYST TESTING AND ANALYSIS OF REACTION PRODUCTS

The experimental set-up and the procedures for the analysis of the reaction products were identical to those described elsewhere [5].

The yield in product *i* was calculated by the relationship:

$$Y_i (\text{C atom } \%) = \frac{N_i}{N(\text{iso})} \times 100$$

where N_i and $N(\text{iso})$ are the numbers of carbon atoms of, respectively, product *i* which can be MTBE, ETBE or C8 products (diisobutene and its isomer), and feed isobutene.

In particular, in the synthesis of ETBE, the yield in diethyl ether is expressed as:

$$Y_{\text{DEE}} (\text{C atom } \%) = \frac{N(\text{DEE})}{N(\text{ETOH})} \times 100$$

where $N(\text{DEE})$ and $N(\text{ETOH})$ are the numbers of carbon atoms of product diethyl ether and feed ethanol, respectively. In addition, the yield in hydrocarbons other than oligomers of isobutene is expressed as :

$$Y_{\text{HC}} (\text{C atom } \%) = \frac{N(\text{HC})}{N(\text{ETOH})} \times 100$$

where $N(\text{HC})$ is the number of carbon atoms of such hydrocarbons.

Product yields are expressed in C atom % rather than in the usual moles % . This allows us to visualize the numbers of C atoms of isobutene or the alcohol converted into carbon containing products, independently from the molecular length or chemical composition of such products.

The reagent contact time is defined as :

$$T_c (\text{expressed in h}) = \frac{W}{F_r}$$

where W and F_r are the weight of catalyst (in g) and the total flow-rate of the reagents (in g/h), respectively. The molar ratio (methanol/isobutene) was set at 1.2 - 1.5.

The determination of the apparent activation energy derived from the Arrhenius formula was done using the initial rates of MTBE formation at several reaction temperatures ranging from 345 K (72 °C) to 371 K (98 °C). Higher temperatures are not recommended because of MTBE decomposition [6]. The apparent activation energy was determined using the linear regression fitting of the curves of MTBE yield as a function of reagent contact time. Such a technique is applicable only for MTBE yields corresponding to contact times lower than 1.7 h, i.e. for MTBE yields lower than 10 (C-atom) %.

RESULTS AND DISCUSSION

There are two values of surface area and volume of nitrogen adsorbed (BJH method), obtained with the parent H-Y zeolite and the H-Y/TFA sample (Table 1): the first corresponds to the zeolite-type micropores and the other, to the mesopores. Figure 1 shows the pore size distribution of the H-Y/TFA catalyst; there is a sharp peak (not shown here) in the micropore region and another peak at 4nm in the mesopore region. Such a bimodal pore size distribution was also observed with the parent zeolite.

Although there was no significant loss in the degree of crystallinity upon loading of triflic acid onto the Y-zeolite, there was an important decrease in the surface area and the volume of nitrogen adsorbed (Table 1). These decreases are mainly related to the micropore region of the zeolite. Previous works have evidenced that: i) triflic acid species could form "chemical-type" bonds with the zeolite surface and thus become more thermally stable than free triflic acid [5, 8-11]; ii) serious steric hindrance was observed for the zeolite pore system upon triflic acid incorporation [5, 7-11]. Therefore, the lower volume of nitrogen adsorbed by the H-Y/TFA sample might be due to a lower accessibility to the micropores whose surface was covered with triflic acid species. While methanol and ethanol had already some difficulty to enter such reduced-sized micropores [10], the much bulkier isobutene molecule was probably even more constrained. Therefore, it is probable that only the mesopores and a portion of the micropores of the H-Y/TFA catalyst were involved in the catalytic reaction. These problems notwithstanding, the yield of MTBE obtained with the H-Y/TFA was twice as high as that obtained with the parent H-Y [5] and was practically equal to that of the Amberlyst 15. Such an enhanced activity is due to the enhanced acidity upon incorporation of triflic acid [9 -11]. The presence of relatively narrow mesopores in the H-Y zeolite is advantageous because it contributes to solve the problem of diffusion limitation within the modified zeolite particles without losing the shape selectivity of such a porous system.

Figure 2 shows the experimental data which were used to determine the apparent activation energy. The value found was 64 ± 6 KJ/mol. The corresponding literature values range from 71 KJ/mol [1] to 82 KJ/mol [6] for the Amberlyst 15 resin, and are greater than 91 KJ/mol for an acid in solution (methyl sulfuric acid [12] and paratoluene sulfonic acid [1]). As pointed out by Gicquel and Torck [6], lower values of the apparent activation energy are partly due to diffusion limitations. The other possible cause of such variations stems from the saturation of the reaction sites by methanol [6].

Figure 3 shows the yields of MTBE plotted against the contact time, observed at 345 K, 360 K and 371 K, respectively. The yield in C8 products at 360 K, which is also reported in this figure, did not exceed 1.5 C-atom % at high contact times. At the reaction temperatures tested, the production of dimethyl ether (DME) and other hydrocarbons was practically negligible (less than 1 C atom %). Lower production of DME was also observed by Chang

Table 1 Textural properties of the H-Y and H-Y/TFA catalysts

Sample	Degree of crystallinity (%)	B.E.T. surface area (m ² /g)	BJH [7] cumulative surface area (m ² /g)		desorption method volume of N ₂ adsorbed (cc/g)	
			mi (1)	mes+ma (2)	mi (1)	mes+ma (2)
H-Y	100	428	348 (79%)	92 (21%)	0.165 (52%)	0.150 (48%)
H-Y/ TFA	99	222	154 (67%)	75 (33%)	0.073 (35%)	0.136 (65%)

(1) micropores having diameter less than 2 nm

(2) mesopores and macropores having diameters in the range of 2 - 300 nm.

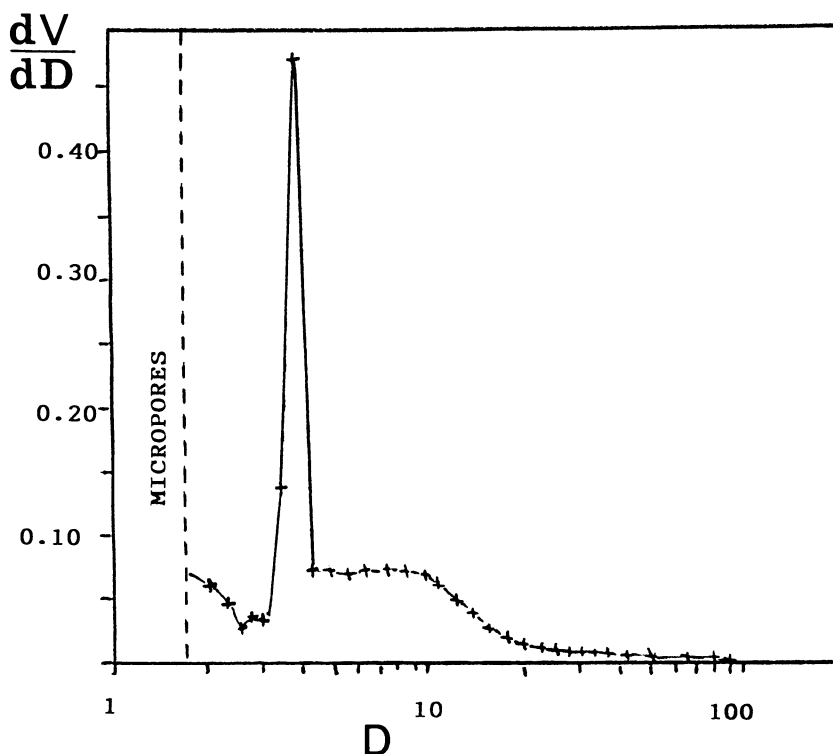


Figure 1 Pore size distribution (mesopore region) of the H-Y/TFA catalyst. V (Volume of nitrogen adsorbed) and D (pore diameter) are expressed in cc/g and nm (10^{-9} m), respectively.

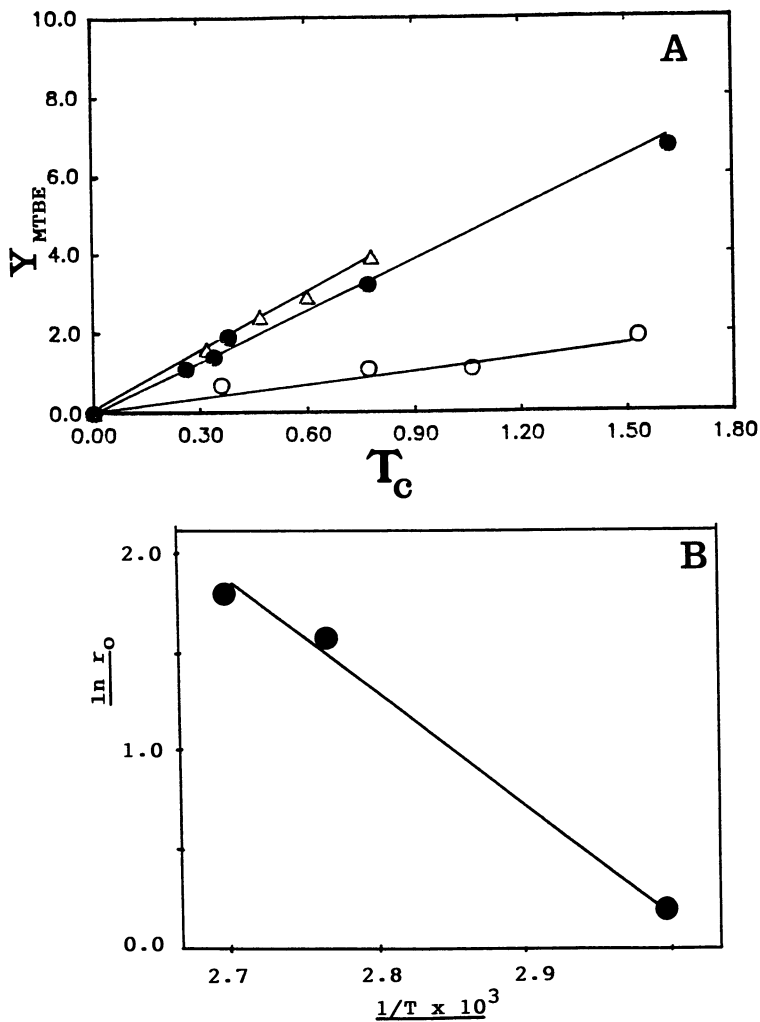


Figure 2 A) Yield of MTBE versus contact time. (○) = 345 K, (●) = 360 K and (△) = 371 K at short contact times. B) Arrhenius plot.

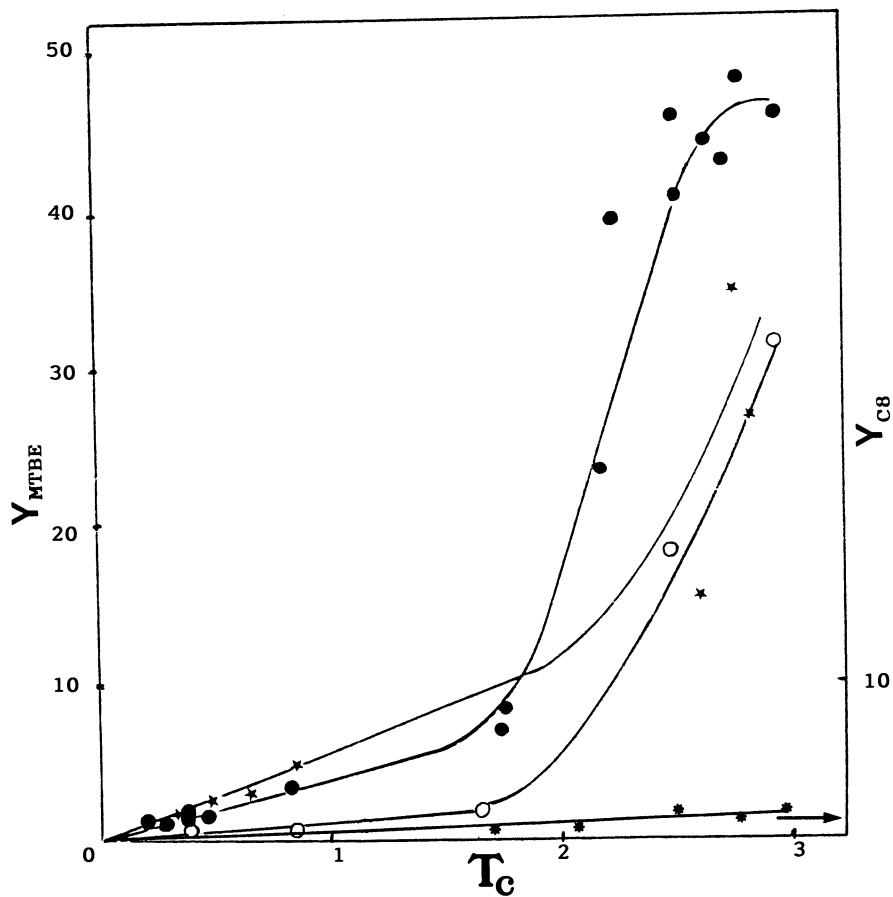


Figure 3 Yield of MTBE versus contact time. (○) = 345 K, (●) = 360 K and (★) = 371 K. (*) = yield in C8 products at 360 K.

et al [13]. At 360 K the production of MTBE reached a maximal value at a contact time of ca 2.5 h. At higher reaction temperatures, there was probably competition between formation and MTBE decomposition which might significantly reduce the final yield of MTBE [6]. Oligomers of isobutene higher than C8 (actually C12) were observed through GC and GC-MSD at reaction temperatures higher than 363 K.

In terms of catalyst stability, runs totalizing more than 50 hours were performed (temperature = 360 K, contact time = 2.6 h and methanol/isobutene ratio = 1.2). There was no significant loss of activity.

The same trends (activity maximum with respect to temperature and contact time) were obtained with the ETBE synthesis at 355 K, 363 K and 378 K, respectively (Figure 4). However, the yield of ETBE was much lower because of a parallel competitive reaction with the ETBE formation: the dehydration of ethanol to diethyl ether (Figure 5). The effect of this reaction was to decrease the concentration of ethanol adsorbed on the catalyst sites. The ethanol molecules which underwent dehydration to diethyl ether were no longer available to react with isobutene, since diethyl ether did not seem to be a precursor of ETBE (Figures 4 and 5). At reaction temperatures above 353 K, some hydrocarbons (C₁ - C₁₁) other than C8 and higher oligomers of isobutene are produced, mostly at longer contact times (Figure 5). As also shown in Figure 5, these hydrocarbons were derived from diethylether, in accord with earlier results obtained in a study of ethanol dehydration [14]. It is well known that the dehydration of ethanol to diethyl ether (activation energy = 56 KJ/mol [14]) is much easier than that of methanol (higher activation energy [15]). On the other hand, it is worth noting that for both MTBE and ETBE syntheses, the yields of C8 hydrocarbons which derived from isobutene by acid-catalyzed oligomerization, were - as expected - practically equal (Figures 3 and 4).

Some attempts were made to calculate the apparent activation energy for the ETBE synthesis. However, the value obtained (133 ± 15 KJ/mol) is tenuous owing to the presence of competitive reactions such as the ethanol dehydration to diethyl ether (already significant at 363 K) and ETBE decomposition at higher temperatures (above 373 K). The lower concentration of ethanol, which is normally available for the ether synthesis, was probably the cause for such a high value of the apparent activation energy [6].

Finally, dilution of the ethanol feed with water reduced significantly the production of diethylether. However, at high water dilution, the yield in ETBE decreased markedly (Table 2) because of the strong competition for adsorption of water with ethanol on the acidic reaction sites.

CONCLUSION

The gas phase syntheses of MTBE and ETBE over triflic acid loaded Y zeolite catalyst are temperature and contact time sensitive reactions. The activity maxima are observed at 358 K (85 °C) / 363 K (90 °C) and contact

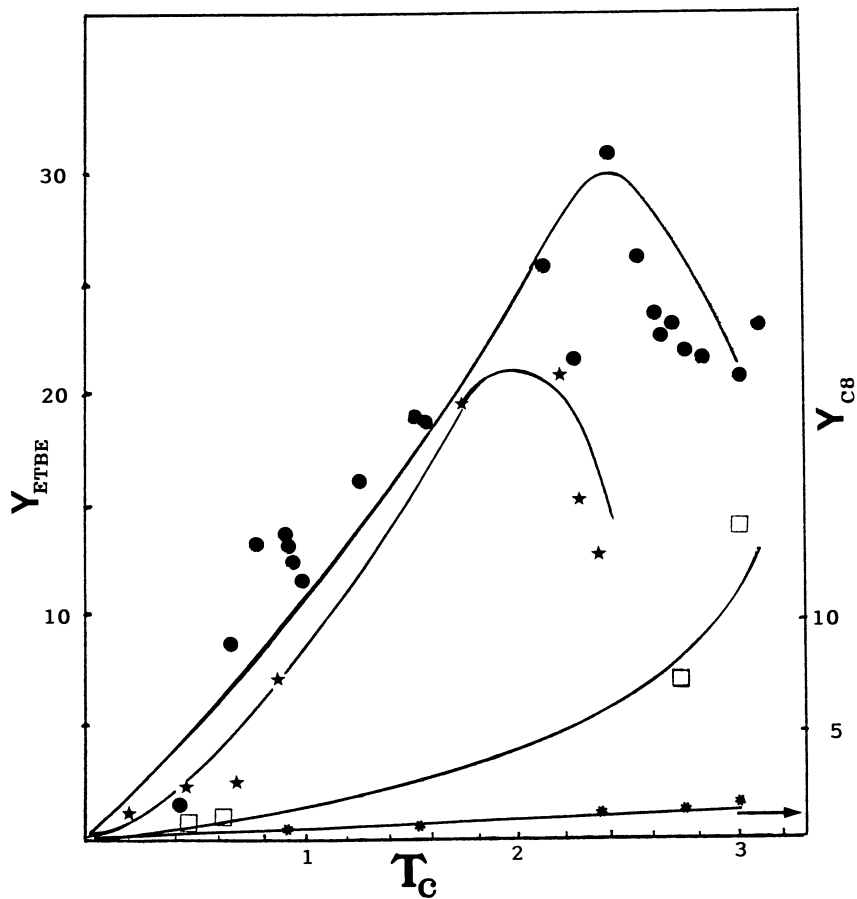


Figure 4 Yield of ETBE versus contact time. (\square) = 355 K, (\bullet) = 363 K and (\star) = 378 K. (\ast) = yield in C8 products at 363 K.

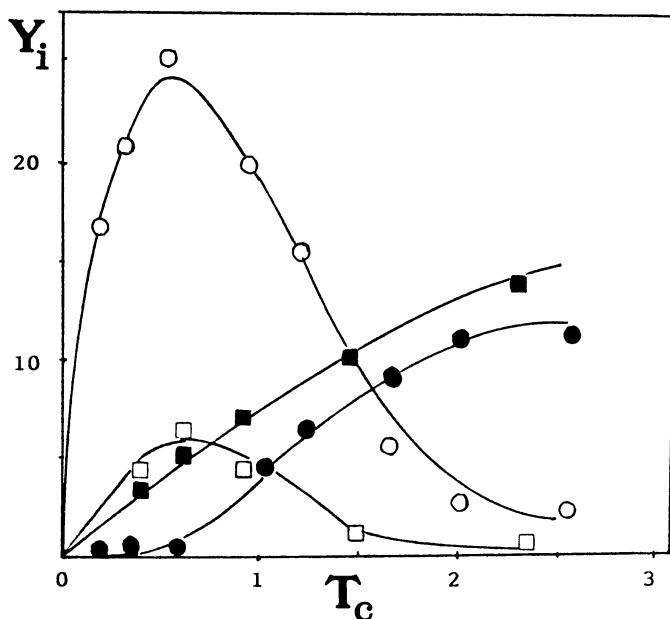


Figure 5 Yield of DEE (\circ = 363 K and \square = 378 K), and yield of hydrocarbons (oligomers of isobutene excluded, \bullet = 363 K and \blacksquare = 378 K), versus contact time.

Table 2 Effect of the dilution of feed ethanol with water (Reaction conditions: temperature = 363 K, contact time = 1.5 h and ethanol/isobutene ratio = 1.2).

Feed	Y_{ETBE}	Y_{DEE}	Y_{CB}	Y_{HC} (1)
100 % Ethanol	20	11	0.6	10
50 vol % Ethanol/ 50 vol % water	22	8	0.5	8 (2)
10 vol % Ethanol/ 90 vol % water	16	1	0.2	0.5 (2)

(1) yield in $C_1 - C_{11}$ hydrocarbons excluding diisobutene and other isobutene oligomers

(2) mostly ethylene

time of 2.5 ± 0.3 h. The presence of mesopores within the H-Y zeolite particles seems to favor the yield of MTBE. The lower yields of ETBE are due to the competitive dehydration of ethanol which alters the concentration of ethanol normally available for the ether synthesis.

ACKNOWLEDGEMENTS

We thank the following agencies: NSERC of Canada and Quebec's Action Structurante Program for their financial support. We also thank Prof. Nick Serpone, Mrs J. Yao and Mr. B. Sjiariel for their technical assistance.

REFERENCES

- [1] F. Ancillotti, M.M. Mauri and E. Pescarollo, *J. Catal.* (1977), **46**, 49.
- [2] G. Pecci and T. Floris, *Hydrocarbon Process.* (1997), **56**, 98.
- [3] L.M. Tau and B.H. Davis, *Appl. Catal.* (1989), **53**, 263.
- [4] P. Chu and G.H. Kuhl, *Ind. Eng. Chem. Res.* (1987), **26**, 365.
- [5] R. Le Van Mao, R. Carli, H. Ahlafi and V. Ragaini, *Catal. Lett.* (1990), **6**, 321.
- [6] A. Gicquel and B. Torck, *J. Catal.* (1983), **83**, 9.
- [7] E.P. Barrett, L.G. Joyner and P.P. Halenda, *J. Am. Chem. Soc.* (1951), **73**, 373.
- [8] R. Le Van Mao, T.M. Nguyen and G.P. McLaughlin, *Appl. Catal.* (1989), **48**, 267.
- [9] R. Le Van Mao, D. Ly and J. Yao, *Novel Production Methods for Ethylene, Light Hydrocarbons and Aromatics (ACS 1990 Natl Meeting, Boston)*, L. Albright, B.L. Crynes and S. Nowak (Ed.), Marcel Dekker (Publ.), New York (1992), p 409 - 424.
- [10] R. Le Van Mao and L. Huang, *Novel Production Methods for Ethylene, Light Hydrocarbons and Aromatics (ACS 1990 Natl Meeting, Boston)*, L. Albright, B.L. Crynes and S. Nowak (Ed.), Marcel Dekker (Publ.), New York (1992), 425 - 442.
- [11] R. Le Van Mao, T.M. Nguyen and G.P. McLaughlin, *Appl. Catal.* (1989), **48**, 267.
- [12] J.P. Beaufiles and M. Hellin, *Internal Report, Institut Francais du Petrole* (1963), mentioned in reference 6.
- [13] K.H. Chang, G. J. Kim and W.S. Ahn, *Ind. Eng. Chem. Res.* (1992), **31**, 125.
- [14] T.M. Nguyen and R. Le Van Mao, *Appl. Catal.* (1990), **58**, 119.
- [15] F. Figueras Roca, L. De Mourgues and Y. Trambouze, *J. Catal.* (1969), **14**, 107.

RECEIVED July 21, 1992

Chapter 17

Design of Layered Phosphate Hosts Containing Multiply Bonded Bimetallic Guest Species

Yeung-gyo K. Shin, Eric A. Saari, Mark R. Torgerson, and
Daniel G. Nocera

Department of Chemistry and the Center for Fundamental Materials
Research, Michigan State University, East Lansing, MI 48824

Layered metal phosphates offer two-dimensional crystalline environments in which to intercalate multielectron photoactive centers. Such solids may ultimately be effective in promoting selective photochemical transformations. Our recent discovery that quadruply bonded metal-metal ($M^{\text{---}4}M$) complexes can undergo multielectron photochemistry with small molecule substrates has prompted us to explore the intercalation chemistry of these complexes with layered metal phosphate host structures. The design of layered phosphates containing photoactive $M^{\text{---}4}M$ cores has developed along three lines: the direct intercalation of solvated $M^{\text{---}4}M$ cores into layered phosphates wherein the phosphate groups of the layers form the ligation sphere for the bimetallic core; acid-base reaction of specially functionalized ligands on the bimetallic core with protons from the layers; and, replacement of the phosphate groups with functionalized phosphonates that offer well-defined coordination sites for the $M^{\text{---}4}M$ core. Recent progress in each of these areas is presented.

Intracrystalline environments of host structures provide the architectural framework to assemble photochemical subunits for catalysis. The events that form the underpinning for light-to-energy conversion processes can be significantly modified in the solid state environment. A common design of many photochemical energy conversion schemes is predicated on the electron transfer chemistry of the photosynthetic reaction center in which an absorbed photon promotes efficient transmembrane separation of an electron/hole pair (1-4). Artificial systems aimed at mimicking photosynthesis have centered on the elaborate design of 'triads', whose structures consist of a donor and acceptor covalently attached to a light harvesting center (5-11).

The vectorial transport of an electron/hole pair away from a light harvesting center occurs by sequential charge separating electron transfer events (i.e. $DP^*A \rightarrow DP^+A^- \rightarrow D^+PA^-$). The complexity associated with molecularly engineered triads is greatly reduced when the electron transfer components of the triads are organized within solid state architectures (12-14). For instance, Mallouk et al. have catenated a metalloporphyrin (15) or $Ru(bpy)_3^{2+}$ (16) photosensitizer to a methylviologen charge transfer/Pt catalyst self-assembly organized within the channels of Zeolite-L. The dimensions of the channels confine the large photosensitizer to the exterior of the zeolite surface but juxtaposed to the long, cylindrical viologens residing within the zeolite. Excitation prompts electron transfer from the photosensitizer to the viologen, which in turn relays the electron to metallic Pt sites where proton reduction to hydrogen occurs. In this manner, a triad (sacrificial electron donor, photosensitizer, electron transfer carrier) is spatially organized at the zeolite/solution interface without the need for covalent attachment of a donor-photoreceptor-acceptor assembly.

Whereas the charge separated states of triads may persist in the microsecond range, the quantum yield for their production may be low owing to simple charge recombination of the electron/hole pair. In addition, photocatalysis based on triad systems requires that the initial electron/hole pair be stored in catalytic centers at the terminus of the network, and the overall process must be repeated to build up the necessary equivalents of holes and electrons needed for reaction. Alternatively, the structural complexity demanded for efficient charge separation and storage may be relaxed if more than one electron can be moved from a discrete excited state. Moreover, multielectron reaction from an electronically excited core obviates the necessity for charge storage coupled to catalytic redox centers.

To this end, we have become interested in designing solid state assemblies in which a multielectron photoactive center is incorporated between redox active layers of a host structure. An objective of our research is to develop photocatalytic cycles of the type depicted in Figure 1. In this schematic the substrate is activated at a multielectron photoactive center (MPC) in the intracrystalline environment. In principle, regeneration of the oxidized photoactive core can be achieved with auxiliary redox-active metal centers in the solid state support. Subsequent oxidation of substrate at the layers will re-establish the formal oxidation state of the metals composing the host layers thereby completing the catalytic cycle. In this approach, multielectron activation occurs in a discrete step at the MPC and thus does not rely on charge propagation via one-electron intermediates of a charge separating network. The exclusion of the relay system leads to an important advantage of this approach in that the intricate structural engineering of photoactive solids needed to prevent charge recombination is circumvented. Our recent discovery of two-electron photoreactions of quadruply-bonded metal-metal (M^4-M) systems with small molecule substrates (17-19) has prompted us to begin designing structures in which the MPC is a M^4-M complex. Of course the design of such structures requires physical and chemical compatibility between supporting host structures and M^4-M bimetallic complexes. Our early studies concentrated on complex layered

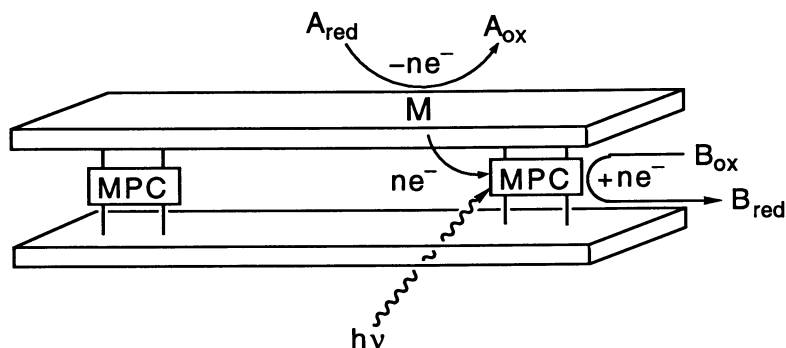


Figure 1. Schematic of a possible photocatalytic cycle based on the photochemistry of a multielectron photoactive center (MPC) intercalated within redox active layers of a host structure.

oxides (CLOs) as layered supports (20), but we soon realized that CLOs are not readily adapted to Figure 1 because the metals composing the layers of CLO structures are generally redox-inactive (21), the basicity of CLOs is not compatible with M^{4+} - M species, which are susceptible to the formation of hydroxo and oxo complexes (22), and the chemical properties of CLOs, for the most part, are too irreproducible for reliable photochemical study. Conversely, layered metal phosphates (LMPs) are superb host compounds for binuclear metal cores because they are acidic and may be synthesized to yield pure crystalline materials featuring redox-active metals composing the layered host structure (23,24). In addition, LMPs display high stability toward temperature, irradiation, and most organic and inorganic environments.

Structures and Exchange Properties of Layered Metal Phosphate Hosts

The structures of two classes of LMPs are shown in Figure 2. Vanadyl phosphate ($VOPO_4$) consists of an array of alternating VO_6 octahedra and PO_4 tetrahedra that share their corners. Specifically, four equatorial oxygens of the VO_6 octahedra are provided by four different adjacent phosphate groups. The apical positions are completed with a terminal $V=O$ bond and a coordinating oxygen from one of two gallery waters. This corner sharing of phosphates to the V^{5+} center is extended in two-dimensions to produce sheets of $[(H_2O)VOPO_4]_n$ that are stacked in the crystallographic *c*-direction (25,26). The second water molecule resides in the gallery between phosphate groups of adjacent layers. The $Zr(HPO_4)_2$ structure consists of layers formed from the octahedral coordination of Zr^{4+} by oxygens of the tripodal bases of six different phosphate tetrahedra in a D_{3d} arrangement (27,28). Three of the phosphate oxygens are bound to metal centers leaving an apical oxygen bearing an exchangeable proton directed into the gallery region.

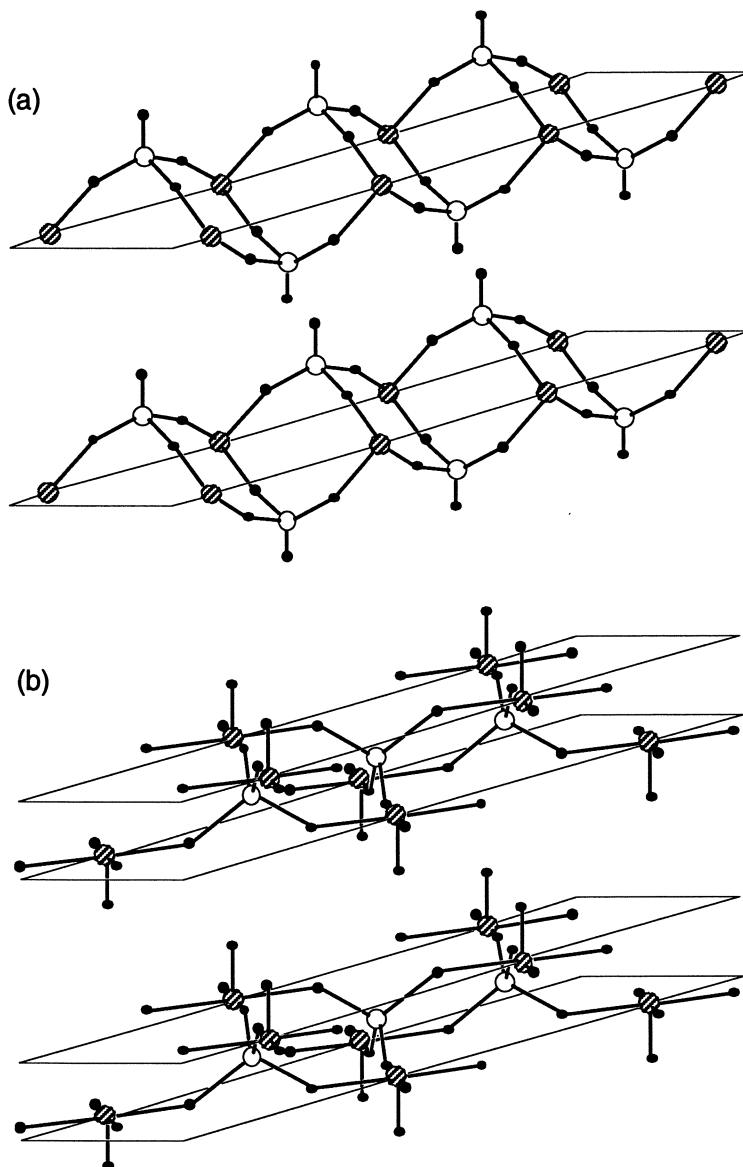


Figure 2. Idealized structures of the layered hydrates of (a) zirconium phosphate and (b) vanadyl phosphate. The metal atoms are shown by the hatched circles, phosphorus atoms by open circles, and oxygen atoms by small black circles. For clarity, the oxygens of intra- and intergallery water molecules in vanadyl phosphate structure are not shown.

The differences in the structures of layered zirconium and vanadyl phosphates are manifested in their disparate intercalation chemistries. Owing to the phosphate's apical hydroxyl group, which protrudes into the gallery of $\text{Zr}(\text{HPO}_4)_2$, incorporation of guests into this solid occurs by Brønsted acid/base chemistry or simple cation exchange (29,30). In contrast, there are no exchangeable protons associated with VOPO_4 layers. Instead the vanadium centers, which are in their highest formal oxidation state, are susceptible to reduction. In fact, metal centers in the reduced V^{4+} state are one of the most common defects in VOPO_4 layered compounds (31). Incorporation of guest ions into the gallery proceeds by an intercalative process whereby the layers are reduced ($\text{V}^{5+} \rightarrow \text{V}^{4+}$) with the concomitant insertion of cationic guests to maintain charge neutrality (32-34). A second mode of intercalation for these solids is seen in the replacement of the vanadium-coordinated water by Lewis bases such as organic amines (35); this formally represents a non-reductive intercalation pathway.

On the basis of these properties, the three approaches summarized in Figure 3 have been elaborated specifically for the introduction of photoactive $\text{M}^{4+}\text{-M}$ cores into layered phosphate host structures. These are: (1) the direct intercalation of solvated $\text{M}^{4+}\text{-M}$ cores into layered phosphates wherein the phosphate groups of the layers form the ligation sphere for the bimetallic core; (2) acid-base reaction of specially functionalized ligands on the bimetallic core with protons from the layers; and (3) replacement of the phosphate groups with functionalized phosphonates that offer well-defined coordination sites for the $\text{M}^{4+}\text{-M}$ core. We now discuss each of these methodologies.

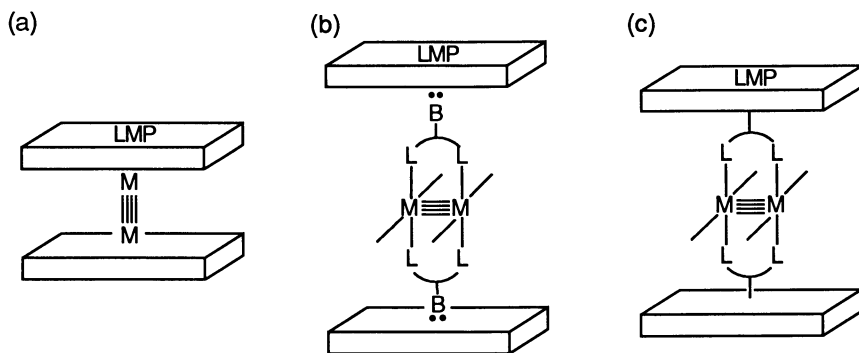


Figure 3. Three basic strategies for the incorporation of multiply bonded metal-metal guest species into vanadyl and zirconium phosphate host layers. (a) The direct intercalation of solvated $\text{M}^{4+}\text{-M}$ cores into the native layered phosphate host structure. (b) Incorporation of $\text{M}^{4+}\text{-M}$ complexes with ancillary ligands containing a Lewis basic site. (c) Coordination of $\text{M}^{4+}\text{-M}$ cores with ligands provided from modified phosphate layers.

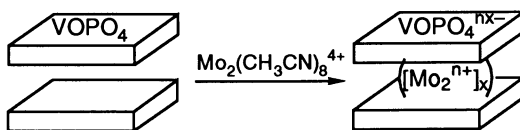
Incorporation of M^{4+} - M Complexes into Layered Metal Phosphates

Redox Intercalation of a Multiply Bonded Dimolybdenum Core into Layered Vanadyl Phosphate. Layered solids described by Figure 3a were explored by studying the chemistry of dimolybdenum guest cations in the intergallery region of VOPO_4 . The motivation for this work was provided by an extensive background knowledge of the structure, spectroscopy, and chemistry of the quadruply bonded $\text{Mo}_2(\text{II,II})$, mixed-valence $\text{Mo}_2(\text{II,III})$, and triply bonded $\text{Mo}_2(\text{III,III})$ cores (36-40) coordinated by phosphate ions.

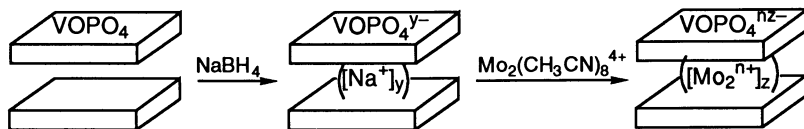
A dimolybdenum core is most easily introduced into LMPs by employing $\text{Mo}_2(\text{CH}_3\text{CN})_8^{4+}$ as a source. Oxidation of Mo_2^{4+} cores to mixed-valence Mo_2^{5+} or triply bonded Mo_2^{6+} cores (36) provides the driving force for the redox intercalation chemistry. Alternatively, the high positive charge of the Mo_2^{4+} solvate permits its ion-exchange with simple inorganic cations intercalated within the galleries of layered vanadyl phosphate.

We have prepared dimolybdenum intercalates of $\text{VOPO}_4 \cdot 2\text{H}_2\text{O}$ by the two separate routes shown in Schemes I and II (41). Scheme I summarizes a redox intercalation pathway where $\text{Mo}_2(\text{CH}_3\text{CN})_8^{4+}$ is reacted directly with the native layered material. Interestingly, ESCA reveals that the stoichiometry ($\text{VOPO}_4 \cdot \text{Mo}_{0.19}$) of solids obtained by ion-exchange of the Na^+ intercalate with $\text{Mo}_2(\text{CH}_3\text{CN})_8^{4+}$ (Scheme II) is virtually identical to that ($\text{VOPO}_4 \cdot \text{Mo}_{0.19}$) observed for the redox-intercalation pathway of Scheme I. We believe that the observed metal contents obtained by Schemes I and II represent the highest possible loading for these layers because the same loadings are obtained even when ion-exchange is performed from solutions containing the guest complex at concentrations ~ 5 times the maximum redox capacity of host layers.

Scheme I



Scheme II



The nature of the molybdenum species within the LMP prepared by Schemes I and II is revealed by electronic and magnetic spectroscopy, which are particularly useful because the spectroscopic behavior of multiply bonded dimolybdenum cores coordinated by phosphate ions is well

established (36,40). Whereas the observation of absorption bands from a dimolybdenum guest in a VOPO₄ host is difficult owing to layer absorption throughout the visible spectral region (transitions associated with the reduced V⁴⁺ centers occur at λ_{\max} = 850, 640, 470 and 300 nm) (36), absorptions of the dimolybdenum guest in the isostructural LMP of NbOPO₄ are easily distinguished. Reaction of NbOPO₄ with Mo₂(CH₃CN)₈⁴⁺ yields solids that are chemically similar to the vanadium system. Absorption spectra of these solids show bands at ~480 nm and ~550 nm in the visible and at 1400 nm in the near-IR spectral region, which are characteristic of the mixed-valence Mo₂(II,III) tetraphosphate (λ_{\max} = 420, 595, and 1400 nm for Mo₂(HPO₄)₄³⁻ (40)). The intercalation of a Mo₂(II,III) core into LMP is further established by EPR studies. The narrow EPR signal, observed for the d¹ (V⁴⁺) spin centers in reduced layers of Na⁺-intercalated VOPO₄, is broadened significantly upon intercalation of a dimolybdenum guest (41). The increase of the EPR line width to ~750 G peak-to-peak separation upon incorporation of a dimolybdenum guest is consistent with a spin-spin interaction between the d¹ centers of the layer and the nearby paramagnetic Mo₂(II,III) centers. Furthermore the observation of line narrowing (by ~100 G) upon exposure of the layered intercalate to air is consistent with the depletion of the Mo₂(II,III) paramagnet by oxidation to the diamagnetic Mo₂(III,III) triply-bonded metal-metal species, which occurs rapidly for the molecular Mo₂(II,III) tetraphosphate ion in air (38,39).

It is interesting that a Mo₂(II,III) intercalate is obtained by either Schemes I or II. Our studies on Mo₂(II,II) coordinated by tetraphosphate anion, Mo₂(HPO₄)₄⁴⁻, show that it is extremely susceptible to oxidation to the mixed-valence Mo₂(HPO₄)₄³⁻ dimer (36). Indeed, solutions of Mo₂(HPO₄)₄⁴⁻ are smoothly converted to Mo₂(HPO₄)₄³⁻ by the weakly oxidizing M—M complex Mo₂(HPO₄)₄²⁻ in a simple comproportionation reaction. Presumably, the Mo₂(II,II) core is not stable in a phosphate environment, and parallel to the molecular solution chemistry, the mixed-valence Mo₂(II,III) bimetallic center is the thermodynamic product.

This "solid state" coordination environment of the intercalated Mo₂⁵⁺ core is similar to that when coordinated by molecular phosphate ion. A reduction in the gallery height (d_{001} = 7.49 Å for VOPO₄·2H₂O, and d_{001} = 6.45 and 6.41 Å for the intercalate prepared by Schemes I and II, respectively) is observed when the Mo₂⁵⁺ core is introduced into the VOPO₄ layers. This compression of layers about a small positively charged cation is attributed to the electrostatic interactions in the intercalate being much stronger than the hydrogen bonding interactions of the native LMP structure. Based on the crystallographic data of Tietze (42), the 2.9 Å d-spacing of the Mo₂⁵⁺-intercalated LMP is consistent with a transverse disposition of the Mo₂⁵⁺ core between LMP interlayers, where each molybdenum center of the binuclear core is keyed into a tetragonal oxygen pocket of the layer. The four oxygens of the tetragonal pocket are corner-shared between vanadium octahedra and phosphate tetrahedra, and are available for coordination to guest cations (43). As shown in Figure 4, this solid-state coordination environment approximates the molecular crystal structure of the mixed-valence diphenylphosphate, Mo₂[O₂P(OC₆H₅)₂]₄-

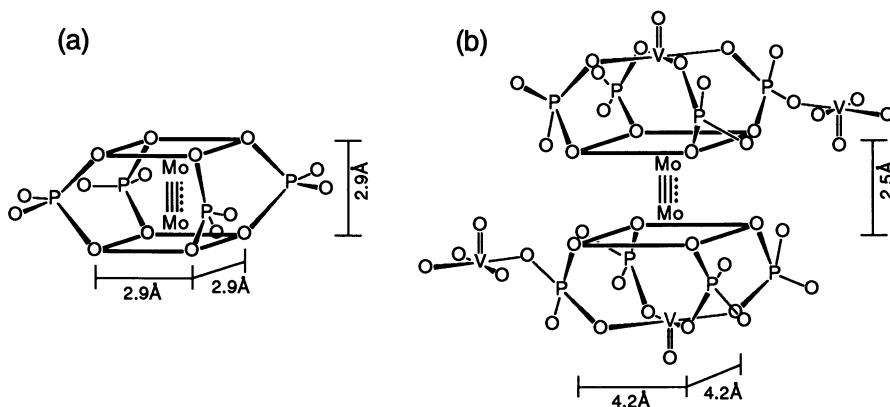


Figure 4. The dimensions of (a) the oxygen environment of $\text{Mo}_2[\text{O}_2\text{P}(\text{OC}_6\text{H}_5)_2]_4(\text{BF}_4)$ as determined from the X-ray crystallographic data of reference 37; and (b) the tetragonal oxygen coordination environment for Mo_2^{5+} -intercalated VOPO_4 .

(BF_4) (37) and, more generally multiply bonded “ Mo_2O_8 ” coordination spheres (44). The interlayer keying of a host with a guest has been observed previously by us in the ion-exchange chemistry of *trans*-dioxorhenium(V) complexes in layered oxides (20), and may give rise to interesting magnetic behavior of the Mo_2^{5+} intercalate (41).

In the context of designing photoactive LMP intercalates, the introduction of solvated $\text{M}^4\text{—M}$ cores into native LMP structures is restrictive inasmuch as the coordination environment of the $\text{M}^4\text{—M}$ center is limited to phosphate. Whereas *tetrakis*(phosphato)dimolybdenum complexes promote the two-electron photoreductions of protons and halocarbons, substrate activation occurs by one-electron radical pathways only upon ultraviolet irradiation (36,37,45). A richer visible photochemistry of $\text{M}^4\text{—M}$ complexes can occur, but it requires ligands other than phosphate in the intergallery environment (17-19,46). Accordingly, methodologies aimed at designing LMPs that contain photochemically active $\text{M}^4\text{—M}$ complexes with modified ligation environments are presented in the following sections.

Intercalation of Multiply Bonded Dimolybdenum Complexes Featuring Lewis Bases as Ligands. Alkyl and aryl amines readily intercalate into $\text{Zr}(\text{HPO}_4)_2 \cdot \text{H}_2\text{O}$ (24,47), $\text{VOPO}_4 \cdot 2\text{H}_2\text{O}$ and their related structures (35) to form bilayers. For the former phosphate, the driving force for intercalation is the formation of alkylammonium ions whereas in the latter, strong intermolecular and ion-dipole interactions provide the driving force for intercalation of the amine. Metal complexes have been introduced within the

layers of LMPs when one or more of the ligands of the complex has an ancillary amine (48). Thus the strategy for introducing $M^{4+}-M$ cores into layered phosphates described by Figure 3b can be developed by including amine or pyridine functionalities directly onto the ligands of an $M^{4+}-M$ core.

The uncoordinated heterocyclic nitrogen of the pyrimidine ligand of $Mo_2(dmhp)_4$ ($dmhp = 2,4\text{-dimethyl-6-hydroxypyrimidine}$) (49) makes this complex an good intercalant of LMPs. The absorption profile, exhibiting visible bands at 370 ($\epsilon/M^{-1}cm^{-1} = 15200$) and 490 ($\epsilon/M^{-1}cm^{-1} = 880$) nm in methanol, is characteristic of $M^{4+}-M$ species coordinated by hydroxypyridines (e.g. $Mo_2(mhp)_4$ (λ/nm ($\epsilon/M^{-1}cm^{-1}$) = 405 (13270); 495 (2450) (50)) with the lowest energy absorption corresponding to the well-known $^1(\delta^2 \rightarrow \delta\delta^*)$ transition (51). Yellow-orange solutions of $Mo_2(dmhp)_4$ turn red upon protonation of the $dmhp$ ligands. Excitation of the $\delta^2 \rightarrow \delta\delta^*$ absorption of the compound in aprotic solutions leads to red luminescence (Figure 5, trace (o)), the energy and intensity of which is comparable to $Mo_2(mhp)_4$. The luminescence is significantly red-shifted and attenuated upon protonation of the uncoordinated heterocyclic nitrogen(s) (Figure 5, traces (i) - (iv)). This proton dependence of $Mo_2(dmhp)_4$ luminescence provides a convenient experimental handle in the study of the intercalation chemistry of this compound with LMPs.

We specifically have studied the reactivity of the $Zr(HPO_4)_2$ system with $Mo_2(dmhp)_4$ and found that the reaction is facilitated by swelling the layers with alcohols or amines. In the latter case, the d_{001} spacing of 7.6 Å of $Zr(HPO_4)_2 \cdot H_2O$ significantly increases to 19.8 Å upon intercalation with *tert*-octylamine (TOA), which is accomplished by stirring the layered phosphate in slightly acidified solutions of 0.4 M TOA. The amine pre-treated material turns pale yellow upon reaction with $Mo_2(dmhp)_4$ and the final product exhibits a slightly contracted d-spacing of 17.9 Å. Under illumination the solid is strongly emissive. Trace (v) of Figure 5 shows that the emission arises mostly from the deprotonated form of $Mo_2(dmhp)_4$, which is not too surprising inasmuch as pre-treatment with TOA renders the proton unavailable for reaction with $Mo_2(dmhp)_4$. Infrared analysis shows that TOA is retained in the layers, even after reaction with the bimetallic complex. However, the orientation of the $Mo_2(dmhp)_4$ in the gallery is not known.

Alcohols are thought to swell $Zr(HPO_4)_2$ layers by weakly associating with the proton of the gallery phosphate, and are displaced upon reaction with other intercalates. Ethanol can be introduced into the layers by stirring the half-exchanged Na^+ -pentahydrate form with ethanol containing 1% perchloric acid (52). The ethanol-swelled product has a d_{001} spacing of ~14 Å, which significantly contracts to 10.6 Å upon reaction with $Mo_2(dmhp)_4$. The intercalated product is weakly luminescent, and as shown in trace (vi) of Figure 5, the emission spectrum is consistent with a $Mo_2(dmhp)_4$ complex in which each of the pyrimidine ligands are protonated. The short interlayer spacing of the ethanol pre-treated material necessarily demands that the $Mo_2(dmhp)_4$ complex be tilted end-on with its metal-metal axis normal to the plane of the layers; accommodation of $Mo_2(dmhp)_4$ with the $Mo^{4+}-Mo$ core parallel to the layers would require a d-spacing of ~13 Å with keying

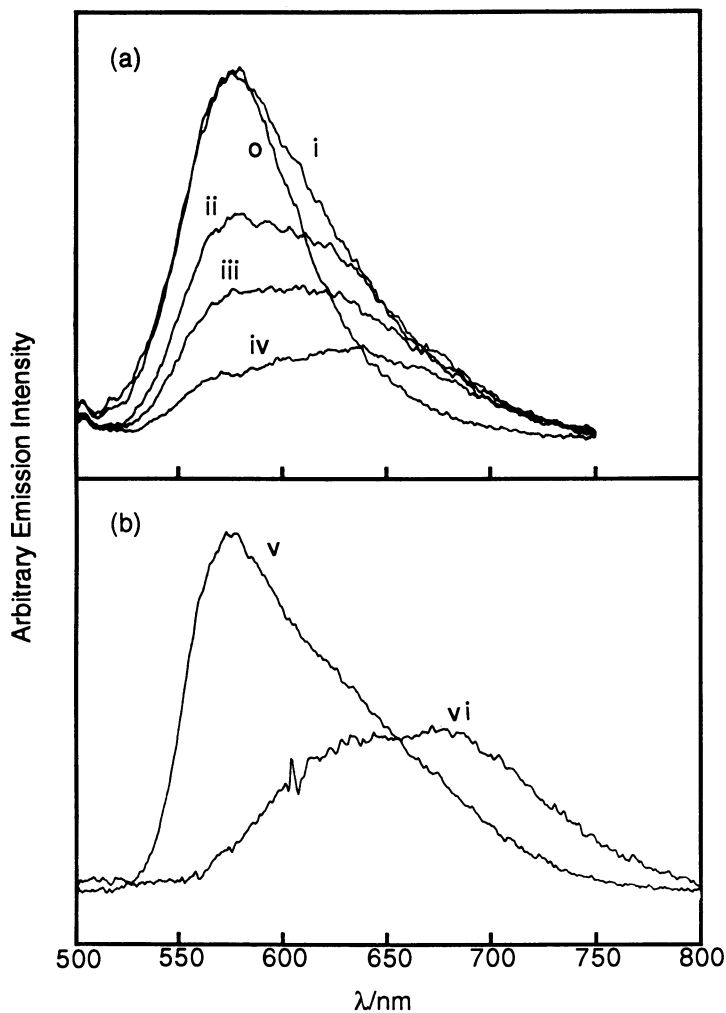


Figure 5. (a) Emission spectra ($\lambda_{\text{exc}} = 436$ nm) of $\text{Mo}_2(\text{dmhp})_4$ (dmhp = 4,6-dimethyl-2-hydroxypyrimidine) in (o) methanol, and HCl-acidified methanol with (i) 1-, (ii) 2-, (iii) 3-, and (iv) 4-equivalents of HCl per equivalent of metal complex. (b) Emission spectra ($\lambda_{\text{exc}} = 436$ nm) of (v) *tert*-octylamine-intercalated zirconium phosphate and (vi) ethanolic pre-swelled zirconium phosphate treated with $\text{Mo}_2(\text{dmhp})_4$. Traces (o) - (v) show relative emission intensities and traces (v) and (vi) are arbitrary and unrelated to each other.

into the lattice and $\sim 15 \text{ \AA}$ without keying. An end-on orientation may be preferred because the heterocyclic nitrogens of the pyrimidine are directed towards the phosphate layers. This orientation thus permits protons to form strong hydrogen bonds to the uncomplexed nitrogens of the ligands.

Design of Layered Phosphonates Possessing Functionalities for Coordination to Multiply Bonded Bimetallic Cores. Solids shown in Figure 3c can be designed readily with LMPs because their galleries can be modified by pendant functionalities covalently anchored to the layers with the methods introduced by Alberti (28,53) and Dines (54-57). Reaction of organic phosphonic or arsonic acids with M^{4+} oxides, oxychlorides, and halides yields $M(O_3XR)_2$ ($X = P$ or As ; $M = Ti, Zr, U, Th,$ and Ce) layered materials,



The backbone of these new layers is similar to that in simple zirconium phosphate layers with M^{4+} coordinated by six oxygens from six different phosphonates. However, the apical oxygen, which is protonated in $Zr(HPO_4)_2 \cdot H_2O$, is replaced by alkyl or aromatic groups. These pendant organic groups are normal to the layer, giving rise to hybrid solids with alternating inorganic and organic sheets (23,29,58-60). Jacobson and Johnson (61) have further elaborated the basic strategy of Alberti and Dines to include vanadyl phosphates. For example, the reaction V_2O_5 with organic phosphonates yields $VO(O_3PR) \cdot nH_2O$ ($n = 1$ or 2),



In the case of $n = 2$, a newberyite structure (62) has been proposed on the basis of X-ray diffraction analysis (63). The structure consists of VO_6 octahedra with the vanadyl oxygen normal to the phosphate layers. Four equatorial oxygens are from three different neighboring phosphonates and a water molecule. A second weakly coordinating water molecule occupies the final coordination site *trans* to the vanadyl oxygen. As in the case for the $Zr(O_3PR)_2$ structure, the phosphonate R groups are directed into the gallery region.

The ability to modify the backbones of LMP structures with phosphonates allows for wide flexibility in the design of new materials containing photoactive binuclear metal cores. The goal of our initial studies has been to demonstrate that a ligating functionality within the gallery is accessible for reaction with a bimetallic core. To demonstrate these initial objectives, we have chosen to study zirconium phosphate modified with alkyl carboxylate, which is a good ligand of bimetallic cores.

The layered phosphonates of zirconium, $Zr(O_3PCH_2CH_2COOH)_2$, and vanadium, $VO(O_3PCH_2CH_2COOH)_2$, were prepared by following Dine's (reaction 1) and Jacobson and Johnson's (reaction 2) procedures, respectively, with $X = P$ and $R = CH_2CH_2COOH$. For the vanadium system, we get the interdigitated material shown in Figure 6, where a chain assumes a *trans* conformation, directed toward an alcohol co-solvate (which occupies

the axial site of the d^1 V(IV) center in the neighboring layer). The material's d-spacing varies as a function of the chain length of the alcohol. The zirconium layered compound exhibits a d-spacing of 12.7 Å; this interlayer spacing agrees nicely with the formation of an organic bilayer structure in which the propyl groups are in an all *trans* configuration. This bilayer arrangement of alkyl chains has been reported in many other layers when guests are long chain amines and alcohols (24,53,64-67). A broad C=O band at 1701 cm^{-1} establishes hydrogen bonding of the COOH moieties in the bilayer arising from cyclic dimer formation between COOH groups of adjacent layers and/or hydrogen bonding to the interlayer solvent (68). These alkyl acid modified layers are very stable toward intercalation reactions that utilize the acid group as a ligand. An attempt to introduce $\text{Mo}_2(\text{CH}_3\text{CN})_8^{4+}$ into the phosphonate to obtain layer-analogs of molecular $\text{Mo}-^4-\text{Mo}$ carboxylates was not successful. No molybdenum was detected by ESCA and no color change was observed upon reaction. The organized assembly of hydrogen bonding between layers apparently stabilizes the carboxylate with respect to their reaction with bimetallic guests.

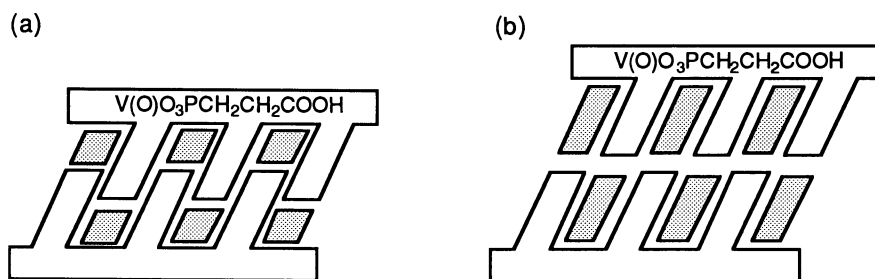


Figure 6. Schematic representation of $\text{VO}(\text{O}_3\text{PCH}_2\text{CH}_2\text{COOH})$ prepared by reaction 2. Pendant phosphonates, which are directed into the layer in a gauche conformation, are (a) interdigitated when the alcohol co-solvate (indicated by shaded rectangles) is ≤ 3 carbons and (b) in a head-to-tail conformation for > 3 carbons. The d-spacings for the MeOH, EtOH, PrOH, BuOH, and BzOH materials are 13.8, 14.8, 16.4, 18.2, and 18.6 Å, respectively.

This exceptionally strong association of layers can be broken by base. Thompson and Burwell (69) have shown that interlayer hydrogen bonding of carboxylic acid chains is alleviated by treating the layers with anhydrous NH_3 to produce ammonium carboxylate. In principle the ammonium ion may be displaced by ion-exchange. Accordingly, the ammonium pre-intercalate $[\text{Zr}(\text{O}_3\text{PCH}_2\text{CH}_2\text{COO}^-)_2](\text{NH}_4^+)_2$ was treated with a deep blue acetonitrile solution of $\text{Mo}_2(\text{CH}_3\text{CN})_8(\text{PF}_6)_4$. The white solid turns light red-orange as ion-exchange proceeds. Although we do not know the stereochemistry or extent of carboxylate ligation to dimolybdenum cores, it is known that *cis*-

$\text{Mo}_2(\text{OAc})_2(\text{CH}_3\text{CN})_4^{2+}$ is red (70). ESCA spectra reveal that 50% of the carboxylate sites are occupied by dimolybdenum cores.

Summary and Conclusions

Layered metal phosphates appear to be ideal host structures for M^{4+}M guests. The physical and chemical properties of LMPs are compatible with those properties of M^{4+}M cores, and indeed the coordination environments of M^{4+}M centers in molecular solids can be achieved within the gallery regions of LMPs by using a variety of approaches. In the context of designing photoactive M^{4+}M -LMP intercalates according to the approaches schematically represented in Figure 3, pathways a and b are somewhat restrictive in that the coordination environment is limited to phosphate or a ligand possessing a free Lewis basic site, respectively. For this reason, pathway c appears to be the more promising because of the broad flexibility in affixing a variety of ligands to the layers according to reactions 1 and 2. The commercial availability of several phosphonates coupled with standard Abruzov (71), Bart (72), and Michaelis-Becker (73) chemistry should permit layers with amines, pyridines, carboxylic acids, nitriles, isonitriles, phosphines, and arsines to be tailored.

New approaches to the design of M^{4+}M -LMPs remain to be explored. Whereas Figure 3 relies on the incorporation of M^{4+}M centers into pre-formed layers, the phosphate host may also be synthesized about the photoactive cores. By carrying out reactions 1 and 2 with M^{4+}M centers coordinated by $\text{L}^{\text{vw}}\text{PO}(\text{OH})_2$ (i.e. L is a ligand pre-attached to the metal cores), layers can be condensed about the bimetallic core. Additionally, Mallouk (74), Katz (75), and Umemura (76) and their co-workers have demonstrated that metal phosphonates can be synthesized layer-by-layer. Such an approach may be adapted to the design of photoactive solids by attaching $\text{L}^{\text{vw}}\text{PO}(\text{OH})_2$ to a surface and then treating repetitively with M^{4+}M solvates followed by $\text{L}^{\text{vw}}\text{PO}(\text{OH})_2$ and MOCl_2 . These new approaches benefit from the advantage that the M^{4+}M cores can be homogeneously dispersed throughout the gallery. This is probably not the case for the methodologies outlined in Figure 3, which are likely to give a heterogeneous distribution of M^{4+}M cores within the layers.

The synthesis of M^{4+}M -LMP materials pose many interesting issues in regard to the design of photocatalytic solids described by Figure 1. These include: how are the excited state properties of the MPC system perturbed by the layers?; is multielectron photoactivity of M^{4+}M core retained within the layers?; can the photoactive M^{4+}M core communicate with metals of the layers by energy transfer?, electron transfer?; and, can the photoreacted M^{4+}M core undergo redox reactions with the layers? We believe that the ability to assemble a 'molecular' coordination environment within the layered phosphates will permit us to use our knowledge of M^{4+}M photophysics and photochemistry as a benchmark for addressing these issues in the solid state.

Acknowledgments

Our studies of layered metal phosphates has generously been supported by the National Science Foundation (CHE-9100532).

Literature Cited

1. Babcock, G. T.; Barry, B. A.; Debus, R. J.; Hoganson, C. W.; Atamian, M.; McIntosh, L.; Sithole, I.; Yocum, C. F. *J. Am. Chem. Soc.* **1989**, *28*, 9557.
2. Kirmaier, C.; Holten, D. In *The Photosynthetic Bacterial Reaction Center—Structure and Dynamics*; Breton, J., Vermeglio, A., Eds.; Plenum: New York, 1988; p 219.
3. Hochstrasser, R. M.; Johnson, C. K. In *Ultrafast Laser Pulses and Applications*; Kaiser, W., Ed.; Topics in Applied Physics, Vol. 60; Springer-Verlag: New York, 1988; p 357.
4. Fox, M. A. *Photochem. Photobiol.* **1990**, *52*, 617.
5. Meyer, T. J. *Acc. Chem. Res.* **1989**, *22*, 164.
6. Duesing, R.; Tapolsky, G.; Meyer, T. J. *J. Am. Chem. Soc.* **1990**, *112*, 5378.
7. Perkins, T. A.; Humer, W.; Netzel, T. L.; Schanze, K. S. *J. Phys. Chem.* **1990**, *94*, 2229.
8. Schmehl, R. H.; Ryu, C. K.; Elliott, C. M.; Headford, C. L. E.; Ferrere, S. In *Electron Transfer in Biology and the Solid State*; Johnson, M. K.; King, R. B.; Kurtz, Jr., D. M.; Kutal, C.; Norton, M. L.; Scott, R. A., Eds.; Advances in Chemistry Series No. 226; American Chemical Society: Washington, DC, 1990; p 211.
9. *Photoinduced Electron Transfer II*; Mattay, J., Ed.; Springer-Verlag: New York, 1990.
10. Gust, D.; Moore, T. A.; Moore, A. L.; Gao, F.; Luttrull, D.; DeGraziano, J. M.; Ma, X. C.; Making, L. R.; Lee, S.-J.; Trier, T. T.; Bittersmann, E.; Seely, G. R.; Woodward, S.; Bensasson, R. V.; Rougée, M.; De Schryver, F. C.; Van der Auweraer, M. *J. Am. Chem. Soc.* **1991**, *113*, 3638.
11. Wasielewski, M. R.; Gaines III, G. L.; O'Neil, M. P.; Svec, W. A.; Niemczyk, M. P. *J. Am. Chem. Soc.* **1990**, *112*, 4559.
12. Ramamurthy, V. In *Photochemistry in Organized and Constrained Media*; Ramamurthy, V., Ed.; VCH: New York, 1991; Chapter 10.
13. Grätzel, M. *Heterogeneous Photochemical Electron Transfer*; CRC Press: Boca Raton, FL, 1989.
14. Kalyanasundaram, K. *Photochemistry in Microheterogeneous Systems*; Academic Press: Orlando, FL, 1987; Chapter 10.
15. Persaud, L.; Bard, A. J.; Campion, A.; Fox, M. A.; Mallouk, T. E.; Webber, S. E.; White, J. M. *J. Am. Chem. Soc.* **1987**, *109*, 7309.
16. Krueger, J. S.; Mayer, J. E.; Mallouk, T. E. *J. Am. Chem. Soc.* **1988**, *110*, 8232.
17. (a) Partigianoni, C. P.; Turró, C.; Chang, I.-J.; Nocera, D. G. In *Photosensitive Metal-Organic Systems*; Kutal, C., Ed.; Advances in Chemistry Series; American Chemical Society: Washington, DC, in press.

18. Partigianoni, C. P.; Turró, C.; Shin, Y.-g. K.; Motry, D. H.; Kadis, J.; Dulebohn, J. I.; Nocera, D. G. *Mixed Valency Systems: Applications in Chemistry, Physics, and Biology*; Prassides, K. Ed.; Kluwer Academic: Dordrecht, 1991; p 91.
19. Partigianoni, C. P.; Chang, I.-J.; Nocera, D. G. *Coord. Chem. Rev.* **1990**, *97*, 105.
20. Newsham, M. D.; Giannelis, E. P.; Pinnavaia, T. J.; Nocera, D. G. *J. Am. Chem. Soc.* **1988**, *110*, 3885.
21. King, R. D.; Nocera, D. G.; Pinnavaia, T. J. *J. Electroanal. Chem.* **1987**, *236*, 43.
22. Dulebohn, J. I.; Ward, D. L.; Nocera, D. G. *Polyhedron* **1991**, *10*, 2813.
23. Clearfield, A. *Comm. Inorg. Chem.* **1990**, *10*, 89.
24. Alberti, G. In *Intercalation Chemistry*; Whittingham, M. S.; Jacobson, A. J., Eds.; Academic Press: New York, 1982; Chapter 5.
25. Tachez, M.; Theobald, F.; Bernard, J.; Hewat, A. W. *Rev. Chim. Miner.* **1982**, *19*, 291.
26. Jordan, B.; Calvo, C. *Can. J. Chem.* **1973**, *51*, 2621.
27. Troup, J. M.; Clearfield, A. *Inorg. Chem.* **1977**, *16*, 3311.
28. Alberti, G. In *Recent Developments in Ion Exchange*; Williams, P. A., Hudson, M. J., Eds.; Elsevier Applied Science: New York, 1987; p 233.
29. Clearfield, A. *Chem. Rev.* **1988**, *88*, 125.
30. Alberti, G. *Acc. Chem. Res.* **1978**, *11*, 163
31. R'kha, C.; Vandenborre, M. T.; Livage, J.; Prost, R.; Huard, E. *J. Solid State Chem.* **1986**, *63*, 202.
32. Jacobson, A. J.; Johnson, J. W.; Brody, J. F.; Scanlon, J. C.; Lewandowski, J. T. *Inorg. Chem.* **1985**, *24*, 1782.
33. Martinez-Lara, M.; Moreno-Real, L.; Jimenez-Lopez, A.; Bruque-Gamez, S.; Rodriguez-Garcia, A. *Mater. Res. Bull.* **1985**, *20*, 549.
34. Matsubayashi, G.-e.; Ohta, S.; Okuno, S. *Inorg. Chim. Acta* **1991**, *184*, 47.
35. Beneke, K.; Lagaly, G. *Inorg. Chem.* **1983**, *22*, 1503.
36. Chang, I.-J.; Nocera, D. G. *J. Am. Chem. Soc.* **1987**, *109*, 4901.
37. Chang, I.-J.; Hsu, C.; Hammermesh, M. A.; Nocera, D. G., submitted for publication.
38. Bino, A. *Inorg. Chem.* **1981**, *20*, 623.
39. Bino, A.; Cotton, F. A. *Inorg. Chem.* **1979**, *18*, 3562.
40. Hopkins, M. D.; Miskowski, V. M.; Gray, H. B. *J. Am. Chem. Soc.* **1988**, *108*, 959.
41. Shin, Y.-g. K.; Nocera, D. G. *J. Am. Chem. Soc.* **1992**, *114*, 1264.
42. Tietze, H. R. *Aust. J. Chem.* **1981**, *34*, 2035.
43. Antonio, M. R.; Barbour, R. L.; Blum, P. R. *Inorg. Chem.* **1987**, *26*, 1235.
44. Cotton, F. A.; Walton, R. A. *Multiple Bonds Between Metal Atoms*; Wiley-Interscience: New York, 1982.
45. Chang, I.-J.; Nocera, D. G. *Inorg. Chem.* **1989**, *28*, 4309.
46. Partigianoni, C. P.; Nocera, D. G. *Inorg. Chem.* **1990**, *29*, 2033.
47. Clearfield A. In *Inorganic Ion-Exchange Materials*; Clearfield, A., Ed.; CRC Press: Boca Raton, FL 1982.

48. Lee, C. F.; Thompson, M. E. *Inorg. Chem.* **1991**, *30*, 4.
49. Cotton, F. A.; Niswander, R. H.; Sekutowski, J. C. *Inorg. Chem.* **1979**, *18*, 1152.
50. Fanwick, P. E.; Bursten, B. E.; Kaufmann, G. B. *Inorg. Chem.* **1985**, *24*, 1165.
51. Manning, M. C.; Trogler, W. C. *J. Am. Chem. Soc.* **1983**, *105*, 5311.
52. Constantino, U. *J. Chem. Soc., Dalton Trans.* **1979**, 402.
53. Alberti, G.; Constantino, U.; Allulli, S.; Tomassini, N. *J. Inorg. Nucl. Chem.* **1978**, *40*, 1113.
54. Dines, M. B.; DiGiacomo, P. M. *Inorg. Chem.* **1981**, *20*, 92.
55. Dines, M. B.; Griffith, P. C. *Polyhedron* **1983**, *2*, 607.
56. Dines, M. B.; Griffith, P. C. *Inorg. Chem.* **1983**, *22*, 567.
57. Dines, M. B.; Cooksey, R. E.; Griffith, P. C.; Lane, R. H. *Inorg. Chem.* **1983**, *22*, 1004.
58. Alberti, G.; Constantino, U.; Marmottini, F. In *Recent Developments in Ion Exchange*; Williams, P. A., Hudson, M. J., Eds.; Elsevier Applied Science: New York, 1987; p 249.
59. Cao, G.; Lynch, V. M.; Swinnea, J. S.; Mallouk, T. E. *Inorg. Chem.* **1990**, *29*, 2112.
60. Burwell, D. A.; Valentine, K. G.; Timmermans J. H.; Thompson, M. E. *J. Am. Chem. Soc.* **1992**, *114*, 4144.
61. Johnson, J. W.; Jacobson, A. J.; Brody, J. F.; Lewandowski, J. T. *Inorg. Chem.* **1984**, *23*, 3844.
62. Abbona, F.; Boistelle, R.; Haser, R. *Acta Cryst.* **1979**, *B35*, 2514.
63. Huan, G.; Jacobson, A. J.; Johnson, J. W.; Corcoran, E. W., Jr. *Chem. Mater.* **1990**, *2*, 91.
64. Alagna, L.; Tomlinson, A. A. G.; Rodriguez-Castellon, E.; Olivera, P. P.; Bruque, S. *J. Chem. Soc., Dalton Trans.* **1990**, 1183.
65. Choy, J.-H.; Kim, Y.-g.; Weiss, A. *Mat. Res. Bull.* **1985**, *20*, 1401.
66. Ferragina, C.; Massucci, M.; La Ginestra, A.; Patrono, P.; Tomlinson, A. A. G.; *J. Chem. Soc., Chem. Commun.* **1984**, 1024.
67. Basini, L.; Raffaelli, A.; Zerbi, G. *Chem. Mater.* **1990**, *2*, 679.
68. Környei, J.; Szirtes, L. *J. Radioanal. Nucl. Chem.* **1985**, *89/2*, 331.
69. Burwell, D. A.; Thompson, M. E. *Chem. Mater.* **1991**, *3*, 14.
70. Cotton, F. A.; Reid, A. H. Jr.; Schwotzer, W.; *Inorg. Chem.* **1985**, *24*, 3965.
71. Binz, A.; Rath, C. *Ann. Chem.* **1927**, *455*, 127.
72. Hudson, R. F. *Structure and Mechanism in Organophosphorus Chemistry*; Academic: New York, 1965.
73. Worms, K. H.; Schmidt-Dunker, M. In *Organic Phosphorus Compounds*, Vol. 7; Kosolapoff, G. M., Ed.; Wiley: New York, 1976.
74. Lee, H.; Kepley, L. J.; Hong, H.-G.; Akhter, S.; Mallouk, T. E. *J. Phys. Chem.* **1988**, *92*, 2597.
75. Putvinski, T. M.; Schilling, M. L.; Katz, H. E.; Chidsey, C. E. D.; Mujsce, A. M.; Emerson, A. B. *Langmuir* **1990**, *6*, 1567.
76. Umemura, Y.; Tanaka, K.; Yamagishi, A. *J. Chem. Soc., Chem. Comm.* **1992**, 67.

Chapter 18

Nuclear Magnetic Resonance Imaging of Anisotropic Solid-State Chemical Reactions

Leslie G. Butler¹, David G. Cory^{2,4}, Joel B. Miller², Kerry M. Dooley³, and
Allen N. Garroway²

¹Department of Chemistry, Louisiana State University,
Baton Rouge, LA 70803-1804

²Code 6122, Chemistry Division, Naval Research Laboratory,
Washington, DC 20375-5000

³Department of Chemical Engineering, Louisiana State University,
Baton Rouge, LA 70803-7303

Imaging an anisotropic chemical reaction, either a reaction in a catalysis bed or at an interface between two phases, is challenging. NMR imaging offers special advantages for following chemical changes, even though techniques for imaging solids are still under rapid development. Herein, we report the application of a recently developed NMR pulse sequence that enables the efficient observation of organic solids in spite of the large proton dipolar coupling in the solid. The reactions of substituted benzoic acid crystals and powders with ammonia gas have been monitored. The reactions are inherently (crystal) or by design (powder) spatially anisotropic.

NMR imaging is well known for its biomedical applications, but has few demonstrated applications in materials chemistry or catalysis. The major obstacle has been the large intrinsic line widths for ¹H NMR resonances in most solids. Recently, techniques have been developed that both reduce the ¹H NMR line width and are compatible with the magnetic field gradients used in NMR imaging. Herein, we describe the application of ¹H NMR imaging for observing anisotropic gas-solid chemical reactions. One reaction, that of ammonia with a bed of powdered toluic acid, was chosen as a model system for imaging a catalytic reactor.

Solid-State NMR Imaging

NMR imaging of solids is a technique that can be divided into two areas, depending upon the characteristics of the sample (1-6). For "soft" solids, the presence of local, rapid molecular motions reduces homonuclear dipolar coupling and averages anisotropic chemical shielding. Thus, the natural line width is narrow (long T₂) and it is relatively easy to encode spatial information with a magnetic field

⁴Current address: Bruker Instruments, Inc., Manning Park, Billerica, MA 01821

gradient. However, in "rigid" solids there is an absence of local, rapid molecular motions. Therefore, homonuclear dipolar coupling and anisotropic chemical shielding contribute to a large line width and it becomes exceedingly difficult to encode spatial information within the time allowed by the short T_2 . For protons, one solution is to employ multiple-pulse ^1H NMR techniques to diminish either homonuclear dipolar coupling or both homonuclear dipolar coupling and chemical shielding interactions, thus artificially narrowing the resonance and increasing the effective T_2 (7-9). Listed in Table I are some representative examples of ^1H NMR imaging using multiple-pulse techniques. The resolution quoted is that demonstrated on the respective phantoms and does not necessarily represent an inherent limitation of that approach. A wide variety of NMR imaging pulse sequences have been used, in particular, the CMG-48 pulse sequence (10) is used for the work described here. Also of note in Table I is the imaging of a solid using a surface coil. In principle, this allows for more flexibility in sample geometry, as opposed to a solenoidal RF coil (used in the other imaging studies) which must encompass the sample.

Table I
Overview of Multiple-Pulse Solid-State NMR Imaging Studies

Sample	Resolution ^a	Comments	Ref.
camphor phantom	50 μm	first use of multiple-pulse for 1D NMR imaging	(11,12)
theory	—	RF gradients	(13)
adamantane cylinder/neoprene tube	1 mm	2D images; MREV-8	(14)
coal (resinite and vitrinite)	200 μm	2D images; MREV-8	(15)
adamantane phantom	~1 mm	magic angle in rotating frame	(16)
poly(methyl methacrylate)	200 μm	surface coil, 1D image	(17)
rubber and Teflon phantoms	1 mm	2D ^1H and ^{19}F images	(18)
hexamethylbenzene phantom	1.7 mm	Jeener-Broekaert phase encoding	(19)
poly(methyl methacrylate)	100 μm	gradient pulses interleaved into MREV-8 for 2D imaging	(20,21)
polyethylene phantom	300 μm	CMG-48 pulse sequence,	(10)
ferrocene phantom	30 μm	1D images	"
adamantane phantom	—	RF gradient, 2D image	(22)

^aNumbers only approximate as two different procedures exist for defining the resolution, either based on a qualitative visual assessment of the image or based upon an effective T_2 . For the latter procedure, the resolution is given by $(\gamma G T_2)^{-1}$, where G is the magnetic field gradient.

Aside from the technical issue of reducing the ^1H NMR line width so that NMR imaging can be accomplished with high sensitivity, the next question is what are the special advantages of NMR imaging as opposed to some other imaging technique. In Table II, we list several studies using mostly solution-state NMR imaging techniques.

Almost all of these examples involve diffusion of a chemical species; measuring diffusion rates has long been a specialty of NMR spectroscopy. The studies of KBr and drawn polyethylene produced unique information; in the latter case, the known orientation of the deuterium electric field gradient in C–D bonds is used to determine the orientation, with respect to the magnetic field, of a polymer chain of a uniaxially ordered polyethylene fiber. The real time imaging of the polymerization of methyl methacrylate is very interesting and may represent a major direction for NMR imaging applications to polymer science.

Table II
Survey of Imaging Studies of Chemical Reactions and/or Diffusional Processes

Sample	Resolution	Comments	Ref.
graphite-AsF ₅ intercalation	1 mm	¹⁹ F solution-state 1D imaging	(23)
B-Z chemical oscillator	1 mm	¹ H solution-state 2D imaging	(24)
ESR spin probe in a nematic phase	—	D = 10 ⁻⁹ — 10 ⁻⁵ cm ² s ⁻¹	(25)
polystyrene + CCl ₄	1 mm	stepped gradients, 1D image	(26)
poly(methyl methacrylate)+acetone	100 μm	stray field gradient, 1D image	(27)
poly(methyl methacrylate)+methanol	68 μm	Case II diffusion, 2D image	(28)
(Na _{1-x} K _x)β-alumina crystal	1 mm	²³ Na diffusion, 2D image	(29)
KBr in a temperature gradient	1 mm	⁸¹ Br T ₁ temperature map	(30)
ivy leaf	500 μm	ivy plant grown in 50% D ₂ O	(31)
polymer blends	50 μm	MAS NMR imaging, 2D image	(32)
drawn polyethylene	1 mm	² H imaging for orientation	(33)
methylmethacrylate polymerization	256 ms ^a	3D FLASH imaging	(34)

^amilliseconds

Experimental

Instrumentation. A home-made 100 MHz (¹H) NMR with an 11 cm bore solenoidal magnet was used for all experiments. For the 10 mm solenoidal rf coil used herein, the 90° pulse length was 3 μs. The short windows of the CMG-48 (10) multiple pulse sequence are 2 μs and the long windows are 7 μs. The axis of the gradient coil is aligned with the static magnetic field. The 5 μs gradient pulses have an effective average gradient of 0.042 T m⁻¹, as determined from the image and the known sample geometry; a delay of 2 μs is allowed for gradient pulse decay before the next rf pulse is applied. Additional features of the gradient coil have been published elsewhere (20,21) as have further details of the spectrometer (35).

One-dimensional images of toluic acid were obtained with a stationary sample. For two-dimensional images, the 4-bromobenzoic acid crystal was rotated about an axis orthogonal to the gradient direction in constant increments of either 3° or 6° over a range of 180° to collect sets of 60 or 30 one-dimensional projections, respectively. The two-dimensional images were calculated with the filtered back-projection reconstruction algorithm (36).

Samples. For the purposes of demonstrating NMR imaging of anisotropic chemical reactions (37,38), the reactions of ammonia with solid organic acids were used. It has been shown that single crystals of acids such as 4-chlorobenzoic acid react anisotropically with ammonia. Most faces of the crystal react rapidly; however, the (100) face reacts slowly as this face has an array of C-Cl units on the surface that protect the carboxylic acid function from ammonia (39). Powders of organic acids react with ammonia in 1:1 ratio to form the simple ammonium salts.

1D NMR Imaging of a Powder. Toluic acid (Aldrich) was used as received in the form of a fine powder. A 78 mg sample of toluic acid was packed into the sample holder, shown in Figure 1. Tygon tubing was used to connect the sample holder, while in the NMR probe and in the magnet, to the NH_3/Ar supply. A mixture of 9.85 mole % ammonia in argon was used for ammonia exposures, all of which were performed at room temperature and with an absolute pressure of about one atmosphere. Note: The use of ammonia diluted in argon was fortuitous and based upon convenient availability; however, it is likely that dilution reduced the rate of reaction so that monitoring the reaction by NMR imaging was made easier. A flow rate of 0.002 L s^{-1} was used. Also shown in Figure 1 is a representative 1D NMR image of the toluic acid sample showing that the rectangular sample profile is imaged as a rectangular function in the NMR spectrum.

2D NMR Imaging of a Crystal. 4-Bromobenzoic acid was purchased from Aldrich and recrystallized from acetone. A crystal with dimensions of [6.6 to 7] x 4 x 0.4 mm was selected and attached to a glass capillary tube with a minimum amount of poly(α -cyanoacrylate) (super glue). The crystal was placed in a low velocity NH_3/Ar gas stream, about 0.002 L s^{-1} , in a laboratory hood. During one NH_3 exposure, a portion of the crystal broke off and was recovered, but not used. Mounted in the sample holder and near the crystal was a capillary tube containing a few crystals of ferrocene. The purpose of the ferrocene was to provide a readily observable marker in the 1D projections; this marker was used to align the projections prior to the back-projection reconstruction. For projections of the unreacted crystal in which the 1D image of the marker was separate from that of the crystal, the peak height of the marker was slightly smaller than that of the crystal. The ferrocene marker was also used to normalize the intensity scale of images taken before and after ammonia exposure. Optical photographs of the crystal before and after ammonia exposure are given elsewhere (35).

Results

1D NMR Imaging of a Powder. Saturation-recovery ^1H NMR images taken before and after ammonia exposure are shown in Figures 2a and 2b, respectively. The relaxation delays for both experiments are 0.05, 0.1, 0.3, 0.5, 1, 3, 5, 10, 30, and 50 s. Small deviations from a rectangular profile are most likely due to either packing and/or sample holder imperfections. After exposure to ammonia gas, the sample holder was reweighed. A mass gain of 9 mg indicated that the reaction to form ammonium toluate proceeded to at least 92 % conversion, perhaps more as some traces of ammonium toluate were found in the tubing downstream from the sample

holder. The increase in the equilibrium magnetization, calculated from the spectra in Figure 2, also indicates at least 90 % conversion of the sample to ammonium toluate.

In the absence of a gradient, the line width of toluic acid is less than the digital resolution of 43 Hz. In the results shown in Figure 2, eleven data points define the images of the 5 mm toluic acid sample, corresponding to a spatial resolution of about 500 μm . Thus, the conversion of toluic acid to ammonium toluate can be independently monitored for eleven different layers.

The spin-lattice relaxation times for toluic acid and ammonium toluate are quite different, 31 s and 0.86 s, respectively. Thus, the ^1H T_1 can be used as an effective contrast agent in the NMR imaging experiment. Demonstration of ^1H T_1 weighted imaging is provided by the results of a set of images acquired during the reaction of toluic acid with ammonia.

NMR images for the first few minutes of the reaction are shown in Figure 3 and are selective for observation of the reaction product only. The images are acquired with a relaxation delay of 0.4 s. Therefore, the product is detected while the reactant is rendered invisible due to a ^1H T_1 value that is long with respect to the relaxation delay. Based on the images shown in Figure 3, it is clear that the top layers of the sample are reacting with ammonia faster than the bottom layers.

2D NMR Imaging of a Crystal. An inversion-recovery experiment showed that the ^1H T_1 of unreacted 4-bromobenzoic acid crystals is quite long, 140 s. A separate sample of powdered 4-bromobenzoic acid was exposed to ammonia; the ^1H T_1 of ammonium 4-bromobenzoate is 3 s. Thus, T_1 is an appropriate contrast agent for reacted and unreacted 4-bromobenzoic acid. However, the long T_1 of the unreacted form makes it quite difficult, though not impossible, to image a 7 mm long, flat crystal of 4-bromobenzoic acid, a relatively small sample for solid-state NMR. Shown in Figure 4 is a contour plot of the 2D NMR image of a crystal of 4-bromobenzoic acid before exposure to ammonia gas. The image is reconstructed from 30 projections acquired in 60 hours. Each projection consists of 40 acquisitions and is obtained with a relaxation delay of 180 s. The data sets were processed as described earlier and without application of any line broadening. The contour levels are based on the most intense pixel of the ferrocene marker having an assigned intensity of 100 %; contour levels are drawn at 20 to 90 % levels in increments of 10 %. In spite of the small crystal size and the unfavorably long ^1H T_1 , the quality of the image is acceptable. An important result here is that the signal intensity is rather uniform across the face of the crystal. Most of the crystal has an uncorrected intensity value between 20 to 40 % relative to the ferrocene marker; when corrected for T_1 saturation effects of the 4-bromobenzoic acid, the intensity levels range between 27 and 55 % of the ferrocene marker.

The crystal was exposed to ammonia for 12 hours. During this exposure, a portion of the crystal broke off from the main body. Visually, some whitening or powdering was observed on the crystal due to the formation of ammonium 4-bromobenzoate. Two-dimensional NMR images were acquired with relaxation delays of 5 and 30 s; the short relaxation delay yields images of only the reaction product. Some reaction was noted in the center of the crystal and at one spot displaced to the left of center.

The crystal was then exposed to ammonia for an additional 24 hours. Shown in Figure 5 is a contour plot of the 2D NMR image of the crystal reconstructed from 60 projections acquired in 5.3 hours. Each projection consists of 64 acquisitions and obtained with a relaxation delay of 5 s. The data sets were processed as described earlier and with an exponential line broadening of 33 Hz. The contour levels are based on the most intense pixel of the ferrocene marker having an assigned intensity of 100 %; contour levels are drawn at 20 to 90 % levels in increments of 10 %. As for the images taken at 12 hours, signal due to ammonium 4-bromobenzoate is observed in the center of the crystal and at a spot to the left of center. Also, a new region to the

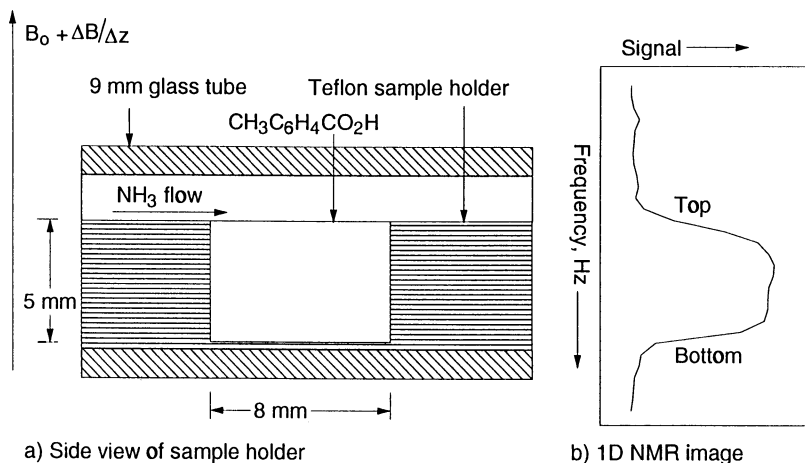


Figure 1. (a) Sample holder for one-dimensional imaging of powdered toluic acid reacting with ammonia gas. (b) Projection of sample into an NMR image.

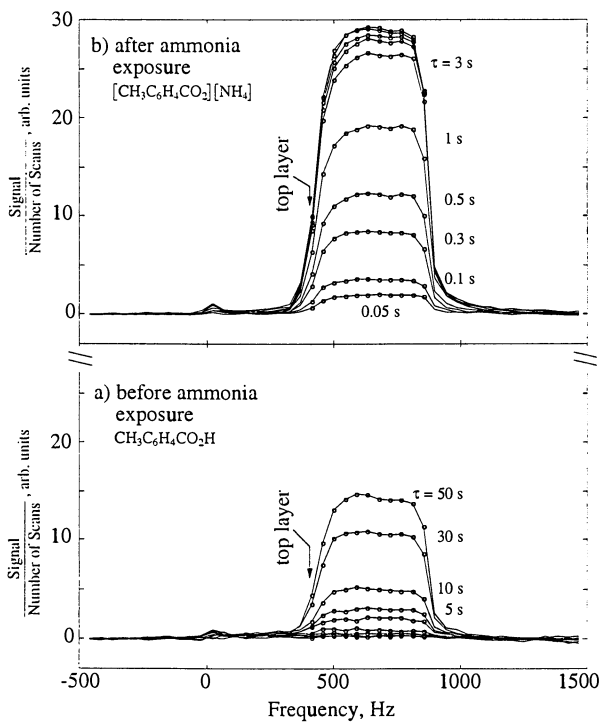


Figure 2. Combination one-dimensional (1D) ^1H NMR imaging and saturation–recovery spectra for powdered toluic acid before (a) and after (b) exposure to ammonia.

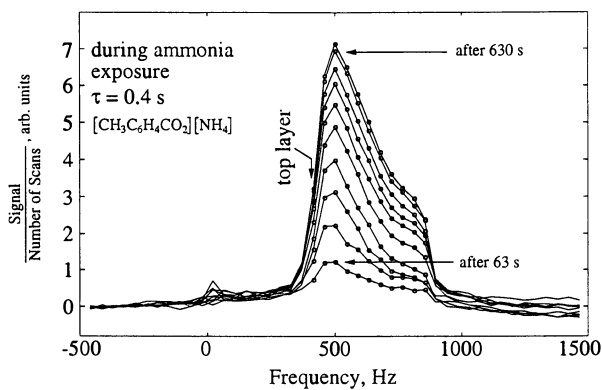


Figure 3. 1D ^1H NMR imaging and saturation–recovery spectra for powdered toluic acid during the first few minutes of ammonia exposure.

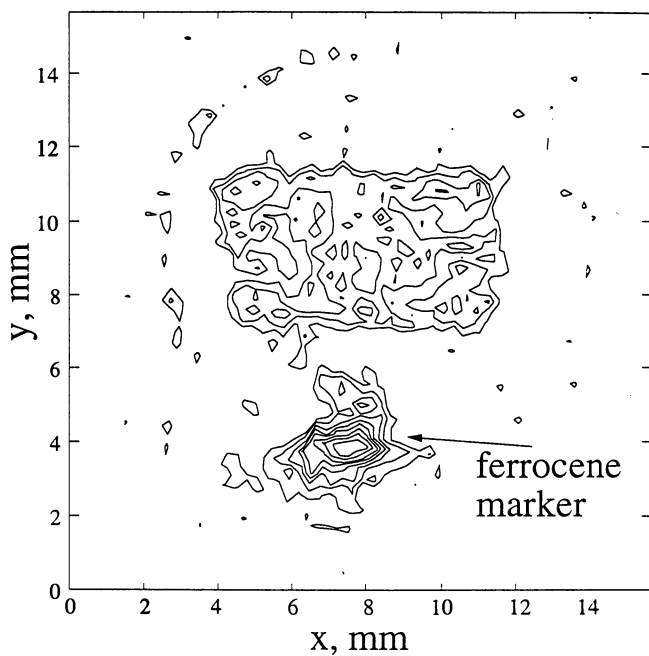


Figure 4. Contour plot of a 2D NMR image of a crystal of 4-bromobenzoic acid before exposure to ammonia.

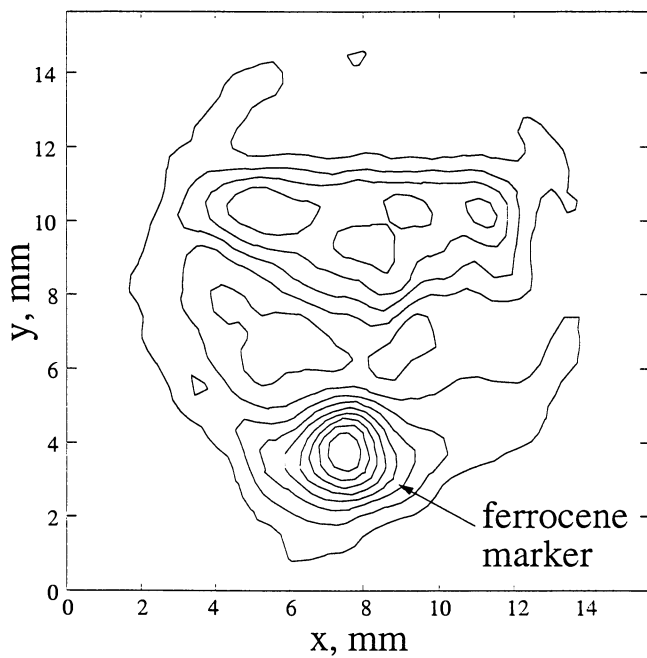


Figure 5. Contour plot of a 2D NMR image of a crystal of 4-bromobenzoic acid after exposure to ammonia for 36 hours.

right of center, not observed at 12 hours, gained intensity. An image taken with a relaxation delay of 10 s also showed similar regions of reactivity. Visually, the crystal after 36 hours ammonia exposure is somewhat opaque and white, in contrast to the clear crystal prior to ammonia exposure.

We can estimate the extent of conversion from 4-bromobenzoic acid to ammonium 4-bromobenzoate of portions of the crystal by using the contour plots shown in Figures 4 and 5 and by making corrections for saturation effects. Before ammonia exposure, most areas of the crystal had an intensity, relative to the ferrocene marker, of about 30 % (41 % after correction for saturation of 4-bromobenzoic acid) while after ammonia exposure the more reacted portions of the crystal have an intensity of 50 % (28 % after correction for saturation of ferrocene and ammonium 4-bromobenzoate). The extent of conversion is then given by

$$\frac{M^{\text{eq}}([\text{BrC}_6\text{H}_4\text{CO}_2][\text{NH}_4]) = 28 \%}{M^{\text{eq}}(\text{BrC}_6\text{H}_4\text{CO}_2\text{H}) = 41 \%} \times \frac{5}{8} \times 100 = 43 \% \text{ conversion}$$

where the factor of 5/8 accounts for the change in the number of protons in the sample.

Discussion

The reaction of a bed of powdered toluic acid with ammonia gas clearly shows reaction heterogeneity in the 1D ^1H NMR images. As expected, the top layers of the sample react more rapidly than do the bottom layers. A simple isothermal simultaneous diffusion with reaction model is sufficient to extract an apparent reaction rate constant and an effective diffusivity from the total conversion data (40). Important parameters in the model are the reaction rate, k , the effective diffusivity, D_e , and the thickness of the sample. For a given set of parameters, the model can be used to generate the extent of conversion as a function of reaction time. The total conversion data are obtained by summing each image over all layers; the normalized total conversion data are plotted in Figure 6. Also shown in Figure 6 is a best fit of a simultaneous diffusion with reaction model along with the residuals of the fit. The reaction rate is $5(2) \times 10^{-4} \text{ mol}^{-1}\text{m}^3 \text{ s}^{-1}$ and the effective diffusivity is $1.0(4) \times 10^{-5} \text{ m}^2 \text{ s}^{-1}$. A more advanced analysis, employing techniques such as finite element analysis, could be used to individually fit the conversion data for each layer. In the event of nonisothermal reaction conditions, such an approach might be necessary, but was not done for images acquired here.

The reaction of ammonia with the crystal of 4-bromobenzoic acid had been expected to occur most rapidly at the edges of the flat crystal. However, this pattern of reactivity was not observed, neither visually nor by 2D NMR imaging. Apparently, crystal quality was not great enough to support the reaction anisotropy reported by Paul and Curtin (41). Nevertheless, reaction anisotropy of a more random nature was observed, roughly corresponding to the features observed on the face of the crystal before the reaction.

Conclusions

Shown herein are the first 2D ^1H multiple-pulse NMR images following a chemical reaction for which the image contrast is T_1 rather than T_2 . A multiple pulse line narrowing sequence is critical to efficient image acquisition where broad lines are expected. The gas-solid reaction between ammonia and a crystal of 4-bromobenzoic acid was monitored optically and by NMR imaging. Some anisotropy in the reaction

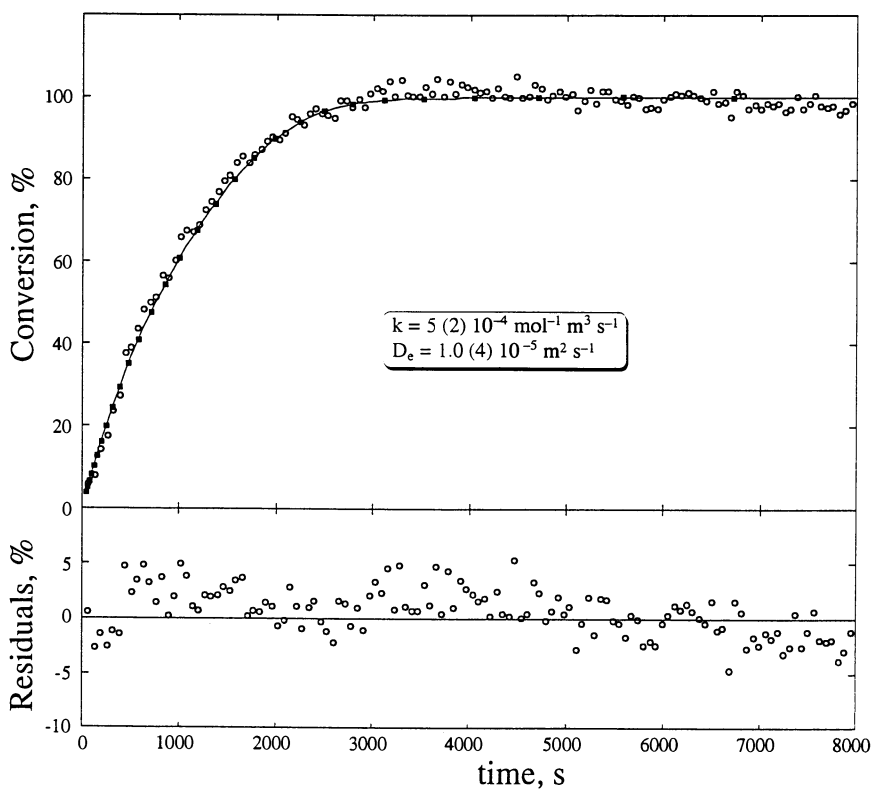


Figure 6. The total conversion of toluic acid into ammonium toluate is shown here as a function of ammonia exposure time.

was observed and the extent of reaction was obtained from the NMR images. The more reactive regions of the crystal are about 40 % converted from 4-bromobenzoic acid to the ammonium salt. A gas-solid reaction between ammonia and a bed of powdered toluic acid showed clear reaction anisotropy; the top layers of the bed reacted faster than the bottom. The averaged conversion of toluic acid to ammonium toluate was analyzed with an isothermal simultaneous diffusion-reaction model which yielded realistic D_e and k values.

It is clear that ^1H multiple pulse NMR imaging yields images that detail chemical reactivity at interfaces. However, it is difficult to predict the full impact of NMR imaging of solid-state chemical reactions. On one hand, one-dimensional NMR images contain sufficient information to allow one to extract kinetic information. On the other hand, three-dimensional NMR images would have enabled monitoring the toluic acid/ammonia reaction at the boundaries of the sample holder. In either case, NMR imaging provides chemically useful information. Since the chemistry of interfaces is so important (for example, the curing of coatings, catalyst bed deactivation, adhesion, just to name a few), a technique which has the capability to selectively and quantitatively image a component within the interface will likely become extremely useful.

Other imaging techniques have also been used to monitor chemical reactions. For example, the catalytic oxidation of CO over a platinum/ceria catalyst has been monitored with 1D positron emission tomography (42). The experimental constraints on the PET experiment are quite different from those of solid-state ^1H NMR imaging. In general terms, PET appears to be more suitable for monitoring large samples (on the order of tens of centimeters) whereas NMR imaging yields greater access to chemical information within the sample by virtue of ^1H T_1 weighting, chemical shift selective imaging, homo- and heteronuclear dipolar coupling, and so forth. One can imagine a wide range of NMR imaging experiments based upon a various constraint mechanisms, and tailored to address a particular catalytic question. For example, chemical shift can be used simply to measure the abundance of chemical species across a reaction front, whereas accessing the anisotropic chemical shift tensor could enable differentiation between bound and mobile components of the same chemical component.

Acknowledgments

This work was supported in part by the Office of Naval Research. The sabbatical hospitality of the Naval Research Laboratory is gratefully acknowledged by one of us (LGB). Leslie G. Butler is a Fellow of the Alfred P. Sloan Foundation (1989-1991). David G. Cory acknowledges a National Research Council/Naval Research Laboratory postdoctoral associateship. All figures adapted from ref. (35).

Literature Cited

1. Mansfield, P.; Morris, P. G., *NMR Imaging in Biomedicine*, in *Adv. Magn. Reson. Suppl.* 2, 1982.
2. Morris, P. G. *Nuclear Magnetic Resonance Imaging in Medicine and Biology*; Clarendon Press: Oxford, 1986.
3. Ernst, R. R.; Bodenhausen, G.; Wokaun, A. *Principles of Nuclear Magnetic Resonance in One and Two Dimensions*; Oxford University Press: Oxford, 1987.
4. Listerud, J. M.; Sinton, S. W.; Drobny, G. P. *Anal. Chem.* 1989, 61, 23.
5. Cory, D. G. *Ann. Rep. NMR* 1991, 25, in press.
6. Jezzard, P.; Attard, J. J.; Carpenter, T. A.; Hall, L. D. *Prog. NMR Spect.* 1991, 23, 1.
7. Waugh, J. S.; Wang, C. H.; Huber, L. M.; Vold, R. I. *J. Chem. Phys.* 1968, 48, 662.

8. Garroway, A. N.; Mansfield, P.; Stalker, D. C. *Phys. Rev. B* **1975**, *11*, 121.
9. Haeberlen, U. *High Resolution NMR in Solids: Selective Averaging*; Academic Press: New York, 1976.
10. Cory, D. G.; Miller, J. B.; Garroway, A. N. *J. Magn. Reson.* **1990**, *90*, 205.
11. Mansfield, P.; Grannell, P. K.; Garroway, A. N.; Stalker, D. C. In *Proc. 1st Spec. Colloque Ampere*; Hennel, J. W., Ed.; Krakow, 1973, 16.
12. Mansfield, P.; Grannell, P. K. *Phys. Rev. B* **1975**, *12*, 3618.
13. Cho, H. M.; Lee, C. J.; Shykind, D. N.; Weitekamp, D. P. *Phys. Rev. Lett.* **1985**, *55*, 1923.
14. Chingas, G. C.; Miller, J. B.; Garroway, A. N. *J. Magn. Reson.* **1986**, *66*, 530.
15. Dieckman, S. L.; Gopalsami, N.; Botto, R. E. *Energy & Fuels* **1990**, *4*, 417.
16. De Luca, F.; Nuccetelli, C.; De Simone, B. C.; Maraviglia, B. *J. Magn. Reson.* **1986**, *69*, 496.
17. Miller, J. B.; Garroway, A. N. *J. Magn. Reson.* **1989**, *85*, 432.
18. McDonald, P. J.; Tokarczuk, P. F. *J. Phys. E; Sci. Instrum.* **1989**, *22*, 948.
19. Rommel, E.; Hafner, S.; Kimmich, R. *J. Magn. Reson.* **1990**, *86*, 264.
20. Cory, D. G.; Miller, J. B.; Turner, R.; Garroway, A. N. *Mol. Phys.* **1990**, *70*, 331.
21. Miller, J. B.; Cory, D. G.; Garroway, A. N. *Phil. Trans. R. Soc. Lond. A* **1990**, *333*, 413.
22. Werner, M. H.; Marohn, J. A.; Shykind, D. N.; Weitekamp, D. P. *Two Dimensions of Solid-State Imaging with One RF-Gradient Coil*. in *32nd ENC.* 1991. St. Louis., Mo., April 7-11: Abstract P240.
23. Chingas, G. C.; Milliken, J.; Resing, H. A.; Tsang, T. *Synth. Metals* **1985**, *12*, 131.
24. Tzalmona, A.; Armstrong, R. L.; Menzinger, M.; Cross, A.; Lemaire, C. *Chem. Phys. Lett.* **1990**, *174*, 199.
25. Moscicki, J. K.; Shin, Y.-K.; Freed, J. H. *J. Magn. Reson.* **1989**, *84*, 554.
26. Corti, M.; Borsa, F.; Rigamonti, A. *J. Magn. Reson.* **1988**, *79*, 21.
27. Samoilenko, A. A.; Artemov, D. Y.; Sibel'dina, L. A. *Russ. J. Phys. Chem.* **1987**, *61*, 1623.
28. Weisenberger, L. A.; Koenig, J. L. *Macromolecules* **1990**, *23*, 2454.
29. Suits, B. H.; White, D. *Solid State Comm.* **1984**, *50*, 291.
30. Suits, B. H.; White, D. *J. Appl. Phys.* **1986**, *60*, 3772.
31. Link, J.; Seelig, J. *J. Magn. Reson.* **1990**, *89*, 310.
32. Cory, D. G.; de Boer, J. C.; Veeman, W. S. *Macromolecules* **1989**, *22*, 1618.
33. Günther, E.; Blümich, B.; Spiess, H. W. *Mol. Phys.* **1990**, *71*, 477.
34. Jackson, P.; Clayden, N. J.; Walton, N. J.; Carpenter, T. A.; Hall, L. D.; Jezzard, P.; Wiggins, C. *NMR Imaging Studies of the Polymerization of Methylmethacrylate*. in *10th EENC.* 1990. May 28-June 1, Veldhoven, The Netherlands, Abstract C.6:
35. Butler, L. G.; Cory, D. G.; Dooley, K. M.; Miller, J. B.; Garroway, A. N. *J. Am. Chem. Soc.* **1992**, *114*, 125.
36. Brooks, R. A.; Di Chiro, G. *Radiology* **1975**, *117*, 561.
37. Dunitz, J. D. *Pure and Appl. Chem.* **1991**, *63*, 177.
38. Weissbuch, I.; Addadi, L.; Lahav, M.; Leiserowitz, L. *Science* **1991**, *253*, 637.
39. Miller, R. S.; Paul, I. C.; Curtin, D. Y. *J. Am. Chem. Soc.* **1974**, *96*, 6334.
40. Dudukovic', M. P. *AIChE J.* **1976**, *22*, 945.
41. Paul, I. C.; Curtin, D. Y. *Science* **1975**, *187*, 19.
42. Jonkers, G.; Vonkeman, K. A.; van der Wal, S. W. A.; van Santen, R. A. *Nature* **1992**, *355*, 63.

Chapter 19

Homogeneous Adsorption of Benzene on NaX and NaY Zeolites

Shang-Bin Liu¹, Jin-Fu Wu^{2,3}, Long-Ja Ma¹, May-Whei Lin¹, and Tun-Li Chen²

¹Institute of Atomic and Molecular Sciences, Academia Sinica, P.O. Box 23-166, Taipei, Taiwan 10764, Republic of China

²Department of Chemistry, Tamkang University, Tamsui, Taiwan 25137, Republic of China

The adsorption behavior of benzene on dehydrated NaX and NaY zeolites has been investigated directly by ¹H and ¹³C NMR measurements of the adsorbed benzene and indirectly by the combination of ¹²⁹Xe NMR and isotherm measurements of the co-adsorbed xenon. Powdered zeolite samples of various Si/Al ratios and with varied adsorbate concentrations were investigated. Detailed macroscopic and microscopic adsorption phenomena of benzene in NaX and NaY zeolites, including the loading capacity, mobility, and sites of adsorption are presented in terms of measurements of NMR linewidths and chemical shifts.

The transport and adsorption properties of hydrocarbons on microporous zeolites have been of practical interest due to the important properties of zeolites as shape-selective adsorbents and catalysts. The system of benzene adsorbed on synthetic faujasite-type zeolites has been thoroughly studied because benzene is an ideal probe molecule and the related role of aromatics in zeolitic catalysts for alkylation and cracking reactions. For instance, its mobility and thermodynamic properties have been studied by conventional diffusion (1-6) and adsorption (7-9) techniques. Moreover, the adsorbate-zeolite interactions and related motion and location of the adsorbate molecules within the zeolite cavities have been investigated by theoretical calculations (10-15) and by various spectroscopic methods such as UV (16, 17), IR (17-23), neutron (24-27), Raman (28), and NMR (29-39).

Adsorption Properties of Benzene in Faujasite-type Zeolites

Despite extensive study of the adsorption of benzene on zeolites, little attention has been devoted to the equilibrium state of adsorption and the

³Current address: Department of Chemistry, National Tsinghua University, Hsinchu, Taiwan, Republic of China

distribution of adsorbate within zeolite cavities. Sorption diffusivities, which are characteristic of related transport processes, are commonly inconsistent when obtained from different techniques (40–43). The possible origins of the discrepancies arising from transport resistances (44–49) and from adsorbate/adsorbent characteristics (1–4, 38, 49–53) have been discussed. When benzene molecules are adsorbed on dehydrated faujasite-type zeolites, the common assumption is that the molecules are adsorbed within the zeolite supercage and disperse uniformly. This assumption was first questioned by Pines and co-workers (54, 55) who observed a uniform benzene adsorption on NaY zeolite only after an extensive adsorbate/adsorbent sample thermal pretreatment. Using ^{129}Xe , ^1H , and ^{13}C NMR (56), we confirmed that a prolonged thermal treatment at temperature $\geq 250^\circ\text{C}$ (much greater than the boiling point of bulk benzene) is necessary to ensure an homogeneous benzene distribution within cavities of NaX and NaY zeolites. Moreover, this effect depends not only on the nature of the adsorbent samples and related sample-bed configurations but also on the adsorbate concentrations.

Following the pioneering works of Ito and Fraissard (57) and Ripmeester (58), ^{129}Xe NMR of xenon adsorbed on zeolite has proven sensitive probe of its local environment due to its chemical inertness and excellent sensitivity (59). In this work, we used ^1H and ^{13}C NMR measurements of the adsorbed benzene in conjunction with ^{129}Xe NMR and adsorption isotherm measurements of the co-adsorbed xenon to study the homogeneous adsorption behavior of benzene on faujasite-type zeolites with various Si/Al ratios. Detailed macroscopic and microscopic adsorption states of the benzene in various NaX and NaY zeolites are discussed in terms of NMR linewidths and chemical shifts and are compared with results obtained from other studies.

Experimental Section

Materials and Sample Preparation. Powdered, binderless, sodium-form zeolite X (Si/Al = 1.23) and zeolite Y (Si/Al = 2.49, 2.70) were obtained from Strem Chemicals. The crystalline framework structure of these materials was confirmed by x-ray diffraction (XRD). Their chemical compositions were determined by ICP-AES and their respective Si/Al ratios were further confirmed by ^{29}Si MAS NMR measurements. Before adsorption of guest molecule, a known amount (typically ca. 1 g) of hydrated zeolite sample in the sample tube was dehydrated by gradual heating to 400°C in vacuum ($< 10^{-5}$ torr) and was then maintained at this temperature for at least 15 hours. The sample tube configuration was designed so that a 10 mm standard NMR tube joined to a vacuum valve could be conveniently setup for adsorption or desorption of adsorbate molecules on a vacuum apparatus and for isolation of the sample from the atmosphere during NMR experiments. After dehydration, benzene guest molecules (adsorbates) were introduced into the samples of host zeolites (adsorbents) by vapor transfer at room temperature (22°C). Prior to the experiments, samples with various benzene concentrations were subjected to thermal treatment at 250°C for 10 hours to render uniform adsorbate distribution within zeolite cavities.

Xenon Adsorption Experiments. Gaseous xenon was co-adsorbed onto the samples on a vacuum manifold; the xenon equilibrium pressure was measured by an absolute-pressure transducer (MKS Baratron) capable of measuring pressure with accuracy ± 0.1 torr. The adsorption isotherms of the co-adsorbed xenon in the samples were measured volumetrically at 22°C .

NMR Experiments. All NMR experiments were done at 22 °C on a spectrometer (Bruker MSL-300) using a broadband NMR probe with proton decoupling option. The field strength of the wide-bore superconducting magnet was 7.05 tesla, corresponding to resonance frequencies 300.13, 75.47 and 83.01 MHz for nuclei of ^1H , ^{13}C and ^{129}Xe , respectively. For the ^{129}Xe NMR experiments, free induction decays (FID) were recorded at room temperature following a single radio-frequency pulse (ca. 30°) at 0.3 s intervals. We followed this procedure because the adsorbed xenon has a large spin-lattice relaxation time ($T_1 \geq 3$ s). In order to ensure adequate signal-to-noise (S/N) ratios, we accumulated typically 1,000–240,000 FID depending on the amount of xenon adsorbed on the sample. The reference for the ^{129}Xe chemical shift values was that of xenon gas extrapolated to zero density following the equation given by Jameson (60). All resonance signals of ^{129}Xe adsorbed on the samples were shifted to higher frequency relative to the reference, which we define to be the positive direction. The ^1H NMR spectra were also obtained by the single-pulse sequence using 2 s recycle delay. Typically, 120 accumulated FID were sufficient to generate spectra with adequate S/N ratio. The ^{13}C NMR spectra, on the other hand, were obtained with proton decoupling; typically 6,000 scans were averaged every 0.6 s. The reference for the chemical shifts of both ^1H and ^{13}C was liquid benzene (adjusted to tetramethylsilane, or TMS, as standard) at the same spectrometer settings.

Results and Discussion

Xenon Adsorption Isotherms and ^{129}Xe NMR Measurements. Figure 1 displays the room temperature (22 °C) xenon adsorption isotherms of the co-adsorbed xenon for the three different zeolite samples loaded with various amounts of benzene. A consistent decrease of adsorption with increasing θ was found for each benzene/zeolite system. By comparing the slope at low xenon pressures, i.e. in the Henry's Law region, we obtained for the adsorption strength $\text{NaX}(1.23) > \text{NaY}(2.49) > \text{NaY}(2.70)$. Moreover, the saturation benzene concentration in faujasite-type zeolites with different Si/Al ratios follows the relation: $\text{NaX}(1.23) < \text{NaY}(2.49) < \text{NaY}(2.70)$.

The dependence on xenon pressure of the measured ^{129}Xe NMR chemical shift (δ) and linewidth ($\Delta\omega$) was also recorded for each adsorbate/adsorbent sample system. In combination with the adsorption data in Figure 1, the dependence of the ^{129}Xe chemical shift on the density of adsorbed xenon is presented in Figure 2. For given θ , the observed δ increases with increasing xenon pressure due to increasing interactions among xenon atoms. In contrast, for a given xenon loading, the increase of δ with increasing θ characterizes a decrease in the internal void space of the benzene/zeolite samples, hence a decrease in the mean free path of xenon (57). The measured xenon chemical shift is described as the sum of three terms:

$$\delta = \delta_0 + \delta_s + \sigma_{\text{xe-xe}} \cdot \rho_{\text{xe}} ; \quad (1)$$

here $\delta_0 = 0$ is the reference; δ_s corresponds to the shift at zero xenon loading which represents in turn the sum of two contributions, $\delta_s = \delta_s(0) + \delta_s(\theta)$, and can be obtained by extrapolation of the straight lines (for various θ) in Figure 2; the results are presented in Figure 3a. The term $\delta_s(0)$ arises from the interactions between xenon and the zeolite walls in the absence of benzene (i.e. $\theta = 0$) and hence should be independent of θ . The term $\delta_s(\theta)$ arises from the interactions between xenon and the adsorbed benzene. The

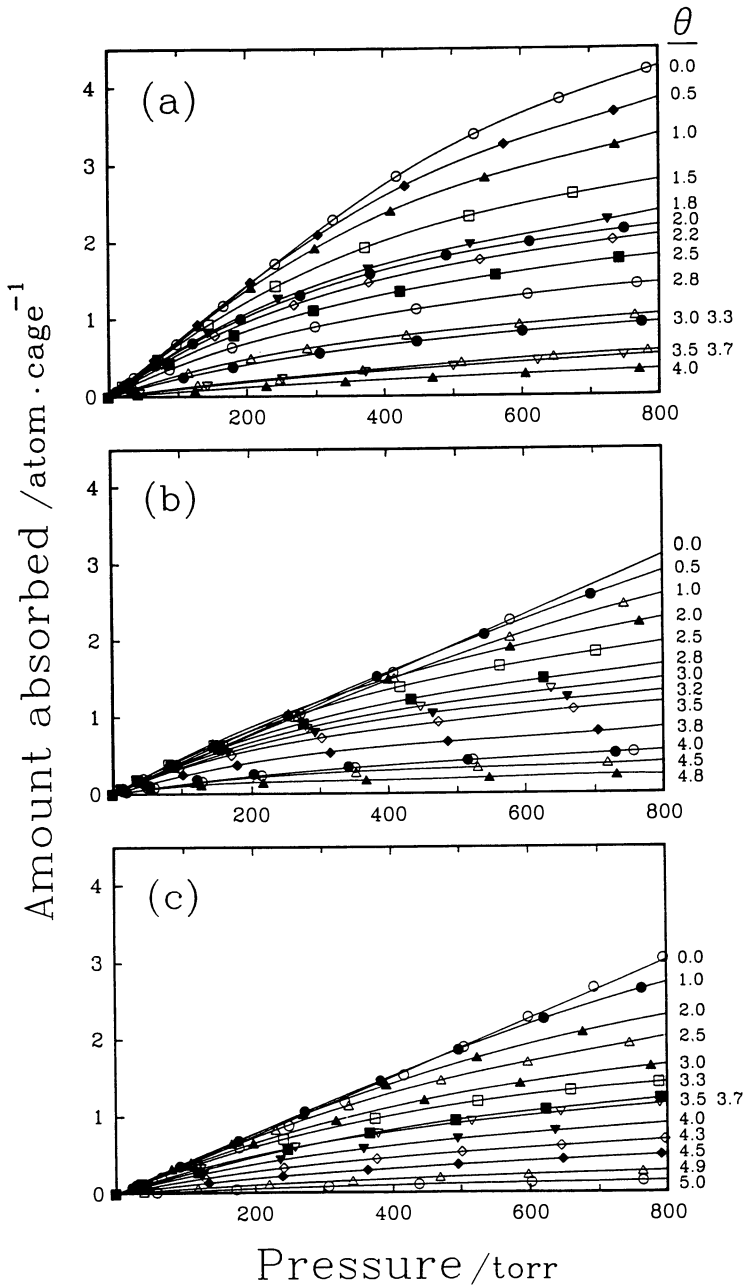


Figure 1. Room temperature (22 °C) adsorption isotherms of xenon co-adsorbed with various amount of benzene in various zeolites (a) NaX, Si/Al = 1.23, (b) NaY, Si/Al = 2.49, (c) NaY, Si/Al = 2.70.

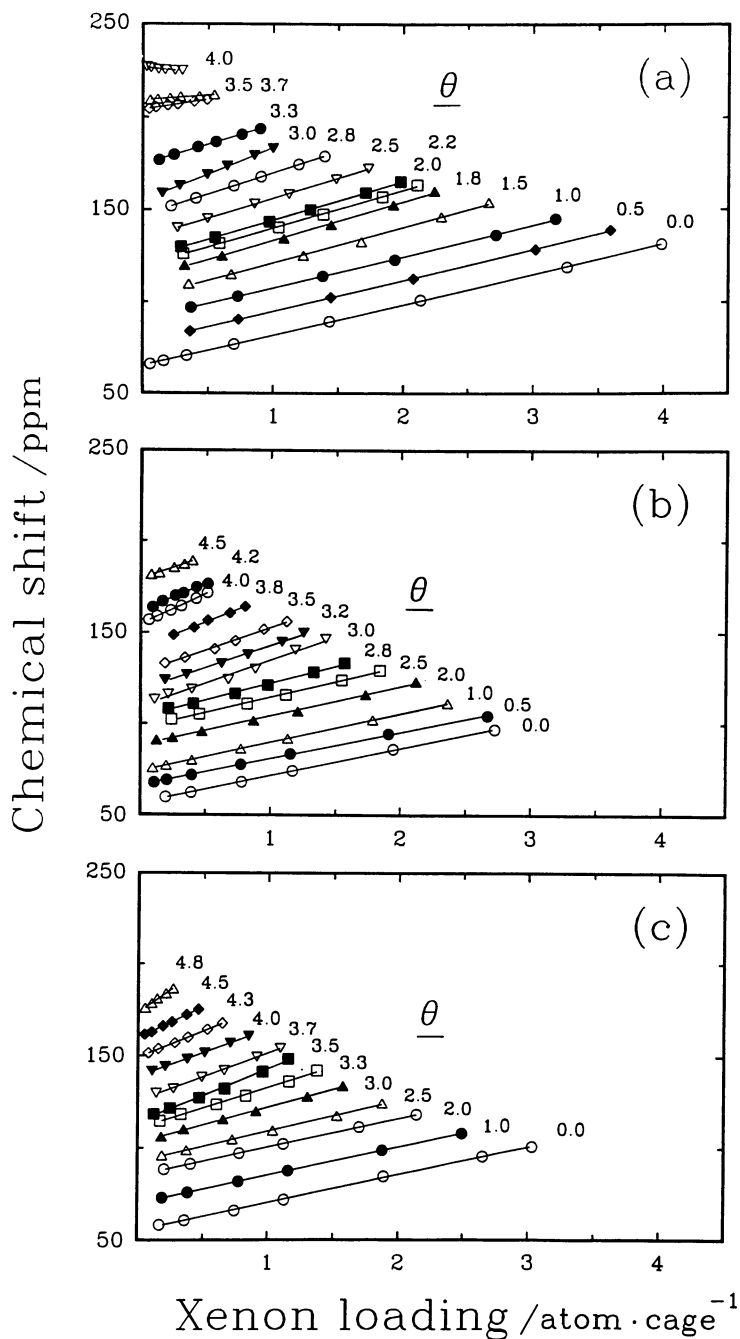


Figure 2. The variations of ^{129}Xe chemical shift with the number of xenon atoms co-adsorbed per supercage for various benzene/zeolite systems (a) NaX , $\text{Si/Al} = 1.23$, (b) NaY , $\text{Si/Al} = 2.49$, (c) NaY , $\text{Si/Al} = 2.70$.

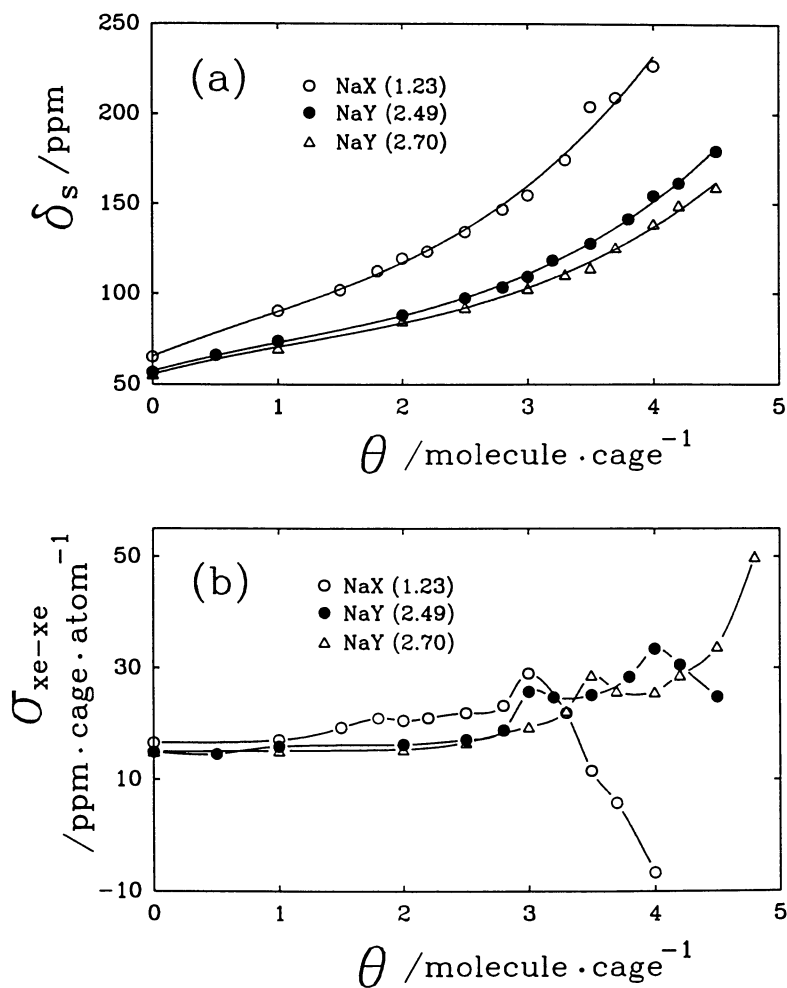


Figure 3. Dependence of (a) ^{129}Xe chemical shift at zero xenon loading (δ_s), and (b) slopes ($\sigma_{\text{xe-xe}}$), both obtained from Figure 2, on benzene coverage (θ) for various benzene/zeolite systems.

last term in equation 1, being characteristic of xenon-xenon interactions in which binary collisions of xenon atoms dominate, is proportional to the density of the adsorbed xenon. The variations of $\sigma_{\text{Xe-Xe}}$ with θ , in Figure 3b, which were obtained from the slopes of the straight lines in Figure 2, therefore reflect changes of the microscopic environments of the adsorbates within the zeolite supercages.

A nonlinear increase of δ_s upon increasing θ is evident for all the adsorbate/adsorbent systems (Figure 3a); the curvatures reflect many-body interactions between a single xenon atom with benzene molecules within the zeolite supercage. Regressional fitting by a third-degree polynomial to the experimental values produces:

$$\delta_s = \delta_s(0) + A_1 \cdot \theta + A_2 \cdot \theta^2 + A_3 \cdot \theta^3; \quad (2)$$

in which θ is the benzene loading per supercage; the resultant data for $\delta_s(0)$, A_1 , A_2 , and A_3 are listed in Table I. At constant benzene coverage, the offset of δ_s values among the three different adsorbate/adsorbent systems (Figure 3a) depends on only the number of Na^+ cations present in the respective zeolite supercage. The Na^+ cation distributions in the zeolite samples are also included in Table I; they were deduced from the XRD results of Mortier and co-workers (61). The difference between dehydrated NaX and NaY zeolites, with regard to benzene adsorption, is the number of Na^+ cations at sites II and III within the supercage (62). The values of $\delta_s(0)$, i.e. at $\theta = 0$, also increase with decreasing Si/Al ratio of the adsorbents consistent with the greater number of cations in the NaX vs. NaY zeolite supercage. This observation contradicts the previous results obtained by Ito and Fraissard who concluded that $\delta_s(0)$ is independent of the Si/Al ratio in faujasite-type zeolites.

For benzene adsorbed on faujasite-type zeolites, it is generally believed that benzene adsorption sites are of two types (22-27,36,37); one corresponds to the site II Na^+ cations within the NaY supercage, and the other is centered in the window formed by the 12-membered oxygen ring between adjacent supercages. Presumably, the adsorption state depends not only on the benzene coverage but also on the properties of zeolite adsorbents such as the nature of the cation and the Si/Al ratio. From Figure 3b, that the values of $\sigma_{\text{Xe-Xe}}$ for $\theta \leq 1.5$, are nearly independent of θ indicates a weak influence of adsorbed benzene within supercages of different zeolites seen by the co-adsorbed xenon. For $\theta > 1.5$, several anomalous apices locate at various values of θ for different adsorbate/adsorbent systems are observed which can be *a priori* related to the microscopic adsorption state of benzene, as we discuss below in conjunction with the corresponding ^{129}Xe linewidth measurements.

The variation of ^{129}Xe NMR linewidth ($\Delta\omega$, measured by full width at half maximum; FWHM) with respect to θ is illustrated in Figure 4. For benzene/NaX(1.23) system in Figure 4a, two linewidth maxima located at $\theta \approx 2.0$ and 3.0 were observed; the location of the linewidth maxima (denoted θ_{max}) are found to decrease linearly with increasing xenon loading as displayed in Figure 5. The xenon loadings specified in Figure 5 were obtained in conjunction with xenon adsorption isotherms (cf. Figure 1) at various benzene coverages. At $\theta \approx 2.0$ and 3.0, two anomalous $\sigma_{\text{Xe-Xe}}$ apices are found in Figure 3b for benzene/NaX(1.23) system. Similar statements also apply for benzene/NaY(2.49) and benzene/NaY(2.70) systems except that in these systems only one linewidth maximum is observable because site III

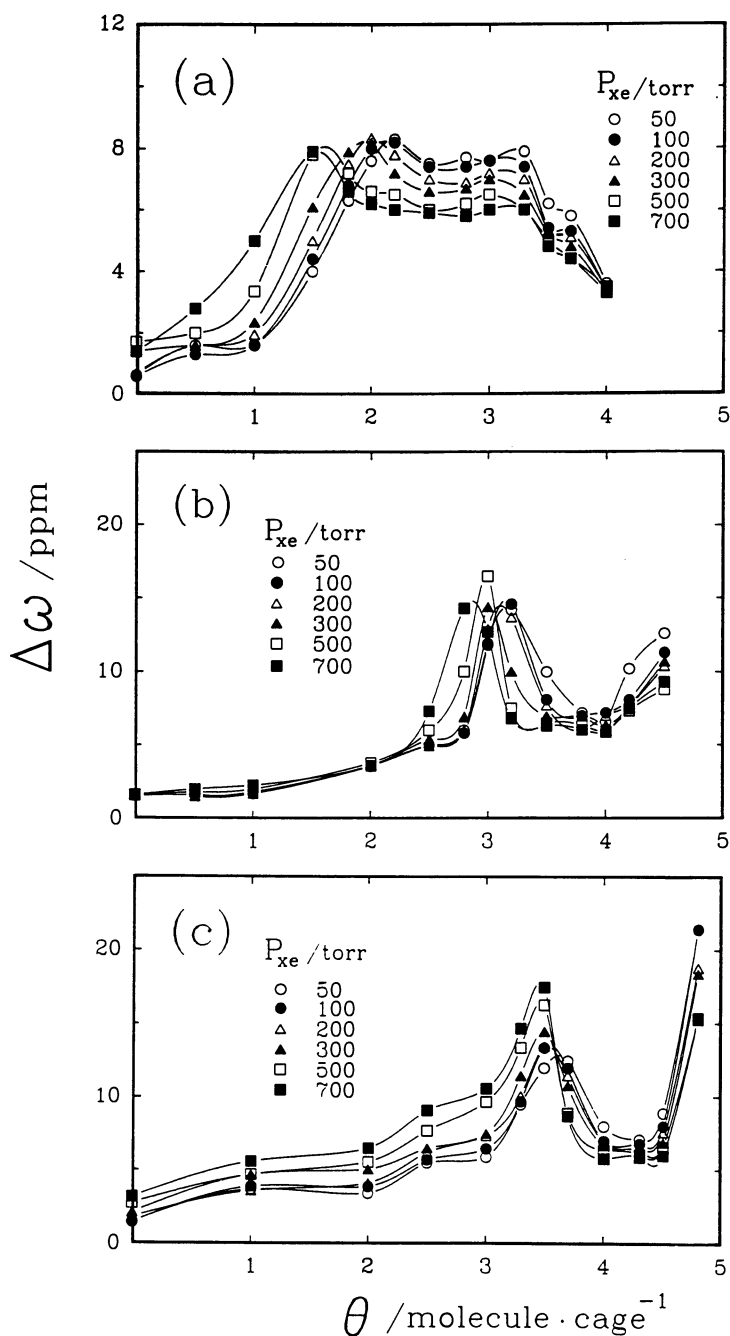


Figure 4. The variations of ^{129}Xe NMR linewidth ($\Delta\omega$) with respect to benzene coverage (θ) for various benzene/zeolite systems (a) NaX, Si/Al = 1.23, (b) NaY, Si/Al = 2.49, (c) NaY, Si/Al = 2.70.

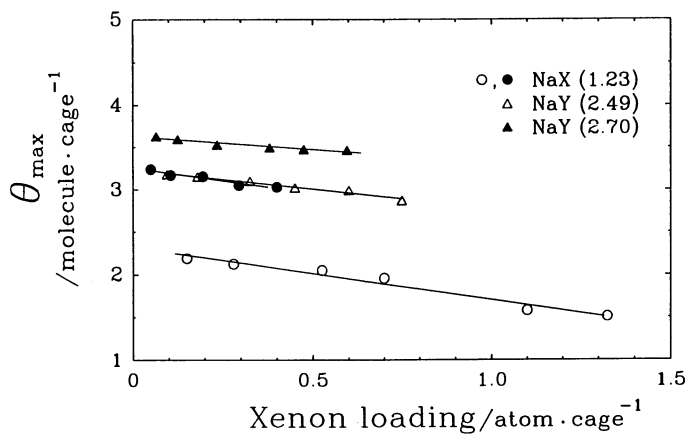


Figure 5. A linear fit between the location of maximum ^{129}Xe NMR linewidth (θ_{max}) and xenon loading for various benzene/zeolite systems.

Na⁺ cations are absent. The occurrence of the linewidth and $\sigma_{\text{Xe-Xe}}$ maxima therefore reflect the same microscopic phenomena originated from the detailed changes of the benzene adsorption states.

Table I. Na⁺ Distribution and Related Experimental Results for Benzene Adsorbed in Different Zeolites

Zeolite(Si/Al)	NaX(1.23)	NaY(2.49)	NaY(2.70)
Number of site II Na ⁺ cations per supercage	4.0	3.9	3.5
Number of site III Na ⁺ cations per supercage	3.0	0.0	0.0
Fitting parameters ^a			
$\delta_s(0)$	65.64	57.36	55.58
A ₁	27.80	19.59	19.11
A ₂	-5.52	-5.30	-5.30
A ₃	2.24	1.56	1.40
$\delta_{\text{ads}}(^1\text{H})^{\text{b}}$	9.1	9.3	9.5
$\delta_{\text{ads}}(^{13}\text{C})^{\text{b}}$	130.9	131.1	132.3
Benzene saturation Coverage ^c	4.0–4.2	4.9–5.2	5.1–5.3

^aObtained by regressional fitting from equation 2; $\delta_s(0)$ in ppm, A₁ in ppm·(molecules/cage)⁻¹, A₂ in ppm·(molecules/cage)⁻², A₃ in ppm·(molecules/cage)⁻³.

^bChemical shifts of benzene obtained by ¹H and ¹³C NMR below saturation benzene coverages; both in (± 0.1) ppm.

^cEstimated from ¹²⁹Xe, ¹H and ¹³C NMR results.

At small θ , the ¹²⁹Xe linewidth increases with increasing θ whereas that the $\sigma_{\text{Xe-Xe}}$ values are nearly independent of θ and Si/Al ratio of the adsorbents indicates that xenon atoms are relatively free to move rapidly between zeolite supercages and that the benzene molecules are fixed on the site II cations for $\theta \leq 1$, in accord with the previous studies (23–25, 20, 34, 38). From the θ dependence of $\sigma_{\text{Xe-Xe}}$ and $\Delta\omega$ in Figure 3b and Figure 4, the first anomalous peak occurring near $\theta \simeq 2.0$ for benzene/NaX(1.23) is associated with the existence of site III Na⁺ ions in the supercage (38), whereas the anomalous peak that occurs at $2.5 < \theta < 4.0$ for all three benzene/adsorbent systems is associated with the site II cations. The linear dependence of the linewidth maximum (θ_{max}) with xenon loading displayed in Figure 5 therefore reflects a competition or mutual hindrance between the xenon and benzene molecules when both species are co-adsorbed in the supercage. This behavior is ascribed to the delocalization and/or rearrangement of benzene molecules within the zeolite supercage. Recent results from molecular dynamics calculations based on the system of two benzene mole-

cules adsorbed per supercage on NaY zeolite (Si/Al = 3.0) illustrated that the adsorbed benzene molecules, which have highly anisotropic motions, are confined largely to the cage walls (12). Previous neutron studies (25,26) using NaY zeolites with Si/Al = 2.78 and 2.43 have also shown that, for $\theta \geq 2.5$, benzene molecules tend to aggregate and migrate toward the center of the supercage. From their low temperature (4 K) results, the authors further concluded that the average distance between benzene and site II Na⁺ cation decreases from 0.270 nm at low benzene coverage to 0.264 nm at high benzene coverage whereas the site II Na⁺ cation, while binding to the benzene molecule, displaced ca. 0.01 nm toward the center of the supercage. However, theoretical calculations (11) and ¹H NMR second-moment measurements made at 77 K (34) indicated that the most favorable distance between a benzene molecule and an Na⁺ cation is 0.32 nm. Moreover, site-specific IR adsorption data (23) for benzene adsorbed on NaY zeolite (Si/Al = 2.5) have indicated that, for $\theta \geq 2.5$, while benzene molecules are sorbed preferentially at site II Na⁺ cations, the possibility of adsorption in the window site increases with increasing benzene concentration. Hence, the results obtained from this study are consistent with the literature cited above.

For benzene/NaX(1.23) with $\theta < 2.5$, the first linewidth maximum gives a range for θ_{\max} from 2.3 at zero xenon loading down to about 1.7 at the greatest observable xenon loading that provides an onset of benzene rearrangement due to the presence of Na⁺ cations at site III. However, as have been demonstrated by the IR measurements of benzene adsorbed on CsNaX zeolites (22), the possibility of benzene first occupying the window sites may not be excluded based on the present ¹²⁹Xe NMR results. For $2.5 < \theta < 4.0$, the overlapped straight lines in the observable range of θ_{\max} for benzene/NaX(1.23) (from 3.0 to 3.3) and benzene/NaY(2.49) (from 2.8 to 3.3) in Figure 5 provide a direct indication of nearly the same number of site II cations existing in the two adsorbents (Table I); the fact that the latter has a greater range is consistent with the absence of site III cations. The greater values of θ_{\max} for benzene/NaY(2.70), ranging from 3.4 to 3.6, therefore signify the deficiency of site II cations. Furthermore, for benzene/NaX(1.23) systems at large benzene coverages, the decrease in both $\sigma_{\text{Xe-Xe}}$ (Figure 3b) and ¹²⁹Xe NMR linewidths (Figure 4a) upon increasing θ is due to the interaction between xenon and highly mobile benzene-Na⁺ complexes, in accord with the notion that the nonlocalizable site III cations are responsible for the greater benzene mobility in NaX than NaY zeolites (38). In contrast, for benzene adsorbed on NaY(2.49) and NaY(2.70) at $\theta \geq 4.0$, the observed ¹²⁹Xe NMR linewidths remain almost constant at first, but increase with increasing θ where the benzene molecules also start to occupy the less favorable window sites after all site II Na⁺ have been occupied. The decrease of $\sigma_{\text{Xe-Xe}}$ in benzene/NaY(2.49) and the increase in benzene/NaY(2.70) at $\theta > 4.0$ may be *a priori* ascribed to the variation in the geometric arrangement of benzene-Na⁺ complexes.

As described earlier, for $2.5 < \theta < 4.0$, benzene molecules tend to aggregate and migrate toward the center of the supercage possibly due to the charge distribution of site II Na⁺ cations (63) and the related charge balance scheme upon increasing benzene coverage or formation of benzene-Na⁺ complexes. From the measurements of the heat adsorption, Neddenriep (64) estimated an effective Na⁺ cation charge in NaY zeolite, about 2/3 of a unit charge. Assuming that there are four Site II Na⁺ cations per NaY supercage, the number of effective 'active sites' for the formation of benzene-Na⁺ complexes amounts to $4 \times (2/3) = 2.7$. By the above simple argument we explain the occurrence of θ_{\max} shown in Figure 5. Due to the

deficiency of site II Na⁺ cations (or a decrease in aluminum content) in the benzene/NaY(2.70) system, the geometrical arrangement of the benzene–Na⁺ complexes within the zeolite supercage for $\theta \geq 4.0$ is less symmetrical than that in benzene/NaY(2.49) and is responsible for the increase of $\sigma_{\text{Xe-Xe}}$ found above $\theta = 4.0$. Moreover, the ¹²⁹Xe NMR results, when combined with xenon adsorption isotherms, also provide macroscopic information related to adsorption capacities in various adsorbate/adsorbent systems. The saturation benzene concentrations estimated from the above results are listed in Table I for the three systems examined; the data were confirmed by the ¹H and ¹³C NMR data discussed in the following section.

¹H and ¹³C NMR Measurements. In order to confirm these ¹²⁹Xe NMR results obtained indirectly from the co-adsorbed xenon, we performed separate NMR experiments on the adsorbed benzene. Specifically, the ¹H and ¹³C NMR of benzene were measured with the same samples used in the ¹²⁹Xe NMR experiments but without xenon. The variations of ¹H and ¹³C NMR FWHM linewidth ($\Delta\omega$) with benzene coverage (θ) are summarized in Figure 6. The results obtained from the two different nuclei give a similar profile; for $\theta < 4.0$, the observed ¹H and ¹³C linewidths were independent of θ , but for $\theta > 4.0$, abrupt increases of linewidth with increasing θ were observed. The above observations are explained by a progressive occupancy of Na⁺ cations by the benzene molecules within the zeolite supercage. For $\theta < 4.0$, the benzene molecules are adsorbed at site II Na⁺ cations progressively; while still confined in the supercage, they undergo vigorous molecular motions which effectively average the ¹H and ¹³C resonances. On the other hand, for $\theta \geq 4.0$, cooperative interactions or mutual hindrance among adjacent benzene molecules inside the limited space of the supercage results in decrease of benzene mobility and hence the observed line broadening. At the same benzene coverage, the overall ¹H and ¹³C NMR linewidths increase with increasing Si/Al ratio of the adsorbents inconsistent with the decrease in benzene mobility (7,8,33,38).

For the benzene/NaY(2.49) system, samples with benzene coverages exceeding saturation coverage were also examined. Both ¹H and ¹³C spectra for samples with benzene coverage exceeding saturation show a narrow line superimposed on a broad line, depicted in Figure 7; although the linewidth of the narrow line decreased with increasing θ , the linewidth of the broad component remained almost unchanged. Similar behavior have been demonstrated for ¹³C NMR (Si/Al ratio not specified) by Borovkov and co-workers (39) and for ¹H NMR (Si/Al = 1.18, 2.50 and 2.71) by Lechert and co-workers (32,33) but with somewhat greater linewidths. All these authors have elucidated that a decrease in benzene mobility due to mutual disturbance of the molecules inside the limited space of the supercages, which also favors an increase in molecular dipole–dipole interaction, is responsible for the increase in ¹H and ¹³C linewidths at $\theta > 4.0$. The occurrence of the superimposed narrow line has been regarded as resulting from mobile benzene molecules (i.e. those not paired with any of the four Na⁺ cations) inside the zeolite supercage. The latter argument is, however, in contrast to our recent finding (56) that the superimposed narrow line arises from excess (free) benzene sorbed on the external surfaces of the zeolite crystallites. Therefore, the appearance of the superimposed narrow line may be considered the onset of saturation coverage and in conjunction with the ¹²⁹Xe NMR results, may be used to estimate the saturation benzene coverage in different zeolite adsorbates (Table I). The values of the saturation benzene coverages which increase with increasing Si/Al ratio of the adsorbents, agree with previous results (34,65).

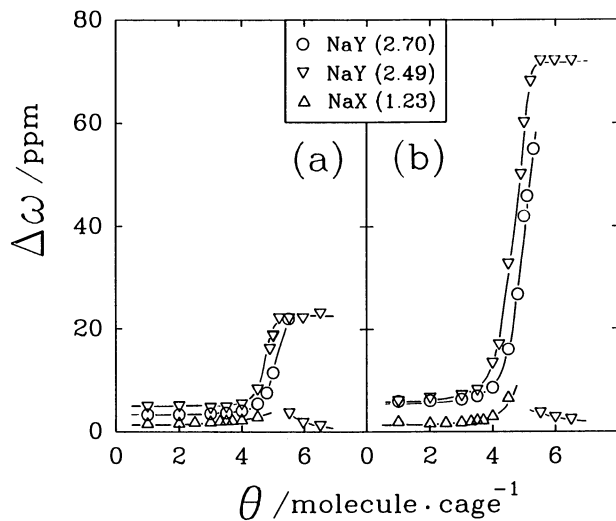


Figure 6. Dependence of (a) ^1H , and (b) ^{13}C NMR linewidth ($\Delta\omega$) on benzene coverage (θ) for various benzene/zeolite systems.

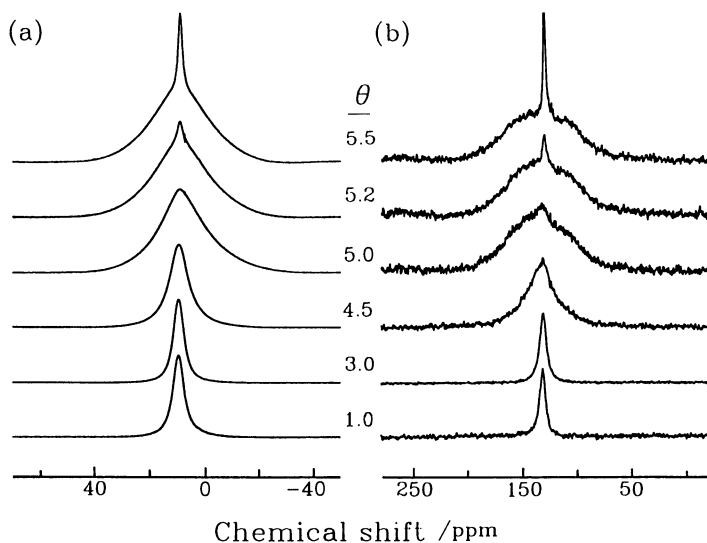


Figure 7. Room temperature (a) ^1H , and (b) ^{13}C NMR spectra of benzene adsorbed on NaY (Si/Al = 2.49) zeolite at various benzene coverages (θ).

Below saturation benzene coverage, the observed ^1H and proton-decoupled ^{13}C chemical shifts, denoted $\delta_{\text{ads}}(\text{H})$ and $\delta_{\text{ads}}(\text{C})$, were both found to increase slightly with Si/Al ratio of the adsorbents but independent of adsorbate coverage; their values are listed in Table I. These values being greater than the well known $\delta_{\text{liq}}(\text{H}) = 7.24$ ppm and $\delta_{\text{liq}}(\text{C}) = 128.7$ ppm (with proton decoupling) values for the bulk liquid benzene have been ascribed to corrections for medium effects (66). However, such a down field shift was not observed in previous ^{13}C NMR studies on similar systems (12, 13,39). Although no ^1H chemical shift data are available for comparison, a small (< 1 ppm) down field shift was observed for benzene adsorbed on Pt/ Al_2O_3 with ^1H NMR (67,68). For benzene/NaY systems with θ near the saturation coverage, the ^1H and ^{13}C chemical shifts both decrease slightly because the deficiency of Na^+ cations at site II and hence the enhancement of benzene-benzene interactions. In contrast, for the benzene/NaX system, a slight increase in chemical shifts was observed because of surplus Na^+ cations at site III.

Summary and Conclusions

Through the analysis of adsorption isotherms and ^{129}Xe NMR results of the co-adsorbed xenon, we have shown that the dispersal of benzene molecules depends on not only the cation distribution but also the amount of benzene adsorbate within the supercage of zeolite adsorbents. We have also demonstrated for the first time that this well known indirect technique has the capability not only to probe the macroscopic distribution of adsorbate molecule in zeolite cavities but also to provide dynamic information about the adsorbate at the microscopic level. Conventional ^1H and ^{13}C NMR which directly detect the adsorbate species, although providing complimentary results, are relatively less sensitive.

In summary of our results obtained from the benzene/zeolite systems, the adsorption strength for xenon decreases with increasing Si/Al ratio of zeolite adsorbents but, in contrast, the mobility and saturation coverage of benzene increase with increasing Si/Al ratio of zeolites. At low benzene coverages, benzene molecules tend to adsorb on Na^+ cations at site III or the 12-oxygen rings window sites rather than site II and, while being confined mostly within the supercage, the benzene- Na^+ complexes may still undergo vigorous motion. At intermediate benzene coverage, rearrangement of benzene molecules by cooperative migration of benzene- Na^+ complexes toward the center of zeolite supercage was confirmed by ^{129}Xe NMR. At high benzene coverages, a decrease in benzene mobility due to mutual hindrance of benzene molecules inside the limited space of the zeolite cavities has been observed. Above saturation benzene coverages at which the zeolite supercage is packed with benzene molecules so that xenon atom can no longer enter, both ^1H and ^{13}C NMR spectra showed a sharp line superimposed on the broad line which we assign to excess benzene adsorbed in the intercrystalline voids.

Acknowledgments

The authors express their appreciation to Professor D. Barthelemy and Professor H. Lechert for helpful discussions. The support of this work by the National Science Council of the Republic of China, grant no. NSC80-0208-M001-48, is gratefully acknowledged.

Literature Cited

1. Kärger, J.; Ruthven, D. M. *J. Chem. Soc. Faraday Trans. I* 1981, 77, 1485.
2. Bülow, M.; Mietk, W.; Struve, P. and Lorenz P. *J. Chem. Soc. Faraday Trans. I* 1983, 79, 2457.
3. Forni, L.; Viscardi C. F. *J. Catal.* 1986, 97, 480.
4. Eic, M.; Goddard, M. and Ruthven, D. M. *Zeolites* 1988, 8, 327.
5. Kärger, J.; Pfeifer, H.; Walther, P.; Dyer, A. and Williams, C. D. *Zeolites* 1988, 8, 251.
6. Germanus, A.; Kärger, J.; Pfeifer, H.; Samulevic, N. N. and Zandov, S. P. *Zeolites* 1985, 5, 91.
7. Barthomeuf, D.; Ha, B.-H. *J. Chem. Soc. Faraday Trans. I* 1973, 69, 2147.
8. Dzhigit, O. M.; Kiselev, A. V. and Rachmanova, T. A. *Zeolites* 1984, 4, 389.
9. Anderson, M. W.; Klinowski, J. *J. Chem. Soc. Faraday Trans. I*, 1986, 82, 3569.
10. Sauer, J.; Deininger, D. *J. Phys. Chem.* 1982, 86, 1327.
11. Sauer, J.; Deininger, D. *Zeolites* 1982, 2, 114.
12. Demontis, P.; Yashonath, S. and Klein, M. L. *J. Phys. Chem.* 1989, 93, 5016.
13. Geschke, D.; Hoffmann, W.-D. and Deininger, D. *Surf. Sci.*, 1976, 57, 559.
14. Deininger, D.; Michel, D. and Heidrich, D. *Surf. Sci.* 1980, 100, 541.
15. Monduzzi, M.; Monaci, R. and Solinas, V. *J. Colloid Interf. Sci.* 1987, 120, 8.
16. Unland, M. L.; Freeman, J. J. *J. Phys. Chem.* 1978, 82, 1036.
17. Primet, M.; Garbowski, E.; Mathieu, M. V. and Imelik, B. *J. Chem. Soc. Faraday Trans. I*, 1980, 76, 1942.
18. Angell, C. L.; Schaffer, P. C. *J. Phys. Chem.* 1965, 69, 3463.
19. Angell, C. L.; Howell, M. V. *J. Colloid Interf. Sci.* 1968, 28, 279.
20. Datka, J.; *J. Chem. Soc. Faraday Trans. I* 1981, 77, 511.
21. Coughlan, B.; Carroll, W. M.; O'Malley, P. and Nunan, J. *J. Chem. Soc. Faraday Trans. I* 1981, 77, 3037.
22. de Mallmann, A.; Barthomeuf, D. *Zeolites* 1988, 8, 292.
23. de Mallmann, A.; Barthomeuf, D. *J. Phys. Chem.* 1989, 93, 5636.
24. Fitch, A. N.; Jobic, H. and Renouprez, A. *J. Chem. Soc. Chem. Commun.* 1985, 284.
25. Fitch, A. N.; Jobic, H. and Renouprez, A. *J. Phys. Chem.* 1986, 90, 1311.
26. Renouprez, A. J.; Jobic, H. and Oberthür, R. C. *Zeolites* 1985, 5, 222.
27. Jobic, H.; Renouprez, A.; Fitch, A. N. and Lauter H. J. *J. Chem. Soc. Faraday Trans. I* 1987, 83, 3199.
28. Freeman, J. J.; Unland M. L. *J. Catal.* 1978, 54, 183.
29. Nagel, M.; Michel, D. and Geschke, D. *J. Colloid Interf. Sci.* 1971, 36, 254.
30. Nagel, M.; Pfeifer, H. and Winkler, H. *Z. Phys. Chemie, Leipzig* 1974, 255, 283.
31. Hoffmann, W.-D. *Z. Phys. Chemie, Leipzig* 1976, 257, 315.
32. Lechert, H.; Haupt, W. and Wittern, K. P. *J. Catal.* 1976, 43, 356.
33. Lechert, H. *Catal. Rev.-Sci. Eng.* 1976, 14, 1.
34. Lechert, H.; Wittern, K.-P. *Ber. Bunsenges. Physik. Chem.* 1978, 82, 1054.

35. Basler, W.; Lechert, H. *Ber. Bunsenges. Physik. Chem.* 1974, 78, 667.
36. Lechert, H.; Basler, W. D. *J. Phys. Chem. Solid* 1989, 50, 497.
37. Lechert, H.; Basler, W. D. and Wittwen, K. P. In *Proceedings of the 7th International Zeolite Conference*; Murakami, Y.; Iijima, A.; Ward, J., Eds.; Elsevier, Amsterdam, 1986; pp. 595–600.
38. Pfeifer, H. In *Magnetic Resonance in Colloid and Interface Science*; Resing, H. A.; Wade C. G., Eds; ACS Symposium Series; American Chemical Society: Washington, DC, 1976, vol. 34; pp 36–47.
39. Borovkov, V. Yu.; Hall, W. K. and Kazanski, V. B. *J. Catal.* 1978, 51, 437.
40. Ruthven, D. M.; Doetsch, I. H. *Amer. Inst. Chem. Engin. J.* 1976, 22, 882.
41. Forni, L.; Viscardi, C. F. and Oliva, C. *J. Catal.* 1986, 97, 469.
42. Kärger, J.; Pfeifer, H. *Zeolites* 1987, 7, 90.
43. Kärger, J.; Caro, J. *J. Chem. Soc. Faraday Trans. I* 1977, 9, 1363.
44. Lee, L.-K.; Ruthven, D. M. *J. Chem. Soc. Faraday Trans. I* 1979, 75, 2406.
45. Yucel, H.; Ruthven, D. M. *J. Chem. Soc. Faraday Trans. I* 1980, 76, 71.
46. Kärger, J.; Kocirik, M. and Zikánová, A. *J. Colloid Interf. Sci.* 1981, 84, 240.
47. Kärger, J.; Bülow, M.; Struve, P.; Kocirik, M. and Zikánová, A. *J. Chem. Soc. Faraday Trans. I* 1978, 74, 1210.
48. Bülow, M.; Struve, P.; Finger, G.; Redszus, C.; Ehrharst, K.; Schirmer, W. and Kärger, J. *J. Chem. Soc. Faraday Trans. I* 1980, 76, 597.
49. Kärger, J.; Heink, W.; Pfeifer, H.; Rauscher, M. and Hoffmann, J. *Zeolites* 1982, 2, 275.
50. Bülow, M.; Struve, P. and Mietk, W. *Z. Chem.* 1983, 23, 313.
51. Bülow, M.; Mietk, W.; Struve, P. and Zikánová, A. *Z. Phys. Chemie. Leipzig* 1983, 264, 3, S. 598.
52. Cohen de Lara, E. In *Proceedings of the 5th International Zeolite Conference*; Rees, L. V. C, Ed.; Heyden: London, 1980; pp 414–423.
53. Kärger, J.; Pfeifer, H.; Rauscher, M.; Bülow, M.; Samulevic, N. N. and Zandov, S. P. *Z. Phys. Chemie. Leipzig* 1981, 262, 3, S. 567.
54. de Menorval, L. C.; Raftery, D.; Liu, S. B.; Takegoshi, K.; Ryoo, R. and Pines, A. *J. Phys. Chem.* 1990, 94, 27.
55. Chmelka, B. F.; Pearsons, J. G.; Liu, S. B.; Ryoo, R.; de Menorval, L. C. and Pines, A. *J. Phys. Chem.* 1991, 95, 303.
56. Wu, J.-F.; Chen, T.-L.; Ma L.-J.; Lin M.-W. and Liu S.-B. *Zeolites* 1992, 12, 86.
57. Ito, T.; Fraissard, J. *J. Chem. Phys.* 1982, 76, 5225.
58. Ripmeester, J. A. *J. Am. Chem. Soc.* 1982, 104, 289.
59. Reisse, J. *Nouv. J. Chim.* 1986, 10, 665.
60. Jameson, C. J. *J. Chem. Phys.* 1975, 6, 5296.
61. Mortier, W. J.; van den Bossche, E. and Uytterhoeven, J. B. *Zeolites* 1984, 4, 41.
62. Breck, D. W. *Zeolite Molecular Sieves: Structure, Chemistry, and Use*; John Wiley & Sons: New York, NY, 1974, pp 92–100.
63. Dempsey, E. *J. Phys. Chem.* 1969, 73, 3660.
64. Neddenriep, R. J. *J. Colloid Interf. Sci.* 1968, 28, 293.
65. Barrer, R. M.; Bultitude, F. W. and Sutherland, J. W. *Trans. Faraday Soc.* 1957, 53, 1111.

66. Engelhardt, G.; Michel, D. *High-Resolution Solid-State NMR of Silicates and Zeolites*; John Wiley & Sons: New York, NY, 1987, Chapter VII.
67. Taarit, Y. B.; Naccache, C. M. and Imelik, B. *Chem. Phys. Lett.* 1977, 47, 479.
68. Tirendi, C. F.; Mills, G. A. and Dybowski, C. *J. Chem. Phys.* 1984, 88, 5765.

RECEIVED July 9, 1992

Chapter 20

Reaction Pathway Analysis

Global Molecular and Mechanistic Perspectives

Michael T. Klein, Matthew Neurock, Linda Broadbelt, and Henry C. Foley

Center for Catalytic Science and Technology, Department of Chemical Engineering, University of Delaware, Newark, DE 19716

Reaction pathway analysis and the closely associated topic of applied chemical kinetics are at the heart of both the practice and study of chemical reactions. They often form the basis of the process engineer's conservation equations and subsequent reactor design, but also can be the starting point for fundamental mechanistic inference. This centrality of reaction pathways guarantees their relevance and motivated this ACS symposium on the topic.

Figure 1 summarizes three hierarchical levels at which reaction pathways can be studied experimentally and modelled. These levels collectively represent a connection between the mechanistic chemistry of elementary steps and industrially relevant process chemistry. Each has its own advantages and limitations, which are evident upon consideration of related reaction models.

Mechanistic models, i.e., those involving the elementary transitions (steps) of active centers and therefore often free-radical or ionic intermediates, have the advantage of being rich in chemical significance. The large number of parameters they contain is a true reflection of the diversity of nature's reactions, but often imposes serious limitations related to the lack of a quantitative kinetics database. Moreover, these models are often numerically stiff and can impose a considerable CPU demand. An acceptable "research" CPU demand will often not meet the needs of industrial practice.

This CPU issue along with historical limitations in analytical chemistry have often forced "practice-oriented" reaction models to be at a global level. These models traditionally involve the relevant boiling point or solubility defined reactants, and not the controlling molecules or intermediates. Thus they will often appear to suffer from the point of view of chemical significance; however they are generally much easier to solve. Most importantly, these models are relevant; the reactants and products in these models are bought and sold!

Increases in the molecular detail provided by modern analytical chemistry have motivated the formation of intermediate-level, molecular models. These hybrid models have molecules as reactants and products, not intermediate active centers (radicals or ions) or globally lumped product fractions. They embody more chemistry and rate constants

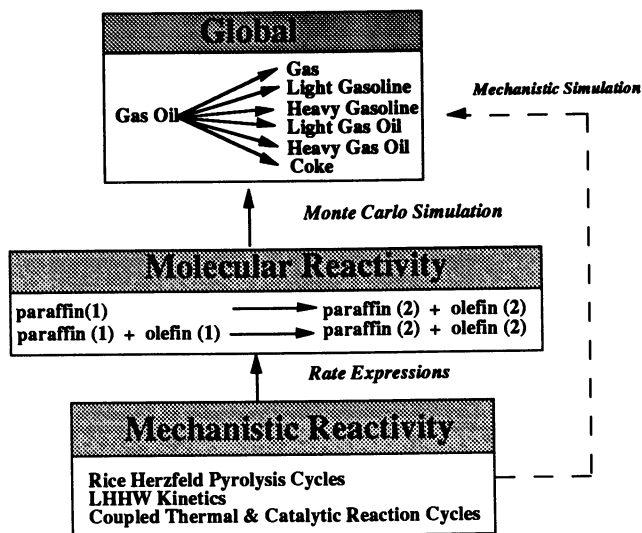


Figure 1. Three hierarchical levels of reaction chemistry and reaction modelling.

than global models, but require subsequent product oriented lumping to ascertain relevant product fractions.

These "pathways-level" models have two key advantages. First, they generally provide a better basis for extrapolation than global models because of their chemical richness. Second, and perhaps trivially obvious, they are fashioned to answer new questions concerning product quality and properties. For example, as environmental issues dictate the allowable aromatics content of gasoline, it is important to have models which can specify, e.g., the benzene content.

The objective of this review is to consider each of these levels of modelling through the view of three important commercial chemistries: pyrolysis, hydrotreating and catalytic cracking. We first review the chemistry in each of the three levels in Figure 1. This is followed by a summary of available experimental information and kinetics data in terms of molecular pathway models. The hope is to expose this intermediate level molecular modelling as an attractive compromise between the chemically rich but CPU intensive mechanistic models and the CPU friendly but chemically poor global modelling approaches.

Global Reaction Models

Global reactions models are those where the reactants and products are defined by available analytical separation schemes. They generally represent the interconversion of lumps or pseudocomponents, i.e., aggregates of many molecules with common attributes. In general, the characteristics which assemble given sets of molecules into a lump will not be reactivity. For example, perhaps the two most commonly found globally lumped models are based on boiling point or solubility characteristics.

Global reactions models have historical significance. Their formulation is largely due to the global nature of analytical output of hydrocarbon mixtures in the 1940s and 50s. Additional advantages of these models include their easy formulation and solution.

Often analytical solutions are permitted. Moreover, on today's high-speed computers they impose only minor CPU requirements, and therefore could find considerable use in process control, design and optimization. They also become very attractive models for solution on inexpensive personal computers which could be placed in a remote location or refinery.

Asphaltene and resid pyrolysis provide two relevant examples of global pyrolysis models. The pyrolysis of an isolated asphaltene feedstock typically yields the type of data summarized in Figure 2, a plot of the temporal variation of weight based product fractions as a function of time (t). This figure illustrates the exponential disappearance of asphaltene accompanied by the formation of coke, maltene and gas product fractions. Consideration of the initial slopes for the formation of coke, maltene and gas fractions led to the type of reaction network shown in Figure 3. Since resid and its reaction products can likewise be defined in terms of the solubility and volatility-based product groups asphaltene,

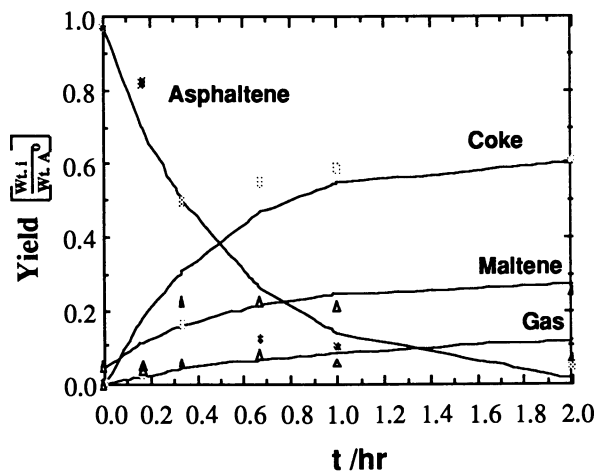


Figure 2. An example of the global reaction product yields for the pyrolysis simulation of a Hondo-derived Asphaltene feedstock at 400°C [1].

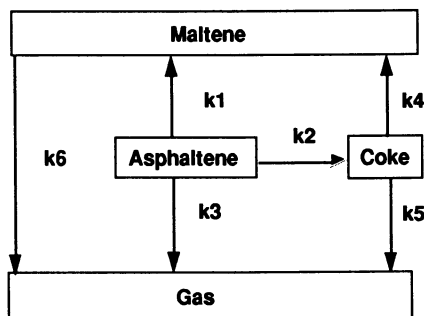


Figure 3. Global reaction network for asphaltene and resid pyrolysis systems [1].

maltene, coke and gas, the reaction network of Figure 3 is applicable to resid as well as isolated asphaltenes (2).

Table I summarizes relevant data for the pyrolysis of a series of isolated asphaltene feedstocks. This table highlights the dependence of reaction product yields and selectivities on the resid origin. Clearly the reactivity of each feed depends upon its source (1).

Table I. Summary of global asphaltene pyrolysis experiments. The ultimate yields and final selectivities for a series of different asphaltene feedstocks which were pyrolyzed for two hours at 400°C (1)

Product/Feedstock	Calif.	Maya	Jobo	Athab.	Hondo
Ultimate Yields					
Asphaltene	22	19	9	9	5
Coke	51	41	51	54	61
Maltene	21	20	27	21	25
Gas	5	20	13	16	7
Final Selectivities					
Coke	65	53	62	60	64
Maltene	27	23	3	23	26
Gas	6	25	33	18	7

This point is underscored more dramatically in Figure 4, a compilation of the global rate parameters of Figure 3 for the various feedstocks of Table I. Clearly these parameters are feedstock dependent. This tends to undermine the value of a reaction

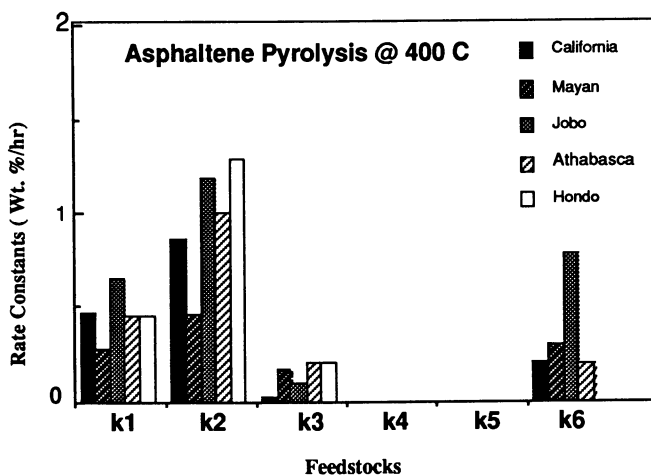


Figure 4. The effect of asphaltene source on the global kinetic rate parameters for the pathways illustrated in Figure 3 (1).

model, and highlights one of the main limitations of global reaction models. This may well be the strongest motivation for molecule-based reaction models.

Hydrotreating reaction models are nicely exemplified by the Amoco Easy-Hard lump model of Figure 5. The global paths and the kinetics reported in this figure were taken from the review by Beaton and Bertolacini (3), which summarizes experimental results, the modelling, and commercialization of Amoco's hydrotreating unit. In short, the subdivisions of resid into "hard" and "easy" fractions and gas oil into reactant and product fractions were required to account for kinetic nonlinearities. The seven lumps and 14 rate constants provided significant flexibility and were able to describe the kinetics of several relevant product fractions.

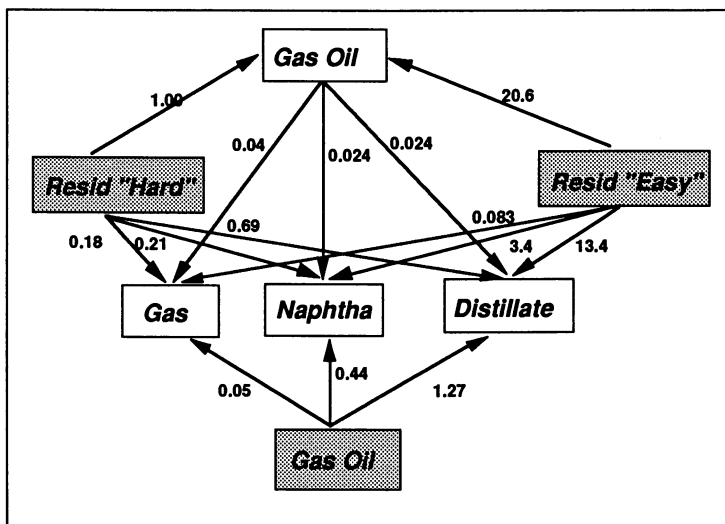
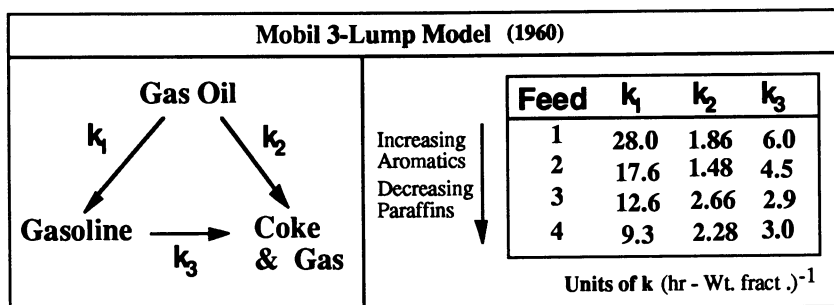


Figure 5. The Amoco Easy-Hard kinetic model for resid hydrotreating. The reaction products are characterized by seven distinct lumps, the three feedstock species which are shaded in gray (resid hard, resid easy, and gas oil) and the four new components which are not shaded (gas, naphtha, distillate, and gas oil). The kinetic interconversion of these groups is described by the 14 constants (3).

Catalytic cracking modelling is nicely illustrated by a series of Mobil publications over the past 30 years. Chronologically, the Mobil models have increased in the number of model lumps, in an effort to describe more chemical detail. The early "three lump" cracking model followed the kinetic evolution of the reactant gas oil and the desirable gasoline product and the undesirable coke and gas fraction (4-6). This model is illustrated in Figure 6a. Weekman has published an extensive review of this approach (7). The need for additional information and better feedstock independence motivated the "ten lump model" (8), which is illustrated in Figure 6b. Finally, the molecule-based modelling approach articulated by Quann and Jaffe (9) follows the evolution of hundreds of pseudocomponents which are resolved from detailed modern analytical chemical analysis. In short, the identified trend is that as the sophistication in the available analytical tools

a)



b)

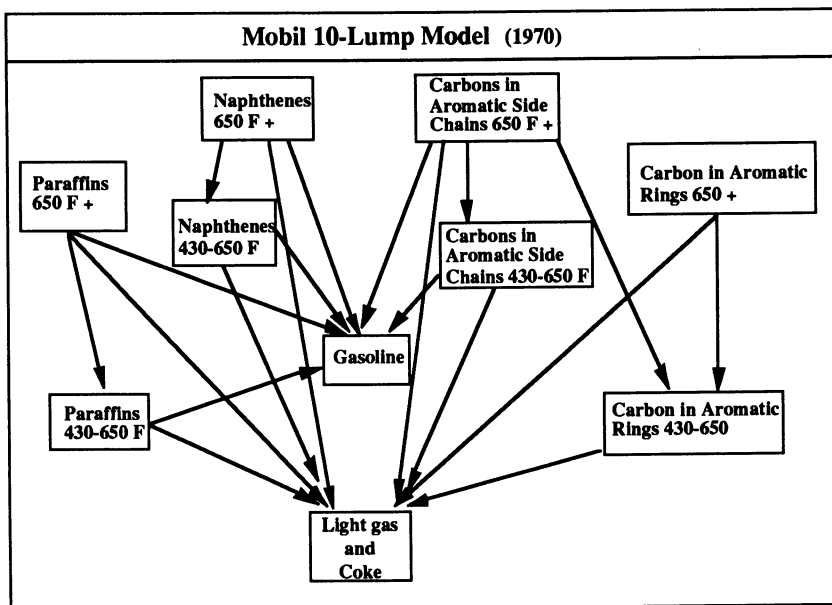


Figure 6. The Mobil series of catalytic cracking reaction models. a) The Mobil 3-Lump model b) the Mobil 10-Lump model (4,5,7).

and modelling issues rose, so too did the number of model lumps. In a sense, the increase in the number of lumps in global models showed the beginnings of the formulation of molecular models. It is these intermediate levels to which we now turn our attention.

Molecular Reaction Models.

Molecular reactions models are those in which the reactants and products are defined by actual molecules. The mechanistic chemistry is implicit, as active centers such as free radical and/or ion intermediates are not addressed explicitly. This pathway-oriented model is thus the "expression" of a sequence of elementary steps, governed by fundamental chemical phenomena such as the transition state activation barriers. The corresponding

kinetics for the mechanism are indirectly accounted for through the development of detailed rate expressions which are functions of the elementary rate constants.

These models require an extensive data base. Often this will be compiled from pure component or model compound reaction pathways and kinetics. Model compound experiments allow for the quantitative deduction of "intrinsic" reaction kinetics and, in favorable circumstances, reaction mechanism information.

The true benefit from molecular models is that they permit the quantitative structural description of complex feeds. As noted above, this allows for easy extrapolation to unstudied systems and also permits product quality and properties issues to be addressed. The kinetics, while formulated at the molecular level, are nevertheless still implicitly tied to the mechanism. The CPU demands, however, are relatively small compared to those of mechanistic models.

Returning to the asphaltene and resid pyrolysis chemistry, their molecular reaction models require a significant data base of hydrocarbon reaction pathways and kinetics. These feeds contain molecules that can be organized into one of five hydrocarbon types. In general, the reactants will contain alkylaromatics, alkyltetralins, alkyl-naphthenes, paraffins, and olefins (10,11). Figure 7 provides a succinct summary of representative reaction pathways for each one of these families. Notice that the reactions are from one molecule to another, and that the selectivities are provided by stoichiometric coefficients. The controlling free-radical intermediates are well-known and have been modelled (11-15), but are nevertheless only implicitly accounted for in the pathways and kinetics of Figure 7. Additional reaction paths not shown in Figure 7 but nevertheless relevant to asphaltene and resid pyrolysis include dehydrogenation, condensation, and ring opening. The first two paths lead to aromatization and coke formation, respectively, whereas the latter allows for additional molecular weight reduction.

The kinetics associated with the reactions shown in Figure 7 are summarized in Table II. Detailed mechanistic studies on the pyrolysis of alkylaromatics (12,13,15), alkyl-naphthenes (14) and alkyltetralins (14) have allowed for the formulation of the Arrhenius parameters and stoichiometric coefficients shown. The kinetics for paraffin and olefin pyrolyses were extracted from the abundant literature data (16-18). Finally, the issue of kinetic interactions have been both theoretically and experimentally addressed (11,19). These interactions in general cause the reaction of the mixture to be different than the linear combination of the pure component rates.

Resid hydrotreating contains a significant thermal component (3), but its key distinction from coking or asphaltene and resid pyrolysis is the inclusion of a catalytic hydrogenation component and, often, an acid cracking reaction. Thus hydrogenation reaction pathways are of considerable relevance. Hydrogenation reaction pathways are typically reversible under relevant process conditions and thus the issues of not only activity but also thermodynamic limitations and hydrogen solubility are real. Table III is a summary of the pathways and kinetics of hydrogenation of an exhaustive set of polynuclear aromatic (PNA) hydrocarbons taken from the literature (20-34). A detailed review and analysis of many of these paths has been provided by Girgis and Gates (24). The kinetics provided in Table III are clearly dependent upon both process conditions, e.g., temperature, pressure, pellet size, and linear velocity, and catalyst properties. These issues suggest that perhaps not all the data in the literature can be considered intrinsic.

Table IV is a concise summary of the effect of the number of aromatic rings and their configurational arrangement on the hydrogenation kinetics of relevant polynuclear

Table II. Kinetics for representative reaction pathways for hydrocarbon pyrolysis


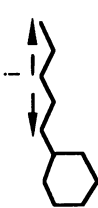
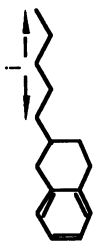
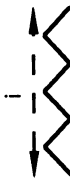
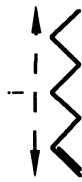
Molecular Components	Expt.	$\log_{10} A$	E^*	v_1	v_2	v_3	v_4	Conditions	w	Ref.
	PDB	14.0	55.5	0.312	0.117	0.571	-	T= 400°C	(i/15) 1/2	12, 13
				0.454	0.117	0.429	-	T= 425°C		
Alkylaromatics				0.510	0.108	0.382	-	T= 450°C		
	TDC	14.9	59.4	0.08	0.07	0.85	-		(i/13)	14
Alkylnaphthenes										
	2ET	12.7	53.5							14
Alkyltetralins										
	C4-	12.8	56.0	0.286	0.571	0.095	0.048	CA=0.001 M		16
Paraffins	C20	16.7	70.2	0.286	0.571	0.095	0.048	CA=1.0 M		
	C4-	13.8	56.0							16
Olefins	C20	17.8	70.2							

Table III. The Pathways and Kinetics of Hydrogenation of Polynuclear Aromatic Hydrocarbons

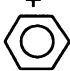
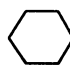
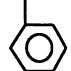

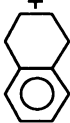

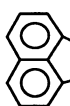

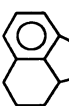
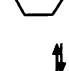
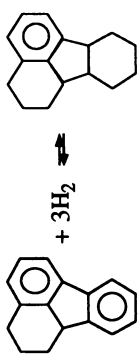
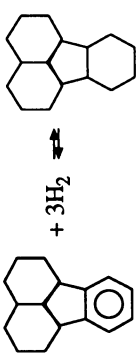

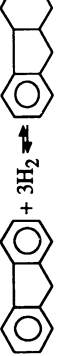
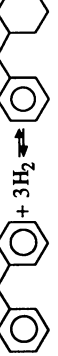
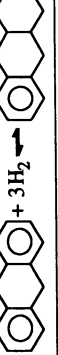
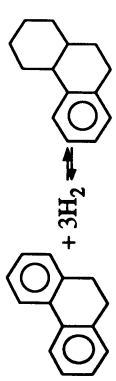
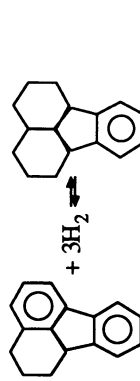

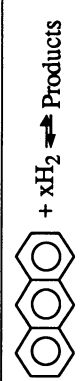
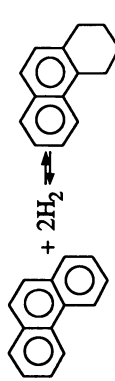
Reaction Pathway	Temp (°C)	Pressure (atm)	Catalyst	Reactor	kf	kr	Units of k	Ref.
 + 3H ₂ ⇌ 	325 C 340 C 340 C 340 C 340 C 340 C	75 atm 71 atm 71 atm 71 atm 71 atm 71 atm	Co-Mo MoS ₂ WS ₂ CoMo NiW NiMo	Batch AC Batch AC Batch AC Batch AC Batch AC Batch AC	0.0101 1*** 1*** 1*** 1*** 1***	0.0004	L/gcat-hr Relative Relative Relative Relative Relative	Sapre Moreau Moreau Moreau Moreau Moreau
 + 3H ₂ ⇌ 	325 C	75 atm	Co-Mo	Batch AC	0.0022	—	L/gcat-hr	Sapre
 + 3H ₂ ⇌ 	325 C	75 atm	Co-Mo	Batch AC	0.005 (T) 0.015 (C)	—	L/gcat-hr	Sapre
 + 3H ₂ ⇌ 	300-400 C	185-190 atm	Ni-Mo	Flow	0.228	0.0739	L/gcat-hr	Girgis
 + 3H ₂ ⇌ 	380 C 300-400 C	153 atm 185-190	Ni-W Ni-Mo	Batch AC Flow	0.30 0.387	0.023 0.365	cm ³ /gcat-s L/gcat-hr	Lapinas Girgis



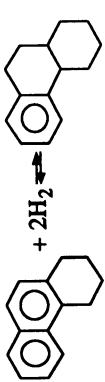
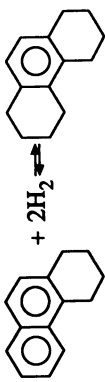
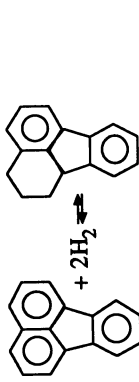
Table III. The Pathways and Kinetics of Hydrogenation of Polynuclear Aromatic Hydrocarbons (continued)

 $+ 3H_2 \rightleftharpoons$	380 C	153 atm	Ni-W	Batch AC	cm ³ /gcat-s	Lapinas
 $+ 3H_2 \rightleftharpoons$	380 C	153 atm	Ni-W	Batch AC	cm ³ /gcat-s	Lapinas
 $+ 3H_2 \rightleftharpoons$	325 C	75 atm	Co-Mo	Batch AC	0.002 4***	Sapre Moreau
 $+ 3H_2 \rightleftharpoons$	350 C	71 atm	Ni-W	Batch AC	0.13	Lapinas
 $+ 3H_2 \rightleftharpoons$	340 C	71 atm	Sulfided	Batch AC	1.5***	Moreau
 $+ 3H_2 \rightleftharpoons$	340 C	71 atm	Sulfided	Batch AC	4.0***	Moreau

Continued on next page

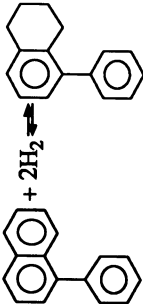
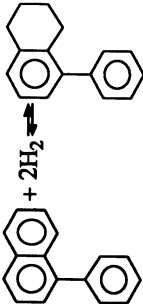
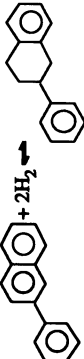
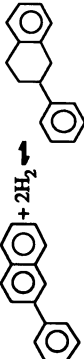
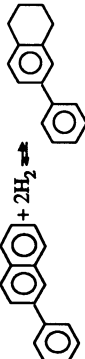
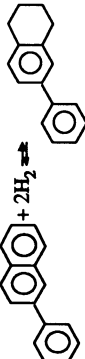

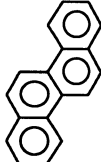
Table III. The Pathways and Kinetics of Hydrogenation of Polynuclear Aromatic Hydrocarbons (continued)

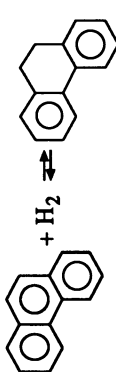
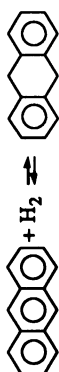
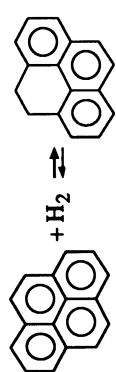
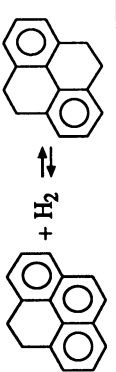
Reaction Pathway	Temp (°C)	Pressure (atm)	Catalyst	Reactor	kf	kr	Units of k	Ref.
 $+ 3H_2 \rightleftharpoons$	340 C	71 atm	Sulfided	Batch AC	2.0***	relative	Moreau	
 $+ 3H_2 \rightleftharpoons$	300-400 C	185-190	NiMo	Flow	0.387	L/gcat-hr	Girgis	
 $+ 2H_2 \rightleftharpoons$	325 C	75 atm	Co-Mo	Batch AC	0.2081	L/gcat-hr	Sapre	
	340 C	71 atm	MoS ₂	Batch AC	14	Relative	Moreau	
	340 C	71 atm	WS ₂	Batch AC	23	Relative	Moreau	
	340 C	71 atm	CoMo	Batch AC	21	Relative	Moreau	
	340 C	71 atm	NiW	Batch AC	18	Relative	Moreau	
	340 C	71 atm	NiMo	Batch AC	10	Relative	Moreau	
 $+ xH_2 \rightleftharpoons$ Products	220-435 C	102 atm	Ni-W	Batch AC	NA	—	Wiser	
 $+ 2H_2 \rightleftharpoons$	300-400 C	185-190	Ni-Mo	Flow	0.157	L/gcat-hr	Girgis	
	200-380 C	102 atm	Ni-W	Batch AC	NA	—	Shabai	
	402-543 C	136-204	Chromia	Flow	NA	—	Haynes	
	430 C	100 atm	Ni-Mo	Batch	NA	—	Lemberton	

	325 C	75 atm	Co-Mo	Batch AC	0.1631	0.0222	L/gcat-hr	Sapre
	325 C	75 atm	Co-Mo	Batch AC	0.094	0.0224	L/gcat-hr	Sapre
	300-400 C	185-190	Ni-Mo	Flow	0.043	—	L/gcat-hr	Girgis
	300-400 C	185-190	Ni-Mo	Flow	0.202	—	L/gcat-hr	Girgis
	380 C 300-400 C	153 185-190	Ni-W Ni-Mo	Batch AC Flow	1.4 1.73	0.072 1.81	cm ³ /gcat-s L/gcat-hr	Lapinas Girgis

Continued on next page

Table III. The Pathways and Kinetics of Hydrogenation of Polynuclear Aromatic Hydrocarbons (continued)

Reaction Pathway	Temp (°C)	Pressure (atm)	Catalyst	Reactor	kf	kr	Units of k	Ref.
 $+ 2H_2 \rightleftharpoons$ 	300-400 C	185-190	Ni-Mo	Flow	0.255	—	L/gcat-hr	Girgis
 $+ 2H_2 \rightleftharpoons$ 	300-400 C	185-190	Ni-Mo	Flow	0.141	—	L/gcat-hr	Girgis
 $+ 2H_2 \rightleftharpoons$ 	300-400 C	185-190	Ni-Mo	Flow	0.256	—	L/gcat-hr	Girgis
 $+ xH_2 \rightleftharpoons$ Products	341 C 375 C 348-400 C	69-205 72.5 35-137	Ni-W Co-Mo Ni-Mo	Batch AC Batch AC	NA NA NA	— — —	— — —	Shabtai Johnston Stephans
 $+ xH_2 \rightleftharpoons$ Products	400 C	98 atm	ZnCl ₂ / CuCo	Batch AC	NA	—	—	Nakatsuji

 $+ \text{H}_2 \rightleftharpoons$	300-400 C	185-190	Ni-Mo	Flow	0.288	1.19	L/gcat-hr	Girgis
 $+ \text{H}_2 \rightleftharpoons$	340 C 340 C 340 C	71 atm 71 atm 71 atm	W ₂ -S ₂ Ni-W Ni-Mo	Batch AC Batch AC Batch AC	62*** 40*** 36*** EA=	relative relative relative		Moreau Moreau Moreau Qadar
 $+ \text{H}_2 \rightleftharpoons$	300-400 C	185-190	Ni-Mo	Flow	1.33	5.04	L/gcat-hr	Girgis
 $+ \text{H}_2 \rightleftharpoons$	300-400 C	185-190	Ni-Mo	Flow	2.87	25.3	L/gcat-hr	Girgis

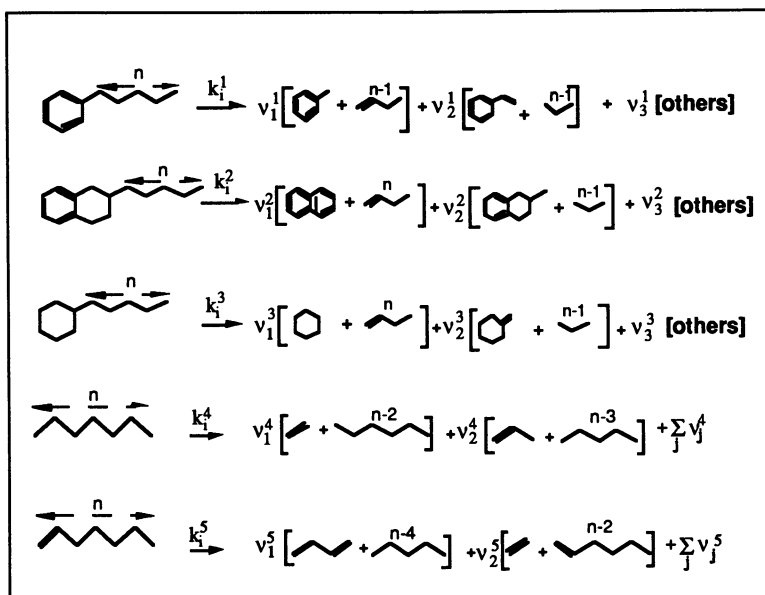
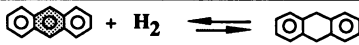
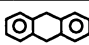
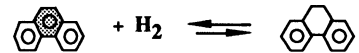
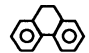
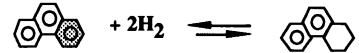
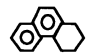
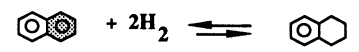
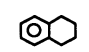
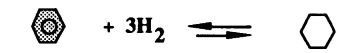



Figure 7. Representative molecular reaction pathways for heavy hydrocarbon pyrolysis systems. Molecules are classified by one of five hydrocarbon types alkylaromatics, alkyltetralins, alkylnaphthenes, paraffins, or olefins. The kinetics are summarized by the rate constant k_j^i , and v_j^i , the stoichiometric coefficient, where i refers to the alkyl carbon chain length and j to the molecule type, and are given in Table II (35)

Table IV. Summary of the effect of the number and configurational arrangement of aromatic rings on the hydrogenation kinetics of aromatic model compounds (54)

REACTION	Reference	k (s ⁻¹) Forward	k (s ⁻¹) Reverse
 + H ₂ ⇌ 	1	0.548	1.82e-03
 + H ₂ ⇌ 	2	4.98e-02	1.66e-03
 + 2H ₂ ⇌ 	2	3.06e-02	2.31e-03
 + 2H ₂ ⇌ 	3	6.06e-04	2.21e-05
 + 3H ₂ ⇌ 	3	9.47e-06	3.75e-07

aromatic model compounds (35). This data base serves both hydrotreating and hydrocracking reaction models. Neurock has shown that much of the kinetics information of Tables III and IV can be summarized concisely by the strategy of linear-free energy relationships (36). This has the effect of reducing the number of model parameters enormously such that a large set of reaction rate constants can be summarized by the smaller number of parameters of a linear-free energy relationship.

Molecular catalytic cracking chemistry is summarized in Figures 8 and 9. The key reactants and intermediates in FCC processes include paraffins, olefins, isoparaffins, isoolefins, alkylaromatics, alkyltetralins, and alkyl naphthenes. Figure 8 summarizes the relevant single component reaction pathways for each of these species. For example, paraffins and isoparaffins can undergo cracking to form smaller olefin and paraffin fragments, skeletal isomerization to create branched isoparaffins, hydrodecyclization to generate naphthenes, with subsequent dehydrogenation to form aromatics, and possible condensation to yield coke and coke precursors. Olefins and isoolefin components follow a similar spectrum of reaction pathways with the addition of double bond isomerization to convert the intermediate α -olefin to other olefin forms. The reaction chemistry of the alkyl naphthenes and alkylaromatics can be divided into pathways involving only transformations of the aliphatic substituents and those involving only the ring structure. The alkyl-substituent paths are similar to those set forth for paraffins and isoparaffins. The ring-containing pathways, on the other hand, included dealkylation of aliphatic chains, dehydrogenation to aromatic structures, and ring-opening pathways (37,38).

Figure 9 summarizes some of the intermolecular reaction pathways deemed important in catalytic cracking. For example, hydrogen transfer between paraffin and olefin and between olefin and naphthenes can occur to form energetically more stable reaction products (37,38). Transalkylation, i.e., scrambling of short chain alkyl groups on aromatics, is also prevalent. Condensation reactions have been implicated in coke formation pathways.

The guidelines of linear-free energy relationships have also been used to capture not only the hydrocarbon structure/function but also catalyst structure/function relationships. Thus Liguras et al. (39) have fashioned a model where the rate constant is a function of the reactant, the reaction family, and the catalyst silicon to aluminum ratio. This fledgling approach considerably reduces the number of kinetic parameters and appears to be quite useful in the modelling of complex kinetics of hydrocarbon feedstocks.

Mechanistic Models.

The most detailed modelling approach summarized in Figure 1 is found at the mechanistic level. These models are explicit accounts of the chemistry of elementary steps. Thus the hierarchy of the levels, i.e., reaction models in Figure 1, now becomes quite clear. Mechanistic models, which provide the temporal and many times spatial variation of the composition of each component and reaction intermediate, are based at the lowest modelling level. Their output, however, is typically phrased in terms of ensembles of stable molecular constituents which is more characteristic of the intermediate level molecular models. The molecular models, in turn, require subsequent organization in order to connect to the global reaction models and relevant product fractions at the top or global level.

As regards the kinetics of the mechanistic models, they are governed quantitatively by the formation and destruction of various active centers. These kinetics can be

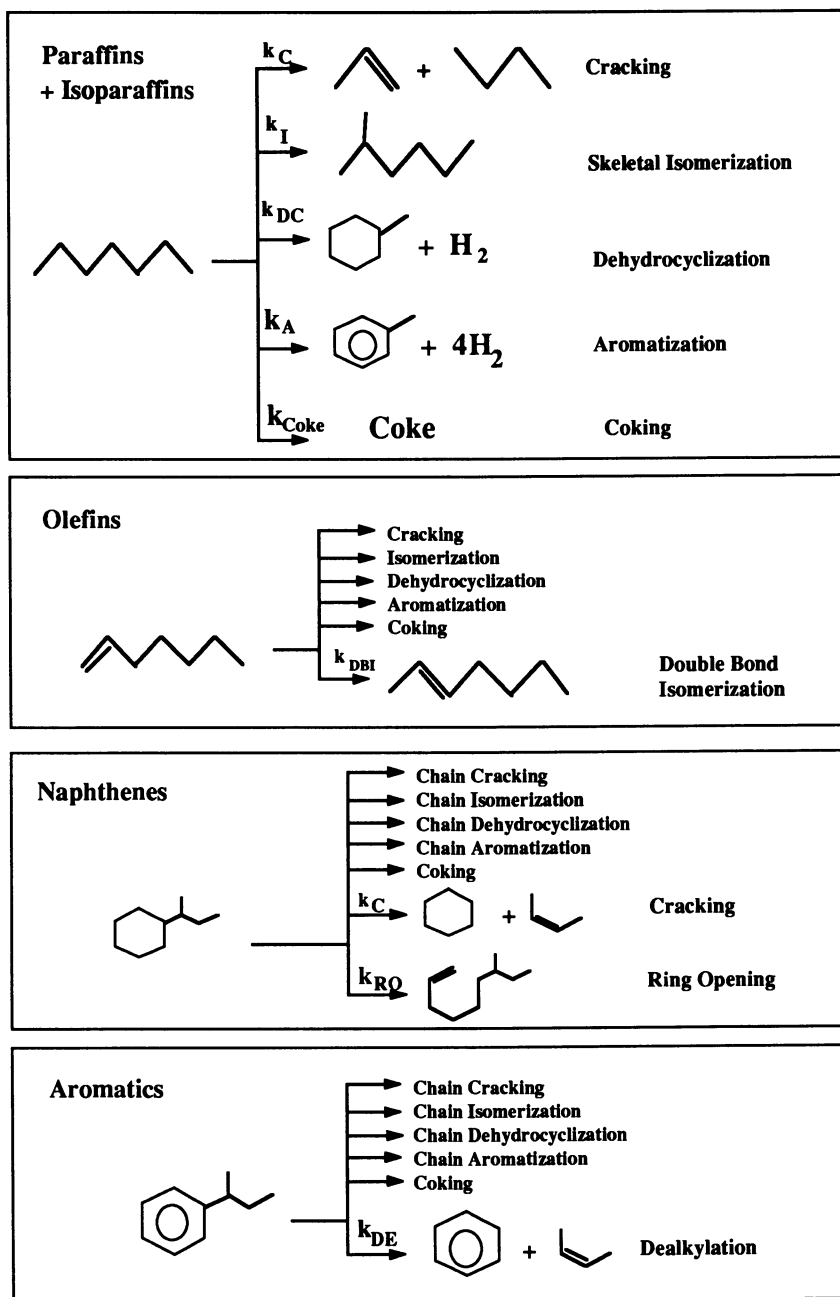


Figure 8. Prototypical molecular reaction pathways for the catalytic cracking of gas oil feedstocks.

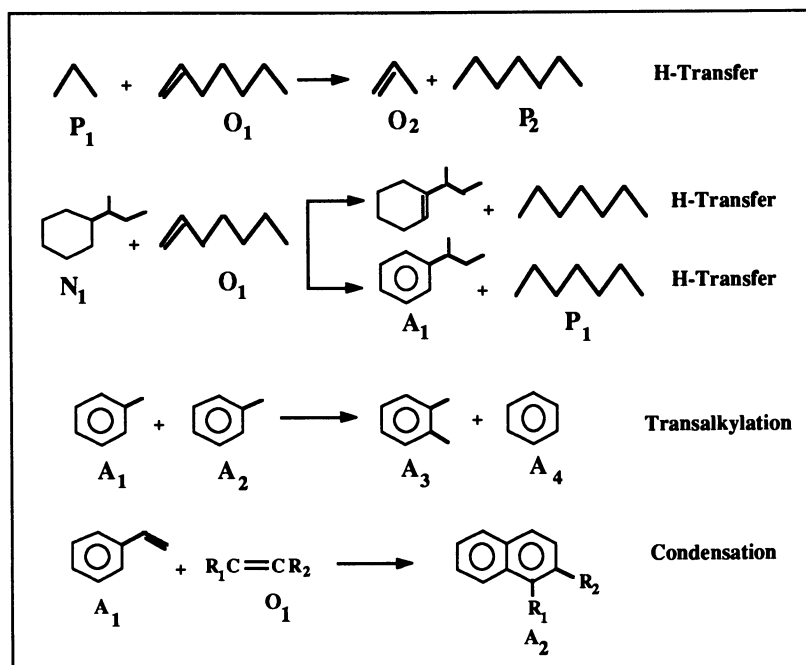


Figure 9. Important intermolecular pathways in the analysis of catalytic cracking of gas oil feedstocks.

estimated from experiments and, in principle, be derived from theory. This is a unique characteristic of the mechanistic level of modelling. For example, semiempirical and ab initio quantum calculations have been reasonably successful in computing chemical bond strengths (35,40,41) which in some instances provides a quantitative estimate of the actual activation energy of the associated elementary step.

Returning to the asphaltene/resid pyrolysis example, the mechanistic models of these processes are based on free radical chemistry. That is, the elementary steps which describe the reaction chemistry are written in terms of free radical species. Thus the development of a mechanistic model requires the time-dependent solution of an extensive set of material balance equations for every component as well as for each of the active centers.

Table V shows the efficient organization of this reaction chemistry into five reaction families. Bond fission, for example, is the elementary step that creates two free radicals from a parent molecule. In chain processes this will often be the "initiation" step. Thermochemical estimates often show that the logarithm of the Arrhenius A factor ($\log_{10}A$) is of the order 14-17, whereas the activation energy is essentially equivalent to the bond dissociation energy (19,42). This equality is the result of the essentially unactivated reverse reaction step, radical recombination.

Hydrogen abstraction provides the chain propagation step that transfers hydrogen from a molecule to attacking radical. The kinetics of these processes often follow a Polanyi relation where $E^* = E_0^* + \alpha(\Delta H_{rxn}^0)$. Estimates of the pre-exponential factor sug-

Table V. Examples of Kinetics for Important Mechanistic Pyrolysis Steps

Event	Example	Activation Energies	$\log_{10} (A/s^{-1} \text{ or } \ell \text{ mol}^{-1} s^{-1})$
Bond Fission	$CH_2 - CH_3 \xrightarrow{k_I} 2CH_3 \cdot$	$E^* = \text{BDE}$	14–17
Hydrogen Abstraction	$CH_3 \cdot + CH_3CH_3 \xrightarrow{k_H} CH_4 + CH_3CH_2 \cdot$	$E^* = E_o^* + \alpha (\Delta H_{\text{rxn}}^\circ)$ $E^* (\text{kcal/mol}) = 12.54 + 0.54 (\Delta H_{\text{rxn}}^\circ)$	8.5–9.0
β -Scission	$CH_3CH_2CH_2\dot{C}HCH_3 \xrightarrow{k_B} CH_3CH_2 \cdot + CH_2 = CHCH_3$	$E^* (\text{kcal/mol}) = 15.2 + 0.60 (\Delta H_{\text{rxn}}^\circ)$	13–15
Radical Addition	$CH_3CH_2 \cdot + CH_2 = CHCH_3 \xrightarrow{k_{RA}} CH_3CH_2CH_2\dot{C}HCH_3$	$E^* (\text{kJ/M}) = 9.2 - 8.3 \text{ EA (eV)}$ $\log k_{300} (\text{M}^{-1} \text{S}^{-1}) = 5.7 + 1.4 \text{ EA (eV)}$	7.1–10
Radical Recombination	$CH_3 \cdot + CH_3CH_2 \cdot \xrightarrow{k_T} CH_3CH_2CH_3$	$E^* (\text{kcal/mol}) = 0 - 2$	8.5–10.1

gest that the value of $\log_{10}A$ is of order 8.5-9.0 (19,42). The second chain propagation step is β -scission where the bond β to the radical center is cleaved to afford an olefin and smaller free radical. Estimates of $\log_{10}A = 13-15$ are reasonable for this process and the activation energy can be phrased in terms of a Polanyi relation as well (19,42). Radical addition is the reverse of the β -scission reaction where the active center adds to an olefin. The kinetics for these systems have been well documented and are especially relevant at lower reaction temperatures. Structure/reactivity relationships for this reaction have focused on estimating the energy barrier of promoting the electron in the singly occupied molecular orbital (SOMO) of the radical to the lowest unoccupied molecular orbital (LUMO) of the olefin (43). One such relationship views the various radicals as having similar SOMO energy values, and therefore correlates the relative activation barrier with the electron affinity, a measure of the E_{Lumo} , for olefin reactant (44). The corresponding Arrhenius parameters have been reported to be of the order $\log_{10}A = 7.1-10$.

Whereas the chain propagation reactions are in radical balance, and the bond fission reaction creates two free radicals from the parent molecule, radical recombination and disproportionation consume two free radicals in the formation of molecular species. The kinetics of this step are essentially collision controlled, as $\log_{10}A = 8.5-10$ is quite reasonable. For reasonably sized hydrocarbon free radicals, E^* is essentially zero.

In addition to the summary and correlations described here, important experimental information and literature exists for pyrolysis of hydrocarbon systems. The review of Poutsma (18) is quite extensive and should be consulted for the chemistry related to heavy hydrocarbon systems.

Several models which are based on mechanistic chemistry similar to that shown in Table V have appeared in the literature to describe hydrocarbon pyrolysis systems. The publications of Froment (45,46) are an example of this type of modelling.

The relative lack of mechanistic modelling effort for hydrotreating and catalytic cracking chemistry compared to that for pyrolysis modelling is primarily due to the less mature understanding of the underlying physical chemistry. Hydrotreating chemistry is typically much more difficult to formalize because of the complexities of adsorption, surface reaction, and desorption, let alone the physical intrusions of internal and external diffusion phenomena. The same is true in catalytic cracking chemistry, where the subtleties of carbenium ion formation, β -scission, isomerization and hydrogen transfer make modelling efforts somewhat less tractable than those for free radical systems.

The aforementioned difficulties in posing mechanistic-based catalytic models is by no means indicative of an insufficient understanding of catalytic hydrotreating and catalytic cracking chemistry. In fact, there are several important reviews on the mechanistic chemistry of hydrotreating and catalytic cracking. Wojciechowski's mechanistic formulation for catalytic cracking cycle for normal alkanes, depicted in Figure 10, explains many features of the observed kinetics (38). It may well be that models are limited by the additional heterogeneity of the solid acid catalyst that couples with the heterogeneities of complex feedstocks to raise the level of complexity beyond that currently contemplated.

We have alluded several times to the fact that mechanistic models provide the most direct expression of the underlying physical and organic chemistry. The controlling thermal and catalytic chemistry, for example, is governed by the energetics of primary, secondary and tertiary free radicals or carbenium ions which provides quantitative measures of reactivity. These advantages, however, are somewhat offset by the computational

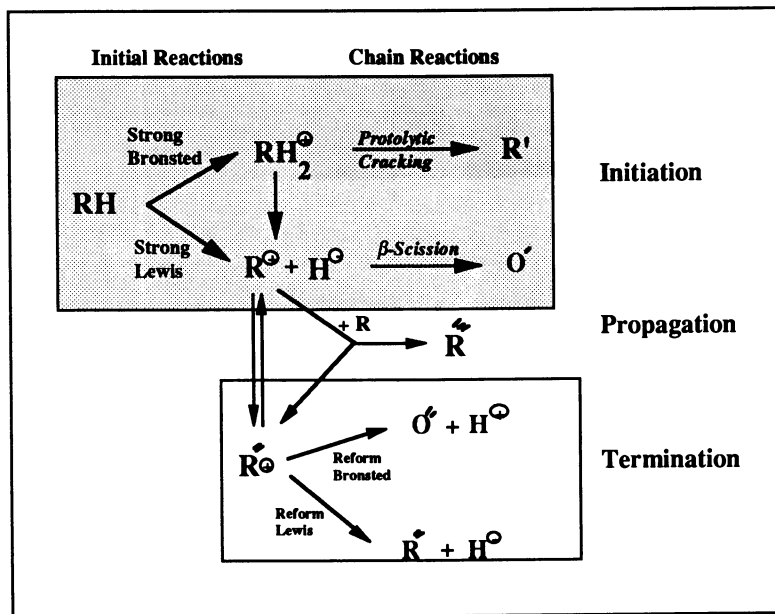


Figure 10. Wojciechowski's mechanistic formalism for the catalytic cracking cycle for normal paraffins [38].

difficulties and intensive CPU requirements involved in mechanistic simulations. The complexity associated with describing the reactivity of thousands of different feedstock components, their reaction intermediates, and their interactions with an extensive data base of catalyst formulations would require an extraordinary number of potential reaction parameters. While a cohesive organizational scheme has yet to be developed, we can point to some emerging progress in this area (49–52).

Discussion

It is worth reconsidering the reaction modelling hierarchy of Figure 1 in the light of the foregoing discussion. Clearly, the relevant global models are easily formulated and nicely adaptable to process engineering models. However, they do so at the expense of chemical fundamentals and therefore can only be used as interpretative correlations. At the other extreme, mechanistic models provide detailed chemical analyses of reaction systems. However, they bear the burden of extensive computational requirements and face the reality of the paucity of experimental data. Molecular models provide a convenient compromise between the two. The CPU requirements are reasonable, while at the same time chemical fundamentals are retained because of the implicit connection to reaction mechanisms.

The hierarchy of Figure 1 is also in many ways a road map. The hierarchy helps to illustrate the manner in which the different models communicate. Traditionally, the mechanistic model could only communicate with global models through molecular models. That is, thermal and catalytic cycles based on mechanistic chemistry, such as Rice-

Herzfeld and Langmuir-Hinshelwood-Hougen-Watson cycles, could be formulated and solved in terms of analytical rate expressions (19,53). These rate expressions, which were derived from mechanistic cycles, are phrased, however, in terms of the formation and destruction of molecular species without the need for computing the composition of reactive intermediates. Thus, these expressions are the relevant kinetics required for molecular models and are rooted to the mechanistic cycles only implicitly by the mechanistic rate constants. The molecular model, in turn, transforms a vector of reactant molecules into a vector of product molecules, either of which is susceptible to thermodynamic analysis. This thermodynamic analysis helps to organize these components into relevant boiling point or solubility product classes. Thus the sequence of mechanistic to molecular to global models is intact.

In anticipation of future requirements and resources, it is reasonable to expect that mechanistic models may very well be able to communicate directly with global models or take on the role of process models. With the advent of increasingly sophisticated serial computers and an advanced understanding of the paradigm of parallel computing, it is reasonable to extrapolate today's advances to the year 2000 where mechanistic models may well provide all three levels (mechanistic, molecular, and global) of product information.

Simulation of the mechanism actually obviates many of the difficulties involved in establishing the links in the mechanism-molecular-global model network. For example, the development of the mechanistic-based rate expression required in the molecular/mechanistic modelling link is nontrivial for complex hydrocarbon mixtures. All possible permutations of molecular interactions must be considered and worked into analytical rate expressions (19).

In mechanistic models these interactions can be directly simulated. Thus the issue of kinetic coupling (molecular interactions) may well be somewhat artificial and only introduced by analysis at the less detailed molecular or global levels. Likewise, the intrusions of diffusion may also be somewhat artificial and a result of modelling at the molecular or global level. That is, mechanistic simulations can now account for the movement as well as reaction of molecules and active centers (54). This becomes especially convenient when the device of a percolation lattice is used. Molecules can then be assembled, moved and reacted on the lattice which, in addition to allowing for simulation of the mechanism of diffusion in reaction, can also provide information about global product fractions, such as polymer gel fraction and cross-link density. The literature of polymer science is rich in these types of applications.

A reasonable generalization is that simulation at the molecular or global level is favored for processes in which kinetic coupling and transport limitations are either nonexistent or can easily be described by overall average compositions. However, for systems in which composition gradients exist and may significantly affect the kinetics, the selection of an optimal modelling method becomes a quantitative trade-off between the complexity of implementation and the CPU expenditures allotted. Two examples of systems where these trade-offs need to be considered carefully include the analysis of multiple steady state phenomena induced by surface catalysis and the prediction of gelation behavior in linear polymer systems. In the first example, Vlachos et al. (53,54) have simulated mechanistic surface adsorption, reaction and diffusion to compute nonlocal composition gradients, local hot spots on the catalyst surface and the conditions leading to multiple steady state behavior (55,56). The second example is illustrated in the mechanistic simu-

lation of the degradation process of poly(arylether)sulfones provided by Libanati et al. (54). In this work, the on-set of gelation was computationally determined by analyzing each polymeric cluster for one which spans the entire simulation grid. Compositional gradients induced by regional active centers (free radicals) were critically important. In both examples, the extensive CPU requirements were tolerated at the expense of the detailed programming required to formulate a molecule-based approach.

In summary, the prospects of mechanistic-based modelling appear to be several years away. However, it is clear that global reaction models are already losing favor because of their inability to answer current and future questions. We may look back and see the Clean Air Act as the beginning of the need for molecule-based models, where the input and output has to be commensurate with the nature of the questions being asked.

Literature Cited

1. Neurock, M., A. Nigam, D.T. Trauth, and M.T. Klein, *Asphaltene Pyrolysis Pathways and Kinetics: Feedstock Dependence*, in Tar Sand and Oil Upgrading Technology, S. Shih and M.C. Oballa, eds., AIChE Symposium Series, 72-79, 1991.
2. Trauth, D.T., M. Yasar, M. Neurock, A. Nigam, and M.T. Klein, *Asphaltene and Resid Pyrolysis: Effect of Asphaltene Environment.*, Energy and Fuels, (accepted), 1992.
3. Beaton, W.I. and R.J. Betolacini, *Resid Hydroprocessing at Amoco.*, Catal. Rev.-Sci. Eng., **33**, ((3&4)), 281-317, 1991.
4. Weekman Jr., V.W. and D.M. Nace, *Kinetics and Catalytic Cracking Selectivity in Fixed, Moving and Fluid-Bed Reactors.*, AIChE Journ., **16**, 397, 1970.
5. Nace, D.M., S.E. Voltz, and V.W.W. Jr., *Application of a Kinetic Model for Catalytic Cracking Effects of Charge Stocks.*, Ind. Eng. Proc. Des. Devt., **10**, 530, 1971.
6. Krambeck, F.J., *An Industrial Viewpoint on Lumping*, in Kinetic and Thermodynamic Lumping of Multicomponent Mixtures, G. Astarita and S.I. Sandler, eds., Elsevier Science Publishers B.V., 111-130, 1991.
7. Weekman Jr., V.W., *Lumps, Models, and Kinetics in Practice.*, Chem. Eng. Prog. Monog. Ser., **79**, (11), 3-29, 1979.
8. Jacob, S.M., S. E. Gross, S.E. Voltz, and J. V.W. Weekman, *A Lumping and Reaction Scheme for Catalytic Cracking.*, AIChE Journ., **22**, 701-713, 1976.
9. Quann, R.J. and S.B. Jaffe, *Structure Oriented Lumping: Describing the Chemistry of Complex Hydrocarbon Mixtures.*, Ind. and Eng. Chem., (accepted), 1992.
10. Neurock, M., C. Libanati, A. Nigam, and M.T. Klein, *Monte Carlo Simulation of Complex Reaction Systems: Molecular Structure and Reactivity in Modelling of Heavy Oils.*, Chem. Eng. Sci., **45**, (8), 2083-2088, 1990.
11. Nigam, A., M. Neurock, and M.T. Klein, *Reconciliation of Molecular Detail and Lumping: An Asphaltene Thermolysis Example*, in Kinetic and Thermodynamic Lumping of Multicomponent Mixtures, G. Astarita and S.I. Sandler, eds., Elsevier Science Publishers B.V., 1991.
12. Savage, P.E. and M.T. Klein, *Asphaltene Reaction Pathways. 2. Pyrolysis of n-Pentadecylbenzene.*, Ind. and Eng. Chem. Res., **26**, (3), 488-494, 1987.
13. Savage, P.E. and M.T. Klein, *Discrimination Between Molecular and Free-Radical Models of 1Phenyldodecane Pyrolysis.*, Ind. and Eng. Chem. Res., **26**, 374, 1987.

14. Savage, P.E. and M.T. Klein, *Asphaltene Reaction Pathways. 4. Pyrolysis of Tridecylcyclohexane and 2-Ethyltetralin.*, Ind. and Eng. Chem. Res., **27**, 1348-1356, 1988.
15. Savage, P.E. and M.T. Klein, *Kinetics of Coupled Reactions: Lumping Pentadecylbenzene Pyrolysis into Three Parallel Chains.*, Chem. Eng. Sci., **44**, (2), 393-404, 1989.
16. Fabuss, B.M., J.O. Smith, and C.N. Satterfield, *Thermal Cracking of Pure Saturated Hydrocarbons.*, Adv. Pet. Chem. Refin., **9**, 157, 1964.
17. Rebick, C., *Pyrolysis of Alpha-Olefins-A Mechanistic Study*, in Thermal Hydrocarbon Chemistry, A. G. Oblad, H.G. Davis, and R.T. Eddinger, eds., Amer. Chem. Soc., 1-19, 1979.
18. Poutsma, M., *A Review of Thermolysis of Model Compounds Relevant to Processing of Coal*, ORNL/TM-10637, Oak Ridge National Laboratory: Chemistry Division, 1987
19. LaMarca, C., *Kinetic Coupling in Multicomponent Pyrolysis Systems*, Ph.D. Dissertation, Univ. of Delaware, 1992.
20. Sapre, A.V. and B.C. Gates, *Hydrogenation of Aromatic Hydrocarbons Catalyzed by Sulfided CoO-MoO₃/γ-Al₂O₃. Reactivities and Reaction Networks.*, Ind. Eng. Chem. Proc. Des. Dev., **20**, (1), 68-73, 1981.
21. Moreau, C. and P. Geneste, *Factors Affecting the Reactivity of Organic Model Compounds in Hydrotreating Reactions.*, Catalysis Today, **4**, (1), 256-310, 1988.
22. Sapre, A.V. and B.C. Gates, *Hydrogenation of Biphenyl Catalyzed by Sulfided CoO-MoO₃/γ-Al₂O₃. The Reaction Kinetics.*, Ind. and Eng. Chem. Process Des. Dev., **21**, (1), 86-94, 1982.
23. Girgis, M.J., *Reaction Networks, Kinetics, and Inhibition in the Hydroprocessing of Simulated Heavy Coal Liquids*, Ph.D. Dissertation, Univ. of Delaware, 1988.
24. Girgis, M.J. and B.C. Gates, *Reactivities, Reaction Network, and Kinetics in High-Pressure Catalytic Hydroprocessing*, Ind. and Eng. Chem. Res., **30**, 2021, 1991.
25. Lapinas, A.T., M.T. Klein, A. Macris, J.E. Lyons, and B.C. Gates, *Catalytic Hydrogenation and Hydrocracking of Fluoranthene Reaction Pathways and Kinetics.*, Ind. and Eng. Chem. Res., **26**, 1026, 1987.
26. Lapinas, A.T., M.T. Klein, A. Macris, J.E. Lyons, and B.C. Gates, *Catalytic Hydrogenation and Hydrocracking of Fluorene: Reaction Pathways and Kinetics.*, Ind. and Eng. Chem. Res., **29**, 42-50, 1991.
27. Wisner, W.H., S. Singh, S.A. Qader, and G.R. Hill, *Catalytic Hydrogenation of Multiring Aromatic Coal Tar Substituents.*, Ind. and Eng. Chem. Prod. Res. Dev., **9**, (3), 350-357, 1970.
28. Shabtai, J., L. Veluswamy, and A.G. Oblad, *Steric Effects in Phenanthrene and Pyrene Hydrogenation Catalyzed by Sulfided Ni-W/Al₂O₃.*, ACS Div. Fuel Chem. Prep., **23**, (4), 107-113, 1978.
29. Huang, C.S., K.C. Wang, and J. H.W. Haynes, *Hydrogenation of Phenanthrene Over a Commercial Cobalt Molybdenum Sulfide Catalyst Under Severe Reaction Conditions*, in Liquid Fuels from Coal, eds., Academic Press, 1977.
30. Lemberton, J.L. and M. Guisnet, *Phenanthrene Hydroconversion as a Potential Test Reaction for the Hydrogenation and Cracking Properties of Coal Hydroliquefaction Catalysts.*, Appl. Catal., **13**, 181-192, 1984.

31. Johnston, K.P., *Hydrogenation-Dehydrogenation of Pyrenes Catalysed by Sulphided Cobalt-Molybdate at Coal Liquefaction Conditions.*, Fuel, **63**, 463-468, 1984.
32. Stephens, H.P. and R.N. Chapman, *The Kinetics of Catalytic Hydrogenation of Pyrene: Implications for Direct Coal Liquefaction Processing.*, ACS Div. Fuel Chem. Prepr., **30**, (2), 345-353, 1985.
33. Nakatsuji, Y., T. Kubo, M. Nomura, and S. Kikkawa, *The Hydrocracking of Polynuclear Aromatic Hydrocarbons Over Molten Salt Catalysts.*, Bull. Chem. Soc. Jpn., **51**, (2), 618-624, 1978.
34. Qadar, S.A. and G.R. Hill, *Development of Catalysts for the Hydrocracking of Polynuclear Aromatic Hydrocarbons.*, ACS Prepr. Div. of Fuel Chem., **16**, (2), 93, 1972.
35. Neurock, M., *A Computational Chemical Reaction Engineering Analysis of the Molecular Pathways and Kinetics of Complex Heavy Hydrocarbon Reaction Systems*, Ph.D. Dissertation, Univ. of Delaware, 1992.
36. Neurock, M. and M.T. Klein, *Linear Free Energy Relationships in Kinetic Analyses: Applications of Quantum Chemistry.*, Prep. ACS Div. of Petrol. Chem., 1992.
37. Gates, B.C., J.R. Katzer, and G.C.A. Schuit, *Chemistry of Catalytic Processes*. McGraw-Hill, 1979.
38. Wojciechowski, B.W. and A. Corma, *Catalytic Cracking*. Marcel Dekker, 1986.
39. Liguras, D.K., et al., *Monte Carlo Simulation of Complex Reactive Mixtures: An FCC Case Study*, in *AIChE Symposium Series: Advanced FCC Technology*, G. Young and R.M. Benslay, eds., 1992.
40. Dewar, M.J.S., E.G. Zoebisch, E.F. Healy, and J.P. Stewart, *AM1: A General Purpose Quantum Mechanical Molecular Model.*, J. Am. Chem. Soc., **107**, 3902-3909, 1985.
41. Hehre, W.J., L. Radom, and P.v.R. Schleyer, *Ab Initio Molecular Orbital Theory*. John Wiley and Sons, Inc., 1986.
42. Boudart, M., *Kinetics of Chemical Processes*. 2nd Ed. ed. Prentice Hall Inc., 1990.
43. Paltenghi, R., E.A. Ogryzlo, and K.D. Bayes, *Rates of Reaction of Alkyl Radicals with Ozone.*, J. Phys. Chem., **88**, 2595-2599, 1984.
44. Fischer, H., *Substituent Effects on Absolute Rate Constants and Arrhenius Parameters for the Addition of Tert-Butyl Radicals to Alkenes*, in *Substituent Effects in Radical Chemistry*, H.G. Viehe and e. al., eds., D. Reidel Publishing Co., 123-142, 1986.
45. Sundaram, K.M. and G.F. Froment, *Modeling of Thermal Cracking kinetics. 3. Radical Mechanisms for the Pyrolysis of Simple Paraffins, Olefins, and Their Mixtures.*, Ind. and Eng. Chem. Fund., **17**, 174—182, 1978.
46. Froment, G.F., *Fundamental Kinetic Modeling of Complex Processes*, in *Chemical Reactions in Complex Mixtures: The Mobil Workshop*. A.V. Sapre and F.J. Krambeck, eds., Van Nostrand Reinhold, 77-100, 1990.
47. Chianelli, R.R., *Fundamental Studies of Transition Metal Sulfide Hydrodesulfurization Catalysts.*, Catal. Rev. -Sci. Eng., **26**, (3&4), 361-393, 1984.
48. Topsoe, H., *Active-Sites and Support Effects in Hydrodesulfurization Catalysts.*, Appl. Catal., **25**, (1-2), 273-293, 1986.

49. Mochida, I. and Y. Yoneda, *Linear Free Energy Relationships in Heterogeneous Catalysis I. Dealkylation of Alkylbenzenes on Cracking Catalysts.*, J. of Catal., **7**, 386-396, 1967.
50. Mochida, I. and Y. Yoneda, *Linear Free Energy Relationships in Heterogeneous Catalysis II. Dealkylation and Isomerization Reactions on Various Solid Acid Catalysts.*, J. of Catal., **7**, 393-396, 1967.
51. Mochida, I. and Y. Yoneda, *Linear Free Energy Relationships in Heterogeneous Catalysis III. Temperature Effects in Dealkylation of Alkylbenzenes on the Cracking Catalysts.*, J. of Catal., **8**, 223-230, 1967.
52. Yoneda, Y., *Linear Free Energy Relationships in Heterogeneous Catalysis IV. Regional Analysis for Solid Acid Catalysis.*, J. of Catal., **9**, 51-56, 1967.
53. Boudart, M., *Kinetics-Assisted Design of Catalytic Cycles*, in Catalyst Design: Progress and Perspectives, L.L. Hegedus, eds., Wiley-Interscience Publication, 141-162, 1987.
54. Libanati, C., C. LaMarca, M.T. Klein, S.M. Andrews, and R.J. Cotter, *Thermal Degradation of Poly(arylether)Sulfones 2. Monte Carlo Simulation of Polymer Structure, Reaction and Diffusion.*, ACS Div. of Fuel Chem. Prep., **36**, (2), 655-663, 1991.
55. Vlachos, D.G., L.D. Schmidt, and R. Aris, *The Effect of Phase Transitions, Surface Diffusion, and Defects on Heterogeneous Reactions*, **Preprint 90-22**, Army High Performance Computing Research Center, University of Minnesota, 1990
56. Vlachos, D.G., L.D. Schmidt, and R. Aris, *The Effect of Phase Transitions, Surface Diffusion, and Defects on Fluctuations and Oscillations in Surface Catalyzed Reactions*, **Preprint 90-16**, Army High Performance Computing Research Center, University of Minnesota, 1990.

RECEIVED July 17, 1992

Chapter 21

Preparation, Characterization, and Catalysis of a Modified ZSM-5 Zeolite

Anne M. Gaffney¹, C. A. Jones¹, John A. Sofranko¹, Chihji Tsiao², and
Cecil Dybowski²

¹ARCO Chemical Company, 3801 West Chester Pike,
Newtown Square, PA 19031

²Center for Catalytic Science and Technology, University of Delaware,
Newark, DE 19716

Protonated and modified ZSM-5 zeolites were prepared, characterized and used in the conversion of methanol to gasoline and in hydrocarbon cracking. The modified ZSM-5 was prepared by heating Na-ZSM-5 with a protonated, sterically hindered amine salt such that only cationic sites external to the zeolite channels underwent exchange. Its constraint index number was significantly lower than that of the unmodified H-ZSM-5, reflecting external protonic sites. Also, its sodium content was higher due to retention of internal sodium. NMR spectrometry of ¹²⁹Xe gas sorbed in the modified and slightly coked zeolite demonstrated coking occurred primarily on the surface; whereas, the H-ZSM-5 zeolite was shown to deposit coke internally. In the conversion of methanol to gasoline, the modified zeolite was significantly less reactive. However, both zeolites had comparable activity in hydrocarbon cracking reactions carried out at high space velocities, i.e., under diffusion limited conditions.

Catalyst Preparation

A modified Na, H-ZSM-5 was prepared which had protonated, external sites and cationic, internal sites. Initially, the Na-ZSM-5 was prepared according to standard procedures (1). A solution of 200 g of NaSiO₂ in 150 ml of water was mixed with a solution of 75 g of NaCl, 6.7 g of Al₂(SO₄)₃•16 H₂O, 19.6 g of H₂SO₄ in 340 ml of water for 5 minutes. To this mixture was added 25 g of (n-propyl)₄N•Br in 100 ml of water. After 50 minutes of mixing, a portion was charged to an autoclave and heated at 149°C for 16 hours. The zeolite was filtered off and washed thoroughly with water; dried at 110°C; and calcined at 550°C for 16 hours. To 10 g of the Na-ZSM-5, was added 500 ml of a 1 molar aqueous solution of (n-butyl)₃N•HCl. This mixture was heated at 80°C and

stirred for 2 hours. The solids were filtered, washed and recontacted with a fresh 500 ml of solution. This procedure was repeated a total of 5 times. The modified Na,H-ZSM-5 was dried at 110°C and calcined at 550°C for 16 hours. Elemental analysis of the modified zeolite indicated that it contained 0.32 wt % Na as compared to 4.3 wt % Na for Na-ZSM-5 and < 0.02 wt % Na for H-ZSM-5.

Catalyst Coking

Catalyst coking studies were carried out on the protonated and modified ZSM-5 zeolites. Approximately 0.8 g of zeolite was heated to 823 K followed by exposure to 2-butene at 100 ml/min for a specific time to obtain samples with varying degrees of coking, as shown in Table I. To achieve a similar wt % coke, the modified Na, H-ZSM-5 zeolite required a 33% longer exposure time to 2-butene.

The coke content of the zeolite samples was measured on a Perkin-Elmer 240B CHN instrument which uses a combustion method to convert the sample elements to simple gases (CO₂, H₂O and N₂). The sample is first oxidized in a pure oxygen environment; the resulting gases are then controlled to exact conditions of pressure, temperature and volume. Finally, the product gases are separated. Then, under steady-state conditions, the gases are measured as a function of thermal conductivity. The results are accurate to $\pm 0.5\%$, absolute.

Table I. Treatment and Coke Contents of Protonated H-ZSM-5 and Modified Na, H-ZSM-5 Samples

Sample	Exposure to 2-Butene (min)	Coke Content Wt %
A. Na,H-ZSM-5		
Fresh	0	0
Slightly coked	1.6	1
Heavily coked	48	12
B. H-ZSM-5		
Fresh	0	0
Slightly coked	1.2	1
Heavily coked	36	12

¹²⁹Xe NMR Spectrometry

NMR spectrometry of Xenon-129 adsorbed in coked samples of the totally protonated H-ZSM-5 zeolite and the modified Na, H-ZSM-5 showed variations attributable to differences in coke distribution. ¹²⁹Xe NMR spectrometry is extremely useful for probing microporous materials. Ito et al.(2) demonstrated, for example, that NMR spectrometry of adsorbed xenon in coke-fouled H-Y zeolite could probe the deposits after coking and the nature of the internal surfaces after decoking. The NMR results in this study are consistent with a distribution of coke restricted by size selectivity of the acidifying medium.

All coked and uncoked samples were pretreated for ^{129}Xe NMR spectrometry by the following procedure: Approximately 0.4 g of material was placed in an NMR tube with a resealable coaxial Teflon stopcock. The sample was outgassed to a pressure of 1.0×10^{-5} Torr at 295 K. It was slowly heated to 673 K over 6 hours and maintained at that temperature for 12 hours under dynamic vacuum. After cooling to 295 K, the sample was exposed to xenon gas (Air Products and Chemicals, 99.99%) for 15 minutes to allow equilibrium to be reached. Subsequently, the tube was sealed and removed from the manifold. Xenon uptake isotherms were measured at 295 K during this successive adsorption process. They show Langmuir-type dependences of uptake on pressure in the range up to 700 Torr, as can be seen in Figure 1.

^{129}Xe NMR spectra were recorded with a Bruker WM-250 NMR spectrometer at 69.19 M Hz. Each spectrum is the accumulation of 500 transients with a relaxation delay of 0.5 seconds. The chemical shifts are reported with respect to bulk xenon gas extrapolated to $P=0$, using a secondary standard of xenon adsorbed in Na-Y zeolite at 590 Torr⁽³⁾. Positive chemical shifts are to higher frequency than the reference.

Figures 1A and 1B show the adsorption isotherms of xenon on the Na, H-ZSM-5 and H-ZSM-5 zeolites, respectively. From the comparison, one sees that xenon uptake decreases slightly (about 10%) with coke content in the Na, H-ZSM-5 with a low (1%) coke content, on zeolite H-ZSM-5, and decreases only slightly more with heavy coking (12%).

Figures 2A and 2B give the xenon-129 chemical shift as a function of the uptake, ρ , of xenon per gram of dry zeolite for the Na, H-ZSM-5 and the H-ZSM-5 zeolites, respectively. One can see that the chemical shift in these materials obey the truncated form of Fraissard's equation⁽⁴⁻⁵⁾:

$$\sigma(\rho) = \sigma_0 + \sigma_1\rho, \quad (1)$$

where $\sigma(\rho)$ is the observed ^{129}Xe chemical shift at a given uptake. σ_0 is the extrapolated chemical shift at infinitesimally low uptake, a term characteristic of the interactions between the xenon atom and the structure in which it is adsorbed. σ_1 is the first-order coefficient in a virial expansion of the chemical shift and is a measure of the effects of xenon-xenon interactions. From the graphs one obtains the Fraissard parameters for xenon under various conditions of treatment of the ZSM-5 zeolites; these are listed in Table II. Figure 2A shows that, for the Na, H-ZSM-5 zeolite, the plots are nearly parallel, whatever the coke level. The intercepts, σ_0 , do depend on the pretreatment conditions and increase with coke content. From Figure 2B, a much different picture emerges for xenon in H-ZSM-5. Again the plots obey Equation 1. However, coking of H-ZSM-5 alters the slope of the profile, while leaving the intercept at low coverage nearly the same. See Table II.

Discussion on ^{129}Xe NMR Results

Demarquay and Fraissard⁽⁶⁾ have shown that the intercept, σ_0 , can be interpreted in terms of a "mean free path" of xenon in the zeolite and have related this NMR-derived mean free path to structural parameters such as channel diameter by a Monte Carlo simulation procedure. They empirically determined the intercept to depend on mean free path as

$$\sigma_0 = A / (B + \lambda), \quad (2)$$

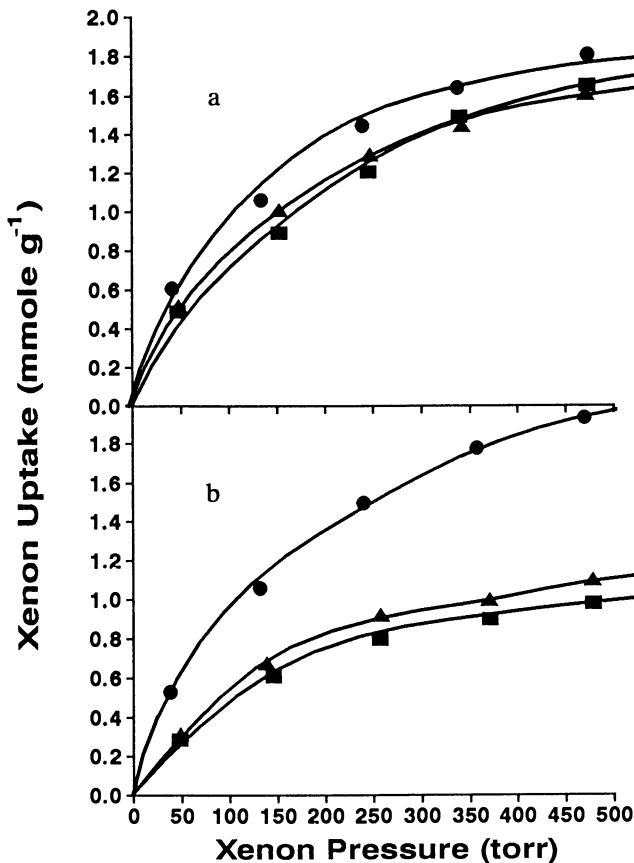


Figure 1. (a) Xenon adsorption isotherms (at 297 K) of the size-selectively modified Na,H-ZSM-5 zeolites having different coke contents: ●--uncoked; ▲--1 wt % coke; ■--12 wt % coke. (b) Xenon adsorption isotherms (at 297 K) of fully protonated H-ZSM-5 zeolites having different coke contents: ●--uncoked; ▲--1 wt % coke; ■--12 wt % coke. (Reproduced with permission from ref. 16. Copyright 1991 Academic Press Inc.)

Table II. Fraissard Parameter, Effective Channel Diameters, and Decrease of Void Volume for Samples after Various Treatments

Sample	σ_0 (ppm)	σ_1 (ppm-g/M mol)	$D_{\text{Channel(A)}}^a$	V/Vo
A. Na, H-ZSM-5				
Fresh	101.3 ± 0.7	23.1 ± 0.5	7.3	---
Slightly Coked	104.6 ± 1.3	23.2 ± 1.1	7.1	1.00 ^b
Heavily Coked	107.7 ± 0.6	23.5 ± 0.5	7.0	0.98 ^b
B. H-ZSM-5				
Fresh	103.1 ± 1.1	18.7 ± 0.8	7.2	---
Slightly Coked	103.4 ± 0.5	31.3 ± 0.6	7.2	0.60 ^b
Heavily Coked	102.9 ± 0.8	39.2 ± 1.0	7.2	0.48 ^b

^a = Calculated using Equations 1 and 2 with A = 499, B = 2.054, and $D_{\text{xenon}} = 4.4 \text{ \AA}$.

^b = These quantities have associated uncertainties of ± 0.05.

where λ is the mean free path in the structure. For an ideal infinitely long straight channel, λ is related to the channel diameter by the equation

$$\lambda = D_{\text{channel}} - D_{\text{xenon}} \quad (3)$$

Cheung and Fu(7) have derived an equation of similar form from a simple physical model. Recently, a relationship between the extrapolated chemical shift at low coverage, σ_0 , and the average pore size of zeolites determined by argon uptake as analyzed by the Horvath-Kawazoe Method(8) has been shown. Such derived parameters as the mean free path and average pore size seem to scale with other measures of the structure, but they do not necessarily correspond quantitatively to measures such as X-ray-derived interatomic distances. However, changes in σ_0 for Na,H-ZSM-5 do indicate slight changes in structural features that affect the xenon NMR response. The data may be interpreted, for example, as a slight change in effective channel diameter. Using the A and B parameters of Demarquay and Fraissard, the effective channel diameters for the samples of ZSM-5 from Equation 3 may be estimated.

As seen in Table II, the effective channel diameter of the modified Na,H-ZSM-5 (as calculated from the ^{129}Xe NMR parameter, σ_0) is reduced by a few tenths of an Angstrom by deposition of coke even at the 1 wt.% level. If one models the ZSM-5 structure as an infinite cylinder, a uniform reduction of the channel diameter by 5% (from 7.3 to 7.0 Å) is sufficient to account for a reduction of approximately 9-10% in volume.

The channels available to xenon in coked H-ZSM-5 appear to be essentially of the same structure, no matter how heavy the coking, as indicated by the essentially constant value of σ_0 for these samples (and the similarly constant value of D_{channel}). Thus, the local environment of xenon atoms is, at most, only

slightly changed by coking in this sample. This is in stark contrast to the 45% loss in uptake upon coking this sample, even at levels as low as 1 wt.%. Perhaps the most startling observation in these experiments is the change in the slope, σ_1 , of the curves for H-ZSM-5 with extent of coking. Ito et al.⁽²⁾ observed similar changes in slope for coked H-Y zeolites.

Generally, σ_1 reflects the effects of two-body collisions between xenon atoms. The change in slope can be interpreted as a change in free volume upon coking. One may estimate effective relative internal volume accessible to xenon gas per gram of material from the slopes⁽²⁾.

$$V/V_0 = \sigma_1 \text{ uncoked} / \sigma_1 \text{ coked}, \quad (4)$$

where V is the internal volume of the coked sample and V_0 is the internal volume of the uncoked material. From the σ_1 values in Table IIB, one would conclude that H-ZSM-5 has lost about 40% of the internal volume per gram due to coking, even at 1 wt.% coke. The isotherms for xenon uptake in Na,H-ZSM-5 show a 9-10% reduction in capacity not detectable in the slopes of the chemical-shift profiles. See Table IIA.

For H-ZSM-5, the expected loss of volume due only to channel filling by the coke, assuming a density of 1.8-2.1 g cm⁻³ for amorphous carbon⁽⁹⁾ and an internal volume for ZSM-5 in the range of 0.10-0.19 cm³g⁻¹^(10,11) may be estimated. For a 1 wt.% loading the coke would occupy 2.5-5.7% of the internal volume, significantly less than the 45% loss observed. The fact that the loss in xenon-accessible volume calculated either from NMR parameters of Figure 2 or from uptake measurements of Figure 1 is larger than expected by a simple model of channel filling by coke indicates that much of the volume not accessible to xenon is not filled with coke in H-ZSM-5.

The internal Brønsted sites in protonated H-ZSM-5 zeolites have been proposed to be located at intersections between the straight and sinusoidal channel⁽¹²⁾. Other investigators indicate that, at low coking, the carbonaceous material resides primarily on the external surfaces of crystallites with each "coke molecule" covering one active site⁽¹⁰⁾. At higher coking levels, highly alkylated aromatic material formed at the channel intersections blocking pores⁽¹³⁾. The modified Na,H-ZSM-5 contains Brønsted sites only external to the channels. Carbonaceous residues will have formed primarily on the outer surfaces only and, perhaps near some channel mouths, as shown in Figure 3. During coking the channels remain effectively accessible to xenon. As indicated by the NMR results, with a slight effective reduction of the channel size, even at 12 wt.% coke. At this level of coking, a calculation similar to the one above would predict a blockage of 30-50% of the Na,H-ZSM-5 channels, if all the coke is formed inside the pores. Thus, most of the coke resides on the external surfaces of the crystallites, with only a minor amount (about 10%) blocking channels in the material.

One model consistent with all these results is shown in Figure 3, in which a few isolated, internal sites of Na,H-ZSM-5 are coked, but with no substantial blockage of large internal volumes, leaving most of the internal volume accessible to xenon. Most of the coke must, therefore, reside on the external surfaces of the Na,H-ZSM-5. For H-ZSM-5, on the other hand, substantial internal volume is blocked from access by the xenon, even at 1 wt.% coking. The inaccessible volume is larger than the volume of coke deposited. Therefore, coke deposited in this material limits access of xenon to areas not

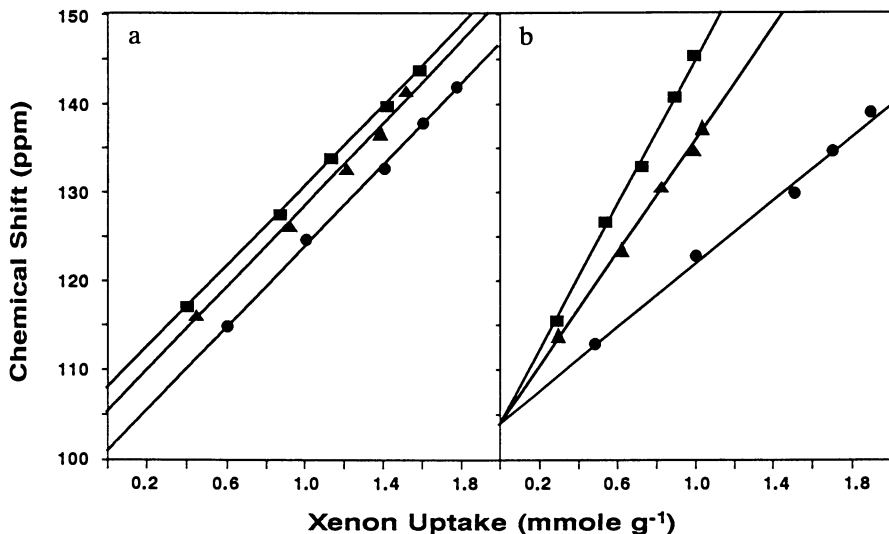


Figure 2. (a) ^{129}Xe chemical shift as a function of xenon uptake for the modified Na,H-ZSM-5 zeolites with different coke contents: ●--uncoked; ▲--1 wt % coke; ■--12 wt % coke. (b) Xenon chemical shift as a function of xenon uptake for fully protonated H-ZSM-5 zeolites having different coke contents: ●--uncoked; ▲--1 wt % coke; ■--12 wt % coke. (Reproduced with permission from ref. 16. Copyright 1991 Academic Press Inc.)

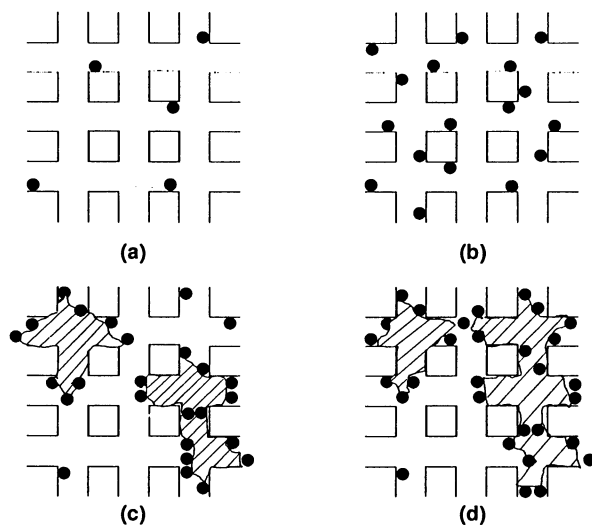


Figure 3. Schematic depiction of coke distributions in zeolite ZSM-5. (a) Lightly coked Na,H-ZSM-5; (b) Heavily coked Na,H-ZSM-5; (c) Lightly coked H-ZSM-5; (d) Heavily coked H-ZSM-5. (Reproduced with permission from ref. 16. Copyright 1991 Academic Press Inc.)

filled with coke. Thus, the coke deposits in H-ZSM-5 occur in sufficiently large volumes to block off xenon movement. These deposits could be either at the surface, at intersections, or in the channels. Comparisons of the xenon results for this material to that of Na,H-ZSM-5, where the sites acidified are at the surface, leads one to conclude that the material is not totally deposited at the surface.

Catalytic Activity

The catalytic activities of the modified Na,H-ZSM-5 and the fully protonated H-ZSM-5 were measured for several reactions. The constraint index experiment was carried according to the literature⁽¹⁴⁾. A 1:1 molar mixture of n-hexane and 3-methylpentane was fed over the catalyst bed at 300°C at a rate of 1 ml/hr with a helium diluent at 12.5 ml/min. The effluent stream was sampled after 20 minutes by syringe and analyzed by gas chromatography. The constraint index is given by Equation 5.

$$\text{Constraint Index} = \frac{\text{Log}_{10} (\text{Fraction of n-hexane remaining})}{\text{Log}_{10} (\text{Fraction of 3-methylpentane remaining})} \quad (5)$$

The fully protonated H-ZSM-5 had a constraint index of 10.8 in agreement with the literature values. The modified Na, H-ZSM-5 had a constraint index of 1.1 which is typical of a larger pore zeolite with a pore diameter greater than 6Å. The modified zeolite reacts with the substrates primarily at external catalytic sites and in a non-discriminating manner. Size and shape selectivity are not major factors since few catalytic sites are located internally.

Catalytic cracking of 2-butene over the modified Na, H-ZSM and the fully protonated H-ZSM-5 at 550°C and 16,000 hr⁻¹ GHSV was carried out. A dilute, fixed bed of 3 wt % zeolite in ∞-alumina was exposed to a 30 second 2-butene pulse followed by a nitrogen purge and a 10 minute air regeneration to determine the coke generated during the run. For both zeolites, conversion was high, 65-67%, and the primary product was propylene. See Table III. At these high space velocities most of the catalytic activity is realized at the external sites. Due to diffusional limitations little reactivity occurs within the channels. By increasing the space velocity sufficiently, it was demonstrated that a C₈ olefin formed from 2-butene coupling was the primary product. This subsequently cracked to the lower hydrocarbon products.

In a similar manner the catalytic cracking of n-octane was carried out over the two zeolites. The feed was passed over the dilute catalyst beds of 3 wt % zeolite in ∞-alumina for two hours. This was followed by a nitrogen purge and a two hour air regeneration to quantify coke. Again a high space velocity, 300 hr⁻¹ WHSV, was used. Both zeolites had comparable activity and gave propylene and butylenes as the major products. See Table IV. At this high space velocity, nearly all the catalytic cracking is occurring externally.

Methanol conversion was carried out over both the fully protonated and modified zeolites at 370°C and 1 atm for 2 hours, according to the methods

Table III. 2-Butene Conversion

Zeolite	% C ₄ ⁼ Conv.	C ₁ -C ₄	Wt. % Selectivity			Coke
			C ₂ ⁼	C ₃ ⁼	C _{5,6}	
H-ZSM-5	67.1	10.6	9.8	49.9	29.0	0.4
Modified Na,H-ZSM-5	64.7	9.9	8.0	49.7	31.9	0.5

Table IV. n - C₈ Conversion

Zeolite	H-ZSM-5	Modified Na,H-ZSM-5
Temp °C	550	550
WHSV, hr ⁻¹	300	300
% Conv.	53.2	52.5
Wt. % Sel.		
CH ₄	0.80	0.65
C ₂ ⁼	7.67	7.88
C ₂	3.35	3.17
C ₃ ⁼	22.31	24.14
C ₃	8.80	10.88
i-C ₄	0.97	1.16
BD	0.03	0.03
n-C ₄	4.49	5.79
C ₄ ⁼	22.65	25.29
C ₅ ⁼	7.07	8.50
C ₅	6.45	6.89
C ₆	3.29	3.73
C ₇	5.53	0.74
C ₈ ⁼	4.21	0.06
C ₉	2.30	1.08
C ₁₀	0.01	0
Coke	0	0

reported in the literature⁽¹⁵⁾. The modified Na, H-ZSM-5 was approximately half as active as the fully protonated H-ZSM-5 for those runs conducted at approximately 100 hr⁻¹ LHSV. The wt % hydrocarbon distributions for the two zeolites were nearly equivalent. See Table V. In this reaction the space velocity was sufficiently low so that a significant portion of the reactivity could have occurred internally. Because the reaction conditions favored lower hydrocarbon formation, size and shape selectivity were not critical in defining the wt % hydrocarbon distributions.

Table V. Methanol Conversion

Catalyst:	H-ZSM-5	H-ZSM-5	Modified Na,H-ZSM-5	Modified Na,H-ZSM-5
LHSV, hr ⁻¹	11	101	10	108
% Conversion	100	46.9	91.1	22.5
Wt % Hydrocarbon Distribution				
CH ₄	1.64	1.48	1.52	1.07
C ₂	0.30	0.16	0.31	0.19
C ₂ =	10.83	18.91	11.26	24.25
C ₃	5.90	3.06	8.46	4.37
C ₃ =	9.72	30.07	6.45	30.03
iC ₄	10.70	6.05	13.76	6.87
nC ₄	2.35	1.24	3.16	4.26
C ₄ =	13.46	20.61	12.57	15.90
iC ₅	3.41	3.56	1.20	2.52
nC ₅	2.76	1.38	1.24	0.88
C ₅ =	5.45	2.71	7.04	2.26
C ₆ =	10.64	4.95	8.39	3.08
Benzene	1.14	2.05	1.02	2.21
C ₇ Olefin	4.86	1.48	4.88	0.79
Toluene	2.11	0.47	1.75	0.74
C ₈ Olefin	8.95	1.43	9.81	0
Xylene	0.89	0.01	11.12	0.42
C ₉₋₁₁	4.63	0.28	5.62	0.15
C ₁₂₊	0.26	0.02	0.26	0
Coke	0.08	0.10	0.12	0

Conclusions

A modified pentasil was prepared in which protonated sites reside externally and cationic sites reside internally. Coked samples of this zeolite were characterized by ¹²⁹Xe NMR. Even at high coke levels, only slight blockage of channels was observed. In contrast the fully protonated H-ZSM-5 was shown to undergo coke deposition resulting in channel blockage. These observations can be rationalized by a model in which deposition of coke in the channels or at

intersections of H-ZSM-5 blocks xenon from accessing large internal volumes even at low coking levels, whereas surface coking of the Na, H-ZSM-5 still permits access to most of the internal volume, even at high coking levels, with only a slight deposition of coke in the internal regions of the material. The modified Na, H-ZSM-5 served as a mechanistic tool for defining those reactions which were occurring primarily at the exterior of the crystallite and were unable to occur to a significant extent internally due to diffusional limitations.

Literature Cited

- (1) Argauer, R.J., and Landolt, G.R., U.S. Patent 3,702,886.
- (2) Ito, T., Bonardet, J.L., Fraissard, J.P., Nagy, J.B., Andre, C., Gabelica, Z., Derouane, E.G., *Appl. Catal.* **43**, L5 (1988).
- (3) Scharpf, E.W., Crecey, R.W., Gates, B.C., and Dybowski, C., *J. Phys. Chem.* **90**, 9 (1986).
- (4) (a) Ito, T., and Fraissard, J.P., *J. Chem. Phys.* **76**, 5225 (1982); (b) Ito, T., and Fraissard, J.P., *Chem. Phys. Lett.* **111**, 271 (1984).
- (5) Tsiao, C., Corbin, D. R., and Dybowski, C., *J. Phys. Chem.*, **94**, 867 (1990).
- (6) Demarquay, J. and Fraissard, J.P., *Chem. Phys. Lett.* **136**, 314 (1987).
- (7) Cheung, T.T.P., and Fu, C.M., *J. Phys. Chem.* **93**, 3740 (1989).
- (8) Cotterman, R.L., Hickson, D.A., Carlidge, S., Dybowski, C., and Tsiao, C., *Zeolites*, **11**, 27 (1991).
- (9) Weast, R. C., Ed., "CRC Handbook of Chemistry and Physics." CRC Press, Boca Raton, FL, (1982).
- (10) Breck, D. W., "Zeolite Molecular Sieves," p. 352, Krieger, Malabar, FL, (1984).
- (11) Flanigen, E.M., Bennett, J.M., Grose, R.W., Cohen, J.P., Patton, R.L., and Kirchner, R.M., *Nature* **271**, 512 (1978).
- (12) Derouane, E.G., and Vadrine, J.C., *J. Mol. Catal.* **4**, 479 (1980).
- (13) Guisnet, M., Magnoux, P., and Caneff, C., in "Proceedings, 7th International Zeolite Conference," p. 701, Kodasha, Tokyo, (1986).
- (14) Frillette, V.J., Haag, W.O., and Lago, R.M., *J. Catal.* **67**, 218 (1981).
- (15) Chang, C.D., and Silvestri, A.J., *J. Catal.* **47**, 249 (1977).
- (16) Tsiao, C., Dybowski, C., Gaffney, A.M., and Sofranko, J.A., *J. Catal.* **128**, 520 (1991).

RECEIVED July 6, 1992

Chapter 22

Effect of Catalyst Preparation on the Aromatization of *n*-Hexane over Pt Clusters Supported on Hydrotalcite

R. J. Davis¹ and E. Mielczarski^{2,3}

¹Department of Chemical Engineering, University of Virginia, Charlottesville, VA 22903-2442

²Department of Chemical Engineering, Virginia Polytechnic Institute and State University, Blacksburg, VA 24061

Calcination of the synthetic anionic clay hydrotalcite, magnesium aluminum hydroxycarbonate, yields a basic mixed oxide of high surface area ($220 \text{ m}^2\text{g}^{-1}$) which can be used as a catalyst support. In this work, the influence of Pt precursor, impregnation method, alloying, and addition of alkali promoter onto calcined hydrotalcite have been investigated by using the aromatization of *n*-hexane as a probe reaction. Monometallic Pt and bimetallic Pt-Au samples prepared by impregnation of acidic metal precursors in aqueous solution yielded the poorest catalysts for aromatization due to significant cracking side reactions occurring over surface acid sites. However, catalysts prepared by a new $\text{Pt}(\text{acac})_2$ impregnation method were superior in aromatization compared to the above samples. Aromatization selectivity is also increased after impregnation of KOH onto a working catalyst. In addition, the terminal cracking index defined as the ratio of C_5 to C_4 hydrocarbons produced over a Pt catalyst increased from 1.6 to 3.1 after KOH impregnation. The observed trends in aromatization selectivity and terminal cracking are interpreted as an influence of K^+ on the surface structure of supported Pt clusters so that (111) surface planes are preferentially exposed and the creation of strong basic surface sites.

Dehydrocyclization of *n*-hexane to form benzene has been a subject of considerable academic and industrial interest since Bernard first reported that platinum clusters supported inside the channels of zeolite L catalyze the reaction with exceptional activity and selectivity (1). The nonacidic nature of the Pt-zeolite L catalyst and correlation of reaction rate with Pt content are consistent with the accepted view that the catalyst is monofunctional, depending solely on Pt metal for catalytic activity (1). However, comparison of aromatization reactivity over nonacidic Pt-zeolites to conventional non-zeolitic catalysts revealed that additional factors contribute to the unusual performance of Pt-zeolites (2).

³Current address: Laboratoire de Catalyse Hétérogène, Université de Nancy I, 54506 Vandoeuvre-les-Nancy, France

Derouane and Vanderveken propose that for dehydrocyclization of n-hexane the spatial constraints inside the channels of zeolite L maximize the Van Der Waals interactions between the channel walls and adsorbed hydrocarbon leading to a stabilized cyclic intermediate that eventually reacts to form benzene (3). A molecular graphics study of n-hexane adsorbed inside zeolite L revealed that adequate space exists for the molecule to curve around on itself and attach both ends to a single Pt atom. However, Tauster and Steger suggest that the only function of the zeolite channels is to collimate a diffusing flux of reactant alkane so that their long axis is parallel to the zeolite channel (4,5). Collimation is suggested to increase the probability for terminal adsorption of n-hexane onto a Pt cluster located within the zeolite and is supported by the large terminal cracking index observed for zeolite catalysts. Terminal adsorption of n-hexane would be expected to enhance a surface reaction pathway involving 1,6 ring closure giving benzene (4,5). However, Lane et al. observed significant terminal cracking for both zeolitic and non-zeolitic catalysts demonstrating that the collimation effect cannot explain the performance of Pt-KL (2).

Varying the zeolite cation alters the intrinsic basicity of the resulting material. Platinum catalysts containing cations that increase the basicity of the zeolite support were reported to be superior for aromatization compared to their less basic counterparts (6). The influence of cation on aromatization is not clear since the catalytic results were reported at different levels of conversion thereby complicating the interpretation. Evidence for a metal-support interaction between the Pt clusters and the cations of zeolite L was reported recently by Larsen and Haller who measured changes in the competitive hydrogenation rates of toluene and benzene over Pt-zeolites containing various alkaline earth cations (7). The ratio of the toluene to benzene adsorption equilibrium constant on Pt was extracted from the hydrogenation kinetic data and was consistent with the Pt being more electron-rich when supported inside the more basic zeolites.

Recently, Pt clusters supported on hydrotalcite-derived magnesia, Mg(Al)O, were shown to catalyze the aromatization of n-hexane as effectively as a Pt/KL catalyst (8). A high surface area basic oxide was chosen to support the metal clusters in order to investigate the influence of carrier structure on aromatization. In that study, significant quantities of cracked products were produced by both the zeolite and non-zeolite catalysts. Since the zeolite catalyst was prepared in a fashion that resulted in residual acidity being present, observation of cracked products is not surprising. However, cracking reactions over Pt/Mg(Al)O are not as easily explained.

In this paper, we investigate the influence of catalyst preparation on the reactivity of hydrotalcite-derived Pt/Mg(Al)O for n-hexane reaction. In specific, the effects of Pt metal incorporation, metal alloying, and adding alkali promoter are examined.

Experimental Methods

All of the hydrotalcite-derived magnesia supports were prepared by first coprecipitating magnesium aluminum hydroxycarbonate in the presence of Mg and Al nitrates, KOH, and K_2CO_3 according to procedures already described (8,9). Hydrotalcites were then decomposed by calcination at 873 K for 12-15 h to yield the binary oxide to be used for a catalyst support. The specific surface area of the hydrotalcites determined by nitrogen adsorption was typically about $220 \text{ m}^2\text{g}^{-1}$ after calcination. X-ray powder diffraction patterns of the materials were recorded on a Scintag X-ray diffractometer.

Several methods were used to incorporate Pt metal onto the magnesia support. One method involved the impregnation of aqueous H_2PtCl_6 onto the dried support until the point of incipient wetness. A second method utilized vapor phase

impregnation of $\text{Pt}(\text{acac})_2$ while a third method involved a liquid phase impregnation of $\text{Pt}(\text{acac})_2$ dissolved in acetone. These catalysts are designated as Pt-I, Pt-VI, and Pt-LI, respectively. The impregnation of $\text{Pt}(\text{acac})_2$ into molecular sieves is discussed elsewhere (Hong, S.B., Mielczarski, E., and Davis, M.E., submitted) and is the same method as used here for hydrotalcites. A bimetallic PtAu catalyst was also prepared by coimpregnating $\text{Mg}(\text{Al})\text{O}$ with an aqueous solution of H_2PtCl_6 and HAuCl_4 having a Pt:Au atomic ratio of 12:88 which is within the miscibility range of Pt-Au alloys. All of the catalysts were calcined in air or oxygen at 623 K for 6 h and reduced in flowing H_2 at 673 K for 2 h. In addition, a reduced Pt/ $\text{Mg}(\text{Al})\text{O}$ catalyst, Pt-LII, (prepared by liquid phase impregnation of $\text{Pt}(\text{acac})_2$) was impregnated with aqueous KOH (giving catalyst Pt-K) to neutralize any acidity of the support due to the presence of aluminum and examine the effect of added alkali cations on Pt/hydrotalcite.

Physical adsorption of argon at 80 K was performed on a Coulter, Omnisorp-100 CX Analyzer. Chemisorption of hydrogen at room temperature was also performed on the Omnisorp Analyzer and was used to estimate the Pt cluster sizes. After reduction at 673 K for 8 h in flowing H_2 , samples were evacuated at 673 K for 1 h and then cooled to RT *in vacuo* before measuring isotherms.

Reaction of n-hexane was carried out in a continuous flow microreactor operating at atmospheric total pressure. A dihydrogen to n-hexane molar ratio in the feed stream was maintained at 6:1 throughout the experiments and no diluent was used. The reactant mixture was fed into a quartz reactor containing the catalyst (-30/+65 mesh) and reaction products were analyzed by on-line gas chromatography. The catalyst was first reduced *in-situ* in flowing H_2 at 733 K for 2 h before admitting reactants and all catalytic results are reported after at least 1 h on stream. The major identified products from n-hexane reaction over Pt catalysts are benzene, methylcyclopentane, 2- and 3- methylpentanes, hexenes, and cracked hydrocarbons ($\text{C}_1\text{-C}_5$).

Results and Discussion

Our support precursor having a Mg:Al molar ratio of about 3:1 shows an x-ray diffraction pattern typical of hydrotalcite (see Figure 1a) (10). After calcination at 873 K the resulting diffraction pattern exhibits diffuse peaks corresponding to MgO (Figure 1b). No evidence for separate crystalline aluminum phases was found so Al cations probably remain closely associated with or dissolved in the MgO structure. However, it is possible that amorphous alumina phases, not detectable by x-ray diffraction, may be present in our mixed oxide.

Earlier work reported that $\text{Mg}(\text{Al})\text{O}$ was non-microporous (8); however, some question remains as to the possibility of micropores being created upon high temperature treatment (11). We have examined the adsorption of argon at low pressure on calcined $\text{Mg}(\text{Al})\text{O}$. Figure 2 compares the argon adsorption isotherms of NaY zeolite, Shell controlled-pore silica spheres (25 nm diameter pores), and calcined $\text{Mg}(\text{Al})\text{O}$. In general, adsorption of Ar at low temperature and $P/P_0 < 10^{-3}$ can be attributed to gas uptake inside micropores having diameters of 20 Å or less (12,13). Adsorption inside the micropores of NaY zeolite is apparent from the large Ar uptake at relative pressures of 10^{-4} - 10^{-3} . Thus, negligible Ar adsorption on $\text{Mg}(\text{Al})\text{O}$ for P/P_0 less than about 10^{-1} is consistent with no micropores being present in the sample. Comparison of the $\text{Mg}(\text{Al})\text{O}$ isotherm with the corresponding isotherm for mesoporous silica reinforces our conclusion.

Incorporation of Pt onto calcined $\text{Mg}(\text{Al})\text{O}$ was accomplished in several ways. Methods involving aqueous impregnation regenerated the hydrotalcite structure since

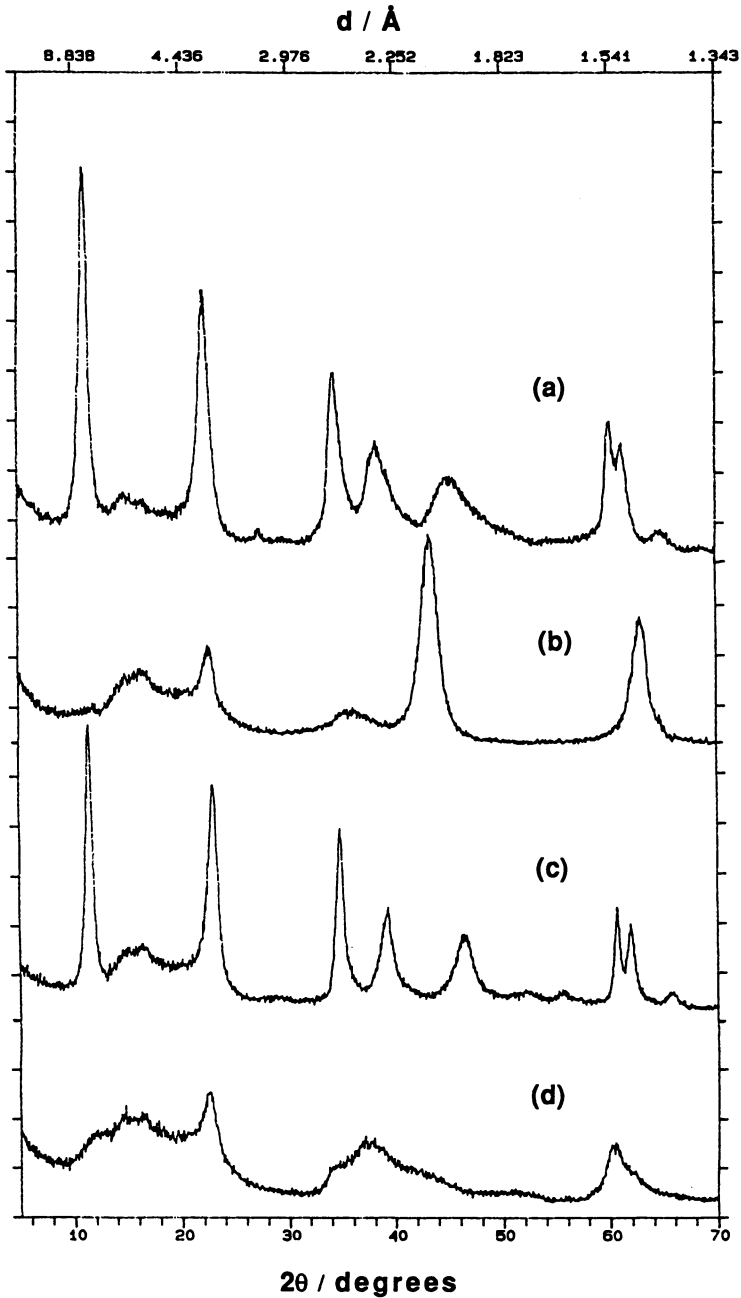


Figure 1. X-ray powder diffraction patterns for (a) synthesized hydrotalcite, (b) hydrotalcite calcined at 873 K to give Mg(Al)O, (c) Mg(Al)O impregnated with aqueous chloroplatinic acid, and (d) sample in (c) calcined in O_2 at 623 K.

no special efforts were taken to ensure the absence of CO₂ in the Pt solution or in the surrounding atmosphere. Figure 1c shows the x-ray diffraction pattern for calcined Mg(Al)O that was impregnated with an aqueous solution of chloroplatinic acid clearly demonstrating the regenerated crystal structure. Calcination of the sample in O₂ at 623 K was sufficient to destroy the ordered layer structure as evidenced by the absence of the peak at about $2\theta = 11^\circ$ in Figure 1d. However, impregnation of Pt followed by calcination at 623 K was not sufficient to produce the distorted MgO pattern typical of calcined hydrotalcite (Fig.1b).

A summary of the catalyst samples used in this work is provided in Table I. The H/Pt ratio determined by hydrogen chemisorption on Pt/Mg(Al)O prepared by vapor phase impregnation of Pt(acac)₂ was 1.37 and corresponds to an average cluster size less than or equal to 1 nm in diameter. An H/Pt ratio of 0.44 was measured for catalyst Pt-LI which was also consistent with Pt/Mg(Al)O prepared by aqueous impregnation of Pt(NH₃)₄Cl₂ (H/Pt = 0.49) having clusters about 2 nm in average diameter (8). Apparently, vapor phase impregnation of Pt(acac)₂ gives the most highly dispersed Pt catalyst. The incorporation of Pt by both liquid and vapor phase impregnation of Pt(acac)₂ has been recently demonstrated for molecular sieve supports (Hong, S.B., Mielczarski, E., and Davis, M.E., submitted), but this is the first time that the method has been used to support Pt on hydrotalcite.

Table I. Summary of Catalysts Used

Sample	Wt% Pt	Preparation Method
Pt-I	0.70	Aqueous Impregnation of H ₂ PtCl ₆
Pt-VI	0.72	Vapor phase impregnation of Pt(acac) ₂
Pt-LI	1.00	Acetone impregnation of Pt(acac) ₂
Pt-Au	0.52 %Pt 3.74 %Au	Aqueous impregnation of H ₂ PtCl ₆ and HAuCl ₄
Pt-LII and Pt-K	0.24 %Pt 4.77 %K	Acetone impregnation of Pt(acac) ₂ and aqueous KOH

The samples in Table I were tested in the reaction of n-hexane at 733 K and atmospheric pressure. Figure 3 shows the selectivity to benzene formation (calculated as the yield of benzene divided by the conversion of n-hexane) as a function of n-hexane conversion for Pt-LI and Pt-VI as circles and squares, respectively. Results recently reported for a 0.88 wt% Pt (H/Pt = 0.49) catalyst prepared by impregnation of aqueous Pt(NH₃)₄Cl₂ are included for comparison (8). However, the results in (8) were obtained at 750 K, H₂/n-hexane = 6 (6 kPa n-hexane) and diluent He at atmospheric total pressure which are slightly different from the experimental conditions used in the current work.

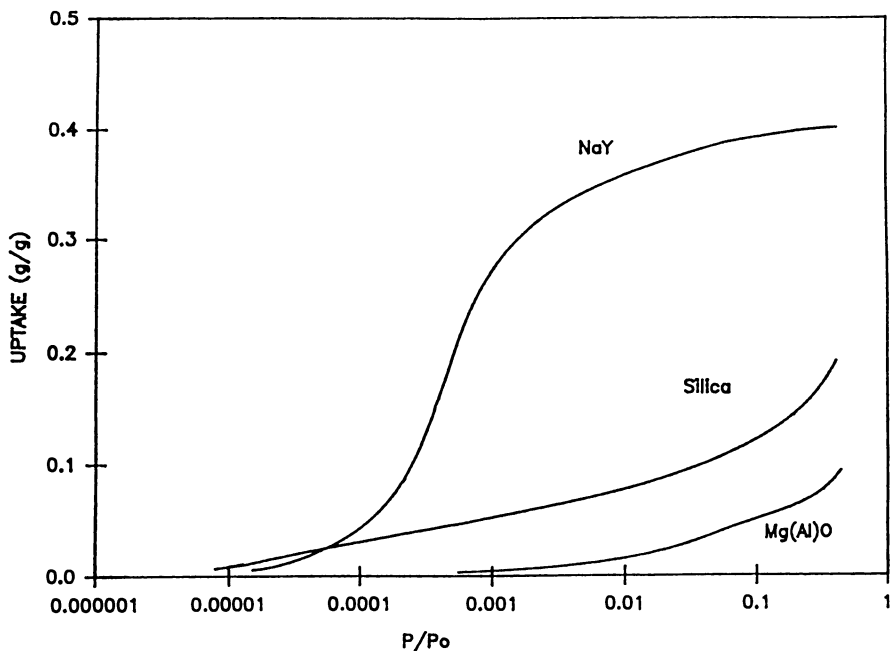


Figure 2. Argon adsorption isotherms for microporous and nonmicroporous catalyst supports. The normalized Ar uptake is plotted as a function of relative saturation pressure.

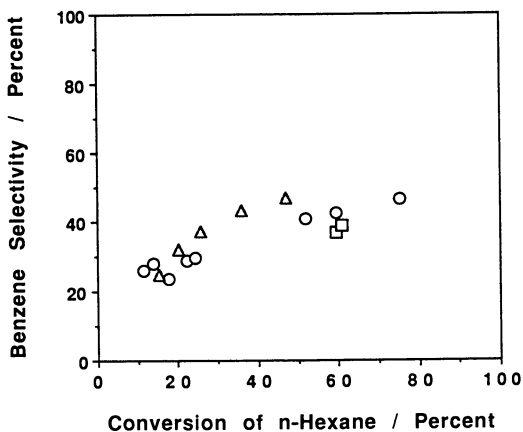


Figure 3. Selectivity to benzene formation as a function of n-hexane conversion at 733 K, H_2/C_6H_{14} molar ratio of 6, and atmospheric total pressure. Circles and squares correspond to results for Pt-LI and Pt-VI, respectively. Catalytic results at 750 K for Pt/Mg(Al)O prepared from $Pt(NH_3)_4Cl_2$ are included as triangles for comparison (Adapted from ref. 8).

The catalysts prepared with $\text{Pt}(\text{acac})_2$ and $\text{Pt}(\text{NH}_3)_4\text{Cl}_2$ precursors showed similar benzene selectivity as a function of conversion over the entire range of conversion studied even though the catalysts had different Pt cluster sizes determined from H_2 chemisorption. These results are consistent with aromatization selectivity being independent of structure over Pt/Mg(Al)O catalysts having cluster sizes between 1 and 2 nm in diameter. Similar activity and selectivity to benzene were found recently for 2 nm Pt clusters on Mg(Al)O compared to 1 nm Pt clusters on KL zeolite (8). In fact, Dautzenberg and Platteuw reported previously that n-hexane isomerization and dehydrocyclization reactions are structure insensitive over monofunctional Pt catalysts having Pt cluster sizes ranging from 1.5 to 5 nm in average diameter (14). However, the similarity of selectivity between Pt-VI (H/Pt = 1.37) and Pt-LI (H/Pt = 0.44) may also result from Pt aggregation of the Pt-VI sample under reaction conditions to yield nearly the same size clusters as Pt-LI. This speculation is partially supported by the measured rates of n-hexane reaction per surface Pt atom. The "turnover frequencies" of reaction are calculated to be 0.12 s^{-1} and 0.067 s^{-1} for Pt-LI and Pt-VI, respectively, when computed as the molecules of n-hexane reacted per surface Pt atom (from H_2 chemisorption) per second. These are not true turnover frequencies since they were calculated from reaction data obtained at 60% conversion which is far from differential. However, they do provide a basis for comparing the catalysts' relative activity. The difference in rate between the two catalysts can be explained by aggregation of the Pt clusters in Pt-VI during reaction. In fact, the normalized rates for the two catalysts would be nearly equal if the Pt clusters in Pt-VI aggregated to the cluster size in Pt-LI. In addition, since the clusters in Pt-VI expose nearly every Pt atom to the surface, a significant interaction of the Pt with the support may explain the lower activity of the sample compared to Pt-LI which has larger clusters. Therefore, further investigation of these catalysts after reaction is needed to demonstrate conclusively that aggregation occurred during reaction.

Comparison of the product selectivity patterns in Table II at two levels of conversion revealed that catalysts prepared by aqueous impregnation of acidic metal precursors (H_2PtCl_6 and HAuCl_4) had a greater tendency to produce cracked products (C_1 - C_5 hydrocarbons) than catalysts prepared by impregnation of $\text{Pt}(\text{acac})_2$. One way to determine if cracked products are produced from metal sites or support acid sites is to examine the distribution of cracked products. Acid-catalyzed cracking has a greater tendency to break internal carbon-carbon bonds resulting in the production of butanes and propanes from n-hexane. Tauster and Steger have defined a terminal cracking index, TCI, to be the ratio of C_5 to C_4 products and we will use the TCI to gauge relative acidity of our samples (4,5). A TCI value greater than about 1.5 appears to be consistent with mostly metal catalyzed cracking over non-acidic catalysts (2,4,5, and Mielczarski, E., Hong, S.B, Davis, R.J., and Davis, M.E., submitted). In addition, Tauster and Steger defined a selectivity parameter to be the wt % benzene / (wt % benzene + wt % C_2 - C_5 gas) which measures a catalyst's tendency to aromatize instead of crack n-hexane (4,5). Table III shows the TCI and benzene selectivity parameter calculated for various Pt catalysts. Evidently, the Pt-Au sample has significant surface acidity that is responsible for internal cracking (low TCI) at the expense of benzene formation (low selectivity parameter). This is not surprising since acidic metal precursors containing chloride were used in the preparation of this sample. In addition, since metal-catalyzed hydrogenolysis is structure sensitive, alloying Au into Pt should also markedly decrease the relative amount of metal-catalyzed cracking compared to acid-catalyzed cracking on the support through an ensemble effect (15). A lower selectivity parameter for Pt-I prepared by impregnation of chloroplatinic acid compared to the $\text{Pt}(\text{acac})_2$ catalysts is evidence for an increase in cracking on surface acid sites. However, the small

decrease in selectivity parameter was not accompanied by a lower TCI like the Pt-Au sample. This discrepancy is probably due to the pronounced influence of the ensemble effect with the alloy catalyst and a larger amount of Cl present per Pt atom in the bimetallic sample.

Table II. Selectivity to Various Products from n-Hexane Reaction over Pt Catalysts at 733 K

Catalyst	% Conv.	C ₁ -C ₅	MP ^a	MCP ^b	Hexenes	Benzene
Pt-I	63.2	33.7%	18.7%	12.2%	4.0%	29.7%
Pt-LI	59.5	19.3	9.7	10.0	18.2	42.2
Pt-LII	17.9	21.2	16.2	31.8	7.3	23.5
Pt-Au	17.5	33.7	15.4	32.0	9.1	9.7

a 2- and 3- methylpentanes

b methylcyclopentane

Table III. Terminal Cracking Index and Benzene Selectivity Parameter at 733 K

Catalyst	TCI ^a	Selectivity Parameter ^b
Pt-I	1.7	0.51
Pt-LI	1.7	0.66
Pt-Au	0.97	0.24
Pt-K ^c	3.1 (1.6)	0.66 (0.56)

a Terminal cracking index is defined as the C₅/C₄ molar ratio.

b Selectivity parameter is defined as:
wt % benzene / (wt % benzene + wt % C₂-C₅ gas).

c Values in parentheses correspond to the TCI and selectivity parameter for the sample before impregnation with KOH.

Although MgO can be considered a basic oxide, the presence of Al in the mixed oxide may induce some surface acidity. For example, decomposition of 2-propanol over calcined hydrotalcite results in the formation of both propene and propanone which is consistent with the presence of both surface acid and base sites (16). We therefore wanted to test the effect of neutralizing all of the support acidity by

impregnating a working catalyst with KOH. In addition to neutralizing support acidity, the presence of K ions may directly influence the Pt-catalyzed reactions of n-hexane. Since Pt/Mg(Al)O prepared with aqueous chloroplatinic acid or chlorinated Pt salts apparently increases the acidity of the final reduced catalyst, we chose to use the liquid phase impregnation of Pt(acac)₂ onto Mg(Al)O since that method should not influence the acidity of the final catalyst. A portion of the reduced Pt/Mg(Al)O was then impregnated with aqueous KOH to give a final K loading of 4.77 wt%. Both samples were tested in the n-hexane reaction at low conversion (12-18%). The TCI for the neutralized sample increased from 1.6 to 3.1 and the benzene selectivity parameter increased from 0.56 to 0.66.

Three explanations for the observed results can be hypothesized. First, residual support acidity due to the presence of Al in the structure may have been neutralized thereby increasing the TCI and benzene selectivity. However, the large increase in TCI to a value of 3.1 cannot be explained solely on the basis of acidity neutralization. In fact, the TCI for non-acidic (verified by NH₃ TPD) Pt/KL catalysts is less than 3 at identical conditions (Mielczarski, E., Hong, S.B, Davis, R.J., and Davis, M.E., submitted). Lane et al., however, have observed a TCI of 3.1 for n-hexane reactions at 420°C over Pt/KY (2). We suggest a second explanation for the unusual increase in TCI and benzene selectivity observed after impregnation of KOH that involves an influence of the cation on the structure of the Pt cluster. Earlier research has shown that alkali metal doping of Pt surfaces induces a rearrangement of the exposed atoms to yield preferentially (111) faces (17). Single crystal studies also demonstrated that the active surface for n-hexane dehydrocyclization and terminal cracking consists of (111) terraces (18). Indeed, Tennison et al. speculate that Na doped Pt/carbon catalysts exhibit high n-hexane aromatization activity because of a Pt surface reorientation induced by Na that exposes the active (111) faces of the Pt clusters (19). The dramatic increase in TCI and selectivity parameter observed in our work by impregnating a catalyst with KOH may result from preferential exposure of Pt(111) faces. A third explanation for the high TCI is that strong basic sites, created on the support surface from impregnation of KOH, may catalyze hydrocarbon reactions in addition to the metal catalyzed reactions.

Conclusions

Several methods of Pt incorporation onto hydrotalcite were found to give active catalysts for aromatization of n-hexane. Impregnation of non-microporous calcined Mg(Al)O with an aqueous solution of chloroplatinic acid (and presumably other aqueous salt solutions) regenerates the layered structure associated with the precursor hydrotalcite. Further calcination and reduction results in Pt clusters supported on an amorphous high surface area binary oxide of magnesium and aluminum that are effective for catalyzing the reactions of n-hexane. In addition, two new methods of vapor phase and liquid phase (acetone) impregnation of Pt(acac)₂ were used to produce highly dispersed Pt clusters onto calcined Mg(Al)O; in fact the vapor phase impregnation method produced a catalyst having all of the Pt atoms exposed to the surface (H/Pt=1.37).

No effect of Pt cluster size in the range of 1 to 2 nm in average diameter was found for the selectivity to benzene formation as long as the preparation method did not involve acidic precursors. A Pt-Au bimetallic catalyst exhibited the worst performance due to excessive internal cracking presumably due to surface acid sites.

Impregnation of Pt/Mg(Al)O with aqueous KOH resulted in a greater selectivity toward benzene production and a significant increase in the terminal cracking index. The large effect of KOH is attributed to the neutralization of surface acid sites, alkali

metal induced reorientation of the Pt clusters, and the creation of strong surface base sites that participate in hydrocarbon reactions.

Acknowledgments

This work was supported by the National Science Foundation (Grant No. CTS-9108206). E.M. acknowledges support from Akzo America, Inc.

Literature Cited

1. Bernard, J.R. in *Proc. 5th Int. Zeolite Conf.*; L.V. Rees, Ed.; Heyden: London, 1980, 686.
2. Lane, G.S.; Modica, F.S.; Miller, J.T. *J. Catal.* 1991, *129*, 145.
3. Derouane, E.G.; Vanderveken, D. *Appl. Catal.* 1988, *45*, L15.
4. Tauster, S.J.; Steger, J.J. *Mat. Res. Soc. Proc.* 1988, *111*, 419.
5. Tauster, S.J.; Steger, J.J. *J. Catal.* 1990, *125*, 387.
6. Besoukhanova, C.; Guidot, J.; Barthomeuf, D.; Breysse, M.; Bernard, J.R. *J. Chem. Soc., Faraday Trans. 1* 1981, *77*, 1595.
7. Larsen, G.; Haller, G.L. *Catal. Lett.* 1989, *3*, 103.
8. Davis, R.J.; Derouane, E.G. *Nature* 1991, *349*, 313.
9. Reichle, W.T. *Solid State Ionics* 1986, *22*, 135.
10. Schaper, H.; Berg-Slot, J.J.; Stork, W.H.J. *Appl. Catal.* 1989, *54*, 79.
11. Reichle, W.T.; Kang, S.Y.; Everhardt, D.S. *J. Catal.* 1986, *101*, 352.
12. Hathaway, P.E.; Davis, M.E. *J. Catal.* 1989, *119*, 497.
13. Hathaway, P.E.; Davis, M.E. *Catal. Lett.* 1990, *5*, 333.
14. Dautzenberg, F.M.; Platteeuw, J.C. *J. Catal.* 1970, *19*, 41.
15. Sinfelt, J.H. *Bimetallic Catalysts-Discoveries, Concepts, and Applications*; Exxon Monograph; John Wiley: New York, 1983.
16. Kelkar, C.P.; Shutz, A.; and Marcelin, G. in *Perspectives in Molecular Sieve Science* 1988, *368*, 324.
17. McCarroll, J.J. *Surf. Sci.* 1975, *53*, 297.
18. Davis, S.M.; Zaera, F.; Somorjai, G.A. *J. Catal.* 1984, *85*, 206.
19. Tennison, S.R.; Foster, A.L.; McCarroll, J.J.; Joyner, R.W. in *ACS Petroleum Division Preprints*, Seattle Meeting, March 20-25, 1983.

RECEIVED June 22, 1992

Chapter 23

Reactions of Ethylene over RuY Zeolite

Y. S. Kye, S. X. Wu, and Tom M. Apple¹

Department of Chemistry, Rensselaer Polytechnic Institute,
Troy, NY 12180

¹³C NMR has been used to probe the reaction of ethylene on Ru-Y zeolite. Self hydrogenation of ethylene to ethane and butane is the primary reaction at room temperature. 2-butenes are observed as intermediates in the reaction. A co-cation dependence of the rate is also observed in the order Ru-H-Y > Ru-Ca-Y > Ru-Na-Y, however little change in selectivity is observed. At intermediate temperatures butane isomerizes to isobutane, presumably through a carbocation intermediate formed at the acid sites. At temperatures above 623 K carbon-carbon bond cleavage is complete yielding only methane.

The adsorption and subsequent reaction of ethylene on Group VIII metal surfaces provides a rich chemistry, which depends upon the adsorption temperature and the Group VIII metal. ¹³C NMR offers great potential to investigate the adsorbed states and to follow the reaction of ethylene on the surface. The study of the reactions of ethylene on Ru surfaces by ¹³C NMR has been reported by Gerstein and co-workers.(1,2) They have shown that ethylene on silica-supported ruthenium is converted to ethane, n-butane, 2- butenes and strongly adsorbed alkyl groups.

Other Group VIII metal-ethylene systems have been studied by NMR. Slichter et al.(3) have used dipolar couplings between carbons and carbon and Pt to show that upon adsorption of ethylene on supported Pt, half of the carbons were non-protonated and half were present as rotating methyl groups. They concluded that ethylene forms ethylidyne on supported Pt at room temperature, with carbon- carbon bond scission beginning at 450K. Gay(4) also studied the adsorption of ethylene on supported Pt by ¹³C NMR, but found no evidence for non-protonated carbon. His results were consistent with adsorption as pi-bonded olefin. However, when Pt was supported on Al₂O₃ or on catalysts containing Cl⁻, reactions to di- adsorbed species which retained the double bond along with some surface alkyls were reported.

We have used ¹³C solid state NMR to probe the adsorption of ethylene on Ru-Y zeolite. The influence of co-cations, temperature changes and hydrogen on the reaction has been investigated.

¹Corresponding author

Experimental

The Na-Y and H-Y zeolite starting materials were obtained from the Union Carbide Co. and the PQ Corp., respectively. The hexammineruthenium (III) chloride was obtained from Strem Chemical Inc. Ca-Y zeolite was made from Na-Y zeolite by ion exchange.⁽⁵⁾ The Ru exchanged Y zeolites were made from Na-Y, Ca-Y, and H-Y zeolites by the same cation exchange method. During ion-exchange at 343 K, the white color of the 15g Na-Y (Ca-Y or H-Y) and 2.2g Ru(NH₃)₆Cl₃ mixture changed to pink then purple due to the formation of "ruthenium red".⁽⁶⁾ In the oven, the color became gray. The ruthenium weight percent was determined by analysis of the supernatant. RuNa-Y, RuCa-Y, RuH-Y were 1.29, 1.28, 0.95% Ru by weight, respectively.

All Ru exchanged Y zeolites were dehydrated in a glass vacuum line at 623 K and reduced under static hydrogen at the same temperature using a procedure similar to that of Uytterhoeven et al..^(7,8) Dispersions for all samples exceeded 0.9. For coadsorption studies of ethylene and hydrogen, ethylene was preadsorbed at 77 K and hydrogen was introduced immediately afterwards.

The double labelled ¹³C-ethylene (99%) used for adsorption was obtained from ICON isotope Co.. Instrument grade isobutane (Matheson) and methane (94.1%, ¹³C) from MSD Co. were used to confirm chemical shifts of NMR peaks.

All adsorptions were performed in a glass vacuum system. The pressures were measured with an MKS capacitance manometer.

Zeolite samples were placed in 5mm O.D. tubes for solid state NMR studies and in 4mm O.D. tube for studies with a liquid state spectrometer. The amount of zeolite packed into each NMR tube was 0.13±0.02g. Glass wool was used to keep the zeolite in the NMR tube during evacuation. Samples were sealed such that all of the catalyst and any dead space above the catalysts was all contained in the NMR coil. In this way all reaction products leaving the zeolite cages could be quantified.

Solid state NMR data was acquired with a Chemagnetics M-100S solid state NMR at a frequency of 25.04 MHz for ¹³C and 99.58 MHz for ¹H. A 9.5mm Kel-F rotor provided by Chemagnetics was used to spin samples sealed under vacuum at 3.0 to 3.3 KHz. Intensity ratios for all resonances were checked as a function of scan repetition rate on several identically prepared samples to insure that the same intensity ratios were obtained with larger repetition delays but fewer scans.

Results and Discussion

In agreement with Denney et al⁽⁹⁾, the NMR spectrum of ethylene adsorbed on Na-Y zeolite at room temperature is consistent with physisorbed ethylene. The spectrum remains unchanged with time indicating that ethylene is unreactive on the unexchanged zeolite.

Room temperature NMR spectra of adsorbed ethylene on Ru- exchanged Y zeolites are shown in Figure 1. These spectra are quite similar to those observed by Gerstein et al.¹ on Ru-SiO₂. Peak (a) (128±2 ppm from TMS) corresponds to carbon-carbon double bonds of unsaturated hydrocarbons. The intensity of this peak decreases with time, while peaks (b), (d) and (e) grow. Peak (e) (2±1 ppm) is due to ethane formed by hydrogenation of ethylene. This peak is very narrow even in the absence of magic-angle spinning, due to the high mobility of ethane in the zeolite. The chemical shifts of peaks (b) (27±2 ppm) and (d) (16±3 ppm) along with the fact that their intensities rise proportionately and that n-butane is detected by mass spectrometry upon evacuation allows their assignment to n-butane. Peak (b) corresponds to

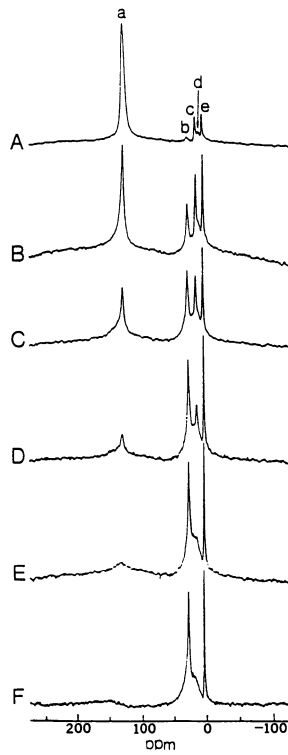


Figure 1. ^{13}C MAS NMR spectra of ethylene adsorbed on Ru-Na-Y zeolite at room temperature: (A) immediately, (B) 2 days, (C) 4 days, (D) 8 days, (E) 12 days, (F) 14 days after sample preparation

secondary carbons ($-\text{CH}_2-$) of butane, while peak (d) is the terminal carbons. During the first several days after sample preparation, the intensity of peak (c) (20 ± 2 ppm) increases very rapidly and then decreases. This suggests that peak (c) derives from intermediates in the reaction. Although ethylene contributes to peak (a) initially, it very rapidly converts to 2-butenes which also give rise to peak (c). The resolution obtained in these experiments does not allow separation of the cis and trans isomer. 2-butene was also released from the catalyst upon evacuation. After 14 days virtually all of the ethylene and butene have been hydrogenated. The lifetime of ethylene on Ru-Y is substantially longer than that observed by Gerstein et al.¹ on Ru-SiO₂. This may be due to a quantum size effect of very small metal particles in zeolites. It has been postulated that small particles in zeolites are "electron deficient".(10)

The coadsorption of 0.222 mg/g H₂ with ethylene accelerates the reaction and increases the relative amount of ethane produced. In another experiment the H₂ dose was reduced by half. The rate and the amount of ethane produced are diminished. The initial rate for ethylene reaction on Ru-Na-Y zeolite is dependent upon hydrogen concentration to approximately first order. This agrees with previous studies of ethylene hydrogenation.(11) Table I lists the rate dependence of loss of ethylene on the initial concentration of hydrogen.

Table I. Rate of ethylene hydrogenation

	initial ¹³ C ₂ H ₄ (mg/g)	initial H ₂ (mg/g)	slope X 10 ⁻⁵ (mg/g·s ⁻¹)	initial rate X 10 ⁻⁵ (mol/Ru·s)
1.	18.705	0.117	9.614	2.43
2.	17.187	0.222	14.85	4.45

NMR results for the adsorption of ethylene on reduced Ru exchanged Ca-Y zeolite are shown in Figure 2. By 3 days only peaks b, d, e and a small broad remnant of peak a remain. The reaction of ethylene to butane and ethane appears to be complete in 5 days. Figure 3 shows the ¹³C NMR spectrum of ethylene coadsorbed with hydrogen on reduced Ru exchanged H-Y zeolite. Data acquisition was complete within 1 hour of adsorption. Ethylene has completely reacted to form butane and ethane. With time no further changes are observed with ¹³C NMR.

The temperature dependence of ethylene's reaction on metal surfaces was studied. Figure 4A is a spectrum of a sample of Ru- Ca-Y exposed to ethylene at room temperature then heated at 373 K for 3 days. While ethane and n-butane are still observed, two new peaks appear at 23 ± 2 ppm and -8 ± 2 ppm. Their assignment was confirmed by observing the scalar coupling (Figure 4B). The splitting indicates that the peak at 23 ppm is due to isobutane. This was further confirmed by adsorbing isobutane on this same sample. The chemical shift agrees exactly with that observed in Figure 4. The formation of isobutane from olefins in Y zeolites has previously been reported.(12,13) The isobutane probably arises from conversion of n-butane by acid sites in the zeolite via a carbonium ion intermediate. The peak observed at -8 ppm corresponds to methane produced by the cleavage of the carbon-carbon bond. Enriched methane adsorbed on this zeolite sample is also found at -8 ppm.

The adsorption was studied at higher temperatures. At 573 K, ethylene adsorbed on Ru-Na-Y zeolite is immediately converted to ethane and some methane.

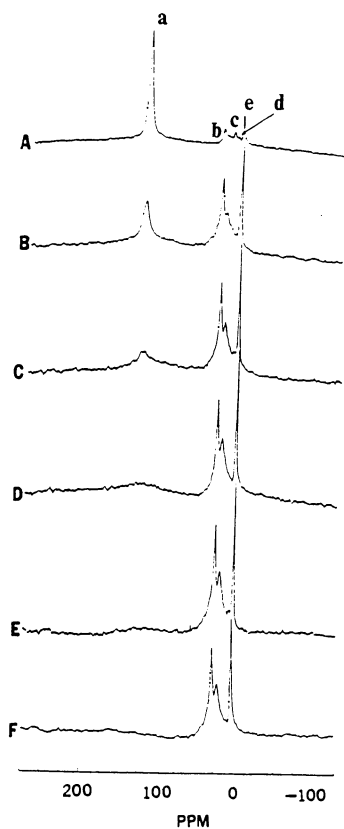


Figure 2. ^{13}C MAS NMR spectra of ethylene adsorbed on Ru-Ca-Y zeolite at room temperature: (A) immediately, (B) 1 day, (C) 2 days, (D) 3 days, (E) 4 days, (F) 5 days after sample preparation

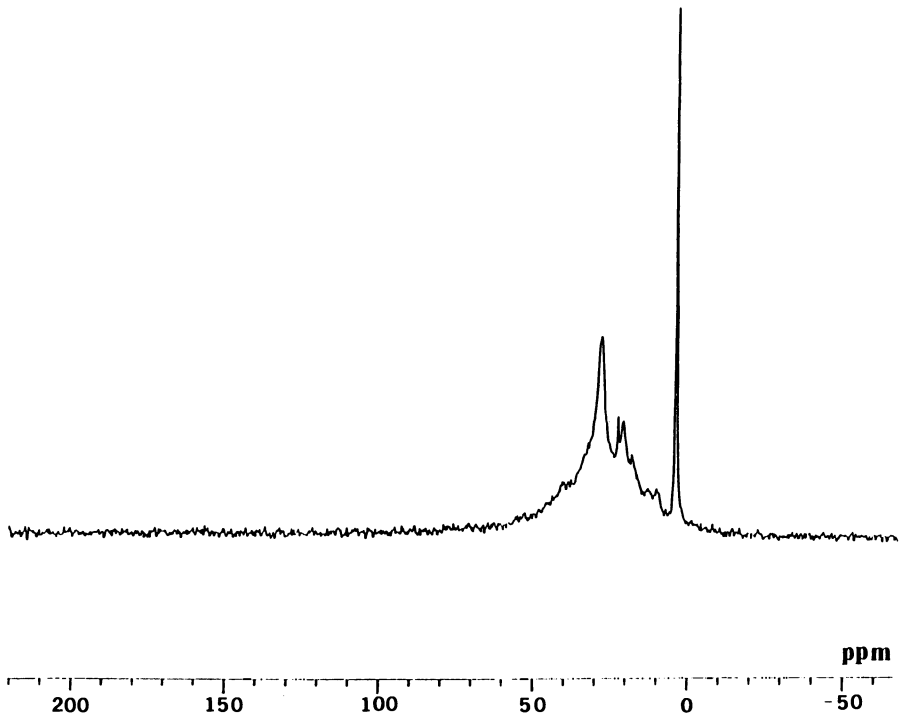


Figure 3. ^{13}C NMR spectrum of ethylene adsorbed on Ru-H-Y at room temperature acquired immediately after sample preparation

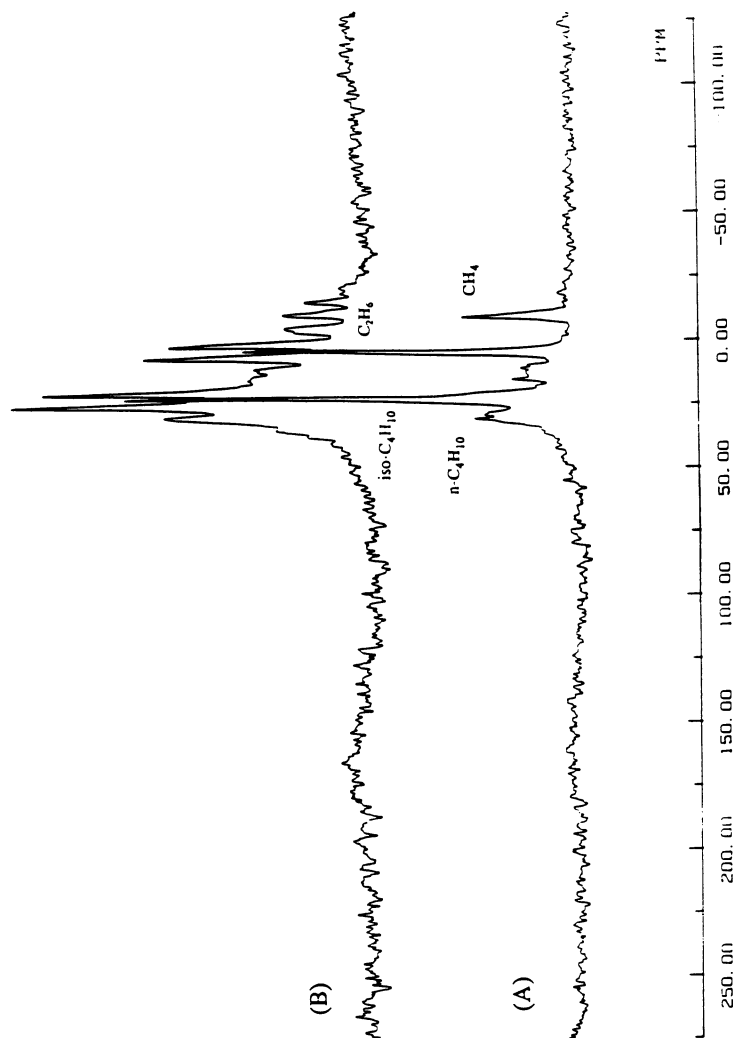


Figure 4. ^{13}C NMR spectrum of ethylene adsorbed on Ru-Ca-Y zeolite heated to 373 K (A) with proton decoupling, (B) without proton decoupling

At 623 K, we observe only methane. Thus, the carbon-carbon bond cleavage is complete between 573 K and 623 K.

Conclusions

A comparison of the reactions of ethylene on three kinds of Ru-Y zeolites shows that the self-hydrogenation rate has the order Ru-H-Y > Ru-Ca-Y > Ru-Na-Y. The hydrogenation rate depends on the amount of coadsorbed hydrogen to roughly first order. The presence of polymerization products beyond butane is not observed. The reactions of ethylene are affected by reaction temperature with some rearrangement of butane to isobutane at intermediate temperatures. Carbon-carbon bond cleavage to methane predominates above 573K.

Acknowledgments

This work was supported by the National Science Foundation under grant CHE8718850.

References

1. Pruski, M.; Kelzenberg, J. C.; Gerstein, B. C.; King, T. S. *J. Am. Chem. Soc.*, **1990**, *112*, 4232.
2. Hwang, S. J.; King, T. S.; Gerstein, B. C. private communication.
3. Wang, P. K.; Slichter C. P.; Sinfelt, J. H. *J. Phys. Chem.*, **1985**, *89*, 3060.
4. Gay, I. D. *J. Catal.*, **1987**, *108*, 15.
5. Breck, D. W. *Zeolite Molecular Sieve*, John Wiley & Sons: New York, NY, 1974; pp.529-588.
6. Cotton F. A.; Wilkinson, G. *Advanced Inorganic Chemistry*, Interscience: New York, NY, 1972; p.1011.
7. Nijs, H. H.; Jacobs, P. A.; Uytterhoeven, J. B. *J.C.S.Chem.Comm.*, **1979**, 180.
8. Verdonck, J. J.; Jacobs, P. A.; Uytterhoeven, J. B. *J.C.S.Chem.Comm.*, **1979**, 181.
9. Denney, D.; Mastikhin, V. M.; Namba, S.; Terkevich, J. *J. Phys. Chem.*, **1978**, *82*, 1752.
10. Rabo, J.; Shomaker, V.; Pickert, P. *Proc. 3rd Intl. Cong. Catalysis*, North Holland Publishing: Amsterdam, NY, 1965; Vol. 2, p 1264.
11. Thomson, S. J.; Webb, G. *Heterogeneous Catalysis*, John Wiley & Sons: New York, NY, 1968; p.118.
12. White, J. L.; Lazo, N. D.; Richardson, B. R.; Haw, J. F. *J. Catal.*, **1990**, *125*, 260.
13. Weitkamp, J. In *Catalysis by Zeolites, Studies in Surface Science and Catalysis 5*, Editor, Imelik, B. et al., Elsevier: Amsterdam, 1980; p.65.

RECEIVED July 29, 1992

Chapter 24

Activation of C–H, C–C, and C–O Bonds of Oxygenates on Rh(111)

N. F. Brown and M. A. Barteau

Center for Catalytic Science and Technology, Department of Chemical Engineering, University of Delaware, Newark, DE 19716

Decarbonylation of oxygenates to liberate CO, H₂, and volatile or adsorbed hydrocarbons has been observed on single crystal surfaces of a number of Group VIII metals. The details of this chemistry hold the promise of providing new insights into catalytic processes which are essentially its reverse, e.g., higher oxygenate synthesis from CO and H₂, and heterogeneous hydroformylation of olefins. The results of our studies of ten C₂ and C₃ oxygenates on Rh(111) demonstrate, however, that the decarbonylation network for these probe molecules is far more complicated than previously recognized. Higher aliphatic aldehydes release CO plus alkyl groups via decarbonylation on Rh(111), these alkyls are hydrogenated to volatile alkanes. Higher alcohols do not dehydrogenate to aldehydes, and do not release volatile hydrocarbon products. Parallels between the reactions of alcohols and epoxides suggest that both form oxametallacycle intermediates on the surface. The divergence of alcohol and aldehyde decarbonylation pathways persists for the unsaturated oxygenates acrolein and allyl alcohol; although both ultimately deposited CO, H, and CH₃C≡ species on the surface, only acrolein liberated volatile C₂ hydrocarbons. Of the ten oxygenates examined, decarbonylation reactions must release at least five different hydrocarbon ligands to the surface in order to account for the range of behavior observed in TPD and HREELS experiments. This suggests that the identities of the primary products of CO insertion on metal catalysts may depend on the identities of the surface hydrocarbon ligands undergoing insertion.

There can be little doubt that oxygen-containing hydrocarbons (oxygenates) will play an increasingly prominent role as components of motor fuels and, potentially, as raw materials for other petrochemical-based processes. The last decade has seen increasing use of oxygenates, including alcohol blends and methyl tertiary butyl ether (MTBE), as octane

enhancers in gasoline. Current trends include the introduction of "environmental gasolines," reduction of some high octane hydrocarbons including butanes and aromatics, and legislative requirements for increased oxygen content as a means of improving air quality (1).

The last decade and a half have seen a great deal of attention devoted to the synthesis of higher molecular weight products from CO and H₂ with supported transition metal catalysts. Strategies for the production of higher oxygenates have centered primarily around two classes of catalysts: supported group VIII metals (typically rhodium) and modified methanol synthesis catalysts (based on Cu/ZnO/Al₂O₃). The operative mechanisms of higher oxygenate synthesis on these two classes of materials are generally proposed to be different. That for group VIII metals has been suggested by numerous workers to involve hydrocarbon chain growth from CH_x units on the surface, with oxygenates formed via termination of chain growth by CO insertion and subsequent hydrogenation (2-4). On modified methanol catalysts chain growth is viewed as the result of various condensation reactions of oxygen-containing intermediates (5-7). While these sequential reaction networks involving competing chain growth and termination steps are adequate to produce the typical Anderson-Schultz-Flory distribution of product chain lengths, it is not clear that they can adequately describe the selectivity to various products having the same number of carbon atoms. For example, it is typically suggested in the above network for metal-catalyzed reactions that C_{n+1} oxygenates are formed by addition of CO to a C_n hydrocarbon ligand on the metal to form an acyl; the sequential hydrogenation of this intermediate leads in succession to aldehyde and alcohol products. Evidence for the sequential hydrogenation of aldehydes to alcohols in the CO + H₂ reaction on rhodium has been provided by Underwood and Bell (8), but conflicting evidence can be found in isotopic tracer studies by Takeuchi and Katzer (9) and Orita et al. (10). In the latter case, ethanol and acetaldehyde were observed to have different distributions of labelled carbon, suggesting that they are not formed by a common mechanism. If so, then the identity of the oxygenate product would depend on the identity of the hydrocarbon ligand to which CO is added, rather than on the extent of hydrogenation of the product after CO insertion.

A second conundrum is evident from the lack of successful exploitation of the analogy between homogeneous and heterogeneous hydrocarbon hydroformylation catalysis. The scheme usually proposed (3-5) and outlined above for supported metal-catalyzed oxygenate synthesis is essentially the hydroformylation of surface hydrocarbon ligands derived from CO and H₂. The exact identity of these hydrocarbon species (alkyl, alkylidene, olefin, etc.) has been much debated. In contrast to the state of affairs in heterogeneous catalysis of higher oxygenate synthesis, homogeneously catalyzed carbonylation and hydroformylation reactions are both well understood and commercially practiced. For example, the essential step in commercial Rh-catalyzed olefin hydroformylation and methanol carbonylation processes is CO insertion into a metal-alkyl bond. The mononuclear rhodium complexes cycle between the +1 and +3 oxidation state in both systems (11). Putative analogies between homogeneous and heterogeneous catalysis have led various workers to postulate and to search for cationic transition metal species on active and selective oxygenate synthesis catalysts. Both the Tamaru (12) and Ponec (13) groups proposed, for example, that zero-valent Pd would not lead to methanol synthesis over supported Pd catalysts. The latter group demonstrated a positive correlation between methanol synthesis activity and the concentration of Pd⁺¹ ions on the catalyst extractable with acetyl acetonate. These conclusions have since been called into question by other workers (14-16). Moreover, the Ponec group demonstrated a *negative* correlation between higher oxygenate activity and Rh⁺¹ extractable from supported rhodium

catalysts (17). Perhaps it is not surprising that the hydroformylation analogy has not advanced much further.

Surface science studies of oxygenate chemistry permit one, in principle, to enter these complex reaction networks via the products and to trace the sequence of reactions back to proposed intermediates and reactants. For example, studies of higher oxygenate decomposition on metals such as Ni (18), Pd (19), and Pt (20) have all demonstrated that the principal reaction pathway is decarbonylation to CO, H(ad), and a hydrocarbon one unit shorter than the parent, in excellent agreement with the picture above of CO insertion as a chain-termination step. On Pd(111) it can even be shown that the decarbonylation of higher alcohols leads precisely through the sequence of steps suggested above; from alcohol to alkoxide to aldehyde to acyl to CO plus a hydrocarbon one unit shorter. On Rh(111) however, in keeping with the confusion noted above, a purely sequential reaction network cannot account for the difference in the decarbonylation behavior of higher oxygenates. This paper describes the complexity of decarbonylation networks on Rh(111), and the menagerie of surface hydrocarbon ligands required to account for them.

Experimental

Temperature Programmed Desorption (TPD) and High Resolution Electron Energy Loss Spectroscopy (HREELS) studies have been carried out after adsorption of three different C₂-oxygenates and seven different C₃-oxygenates on the Rh(111) surface in the apparatus described previously (21). All adsorption experiments described below were carried out to saturation of the first monolayer on a Rh(111)-oriented single crystal, prepared as described (22), with the surface held between 90 K and 100 K. TPD experiments involved ramping the sample temperature at a rate of 4 K s⁻¹ while monitoring the desorbing products with a collimated UTI 100 C mass spectrometer. HREEL spectra were all acquired at the adsorption temperature; spectra characteristic of the adlayers at higher temperatures were obtained after brief heating to the desired temperature followed by cooling to the original temperature. A variety of oxygen-containing reactants were examined including ethanol, acetaldehyde, ethylene oxide, propanal, 1-propanol, acrolein, allyl alcohol, acetone, and 2-propanol; each was dosed onto the surface from the vapor phase via a needle doser connected to a valve external to the chamber. All exposures are reported in Langmuirs (1 L = 10⁻⁶ torr·sec). All other experimental procedures were as previously described (21).

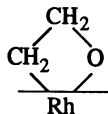
Results

While adsorbed primary alcohols on the Pd(111) surface dehydrogenate sequentially to form the corresponding adsorbed aldehyde and acyl species prior to their decarbonylation (23), we have found no evidence for aldehyde formation from primary alcohols on Rh(111) (21,24). Instead, alcohol and aldehyde decarbonylation pathways on Rh(111) appear to be non-intersecting. This surprising divergence of reaction pathways for such closely related molecules is demonstrated by two critical observations:

1. Volatile hydrocarbon products one unit shorter than the parent were consistently produced by decarbonylation of aldehydes, but *not* of alcohols.
2. CO elimination from ethanol and 1-propanol occurred at lower temperature than from acetaldehyde and propanal, thus the latter cannot be intermediates in the reactions of the former.

Primary alcohols dissociate to form stable alkoxides below 150 K on Rh(111) (21,22,24). The range of possible subsequent bond scission steps is fairly limited, especially for smaller

molecules. For example, if the ethoxide does not undergo C–H scission at the α position to form acetaldehyde, the only alternative C–H scission would be at the β position. β -CH activation would form not an aldehyde, but an oxametallacycle of the form:



There are numerous precedents for such proposed intermediates for mononuclear metal complexes in solution (25), and such cyclic adsorbates on an extended metal surface should experience less ring strain than their mononuclear counterparts in solution.

In order to test the hypothetical formation of surface oxametallacycles, we have examined the decarbonylation reactions of epoxides such as ethylene oxide ($\text{CH}_2\text{CH}_2\text{O}$) and propylene oxide ($\text{CH}_3\text{CHCH}_2\text{O}$) on the Rh(111) surface. Simple ring opening of these molecules by C–O scission should produce oxametallacycles analogous to those postulated for the alkoxides; a 1,2 hydrogen shift accompanied by ring opening would produce the aldehydes which are isomers of these epoxides. In fact, as shown by Figures 1 and 2, the decarbonylation of these epoxides parallels that of the primary alcohols and *not* that of the isomeric aldehydes. Methane desorbed from the Rh(111) surface during the course of acetaldehyde decarbonylation but *not* during those of ethanol or ethylene oxide. Similarly, propanal released ethane, but no hydrocarbons desorbed during TPD experiments with either 1-propanol or propylene oxide. Taking account of the different yields of CO and H_2 from the

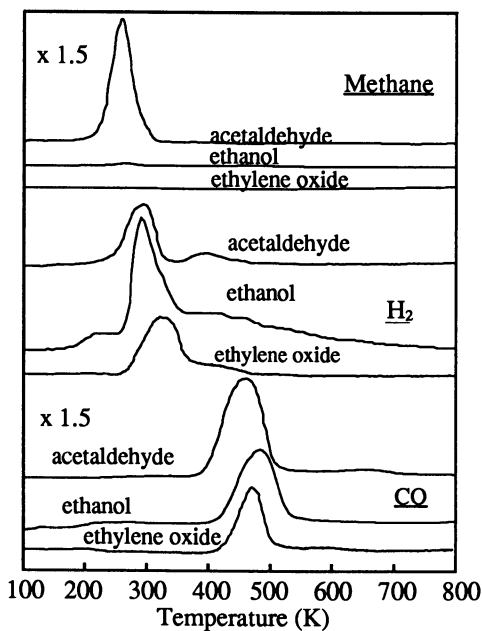


Figure 1. A comparison of product TPD spectra obtained after exposure of 1.5 L acetaldehyde, 1.1 L ethanol, or 3.9 L ethylene oxide to the clean Rh(111) surface at ca. 91K.

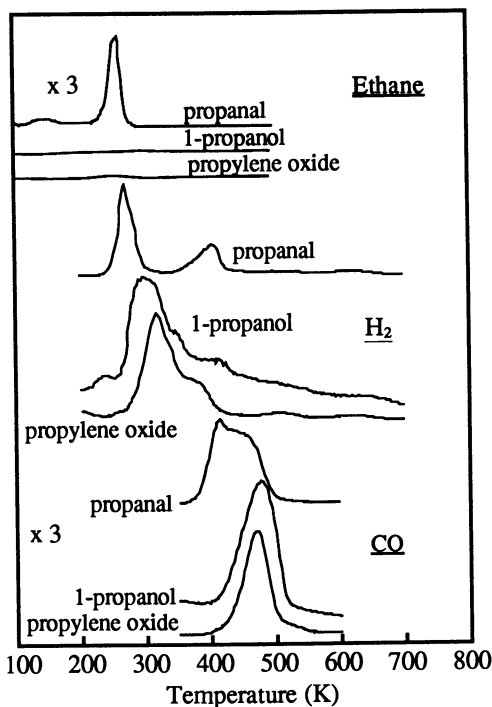


Figure 2. A comparison of product TPD spectra obtained after exposure of 1.6 L propanal, 2.3 L 1-propanol, or 2.1 L propylene oxide to the clean Rh(111) surface at ca. 91 K.

alcohols and epoxides, and the coverage dependence of the kinetics of reactions such as H atom recombination, the TPD spectra for the primary alcohols and epoxides were in excellent agreement, and were distinguishable from those of the aldehydes of the same chain length. For example, the CO desorption peak from propanal was broadened and shifted to lower temperature relative to those for CO from the clean Rh(111) surface or for CO eliminated from 1-propanol or propylene oxide. This CO peak shift has been shown to be characteristic of CO adsorbed in the presence of ethylidyne ($\text{CH}_3\text{C}\equiv$) species (26) and, indeed, ethylidyne formation was observed by HREELS from propanal but not from 1-propanol or propylene oxide (24). Thus the common decarbonylation routes for epoxides and for primary alcohols support the intermediacy of the proposed oxametallacycles in each.

The formation of such multiply coordinated surface intermediates would be expected to be enhanced by adsorption of multi-functional reagents, e.g., oxygenates with hydrocarbon chains more reactive than saturated alkyl ligands. To test this hypothesis, we have also examined the adsorption and reaction of allyl alcohol ($\text{CH}_2=\text{CH}-\text{CH}_2\text{OH}$) and acrolein ($\text{CH}_2=\text{CH}-\text{CHO}$) on the Rh(111) surface. While these molecules do exhibit evidence for interaction with the surface via both their oxygen and vinyl functions, and while they appear to preserve the divergence of decarbonylation pathways observed for their aliphatic counterparts, their reactivity patterns add yet another layer of complexity to the puzzle of oxygenate decarbonylation.

Temperature programmed desorption experiments with acrolein and allyl alcohol were qualitatively consistent with the results for the other C₃-oxygenates depicted in Figure 2. Acrolein decarbonylation gave rise to ethane at ca. 260 K (27) as did that of propanal (24), but small amounts of ethylene were also formed from acrolein (27). Allyl alcohol, like its aliphatic counterparts, produced no volatile hydrocarbon products. However, it differed from 1-propanol in the identity of the hydrocarbon ligand deposited on the surface. As shown by the HREEL spectra of Figure 3, decarbonylation of propanal, acrolein, and allyl alcohol led to the formation of recognizable surface ethylidyne intermediates (fingerprinted by the pattern of peaks at 980, 1135, and 1370 cm⁻¹), but 1-propanol did not. Thus for these four C₃ oxygenates, four different reactivity patterns (and four different decarbonylation temperatures) were observed, as summarized in Table I. Propanal produced ethane and ethylidynes, acrolein produced these plus ethylene, allyl alcohol produced ethylidynes but no ethane or ethylene, and 1-propanol produced neither ethylidynes nor volatile C₂ hydrocarbons. These observations suggest that the divergence of reaction pathways is not just two-fold but four-fold: all four of these C₃ oxygenates follow a different path to CO, producing a different hydrocarbon moiety from each.

Table I. Summary of C₃-O Decarbonylation Reactions

Reactant	Decarbonylation Temperature (K)	Volatile Hydrocarbon Product	Adsorbed Hydrocarbon Intermediate
CH ₃ CH ₂ CHO	251	C ₂ H ₆	CH ₃ C≡
CH ₂ =CHCHO	201	C ₂ H ₆ + C ₂ H ₄	CH ₃ C≡
CH ₂ =CHCH ₂ OH	278	None	CH ₃ C≡
CH ₃ CH ₂ CH ₂ OH	226	None	CH _x

Discussion

Of the ten different C₂ and C₃ oxygenates examined on the Rh(111) surface to date, at least five and as many as seven different hydrocarbon ligands must be involved as initial elimination products to explain the diversity of their behavior in TPD and HREELS experiments. A summary of these observations and proposed sequences of bond activation is contained in Table II; the logic behind this proposal is described below.

Aldehyde decarbonylation on Rh(111) liberates volatile hydrocarbons one unit shorter than the parent. Previous experiments have demonstrated that there is no kinetic isotope effect observed in the kinetics of CH₃CHO vs. CD₃CDO decarbonylation, but CH₃D can be formed cleanly by decarbonylation of CH₃CHO in the presence of adsorbed deuterium atoms (21). These two results strongly suggest that alkyl groups are eliminated intact in the decarbonylation of aliphatic aldehydes; these add one H from the surface to form the corresponding alkanes or, in the case of ethyl ligands, undergo parallel dehydrogenation to form stable ethylidynes. The C-C bond scission step liberating alkyl ligands does not

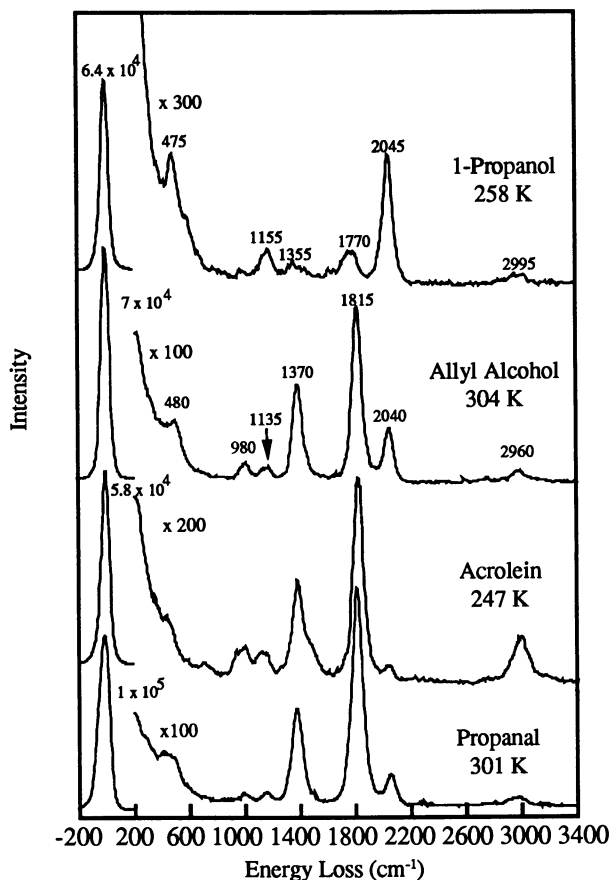


Figure 3. HREEL spectra observed after exposure of 2.2 L propanal, 2.6 L acrolein, 1.3 L allyl alcohol, or 2.3 L 1-propanol to the clean Rh(111) surface and annealing to 301 K, 247 K, 304 K, and 258 K, respectively, to complete the decarbonylation reaction.

necessarily occur for the intact aldehyde, but likely involves acyl ligands formed from aldehydes via an initial C-H bond scission step.

C-C scission in the unsaturated acyl formed from acrolein would release vinyl ($\text{CH}_2=\text{CH}-$) ligands to the surface. Isomerization of these would lead to stable ethylidynes, hydrogenation, to volatile ethylene and ethane. The observation that acrolein decarbonylates at lower temperature than does propanal suggests that these hydrogenation steps must follow C-C scission; propanal cannot be an intermediate in the acrolein decarbonylation sequence.

Oxametallacycle formation from aliphatic alkoxides could occur via C-H scission at the β position, or from epoxides by C-O scission to open the ring. The subsequent C-H and C-C bond activation steps are less clear than those of the aldehydes above. For the oxametallacycle formed from the ethoxide, C-C scission must release CH_2 or perhaps CH

Table II. Summary of Bond Activation Sequences for C₂ and C₃ Oxygenates on Rh(111)

Reactant	Volatile Hydrocarbon Product Observed	Adsorbed Hydrocarbon Product Observed	Proposed Ligand Eliminated	Proposed Bond Activation Sequence (Greek letters designate C-H bonds at that position)
CH ₃ CH ₂ OH β α	none	CH _x	CH ₂	OH, β, α, C-C
CH ₃ CHO β α	CH ₄	CH ₃	CH ₃	α, C-C
CH ₂ CH ₂ O β α	none	CH _x	CH ₂	C-O, α, C-C
CH ₃ CH ₂ CH ₂ OH γ β α	none	CH _x	CCH ₂	O-H, β, α, β, γ, C-C
CH ₃ CH ₂ CHO γ β α	C ₂ H ₆	CCH ₃	C ₂ H ₅	α, C-C
CH ₃ CHCH ₂ O γ β α	none	CH _x	CCH ₂	C-O, α, β, γ, C-C
CH ₂ =CHCH ₂ OH γ β α	none	CCH ₃	HCCH	O-H, γ, C-C
CH ₂ =CHCHO γ β α	C ₂ H ₆ , C ₂ H ₄	CCH ₃	CHCH ₂	α, C-C
CH ₃ CHOHCH ₃ β α β	none	CH _x	CH	O-H, β × 4, C-C × 2
CH ₃ COCH ₃ β α β	none	CH _x	CH	β × 4, C-C × 2

groups to the surface. These do not appear to be hydrogenated to methyl groups or methane under the UHV conditions prevailing in these surface studies. The situation for 1-propanol decarbonylation is less certain. Clearly, additional C-H scissions are necessary to account for the absence of C₂H₆ or ethylidyne formation. Direct C-C scission in the intermediate oxametallacycle would release ethylidene ligands (CH₃CH=) almost any reaction or rearrangement of which should lead to proscribed species such as ethane, ethylene, vinyl or ethylidyne. Thus it appears likely that substantial dehydrogenation occurs along the hydrocarbon tail of the oxametallacycle prior to C-C scission, and the C₂ hydrocarbon eliminated can possess no more than two hydrogen atoms if intersection with the products of propanal

or acrolein dehydrogenation is to be avoided. Allyl alcohol produces ethylidyne, unlike 1-propanol, but does not liberate volatile C_2 hydrocarbons, unlike acrolein. Possible ligands which might be eliminated from allyl alcohol include ethylidyne, $CH_3C\equiv$, vinyl, $CH_2=CH-$, acetylene, $H-C\equiv C-H$, or vinylidene, $CH_2=C=$. Objections can be raised with respect to each of these possibilities. Ethylidyne elimination would require prior H shifts along the hydrocarbon tail, for which there is little evidence among any of the other oxygen-containing adsorbates. Vinylidene elimination would put allyl alcohol and propanol decarbonylation on a common path, but stable ethylidyne were produced only from the former. Acetylene satisfies all of the observations, and has been shown to form ethylidyne and ethylene by hydrogenation on Rh(111), but the absence of volatile C_2H_2 or C_2H_4 products from allyl alcohol is then somewhat troubling. Vinyl elimination from allyl alcohol would put allyl alcohol and acrolein decarbonylation on a common path, and would appear to be in conflict with the observation of volatile hydrocarbons in one case but not the other. However, it should be noted that release of CO from allyl alcohol occurs above 275 K while that from acrolein begins at 200 K. Thus elimination of a vinyl moiety in both cases could still be feasible, provided that the activation barrier for isomerization to ethylidyne is greater than that for hydrogenation to ethylene; the isomerization/hydrogenation selectivity would then increase with increasing temperature. In any case the *minimum* number of different hydrocarbon ligands required to account for the behavior of the first eight reactants in Table II is five: $CH_{x<3}$, CH_3 , C_2H_5 , CH_2CH and $CH_2=C=$. Clearly in spite of their affinity for decarbonylation, the number of routes to this end is nearly as large as the number of reactants. Microscopic reversibility would therefore suggest that carbonylation of different surface hydrocarbon ligands should lead to different primary products, subsequent reactions of which may or may not lead to a common product slate.

A final note concerns oxygenates in which oxygen is not bound to a terminal carbon, e.g., acetone and 2-propanol. CO elimination from either of these prior to C-H scission at a terminal methyl group might be expected to lead to methane formation; in fact no methane was produced from either acetone or 2-propanol on the Rh(111) surface (28,29). The relative intensities of the hydrogen desorption peaks in acetone TPD on the Rh(111) suggests that four H atoms are lost prior to C-C scission, suggesting that CH groups are deposited on the surface. It is not clear that these are distinguishable from the CH_x species eliminated from ethanol or ethylene oxide. Even if they do not differ, the *minimum* number of different hydrocarbon ligands eliminated via decarbonylation of the oxygenates in Table II is one-half the number of reactants. This surprisingly large fraction does not bode well for proposed universal mechanisms of CO insertion and oxygenate production.

Conclusions

Decarbonylation of higher oxygenates on the Rh(111) surface leads to volatile hydrocarbons only in the case of aldehydes. Higher alcohols do not form adsorbed aldehydes, but appear to undergo β -CH scission to form surface oxametallacycles. These postulated intermediates can also be formed by C-O scission in epoxides. Of the ten C_2 and C_3 oxygenates examined, elimination of at least five different hydrocarbon ligands must be involved in the decarbonylation step to explain the variations observed in the identity of adsorbed and volatile products.

Acknowledgment

We gratefully acknowledge the support of the research by the Department of Energy, Office of Basic Energy Sciences, Division of Chemical Sciences (Grant FG02-84ER 13290).

Literature Cited

1. Ecklund, E. F.; Mills, G. A. *Chemtech* **1989**, 19, 549.
2. Bell, A. T. *Catal. Rev.—Sci. Eng.* **1981**, 23, 203.
3. Biloen, P.; Sachtler, W. M. H. *Adv. Catal.* **1981**, 30, 165.
4. Ponec, V. *Catalysis—Specialist Periodical Reports* **1981**, 5, 48.
5. Nunan, J. G.; Bogden, C. E.; Klier, K.; Smith, K. J.; Young, C. W.; Herman, R. G. *J. Catalysis* **1989**, 116, 195.
6. Mazanec, T. J. *J. Catalysis* **1986**, 98, 115.
7. Elliott, D. J.; Pennella, F. *J. Catalysis* **1989**, 119, 359.
8. Underwood, R. P.; Bell, A. T. *Appl. Catalysis* **1986**, 21, 157.
9. Takeuchi, A.; Katzer, J. R. *J. Phys. Chem.* **1982**, 86, 2438.
10. Orita, H.; Naito, S.; Tamaru, K. *J. Catalysis* **1984**, 90, 183.
11. Dekleva, T. W.; Forster, D. *Adv. Catal.* **1986**, 34, 81.
12. Kikuzono, Y.; Kagami, S.; Naito, S.; Onishi, R.; Tamaru, K. *Faraday Disc Chem. Soc.* **1982**, 72, 135.
13. Driessen, J. M.; Poels, E. K.; Hindermann, J. P.; Ponec, V. *J. Catalysis* **1983**, 82, 26.
14. Rieck, J. S.; Bell, A. T. *J. Catalysis* **1985**, 96, 88.
15. Deligianni, H.; Mieville, R. L.; Peri, J. B. *J. Catalysis* **1985**, 95, 465.
16. Berlowitz, P. J.; Goodman, D. W. *J. Catalysis* **1987**, 108, 364.
17. van der Lee, G.; Schuller, B.; Post, H.; Favre, T. L. F.; Ponec, V. *J. Catalysis* **1986**, 98, 522.
18. Gates, S. M., Russell, J. N., Jr.; Yates, J. T., Jr. *Surface Sci.* **1986**, 171, 111.
19. Davis, J. L.; Barteau, M. A. *Surface Sci.* **1987**, 187, 387.
20. Sexton, B. A.; Rendulic, K. D.; Hughes, A. E. *Surface Sci.* **1982**, 121, 181.
21. Houtman, C. J.; Barteau, M. A. *J. Catalysis* **1991**, 130, 528.
22. Houtman, C.; Barteau, M. A. *Langmuir* **1990**, 6, 1558.
23. Davis, J. L.; Barteau, M. A. *Surface Sci.* **1990**, 235, 235.
24. Brown, N. F.; Barteau, M. A. *Langmuir* **1992**, 8, in press.
25. Jørgensen, K. A.; Schiøtt, B. *Chem. Rev.* **1990**, 90, 1483.
26. Blackman, G. S.; Kao, C. T.; Bent, B. E.; Mate, C. M.; Van Hove, M. A.; Somorjai, G. A. *Surface Sci.* **1988**, 207, 66.
27. Brown, N. F.; Barteau, M. A. *J. Am. Chem. Soc.* **1992**, 114, in press.
28. Houtman, C.; Barteau, M. A. *J. Phys. Chem.* **1991**, 95, 3755.
29. Xu, X. P.; Friend, C. M. *Surface Sci.* (submitted).

RECEIVED June 22, 1992

Chapter 25

Continuous Catalytic Conversion of Acetylene to Higher Hydrocarbons over a Metal Modified Shape Selective Zeolite Catalyst

Yigong He, Benjamin W.-L. Jang, and Richard B. Timmons

Department of Chemistry, The University of Texas at Arlington, Box 19065, Arlington, TX 76019-0065

This paper describes the catalytic conversion of C_2H_2 to higher hydrocarbons. The continuous conversion of C_2H_2 is achieved using a bifunctional nickel modified ZSM-5 shape selective zeolite catalyst which combines catalytic activity of the added Ni with the acidic/shape selectivity properties of the ZSM-5. Additionally, the successful conversion process requires the addition of an added reactant (e.g., H_2O) to the C_2H_2 stream. Dependent on reaction conditions employed, significant variations in the hydrocarbon product distributions are observed with respect to the relative amounts of paraffins, olefins and aromatics produced. Evidence is obtained for the intermediate formation of CH_3CHO (i.e., from $C_2H_2 + H_2O$) which is believed to react further with C_2H_2 to provide the hydrocarbon plus CO product yields observed.

The continuous conversion of acetylene to higher hydrocarbons has been the subject of numerous catalytic investigations. Although C_2H_2 oligomerization is promoted by a wide variety of catalysts, the oligomerization reactions have, without exception, been accompanied by rapid catalyst deactivation (1-6). In fact, even catalytic and spectroscopic studies involving only batch and pulse type experiments have revealed significant catalyst modifications after relatively limited contact between the catalyst and C_2H_2 (7-11). Catalytic materials employed in C_2H_2 conversions include various zeolites, aluminum oxide, fluorinated aluminum oxide, single crystal metals and various metal supported catalysts.

The difficulty of maintaining continuous catalytic conversion of acetylene to higher hydrocarbons results from rapid coking of the catalysts. Whereas initial oligomerization of C_2H_2 is easily induced, this process is accompanied with a marked tendency for polymerization of the C_2H_2 to yield various polycyclic aromatics or other high molecular weight polymers. Allenger et al. have provided a detailed recent discussion of many important aspects of these oligomerization and polymerization processes (6).

The purpose of the present study is to describe a new approach to the successful continuous catalytic conversion of C_2H_2 to higher hydrocarbons (12). The rapid catalyst poisoning which has plagued all previous attempts at this

conversion has been overcome using a bifunctional catalyst consisting of a metal modified shape selective ZSM-5 catalyst *coupled* with the addition of an added hydrogen donor reactant (e.g., H₂O) to the C₂H₂ reactant stream. The catalytic conversion process developed provides a remarkably stable conversion of C₂H₂ to higher hydrocarbons, with this conversion having been demonstrated for extended periods of time without noticeable catalyst deactivation. Furthermore, the composition of the hydrocarbon product mix obtained (i.e., the relative proportions of paraffins to olefins to aromatics) can be varied as a function of the reaction conditions employed. The details of this conversion process along with the mechanistic implications involved are described in this paper.

Experimental

A fixed-bed continuous flow microreactor operating at atmospheric pressure was employed in this work. The catalyst was located in the center of a 0.64 cm x 15 cm stainless steel reactor tube mounted vertically in a bored cylindrical block aluminum furnace. The furnace temperature was adjusted and maintained using an Omega Engineering CN-2010 Series programmable temperature controller. Gas flows were measured using calibrated flow meters. The liquid reactants were provided to the reactor by bubbling acetylene through a thermostated container of the liquid. The effluent gas mixture of C₂H₂ + vaporized liquid was fed directly to the catalyst bed using a heated transfer line to prevent liquid condensation. The amount of liquid reactant provided as vapor was determined by periodic weighing of the liquid containing vessel.

The shape selective ZSM-5 catalyst employed had a Si/Al ratio of 30. The sodium cations present in this material were exchanged for NH₄⁺ ions by contacting the catalyst with a solution of (NH₄)₂SO₄. Specifically, this cation exchange was carried out using weight ratios of 1 g (NH₄)₂SO₄ : 1 g ZSM-5 : 10 g H₂O. The NH₄-ZSM-5 material obtained after drying was calcined at 550 °C for 3 hours after which it was mixed with 0.5 M HNO₃ at 70 °C for 3 hours at a mixing ratio of 1 gram of catalyst per 40 mL of HNO₃ solution. The use of the HNO₃ treatment results in a protonated product with a lower sodium content than that produced by ammonium exchange. The solid catalyst, at this point in the form of H-ZSM-5, was filtered from solution and dried at 120 °C. This solid was then blended with Al(OH)₃ at a weight ratio of 40 parts zeolite to 60 parts Al(OH)₃. This ZSM-5/Al(OH)₃ mixture was then added to a solution of nickel(II) nitrate and the resulting solution evaporated to dryness. The extent of nickel loading of the final catalyst is determined by the volume and concentration of the Ni(NO₃)₂ solution employed. Two separate procedures were employed in reducing the Ni²⁺ to the elemental state. In the first procedure, the solid mixture of Ni(NO₃)₂/ZSM-5/Al(OH)₃ was calcined at 550 °C for 2 hours during which time the Ni(NO₃)₂ and Al(OH)₃ are converted to NiO and Al₂O₃, respectively. The resultant NiO/ZSM-5/Al₂O₃ solid was cracked and sieved to 18-50 mesh (i.e., 1000 to 300 micron sized particles). This material was then subjected to a temperature programmed H₂ reduction step to produce Ni⁰ immediately prior to the C₂H₂ conversion studies (13). Alternately, the high temperature calcination of the Ni(NO₃)₂/H-ZSM-5/Al(OH)₃ can be omitted and direct temperature programmed reduction of this solid carried out being careful to follow the temperature program sequence recommended by Bartholomew and Farruato (13). The resultant catalyst activity observed is essentially the same for either mode of catalyst preparation.

In addition to studies with the Ni/ZSM-5/Al₂O₃ catalyst, a large number of control experiments were carried out using either pure components or mixtures of these materials. These control experiments included studies with Na-ZSM-5,

H-ZSM-5, Ni/H-ZSM-5, pure Al₂O₃, H-ZSM-5/Al₂O₃ and Ni/Al₂O₃. The percent Ni loading of any of the catalysts employed is defined with respect to the weight ratio of Ni to the total weight of other material present (e.g., the weight of Ni to the combined weight of ZSM-5 + Al₂O₃ in the case of the complete Ni/ZSM-5/Al₂O₃ catalyst).

Reaction products were determined by on-line chromatography using a 30 meter megabore (0.53 mm) GS-Q column operated in a temperature programmed mode over a temperature range of 70 to 236 °C using helium carrier gas. FID detection was employed. Using this system, excellent separations are obtained for low molecular weight hydrocarbons and oxygenated hydrocarbons up through C₁₁. Hydrocarbon products and GC response factors were determined by calibrations using pure compounds. A Varian Model 4400 integrator was used to compute and record peak areas. The reaction product distributions are reported as product selectivity expressed in terms of carbon atom number. In addition to this FID analysis, a limited number of analyses were carried out using a silica gel column and TCD detector for the express purpose of monitoring CO and CO₂ formation during these conversions.

Results

Initial control experiments were carried out using pure ZSM-5, in either the H⁺ or Na⁺ form, as a catalyst for C₂H₂ conversion. The high initial catalytic activity of the Na-ZSM-5 is somewhat surprising but presumably reflects the relative ease of promoting C₂H₂ oligomerization over weakly acidic sites. The results obtained illustrate both the rapid catalyst deactivation which occurs and the growth of fused ring aromatic products with time on stream. The rapidity of the catalyst deactivation is illustrated in Figure 1 for C₂H₂ conversion at 400 °C over H-ZSM-5 and Na-ZSM-5 catalysts. Despite a relatively low C₂H₂ WHSV of only 0.48 hr⁻¹, catalyst deactivation is virtually complete after only 80 minutes of on-stream conversion. The hydrocarbon product distribution obtained under these conditions is exceptionally rich in aromatics. This is illustrated in Figure 2 for conversions of C₂H₂ using the H-ZSM-5 catalyst. In particular, one notes a rapid increase in the relative yield of fused-ring aromatics as the deactivation process occurs. Undoubtedly, this build-up of fused-ring aromatics leads to increased coking which, in turn, accelerates the catalyst deactivation.

A number of additional control experiments using pure H-ZSM-5 were carried out in which H₂O was added to the C₂H₂ reactant stream. The choice of H₂O addition was based on the nmr studies of Haw and coworkers (10) which provide unequivocal evidence for a ZSM-5 promoted reaction between C₂H₂ and H₂O. However, the pure H-ZSM-5 catalyst again undergoes rapid deactivation in the presence of a C₂H₂ + H₂O reactant stream, as illustrated in Figure 3 for runs at 350 °C [WHSV (C₂H₂) = 3.2 hr⁻¹] and 400 °C [WHSV (C₂H₂) = 0.48 hr⁻¹] at molar ratios of H₂O/C₂H₂ of 0.91 and 0.40, respectively. Again, the source of this catalyst deactivation is associated with increasing relative yields of fused-ring aromatics with increasing time on stream as shown in Figure 4. Although other experiments were carried out using a range of H₂O/C₂H₂ reactant ratios and varying space velocities, a stable catalytic conversion state could not be established using the pure H-ZSM-5 catalyst. The catalyst deactivation observed is consistent with the observations of Haw et al. who report the presence of residual "tarry" hydrocarbons on the zeolite after contacting C₂H₂ + H₂O mixtures, as evidenced by nmr spectra (10).

In sharp contrast to the results observed with the pure ZSM-5 catalyst, conversion of C₂H₂ + H₂O mixtures over a Ni/H-ZSM-5/Al₂O₃ catalyst can be

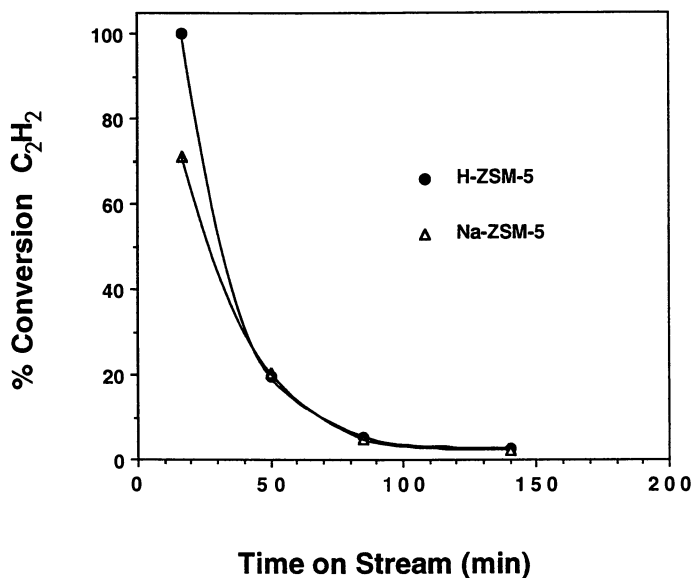


Figure 1. Illustration of the rapid decrease in % C₂H₂ conversion with time on stream over pure H-ZSM-5 and Na-ZSM-5 catalysts at 400 °C and a C₂H₂ WHSV of 0.48 hr⁻¹.

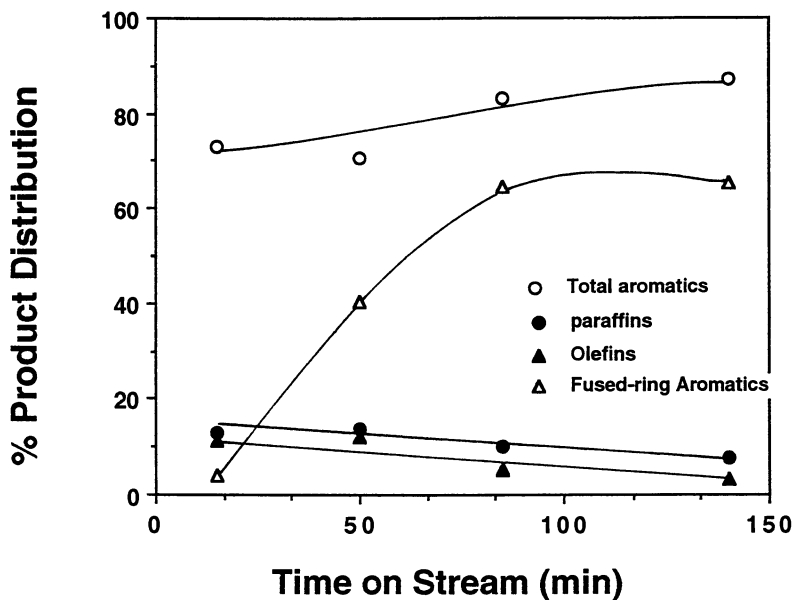


Figure 2. Variation in the normalized hydrocarbon product distribution with time on stream in the conversion of C₂H₂ (WHSV = 0.48 hr⁻¹) over pure H-ZSM-5 at 400 °C. Figure shows both total aromatic and, separately, fused-ring aromatic component of total aromatics.

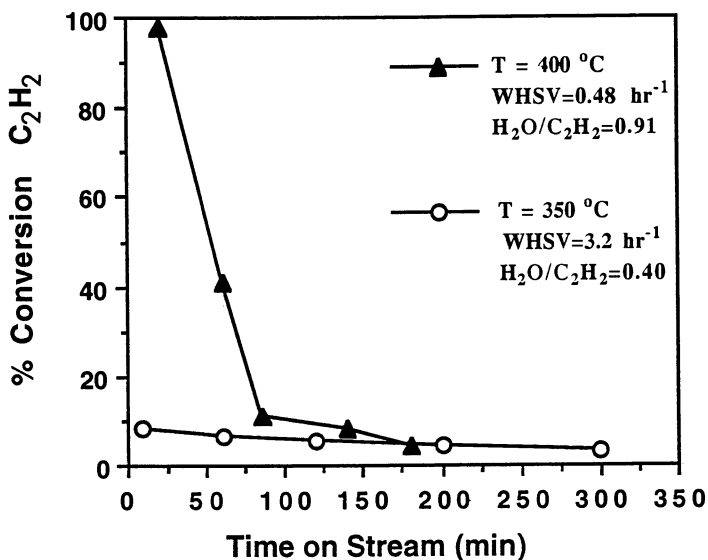


Figure 3. Illustration of the decrease in % C₂H₂ conversion with time on stream in reactions of C₂H₂ + H₂O mixtures over pure H-ZSM-5 catalysts at 350 °C and 400 °C.

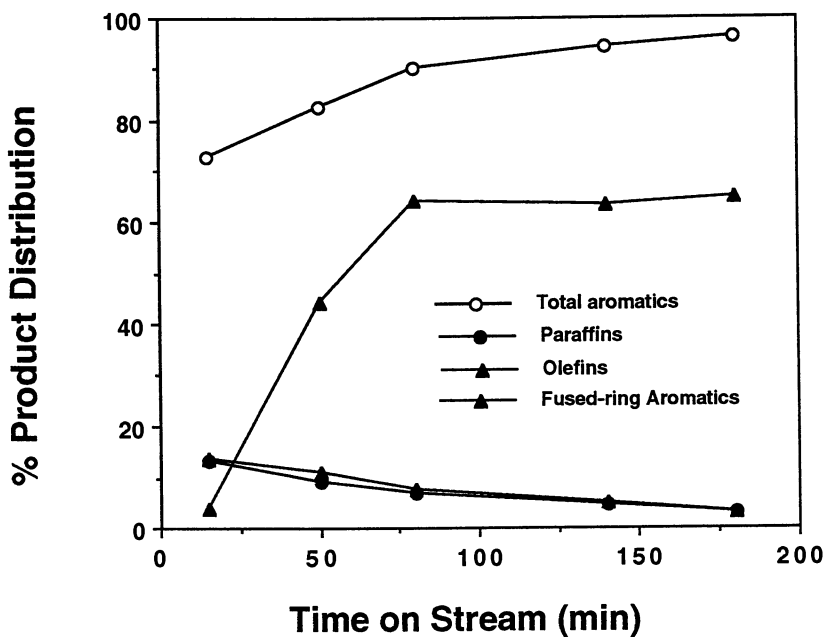


Figure 4. Variation in the normalized hydrocarbon product distribution with time on stream in the conversion of C₂H₂ (WHSV = 0.48 hr⁻¹) + H₂O mixtures over pure H-ZSM-5. [H₂O]/[C₂H₂] = 0.4. Figure shows both total aromatic and, separately, fused-ring aromatic component of total aromatics.

carried out continuously with a relatively stable product distribution. An example of such a conversion is shown in Figure 5 for a 100-hour run at 310 °C using a 13% Ni loaded catalyst, a molar reactant ratio of $\text{H}_2\text{O}/\text{C}_2\text{H}_2$ of 0.6 and a C_2H_2 WHSV of 3.2 hr^{-1} . One hundred percent conversion of the C_2H_2 was maintained throughout this reaction period including up to the point at which the experiment was terminated. The normalized yield of total hydrocarbons is shown in Figure 5. As shown by these data the selectivity with respect to total aromatics is virtually constant over the 100-hour conversion period, while there is a slow, but persistent, shift from olefins to increasing paraffins with increasing time on stream. Furthermore, the aromatic fraction is represented overwhelmingly by mono-cyclic compounds with a relatively small and steady contribution from fused-ring aromatics. Clearly, the catalytic product selectivity control exhibited by the bifunctional metal modified zeolite catalyst is very different from that obtained with pure ZSM-5 (e.g., Figure 4). A detailed breakdown of specific molecules observed in each of the three major hydrocarbon product groups is shown in Table I in which the product selectivity is normalized to 100% for the hydrocarbon fraction.

In addition to the hydrocarbons formed, both CO and CO_2 were observed as reaction products with the sum of the CO + CO_2 amounting to approximately $27 \pm 5\%$ of the C_2H_2 input carbon atoms. The yield of CO was much higher than that of CO_2 with the CO representing approximately 80 to 85% of the combined CO + CO_2 yield. The results of the hydrocarbon FID and CO + CO_2 TCD gas chromatography analyses were combined to provide a measure of the overall carbon atom accountability in C_2H_2 conversion. Typically this C atom accountability was found to lie between 96 and 100%.

A relatively large number of experiments were carried out investigating the effect of key reaction variables on the product distributions observed. These experiments included studies of the following variables: ratio of $\text{H}_2\text{O}/\text{C}_2\text{H}_2$; % Ni loading of the catalyst; reaction temperature; and space velocity. In general, it was observed that relatively large shifts in the hydrocarbon product distributions could be achieved while simultaneously maintaining continued catalytic activity and 100% C_2H_2 conversion. An example of the variability of the hydrocarbon product distribution with changing space velocity is shown in Figure 6 for runs carried out at 350 °C and $[\text{H}_2\text{O}]/[\text{C}_2\text{H}_2] = 0.6$ using a 13% Ni loaded H-ZSM-5 + Al_2O_3 catalyst. As shown in Figure 6, there is a dramatic shift in the relative yields of olefins and paraffins with increasing space velocity (i.e., decreasing catalyst contact time). In contrast, the aromatic yield remains relatively constant except for the very highest space velocities at which a decrease is observed. The increasing yield of olefins with decreasing contact time indicates the reaction sequence proceeds via initial formation of olefins which are subsequently converted to paraffins at longer reaction times. It should be noted that the data shown in Figure 6 represent product distributions after 2 hours of on stream conversion at each of the space velocities employed.

In contrast with the above result, relatively little change in product selectivity was noted with variation of the $[\text{H}_2\text{O}]/[\text{C}_2\text{H}_2]$ ratio in the reactant feed. The results from these experiments are shown in Table II for conversions at 350 °C and a C_2H_2 WHSV of 3.2 hr^{-1} . A variation favoring increasing aromatics and decreasing paraffins is noted with increasing $\text{H}_2\text{O}:\text{C}_2\text{H}_2$ at low values of this ratio, with product selectivity becoming essentially independent of the reactant ratio at values of $[\text{H}_2\text{O}]/[\text{C}_2\text{H}_2]$ above approximately 0.4. The data shown in Table II at a $[\text{H}_2\text{O}]/[\text{C}_2\text{H}_2]$ ratio of 0.10 were obtained after 90 minutes on stream conversions, whereas the data at all other ratios represent 2 hours conversions. The shorter time period was employed for the lowest $[\text{H}_2\text{O}]/[\text{C}_2\text{H}_2]$ as slow catalyst deactivation was observed at this low ratio. A slower catalyst deactivation was noted at $[\text{H}_2\text{O}]/$

Table I. Variation of the Normalized Hydrocarbon Product Distribution with Extended Time on Stream at 310 °C Over a 13% Ni/ZSM-5/Al₂O₃ Catalyst. C₂H₂ Conversion 100% (all runs)

Feed gas composition: C ₂ H ₂ = 5.0 mL/min; H ₂ O = 2.2 mg/min; He = 11.5 mL/min; VHSV (total gas mixture) = 6.9 x 10 ³ hr ⁻¹								
Time on stream (hr):	1.0	10.0	20.0	30.0	40.0	60.0	80.0	100.0
Hydrocarbon Distribution								
<i>Olefins</i>								
C ₂	11.0	6.7	4.7	3.2	3.2	2.2	1.7	1.4
C ₃	13.4	12.3	9.8	8.9	7.5	7.2	6.3	6.2
C ₄	7.9	6.1	7.7	7.2	7.5	6.1	4.6	3.1
C ₅₊	6.1	5.2	8.2	4.0	6.3	6.2	2.4	1.4
Selectivity (%)	38.4	30.3	30.4	23.3	24.5	21.7	15.0	12.1
<i>Paraffins</i>								
C ₁	11.3	16.1	17.4	17.8	18.8	24.4	27.3	35.7
C ₂	12.7	16.7	15.5	14.1	14.4	13.5	18.1	14.4
C ₃	4.1	4.8	4.3	3.6	3.7	3.9	4.8	4.9
C ₄	1.1	2.2	2.4	2.4	2.8	2.9	3.7	3.6
C ₅₊	2.1	1.4	2.5	5.7	6.9	5.5	4.6	2.7
Selectivity (%)	31.3	41.2	42.1	48.5	46.6	50.2	58.5	61.3
<i>Aromatics</i>								
Benzene	7.5	6.8	6.4	6.8	6.4	6.1	6.2	5.8
Toluene	9.8	8.4	7.8	7.6	8.4	8.5	7.4	7.2
Ethylbenzene	1.8	2.1	2.1	1.8	1.9	2.1	1.8	1.4
p+m-Xylene	4.1	4.2	3.5	3.9	4.2	4.3	3.2	3.6
o-Xylene	0.7	0.8	0.6	0.7	0.7	0.8	0.6	1.2
Ethyltoluene	3.2	3.4	3.7	3.7	3.4	2.8	2.6	2.7
Trimethyl benzene	2.4	2.1	2.5	2.7	2.8	2.7	3.3	3.1
Fused-ring aromatics	0.8	0.7	0.9	1.0	1.1	0.8	1.4	1.6
Selectivity (%)	30.3	28.5	27.5	28.2	28.9	28.1	26.5	26.6

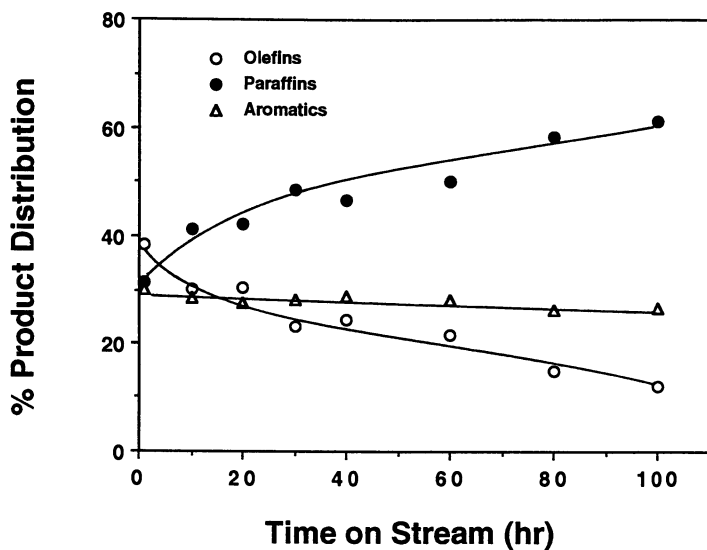


Figure 5. Illustration of the long-term normalized hydrocarbon product distribution obtained in the conversion of $C_2H_2 + H_2O$ mixtures over a 13% Ni/ZSM-5/ Al_2O_3 catalyst at 310 °C. $[H_2O]/[C_2H_2] = 0.6$. $WHSV(C_2H_2) = 3.2 \text{ hr}^{-1}$.

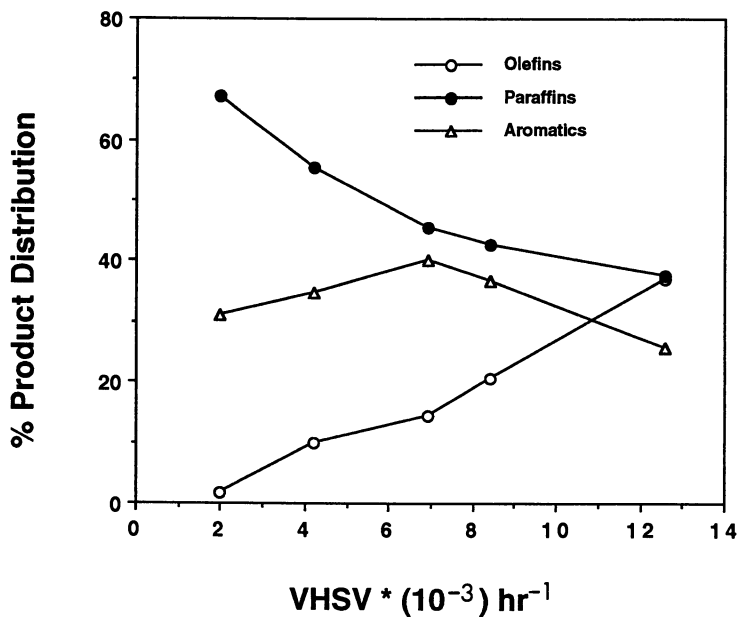


Figure 6. Variation of the normalized hydrocarbon product distribution as a function of catalyst contact time at 350 °C at a fixed $[H_2O]/[C_2H_2]$ of 0.6 and added He to vary the total $VHSV$.

Table II. Variation of Normalized Hydrocarbon Product Distribution at 350 °C as a Function of [H₂O]/[C₂H₂] Ratio All Other Reaction Variables Held Constant^a

[H ₂ O]/[C ₂ H ₂]	0.10	0.20	0.37	0.78	1.74
Hydrocarbon Distribution					
<i>Olefins</i>					
C ₂	0.3	0.2	0.1	0.1	0.0
C ₃	0.5	1.4	2.4	0.6	0.7
C ₄	0.7	0.7	0.8	0.1	0.5
C ₅₊	0.5	0.1	0.6	0.2	0.2
Selectivity (%)	2.0	2.4	3.9	1.0	1.4
<i>Paraffins</i>					
C ₁	52.7	45.6	33.1	26.7	27.4
C ₂	11.1	12.8	14.4	15.8	16.4
C ₃	10.0	12.5	13.1	14.3	15.2
C ₄	2.4	3.1	5.9	8.2	9.0
C ₅₊	0.3	0.2	0.5	0.3	0.7
Selectivity (%)	76.5	74.2	67.0	65.3	68.7
<i>Aromatics</i>					
Benzene	6.0	7.1	6.7	5.6	6.6
Toluene	6.2	7.7	10.3	11.9	11.3
Ethylbenzene	0.1	0.5	0.6	1.4	1.0
p+m-Xylene	2.5	3.4	4.2	7.8	5.8
o-Xylene	0.4	0.8	1.0	1.1	1.5
Ethyltoluene	0.8	0.9	2.6	2.8	1.2
Trimethylbenzene	1.1	0.6	2.7	2.5	2.2
Fused-ring aromatics	4.4	2.4	1.0	0.6	0.3
Selectivity (%)	21.5	23.4	29.1	33.7	29.9

^aCatalyst employed was 13% Ni/ZSM-5/Al₂O₃; WHSV (C₂H₂) = 3.2 hr⁻¹.

[C₂H₂] of 0.2. Very rapid catalyst deactivation is observed when [H₂O]/[C₂H₂] is zero so that reactant ratio is not included in Table II. Experimentally, it is observed that a [H₂O]/[C₂H₂] ≥ 0.4 is required in order to establish the stable catalyst conversion condition.

The effect of reaction temperature on hydrocarbon product distribution is illustrated in Figure 7 for runs carried out at a constant C₂H₂ WHSV of 3.2 hr⁻¹ and a [H₂O]/[C₂H₂] value of 0.4 and temperatures ranging from 175 to 450 °C. The % C₂H₂ conversion, shown on the left-side ordinate, was 100% at temperatures of 350 °C and above for the space velocity employed. The hydrocarbon product distribution as a function of reaction temperature can be read from the right-hand ordinate. As these data show, there is a dramatic change in the paraffin/olefin selectivity with the relative yield of paraffins increasing rapidly with increasing temperature. The aromatic yield, which is virtually non-existent at the lowest conversion temperatures, goes through a maximum at a temperature ~350 °C before decreasing again at higher temperatures.

A number of experiments were carried out in which the effect of varying the extent of Ni atom loading was explored in terms of both catalyst longevity and with respect to the product distribution obtained. It was observed that a minimal Ni atom loading of ~10 wt. % Ni (relative to the combined weight of ZSM-5 + Al₂O₃) was required in order to avoid catalyst deactivation in experiments with C₂H₂ + H₂O reactant feed. Runs carried out with Ni loading of less than 10% resulted in virtually complete catalyst deactivation after only 1 to 2 hours of on-stream conversion. Experiments with Ni atom loadings ranging from 10 to 35 % produced stable catalytic action and a hydrocarbon product distribution which is relatively independent of the extent of Ni atom loading. The results from these studies are summarized in Table III.

In an effort to obtain mechanistic insights into this conversion process, a number of reactions were carried out under conditions of less than 100% C₂H₂ conversion. This was accomplished by employing significantly higher C₂H₂ WHSVs (achieved by reducing the size of the catalyst bed) and by working at lower reaction temperatures. The results are summarized in Table IV. As shown by these data, acetaldehyde represents a major reaction product when low percent conversions of C₂H₂ are involved. For example, CH₃CHO constitutes 35% of the observed product distribution at 250 °C and only 4% C₂H₂ conversion. At higher reaction temperatures (and thus higher C₂H₂ conversions), CH₃CHO is still detected but the relative percent of CH₃CHO to the total hydrocarbon yield decreases rapidly with increasing temperature. At 350 °C and above, no CH₃CHO was detected under the conversion conditions employed. No other oxygenates, other than CH₃CHO, were detected among the reaction products under any of the reaction conditions employed.

In light of the observed formation of CH₃CHO in the C₂H₂ + H₂O conversion reaction, a number of experiments were carried out in which pure CH₃CHO was employed or in which CH₃CHO was added as a reactant to a stream of C₂H₂ or H₂O. It was observed that the reaction of pure CH₃CHO (WHSV = 2.7 hr⁻¹) or a mixture of [CH₃CHO]/[H₂O] = 1.0 (WHSV of CH₃CHO = 2.7 hr⁻¹) at 350 °C results in only partial conversion of the CH₃CHO and the % conversion of the CH₃CHO decreased rapidly with time on stream in conversions over the metal modified zeolite. For example, the conversion of the CH₃CHO was less than 10% after only 360 minutes conversion using the complete Ni (13%)/ZSM-5/Al₂O₃ catalyst. In contrast with this result, good continued catalyst activity was observed in conversion of equimolar mixtures of C₂H₂ and CH₃CHO at the same 2.7 hr⁻¹ CH₃CHO WHSV. Under these conditions, complete consumption of both the C₂H₂ and CH₃CHO is observed and the hydrocarbon product distribution is very

Table III. Catalyst Activity and Hydrocarbon Product Distribution at 350 °C as a Function of % Ni Loading of the Catalyst All Other Reaction Variables Held Constant^a

Reactant Feed: C ₂ H ₂ = 20 mL/min; H ₂ O = 4.7 mg/min						
% Ni Loading	0.0	5.0	10.0	13.2	20.0	35.0
C ₂ H ₂ Conversion (%)	2.2	4.3	99.1	100.0	100.0	100.0
Hydrocarbon Distribution						
<i>Olefins</i>						
C ₂	0.2	0.1	0.9	0.0	0.2	0.2
C ₃	0.2	0.2	1.8	1.5	0.6	0.5
C ₄	4.3	2.0	7.0	0.2	0.4	0.4
C ₅ ⁺	0.4	2.2	7.4	1.5	0.1	0.2
Selectivity (%)	5.1	4.5	17.1	3.2	1.3	1.3
<i>Paraffins</i>						
C ₁	0.2	4.2	24.5	24.9	36.6	32.9
C ₂	0.0	0.4	21.0	16.9	15.0	17.6
C ₃	4.2	11.4	13.4	14.8	10.8	10.5
C ₄	12.5	15.1	1.6	9.4	4.5	5.4
C ₅ ⁺	0.5	0.6	4.8	0.4	0.5	1.2
Selectivity (%)	17.4	31.7	65.3	66.4	67.4	67.6
<i>Aromatics</i>						
Benzene	0.5	6.1	5.6	7.4	11.9	9.7
Toluene	2.2	4.7	5.1	10.3	12.0	13.6
Ethylbenzene	0.0	0.0	0.2	0.4	0.4	0.5
p+m-Xylene	8.8	1.2	3.1	6.1	2.5	3.3
o-Xylene	1.0	0.5	0.8	1.4	0.9	0.6
Ethyltoluene	0.5	0.2	0.7	1.9	1.5	1.2
Trimethylbenzene	0.9	1.1	1.2	2.1	1.4	1.4
Fused-ring aromatics	63.6	50.0	0.9	0.5	0.7	0.8
Selectivity (%)	77.5	63.8	17.6	30.4	31.3	31.1

^aProduct yields and % C₂H₂ conversion recorded after 2 hours of on-stream conversion at each Ni loading shown. WHSV (C₂H₂) was 3.2 hr⁻¹ at each Ni loading. ZSM-5:Al₂O₃ weight ratio was 40:60.

Table IV. Normalized Product Yields in the Conversion of C_2H_2/H_2O Mixtures Under Reaction Conditions in Which C_2H_2 Conversion is Less Than 100%

Temperature ($^{\circ}C$)	250	275	300	350
C_2H_2 Conversion (%)	4.0	19.1	62.4	92.6
Product Distribution (%)				
Acetaldehyde	35.0	15.2	3.8	0.0
Hydrocarbons	65.0	84.8	96.2	100.0
Hydrocarbon Distribution (%)				
Olefins	81.3	75.1	68.7	11.3
Paraffins	18.5	22.5	25.8	67.2
Aromatics	0.2	2.4	5.5	21.5

Note: Catalyst – Ni (13.1%)/H-ZSM-5/ Al_2O_3 ; WHSV (C_2H_2) = 3.8 hr^{-1} ; $[H_2O]/[C_2H_2] = 0.63$; added carrier gas – He.

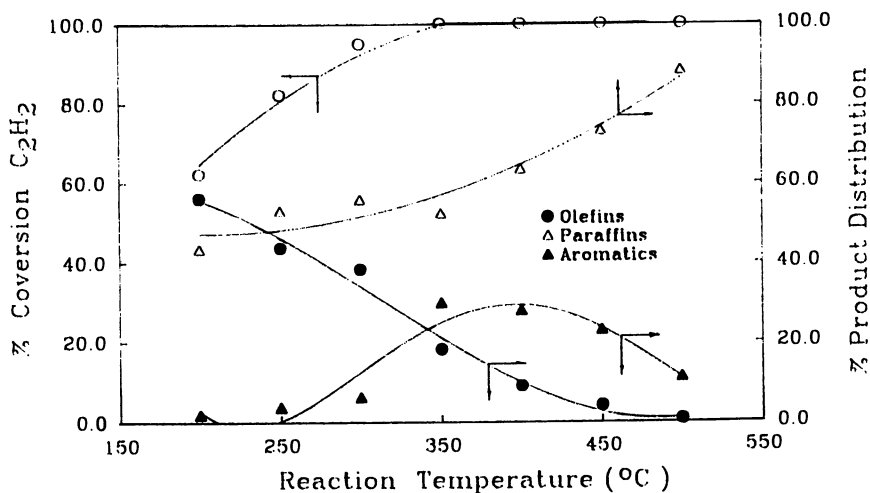


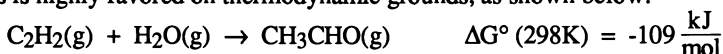
Figure 7. Effect of reaction temperature on % conversion of the C_2H_2 at a fixed reactant ratio of $[H_2O]/[C_2H_2] = 0.4$ and a C_2H_2 WHSV of 3.2 hr^{-1} (left ordinate). Normalized hydrocarbon product distribution as a function of reaction temperature (right ordinate). Catalyst employed was 13% Ni/ZSM-5/ Al_2O_3 .

similar to that obtained in conversions of $C_2H_2 + H_2O$ mixtures (Table V). Additional experiments were carried out using a C_2H_2/CH_3CHO reactant stream and a pure H-ZSM-5 catalyst. Rapid catalyst deactivation was observed under all reaction conditions employed using only the pure ZSM-5 material.

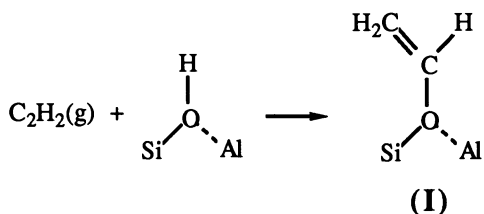
Discussion

As the above results document, the catalytic process developed provides the first successful continuous process for the conversion of acetylene to higher hydrocarbons. This process requires both the bifunctional catalyst and the addition of a hydrogen donor molecule to the reactant stream in order to maintain continuous catalytic activity. The absence of either the added Ni to the zeolite or H_2O (or CH_3CHO) to the C_2H_2 reactant stream results in rapid catalyst deactivation. As shown in this work, the rapid catalyst deactivation observed in the absence of the added Ni or H_2O can be ascribed to enhanced formation of fused-ring aromatics with time on stream. These polycyclic aromatics, in turn, result in coke formation and loss of catalytic activity. In view of the restricted pore size of ZSM-5 which severely limits polycyclic aromatic formation in other conversion [e.g., CH_3OH (14)], it is reasonable to assume that the coke formation observed in C_2H_2 conversions over pure ZSM-5 is associated with exterior pore sites, leading to ultimate pore blockage.

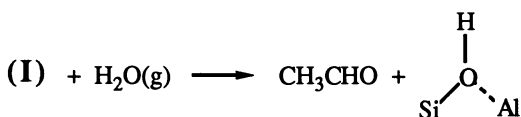
The results from the present study, coupled with those from the recent nmr study of Haw et al. (10), provides strong evidence for an initial facile zeolite catalyzed reaction between C_2H_2 and H_2O leading to CH_3CHO formation. Such a process is highly favored on thermodynamic grounds, as shown below:



Furthermore, as the nmr results show, dissociative adsorption of C_2H_2 on zeolites (including ZSM-5) occurs at temperatures as low as 200 °C. This initial $C_2H_2 +$ zeolite interaction has been interpreted as leading to a vinyl alkoxy intermediate (I):



Subsequent addition of H_2O to this system leads to CH_3CHO formation, via the reaction:



and regeneration of the catalytic site (10). Our observation of significant CH_3CHO product formation under high space times and low temperature reaction conditions is consistent with the nmr results.

Table V. Comparison of Hydrocarbon Product Distributions Obtained in Conversions of C₂H₂/H₂O and C₂H₂/CH₃CHO Under Comparable Reaction Conditions at 350 °C Over a 13% Ni/ZSM-5/Al₂O₃ Catalyst

	C ₂ H ₂ /H ₂ O						C ₂ H ₂ /CH ₃ CHO					
	20.0	20.0	20.0	20.0	20.0	20.0	10.0	10.0	10.0	10.0	10.0	10.0
C ₂ H ₂ (mL/min)	20.0	20.0	20.0	20.0	20.0	20.0	10.0	10.0	10.0	10.0	10.0	10.0
H ₂ O (mg/min)	5.2	5.2	5.2	5.2	5.2	5.2	17.6	17.6	17.6	17.6	17.6	17.6
Time on stream (min)	60	300	600	900	1200	1500	15	80	200	300	420	420
	Hydrocarbon Distribution											
<i>Olefins</i>												
C ₂	0.1	0.0	0.1	0.2	0.1	0.0	0.5	0.7	0.4	0.3	0.2	0.2
C ₃	1.5	1.7	1.4	0.8	0.3	0.3	5.6	4.4	1.8	0.7	0.5	0.5
C ₄	0.2	0.2	0.3	0.5	0.2	0.2	5.2	4.3	2.1	2.1	1.5	1.5
C ₅ ⁺	1.5	0.3	0.3	0.4	0.3	0.2	2.1	2.5	2.0	0.4	0.2	0.2
Selectivity (%)	3.3	2.2	2.1	1.9	0.9	0.7	13.4	11.9	6.3	3.5	2.4	2.4
<i>Paraffins</i>												
C ₁	23.1	32.6	41.0	48.7	53.4	54.1	37.0	40.7	49.9	50.1	51.3	51.3
C ₂	17.9	17.4	14.8	11.7	9.0	8.2	10.3	11.5	9.3	7.8	8.5	8.5
C ₃	15.8	13.1	11.9	9.7	9.0	9.6	11.1	10.1	10.3	12.4	12.3	12.3
C ₄	9.4	5.6	2.5	1.1	1.1	0.9	2.2	2.5	1.4	3.0	4.0	4.0
C ₅ ⁺	0.4	0.2	0.2	0.2	0.1	0.1	1.9	1.1	1.2	0.3	0.3	0.3
Selectivity (%)	66.6	68.9	70.4	71.4	72.6	72.9	62.5	65.0	72.1	74.4	76.1	76.1
<i>Aromatics</i>												
Benzene	7.4	7.8	7.9	8.1	9.4	10.5	4.2	3.7	3.7	5.1	5.0	5.0
Toluene	10.3	10.5	9.3	9.2	8.7	7.9	11.5	10.2	8.4	8.6	8.3	8.3
Ethylbenzene	0.4	0.3	0.3	0.2	0.2	0.1	0.7	0.5	0.6	0.5	0.4	0.4
p+m-Xylene	6.1	4.5	3.7	3.0	2.4	2.1	3.9	4.2	6.4	4.9	5.0	5.0
o-Xylene	1.4	1.1	1.0	0.7	0.6	0.5	1.1	1.0	0.8	1.2	1.0	1.0
Ethyltoluene	1.9	1.6	1.4	1.0	0.6	0.3	1.5	1.5	0.6	0.5	0.5	0.5
Trimethylbenzene	2.1	1.9	1.7	1.5	0.7	0.5	0.5	0.6	0.4	0.3	0.4	0.4
Fused-ring aromatics	0.5	1.2	2.2	3.0	3.9	4.5	0.7	0.8	0.7	1.0	0.9	0.9
Selectivity (%)	30.1	28.9	27.5	26.7	26.5	26.4	24.1	23.1	21.6	22.1	21.5	21.5

Note: The combined moles of C₂H₂ and CH₃CHO employed equaled the moles of C₂H₂ + H₂O runs.

Although CH_3CHO clearly represents an active intermediate in the $\text{C}_2\text{H}_2 + \text{H}_2\text{O}$ conversion process, the overall reaction mechanism must also account for the critical role played by the added Ni in the successful conversion process. The following experimental facts are pertinent in attempting to identify the role exerted by the nickel:

(a) Reactions of $\text{C}_2\text{H}_2/\text{H}_2\text{O}$ or $\text{C}_2\text{H}_2/\text{CH}_3\text{CHO}$ mixtures over pure ZSM-5 (or ZSM-5 + Al_2O_3) catalyst lead to rapid deactivation of the catalyst.

(b) Reactions of CH_3CHO or $\text{CH}_3\text{CHO}/\text{H}_2\text{O}$ mixtures over pure ZSM-5 (or ZSM-5 + Al_2O_3) catalyst show very low CH_3CHO conversion and subsequent catalyst deactivation.

(c) Reactions of pure CH_3CHO or $\text{CH}_3\text{CHO}/\text{H}_2\text{O}$ mixtures over the complete Ni/ZSM-5/ Al_2O_3 catalyst also exhibit low conversion and catalyst deactivation.

(d) Reactions of $\text{C}_2\text{H}_2/\text{H}_2\text{O}$ or $\text{C}_2\text{H}_2/\text{CH}_3\text{CHO}$ over the complete Ni/ZSM-5/ Al_2O_3 catalyst result in continued 100% C_2H_2 conversion and no noticeable catalyst deactivation.

(e) In order to achieve the reaction condition shown in (d) a minimum Ni loading of the catalyst of around 10% is required. Similarly, a minimal ratio of $[\text{H}_2\text{O}]/[\text{C}_2\text{H}_2]$ of at least 0.40 is required to generate catalyst stability.

In light of these observations, it is clear that a simple reaction sequence:

$\text{C}_2\text{H}_2 + \text{H}_2\text{O} \rightarrow \text{CH}_3\text{CHO} \rightarrow \text{hydrocarbons} + \text{CO}$ (or CO_2) is not operative. This direct route is ruled out by the experimental observations that reactant streams of either pure CH_3CHO or $\text{CH}_3\text{CHO} + \text{H}_2\text{O}$ mixtures show poor conversion and rapid catalyst deactivation both with ZSM-5 and the Ni modified ZSM-5 catalysts. On the other hand, reactant mixtures of $\text{C}_2\text{H}_2 + \text{CH}_3\text{CHO}$ result in continuous conversion of both the C_2H_2 and CH_3CHO over the Ni/ZSM-5/ Al_2O_3 but not over the ZSM-5/ Al_2O_3 catalyst. Furthermore, the hydrocarbon product distribution obtained with $\text{C}_2\text{H}_2 + \text{CH}_3\text{CHO}$ reactant mixtures is remarkably similar to those obtained with $\text{C}_2\text{H}_2 + \text{H}_2\text{O}$ when compared under similar space velocities and reaction temperature conditions. If the initial $\text{C}_2\text{H}_2 + \text{H}_2\text{O}$ interaction leads to CH_3CHO as described previously, then the experimental observations noted above are strongly supportive of a nickel mediated subsequent process involving $\text{C}_2\text{H}_2 + \text{CH}_3\text{CHO}$ reactions. Both C_2H_2 and CH_3CHO are known to be strongly absorbed on nickel catalysts. For example, significant spectroscopic evidence exists for the formation of an ethynylidene ($\text{CH}_3\text{-C}\equiv$) type intermediate in the adsorption of C_2H_2 on Ni as well as various other Group VIII metals (9,11). It seems reasonable to suggest that the Ni catalytic centers could be effective in promoting a decarbonylation reaction between C_2H_2 and CH_3CHO leading to CO and hydrocarbon formation. If such a process is occurring it must also involve the zeolite since control experiments with $\text{C}_2\text{H}_2 + \text{CH}_3\text{CHO}$ mixtures reacted over a Ni/ Al_2O_3 catalyst show low conversion and rapid catalyst deactivation.

An overall mechanism of:



followed by:



(in which C_3H_6 formation is simply used as illustrative of a possible hydrocarbon product) is highly favorable on thermodynamic grounds in that the overall reaction stoichiometry has a large negative ΔG :



Additional support of this suggested mechanism comes from the fact that the CO yields in the present work represent about 27% of the input carbon (on a carbon atom basis) which compares with a 25% value predicted by the above overall reaction.

It is clear that a major function of the added Ni is to limit formation of fused-ring aromatics which are generally so prominent in C_2H_2 conversion. Reduction in fused-ring aromatics avoids the rapid coking encountered in all other attempts at continuous C_2H_2 conversion. However, the added Ni is effective ONLY if an added hydrogen donor molecule, such as H_2O or CH_3CHO , is also provided. Conversion of C_2H_2 over a Ni/ZSM-5/ Al_2O_3 catalyst in the absence of the added hydrogen donor reactant results in large yields of fused-ring aromatics and rapid catalyst deactivation as shown in this study. Thus, we believe the role of the added Ni is to promote a C_2H_2 reaction which channels some of the C_2H_2 away from its natural tendency to oligomerize and polymerize over solid acidic type catalysts via a bimolecular reaction involving C_2H_2 and CH_3CHO . A minimum Ni atom loading is required in order to achieve stable catalytic conditions and thus limit the extent of fused-ring aromatic formation.

The suggested formation of an olefinic compound as shown in equation 1 would be consistent with the low conversion-high space velocity experiments which reveal substantial initial olefin product formation. It is well established that olefins undergo reactions over zeolites such as ZSM-5 resulting in both paraffin and aromatic formation. There has been extensive discussion of the various reaction mechanisms which may be operative in the disproportionation reactions of olefins over ZSM-5. Thus, under reaction conditions of longer space times and/or higher reaction temperatures, it would be anticipated that any initially formed olefins would react further to yield paraffins and aromatics. Clearly, subsequent olefin reactions could also include catalyst promoted reactions with acetylene.

Acknowledgment

This material is based, in part, upon work supported by the Texas Advanced Research Program (Advanced Technology Program) under Grant No. 003656-116.

Literature Cited

1. Tsai, P.; Anderson, J. R. *J. Catal.* **1983**, *80*, 207-214.
2. Allenger, V. M.; Fairbridge, C.; McLean, D. D.; Ternan, M. *J. Catal.* **1987**, *105*, 71-80.
3. Allenger, V. M.; McLean, D. D.; Ternan, M. *Fuel* **1987**, *66*, 435-436.
4. Allenger, V. M.; Brown, J. R.; Clugston, D.; Ternan, M.; McLean, D. D. *Appl. Catal.* **1988**, *39*, 191-211.
5. White, N.; Kagi, D. A.; Creer, J. G.; Tsai, P. "Aromatization of Acetylene", *U. S. Patent* **4,424,401** (1984).
6. Allenger, V. M.; McLean, D. D.; Ternan, M. *J. Catal.* **1991**, *131*, 305-318.
7. Leglise, J.; Chevreau, Th.; Cornet, D. *Catal. Zeolites* **1980**, *95*, 195-202.
8. Pichat, P.; Vedrine, J. C.; Gallezot, P.; Imelik B. *J. Catal.* **1974**, *32*, 190-203.
9. Galuszka, J.; Amenomiya, Y. *9th Proc. Int. Congr. Catal.* **1988**, *2*, 697-705.

10. Lazo, N. D.; White, J. L.; Munson, E. J.; Lamregts, M.; Haw, J. F. *J. Am. Chem. Soc.* **1990**, *112*, 4050-4052.
11. Beebe, T. P.; Albert, M. R.; Yates, Y. T., Jr. *J. Catal.* **1985**, *96*, 1-10.
12. He, Y.; Jang, W. L.; Timmons, R. B. *Energy and Fuels* **1991**, *5*, 613-614.
13. Bartholomew, C. H.; Farruato, R. J. *J. Catal.* **1976**, *45*, 41-53.
14. Chang, C. D.; Silvestri, A. J. *J. Catal.* **1977**, *47*, 249-259.

RECEIVED June 22, 1992

Chapter 26

Characterization of RuCl₃-Impregnated NaY Zeolite

Cathy L. Tway¹, Salvatore J. Bonafede¹, A. Mohamad Ghazi²,
Christopher P. Reed³, Robert J. DeAngelis³, and Tom M. Apple⁴

¹Department of Chemistry, ²Department of Geology, and ³Department
of Mechanical Engineering, University of Nebraska,
Lincoln, NE 68588

⁴Department of Chemistry, Rensselaer Polytechnic Institute,
Troy, NY 12180

²⁷Al Magic Angle Spinning (MAS) NMR of RuY zeolite reveals that impregnation of the zeolite with RuCl₃ causes dealumination of the lattice. ²⁹Si MAS NMR indicates that the as-prepared RuY is highly disordered. A loss of crystallinity is observed after ion-exchange, however this is apparently not simply due to the low pH of the exchange solution. Zeolites which were immersed in HCl solutions of identical pH as the RuCl₃ solution show little loss of crystallinity. NaCl treatment of the RuY produces materials with very high percentages of ruthenium by weight. Little structural damage is observed upon low temperature reduction of RuY, however reductions performed at 723 K cause sintering and the formation of large clusters of Ru on the outer edges of the crystallites. Large RuO₂ particles are formed under oxidizing conditions.

Ruthenium is known to catalyze a number of reactions, including the Fischer-Tropsch synthesis of hydrocarbons (1) and the polymerization of ethylene (2). The higher metal dispersions and the shape selectivity that a zeolite provides has led to the study of ruthenium containing zeolites as catalytic materials (3). A number of factors affect the product distribution in Fischer-Tropsch chemistry when zeolites containing ruthenium are used as the catalyst, including the location of the metal (4) and the method of introducing ruthenium into the zeolite (3).

Typically, the amine complexes have been used to ion-exchange ruthenium into Y-type zeolites (5,6). RuCl₃:3H₂O has largely been avoided as an ion-exchange medium because hydrolysis of the Ru⁺³ cation results in acidic solutions which can lead to a loss of crystallinity in less siliceous zeolites (5,7-8). However there appear to be differences in the behavior of the ruthenium if RuCl₃:3H₂O is used as the source of ruthenium instead of Ru(NH₃)₆Cl₃ (3,6,9). Shoemaker and Apple (9) studied the chemistry of ruthenium species in RuY zeolites prepared from RuCl₃:3H₂O under reducing and oxidizing conditions. In contrast to RuY prepared via ion-exchange with Ru(NH₃)₆Cl₃ (6), ruthenium species in RuCl₃-impregnated RuY did not sinter under oxidizing conditions. After oxidation, RuO₂ remained dispersed within the zeolite supercages (9). Large RuO₂ particles were found after oxidation in RuY

prepared from Ru(NH₃)₆Cl₃ (6). In this paper, RuY zeolite prepared via ion-exchange with RuCl₃ solutions will be characterized using a variety of techniques.

Experimental

The starting material for all samples was LZY-52 zeolite obtained from Union Carbide which was used without further pretreatment. The Si/Al ratio of the starting NaY zeolite was determined from ²⁹Si Magic Angle Spinning (MAS) solid state NMR to be 2.7.

RuY was prepared by exchanging 20 grams of NaY zeolite with 500 mL of a .04M solution of RuCl₃ prepared from RuCl₃·3H₂O (Strem Chemicals). Ion-exchange was performed at room temperature for three hours with constant stirring. The resulting RuY zeolite was rinsed with deionized water and dried in air for 17 hours at 383 K.

Zeolite samples were digested using a mixture of HF, HNO₃ and HClO₄ in screw-top teflon bombs (Saville). Ruthenium analyses were performed using a VG PlasmaQuad II Inductively Coupled Plasma Mass Spectrometer. All samples were spiked with indium to serve as an internal standard. Atomic absorption was used to determine aluminum content. The results from the chemical analyses are shown in Table 1.

X-ray powder diffraction data for all samples were collected via a Phillips x-ray diffractometer with a copper target tube and a diffracted beam monochromator. Ruthenium and RuO₂ particle sizes were estimated by x-ray line shape profile analysis using a single profile technique which provides diffracting particle size, microstrain, and the particle size distribution (10).

²⁷Al and ²⁹Si MAS NMR were used to monitor changes in the zeolite structure. ²⁷Al NMR was performed at 93.8 MHz with a homebuilt magic-angle spinning probe. ²⁹Si NMR was performed at 71.3 MHz using the same probe.

Diffuse reflectance Fourier Transform IR spectra were collected using an Analect RFX-65 FTIR spectrometer. KBr was used as the background material. RuY samples were diluted with KBr in order to obtain better transmittance. The position of the asymmetric T-O stretching vibration was used to monitor changes in the Si/Al ratio (11).

All reductions were carried out on a glass vacuum system under static H₂ (Linde 99.999%) which was dried by passing through Drierite and molecular sieves prior to exposure to the sample. H₂ uptakes were monitored using a capacitance manometer (MKS Instruments Inc.) N₂ isotherms at 77 K were performed on the same vacuum system using pre-purified grade N₂ (Linde) which was dried prior to use. Oxidations were performed under flowing O₂ (Linde 99.999%) at 773 K and under static O₂. The samples were evacuated at 623 K to a residual pressure of less than 5 X 10⁻⁵ torr prior to reduction or N₂ isotherm measurements.

Table I. Chemical Analysis of RuY Samples

Zeolite Sample	Percent Ru by Weight	Percent Al by Weight
RuY	11.7	11.9
NaCl Treated RuY	34.6	9.9
AgNO ₃ Treated RuY, 298 K	11.4	10.8
AgNO ₃ Treated RuY, 383 K	11.9	5.6

Results and Discussion

Crystallinity of RuY. The RuY samples which were prepared from RuCl₃ solutions are less crystalline than the starting material. Significant loss of intensity in the X-ray diffraction peaks is observed after the ion-exchange procedure. N₂ isotherm data indicate that ion-exchange results in a loss of around 50% of the original surface area and microporosity (Table 2). The ²⁹Si MAS NMR spectrum shown in Figure 1 illustrates just how severe the structural damage is in these samples. The individual crystallographic silicon species can not be observed and there is a broad component indicating the presence of amorphous material.

Table II. N₂ Adsorption Data

Zeolite	BET Surface Area (m ² /g)	Microporosity (cc/g)
NaY	710	.339
RuY	360	.178
pH=3.2 Treated NaY	612	.313
pH=1.26 Treated NaY	601	.292
NaCl Treated RuY	420	.192
Calcined RuY	326	.152
NaCl Treated Calcined RuY	300	.142
Calcined RuY, Reduced at 773 K	290	.140

The starting ruthenium exchange solution is somewhat acidic, possessing a pH of 3.2. Due to the instability of Ru(H₂O)₆³⁺ in aqueous solution (7), the pH of the solution quickly drops to a pH of 1.26. In order to test whether the lattice destruction was simply due to the pH of the exchange solutions, the ion-exchange procedure was repeated with solutions containing no ruthenium whose pH were adjusted to 1.26 and 3.2 using HCl.

The ²⁹Si MAS NMR results shown in Figure 2 clearly indicate that the structural damage is not simply due to pH. In both of the acid treated samples, the individual crystallographic silicon species can be observed and the shoulder denoting the amorphous material is absent. This conclusion is also supported by the N₂ BET surface area and microporosity results listed in Table 2. In all cases, the values for the RuY are much lower than those of the acid treated samples. Our results are in agreement with the work of Lee and Rees (12) who found that HCl solutions do not dealuminate Y-type zeolites when the hydrogen ion concentration is less than .22 mmole [H⁺]/gram zeolite. For our experimental conditions, this corresponds to a pH of 2.06. Because the solutions start at a pH of 3.2 and rise upon the addition of NaY zeolite to a pH of 5, we would not expect the acid-derived dealumination to be very significant in the RuY samples.

In contrast, Kim *et al.* (13) found that the amount of aluminum removed from the zeolite lattice during ion-exchange with solutions of metal chlorides was directly related to the pH of the solution and that the presence of the metal cation played no part in the dealumination. Our work more closely mirrors that of Bailar and co-workers (14-16) who found that solutions of CrCl₃ under reflux conditions could dealuminate a variety of zeolites to a much greater extent than the pH of the CrCl₃ solutions would predict. To explain their results, they proposed that the chromium cations could complex with hydrolyzed aluminum ions in the zeolite through the formation of "ol bridges" which then diffused out of the zeolite. Therefore,

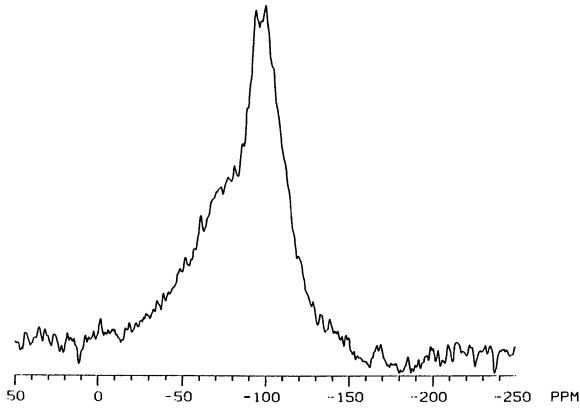


Figure 1. ²⁹Si MAS NMR spectrum of as-prepared RuY.

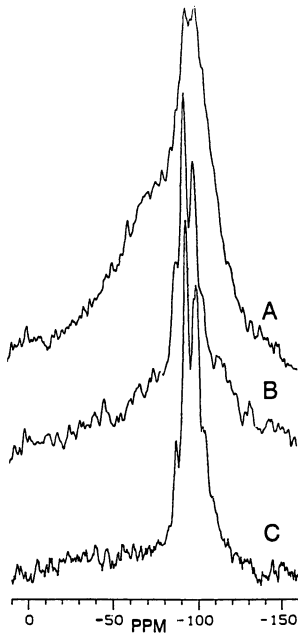


Figure 2. ²⁹Si MAS NMR spectra of: A) as-prepared RuY; B) NaY treated at pH=3.2; C) NaY treated at pH=1.26.

dealumination would proceed until all of the chromium was tied up in these complexes or until the pH of the solution was such that a sufficient amount of hydroxyl groups could not form (14). However, we do not have any evidence to support this type of dealumination process in the RuY system. During the exchange process, greater than 95% of the starting ruthenium is deposited in the zeolite, leaving very little to remain in the solution as a complex with aluminum. ^{27}Al NMR spectra of the exchange solutions feature a single peak at 0 ppm corresponding to an octahedral aluminum species and no signal that would indicate the presence of an aluminum-ruthenium complex. In addition, ^{27}Al MAS NMR spectra of the as-prepared RuY indicate the presence of extra framework detrital aluminum in an octahedral environment (Figure 3). When chelating agents are used to dealuminate zeolites, typically only tetrahedral aluminum species are observed (8). The actual mechanism for dealumination in the RuY system has not yet been determined.

Back Ion-exchange of Ruthenium. Several attempts were made to back ion-exchange the ruthenium out of the RuY in accordance of the work of Bailar *et al.* (14-16). Five grams of RuY were immersed in 100 mL of 1 M AgNO_3 solution, both under room temperature and reflux conditions. No ruthenium was removed from the zeolite during these treatments (Table 1). When the procedure was repeated using 100 mL of a solution of 1 M NaCl at room temperature, significant desilication was observed with no loss of ruthenium. The materials produced from the NaCl treatment contained 36.4 % ruthenium by weight (Table 1). Some extra-framework aluminum is also removed resulting in a material with an Al/Ru ratio of 1.1. Because this Al/Ru ratio is close to one, the ruthenium can not be acting simply as a charge compensating tri-valent cation in the NaCl treated RuY.

The inability to back ion-exchange the ruthenium from the zeolite, suggests that even in the starting RuY the ruthenium is not present in a highly dispersed form. Precipitation of ruthenium species has been observed in RuCl_3 solutions in the pH range of 3-7 (17). Because the addition of NaY zeolite to our solution caused the pH to rise to 5, it is very likely that polymeric ruthenium was deposited in the zeolite.

Bailar *et al.* (14-16) noted that a similar NaCl treatment of their chromium dealuminated samples resulted in desilication. However chromium cations were exchanged at the same time resulting in only small changes in the chromium content in the treated material. In agreement with their findings, we find that the NaCl treated material is more crystalline than the starting RuY. Figure 4 shows ^{29}Si MAS NMR spectra of the as-prepared RuY and the NaCl treated material. Following the NaCl treatment a loss in the intensity of the amorphous shoulder as well as some resolution of the silicon resonances for silicon in different chemical environments is observed. The loss of intensity of the amorphous shoulder without loss of Ru upon NaCl treatment suggest that the amorphous shoulder is not due simply to the presence of a Ru atom in the neighborhood of silicon. The N_2 isotherms for these materials are nearly identical in shape although the NaCl treated material adsorbs more N_2 at lower relative pressures than the starting RuY (Figure 5), which is reflected in a higher microporosity and BET surface area for the NaCl treated material (Table 2). The surface area of the NaCl treated material is actually very similar to that of the starting NaY with a surface area of $660 \text{ m}^2/\text{gram}$ zeolite if the weight of the ruthenium is not included.

Diffuse reflectance Fourier Transform IR was also used to monitor the effect of the NaCl treatment on the RuY sample. The position of the asymmetric stretching T-O vibration is directly related to the Si/Al ratio of the zeolite, with higher wavenumbers corresponding to higher Si/Al ratios (11). After the NaCl treatment, the position of this band drops from 1038 to 1025 cm^{-1} indicating a loss of silicon

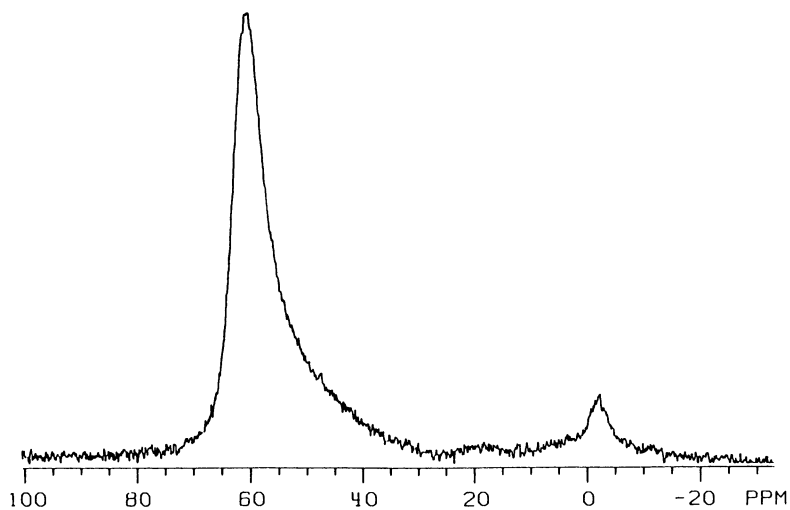


Figure 3. ²⁷Al MAS NMR spectrum of as-prepared RuY.

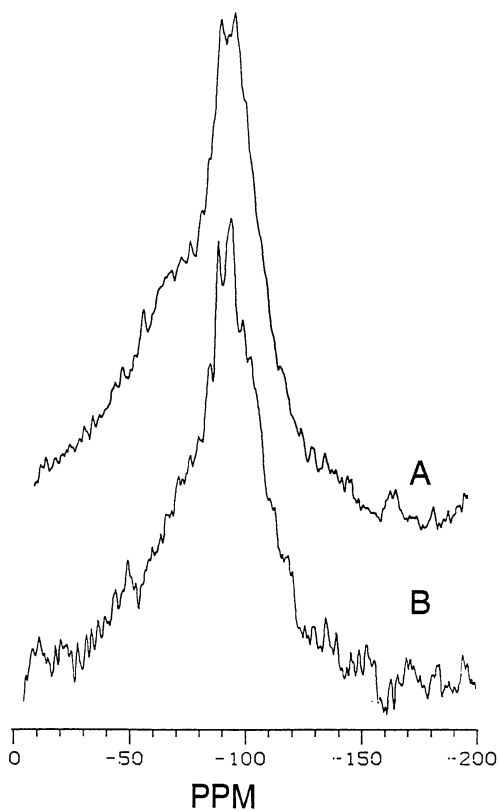


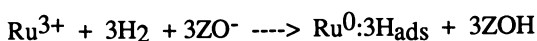
Figure 4. ²⁹Si MAS NMR spectra of: A) as-prepared RuY; B) NaCl treated RuY.

during the NaCl treatment. However, the position of this band in the NaCl treated material is still higher than that of the starting NaY (Table 3).

Table III. Diffuse Reflectance FT-IR Results for RuY Samples

Zeolite	Asymmetric T-O Stretching Vibration (cm ⁻¹)
NaY	1017
RuY	1038
NaCl Treated RuY	1025
Calcined RuY	1042
Calcined RuY, Reduced at 773 K	1071

The NaCl treatment also hinders the reduction of the ruthenium in the zeolite. In the starting RuY 2.6 moles H are used per mole ruthenium during reduction at 298 K. In the NaCl treated material, this ratio drops to 0.4 moles H/mole Ru. However both of these ratios are much lower than the ratio of six predicted from the following reaction:



where ZO⁻ represents the anion sites in the zeolite (9). The low H/Ru ratio in the starting RuY supports the presence of polymeric ruthenium.

The presence of a large amount of Cl⁻ ions in the NaCl solution may allow the formation of ruthenium chloro complexes which would hinder the reduction of ruthenium in the NaCl treated material. Such chloro complexes are known to exist in solutions of RuCl₃ (17). In Ru/Al₂O₃ and Ru/SiO₂ catalysts prepared from RuCl₃ solutions contamination with Cl⁻ ions even after reduction at elevated temperatures has been observed (18-19). The amount of residual Cl⁻ ions in the reduced ruthenium catalyst is also related to the type of support, where Cl⁻ ions are more prevalent in Ru/Al₂O₃ than in Ru/SiO₂ (19). We are currently investigating the amount of residual Cl⁻ ions in the RuY system.

Effects of Reduction. Reduction of both the RuY and the NaCl treated RuY at 773 K results in the formation of large ruthenium particles which have migrated out of the zeolite supercages. This finding is in agreement with prior work with RuY prepared from RuCl₃:3H₂O (9). The x-ray diffraction data feature a strong ruthenium pattern for both samples. Using line width analysis of the x-ray peaks we estimate the size of the ruthenium particles to be 12.0 nm in the RuY and 7.4 nm in the NaCl treated material. The smaller particles in the NaCl treated RuY indicates that this material is harder to reduce even at high temperature, supporting the presence of Cl⁻ contamination in this sample.

The lattice destruction that occurs during the formation of these large particles was followed using N₂ isotherms (Figure 6). Although the adsorption capacity drops with high temperature reduction, the shape of the isotherm does not change. Evidently, the migration of ruthenium during the reduction process does not result in the formation of mesopores.

Effects of Calcination. Calcination of RuY or NaCl treated RuY under flowing O₂ at 773 K results in the formation of large RuO₂ particles which are observable

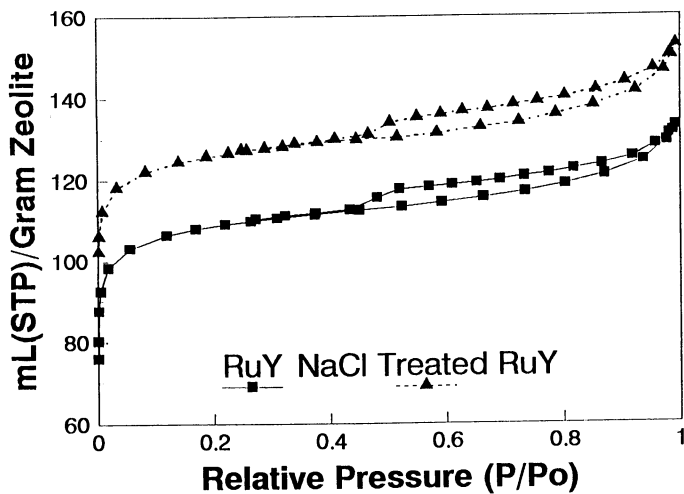


Figure 5. N₂ isotherms at 77 K for as-prepared RuY and NaCl treated RuY.

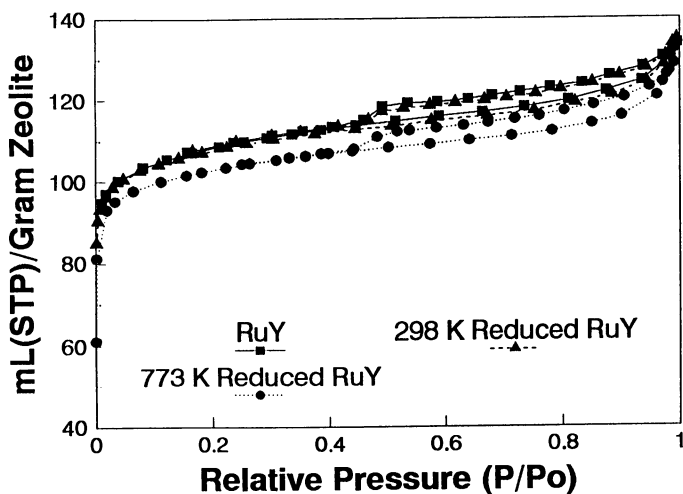


Figure 6. N₂ isotherms at 77 K for RuY before and after various reduction conditions.

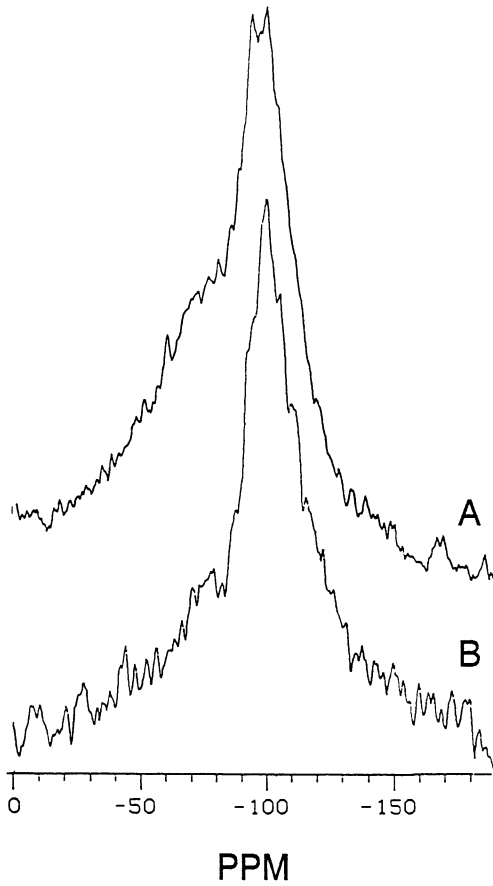


Figure 7. ^{29}Si MAS NMR spectra of: A) as-prepared RuY; B) RuY calcined at 773 K.

using x-ray diffraction. The formation of large RuO₂ particles was observed in RuY zeolite prepared from the Ru(NH₃)₆Cl₃, although the particles were not large enough to be observed with x-ray diffraction analysis (6). However Shoemaker and Apple (9) found no evidence of the migration of ruthenium under oxidizing conditions and the formation of large particles of RuO₂ in their work with RuY prepared from RuCl₃. All of their samples were evacuated prior to oxidation under static conditions (9). When our samples are evacuated at 773 K and then exposed to oxygen at 773 K we observe the formation of large RuO₂ particles, so the reason for the discrepancy is unclear.

Because RuO₂ is not soluble in acidic solutions, only the ruthenium that is not in the zeolite as RuO₂ will be dissolved during the acid digestion used in the ICP/MS analysis. The solutions above the undissolved RuO₂ particles were analyzed and the results indicate that only 3% of the ruthenium is not incorporated into RuO₂ particles in the calcined RuY samples.

Calcination of RuY does provide some stabilization of the silicon, probably due to migration of silicon into the defect sites produced during ion-exchange. Figure 7 shows ²⁹Si MAS NMR spectra of the starting RuY and the calcined material. Calcination results in a decrease in intensity of the amorphous shoulder. In addition, NaCl treatment of the calcined material does not result in an increase in the surface area, but instead a decrease. However, the surface area of the calcined material is lower than that of the starting RuY due to the formation of RuO₂ particles (Table 2).

The RuO₂ particles can not be reduced at room temperature, but reduce readily at 773 K. The ruthenium particles produced after this reduction procedure are estimated to be 16 nm in diameter from x-ray diffraction line width analysis. The reduction results in further loss of crystallinity, reflected by a drop in surface area and microporosity (Table 2). In addition, the position of the asymmetric T-O stretching vibration is at 1071 cm⁻¹, indicating a very silicon-rich material.

Conclusion

Ion-exchange of NaY zeolite with RuCl₃ solutions produces dealuminated materials. However the dealumination is not simply due to the low pH of the exchange solution. NaCl treatment of these materials allows the preparation of zeolitic materials containing very high ruthenium content with good microporosity. These novel materials may prove to be useful for a variety of catalytic reactions. Unfortunately, the ruthenium sinters and migrates out of the zeolite under reducing and oxidizing conditions, limiting the applicability of these materials.

Acknowledgments

This work was supported by the National Science Foundation under grant CHE8718850. This material is based upon work supported under a National Science Foundation Graduate Fellowship. We thank Prof. Bernard C. Gerstein for discussions pertaining to Cl⁻ ion contamination of supported ruthenium catalysts.

Literature Cited

1. Vannice, M. A. In *Solid State Chemistry of Energy Conversion and Storage*; Goodenough, J. B.; Whittingham, M. S., Eds.; Advances in Chemistry Series 163; American Chemical Society: Washington, D. C., 1977, 15-32.
2. Yashima, T.; Ushida, Y.; Ebisawa, M.; Hara, N. *J. Catal.* **1975**, *36*, 320.
3. Chen, Y. W.; Wang, H. T.; Goodwin, J. G. Jr. *J. Catal.* **1983**, *83*, 415.

4. Nijs, H.; Jacobs, P.; Uytterhoeven, J. *J. Chem. Soc., Chem. Commun.* **1979**, 181.
5. Lunsford, J. H. In *Metal Microstructures in Zeolites*; Jacobs, P. A.; Jaeger, P.; Jiru, P.; Schulz-Ekloff, G., Eds.; Studies in Surface Science and Catalysis 12; Elsevier Scientific Publishing Company: Amsterdam, The Netherlands, 1982, 1-13.
6. Verdonck, J. J.; Jacobs, P. A.; Genet, M.; Poncelet, G. *J. Chem. Soc., Faraday Trans. I*, **1980**, *76*, 403.
7. Wehner, P.; Hindman, J. C. *J. Am. Chem. Soc.* **1950**, *72*, 3911.
8. Scherzer, J. In *Catalytic Materials: Relationship Between Structure and Reactivity*; Whyte, T. E., Jr.; Dalla Betta, R. A.; Derouane, E. G.; Baker, R. T. K., Eds.; American Chemical Society Symposium Series, 248; American Chemical Society: Washington, D. C., 1984; 157-200.
9. Shoemaker, R.; Apple, T. *J. Phys. Chem.* **1987**, *91*, 4024.
10. Reed, C. P.; DeAngelis, R. J.; Zhang, Y. X.; Liou, S. H. In *Advances in X-ray Analysis 34*; Barrett, C. S.; Gilfrich, J. V.; Noyan, I. C.; Huang, T. C.; Perdecki, P. K., Eds.; Plenum Press: New York, 1991; 557-565.
11. Flanigen, E. M.; Szymanski, H. A.; Khatami, H. In *Molecular Sieve Zeolites*; Advances in Chemistry Series 101; American Chemical Society, Washington, D. C., 1971, Vol. 1; 201-230.
12. Lee, E. F. T.; Rees, L. V. C. *J. Chem. Soc., Faraday Trans. I* **1987**, *83*, 1531.
13. Kim, J. T.; Kim, M. C.; Okamoto, Y.; Imanaka, T. *J. Catal.* **1989**, *115*, 319.
14. Garwood, W. E.; Chen, N. Y.; Bailar, J. C., Jr. *Inorg. Chem.* **1976**, *15*, 1044.
15. Garwood, W. E.; Lucki, S. J.; Chen, N. Y.; Bailar, J. C., Jr. *Inorg. Chem.* **1978**, *17*, 610.
16. Garwood, W. E.; Chu, P.; Chen, N. Y.; Bailar, J. C., Jr. *Inorg. Chem.* **1988**, *27*, 4331.
17. Khan, M. M. T.; Ramachandraiah, G.; Rao, A. R. *Inorg. Chem.* **1986**, *25*, 665.
18. Narita, T.; Miura, H.; Sugiyama, K.; Matsuda, T.; Gonzalez, R. D. *J. Catal.* **1987**, *103*, 492.
19. Bossi, A.; Garbassi, F.; Petrini, G.; Zanderighi, L. *J. Chem. Soc., Faraday Trans. I*, **1982**, *78*, 1029.

RECEIVED July 29, 1992

Chapter 27

Non-Flory Product Distributions in Fischer–Tropsch Synthesis Catalyzed by Ruthenium, Cobalt, and Iron

Rostam J. Madon¹, Enrique Iglesia, and Sebastian C. Reyes

Corporate Research Laboratories, Exxon Research and Engineering Company, Route 22 East, Annandale, NJ 08801

Hydrocarbon distributions in the Fischer-Tropsch (FT) synthesis on Ru, Co, and Fe catalysts often do not obey simple Flory kinetics. Flory plots are curved and the chain growth parameter α increases with increasing carbon number until it reaches an asymptotic value. α -Olefin/n-paraffin ratios on all three types of catalysts decrease asymptotically to zero as carbon number increases. These data are consistent with *diffusion-enhanced readsorption of α -olefins within catalyst particles*. Diffusion limitations within liquid-filled catalyst particles slow down the removal of α -olefins. This increases the residence time and the fugacity of α -olefins within catalyst pores, enhances their probability of readsorption and chain initiation, and leads to the formation of heavier and more paraffinic products. Structural catalyst properties, such as pellet size, porosity, and site density, and the kinetics of readsorption, chain termination and growth, determine the extent of α -olefin readsorption within catalyst particles and control FT selectivity.

Selectivity in the Fischer-Tropsch (FT) synthesis is directly related to carbon number distributions. These distributions were first discussed by Friedel and Anderson (1), who used an approach suggested by Herrington (2) to relate the rates of formation of hydrocarbon chains to the rates of chain termination. Later, it was shown (3) that the approach in Ref. (1) was similar to that used in

¹Current address: Engelhard Corporation, 101 Wood Avenue, Iselin, NJ 08830

Flory polymerization kinetics (4). Henrici-Olivé and Olivé (5) proposed the use of the related equation of Schulz (6). Over the last decade the Flory equation has been used frequently to describe product distributions in FT synthesis. The Friedel-Anderson (1) or Flory (4) approaches apply when the rates of propagation and termination are independent of carbon number. We do not attempt here to discuss all previous research on FT product distributions except to say that the literature contains many examples of product distributions that obey Flory kinetics within relative narrow carbon number ranges and many that do not.

Recently, we reported detailed descriptions of hydrocarbon chain growth on supported Ru catalysts (7,8); we showed that product distributions do not follow simple polymerization kinetics and proposed a *diffusion-enhanced olefin readsorption model* in order to account for such deviations (7,8). In this paper, we describe this model and show that it also applies to Co and Fe catalysts. Finally, we use this model to discuss a few examples from the literature where catalyst physical structure and reaction conditions markedly influence hydrocarbon product distributions.

The Diffusion-Enhanced Olefin Readsorption Model

This model accounts for the readsorption of α -olefin products during FT synthesis (7,8); the rate and extent of readsorption depend on catalyst type and on experimental conditions. After readsorption on FT sites, α -olefins re-enter the chain growth process by initiating new chains; they in turn may terminate as larger olefins, n-paraffins, or branched isomers. α -Olefins may also readsorb on sites that catalyze secondary hydrogenation or isomerization. Primary and secondary products on Ru catalysts were previously discussed in Ref. (8). Even though α -olefin readsorption onto a FT site is a secondary reaction, the resulting surface chains enter the surface alkyl pool and become indistinguishable from surface alkyls formed directly from CO and H₂. The products obtained as a result of olefin readsorption are indistinguishable from primary FT products. A product formed by a single sojourn of a reaction intermediate on a Fischer-Tropsch site is considered a primary product regardless of the number of surface sojourns actually required to form it. For the purpose of this paper, we will limit ourselves to discussions of the two major primary products: α -olefins and n-paraffins.

We previously proposed that intrapellet (pore) diffusion within liquid-filled catalyst pores decreases the rate of α -olefin removal. This increases the residence time and the fugacity of α -olefins within catalyst pellets and increases the probability that they will readsorb onto FT chain growth sites and initiate new chains. This occurs even for small catalyst particles (~0.1 mm pellet diameter) at normal FT conditions. Larger α -olefins remain longer within catalyst particles because diffusivity decreases markedly with increasing molecular size (carbon number). As a result, readsorption rates increase with increasing carbon number.

We can write the overall termination parameter (β_n) for carbon number n using the Herrington formalism (2), as

$$\beta_n = \beta_o + \beta_h + \beta_i - \beta_{r,n} \quad (1)$$

where β_n is the ratio of the total chain termination rate to the propagation rate, and β_o , β_h , and β_i represent termination pathways to α -olefins, paraffins, and isomers, respectively; $\beta_{r,n}$ is the ratio of α -olefin readsorption to propagation rates. Values of $\beta_{r,n}$ can be obtained from independent measurements of readsorption rates of α -olefins introduced with H_2/CO feeds (7).

Our model suggests that only the readsorption step depends on carbon number; the dependence arises from intraparticle diffusion limitations and not from intrinsic kinetic effects. Rates of termination and propagation remain independent of carbon number; therefore, Flory kinetics still apply at each catalytic site. The readsorption of a C_n α -olefin results in a net decrease in the termination rate of C_n chains. β_n decreases with n until no α -olefins are formed ($\beta_o = \beta_{r,n}$) because $\beta_{r,n}$ increases with n . For higher carbon numbers, β_n remains constant and equal to $\beta_h + \beta_i$. Because β_n is related to the Flory chain growth parameter ($\alpha_n = 1/(1 + \beta_n)$), α will increase with carbon number until it reaches its maximum constant value. Therefore, Flory plots, using the logarithmic form of the Flory equation (4), will not be straight lines but will curve until α reaches a constant value and only unreactive paraffins are observed. The curvature of such a plot, and the increase in α with carbon number, cannot arise simply from α -olefin readsorption processes (22); it requires that the readsorption rates increase with carbon number.

Each time an α -olefin readsorbs, there is a chance that it will desorb as a larger paraffin. Desorption as a paraffin is an irreversible termination step. At high carbon numbers, pore diffusion effects dominate and α -olefins do not exit the catalyst particles unreacted because of enhanced readsorption; only unreactive paraffins are observed. As a result, the olefin/paraffin ratio decreases asymptotically to zero as carbon number increases.

Readsorption of α -olefins is also influenced by bed residence time (i.e., space-velocity). As we discussed previously, space-velocity controls the readsorption rate of small α -olefins (7,8). As α -olefin size increases, the influence of bed residence time decreases and the influence of pore residence time increases until the latter totally controls the secondary reaction chemistry. In some cases, where only bed residence times affect α -olefin readsorption and pore residence times are much smaller than bed residence times, straight line Flory plots with a single value of α can be obtained; such α values, however, are larger than in the absence of secondary readsorption (7,22).

Experimental

The apparatus and procedures have been described elsewhere (7-9). All experiments were carried out in plug-flow reactors; sufficient time was allowed to elapse before product collection in order to ensure steady-state product distributions. The product distribution ($C_1 - C_{150}$) was measured using methods previously described (7,8).

Preparation procedures for Ru supported on Degussa P-25 TiO₂ and Davison grade 62 SiO₂ are described in Ref. (8). A ruthenium nitrate-acetone slurry was used to impregnate the supports. In this paper, we report data on 1% wt. Ru/TiO₂ and 10.8% wt. Ru/SiO₂. The Fe-Cu-K catalyst preparation is described in Refs. (9,10). Ferrous, ferric, and cupric chlorides were mixed to give an aqueous solution containing 75 parts Fe⁺², 25 parts Fe⁺³, and 20 parts Cu⁺². This was heated to 343K and then mixed with a NaOH solution at 363K. The precipitate was washed to reduce sodium and chlorine levels to below 100 ppm, and K₂CO₃ was then added to the mixture. The final composition was 100 Fe : 21.8 Cu : 1 K₂CO₃ by weight. A 11.6% wt. Co/TiO₂ catalyst was prepared by incipient wetness impregnation of Degussa P-25 TiO₂ with an aqueous cobalt nitrate solution. The catalyst was dried, calcined in air at 773 K for 4 h and reduced in flowing H₂ at 723 K for 4 h. All catalysts were sieved to retain the 80-140 mesh fraction (0.17 mm average diameter) and pretreated in flowing H₂ for 4 h at 673 K before use.

Results

Ruthenium. We have previously discussed FT reaction pathways on Ru/TiO₂ and Ru/SiO₂ (8). Here, we compare the two systems at the same reactor temperature and pressure. It is important to compare these two oxide supports, because TiO₂ is an SMSI-support (11) previously shown to influence FT synthesis rates and selectivity (12,13). However, site-time yields and selectivity on Ru are independent of the chemical identity of the support (TiO₂ or SiO₂) (Table 1). The detailed hydrocarbon distributions (Figure 1) and the α -olefin/paraffin ratios (Figure 2) are also very similar on the two catalysts. This shows that the catalytic chemistry occurs predominantly on Ru and that it is unaffected by the support. The hydrocarbon distributions are given as conventional Flory plots in Figure 1. The plots are curved; α increases with carbon number until it reaches its asymptotic value of 0.945, corresponding to a minimum β_n value of 0.058 at high carbon numbers ($n > 25$). The α -olefin/paraffin ratio decreases monotonically with carbon number; it approaches zero for molecules larger than C₂₀ on both supports.

Iron. Fe-Cu-K data are shown in Table 2. Carbon number distribution (Flory plots) and α -olefin/paraffin data are shown in Figures 3 and 4, respectively. As on Ru catalysts, the Flory plot is curved and the α -olefin/paraffin ratio decreases to zero as carbon number increases. The experimental conditions are different for the Ru and Fe systems; therefore, we cannot make direct comparisons. Such comparisons will be made in a later publication (14). However, we comment on three important findings. First, C₂ and C₃ hydrocarbons fall close to the Flory curve (Figure 3) for Fe, in clear contrast with the results on Ru. This suggests that the high rate of ethylene readsorption that leads to low C₂ concentrations on Ru (7,8) does not occur on Fe. Secondly, both α -olefins and β -olefins persist at higher carbon numbers than on Ru; the Flory plot for Fe shows a more pronounced curvature and the asymptotic value of α is reached at higher carbon number than on Ru. Finally, Ru catalysts produce about 40 wt% C₂₀+ product whereas the Fe

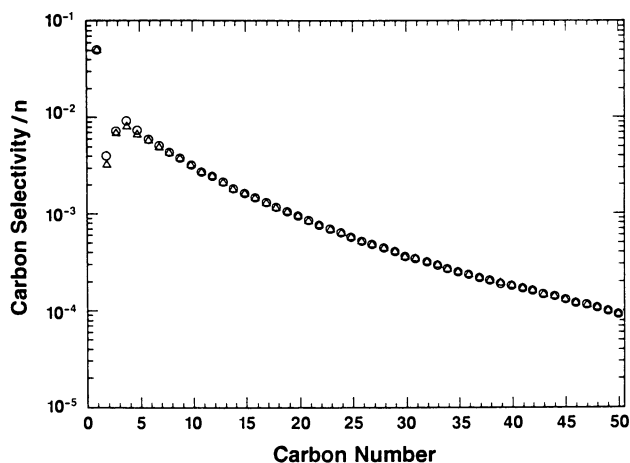


Figure 1: Flory plots for 1% Ru/TiO₂ (○) and 10.8% Ru/SiO₂ (△); (T = 485 K, P = 510 kPa, H₂/CO = 2). (Flory equation (4) used: $\ln (W_n/n) = \ln [(1-\alpha)^2/\alpha] + n \ln \alpha$, where W is the selectivity in wt% of carbon number n and α is the chain growth probability).

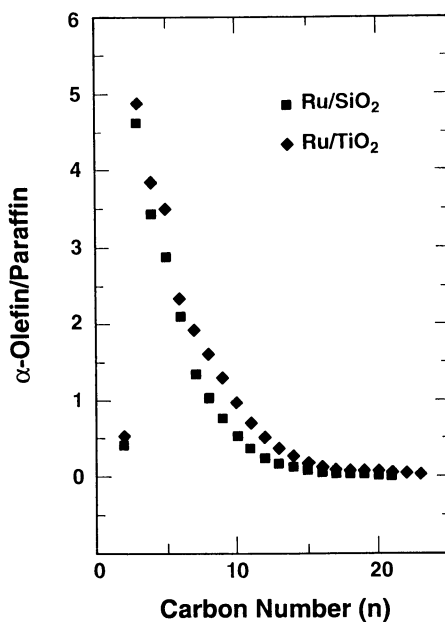


Figure 2: α -Olefin/n-paraffin ratio for 1% Ru/TiO₂ and 10.8% Ru/SiO₂ versus carbon number. (Conditions as in Figure 1).

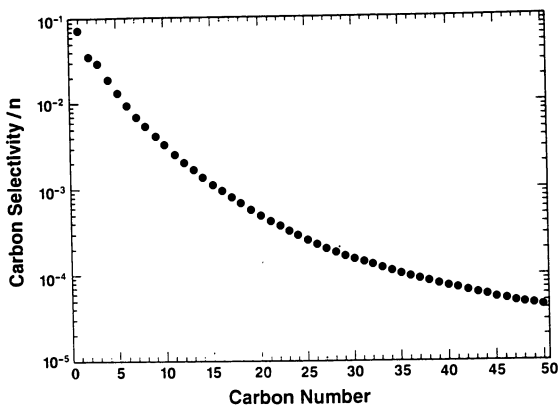


Figure 3: Flory plot for Fe-Cu-K ($T = 489$ K, $P = 1620$ kPa, $H_2/CO = 2$). (See legend for Figure 1).

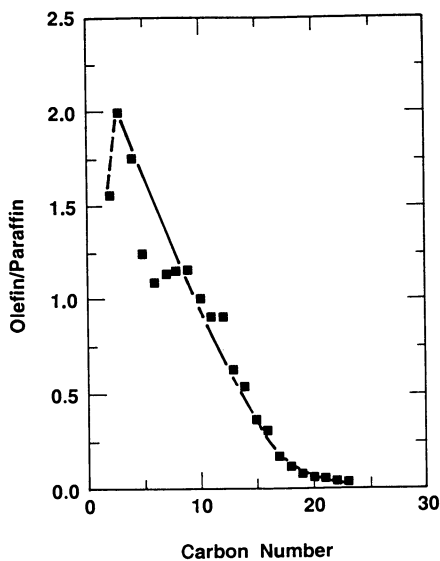


Figure 4: α -Olefin/n-paraffin ratio for Fe-Cu-K versus carbon number. (Conditions as in Figure 3).

Table 1. Comparison of Ru Supported on TiO₂ and SiO₂

Catalyst	1% Ru/TiO ₂	10.8% Ru/SiO ₂
Dispersion, %(a)	45	20
(H ₂ + CO) conversion, %	32	51
Site-time yield x 10 ² , s ⁻¹	2.0	2.4
Selectivity, wt%(b)		
CH ₄	5.0	4.9
C ₂ - C ₄	6.6	6.1
C ₅ - C ₂₀	46.1	45.6
C ₂₁ - C ₅₀	29.2	29.8
C ₅₁ +	12.1	12.5

(a) Ru dispersion measured via microscopy for Ru/TiO₂, and via H₂ chemisorption for Ru/SiO₂

(b) CO₂ and light alcohols ~ 1%.

[485 K, 510 kPa, H₂/CO = 2]

Table 2. Fe-Cu-K Catalyst

Selectivity, wt%(a)	
CH ₄	7.0
C ₂ -C ₄	23.5
C ₅ - C ₂₀	47.0
C ₂₁ - C ₅₀	12.8
C ₅₁ +	9.7

(a) On a CO₂ free basis; CO₂ selectivity = 69 wt%.

[489 K, 1616 kPa, H₂/CO = 2, (H₂ + CO) Conversion = 28%]

catalyst gives 22 wt%, even though the asymptotic termination rate on Fe (0.040) is lower than on Ru (0.058). The asymptotic value of β is equal to β_h (7,8); thus, the ratio of the rate of termination of hydrocarbons as paraffins to the rate of chain propagation is lower on Fe than on Ru at their respective reaction conditions.

Cobalt. Fischer-Tropsch synthesis was studied on 11.6% Co/TiO₂ at 560 kPa pressure, 476 K, and H₂/CO = 2.1. Figures 5 and 6 show results at two CO conversion levels (6 and 45.5%), achieved by varying the space-velocity. The plots show trends similar to those observed on Ru and Fe catalysts. The Flory plots (Figure 5) are curved but to a lesser extent than on Ru or Fe catalysts. At higher conversions, the products are slightly heavier. However, the asymptotic value of α ,

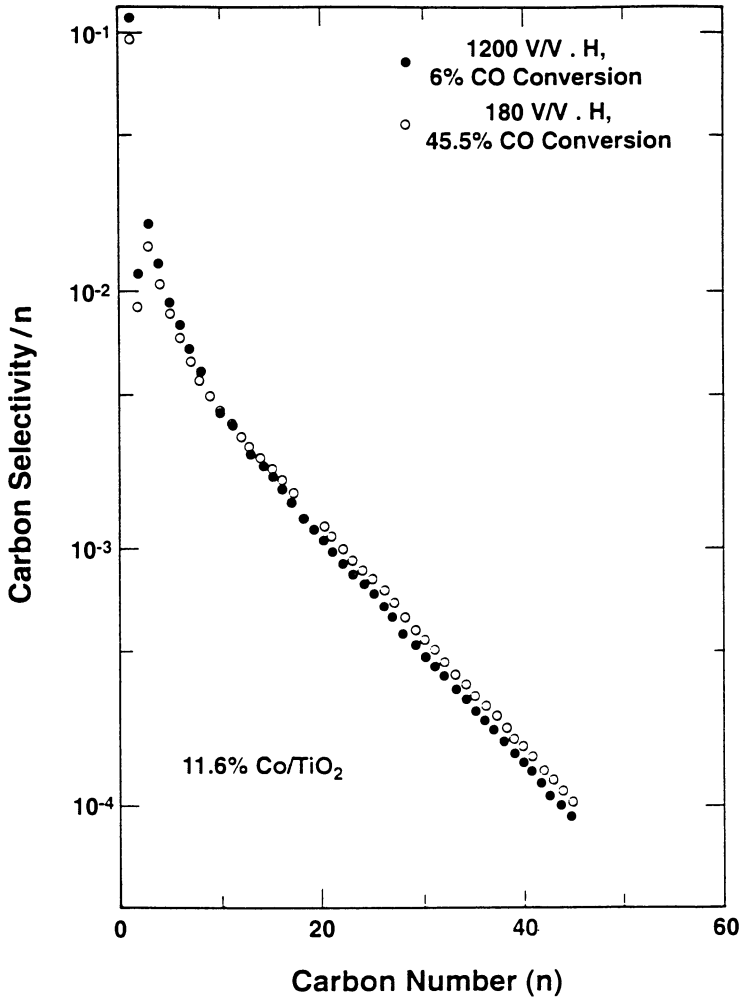


Figure 5: Flory plots for 11.6% Co/TiO₂ (T = 476 K, P = 560 kPa, H₂/CO = 2. 1200 V/V.h -- 6% CO conv. (●), 180 V/V.h -- 45.5% CO conv. (○)). (See legend for Figure 1).

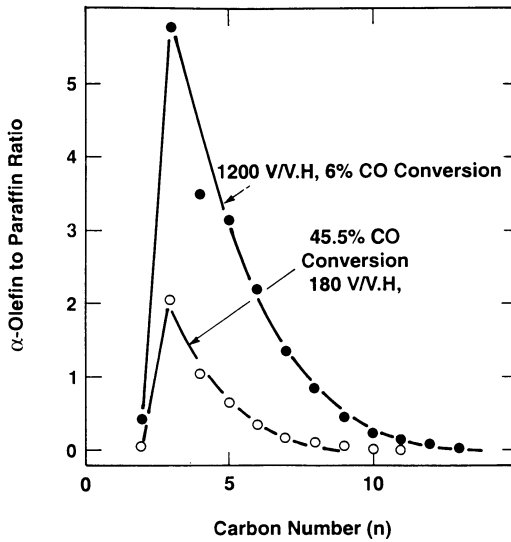


Figure 6: α -Olefin/n-paraffin ratio for Co/TiO₂ (1200 V/V.h -- 6% CO conv. (●), 180 V/V.h -- 45.5% CO conv. (○)).

and therefore of β , is independent of conversion. Similar effects of space-velocity on Ru catalysts were reported in Refs. (7,8); the differences between the two curves in Figure 5 arise from an increase in readsorption probability with increasing bed residence time.

The α -olefin/paraffin ratio on Co also approaches zero as carbon number increases. Here, the ratio decreases more rapidly than on Ru or Fe catalysts. This suggests that the net rate of α -olefin formation on Co rapidly decreases with carbon number. As a result, Flory plots (Figure 5) are linear over a broader carbon number range than on Ru (Figure 1) or Fe (Figure 3). The asymptotic value of β for the cobalt catalyst is 0.11, higher than those obtained with Fe and Ru catalysts, suggesting that the ratio of the rate of chain termination to paraffins to the rate of chain propagation is higher on Co. At very high conversions, only paraffins are observed even for small carbon numbers and Flory plots become linear even though significant intraparticle diffusional restrictions remain. In such cases, the asymptotic value of β is reached at very low carbon numbers.

Discussion

The trends in carbon number distribution and in α -olefin/paraffin ratio on Ru, Fe, and Co, three very different catalytic surfaces, are remarkably similar. All catalysts show a curved Flory plot and an α -olefin/paraffin ratio that decreases with increasing carbon number until only paraffins are observed at high carbon numbers. In each case, diffusion-enhanced olefin readsorption accounts for such trends. Its contribution depends on the catalytic surface, its physical structure, and reaction conditions.

Here, we are concerned with intraparticle diffusion controlling a first-order readsorption reaction; therefore, the Damköhler number (15), which reflects the ratio of reaction to diffusion rates within catalyst particles, is given by:

$$D_a = (k_{r,n}/D_n) \cdot (2L^2\theta\epsilon)/R_p \quad (2)$$

The effective diffusivity D_n decreases rapidly as carbon number increases. The readsorption rate constant $k_{r,n}$ depends on the intrinsic chemistry of the catalytic site and on experimental conditions but not on chain size. The rest of the equation contains only structural catalyst properties: pellet size (L), porosity (ϵ), active site density (θ), and pore radius (R_p). High values of the Damköhler number lead to transport-enhanced α -olefin readsorption and chain initiation. The structural parameters in the Damköhler number account for two phenomena that control the extent of an intrapellet secondary reaction: the intrapellet residence time of α -olefins and the number of readsorption sites (θ) that they encounter as they diffuse through a catalyst particle. For example, high site densities can compensate for low catalyst surface areas, small pellets, and large pores by increasing the probability of readsorption even at short residence times. This is the case, for example, for unsupported Ru, Co, and Fe powders.

Structural parameters are very important but the magnitude of the α -olefin readsorption effect also depends on the relative rates of readsorption (k_r), propagation (k_p), termination (k_h , k_o) and of competing secondary reactions (k_s), as shown schematically in Figure 7. Thus, the overall product selectivity depends on how the propagation rate constant k_p , and the termination rate constants to olefins (k_o), paraffins (k_h), or isomers (k_i) compare with k_r . Diffusion-enhanced α -olefin readsorption will play a major role in determining selectivity to high molecular weight hydrocarbons when $k_o \gg k_h$ and k_r is large, because olefins will be available and will react. In contrast, if $k_h \gg k_o$, or k_r is small, or if α -olefins are rapidly hydrogenated (k_s) on secondary reaction sites, pore diffusion effects on selectivity will be small.

Relative rate constants for α -olefin readsorption decrease as follows: $k_{r,Co} > k_{r,Ru} > k_{r,Fe}$ (7). Although k_r on Fe catalysts is smaller than on Ru or Co, the other parameters in Eq. (2), such as the low diffusivity of large hydrocarbon and the high site density on unsupported Fe catalysts, ultimately increase the probability of α -olefin readsorption; therefore, pore diffusion effects also play a crucial role in Fe-catalyzed FT synthesis (Figures 3 and 4). Fe catalysts, however, give lower C_{20+} selectivity because of lower intrinsic values of k_r , even though asymptotic chain termination probabilities are lower on Fe.

Readsorption effects may explain selectivity differences between Sasol's Fe-based ARGE and Synthol Fischer-Tropsch processes. The ARGE fixed-bed process uses a precipitated high surface area Fe-based catalyst; it produces a significant amount of paraffin wax, ($C_{35+} = 25$ wt%) and about 5% C_4 hydrocarbons (16,17). If we (conservatively) assume that C_4 olefins, with high diffusivity because of their small size, are not influenced by pore diffusion and do not undergo significant readsorption, the chain growth probability for C_4 would be 0.86. If larger α -olefins did not readsorb, then α would remain constant (0.86) for the entire distribution. This constant value of α would lead to a C_{35+} selectivity of 3.2%, much smaller than the observed value (25%). Clearly, the chain growth parameter in this process can not be independent of chain size; it must increase with carbon number. At least 85% of the observed C_{35+} hydrocarbons form because α -olefins readsorb and initiate chains in the ARGE process.

Results for the Synthol entrained-bed process (16) are plotted in Figure 8. The available C_1 to C_{15} data follow the conventional Flory plot with α equal to 0.7. The Synthol process uses a fused Fe catalyst of low surface area and porosity and operates at high temperatures ($\sim 590K$). The products in the reactor are mainly gaseous, wax formation is minimal, and the pellet pore structure remains free of liquid products; therefore, diffusion-enhanced α -olefin readsorption is much less likely than in the ARGE process. Whereas the product selectivity in the ARGE process is altered by diffusion-enhanced α -olefin readsorption, that in the Synthol process is not.

When light hydrocarbons terminate predominantly as paraffins ($k_h \gg k_o$), or when α -olefins are rapidly hydrogenated in secondary reactions ($k_s > k_r$), we should obtain a light product distribution with a low and constant value of α . We describe below two such systems. A Fe-based catalyst (α - Fe_2O_3) at very high H_2/CO ratios (~ 9) gives only C_1 to C_5 paraffins with a constant chain growth

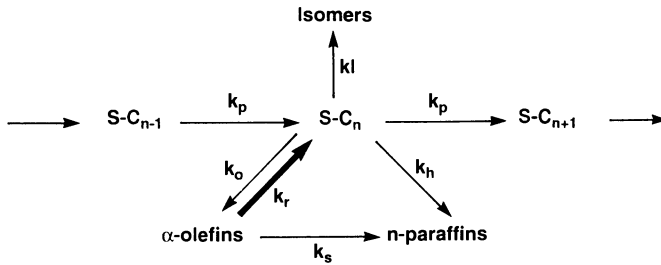


Figure 7: Simplified scheme of hydrocarbon chain growth pathways. (S -- FT chain growth site; k -- rate constants, see text).

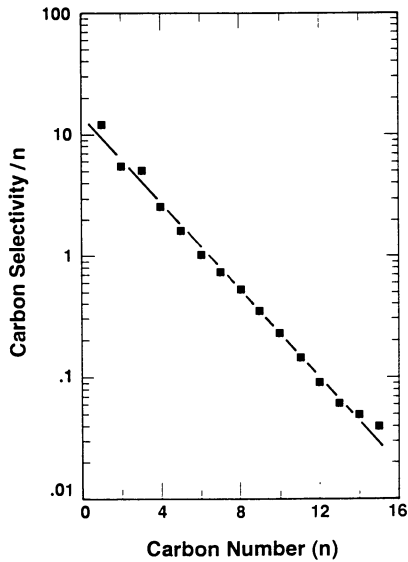


Figure 8: Flory plot of SASOL's Synthol process on Fe-based catalysts. Data from Ref. (17). (See legend for Figure 1).

probability of 0.3 (18). On Mo-based systems (19, 20), only very light paraffins were observed ($\alpha = 0.2$). No α -olefins were observed in either case; therefore no readsorption and chain initiation occur. Sometimes, α -olefin readsorption occurs without the influence of pore diffusion and a single value of α is observed. This value of α is higher than without α -olefin readsorption. Dwyer and Somorjai (21) using a 1-cm² Fe (111) single crystal surface showed that the addition of ethylene to H₂/CO feeds increased α from 0.3 with 2 Torr ethylene to 0.56 with 125 Torr ethylene. They proposed that this increase was directly related to the increased participation of ethylene in chain initiation and growth reactions. Theoretical studies of olefin readsorption without pore diffusion effects are consistent with these results and explanations (7,22).

Many studies address the effect of promoters such as K and Mn on Fe-based catalysts. Dry *et al.* (23) suggest that the alkali promoter weakens the C-O bond and enhances its rate of dissociation; it also strengthens the metal-C bond, the surface residence time of adsorbed chains, and the probability of chain growth. In the presence of Mn, termination to olefins predominates (24-26). Our results suggest that we must also consider the effect of promoters and of catalyst treatment on α -olefin readsorption. Perhaps the presence of alkali also enhances α -olefin readsorption reactions leading to heavier products whereas Mn does not.

Secondary olefin hydrogenation reactions can occur readily on unpromoted, poorly promoted, or oxidized Fe catalysts (27). Secondary hydrogenation can also be enhanced by diffusional restrictions that increase the intrapellet concentration of reactive α -olefins on Fe catalysts (27). The presence of polymeric carbon formed during initial carburization processes leads to transport restrictions that severely limit the yield of light olefins on Fe-Co-K catalysts and leads to their consumption in secondary chain growth and hydrogenation reactions (27). The olefin content decreased markedly with increasing carbon number on catalysts with excess matrix carbon. This effect was weaker on catalysts prepared by techniques that minimize excess carbon formation. Olefin contents in C₄-C₁₀ hydrocarbons became independent of molecular size when much smaller pellets were tested in a stirred tank reactor, where intrapellet transport restrictions are removed (27). Therefore, it appears that the porosity and the size of catalyst pellets are critical design parameters in the control of Fischer-Tropsch selectivity on Fe catalysts.

We suggest that diffusion-enhanced olefin readsorption, the reverse of the chain termination to olefins step, is a critical reaction pathway that controls the product distributions on Ru, Co, and Fe-based catalysts. It is responsible for the observed effects of molecular size on chain growth probability and olefin content, which arise from the higher intraparticle (pore) residence time of larger α -olefins. Molecular size effects do not arise from the higher solubility of larger molecules in liquid hydrocarbons (7). On all three metals, we observe curved Flory plots and chain growth parameters that increase with increasing carbon number; at high carbon numbers, α approaches a constant value and the product becomes essentially paraffinic. The extent to which diffusion enhances readsorption depends on catalyst structure and on readsorption, chain growth, and termination rate constants. Only when olefin readsorption does not occur or when olefin

concentration gradients are not present within catalyst particles, hydrocarbon chain growth processes strictly obey Flory kinetics.

Literature Cited

1. Friedel, R. A., Anderson, R. B., *J. Am. Chem. Soc.* **1950**, *72*, 1212, 2307.
2. Herrington, E. F. G., *Chem. Ind. (London)* **1946**, 347.
3. Madon, R. J., *J. Catal.* **1979**, *57*, 183.
4. Flory, P. J., *J. Am. Chem. Soc.* **1936**, *58*, 1877.
5. Henrici-Olivé, G., Olivé, S., *Angew. Chem. Int. Ed.* **1976**, *15*, 136.
6. Schulz, G. V., *Z. Phys. Chem.* **1935**, *B43*, 25.
7. Iglesia, E., Reyes, S. C., Madon, R. J., *J. Catal.* **1991**, *129*, 238.
8. Madon, R. J., Reyes, S. C., Iglesia, E., *J. Phys. Chem.* **1991**, *95*, 7795.
9. Madon, R. J., Buckner, E. R., Taylor, W. F., Dept. of Energy, Final Report, Contract No. E(46-1)-8008, July 1977.
10. Madon, R. J., Taylor, W. F., *J. Catal.* **1981**, *69*, 32.
11. Tauster, S. J., Fung, S. C., Garten, R. L., *J. Am. Chem. Soc.* **1978**, *100*, 170.
12. Vannice, M. A., Garten, R. L., *J. Catal.* **1979**, *56*, 236.
13. Wang, S-Y., Moon, S. H., Vannice, M. A., *J. Catal.* **1981**, *71*, 167.
14. Madon, R. J., Iglesia, E., *J. Catal.*, submitted for publication.
15. Weisz, P. B., Prater, C. D., *Adv. Catal. Relat. Subj.* **1954**, *6*, 143.
16. Dry, M. E. In *Catalysis, Science and Technology*; Anderson, J. R., Boudart, M., Eds.; Springer-Verlag: 1981. Vol. 1, Chapter 4.
17. Frohning, C. D., Kolbel, H., Ralek, M., Rottig, W., Schnir, F., Schulz, H. In *Chemierstoffe aus Kohle*; Falbe, J., Ed.; Stuttgart Thieme, 1977.
18. Reymond, J. P., Pommier, B., Meriaudeau, P., Teichner, S. J., *Bull. Soc. Chim. Fr.* **1981**, *5-6*, 173.
19. Murchison, C. B., Murdick, D. A., *Hydrocarbon Proc.* **1981**, 151.
20. Murchison, C. B., Murdick, D. A., U. S. Patent 4,151,190, (1979).
21. Dwyer, D. J., Somorjai, G. A., *J. Catal.* **1979**, *56*, 249.
22. Novak, S., Madon, R. J., Suhl, H., *J. Catal.* **1982**, *77*, 141.
23. Dry, M. E., Shingles, T., Boshoff, L. J., Oosthuizen, G. J., *J. Catal.* **1969**, *15*, 190.
24. Kolbel, H., Tillmetz, K. D., U. S. Patent 4,177,203 (1979).
25. Bussmeier, B., Frohning, C. D., Horn, G., Kluy, W., Deutsches Offen. 2,518,964 (1976); U. S. Patent 4,455,395 (1984).
26. Deckwer, W. D., Serpemen, Y., Ralek, M., Schmidt, B., *Ind. Eng. Chem. Proc. Des. Dev.* **1982**, *21*, 222.
27. Soled, S. L., Iglesia, E., Fiato, R. A., *Catal. Lett.* **1990**, *7*, 271.

RECEIVED August 4, 1992

Author Index

- Ahlafi, H., 233
Apple, Tom M., 337,372
Armor, J. N., 168
Barteau, M. A., 345
Bonafede, Salvatore J., 372
Broadbelt, Linda, 290
Brown, N. F., 345
Butler, Leslie G., 260
Chan, A. S. C., 27
Chen, Cong-Yan, 222
Chen, Tun-Li, 272
Cory, David G., 260
Davis, Burtron H., 109
Davis, Mark E., 206,222
Davis, R. J., 327
DeAngelis, Robert J., 372
Dooley, Kerry M., 260
Doyle, Michael P., 40
Dybowski, Cecil, 316
Foley, Henry C., 168,290
Forster, D., 22
Gaffney, Anne M., 316
Garroway, Allen N., 260
Ghazi, A. Mohamad, 372
Hayashi, Tamio, 75
He, Yigong, 355
Humphrey, Mark G., 127
Iglesia, Enrique, 383
Jang, Benjamin W.-L., 355
Johnson, B., 168
Jones, C. A., 316
Khouw, Charles B., 206
Kim, Man-Hoe, 222
Klabunde, Kenneth J., 88,136
Klein, Michael T., 290
Kubo, Akihiko, 75
Kye, Y. S., 337
Lamanna, W. M., 156
Laneman, S. A., 27
Le, T. S., 233
Le Vanmao, R., 233
Li, Yong-Xi, 88,136
Lin, May-Whei, 272
Liu, Shang-Bin, 272
Ma, Long-Ja, 272
Madon, Rostam J., 383
McAteer, Colin H., 127
Mielczarski, E., 327
Miller, Joel B., 260
Miller, R. E., 27
Nerad, B. A., 156
Neurock, Matthew, 290
Newmark, R. A., 156
Nocera, Daniel G., 244
Occelli, Mario L., 185
Olofson, J. M., 156
Ozawa, Fumiyuki, 75
Reed, Christopher P., 372
Reyes, Sebastian C., 383
Riley, D. P., 58
Saari, Eric A., 244
Schaefer, G., 58
Shapley, John R., 127
Shen, Yan-Fei, 185
Shin, Yeung-gyo K., 244
Siedle, A. R., 156
Sofranko, John A., 316
Suib, Steven L., 1,185
Timmons, Richard B., 355
Torgerson, Mark R., 244
Tsiao, Chihji, 316
Tway, Cathy L., 372
Waldman, T. E., 58
Wang, A. W., 168
Wang, Yi, 136
Wu, Jin-Fu, 272
Wu, S. X., 337

Affiliation Index

- 3M Corporate Research Laboratories, 156
 Academia Sinica, 272
 Air Products and Chemicals, Inc., 168
 ARCO Chemical Company, 316
 California Institute of Technology, 206
 Concordia University, 233
 Exxon Research and Engineering Company, 383
 Georgia Technical Research Institute, 185
 Hokkaido University, 75
 Kansas State University, 88,136
 Louisiana State University, 260
 Michigan State University, 244
 Monsanto Company, 22,27,58
 Naval Research Laboratory, 260
 Rensselaer Polytechnic Institute, 337,372
 Tamkang University, 272
 Trinity University, 40
 University of Connecticut, 1,185
 University of Delaware, 168,290,316,345
 University of Illinois, 127
 University of Kentucky, 109
 University of Nebraska, 372
 University of Texas at Arlington, 355
 University of Virginia, 327
 Virginia Polytechnic Institute and State University, 222,327

Subject Index

A

- Acetaldehyde decomposition, reaction pathway control, 14–15
 Acetylene, continuous catalytic conversion over metal-modified shape-selective zeolite catalyst, 355–370
 Acid-catalyzed shape selectivity in zeolites
 primary shape selectivity, 209–211
 secondary shape selectivity, 211–213
 Acid molecular sieves, reactions of *m*-diisopropylbenzene, 222–230
 Activation of C–H, C–C, and C–O bonds of oxygenates on Rh(111)
 bond-activation sequences, 350–353
 divergence of alcohol and aldehyde decarbonylation pathways, 347–351
 experimental procedure, 347
 Additives, selectivity, 7,8f
 Adsorption of benzene on NaX and NaY zeolites, homogeneous, *See* Homogeneous adsorption of benzene on NaX and NaY zeolites
 Alcohol and aldehyde decarbonylation on Rh(111), activation of C–H, C–C, and C–O bonds, 345–353
 Alkane dehydrocyclization with Pt–Sn–alumina catalysts
 aromatic formation, 120
 preparation condition effect, 119
 Alkane dehydrocyclization with Pt–Sn–alumina catalysts—*Continued*
 pressure effect, 120
 PtSn alloy formation, 117–118
 role of Sn, 117
 Sn vs. carbon deposition, 120
 Sn vs. coking, 118–119
 Sn vs. *n*-octane conversion, 120–122
 Sn vs. selectivity, 118
 temperature effect, 119
 Alkene hydroformylation, asymmetric catalysis, 24
 Alkynes, coordination, dimerization, and scission on tungsten–triiridium cluster core, 127–134
 Alloys
 applications and properties, 5
 factors affecting selectivity, 7,9
 Allylic alcohol
 ether formation, stereoselectivity, 2–3
 hydrogenation, asymmetric catalysis, 25
 oxidation, asymmetric catalysis, 24
 Amino acid esters of phenylalanine and tryptophan, selective transport, 15,16f
 Anisotropic solid-state chemical reactions, NMR imaging, 260–269
 Aromatization of *n*-hexane over Pt clusters supported on hydrotalcite, catalyst preparation effect, 327–335

Affiliation Index

- 3M Corporate Research Laboratories, 156
 Academia Sinica, 272
 Air Products and Chemicals, Inc., 168
 ARCO Chemical Company, 316
 California Institute of Technology, 206
 Concordia University, 233
 Exxon Research and Engineering Company, 383
 Georgia Technical Research Institute, 185
 Hokkaido University, 75
 Kansas State University, 88,136
 Louisiana State University, 260
 Michigan State University, 244
 Monsanto Company, 22,27,58
 Naval Research Laboratory, 260
 Rensselaer Polytechnic Institute, 337,372
 Tamkang University, 272
 Trinity University, 40
 University of Connecticut, 1,185
 University of Delaware, 168,290,316,345
 University of Illinois, 127
 University of Kentucky, 109
 University of Nebraska, 372
 University of Texas at Arlington, 355
 University of Virginia, 327
 Virginia Polytechnic Institute and State University, 222,327

Subject Index

A

- Acetaldehyde decomposition, reaction pathway control, 14–15
 Acetylene, continuous catalytic conversion over metal-modified shape-selective zeolite catalyst, 355–370
 Acid-catalyzed shape selectivity in zeolites
 primary shape selectivity, 209–211
 secondary shape selectivity, 211–213
 Acid molecular sieves, reactions of *m*-diisopropylbenzene, 222–230
 Activation of C–H, C–C, and C–O bonds of oxygenates on Rh(111)
 bond-activation sequences, 350–353
 divergence of alcohol and aldehyde decarbonylation pathways, 347–351
 experimental procedure, 347
 Additives, selectivity, 7,8f
 Adsorption of benzene on NaX and NaY zeolites, homogeneous, *See* Homogeneous adsorption of benzene on NaX and NaY zeolites
 Alcohol and aldehyde decarbonylation on Rh(111), activation of C–H, C–C, and C–O bonds, 345–353
 Alkane dehydrocyclization with Pt–Sn–alumina catalysts
 aromatic formation, 120
 preparation condition effect, 119
 Alkane dehydrocyclization with Pt–Sn–alumina catalysts—*Continued*
 pressure effect, 120
 PtSn alloy formation, 117–118
 role of Sn, 117
 Sn vs. carbon deposition, 120
 Sn vs. coking, 118–119
 Sn vs. *n*-octane conversion, 120–122
 Sn vs. selectivity, 118
 temperature effect, 119
 Alkene hydroformylation, asymmetric catalysis, 24
 Alkynes, coordination, dimerization, and scission on tungsten–triiridium cluster core, 127–134
 Alloys
 applications and properties, 5
 factors affecting selectivity, 7,9
 Allylic alcohol
 ether formation, stereoselectivity, 2–3
 hydrogenation, asymmetric catalysis, 25
 oxidation, asymmetric catalysis, 24
 Amino acid esters of phenylalanine and tryptophan, selective transport, 15,16f
 Anisotropic solid-state chemical reactions, NMR imaging, 260–269
 Aromatization of *n*-hexane over Pt clusters supported on hydrotalcite, catalyst preparation effect, 327–335

2-Arylacrylic acids, asymmetric catalytic hydrogenation, 27–38

Asphaltene and resid pyrolysis
global reaction models, 292*f*–294
mechanistic models, 307–309

Asymmetric catalysis

asymmetric Heck reactions, 26

challenges, 22

codimerization of olefins, 24

development, 22–23

epoxidation of olefins, 25

hydroformylation of alkenes, 24

hydrogenation

allylic alcohols, 25

imines, 23

ketones, 24

hydrosilation of ketones, 25

mechanism, 23

oxidation of allylic alcohols, 24

reaction rates, 23

Asymmetric catalytic hydrogenation of
2-arylacrylic acids

base promoter effect, 30,31*t*

catalyst(s), 30*t*

catalyst structure and synthesis, 31–33

commercially feasible processes, 36–38*f*

conditions, 29,30*t*

deuterium-labeling study of reaction

mechanism, 34–36*f*

experimental procedure, 37–38

mechanism for catalyst formation, 33*f*,34

optical yields vs. hydrogen pressure, 29

³¹P-NMR spectrum of catalysts, 32*f*

temperature and pressure effect, 30,31*t*

tertiary amine vs. optical yield, 29

Asymmetric Heck reactions

asymmetric catalysis, 26

catalytic, *See* Catalytic asymmetric
Heck reaction

Asymmetric hydrosilation catalysis,

reduction of cyclopentene-1,4-diones, 59

Asymmetric hydrosilation of ketones,

discrete chiral rhodium phosphine

complexes as catalysts, 58–73

Au atom–Sn atom clusters in cold solvents

cluster growth, 142–145,147

heat treatment of AuSn particles,

145–148*f*

Mössbauer spectra, 146,149*f*

rate processes for cluster growth, 145,147*f*

Au atom–Sn atom clusters in cold solvents—

Continued

solvent properties vs. crystal growth,

142,144*t*,145

viscosity vs. crystal growth, 145

X-ray diffraction pattern, 142,143*f*

X-ray photoelectron studies of

electrons, 146,150–153

Au–Sn alloy system, 140,141*t*

B

β scission, description, 309

Benzene adsorption on synthetic

faujasite-type zeolites, 272–273

Bifunctional platinum–alumina catalyst for

naphtha reforming, 109–110

Bimetallic catalysts

conventional preparation procedure, 91

poisoning studies, 92,99–104

reactivity studies, 92,99–104

solvated metal atom dispersed catalysts, 91

structural elucidation techniques, 91–98*t*

Bimetallic cluster compounds

derivation from heterogeneous catalysts,

89–91

molecular, 88–89

Bimetallic crystal surfaces, evidence for
electronic effects, 89

Bimetallic particles, functions, 88

Bond fission, description, 307,308*t*

2-Butene conversion, protonated and

modified ZSM–5 zeolites, 323,324*t*

C

n-C₈ conversion, use of protonated and
modified ZSM–5 zeolites, 323,324*t*

C–C bond formation, stereoselectivity, 2

C–C, C–H, and C–O bonds of oxygenates,
activation on Rh(111), 345–353

¹³C-NMR spectroscopy, reactions of

ethylene over Ru–Y zeolite, 337–344

η^5 -C₅H₅WIr₃(CO)₁₁ reaction with
diphenylacetylene

bond distances in products, 128,129*t*

experimental description, 127–128

molecular structure of products, 129–131*f*

- $\eta^5\text{-C}_3\text{H}_5\text{WIr}_3(\text{CO})_{11}$ reaction with diphenylacetylene—*Continued*
product analysis, 128
reaction patterns of molecular W–Ir clusters with alkynes, 132,133f
reaction with diphenylacetylene, 128
W–Ir and Mo–Ir cluster-derived catalysts, 132,134f
- $(\eta^5\text{-C}_2\text{H}_5)_2\text{ZrC}_{12}$, exchange reaction with methylaluminoxane, 157
- Calcination
RuCl₃-impregnated NaY zeolite effect, 378,380f,381
vanadium migration, 196–198,200f
- Catalysis, selectivity, 1–17
- Catalyst(s), asymmetric catalytic hydrogenation of 2-arylacrylic acids, 27–38
- Catalyst preparation effect on aromatization of *n*-hexane over Pt clusters supported on hydrotalcite
argon adsorption isotherms for catalyst supports, 329,332f
catalyst cluster size vs. selectivity, 333
catalysts used, 331t
experimental procedure, 328–329
product selectivity vs. catalyst preparation method, 333,334t
Pt incorporation onto calcined MgAlO, 329,331
selectivity of benzene formation vs. *n*-hexane using different catalysts, 331–333
selectivity parameter vs. catalyst, 333–335
support acidity effect, 335
terminal cracking index vs. catalyst, 333–335
X-ray diffraction patterns for catalyst supports, 329,330f
- Catalytic asymmetric arylation of olefins using palladium catalyst
chiral carbon center formation, 76–77
2,3-dihydrofuran, 78–80t
mechanism, 75–77
N-substituted pyrrolines, 78,80
palladium catalyst reactivity toward olefin insertion, 76,79
reaction conditions, 76,78
- Catalytic asymmetric Heck reaction
mechanism, 78–84
reaction for arylation of cyclic olefins, 75–80
- Catalytic asymmetric hydrogenation
2-arylacrylic acid, 29–38
L2-DOPA, 28–29
- Catalytic asymmetric synthesis, production of optically pure compounds, 28
- Catalytic cracking, global reaction models, 294,295f
- Catalytic cracking cycle, mechanistic formalism, 309,310f
- Catalytic cracking of gas oil feedstocks, molecular reaction model, 305–307f
- Catalytic metal carbene transformations, 41–44
- Catalytic olefin polymerization
 $(\eta^5\text{-C}_2\text{H}_5)_2\text{ZrCl}_2\text{-(MeAlO)}_x$ -toluene catalyst system, 156–158
ethylene polymerization, 158–159,161f
free energy of activation, 165–167
hexene polymerization, 159–164
substituent effects, 164–167
technological potential, 156
- Catalytic palladium membrane, hydrogenation effect, 169–183
- Catalytic test reaction for pore structure characterization, 224–230
- Ceramic films, preparation methods, 171
- Chiral alcohols, preparation using catalytic asymmetric hydrosilation, 58–59
- Chiral (camphorquinone dioximato)-cobalt(II) catalysts, structure, 41,44
- Chiral catalysis, zeolites, 218,220
- Chiral catalysts for asymmetric carbenoid transformations
applications, 41,43f
design approach, 41,45,49t
enantioselective cyclopropanation, 45,47t
intermolecular cyclopropanation of alkynes, 48,52–53
intramolecular C–H insertion, 52–55
intramolecular cyclopropanation, 45,48–51
structures, 41,44–46
- Chiral compound(s)
importance, 27
isomer vs. properties, 27
use as starting materials or templates, production of optically pure compounds, 28
- Chiral palladium catalyst, molecular model, 78,81f

Chiral rhodium(II) carboxamides catalysts for enantioselective metal carbene transformations, 40–55
 intermolecular cyclopropanation of alkynes, 48,52–53

Chiral rhodium(II) catalysts, intramolecular carbon–hydrogen insertion, 52–55

Chiral rhodium(II) 2-pyrrolidone-5-carboxylates, intramolecular cyclopropanation, 45,48–51

Chiral (semicorrinato)copper complexes, structure, 41,44

Cinchonidine, role in stereoselectivity, 4

Cl⁻ additives, selectivity, 7,8*t*

Cluster(s)
 applications and properties, 5
 factors affecting selectivity, 7,9

Cluster beam approach, description, 137

Cluster-derived butane hydrogenolysis catalysts, 127–134

Co, Fe, and Fe–Co alloy clusters in zeolites, selectivity, 5

CO hydrogenation, reaction pathway control, 15,17

Cobalt, catalysis of Fischer–Tropsch synthesis, 389–392

Codimerization of olefins, asymmetric catalysis, 24

Cold solvents, Au atom–Sn atom clusters, 142–153

Complex layered oxides, use as layered supports, 245–246

Conjugated dienol and diol formation, stereoselectivity, 3

Constraint index, definition, 323

Continuous catalytic conversion of acetylene to higher hydrocarbons over metal-modified shape-selective zeolite catalyst
 catalyst deactivation
 $C_2H_2 + H_2O$ mixture reactions, 357,359*f*
 vs. C_2H_2 conversion, 357,358*f*
 catalytic activity vs. Ni loading, 364,365*t*
 experimental procedure, 355–357
 fixed-bed continuous flow microreactor, 356
 hydrocarbon product distribution
 vs. CH_3CHO , 364,367,368*t*
 vs. Ni loading, 364,365*t*
 vs. reaction temperature, 364,366*f*

Continuous catalytic conversion of acetylene to higher hydrocarbons over metal-modified shape-selective zeolite catalyst—*Continued*
 hydrocarbon product distribution—
Continued
 vs. time for C_2H_2 conversion, 357,358*f*
 vs. time for $C_2H_2 + H_2O$ mixture conversion, 357,359*f*
 long-term normalized hydrocarbon product distribution for $C_2H_2 + H_2O$ mixture conversion, 357,360–362*f*
 mechanism, 367,369–370
 normalized hydrocarbon product distribution
 vs. $[H_2O] : [C_2H_2]$ ratio, 360,363*t*,364
 vs. space velocity, 360,362*f*
 product yields under conditions of less than 100% C_2H_2 conversion, 364,366*t*
 requirements, 367
 role of added Ni, 369–370

Continuous conversion of acetylene to higher hydrocarbons, catalytic investigations, 355

Copper catalysts
 limitations as catalysts, 41
 role in reaction pathway control, 14

Coreactant-induced modification, 211–213

1,5-Cyclooctadiene isomerization, reaction pathway control, 15

4-Cyclopentene-1,3-dione
 hydrosilation, mechanism, 69,71*f*
 hydrosilation using rhodium phosphine complexes as catalysts, 63–66*f*

D

Damköhler number, definition, 392

Dehydrocyclization of *n*-hexane
 function of catalyst, 327
 zeolite cation effect, 328
 zeolite channel effect, 328

Diastereomeric crystallization, production of optically pure compounds, 27

Diazo compounds, transition metal compounds as catalysts of carbenoid reactions, 40–41

Diffuser, function, 169

Diffusion-enhanced olefin readsorption model, 384–385

2,3-Dihydrofuran

- catalytic asymmetric arylation, 78–80*t*
- mechanism for arylation, 78,81–84*t*
- m*-Diisopropylbenzene reactions on acid
 - molecular sieves for pore structure determination
- adsorption capacities, 225,226*t*
- adsorption measurement procedure, 225
- ammonia temperature-programmed
 - desorption measurement procedure, 225
- catalyst preparation, 224
- catalytic experimental procedure, 225
- catalytic pore size vs. product
 - distributions, 228,229*t*
- comparison of indexes, 230*t*
- experimental conditions, 228
- isomerization effect on product
 - distribution, 228,229*t*
- principle, 228
- temperature-programmed desorption
 - results, 226,227*f*

2,6-Dimethylphenol oxidation, 14,16*f*

- Dimolybdenum cores, multiply bonded,
 - redox intercalation into layered vanadyl phosphate, 249–251*f*

Dirhodium(II) catalysts, advantages for use in carbenoid reactions, 41**E**

- Electrochemical reactions, shape-selective
 - catalysis with zeolites and molecular sieves, 218,219*f*
- Enantioselective metal carbene
 - transformations, catalysis using chiral rhodium(II) carboxamides, 40–55
- Epoxidation of olefins, asymmetric
 - catalysis, 25
- Ethane reaction, selectivities and
 - conversions, 12–14
- Ethanol decomposition, reaction pathway
 - control, 14–15
- Ethanol reaction, selectivities and
 - conversions, 12,13*t*
- Ethyl *tert*-butyl ether, limitations as
 - octane booster, 233–234
- Ethyl *tert*-butyl ether synthesis over
 - triflic acid modified Y zeolite
 - catalyst characterization procedure, 234
 - catalyst preparation, 234

- triflic acid modified Y zeolite—*Continued*
- dehydration of ethanol to diethyl ether,
 - 240,242*f*
- dilution of ethanol feed with water vs.
 - yield, 240,242*t*
- pore-size distribution of catalyst, 236,237*f*
- reagent contact time determination, 235
- textural properties of catalysts, 236,237*t*
- yield calculation procedure, 235
- yield vs. contact time, 240,241*f*
- Ethylene polymerization, procedure using
 - Kaminsky catalyst, 158–159,161*f*
- Ethylene reactions over Ru–Y zeolite
 - ethylene hydrogenation, rate, 340*t*
 - experimental procedure, 338
 - previous studies, 337
 - room-temperature spectra
 - Ru–Ca–Y zeolite vs. time after sample
 - preparation, 340,341*f*
 - Ru–H–Y zeolite, 340,342*f*
 - Ru–Na–Y zeolite vs. time after sample
 - preparation, 338,339*f*
 - spectra of heated sample on Ru–Ca–Y
 - zeolite with and without proton
 - decoupling, 340,343*f*,344

F

- Fischer–Tropsch synthesis
 - carbon number distributions vs.
 - selectivity, 383
 - hydrocarbon, factors affecting product
 - distribution, 372
 - non-Flory product distributions catalyzed
 - by Ru, Co, and Fe, 383–396
 - Flory equation, product distributions in
 - Fischer–Tropsch synthesis, 384
 - Fluid cracking catalysts, SEM–EDX studies
 - of vanadium migration between model
 - compounds, 185–200
 - Fraissard’s equation, form, 318

G

- Global reaction models
 - asphaltene and resid pyrolysis, 292*f*–294
 - catalytic cracking, 294,295*f*

Global reaction models—*Continued*
 description, 291
 historical significance, 291–292
 hydrotreating, 294f
 Gold–tin bimetallic particles, structure
 and catalysis, 136–153
 Group 8 metal surfaces, adsorption and
 subsequent reaction of ethylene, 337–344

H

Heat treatment, AuSn particles, 145–148f
 Heck reaction, *See* Catalytic asymmetric
 Heck reaction
 Heterogeneous catalysts derived from
 bimetallic cluster compounds, 89–91
n-Hexane, catalyst preparation effect on
 aromatization over Pt clusters supported
 on hydrotalcite, 327–335
 Hexene hydrogenation, shape selectivity, 10
 Hexene polymerization using Kaminsky
 catalyst
 kinetics, 160,162–164,166
 mechanistic model, 162–164
 procedure, 159–160
 substituent effects, 164–167
 unsaturated end groups, origin, 160,161f
 Homogeneous adsorption of benzene on
 NaX and NaY zeolites
¹³C-NMR line width vs. benzene coverage,
 283,284f
 experimental materials, 273
¹H-NMR line width vs. benzene coverage,
 283,284f
 location of maximum ¹²⁹Xe-NMR line
 width vs. xenon loading, 278,280f–283
 Na⁺ distribution, 278,281f
 NMR experimental procedure, 274
 NMR line widths at saturation benzene
 coverage, 283,284f,285
 sample preparation, 273
¹²⁹Xe chemical shift
 vs. benzene coverage, 274,277f,278
 vs. density of adsorbed xenon, 274,276f
¹²⁹Xe-NMR line width vs. benzene
 coverage, 278,279f,281
 xenon adsorption experimental
 procedure, 273
 xenon adsorption isotherms, 274,275f

Hydrocarbon conversions, activity of PtSn
 catalysts, 118
 Hydrocarbon hydrogenation, molecular
 reaction model, 296,298–305
 Hydrocarbon pyrolysis, molecular reaction
 model, 295–297t,304f
 Hydroformylation of alkenes, asymmetric
 catalysis, 24
 Hydrogen abstraction, description, 307–309
 Hydrogenation, asymmetric catalysis
 allylic alcohols, 25
 imines, 23
 ketones, 24
 Hydrogenation effect on catalytic palladium
 membrane
 activity suppression at high temperatures
 for pure palladium membranes, 177,180f
 background, 169–171
 ceramic coating, 171
 experimental procedures, 171,173
 hydrogen permeability for pure palladium
 membranes, 174,176t–178f
 hydrogen permeability for Ti–Pd
 hybrid membranes, 177,179,180f
 membrane preparation, 171
 Pt–TiO₂/Pd membranes, 174
 thin films of TiO₂ on
 palladium foils, 173–175f
 membrane reactor, 171,172f
 stability of TiO₂/Pd membranes as
 catalysts, 179,181f
 surface restructuring vs. strength of
 hydrocarbon adsorption, 182–183
 temperature vs. activity, 182
 time and temperature dependence for pure
 palladium membranes, 174–176f
 time on stream vs. activity, 182
 Hydrosilation of ketones, asymmetric
 catalysis, 25
 Hydrotalcite, catalyst preparation effect
 on aromatization of *n*-hexane, 327–335
 Hydrotreating, global reaction models, 294f

I

S-Ibuprofen process, reaction, 36–38f
 Imine hydrogenation, asymmetric
 catalysis, 23
 Intermolecular cyclopropanation of alkynes,
 chiral rhodium(II) carboxamides, 48,52–53

Intracrystalline environments of host structures, framework for assembling photochemical subunits for catalysis, 244
Intramolecular carbon–hydrogen insertion, chiral rhodium(II) catalysts, 52–55
Intramolecular cyclopropanation, chiral rhodium(II) 2-pyrrolidone-5-carboxylates, 45,48–51
Iron, catalysis of Fischer–Tropsch synthesis, 386,388*f*,389*t*
Iron clusters, role in Fischer–Tropsch catalysis, 6

K

Kaminsky catalyst
ethylene polymerization, 158–159,161*f*
hexene polymerization, 159–164
Ketone(s), discrete chiral rhodium phosphine complexes as catalysts for asymmetric hydrosilation, 58–73
Ketone hydrogenation, asymmetric catalysis, 24
Ketone hydrosilation, asymmetric catalysis, 25
Kinetic resolution, production of optically pure compounds, 28

L

Layered double hydroxide, role in stereoselectivity, 4–5
Layered metal phosphate hosts
binuclear metal cores, 246
coordination to multiply bonded bimetallic cores, design, 254–256
exchange properties, 248*f*
multiply bonded metal–metal guest species, strategies for incorporation, 248*f*
quadruply bonded metal–metal complexes, incorporation, 249–256
structures, 246,247*f*
Li₂CO₃, selectivity, 7
Lipase enzymes, stereoselectivity, 4

M

Mechanistic models
applications, 311–312
asphaltene and resid pyrolysis, 307–309

Mechanistic models—*Continued*
catalytic cracking cycle, 309,310*f*
description, 290,305
future, 310–311
kinetics, 305,307
reaction pathway analysis, 290,309–310
types, 309
Membrane separation combined with catalytic reaction, advantages, 169
Membrane surfaces, restructuring and effect on catalytic and transport properties, 170–171
Membrane transport, importance, 169
Metal carbene transformations, enantioselective, catalysis using chiral rhodium(II) carboxamides, 40–55
Metal-catalyzed shape selectivity in zeolites
applications, 213–214
selectivity in oxidations, 213–215
Metal clusters, preparation methods, 137
Metal contaminants, fluid cracking catalyst physicochemical property effect, 185
Metallosilicates, description, 214
Metal-modified shape-selective zeolite catalysts, continuous catalytic conversion of acetylene to higher hydrocarbons, 355–370
Methane reaction, selectivities, 12,14
Methanol conversion, use of protonated and modified ZSM–5 zeolites, 323,325*t*
Methyl *tert*-butyl ether
advantages as octane booster, 233
synthesis over acidic ion-exchange resin, 233
synthesis over trific acid modified Y zeolite
apparent activation energy, 236,238*f*
catalyst characterization procedure, 234
catalyst preparation, 234
pore-size distribution of catalyst, 236,237*f*
reagent contact time determination, 235
textural properties of catalysts, 236,237*t*
yield calculation procedure, 235
yield vs. contact time, 236,239*f*,240
Methyl pyruvate hydrogenation, stereoselectivity, 4
Methylaluminoxane, 156–157
2-Methylnaphthalene disproportionation, shape selectivity, 9–11*f*
Mn additives, selectivity, 7,8*t*

- Modified methanol synthesis catalysts,
production of higher oxygenates, 346–347
- Modified ZSM-5 zeolites
2-butene conversion, 323,324*t*
n-C₈ conversion, 323,324*t*
catalytic activity, 323–325*t*
channel diameter estimation, 320*t*,321
coke contents, 317*t*
coke distributions, 321–323
coking procedure, 317
Fraissard parameters, 318,320*t*
internal Brønsted site location, 321
methanol conversion, 323,325*t*
preparation procedure, 316–317
relative internal volume accessible to Xe
gas, 320*t*,321
Xe adsorption isotherms, 318,319*f*
¹²⁹Xe chemical shift vs. Xe uptake,
318,322*f*
¹²⁹Xe-NMR results, 318,320
¹²⁹Xe-NMR spectrometric procedure,
317–319*f*
- Molecular bimetallic cluster compounds,
examples, 88–89
- Molecular reaction models
catalyst cracking, 305–307*f*
database requirement, 296
description and advantages, 295–296
heavy hydrocarbon pyrolysis systems,
pathways, 296,304*f*
hydrocarbon hydrogenation, kinetics and
pathways, 296,298–305
hydrocarbon pyrolysis, kinetics, 296,297*t*
- Molecular sieves, pore structure
characterization
catalytic test reaction, 224–230
methods, 222,224
- Monsanto L-DOPA process, 28*f*,29
- Multielectron photoactive center, use in
photocatalytic cycle, 245,246*f*
- Multiply bonded dimolybdenum complexes
featuring Lewis bases as ligands, 251–254
- Multiply bonded dimolybdenum cores, redox
intercalation into layered vanadyl
phosphate, 249–251*f*
- N
- N-substituted pyrrolines, catalytic
asymmetric arylation, 78,80
- Nanoscale metal particles, 136
- Naphtha reforming using bifunctional
platinum–alumina catalyst, 109–110
- Naproxen process, reaction, 36,37*f*
- NaX and NaY zeolites, homogeneous
adsorption of benzene, 272–285
- NaY zeolite, RuCl₃ impregnated, *See*
RuCl₃-impregnated NaY zeolites
- NMR imaging, applications in materials
chemistry and catalysts, 260
- NMR imaging of anisotropic solid-state
chemical reactions
extent of conversion, 268
instrumentation, 262–263
one-dimensional imaging experimental
procedure, 263,265*f*
one-dimensional imaging of powder,
263–266*f*
samples, 263
total conversion vs. exposure time, 268,269*f*
two-dimensional imaging experimental
procedure, 263
two-dimensional imaging of crystal,
264,266–268
- Non-Flory product distributions in
Fischer–Tropsch synthesis catalyzed by
ruthenium, cobalt, and iron
cobalt hydrocarbon distribution,
389,390*f*,392
cobalt α -olefin : *n*-paraffin ratio,
389,391*f*,392
diffusion-enhanced olefin readsorption
model, 384–385,395–396
diffusivity vs. carbon number, 392
experimental procedure, 384–386
hydrocarbon chain growth pathway,
393,394*f*
iron carbon number distribution, 386,388*f*
iron α -olefin : *n*-paraffin ratio,
386,388*f*,389
iron selectivity, 386,389*t*
porosity and size of catalyst pellets vs.
selectivity, 395
readsorption vs. selectivity, 393
ruthenium hydrocarbon distribution
vs. support, 386,387*f*
ruthenium α -olefin : *n*-paraffin ratio vs.
carbon number, 386,387*f*
ruthenium yields and selectivity vs.
supports, 386,389*t*

- Non-Flory product distributions in
Fischer–Tropsch synthesis catalyzed by
ruthenium, cobalt, and iron—*Continued*
Synthol entrained-bed process results,
393,394*f*
- O**
- Olefin(s), catalytic asymmetric arylation
using palladium catalyst, 75–84
Olefin codimerization, asymmetric catalysis, 24
Olefin epoxidation, asymmetric
catalysis, 25
Olefin polymerization, catalytic, *See*
Catalytic olefin polymerization
Optically pure compounds, production
methods, 27–28
Oxidation of allylic alcohols, asymmetric
catalysis, 24
Oxygenates
activation of C–H, C–C, and C–O bonds
on Rh(111), 347–353
applications, 345–346
production strategies using catalysts,
346–347
surface science studies, 347
- P**
- Palladium-catalyzed arylation and
alkenylation of olefins, *See* Catalytic
asymmetric Heck reaction
Palladium membrane
activity suppression at high temperatures,
177,180*f*
hydrogen permeability, 174,176*t*–178*f*
time and temperature dependence of
ethylene hydrogenation, 174–176*f*
Palladium membrane, catalytic, 169–183
Palladium membrane technology, 169–170
Pathway-level models for reaction pathway
analysis
description, 290–291
global reaction models, 291–295
mechanistic models, 305,307–310
molecular reaction models, 295–307
Pd, role in reactions on metal oxide
supports, 6–7
Pd²⁺, role in electron transport chain
conversions, 6
Pharmaceutical products, preparation using
asymmetric catalytic hydrogenation of
2-arylacrylic acids, 27–38
Photocatalytic cycle, schematic
representation, 245,246*f*
Photochemical reactions, shape-selective
catalysis with zeolites and molecular
sieves, 216–218
Photosynthesis, artificial system design,
244–245
Platinum–tin bimetallic particles, structure
and catalysis, 136–153
Poison(s), definition, 5
Poisoning studies, bimetallic catalysts,
92,99–104
Practice-oriented reaction models,
reaction pathway analysis, 290
Preferential crystallization, production
of optically pure compounds, 27
Primary shape selectivity, 209–211
Propylene oxide polymerization,
stereoselectivity, 4–5
Protonated ZSM–5 zeolites
2-butene conversion, 323,324*t*
n-C₈ conversion, 323,324*t*
catalytic activity, 323–325*t*
channel diameter estimation, 320*t*,321
coke contents, 317*t*
coke distributions, 321–323
coking procedure, 317
Fraissard parameters, 318,320*t*
internal Brønsted site location, 321
methanol conversion, 323,325*t*
preparation procedure, 316–317
relative internal volume accessible to Xe
gas, 320*t*,321
Xe adsorption isotherms, 318,319*f*
¹²⁹Xe chemical shift vs. Xe uptake,
318,322*f*
¹²⁹Xe-NMR results, 318,320
¹²⁹Xe-NMR spectrometric procedure,
317–319*f*
Pt clusters, catalyst preparation effect on
aromatization of *n*-hexane,
327–335
Pt–Re–alumina catalyst, use for naphtha
re-forming, 110
Pt–Sn–alumina catalysts
alkane dehydrocyclization, 117–122
catalytic properties, 138

Pt–Sn–alumina catalysts—*Continued*
 characterization methods
 temperature-programmed reduction,
 110–111
 tin Mössbauer data, 111–113
 transmission electron microscopy,
 113–115f
 X-ray absorption fine structure, 113
 X-ray diffraction, 113
 X-ray photoelectron spectroscopy, 111
 formation, proposed sequence, 138,139f
 naphtha re-forming, 110
 phase diagram, 110–112f
 preparation methods, 138,139f
 full-solvated metal atom dispersed,
 137–138
 half-solvated metal atom dispersed, 137
 properties, explanation for superiority, 110
 sites, 119–120
 surface structure, 114–117
 Pt–TiO₂/Pd membranes, preparation, 174

Q

Quadruply bonded metal–metal complex
 incorporation into layered metal
 phosphates
 design of layered phosphates for
 coordination to multiply bonded
 bimetallic cores, 254–256
 intercalation of multiply bonded
 dimolybdenum complexes featuring
 Lewis bases as ligands, 251–254
 redox intercalation of multiply bonded
 dimolybdenum core into layered
 vanadyl phosphate, 249–251f

R

Reactant shape selectivity, description,
 209–211
 Reaction pathway analysis, 290,291f
 Reaction pathway control
 acetaldehyde decomposition, 14–15
 amino acid ester transport, 15,16f
 CO hydrogenation, 15,17
 1,5-cyclooctadiene isomerization, 15
 description, 10
 ethanol decomposition, 14–15

Reaction pathway control—*Continued*
 examples, 10,12
 homogeneous reactions, 10
 oxidation reactions, 12–14
 Reactivity studies, bimetallic catalysts,
 92,99–104
 Reagent contact time, definition, 235
 Reduction, RuCl₃-impregnated NaY zeolite
 effect, 378,379f
 Rh(111), activation of C–H, C–C, and C–O
 bonds of oxygenates, 345–353
 Rhodium(II) carboxamides, chiral, *See*
 Chiral rhodium(II) carboxamides
 Rhodium catalysts
 structure, 41–42
 use in carbenoid reactions, 41
 Rhodium phosphine complexes as catalysts
 for asymmetric hydrosilation of ketones
 catalyst preparation procedure, 60–61
 cyclopentene-1,4-dione hydrosilation,
 mechanism, 69,71f
 development of rhodium(I) catalysts, 71–72
 experimental description, 59–60
 hydrosilation mechanisms, 69,71f–73f
 hydrosilation of 4-cyclopentene-1,3-dione,
 63–66f
 hydrosilation procedure, 61
 kinetic study procedure, 61
 optical yield determination procedure, 63
 rhodium μ_3 -enolate trimer preparation
 and isolation procedures, 62–63
 rhodium μ_2 -fluoro trimer
 preparation and isolation, 61–62
 structural determination, 62
 structures of ligands, 59,60f
 tetraphosphine Rh(I) catalyst
 development, 64,67–70
 RuCl₃-impregnated NaY zeolites
 advantages, 372–373
²⁷Al magic angle spinning spectra of
 original RuY sample, 374,376,377f
 back ion exchange of ruthenium,
 376–379f
 calcination effect, 378,380f,381
 chemical analysis of RuY samples, 373t
 crystallinity of RuY samples, 374t–377f
 diffuse reflectance Fourier-transform IR
 spectroscopy, 376,378t
 experimental procedure, 373
 N₂ adsorption data, 374t

- RuCl₃-impregnated NaY zeolites—*Continued*
N₂ isotherms, 376,378,379f
pH vs. ²⁹Si magic angle spinning spectra, 374,375f
reduction effect, 378,379f
²⁹Si magic angle spinning spectrum of original RuY sample, 374,375f
- Ruthenium
catalysis of Fischer–Tropsch synthesis, 386,387f,389t
use as catalyst, 372
- RuY zeolite, adsorption and subsequent reaction of ethylene, 337–344
- S
- Scanning electron microscopy–energy-dispersive X-ray (SEM–EDX) analyses, vanadium migration between model components of fluid cracking catalysts, 185–200
- Secondary shape selectivity, 211–213
- Selectivity in catalysis
areas, 1
clusters, alloys, and poisoning, 5–9
control methods, 1
enhancement techniques, 1–2
reaction pathway control, 10,12–17
shape selectivity, 9–11f
stereoselectivity, 2–5
- Semiconductor thin films, preparation methods, 171
- Shape-selective catalysis with zeolites and molecular sieves
acid-catalyzed shape selectivity, 209–213
chiral catalysis, 218,220
electrochemical reactions, 218,219f
metal-catalyzed shape selectivity, 213–215
photochemical reactions, 216–218
trends in shape selectivity, 215–216
- Shape selectivity
classifications, 9
clay catalysts, 10
hexene hydrogenation, 10
2-methylnaphthalene disproportionation, 9–11f
secondary, 211–213
styrene hydrogenation, 10
trifunctional catalyst system, 10,11f
xylene formation, 9
- Solid-state chemical reactions, anisotropic, NMR imaging, 260–269
- Solid-state NMR imaging areas, 260–261
multiple-pulse techniques, 261t
studies of chemical reactions and diffusional processes, 261,262t
- Solvated metal atom dispersed bimetallic catalysts, 91
- Solvated metal atom dispersed processes, description, 137–139f
- Steaming, mechanism for vanadium migration, 198–200f
- Stereoselective synthesis of organic molecules, importance, 22
- Stereoselectivity
allylic alcohol and ether formation, 2–3
challenge in catalysis, 22–26
cinchonidine, 4
conjugated dienol and diol formation, 3
layered double hydroxide, 4–5
lipase enzymes, 4
methyl pyruvate hydrogenation, 4
propylene oxide polymerization, 4–5
TiCl₄ isomerization of dioxolanes, 3
- Structural elucidation techniques, bimetallic catalysts, 91–98t
- Styrene hydrogenation, shape selectivity, 10
- Supported group 8 metals, production of higher oxygenates, 346–347
- T
- Temperature-programmed reduction, characterization of Pt–Sn–alumina catalysts, 110–111
- Tetraphosphine rhodium(I) catalysts
asymmetric hydrosilation reaction, characteristics, 72
development, 64,67–70
hydrosilation, mechanism, 72,73f
- TiCl₄ isomerization of dioxolanes, stereoselectivity, 3
- Tin Mössbauer data, characterization of Pt–Sn–alumina catalysts, 111–113
- TiO_x thin films on palladium foils, preparation, 173–175f
- Titania–palladium hybrid membranes
hydrogen permeability, 177,179,180f
stability as catalysts, 179,181f

Transition metal compounds, use as catalysts, 40
 Transition-state shape selectivity, 209–211
 Transmission electron microscopy, characterization of Pt–Sn–alumina catalysts, 113–115*f*
 Trends in shape selectivity of zeolites, examples, 215–216
 Triad systems, photocatalysis, 245
 Triflic acid modified Y zeolite, synthesis of methyl *tert*-butyl ether and ethyl *tert*-butyl ether, 233–242
 Tungsten–triridium cluster core, alkyne coordination, dimerization, and scission, 127–134

V

Vanadium, role as poison in zeolites, 5–6
 Vanadium in fluid cracking catalysts, detrimental effect, 185–186
 Vanadium migration between model components of fluid cracking catalysts
 calcination mechanism, 196–198,200*f*
 EDX analyses, 187,188–189*t*
 migration mechanisms, 186
 nomenclature of samples, 187
 sample preparation, 186–187
 SEM–EDX measurement procedure, 187
 steaming mechanism, 198–200*f*
 vanadium porphyrin
 on AAA-alumina, 188,190,192–194
 on EuY, 187–188,190–192
 vanadyl naphthenate
 on AAA-alumina, 193,195*f*–197*f*
 on EuY, 187

X

X-ray absorption fine structure, characterization of Pt–Sn–alumina catalysts, 113

X-ray diffraction, characterization of Pt–Sn–alumina catalysts, 113
 X-ray photoelectron spectroscopy, characterization of Pt–Sn–alumina catalysts, 111
 Xylenes, formation, 9

Y

Y zeolite, triflic acid modified, synthesis of methyl *tert*-butyl ether and ethyl *tert*-butyl ether, 233–242

Z

Zeolite(s)
 acid-catalyzed shape selectivity, 209–213
 building blocks, 206,207*f*
 chiral catalysis, 218,220
 description, 206
 electrochemical reactions, 218,219*f*
n-hexane dehydrocyclization effect, 327–328
 homogeneous adsorption of benzene, 272–285
 metal-catalyzed shape selectivity, 213–215
 photochemical reactions, 216–218
 pore sizes, 206,208*f*,209
 shape-selective catalysts, 222
 shape selectivity, trends, 215–216
 Zeolite catalysts, metal-modified shape-selective, 355–370
 Zeolitelike phosphate-based molecular sieves, shape-selective catalysts, 222
 ZSM–5 zeolites
 modified, *See* Modified ZSM–5 zeolites
 protonated, *See* Protonated ZSM–5 zeolites